

**UNIVERSITA' DELLA CALABRIA**

**Dipartimento di Ingegneria Meccanica, Energetica e Gestionale**

**Dottorato di Ricerca in  
Ingegneria Civile e Industriale**

**CICLO XXIX**

**Dynamic thermal characteristics and energy behaviour of building walls  
containing sensible storage materials and phase change materials (PCM).**

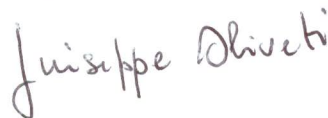
**New analytical and numerical models and experimental validation**

**Settore Scientifico Disciplinare ING-IND/11**

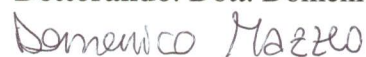
**Coordinatore:** Ch.mo Prof. Franco Furgiuele



**Supervisore:** Ch.mo Prof. Giuseppe Oliveti



**Dottorando:** Dott. Domenico Mazzeo



*Al Prof. Olivetti*

*A Nicoletta*

*Alla mia famiglia*

*Grazie ai quali sono la persona che sono  
e ai quali posso dire solo un sincero grazie*

---

# Index

## **Introduction**..... 1

## **Chapter 1.** A new parameter for the dynamic analysis of building walls using the harmonic method

Abstract.....	15
1. Introduction .....	17
2. Methodology.....	19
3. Analysis of the dynamic response of a wall to single loads .....	22
4. Dynamic analysis of a building component under the contemporaneous action of the three loads.....	29
5. Behavior of some characteristic walls .....	35
6. Comparison and validation.....	42
6.1. Analysis of the dynamic response of a hollow-wall to single loadings .....	42
6.2. Analysis of the dynamic response of a hollow-wall under the contemporaneous action of the three loads .....	46
7. Conclusions .....	47
References .....	48
Nomenclature.....	50

## **Chapter 2.** Influence of internal and external boundary conditions on the decrement factor and time lag heat flux of building walls in steady periodic regime

Abstract.....	53
1. Introduction .....	55
2. Methodology.....	60
2.1. Mathematical formulation of the thermal transfer in the wall with internal and external loadings.....	60
2.2. Dynamic characterization of the wall with sinusoidal loadings.....	67
2.3. Dynamic characterization of the wall with non-sinusoidal loadings .....	69
3. Application of the calculation procedures .....	72
3.1. Considered walls and boundary conditions .....	72
3.2. Periodic sinusoidal condition, results and discussion .....	74
3.3. Periodic non-sinusoidal condition, results and discussion.....	79

3.3.1. Decrement factor and time lag of the maximum heat flux in summer .....	85
3.3.2. Decrement factor and time lag of the minimum peak heat flux in winter .....	88
3.3.3. Decrement factor in terms of energy in the summer and winter period .....	90
3.3.4. Determination of the number of harmonics required by means of the criterion.....	91
4. Conclusions .....	93
References .....	96
Nomenclature.....	101

**Chapter 3.** Mapping of the seasonal dynamic properties of building walls in actual periodic conditions and effects produced by solar radiation incident on the outer and inner surfaces of the wall

Abstract.....	104
1. Introduction .....	106
2. Methodology.....	109
3. Dynamic characterisation of the wall in non-sinusoidal conditions.....	112
4. Walls considered and boundary conditions .....	113
5. Results and discussion .....	116
5.1. Continuous regime and absence of internal radiant loads.....	117
5.2. Continuous regime and presence of radiant internal loads .....	120
5.3. Attenuated regime in the absence of internal radiant loads .....	122
5.4. Attenuated regime in the presence of internal radiant loads .....	124
5.5. Maps for the comparison of the summer and winter dynamic properties.....	126
6. Conclusions .....	133
References .....	134
Nomenclature.....	136

**Chapter 4.** Analytical model for solidification and melting in a finite PCM in steady periodic regime

Abstract.....	139
1. Introduction .....	141
2. Methodology.....	144
2.1. Formulation of physical model .....	144
2.2. Steady thermal field .....	151
2.3. Steady periodic thermal field.....	153
3. Application of the model .....	162

3.1. General analysis of the basic cases considered.....	162
3.2. An example of resolution of a multi-harmonic thermal field .....	172
4. Comparison between analytical and numerical solution .....	177
5. Conclusions .....	179
References .....	180
Nomenclature.....	181

**Chapter 5. Parametric study and approximation of the exact analytical solution of the Stefan Problem in a finite PCM in a steady periodic regime**

Abstract.....	184
1. Introduction .....	186
2. The exact analytical solution of the Stefan problem in steady periodic regime.....	187
3. Parametric study of the exact analytical solution .....	191
4. Frequency response of the Stefan Problem .....	199
5. An approximate solution of the Stefan problem in steady periodic regime .....	205
5.1. Mathematical formulation.....	205
6. Conclusions .....	210
Appendix A .....	211
Appendix B.....	212
References .....	212
Nomenclature.....	216

**Chapter 6. Thermal field and heat storage in PCM walls with multiple bi-phase interfaces under actual periodic boundary conditions**

Abstract.....	219
1. Introduction .....	222
2. Methodology.....	226
2.1. Calculation model .....	226
2.2. Validation of the numerical code.....	233
3. Results and discussion .....	236
3.1. PCM considered and boundary conditions .....	236
3.2. Configuration of phases in the layer and thermal fields .....	238
3.2.1. Absence of phase change .....	239
3.2.2. Presence of a bi-phase interface .....	240
3.2.3. Presence of two bi-phase interfaces .....	244

3.2.4. Presence of three bi-phase interfaces .....	251
3.2.5. Phases configurations in the different PCM for the two considered locations .....	254
4. Conclusions .....	262
Appendix A .....	265
References .....	268
Nomenclature.....	274

**Chapter 7.** Definition of a set of parameters for the energy and dynamic thermal identification of PCM layers in the presence of one or more liquid-solid interfaces

Abstract.....	276
1. Introduction .....	279
1.1. Research background.....	279
1.1.1. Literature investigation on the dynamic characterization .....	280
1.1.2. Literature investigation on the energy performance .....	282
1.2. Objectives of this work .....	284
2. Methodology.....	286
2.1. Calculation model .....	286
2.2. Phase configurations in the layer and surface temperatures and heat fluxes .....	289
2.3. Fluctuating transferred energy and stored energy .....	298
2.4. Definition of the dynamic parameters.....	298
3. Case study description .....	302
4. Results and discussion .....	305
4.1. Configuration of the phases in the different typologies of PCM layers.....	306
4.2. Evaluation of the transferred and stored energy .....	307
4.3. Evaluation of dynamic parameters.....	314
4.3.1. Monthly values.....	314
4.3.2. Influence of the latent storage efficiency on the dynamic characteristics .....	320
4.3.3. Correlations between dynamic parameters.....	326
4.3.4. Parameters required for the dynamic characterization .....	327
5. Conclusions .....	328
References .....	331
Nomenclature.....	338

**Chapter 8.** Experimental verification of the analytical solution of the heat transfer in a PCM layer in a steady periodic regime

Abstract.....	341
1. Introduction .....	344
2. Method and materials .....	348
2.1. Physical model.....	348
2.1.1. Description.....	348
2.1.2. Constitutive equations of the analytical model .....	348
2.2. Equipment for testing steady and dynamic response of a PCM layer.....	355
2.2.1. Test box.....	355
2.2.2. Description of the PCM sample holder Pure Temp 23.....	356
2.2.3. Setting of the experiments.....	361
2.3. Determination of the solid phase and liquid phase thermophysical properties in the test box .....	364
2.3.1. Thermal conductivity and specific heat.....	364
2.3.2. Heat latent of fusion and phase change temperature .....	366
3. Experimental test results for the determination of the thermophysical properties .....	367
3.1. Thermal conductivity and specific heat .....	367
3.2. Heat latent of fusion and phase change temperature.....	369
3.3. Thermophysical properties of PureTemp23 employed for the verification of the analytical model .....	371
4. Verification of the analytical model .....	372
5. Conclusions .....	379
References .....	381
Nomenclature.....	384
 <b>Conclusions .....</b>	 <b>387</b>

## Introduction

The research activities carried out during the PhD related to the study of "dynamic and energetic behavior of the traditional building walls and of the phase change innovative walls".

For the containment of energy needs of buildings, in civil, residential and tertiary sectors, as indicated by recent European regulations, it is necessary to improve the thermal performance of the building envelope. In this context, it is considered crucial to design and efficiently requalify the building envelope in relation to external and internal thermal loadings (convective and radiative heat transfer) and/or employ highly efficient technologies to develop and make the building a "Nearly Zero Energy Building" (NZEB), or more generally a sustainable building in energy, environmental or economic terms. The thermal exchanges through the envelope significantly contribute to the determination of the energy requirements provided by the plant. Their reduction requires a correct evaluation of the dynamic characteristics of the opaque envelope components considering actual boundary conditions.

**In this context, the research activities focused on the study of the dynamic thermal and energy behavior of materials employing the *sensible heat storage capacity* or employing the *latent heat storage capacity*.**

The first is mainly linked to the mass involved, while the latent is able to store significant amounts of heat with small masses. For this reason, Phase Change Materials (PCMs) are currently being studied by the international scientific community, for the potential energy savings that present when applied to the opaque surfaces of buildings.

Chapters 1-3 relate to the study of the thermal behavior of sensible thermal storage materials. Starting from the methodology used in the technical reference standard EN ISO 13786 and the scientific literature regarding the study of the thermal dynamic properties of walls, a new method to dynamically characterize the walls in the actual operating conditions was developed. These conditions concern the simultaneous presence of more temperature and heat flux loadings on the external and internal surfaces with their actual trend upon the variation of time. The harmonic method that requires the condition that the input variables are periodic was used. This is not a significant limitation because in the technical design of air conditioning systems it is usual to use a characteristic day,



representative of a given month, and assume that it will repeat itself, always the same, throughout the considered month. The methodology developed allows for expression in analytical form by means of a Fourier series expansion, which represents the data through a steady mean value and a sum of sinusoids of different frequency, amplitude and argument. Known the Fourier series expansion of the external loadings, the phasor method is applied which supposes that the generic harmonic is the imaginary part of a complex number written in trigonometric form. Once the unknown oscillating thermal quantities are obtained, also in the form of a complex number, to bring them back in the time domain it is necessary to consider only the imaginary part that constitutes the solution for the generic harmonic. Adding the solutions obtained for the various harmonics, and adding the steady term, the response to the input signal, of which initially the Fourier series expansion was made, is obtained.

European reference technical standard EN ISO 13786 is reference for the evaluation of the quality of the building thermal envelope through dynamic indices. It considers the steady periodic regime and contains a procedure that assumes that the temperatures and heat fluxes are sinusoidal, and that, through the wall, they undergo an attenuation and a time lag. In particular, it considers a sinusoidal oscillation of the external air temperature, and adopts simplifications on the outer surface, incorporating the infrared radiation of the sky in the surface heat transfer coefficient and not contemplating the action of solar radiation, and on the inner surface, not considering the presence of convective and radiative loadings. In order to calculate the dynamic thermal characteristics it is necessary to proceed to the product of matrix of complex numbers and the link between the external and internal thermal loadings takes the form of a matrix equation that depends on the thermophysical properties of the component, the arrangement of the layers and the period of the oscillations. The employed dynamic parameters are evaluated in a continuous operating regime of the air-conditioning system, and in the case in which the oscillation of the internal air temperature is zero. These parameters are the periodic thermal admittances, which correlate the heat flux and temperature oscillations on the same face of the component, and the periodic thermal transmittance that binds the temperature oscillations on a face of the component with those of the heat flux on the other face, and it provides the decrement factor and the time lag that the loading undergoes crossing the component. Finally, the periodic heat capacity per unit area quantifies the thermal storage properties. Also, in the scientific literature in general the decrement factor and time lag are determined

by simplifying the actual trends of the external loading. The outdoor environment is sometimes schematized, in analogy to the technical regulations, through the use of a sinusoidal oscillation of external air temperature or by employing the sol-air temperature that is an external equivalent temperature enabling to take account of joint action of the convective and shortwave and longwave radiative exchanges. Finally, it is usual to use the inner surface boundary conditions considered by the reference standard. With this schematisation, the dynamic behavior of the walls only depends on the thickness, the arrangement and the thermophysical properties of the layers. If the actual external loadings are considered, the dynamic parameters also depend on the loading trends. The dynamic behavior of the walls was also studied by some authors to assess the decrement factor and time lag in sinusoidal conditions undergone by the fluctuating heat flux that passes through the wall, rather than the temperature.

In *Chapter 1*, starting from the methodology introduced by the standard, an extension of the dynamic characterization of the building component is proposed, considering the action of different loadings, such as the infrared radiation of the sky, the solar radiation and the convective heat flux exchanged with the external air. First individually these effects have been taken into consideration and then the dynamic behavior of the component when the three loadings act jointly has been analyzed. It was thus possible to define the periodic thermal transmittance in the presence of the individual loadings, external air and sky temperature loadings, and the non-dimensional periodic thermal transmittance in the presence of solar radiation loading. Finally, a new dynamic parameter, the non-dimensional global periodic transmittance, ratio of the heat flux entering the indoor environment and the conductive heat flux entering through the wall from the outer surface, in the case in which the three loadings operate jointly was introduced. In this case, reference is made to the equivalent electric circuit that has been solved with the method of superposition of causes and effects. An expression matrix that binds the oscillating temperature and the heat flux in the indoor environment with the three external loadings was derived. The resolution of the equations system leads to a relation between the internal and external heat flux and the variation of internal energy per unit time to the three loadings.

Another point examined was a simplification adopted by the standard that considers the trends of thermal quantities summarized with a simple sine wave for a period equal to

24 hours. This analysis allowed to highlight that for the correct evaluation of the dynamic parameters it is necessary to take into account the contributions of more harmonics.

For the validation of the proposed procedure the results were compared with those calculated using an implicit finite difference numerical model. The comparison between the trends of the surface heat fluxes evaluated numerically and analytically, proves the correspondence between the two methods with almost negligible differences.

The research activities contained in this chapter led to the publication of the article:

*G. Oliveti, N. Arcuri, D. Mazzeo, M. De Simone, A new parameter for the dynamic analysis of building walls using the harmonic method, International Journal of Thermal Sciences, Volume 88, February 2015, Pages 96-109, ISSN 1290-0729, <http://dx.doi.org/10.1016/j.ijthermalsci.2014.09.006>.*

In the air conditioning of environments the dynamic behavior of the walls depends, in addition to the external loadings, also on the convective and internal radiative loadings.

In *Chapter 2*, a more general dynamic characterization of opaque envelope components, subject to the joint action of periodic non-sinusoidal loadings acting on the outer and inner surfaces, was thus developed. The external loadings are the air temperature, the sky temperature and the absorbed solar radiation. The internal loadings are the air temperature, the absorbed shortwave radiative heat flux, the heat flux associated with the infiltration flow rate, the convective heat fluxes contributions and the heat flux supplied by the plant.

In this case, the resolution of the electrical circuit provides a new matrix expression that links, for each harmonic, the oscillating temperature and heat flux in the indoor environment with both the external and internal loadings. Starting from the expression matrix, the relationships between the internal and external heat flux and the variation of internal energy per unit time to the internal and external loadings was derived. The generic  $Y$  complex parameter contained in the relations obtained provides the contribution, in amplitude and argument, for the calculation of internal and external heat fluxes, or of variation of internal energy per unit time. The  $Y$  parameters were correlated to the periodic thermal transmittance, to the periodic thermal admittances and to the periodic heat capacity per unit area, defined in EN ISO 13786.

The simultaneous presence of more loadings of temperature and heat flux on the outer and inner surface, unlike the schematization provided by EN ISO 13786, requires for the dynamic characterization the use of heat fluxes entering and exiting the wall. The use of

the heat flux allows for the joint action of all the loadings to be taken into account, to assess the peaks of thermal loads to be used for the dimensioning of the plant and, in addition, to determine the energy transferred.

With reference to the generic harmonic, in the case that the heat flux penetrates from the outside towards the inside, the new expression of non-dimensional global periodic transmittance was obtained. This parameter depends, besides the  $Y$  complex parameters, function of thermophysical properties, of the surface heat transfer coefficients on the inner and outer surface and of the oscillation period, also on internal and external loadings. The parameter is a phasor and defines the attenuation and time lag undergone by the external heat flux crossing the wall. Furthermore, the ratio between the energy stored per unit time and the external heat flux entering the wall, namely the instantaneous periodic efficiency of storage of the wall, was defined.

In the actual operating conditions, the loadings that act on the building walls are non-sinusoidal. In the presence of non-sinusoidal loadings, the identification of the dynamic behaviour of the wall was obtained using several dynamic parameters, with the aim of dynamically characterising the wall in energy terms and in terms of heat flux. The energy decrement factor and the decrement factor of the heat flux maximum peak and that of the heat flux minimum peak were introduced. The first is the ratio between the energy in a semi-period entering and exiting the wall, while the second and the third identify, according to the direction of the steady heat flux, respectively the heat flux peak in summer and winter conditions. The calculation of the previous parameters requires the use of all the harmonics. In order to determine the number of required harmonics, a criterion that is useful in quantifying the deviation of a non-sinusoidal periodic trend from a sinusoidal trend, and which consists in the evaluation of the Total Harmonic Distortion (THD), was developed. The introduced criterion foresees that the number  $k$  of harmonics to be considered in the calculation of the internal and external heat flux is that which gives rise to a contained relative percentage error (2-3%) of the most distorted heat flux to which a higher THD value corresponds.

The methodology developed was used to evaluate the influence of external and internal loadings on the dynamic characteristics of two common use walls on a monthly and seasonal basis. The first wall is isolated and has a high heat capacity while the second is not isolated and has a low heat capacity. The external loadings were changed considering two climatically different locations and different orientations of the walls. For each location was defined a characteristic day of each month through the use of the software

TRNSYS 17 that, starting from the monthly average daily values, has allowed the obtainment of the hourly average values of the external loadings. Inside, two boundary conditions corresponding to winter heating and summer cooling, in continuous regime and with nocturnal attenuation, in the absence and presence of a shortwave radiative heat flux on the internal surface, were considered. In total for each orientation 16 cases were considered, relating to the two walls, to the two locations, to the two plant operating regimes in the absence and the presence of internal radiant loads. The results obtained were used to plot maps, for the various orientations, which report the seasonal mean values of the decrement factor of the heat flux maximum peak as a function of the relative time lag in the summer period. These maps were also plotted with reference to the winter season considering the decrement factor and the time lag of the heat flux minimum peak. Finally, in a last map, the energy decrement factor in the summer season as a function of that in the winter season was reported. The latter representation allows for the highlighting of season in which the decrement factor is lower.

The research activities contained in this chapter led to the publication of the article:

*D. Mazzeo, G. Oliveti, N. Arcuri, Influence of internal and external boundary conditions on the decrement factor and time lag heat flux of building walls in steady periodic regime, Applied Energy, Volume 164, 15 February 2016, Pages 509-531, ISSN 0306-2619, <http://dx.doi.org/10.1016/j.apenergy.2015.11.076>.*

In **Chapter 3**, the procedure developed was used to evaluate, on a seasonal basis, the influence of the solar radiation incident on the outer surface and of the shortwave radiation that incides on the inner surface, on the dynamic characteristics of two commonly used walls. The trend of the solar radiation, in addition to changes with the orientation of the wall, varies with the solar absorption coefficient of the outer surface. For each wall, a total of 160 cases were considered by varying the location, the plant operating regime, the shortwave radiant contribution on the inner surface, the orientation and the solar absorption coefficient of the wall. For the two considered walls, the seasonal average dynamic parameters, related to the summer and winter air-conditioning regime, were determined. The results obtained were used to plot additional maps that show, upon variation of the absorption coefficient, the dynamic behaviour of the walls in the summer and in the winter period, and the comparison between the two seasons of air-conditioning.

The research activities contained in this chapter have led to the publication of the article:

---

*D. Mazzeo, G. Oliveti, N. Arcuri, Mapping of the seasonal dynamic properties of building walls in actual periodic conditions and effects produced by solar radiation incident on the outer and inner surfaces of the wall, Applied Thermal Engineering, Volume 102, 5 June 2016, Pages 1157-1174, ISSN 1359-4311, <http://dx.doi.org/10.1016/j.applthermaleng.2016.04.039>.*

Chapters 4-8 relate to the study of the thermal behavior of latent heat storage materials, namely phase change materials (PCM). The PCM utilize the solid-liquid phase change to store and release heat through an isothermal transformation, at the melting temperature. Providing a heat flux, they store energy in the form of latent heat, while subtracting heat flux they return the energy stored maintaining their temperature constant. The presence of a PCM layer in the building envelope modifies the trends of the temperature and heat flux with a consequent reduction in energy lost by the indoor environment in the winter period and in energy entering the indoor environment, mainly due to the solar load, in the summer period, and a consequent reduction of power peaks used for the dimensioning of the plant. In the internal walls, the presence of a PCM layer increases the heat storage capacity with a consequent reduction of the internal air temperature fluctuations. The problem of the determination of the thermal field in a layer subject to phase changes presents some characteristics, which render the solving of differential equations that describe the phenomenon particularly difficult. In particular, the domains of the differential equations are variable in time and depend, as well as on the external surface boundary conditions, on the bi-phase interface conditions. These conditions are expressed by an instantaneous thermal balance equation, which describes conductive heat flux discontinuity, and by the condition at the temperature interface that is equal to the melting temperature. This problem is known as the Stefan or Moving Boundary Problem. Upon variation of the boundary conditions, the PCM layer may be either totally in solid phase or in liquid phase or both phases may be present separated by a bi-phase interface. It may also occur that in the layer there are multiple bi-phase interfaces. Only in special cases, different authors have provided exact analytical solutions to the Stefan Problem, i.e. in semi-infinite monodimensional domains with simple initial and boundary conditions. For example, Neumann formulated the exact analytical solution for a Stefan Problem in a semi-infinite monodimensional domain in the case of heat conduction with a constant temperature assigned on the boundary. The examined scientific literature

---

showed that the Stefan Problem exact analytical solution in a finite PCM layer in a steady periodic regime was not available.

*Chapter 4* deals with the formulation of a new analytical model that solves the problem of the heat transfer in a finite layer of PCM subject to steady periodic boundary conditions. The boundary conditions are such as to give rise to a single bi-phase interface, in motion in the layer, which separates the solid phase from the liquid phase. In particular, temperature fluctuations on a face always higher than the melting temperature and temperature fluctuations always lower than the melting temperature on the other face were considered. The obtained solution allows evaluation, upon variation of the time, of the bi-phase interface position, of the temperature and heat flux fields, and of the energy stored in the sensible and latent form. The problem was solved by breaking it down into a steady subproblem and a fluctuating subproblem, the solution of which was obtained separately. Regarding the steady subproblem, the monodimensional heat conduction equation with the bi-phase interface position at the melting temperature and not time dependent was considered. For the determination of the oscillating thermal field, with reference to a generic harmonic, the phasor method was applied. Such a method allows transformation of the partial differential equation in the time domain, which describes the heat conduction in the solid and liquid phase, in ordinary differential equations in the complex domain, and the heat balance equation at the bi-phase interface in an algebraic equation. The Stefan Problem was then reduced to a system of algebraic equations whose solution gives the equation for determining the oscillating component of the bi-phase interface position and, starting from this, the expressions of the oscillating temperature and heat flux at each point of the layer at each time instant, the advancement velocity of the bi-phase interface and the latent and sensible heat stored/released per unit time. The equations that describe the thermal field in the two phases and the balance equation at the bi-phase interface were rendered dimensionless by introducing the dimensionless abscissa, the Fourier and the Stefan numbers calculated in the liquid phase and in the solid phase. The oscillating component of the bi-phase interface position, for a generic harmonic, is the solution of an implicit transcendental complex equation with complex parameters and unknowns. This equation has a structure that is very similar to the Neumann solution obtained in a semi-infinite layer with a face that is maintained at a constant temperature. The solution obtained can be used to evaluate the thermal performance of a PCM layer both in the case

in which it is subjected to sinusoidal thermal loadings and in the case in which it is subjected to the actual thermal loadings (non-sinusoidal).

The obtained solution was thus used to evaluate the temperature and the heat flux fields in a PCM layer for different sinusoidal boundary conditions and for boundary conditions expressed by a Fourier series expansion.

The research activities contained in this chapter led to the publication of the article:

*D. Mazzeo, G. Oliveti, M. De Simone, N. Arcuri, Analytical model for solidification and melting in a finite PCM in steady periodic regime, International Journal of Heat and Mass Transfer, Volume 88, September 2015, Pages 844-861, ISSN 0017-9310, <http://dx.doi.org/10.1016/j.ijheatmasstransfer.2015.04.109>.*

In this new form, a parametric study of the amplitude and of the argument of the oscillating component of the bi-phase interface position upon variation of the five dimensionless parameters, was conducted.

In **Chapter 5**, the equation for determining the oscillating component of the bi-phase interface position was rewritten in a new dimensionless form in which five parameters appear: the dimensionless abscissa, the root of the Fourier number and the Stefan number in one phase, the ratio of the roots of the Fourier numbers in the two phases, that is the ratio of the thermal diffusivity of the two phases, and another ratio that also takes into account the attenuation and the time lag between the temperature loadings applied on the boundary of the layer. In this new form, a parametric study of the amplitude and the argument of the oscillating component of the bi-phase interface position upon the variation of the five dimensionless parameters was conducted. For the parametric study, the thermophysical properties of the most commonly used PCM and the variation range of attenuation and time lag between the temperature loadings operating on the internal and external surfaces were considered. The study of the phasor that describes the oscillating component of the bi-phase interface position, as a function of the Fourier number in one phase, namely in the frequency domain, and upon variation of the other thermal parameters, has highlighted how the trends of the amplitude and the argument are very similar to a frequency response that in the Laplace domain is equal to the transfer function of a dynamic linear system of the third order with a finite time-delay. Two of the three poles are complex conjugates and they describe the maximum overshoot of the amplitude and the discontinuity of the argument of the oscillating component of the bi-phase interface position. The inverse of the Fourier number, proportional to the pulsation, is used to plot



the Bode diagram describing the frequency response of a PCM. The comparison of the Bode plot traced analytically and that obtained by the frequency response function shows a good adherence between the two trends. Such a trends can be rendered more accurate with a transfer function with an order higher than the third obtainable by adding, in the same number, more poles and zeros.

In the thermal analysis of a PCM layer, it is useful to have an expression in an explicit form of the oscillating component of the bi-phase interface position to be substituted in the other relations to obtain the mathematical expression of the temperature and heat flux fields as a function of only dimensionless thermal parameters and boundary loadings. This was obtained approximating hyperbolic functions with a MacLaurin series expansion. The implicit transcendental equation has been simplified in an algebraic equation of the third degree with coefficients that are in part real and in part complex, which admit three roots, of which only one is the solution of the exact equation. Such an approximate solution, acceptable for wide intervals of variation in thermal parameters, is only a function of the dimensionless steady component of the bi-phase interface position and of two new dimensionless thermal parameters: the product between the Fourier number and the Stefan number calculated in each phase. This product has a definite physical significance. Furthermore, the errors committed by employing the approximate solution upon the variation of the dimensionless parameters were evaluated.

The research activities contained in this chapter led to the publication of the article:

*D. Mazzeo, G. Oliveti, Parametric study and approximation of the exact analytical solution of the Stefan Problem in a finite PCM layer in a steady periodic regime, International Communications in Heat and Mass Transfer, Volume 84, May 2017, Pages 49-65, ISSN 0735-1933, <http://doi.org/10.1016/j.icheatmasstransfer.2017.03.013>.*

The analytical model developed is valid when a sole bi-phase interface originates in the layer. In the building walls, the boundary conditions that characterize the outdoor environment and the air-conditioned indoor environment can give rise to temperatures on the boundary surfaces that oscillate around the melting temperature giving origin during the year, to several bi-phase interfaces in the PCM layer.

In **Chapter 6**, the formulation of a numerical model that determines the dynamic behavior of a layer of PCM in the presence of one or more bi-phase interfaces has developed. In particular, among those available in the literature, the numerical model and the resolution algorithm proposed by Halford et al. (2009) were reformulated in order to

take into account the presence of several bi-phase interfaces and by removing some simplifications, such as the uniformity of the spatial discretization of the subvolumes of the layer, the invariance in space and time of the thermal resistances and the areal heat capacities, in order to obtain a more accurate representation of heat flux discontinuity in the subvolumes involved in the phase change. Reference was made to an equivalent electrical circuit of a PCM layer, discretized with  $N$  subvolumes, subject to the external air temperature loading, sky temperature loading and absorbed solar radiation loading, and to the constant value of the internal air temperature loading. The numerical discretization of the system of differential equations according to an explicit finite difference scheme leads to a system of algebraic equations representing the heat balance of all the subvolumes. Such equations provide the temperature of the nodes that are not subject to phase change and liquid fraction in the nodes at the melting temperature at the successive time instant through thermal quantities calculated at the preceding time instant. The position of the bi-phase interfaces is calculated as a function of liquid fraction in the considered node and the bi-phase interface type. The calculation algorithm developed consists of three subroutines to determine the temperature and the liquid fraction present in the node in different instants; the node can be entirely in the solid phase, or in liquid phase or in phase change. The thermal resistances and the heat capacity are updated in each time instant as a function of the temperature and of the liquid fraction. The analytical solution developed, described in Chapter 5, was used to validate the numerical model.

The developed calculation procedure is employed for the evaluation of the effective thermal field and for the study of the thermal behaviour of PCM layers, with different melting temperatures and thermophysical properties, with boundary conditions characteristics of two localities with a continental climate and a mediterranean climate. Such a procedure allows for the determination, at different time instants of the period  $P=24$  hours, of the position of the bi-phase interfaces present in the layer, the temperature and heat flux fields and the energy released and stored per unit time of each interface. The numerical results have revealed interesting phenomena that for such boundary conditions and in such detail have never previously been reported in the literature.

The PCM layer have presented different configurations of the phases in the different months of the year and it was found that the thermal fields depend on the advancement velocity of the bi-phase interfaces which define the law of storage and release of latent energy at the melting temperature in the involved layer portions.

The research activities contained in this chapter led to the publication of the article:

*D. Mazzeo, G.Oliveti, Thermal field and heat storage in PCM walls with multiple bi-phase interfaces under actual periodic boundary conditions.*

The article was submitted to the International Journal of Thermal Sciences and is currently under review.

In *Chapter 7*, the numerical model is employed for the definition of the energetic and dynamic behavior of a layer subject to phase change (PCM) with boundary conditions characterizing the external walls of air-conditioned buildings. The surface heat fluxes are used to evaluate the PCM layer energetic behavior in terms of energy transferred through the boundary surfaces and of stored energy in sensible and latent form. Furthermore, the trends of surface temperatures and heat fluxes, the fluctuating energy transferred and stored in sensible and latent form, are used in order to define the parameters necessary for the complete dynamic characterization of the layer. The defined parameters are: the latent storage efficiency; the fraction of latent energy stored compared to the total energy stored; the decrement factor of the maximum excursion of the temperature and heat flux; the energy decrement factor; the maximum peak and minimum peak time lags of the temperature and heat flux; the fraction of the period in which the maximum or minimum peak of the temperature and heat flux on the internal surface are constant in time. The proposed parameters are to be used for the thermal design of innovative walls of air conditioned buildings, targeting the reduction of power peaks entering the environment, in order to reduce the energy requirements and also to improve indoor thermal comfort.

The methodology developed is applied to PCM layers with different melting temperatures and thermo-physical properties and subject to climatic conditions of two locations, one with a continental climate and the second one with a Mediterranean climate. The results obtained allowed to identify which PCM is more suitable in improving the energetic performances in the heating or cooling period and to determine the dynamic characteristics during the year. In particular, it was found that all the defined dynamic parameters, irrespective of locality and of typology of PCM, are related to the latent storage efficiency. Furthermore, the results show that it was sufficient to reach the phase change in a portion of the layer of about 35% to obtain: complete attenuation of the maximum excursion of the temperature and heat flux on the internal surface; an annulment of the fluctuating energy transferred in the indoor environment; unitary values of the latent energy fraction; a higher increase of the time lag of maximum peak of the temperature and heat flux, of the

minimum peak of the temperature and of the minimum peak of the heat flux in the summer time; a high reduction of the minimum peak of the heat flux in the winter period.

Furthermore, a strict correlation between the decrement factor of the maximum excursion of the heat flux and the energy decrement factor was found, and as well as between the time lag of the maximum peak of the temperature and the time lag of the maximum peak of the heat flux.

The research activities contained in this chapter have led to the publication of the following articles:

- 1) D. Mazzeo, G. Oliveti, N. Arcuri, *Definition of a new set of parameters for the dynamic thermal characterization of PCM layers in the presence of one or more liquid-solid interfaces*, *Energy and Building*, Volume 141, 15 April 2017, Pages 379-396, ISSN 0378-7788, <http://doi.org/10.1016/j.enbuild.2017.02.027>.
- 2) D. Mazzeo, G. Oliveti, N. Arcuri, *Data demonstrating the influence of the latent storage efficiency on the dynamic thermal characteristics of a PCM layer*, *Data in Brief*, Volume 12, June 2017, Pages 274-276, ISSN 2352-3409, <http://doi.org/10.1016/j.dib.2017.04.005>.
- 3) D. Mazzeo, G. Oliveti, N. Arcuri, *A method for thermal dimensioning and for energy behavior evaluation of a building envelope PCM layer by using the characteristic days*, *Energies*, *Energies* Volume 10(5), May 2017, 659-678; doi:10.3390/en10050659

In **Chapter 8**, the analytical solution developed has been subjected to experimental verification. This verification was conducted during a period of research at the research center Innovació GREA Concurrent (Lleida, Spain). The experimental investigation was conducted by subjecting the two flat faces of a cylindrical PCM sample, mounted inside a test-box, to different boundary conditions upon time variation and measuring the temperature at different heights and the surface heat fluxes. The choice of the PCM was made so that the thermophysical and thermochemical behaviour was very close to these hypothesised in the formulation of the analytical model. For the evaluation of the thermophysical properties of the PCM sample used (thermal conductivity and specific heat in the two phases, latent heat and phase change temperature), an experimental procedure created by the authors was used. The experimental procedure consists of subjecting the sample, mounted in the test-box for validation of the model, to the different tests. Each of these tests consists of a thermal transient from an initial steady state to a final steady state.

The sample in the first test is entirely in solid phase, in the second test it is entirely in liquid phase and in the third test it undergoes a complete solid-liquid phase change.

Verification of the analytical model was conducted: in a sinusoidal periodic regime, setting temperature boundary conditions on the two faces of the sample varying the decrement factor, the time lag and the oscillation period; in a non-sinusoidal periodic regime, considering temperature boundary conditions with a different shape on the two sample faces, represented by means of a Fourier series expansion. In all the cases, the comparison between the measured and calculated temperature trends and of the surface heat fluxes resulted as being in excellent agreement, as the thermal fluctuations present very close steady mean values, and amplitudes and arguments. Moreover, also having verified the comparison between the total stored energy, the analytical model constitutes a valid instrument for the evaluation of the latent and sensible contribution and the trend of the position of the bi-phase interface in function of time.

The research activities contained in this chapter have led to the publication of the article:

*D. Mazzeo, G.Oliveti, A. de Gracia, J. Coma, A. Solè, L. F. Cabeza, Experimental validation of the exact analytical solution of the steady periodic heat transfer problem in a PCM layer.*

The article has been submitted to the Energy Journal and is currently under review.

# **Sensible heat storage materials**

# Chapter 1

## **A new parameter for the dynamic analysis of building walls using the harmonic method**

### **Abstract**

The authors propose a methodology to schematize correctly the capacitive effects in the transmission of heat in the multilayered walls of buildings.

An analytical study is presented related to a steady periodic regime allowing consideration of three external loads acting singularly or simultaneously: air temperature, apparent sky temperature and incident solar irradiation.

Such a study is applied in the case of four traditional types of wall (A – brick wall, B - hollow wall, C – polarized brick wall, D – prefabricated wall).

The expression of the oscillating heat flux, which penetrates the internal environment, and the conductive heat flux which penetrates the wall in contact with the external air, was obtained by means of the electrical analogy and the resolution of the equivalent circuit. It is demonstrated that the non-dimensional periodic global transmittance, the ratio between the heat flux which is

transferred to the indoor environment and the external heat flux, with the plant turned on, is the most suitable non-dimensional parameter for the dynamic analysis of the walls. This parameter allows for the evaluation of all the typical dynamic quantities for the complete description of the thermal behavior of the walls.

*Keywords:* harmonic method, dynamic analysis, building walls, thermal parameters, time lag, decrement factor.

- The thermal behavior of building walls by the harmonic method is analyzed
- Three forcings for the thermal dynamic characterization of the walls are considered
- New methodology and parameters for the dynamic analysis of the walls are formulated
- The parameters are applied to compare the thermal performance of different walls

*In questioni di scienza, l'autorità di un migliaio di persone non vale tanto quanto l'umile ragionamento di un singolo individuo.*

*(Galileo Galilei)*



## 1. Introduction

In the air-conditioning of buildings, the spread of cooling systems has determined a significant increase in annual energy requirement. In order to contain the energy consumption, as indicated by the recent regulations regarding energy efficiency [1, 2], it is necessary to improve the thermal performance of the building shell and use more efficient plant systems. In many cases the evaluation of heat fluxes, through the external components of the building shell, is carried out with simplified procedures when one is interested in the determination of energy uses [3], while plants dimensioning requires the determination of the peak powers, which are obtained using calculation codes which can simulate the effective behavior of the building air conditioning system in dynamic conditions.

Often, during the preliminary phase of thermal design and the performance evaluation and diagnosis of buildings, the use of simplified models results as being convenient [4, 5]. In [6, 7] it is highlighted how, in the formulation of simplified models, it is important to correctly schematize the thermal capacitive effects and identify the parameters necessary to describe accurately the phenomena of thermal exchange and storage.

A further issue, which can arise during the planning phase, consists in the evaluation of the influence of the stratigraphical composition of the walls on the dynamic properties of the building shell [8, 9]. In [10-13] the time lag and the decrement factor of a wall are determined by varying the thermophysical properties of the materials, the thickness and the position of the insulation layer, considering the sol-air temperature as the external load with a sinusoidal trend equal to 24 hours. A similar approach was adopted in [14] in which an analytical study on the influence of the color, or rather of the optical properties, of the external surfaces of a building component on the transfer of heat in a steady periodic regime is presented.

A sophisticated model that takes into account the heat transfer and moisture transfer in walls whose layers are made with nonhomogeneous materials is shown in [15].

In Refs. [16, 17] traditional methods for the resolution of the conduction equation (numerical methods, harmonic methods, response factor methods and methods based on conduction transfer functions (CTF)) are compared, and the advantages and disadvantages of each method are shown.

In particular, the harmonic method presents the advantage of providing analytical expressions of the parameters which identify the dynamic behavior of the building components. Such a setting is found in recent Standards such as EN ISO 13792:2012 [18] and EN ISO 13786:2010 [19]. The

latter uses harmonic analysis in a steady periodic regime for the dynamic characterization of building components. The boundary conditions on the two faces which delimit the wall are temperature or heat flux that vary sinusoidally.

The shell walls are generally subjected to variable loads over time, prevalently due to the external air temperature, to the incident solar radiation and to the infrared radiation from the sky. From a mathematical standpoint, it is possible to approximate the variation law of such loads over time as the sum of infinite contributions (harmonics) whose variations are sinusoidal over different periods. The first is called fundamental harmonic and has period  $P = 24$  hours; the successive ones have  $P_k = P/k$  with  $k$  integer.

The resolution of the general equation of conduction is obtained in the entire domain and, by means of the heat transfer matrix, allows the calculation of the complex amplitudes of the temperature and the heat flux on the internal side, starting from the complex amplitudes of the loads which act on the external surface.

The characteristics used are the periodic thermal admittances and the properties of dynamic heat transfer; specifically, the periodic thermal admittance correlates the oscillating heat flux with the oscillation of the temperature on the same face of the component, while the dynamic heat transfer properties correlate the oscillations of a quantity on a face of the component with the corresponding one on another face.

Among the dynamic heat exchange properties, the Standard [19] considers the periodic thermal transmittance, a complex number which provides the decrement factor of the amplitude of the oscillation and the time lag to which the load is subjected when it crosses the component. The periodic thermal admittances and transmittance are used to determine the areal heat capacity which quantifies the storage properties. It is possible to define an admittance and a thermal capacity on each side for each component.

In this chapter, the dynamic characterization of the walls, in steady periodic regime, is widened through the consideration of three distinct loads: the external air temperature, the apparent sky temperature and the incident solar radiation. Moreover, a dynamic analysis of the building component is developed considering the joint action of the three periodic loads, with the formulation of a matrix expression, obtained by means of the electrical analogy and the overlapping of the causes and effects, which permits the calculation of the heat flux which appears within the indoor environment when the three loads act externally.

The procedure was specially created and used in order to identify further characteristic dynamic parameters, with the aim of describing the heat transfer phenomena in a more complete manner.

Verification of the results obtained with the analytical procedure was carried out by means of a

numerical model of the wall using the finite difference method.

The external loads trend was obtained starting from the experimental data of the external variables, air temperature, solar irradiation and sky temperature, recorded in clear sky conditions.

## 2. Methodology

The experimental values of each external load are expressed in an analytical form through a discrete Fourier series [20] with interruption of the tenth harmonic, which approximates the data by a mean steady value and a sum of sinusoids of different frequencies, amplitude and argument according to the equation:

$$y(t) = \bar{y} + \sum_{k=1}^{10} \tilde{y}_k = \bar{y} + \sum_{k=1}^{10} |\tilde{y}_k| \sin(k\omega t + \psi_k) \quad (1)$$

in which  $\bar{y}$  represents the mean value,  $\tilde{y}_k$  the amplitude,  $k\omega$  the angular frequency and  $\psi_k$  the argument of the  $k$ -th harmonic. Figure 1 reports the experimental data of the loads and the trends, obtained by setting the angular frequency  $\omega$  equal to 0.262 rad/s, corresponding to a period of 24 hours, and the steady value equal to the mean in the entire period.

In Tables 1-3 the mean value and the characteristic parameters of the first ten harmonics are reported.

Starting from the entering signals and the transfer matrix of the wall, the symbolic or phasors method is applied which, for each generic harmonic  $\tilde{y}_k$  supposes the entering signal as an imaginary part of the more general signal [21]:

$$\hat{y}_k = |\hat{y}_k| [\cos(k\omega t + \psi_k) + j \text{sen}(k\omega t + \psi_k)] = |\hat{y}_k| e^{j(k\omega t + \psi_k)} \quad (2)$$

Once the exiting signal has been obtained in its complex form, it is necessary to multiply it by the complex operator  $e^{jk\omega t}$  and select solely the imaginary part, which forms the solution for the generic harmonic of angular frequency  $k\omega$ . By summing the responses obtained for the various harmonics, and adding the term relative to the null angular frequency component (steady conditions), the response to the entering signal, of which the Fourier finite series was initially broken down, is obtained. Therefore, an entering fixed sinusoid is first transformed into a complex form and then multiplied by the transfer matrix of the same period, in order to obtain

the corresponding exiting sinusoid in a complex form. In order to pass from a complex domain to a time domain, it is necessary to consider the imaginary part of this result.

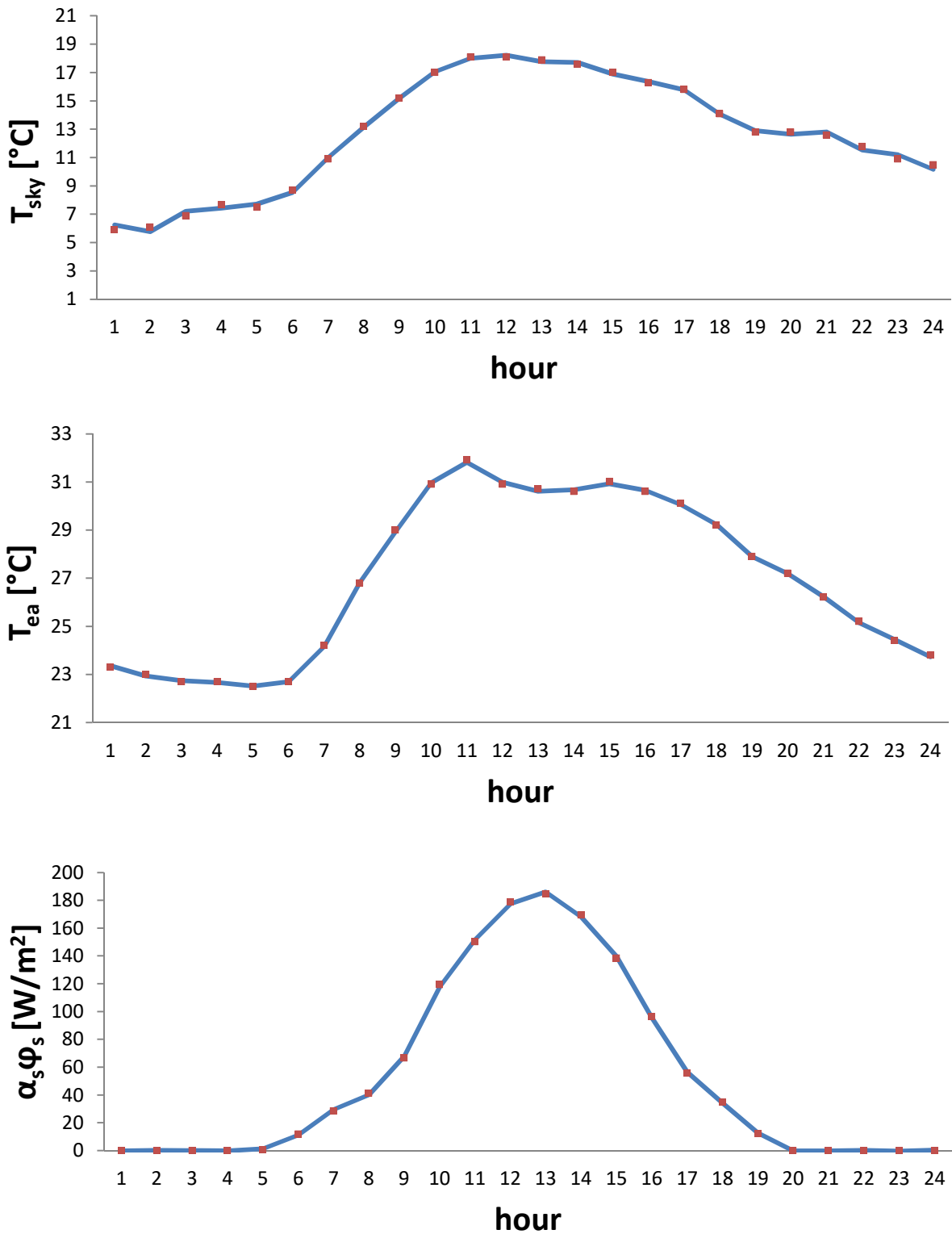


Figure 1. Experimental trends of the loads: external air temperature  $T_{ea}$ , apparent sky temperature  $T_{sky}$  and absorbed solar irradiation  $\alpha_s \phi_s$  (solar absorption coefficient  $\alpha=0.40$ ).

Table 1. External air temperature. Mean value  $\bar{T}_{ea}$ , amplitude and argument of the first ten harmonics  $\hat{T}_{ea}$ .

$\bar{T}_{ea}$ [°C]	26.98			
$\hat{T}_{ea}$ [°C]	$\omega$ [rad/h]	<b>T</b> [h]	$\rho$ [°C]	$\alpha$ [h]
1	0.262	24.0	-4.52	3.80
2	0.524	12.0	0.85	4.01
3	0.786	8.0	0.73	0.06
4	1.048	6.0	-0.43	0.65
5	1.310	4.8	0.10	0.64
6	1.572	4.0	0.04	1.41
7	1.834	3.4	0.12	0.17
8	2.096	3.0	-0.08	0.24
9	2.358	2.7	-0.05	-0.29
10	2.620	2.4	-0.08	0.75

Table 2. Apparent sky temperature. Mean value  $\bar{T}_{sky}$ , amplitude and argument of the first ten harmonics  $\hat{T}_{sky}$ .

$\bar{T}_{sky}$ [°C]	12.73			
$\hat{T}_{sky}$ [°C]	$\omega$ [rad/h]	<b>T</b> [h]	$\rho$ [°C]	$\alpha$ [h]
1	0.262	24.0	-5.36	-0.85
2	0.524	12.0	-1.47	-0.47
3	0.786	8.0	-0.23	-0.11
4	1.048	6.0	-0.59	-0.37
5	1.310	4.8	-0.29	-0.23
6	1.572	4.0	-0.31	-0.30
7	1.834	3.4	-0.38	-0.43
8	2.096	3.0	-0.21	-0.26
9	2.358	2.7	0.13	0.19
10	2.620	2.4	-0.18	-0.28

Table 3. Absorbed solar irradiation. Mean value  $\alpha\bar{\phi}_s$ , amplitude and argument of the first ten harmonics  $\alpha\hat{\phi}_s$ .

$\alpha\bar{\phi}_s$ [W/m <sup>2</sup> ]	53.74			
$\alpha\hat{\phi}_s$ [W/m <sup>2</sup> ]	$\omega$ [rad/h]	<b>T</b> [h]	$\rho$ [W/m <sup>2</sup> ]	$\alpha$ [h]
1	0.262	24.0	-83.68	5.25
2	0.524	12.0	37.82	2.17
3	0.786	8.0	9.26	-2.95
4	1.048	6.0	2.17	1.05
5	1.310	4.8	0.93	-0.62
6	1.572	4.0	-2.43	-7.56
7	1.834	3.4	1.22	0.55
8	2.096	3.0	1.73	0.02
9	2.358	2.7	1.69	1.32
10	2.620	2.4	0.51	0.13

### 3. Analysis of the dynamic response of a wall to single loads

The Standard EN ISO 13786:2010 [19] exemplifies the dynamic characterization of building components considering the external air temperature of a period equal to 24 hours as a load. The convective-radiative heat transfer coefficient for internal and external surface heat exchanges are used for these evaluations. In the present chapter, a more accurate investigation is developed and the characterization of the building component is obtained considering the three loads and effective boundary conditions on the external surface singularly, whereas on the internal surface the thermal exchange was modelled by means of the surface heat coefficient.

For each load, the contribution of a single harmonic is evaluated considering the relation between the complex amplitudes of the temperature and of the heat flux inside and those corresponding which act on the outside [22]. The expressions obtained are:

a) external air temperature (“*ea*” load)

$$\begin{bmatrix} \hat{T}_{ia,ea} \\ \hat{\Phi}_{i,ea} \end{bmatrix} = \begin{bmatrix} 1 & -\frac{1}{h_i} \\ 0 & 1 \end{bmatrix} [Z] \begin{bmatrix} 1 & -\frac{1}{h_{e,c}} \\ 0 & 1 \end{bmatrix} \begin{bmatrix} \hat{T}_{ea} \\ \hat{\Phi}_{e,c} \end{bmatrix} = \begin{bmatrix} S_{11,ea} & S_{12,ea} \\ S_{21,ea} & S_{22,ea} \end{bmatrix} \begin{bmatrix} \hat{T}_{ea} \\ \hat{\Phi}_{e,c} \end{bmatrix} = S_{ea} \begin{bmatrix} \hat{T}_{ea} \\ \hat{\Phi}_{e,c} \end{bmatrix} \quad (3)$$

b) apparent sky temperature (“*sky*” load)

$$\begin{bmatrix} \hat{T}_{ia,sky} \\ \hat{\Phi}_{i,sky} \end{bmatrix} = \begin{bmatrix} 1 & -\frac{1}{h_i} \\ 0 & 1 \end{bmatrix} [Z] \begin{bmatrix} 1 & -\frac{1}{h_{e,r}} \\ 0 & 1 \end{bmatrix} \begin{bmatrix} \hat{T}_{sky} \\ \hat{\Phi}_{e,r} \end{bmatrix} = \begin{bmatrix} S_{11,sky} & S_{12,sky} \\ S_{21,sky} & S_{22,sky} \end{bmatrix} \begin{bmatrix} \hat{T}_{sky} \\ \hat{\Phi}_{e,r} \end{bmatrix} = S_{sky} \begin{bmatrix} \hat{T}_{sky} \\ \hat{\Phi}_{e,r} \end{bmatrix} \quad (4)$$

c) solar irradiation (“*s*” load)

$$\begin{bmatrix} \hat{T}_{ia,s} \\ \hat{\Phi}_{i,s} \end{bmatrix} = \begin{bmatrix} 1 & -\frac{1}{h_i} \\ 0 & 1 \end{bmatrix} [Z] \begin{bmatrix} \hat{T}_{2,s} \\ \alpha \hat{\Phi}_s \end{bmatrix} = \begin{bmatrix} S_{11,s} & S_{12,s} \\ S_{21,s} & S_{22,s} \end{bmatrix} \begin{bmatrix} \hat{T}_{2,s} \\ \alpha \hat{\Phi}_s \end{bmatrix} = S_s \begin{bmatrix} \hat{T}_{2,s} \\ \alpha \hat{\Phi}_s \end{bmatrix} \quad (5)$$

The heat transfer matrix of the multilayered wall from surface to surface is:

$$[Z] = [Z_N] \cdot \dots \cdot [Z_1] \quad (6)$$

where  $[Z_1], \dots, [Z_N]$ , are the heat transfer matrices of the various layers of the wall of the building, beginning from layer 1. As a convection for building envelope components, layer 1 shall be the outermost layer.

The matrix elements  $Z_{mn}$  of a generic layer are calculated as follows:

$$Z_{11} = Z_{22} = \cosh(\xi)\cos(\xi) + j \sinh(\xi)\sin(\xi) \quad (7)$$

$$Z_{12} = -\frac{\delta}{2\lambda} \{ \sinh(\xi) \cos(\xi) + \cosh(\xi) \sin(\xi) + j [ \cosh(\xi) \sin(\xi) - \sinh(\xi) \cos(\xi) ] \} \quad (8)$$

$$Z_{21} = \frac{\lambda}{\delta} \{ \sinh(\xi) \cos(\xi) - \cosh(\xi) \sin(\xi) + j [ \cosh(\xi) \sin(\xi) + \sinh(\xi) \cos(\xi) ] \} \quad (9)$$

With  $\lambda$  thermal conductivity and  $\xi$  ratio of the thickness of the layer  $d$  to the periodic penetration depth  $\delta$ , given by the relation:

$$\xi = \frac{d}{\delta} = \frac{d}{\sqrt{\frac{aP}{\pi}}} \quad (10)$$

with  $P$  period of oscillation and  $a$  thermal diffusivity.

The heat transfer matrix from environment to environment  $S_{ea}$ ,  $S_{sky}$  and  $S_s$  are determined by the thermophysical properties of the material, by the external convective and radiative heat transfer coefficients,  $h_{e,c}$  and  $h_{e,r}$ , by the internal heat transfer coefficient  $h_i$  and are calculated for each harmonic contribution.

In the case in which the temperature within the environment is constant and controlled by an air-conditioning plant, the amplitude of the oscillation is null and the preceding equation systems provide, for the heat flux  $\hat{\varphi}_i$ , respectively the following equations:

$$\hat{\varphi}_{i,ea} = -\frac{1}{S_{12,ea}} \hat{T}_{ea} = Y_{12,ea} \hat{T}_{ea} \quad (11)$$

$$\hat{\varphi}_{i,sky} = -\frac{1}{S_{12,sky}} \hat{T}_{sky} = Y_{12,sky} \hat{T}_{sky} \quad (12)$$

$$\hat{\varphi}_{i,s} = \frac{1}{S_{11,s}} \alpha \hat{\varphi}_s = Y_{11,s} \alpha \hat{\varphi}_s \quad (13)$$

The decrement factor and the time lag for the loading  $ea$  assume the form shown in the equation:

$$f_{ea} = \frac{|\hat{\Phi}_{i,ea}|}{|\hat{T}_{ea}|U_{ea}} = \frac{|Y_{12,ea}|}{U_{ea}}; \quad \Delta t_{ea} = \frac{P}{2\pi} \arg(S_{12,ea}) \quad (14)$$

with  $U_{ea}$  steady thermal transmittance of the component calculated considering only the convective heat transfer coefficient  $h_{e,c}$  on the outer surface and  $|Y_{12,ea}|$  amplitude of the periodic thermal transmittance for the loading  $ea$ .

Analogously the decrement factor and the time lag for the  $sky$  load can be defined considering in  $U_{sky}$  only the radiative heat transfer coefficient  $h_{e,r}$  on the outer surface. For the solar load, the dynamic parameters are:

$$f_s = \frac{|\hat{\Phi}_{i,s}|}{|\alpha\hat{\Phi}_s|} = |Y_{11,s}|; \quad \Delta t_s = \frac{P}{2\pi} \arg(S_{11,s}) \quad (15)$$

where  $|Y_{11,s}|$  is the non-dimensional periodic solar thermal transmittance amplitude, thus defined:

$$|Y_{11,s}| = \left| \frac{1}{S_{11,s}} \right| \quad (16)$$

For each harmonic of the single load, the preceding relations were used to determine the decrement factor and the time lag relative to four types of walls, A, B, C and D, represented in Figure 2, and whose thermophysical properties are reported in Tables 4-7.



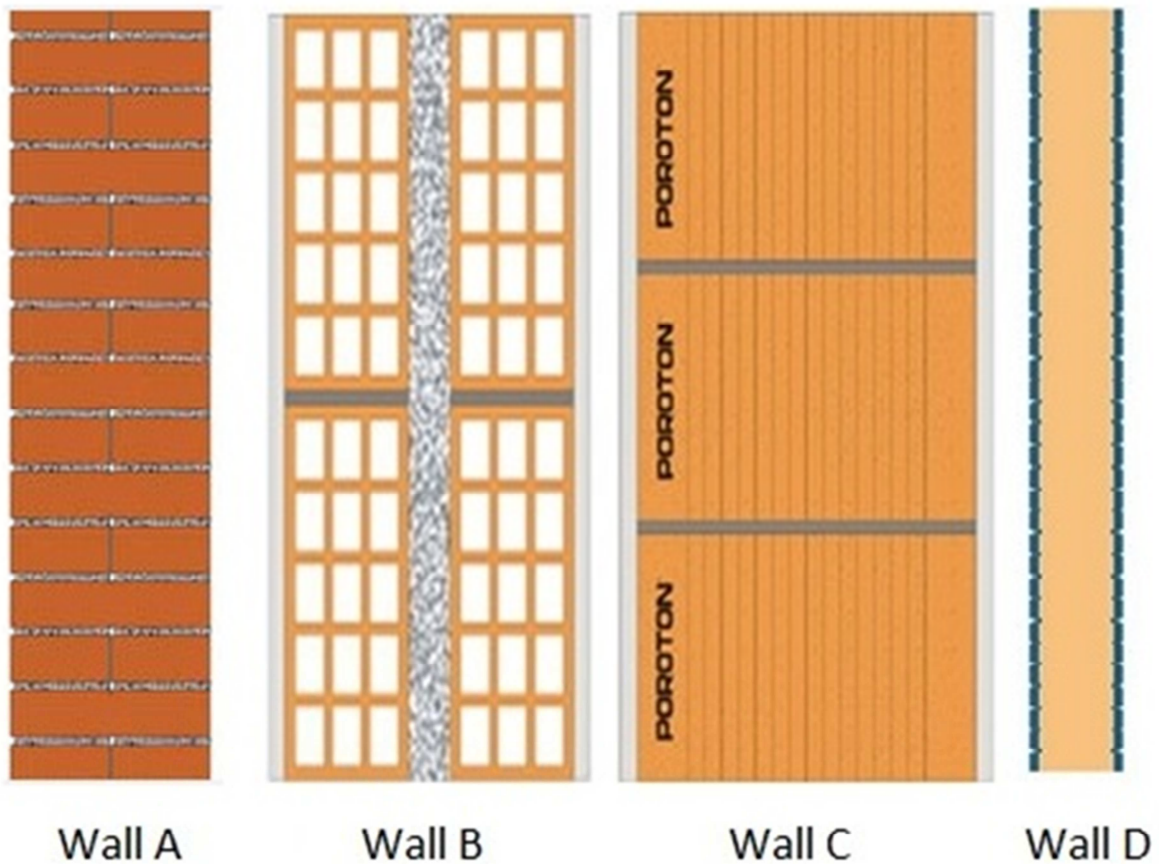


Figure 2. Stratigraphy of the four types of walls considered.

Table 4. Type A: Monolayer external wall of bricks.

	Thickness [m]	Thermal conductivity [W/m K]	Specific heat [J/kg K]	Density [kg/m <sup>3</sup> ]
External plaster	0.01	0.9	1000	1800
Brick	0.12	0.89	1000	800
Air gap	0.04			
Insulation	0.04	0.04	1450	20
Brick	0.12	0.89	1000	800
Internal plaster	0.01	0.7	1000	1400
Thermal transmittance $U=0.608 \text{ W/m}^2\text{K}$ - Heat capacity $C=225 \text{ kJ/m}^2\text{K}$				

Table 5. Type B: External wall with insulated hollow.

	Thickness [m]	Thermal conductivity [W/m K]	Specific heat [J/kg K]	Density [kg/m <sup>3</sup> ]
External plaster	0.01	0.9	840	1800
Poroton	0.38	0.17	840	630
Internal plaster	0.01	0.7	840	1400
Thermal transmittance $U=0.412 \text{ W/m}^2\text{K}$ - Heat capacity $C=228 \text{ kJ/m}^2\text{K}$				

Table 6. Type C: External wall in polarized brick.

	Thickness [m]	Thermal conductivity [W/m K]	Specific heat [J/kg K]	Density [kg/m <sup>3</sup> ]
Steel	0.005	50	500	7850
Polyurethane	0.08	0.032	1400	30
Steel	0.005	50	500	7850
Thermal transmittance U=0.375 W/m <sup>2</sup> K - Heat capacity C=42.6 kJ/m <sup>2</sup> K				

Table 7. Type D: Panel for prefabricated construction.

	Thickness [m]	Thermal conductivity [W/m K]	Specific heat capacity [J/kg K]	Density [kg/m <sup>3</sup> ]
Steel	0.005	50	500	7850
Polyurethane	0.08	0.032	1400	30
Steel	0.005	50	500	7850
Steady thermal transmittance U=0.375 W/m <sup>2</sup> K – Steady areal heat capacity C=42.6 kJ/m <sup>2</sup> K				

The boundary conditions considered are:

$$T_{ia} = T_{ia,ea} = T_{ia,sky} = T_{ia,s} = 26^{\circ}\text{C} \quad ; \quad h_i = 7.7 \frac{\text{W}}{\text{m}^2\text{K}} \quad ; \quad h_{e,c} = 20 \frac{\text{W}}{\text{m}^2\text{K}} \quad ; \quad h_{e,r} = 5.35 \frac{\text{W}}{\text{m}^2\text{K}}$$

The radiative heat transfer coefficient on the outer surface was evaluated with an experimental investigation carried out by the authors [23].

The results obtained for the temperature loadings can be thus summarized. The temperature oscillation of the sky is more attenuated and delayed compared to that of the external air for each period considered:

$$f_{sky} < f_{ea} \quad \Delta t_{sky} > \Delta t_{ea} \quad (17)$$

If the dynamic parameters obtained for the four walls A, B, C and D are compared, the following relations are valid:

$$f_{ea,C} < f_{ea,A} < f_{ea,B} < f_{ea,D} \quad f_{sky,A} < f_{sky,C} < f_{sky,B} < f_{sky,D} \quad (18)$$

$$\Delta t_{ea,C} > \Delta t_{ea,A} > \Delta t_{ea,B} > \Delta t_{ea,D} \quad \Delta t_{sky,C} > \Delta t_{sky,A} > \Delta t_{sky,B} > \Delta t_{sky,D}$$

Wall C and wall A show the best dynamic characteristics in that they present the smallest decrement factor and the highest time lag for each harmonic.

The previous results were compared with those obtained following the methodology of the Standard, which models the external convective-radiative exchange in a different manner.

Table 8 shows the decrement factors and the time lag obtained, with reference to the fundamental harmonic  $P = 24$  hours and it highlights that the Standard is conservative in that it provides a higher decrement factor and a lower time lag.

It should be pointed out that such evaluations, relative to the temperature loads of the air and the sky are held to be sufficiently accurate.

*Table 8. Dynamic parameters  $f$  and  $\Delta t$  evaluated according to the Standard methodology, and parameters obtained subjecting the wall to the separate action of the external air temperature,  $f_{ea}$  and  $\Delta t_{ea}$ , and of the apparent temperature of the sky,  $f_{sky}$  and  $\Delta t_{sky}$ .*

Wall type	$f$ [-]	$\Delta t$ [h]	$f_{ea}$ [-]	$\Delta t_{ea}$ [h]	$f_{sky}$ [-]	$\Delta t_{sky}$ [h]
A	0.172	12.10	0.164	12.25	0.106	13.25
B	0.512	7.02	0.500	7.21	0.328	8.71
C	0.150	14.11	0.147	14.20	0.120	15.06
D	0.980	1.32	0.978	1.38	0.947	2.08

The comparison among the four types of wall regarding the solar radiation was obtained by applying Eq. (13) to each individual harmonic whose characteristics are shown in Table 3. This equation evaluates the solar flux which penetrates the internal environment, set at constant temperature, starting from the solar flux absorbed by the wall on the external surface. To evaluate the contribution of the individual harmonics in the calculation of the decrement factor and that of the time lag, the external and internal heat fluxes were determined considering as well as the first harmonic, the sum of the first two, the first three, and finally the contribution of all the harmonics. Table 9 shows the decrement factors and the time lags obtained, in the case of the first harmonic with Eq. (15), and in the other cases comparing the profiles resulting from the sum of the harmonics.

Table 9. Incidence of the harmonics on the calculation of the decrement factor and the time lag of the solar radiation for the four types of walls.

	$f_s$ [-]	$(f_s - f_{s,\Sigma})/f_{s,\Sigma}$ [%]	$\Delta t_s$ [h]	$(\Delta t_s - \Delta t_{s,\Sigma})/\Delta t_{s,\Sigma}$ [%]
Wall A				
1	0.0354	67.39	14	7.69
$\Sigma$ 1-2	0.0232	9.69	13	0
$\Sigma$ 1-3	0.0214	1.41	13	0
$\Sigma$ 1-10	0.0211	0	13	0
Wall B				
1	0.0490	63.96	10	11.11
$\Sigma$ 1-2	0.0330	10.61	9	0
$\Sigma$ 1-3	0.0303	1.31	9	0
$\Sigma$ 1-10	0.0300	0	9	0
Wall C				
1	0.0199	67.33	17	0
$\Sigma$ 1-2	0.0130	8.90	17	0
$\Sigma$ 1-3	0.0121	1.47	17	0
$\Sigma$ 1-10	0.0119	0	17	0
Wall D				
1	0.239	40.48	5	0
$\Sigma$ 1-2	0.187	10.32	5	0
$\Sigma$ 1-3	0.173	2.15	5	0
$\Sigma$ 1-10	0.170	0	5	0

These profiles do not have a sinusoidal trend since they are obtained by totaling harmonics with different angular frequencies. The table shows that the greatest contribution to the decrement factor and to the time lag is to be attributed to the first harmonic whereas the contribution of the other harmonics is lower and decreases at an increase of the angular frequency. Moreover, the table shows the percentage deviation of the decrement factor and the time lag of the different compositions of the harmonics with respect to the values obtained from totaling all the harmonics.

If, for an accurate evaluation of the time lag, the fundamental harmonic and that of the period of 12 hours are sufficient, in order to determine an decrement factor value which deviates at most by 2% from that which would be obtained without neglecting any harmonic contribution, it is necessary to compose the first three harmonics.

From the comparison of the dynamic parameters reported in Tables 8 and 9, it is possible to infer that the characterization of the component by means of the external air temperature loading is not ideal to qualify the component compared to the solar load dynamically. The difference is very marked with regards to the decrement factor.

#### 4. Dynamic analysis of a building component under the contemporaneous action of the three loads

The thermal behavior of walls which are subjected to the combined presence of the three loads, external air temperature, apparent sky temperature and absorbed solar irradiation, was studied. Reference was made to the equivalent electrical circuit in Figure 3 which was resolved with the superposition method of the causes and effects.

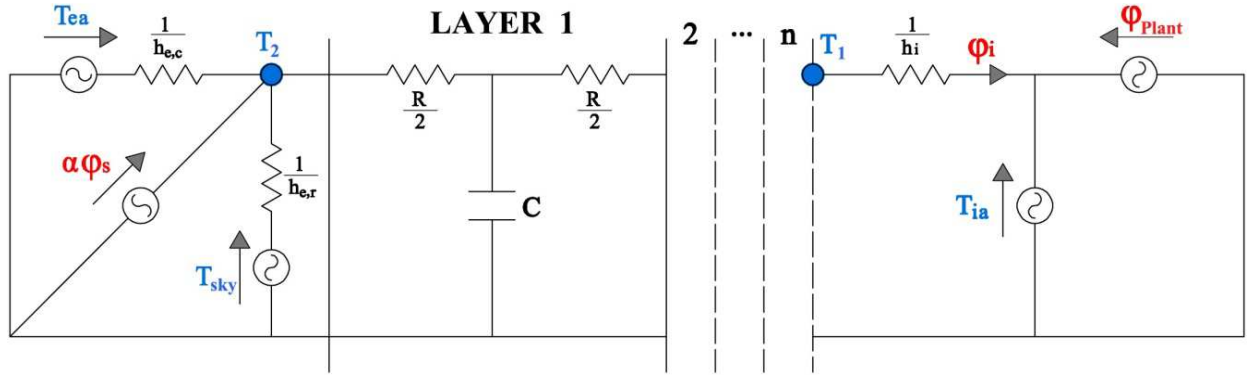


Figure 3. Electrical circuit equivalent to a multilayer wall subject to three loadings: external air temperature  $T_{ea}$ , apparent sky temperature  $T_{sky}$  and absorbed solar irradiation  $\alpha\phi_s$ .

The solution of the electrical circuit provides a matrix expression which links the oscillating amplitudes of the temperature and the heat flux on the internal side with the external loads  $T_{ea}$ ,  $T_{sky}$  and  $\alpha\phi_s$ :

$$\begin{aligned}
 \begin{bmatrix} \hat{T}_{ia} \\ \hat{\phi}_i \end{bmatrix} &= \begin{bmatrix} 1 & -\frac{1}{h_i} \\ 0 & 1 \end{bmatrix} [Z] \begin{bmatrix} \frac{h_{e,r}}{h_{e,r} + h_{e,c}} & \frac{h_{e,c}}{h_{e,r} + h_{e,c}} & -\frac{1}{h_{e,r} + h_{e,c}} \\ 0 & 0 & 1 \end{bmatrix} \begin{bmatrix} \hat{T}_{sky} \\ \hat{T}_{ea} \\ \hat{\phi}_e \end{bmatrix} \\
 &+ \begin{bmatrix} 1 & -\frac{1}{h_i} \\ 0 & 1 \end{bmatrix} [Z] \begin{bmatrix} \frac{\alpha\hat{\phi}_s}{h_{e,r} + h_{e,c}} \\ 0 \end{bmatrix} = \\
 &= \begin{bmatrix} A_{11} & A_{12} & A_{13} \\ A_{21} & A_{22} & A_{23} \end{bmatrix} \begin{bmatrix} \hat{T}_{sky} \\ \hat{T}_{ea} \\ \hat{\phi}_e \end{bmatrix} + \begin{bmatrix} B_{11} & B_{12} \\ B_{21} & B_{22} \end{bmatrix} \begin{bmatrix} \frac{\alpha\hat{\phi}_s}{h_{e,r} + h_{e,c}} \\ 0 \end{bmatrix} = \\
 &= [A] \begin{bmatrix} \hat{T}_{sky} \\ \hat{T}_{ea} \\ \hat{\phi}_e \end{bmatrix} + [B] \begin{bmatrix} \frac{\alpha\hat{\phi}_s}{h_{e,r} + h_{e,c}} \\ 0 \end{bmatrix} \quad (19)
 \end{aligned}$$

In the preceding relation the elements of the matrices [A] and [B] are complex numbers, and  $\hat{\varphi}_e$  represents the conductive heat flux which penetrates the wall at the interface with the external air. If the oscillating amplitude of the internal environment temperature is null, owing to the effect of the power supplied by the plant, the resolution of the equation system leads, for the internal heat flux, to the expression:

$$\hat{\varphi}_i = \left( A_{22} - \frac{A_{23}A_{12}}{A_{13}} \right) \hat{T}_{ea} + \left( A_{21} - \frac{A_{23}A_{11}}{A_{13}} \right) \hat{T}_{sky} + \left( B_{21} - \frac{B_{11}A_{23}}{A_{13}} \right) \frac{\alpha \hat{\varphi}_s}{(h_{e,r} + h_{e,c})} \quad (20)$$

It is possible to demonstrate that in Eq. (20) the multiplicative complex terms of the three loadings are a function of the periodic thermal transmittance  $Y_{12}$ , evaluated according to the Standard procedure considering only the oscillation of the external air temperature as the load. Eq. (20) can be expressed as:

$$\hat{\varphi}_i = Y_{ea}^i \hat{T}_{ea} + Y_{sky}^i \hat{T}_{sky} + Y_s^i \alpha \hat{\varphi}_s \quad (21)$$

With the parameters  $Y^i$  given by the relations:

$$Y_{ea}^i = \frac{h_{c,e}}{h_{c,e} + h_{r,e}} Y_{12} \quad (22)$$

$$Y_{sky}^i = \frac{h_{r,e}}{h_{c,e} + h_{r,e}} Y_{12} \quad (23)$$

$$Y_s^i = \frac{1}{h_{c,e} + h_{r,e}} Y_{12} \quad (24)$$

The peak power per area unit which is transferred indoors  $\varphi_{i,p}$  is given by the sum of the steady component  $\bar{\varphi}_i$  and by the amplitude of the fluctuating component, obtained as the maximum value of the sum of all the harmonics:

$$\varphi_{i,p} = \bar{\varphi}_i + \max_{0 \leq t \leq P} \left( \sum_{k=1}^{10} \tilde{\varphi}_{i,k} \right) \quad (25)$$

With regards to the calculation of the energy that penetrates the indoor environment during the 24 hours, it is possible to identify two cases: case (a) (Figure 4) when the steady heat flux is greater than the maximum oscillating value in respect to the steady value and case (b) (Figure 5) when the peak of the oscillating heat flux in respect to the steady value is greater than the steady heat flux.

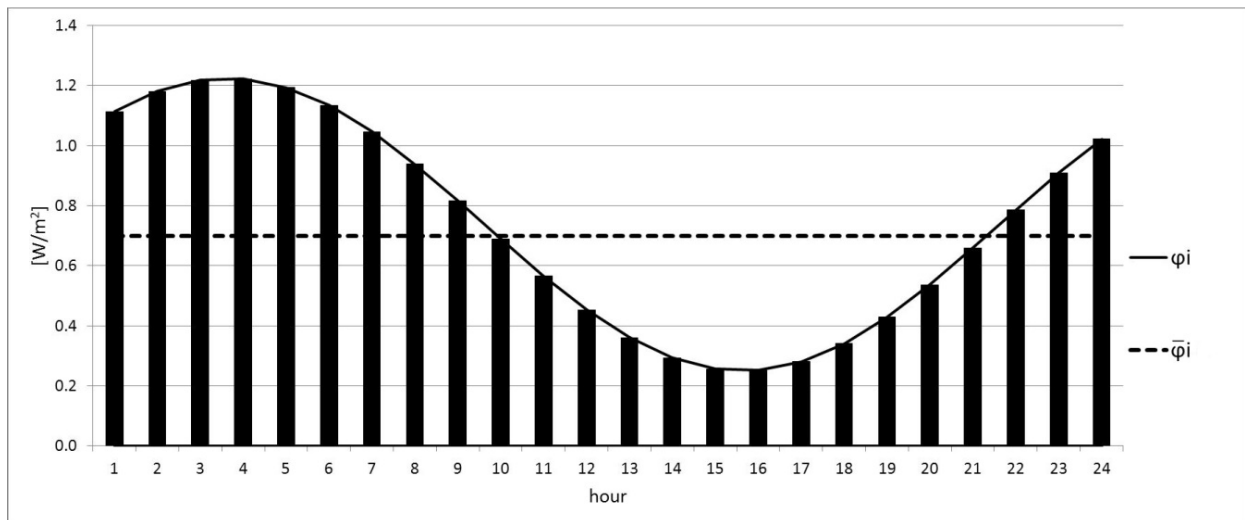


Figure 4. Temporal trend of the total internal heat flux  $\varphi_i$  and of the steady heat flux  $\bar{\varphi}_i$  in case (a).

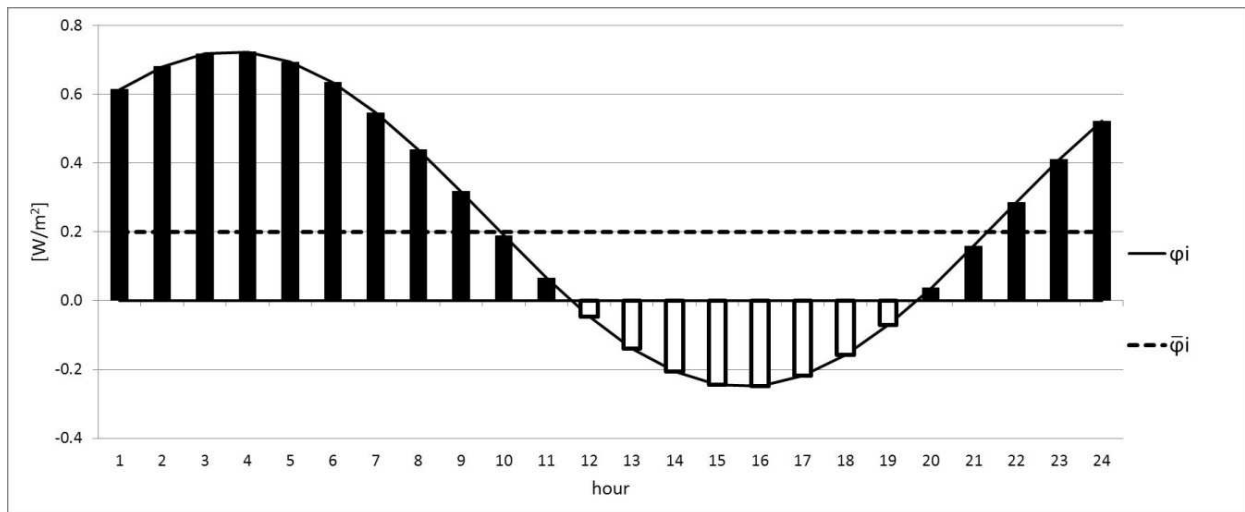


Figure 5. Temporal trend of the total internal heat flux  $\varphi_i$  and of the steady heat flux  $\bar{\varphi}_i$  in case (b).

In case (a) there is a compensation of the energy associated with the fluctuating components and therefore the daily energy is provided by one steady component.

In case (b) there is an inversion of the total heat flux and the total energy of the 24 hours is still given by the area subtended to the steady heat flux. The total entering energy and that exiting the environment can be distinguished and can be calculated respectively with the equations:

$$E_i^+ = \frac{\bar{E}_i}{2} + \tilde{E}_i \quad (26)$$

$$E_i^- = \frac{\bar{E}_i}{2} - \tilde{E}_i \quad (27)$$

with

$$\tilde{E}_i = \int_0^P \left| \sum_{k=1}^{10} \tilde{\varphi}_{ik} \right| dt / 2 \quad (28)$$

which represent the energy associated with the fluctuating component during a half period, while  $\bar{E}_i$  is the steady energy. Similarly, the total conductive heat flux entering the wall from the external side is equal to:

$$\hat{\varphi}_e = Y_{ea}^e \hat{T}_{ea} + Y_{sky}^e \hat{T}_{sky} + Y_s^e \alpha \hat{\varphi}_s \quad (29)$$

With the parameters  $Y_{ea}^e, Y_{sky}^e, Y_s^e$ , functions of the admittance on the external side  $Y_{22}$  determined according to the Standard, which can be calculated with the relations:

$$Y_{ea}^e = -\frac{h_{c,e}}{h_{c,e} + h_{r,e}} Y_{22} \quad (30)$$

$$Y_{sky}^e = -\frac{h_{r,e}}{h_{c,e} + h_{r,e}} Y_{22} \quad (31)$$

$$Y_s^e = -\frac{1}{h_{c,e} + h_{r,e}} Y_{22} \quad (32)$$

The comparison between the oscillating heat flux entering the wall (Eq. 29) and the heat flux transferred to the indoor environment (Eq. 21), allows for the evaluation of the decrement factor and time lag operated by the wall, while the difference between the two heat fluxes provides the variation of energy in the wall in the time unit. The following form can be given to the latter:

$$\Delta \hat{U} = Y_{ea}^u \hat{T}_{ea} + Y_{sky}^u \hat{T}_{sky} + Y_s^u \alpha \hat{\varphi}_s \quad (33)$$



with parameters  $Y_{ae}^u, Y_c^u, Y_s^u$ , determined by the periodic areal heat capacity on the external side of the wall indicated by the Standard with  $\kappa_2$ :

$$Y_{ea}^u = -\frac{h_{c,e}}{h_{c,e} + h_{r,e}} \frac{2 \pi}{P} \kappa_2 \quad (34)$$

$$Y_{sky}^u = -\frac{h_{r,e}}{h_{c,e} + h_{r,e}} \frac{2 \pi}{P} \kappa_2 \quad (35)$$

$$Y_s^u = -\frac{1}{h_{c,e} + h_{r,e}} \frac{2 \pi}{P} \kappa_2 \quad (36)$$

When the loads act externally, the building component will store a quantity of energy equal to:

$$\tilde{E}_u = \int_0^P \left| \sum_{k=1}^{10} \Delta \tilde{U}_k \right| dt / 2 \quad (37)$$

Resulting from a periodic variation of all harmonics of the three loads on the external side from  $-|\tilde{T}_{ea}|$  to  $|\tilde{T}_{ea}|$ , from  $-|\tilde{T}_{sky}|$  to  $|\tilde{T}_{sky}|$  and from  $-|\alpha\tilde{\varphi}_s|$  to  $|\alpha\tilde{\varphi}_s|$  during a half period.

A schematization of the dynamic parameters, which characterize the phenomenon when the periodic variations in temperature and in heat flux on the external side have unitary dimensions, is represented in Figure 6.

The ratio between the heat flux entering the internal environment and the conductive heat flux entering the wall, defined as the non-dimensional periodic global thermal transmittance  $\tau_G$  assumes the form:

$$\tau_G = \frac{\hat{\varphi}_i}{\hat{\varphi}_e} = \frac{Y_{ea}^i \hat{T}_{ea} + Y_{sky}^i \hat{T}_{sky} + Y_s^i \alpha \hat{\varphi}_s}{Y_{ea}^e \hat{T}_{ea} + Y_{sky}^e \hat{T}_{sky} + Y_s^e \alpha \hat{\varphi}_s} \quad (38)$$

The previous relations (Eqs. 22-24, Eqs. 30-32) lead to the equalities:

$$\frac{Y_{ea}^i}{Y_{ea}^e} = \frac{Y_{sky}^i}{Y_{sky}^e} = \frac{Y_s^i}{Y_s^e} \quad (39)$$

For which the expression of the non-dimensional periodic global thermal transmittance can be written as:

$$\tau_G = -\frac{Y_{12}}{Y_{22}} \quad (40)$$

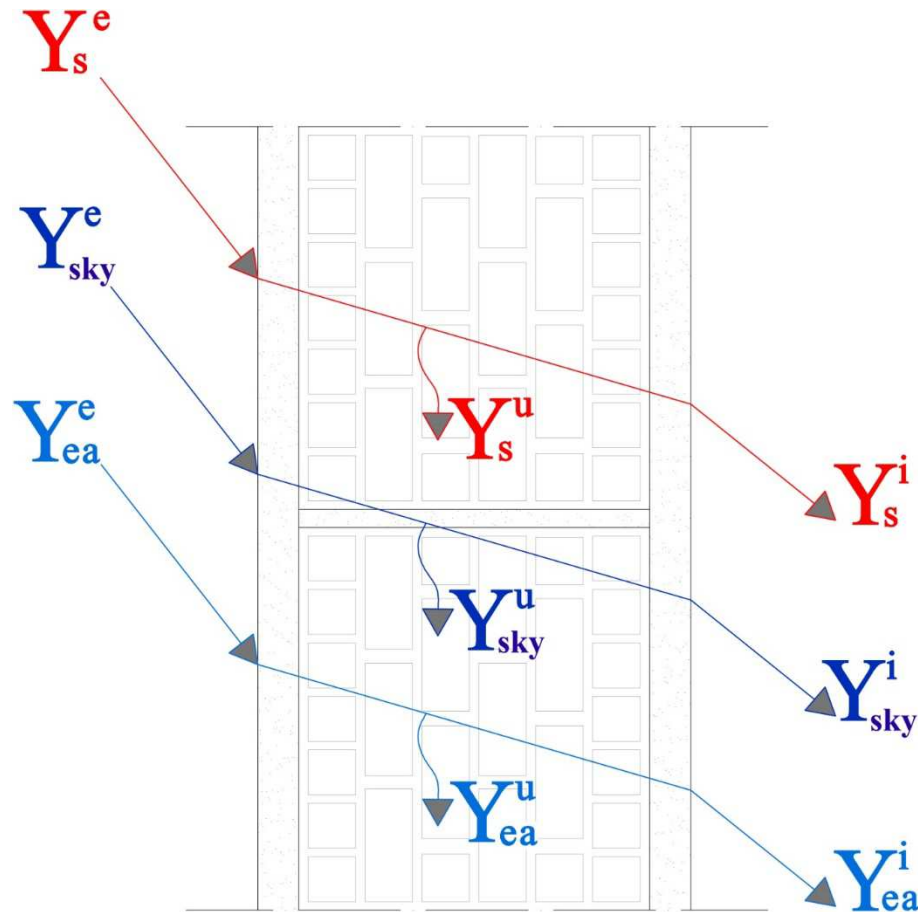


Figure 6. Representation of the dynamic parameters which intervene in the definition of the heat fluxes on two sides of the wall and the variation in internal energy in the time unit.

In order to characterize the thermal storage capacity of the wall it can be useful to evaluate the relation between the energy accumulated in the time unit and the entering heat flux, which represents the global periodic thermal storage efficiency of the wall:

$$\varepsilon_G = \frac{\Delta\hat{U}}{\hat{\varphi}_e} = 1 - \tau_G = \frac{\frac{2\pi}{P} \kappa_2}{Y_{22}} \quad (41)$$

The non-dimensional periodic global thermal transmittance  $\tau_G$  and the storage parameter  $\varepsilon$  are

evaluated using the periodic areal heat capacity  $\kappa_2$  and the admittance  $Y_{22}$ , both referred to the external side, and the periodic thermal transmittance  $Y_{12}$ , calculated following the Standard procedure.

It is possible, by means of the parameter  $\tau_G$ , to define the global decrement factor  $f_G$  and the global time lag  $\Delta t_G$  of the wall:

$$f_G = |\tau_G| ; \quad \Delta t_G = \frac{P}{2\pi} \arg(\tau_G) \quad (42)$$

The parameter  $\tau_G$ , when calculated considering reference boundary conditions, can be used for the dynamic characterization of building components in specification of product.

Furthermore, it can be used in the dynamic thermal analysis in real use conditions for the evaluation of the oscillating heat flux  $\tilde{\varphi}_i$ , of the internal energy variation  $\Delta\tilde{U}$  in the time unit, of the energy which is transferred to the indoor air  $\tilde{E}_i$  and of the energy stored by the wall  $\tilde{E}_u$ .

## 5. Behavior of some characteristic walls

The previous relations were used in order to determine the dynamic performance of the previously defined walls subjected to the joint action of the three loads.

This required the reconstruction of the external and internal heat flux trends, by means of the composition of harmonics, in such a way as to carry out the characterization and evaluation of the performance of the walls considered.

Starting from the characteristic parameters of the different harmonics, reported in Tables 1-3, and the values of the parameters  $Y^i$  (Eqs. 22-24) and the parameters  $Y^e$  (Eqs. 30-32), by means of the Eqs. (21) and (29) the conductive heat flux trend entering the external side of the wall and that transferred to the inside was reconstructed.

Specifically, the time trends of the first harmonic, and the sum of the harmonics up to the fifth in order to make a comparison with the trend which is obtained considering the sum of all the oscillations, were determined. The results obtained for the external  $\tilde{\varphi}_e$  and internal  $\tilde{\varphi}_i$  heat flux, for the four types of walls, are reported in Figure 7.

For all the walls, the fundamental harmonic is not sufficient to represent the trend of the conductive heat flux which penetrates the wall. It is necessary to consider at least two or more harmonics in order to obtain increased accuracy. Instead, with regards to the internal heat flux,

the use of the first two sinusoids always proves adequate.

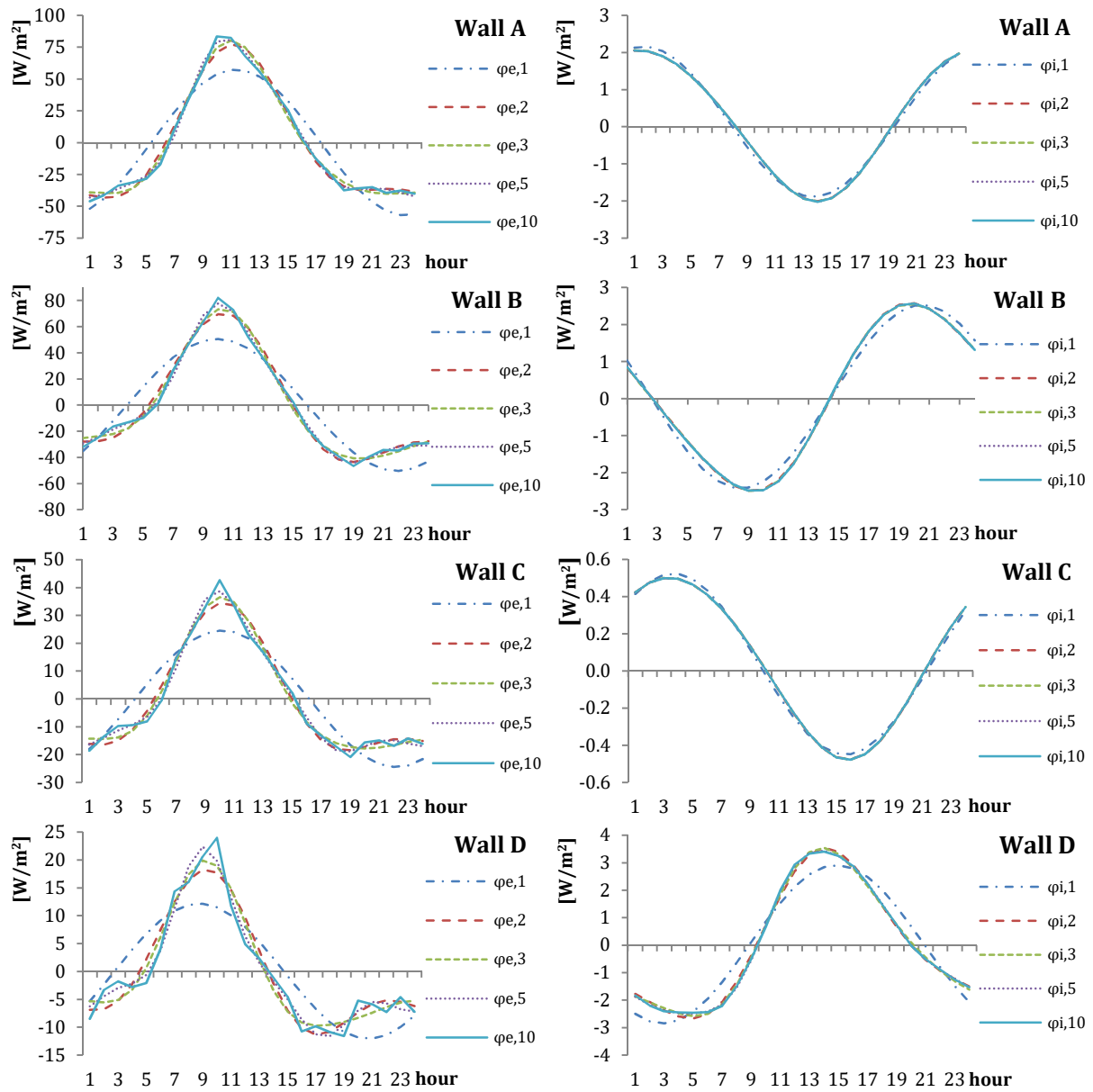


Figure 7. Internal heat flux and external conductive heat flux trend resultant from the harmonic composition for the walls A, B, C and D considered.

The non-dimensional periodic global thermal transmittance  $\tau_G$  (Eq. 40) and the relative dynamic parameters  $f_G$  and  $\Delta t_G$  (Eq. 42) were determined for each wall.

The results obtained for each individual harmonic are compared in Table 10.

Table 10. Amplitude and argument of the non-dimensional periodic global thermal transmittance  $\tau_G$  for each harmonic of the considered walls.

k-th harmonic	$\tau_G$							
	Wall A		Wall B		Wall C		Wall D	
	$f_G$ [-]	$\Delta t_G$ [h]	$f_G$ [-]	$\Delta t_G$ [h]	$f_G$ [-]	$\Delta t_G$ [h]	$f_G$ [-]	$\Delta t_G$ [h]
1	0.0354	14.31	0.0491	10.59	0.0199	17.45	0.2382	6.14
2	0.0072	9.91	0.0142	6.70	0.0029	0.30	0.1154	3.81
3	0.0022	0.002	0.0061	5.14	0.0007	2.01	0.0713	2.91
4	0.0008	0.87	0.0032	4.28	0.0002	2.64	0.0485	2.42
5	0.0003	1.31	0.0019	3.73	0.00007	2.91	0.0349	2.10
6	0.0002	1.55	0.0012	3.34	0.00002	3.02	0.0260	1.87
7	0.0001	1.69	0.0007	3.05	0.00001	3.06	0.0199	1.70
8	0.00004	1.77	0.0005	2.82	0.000004	0.06	0.0156	1.56
9	0.00002	1.82	0.0003	2.63	0.000002	0.37	0.0124	1.45
10	0.00001	1.85	0.0002	0.08	0.0000009	0.60	0.0100	1.35

In order to obtain the effective decrement factor and time lag it is necessary to arrange the results of the previous table.

The results of the deviation of the two parameters of the effective value obtained by arranging the different harmonics are reported in Table 11.

The table shows that with the first five harmonics it is possible to obtain a deviation of the effective global decrement factor at most of 10%, whereas with regard to the effective global time lag the reconstruction proves more random, in that the first two harmonics are necessary for walls B and C, and more than five for walls D and A.

From the analysis of the dynamic parameters, wall B proves to be that with the smallest global decrement factor and the highest global time lag.

The comparison between the dynamic parameter values of Tables 7 and 10 shows that the characterization of the walls in the effective conditions of use differs from that obtained only considering temperature oscillation, which provides only qualitative type indications.

The effectiveness of this analysis, for the evaluation of the dynamic performance of the walls, is shown by the comparison between the internal and external heat flux trend, obtained composing the steady heat flux with the oscillating heat flux, reported in Figure 8.

In such a way it is possible to evaluate the instant and the peak value of the heat flux which penetrates the wall and the instant and the corresponding maximum heat flux value which is transferred to the indoor environment. Specifically, walls A and B, with higher steady thermal transmittance, prove to have a greater heat flux which penetrates from the external surface of the wall, while wall D, characterized by lower steady thermal transmittance, presents a more reduced

heat flux on the external side. The heat flux which is transferred to the indoor environment is determined by the dynamic properties of the walls.

Table 11. Deviations from the effective global decrement factor and time lag value obtained composing the harmonics.

	$f_G$ [-]	$(f_G - f_{G,\Sigma})/f_{G,\Sigma}$ [%]	$\Delta t_G$ [h]	$(\Delta t_G - \Delta t_{G,\Sigma})/\Delta t_{G,\Sigma}$ [%]
Wall A				
1	0.0354	53.51	15	0
$\Sigma$ 1-2	0.0249	7.97	14	-6.67
$\Sigma$ 1-3	0.0240	4.06	14	-6.67
$\Sigma$ 1-5	0.0238	3.27	14	-6.67
$\Sigma$ 1-10	0.0230	0	15	0
Wall B				
1	0.0491	60.25	11	10
$\Sigma$ 1-2	0.0362	18.38	10	0
$\Sigma$ 1-3	0.0341	11.29	10	0
$\Sigma$ 1-5	0.0323	5.57	10	0
$\Sigma$ 1-10	0.0306	0	10	0
Wall C				
1	0.0199	83.10	18	5.88
$\Sigma$ 1-2	0.0134	23.46	17	0
$\Sigma$ 1-3	0.0127	16.68	17	0
$\Sigma$ 1-5	0.0120	10.11	17	0
$\Sigma$ 1-10	0.0109	0	17	0
Wall D				
1	0.2382	68.92	6	50
$\Sigma$ 1-2	0.1919	36.07	5	25
$\Sigma$ 1-3	0.1770	25.49	5	25
$\Sigma$ 1-5	0.1524	8.07	5	25
$\Sigma$ 1-10	0.1410	0	4	0

The variation of the internal energy in the time unit, formed through the sum of the various harmonic components, given that the steady component is null, is shown in Figure 9. Also in this case, the heat storage entity is closely linked to the steady areal heat capacity and to the quantity of energy that penetrates the wall, and therefore the considerations made previously are valid.

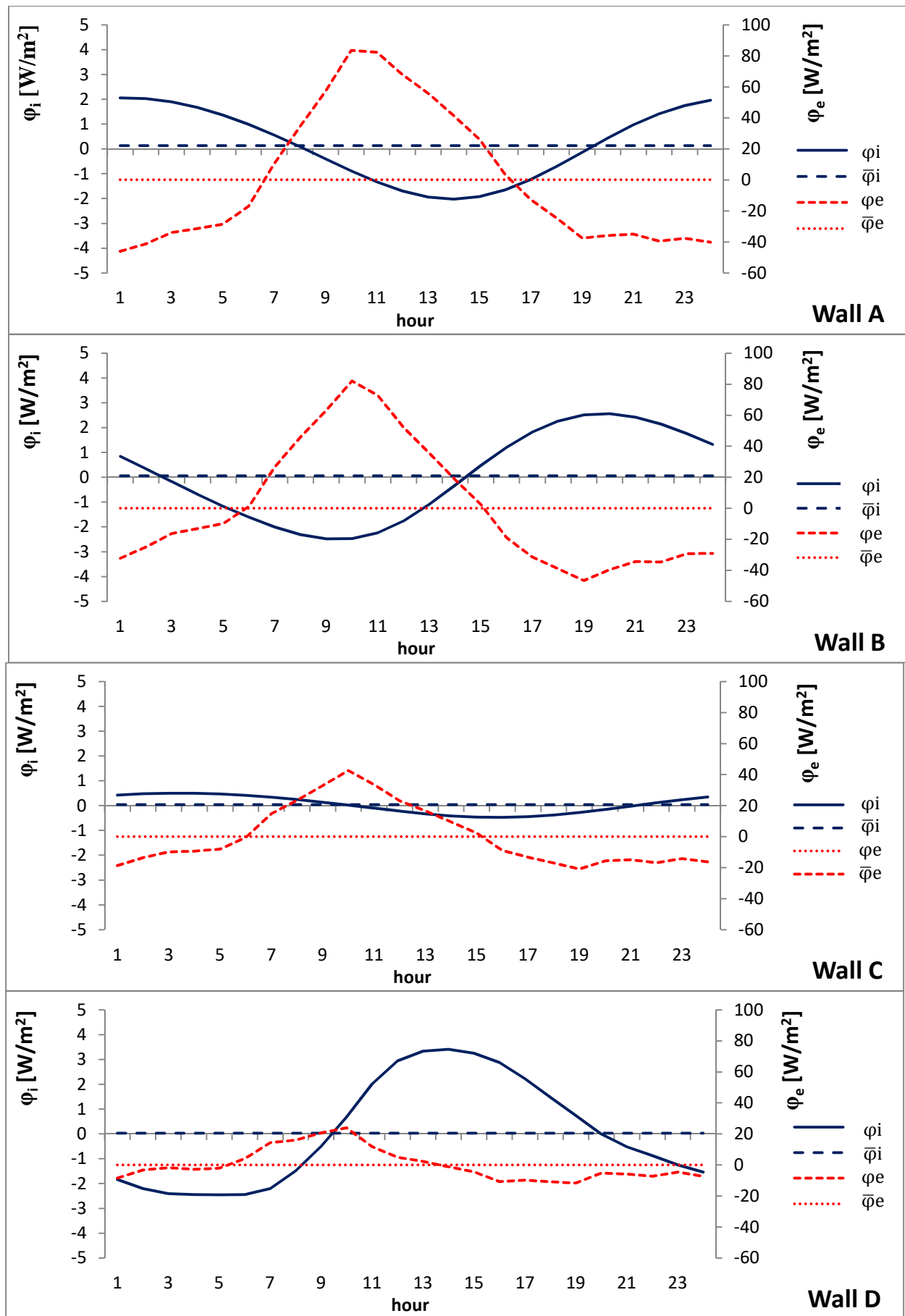


Figure 8. Trend of the internal heat flux  $\phi_i$  and of the external conductive heat flux  $\phi_e$ , and value of the steady heat

flux  $\bar{\varphi}_i = \bar{\varphi}_e$  for the four types of walls considered.

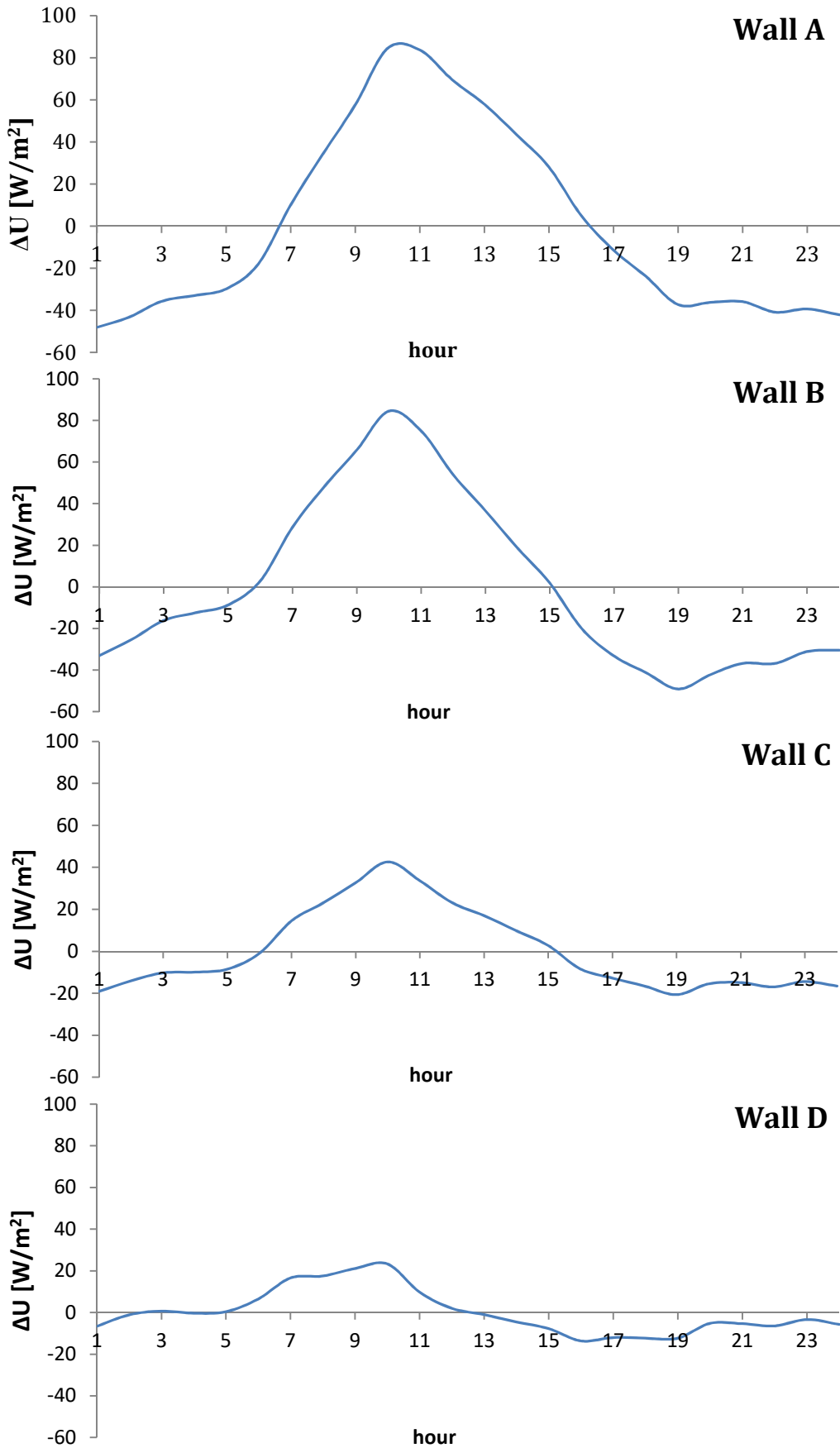




Figure 9. Variation in the internal energy in the time unit  $\Delta U$  for the four walls considered.

For the walls considered, the steady and dynamic parameters necessary for the evaluation of the total energy entering and exiting the internal environment are reported in Table 12.

Table 12. Steady internal heat flux  $\bar{\varphi}_i$ , maximum heat flux associated with the fluctuating components of the internal heat flux  $\max_{0 \leq t \leq P} (\sum_{k=1}^{10} \tilde{\varphi}_{i,k})$ , steady energy which enters the environment  $\bar{E}_i$ , fluctuating energy in a semiperiod which enters the internal environment  $\tilde{E}_i$ , total entering energy  $E_i^+$  and total exiting energy  $E_i^-$  in the case of inversion of the heat flux and stored energy  $\tilde{E}_u$  for the four walls considered.

	Wall A	Wall B	Wall C	Wall D
$\bar{\varphi}_i$ [W/m <sup>2</sup> ]	0.136	0.055	0.037	0.034
$\max_{0 \leq t \leq P} \left( \sum_{k=1}^{10} \tilde{\varphi}_{i,k} \right)$ [W/m <sup>2</sup> ]	2.056	2.508	0.463	3.376
$\bar{E}_i$ [kJ/m <sup>2</sup> ]	11.73	4.77	3.23	2.94
$\tilde{E}_i$ [kJ/m <sup>2</sup> ]	55.79	68.47	13.44	81.44
$E_i^+$ [kJ/m <sup>2</sup> ]	61.65	70.86	15.06	82.91
$E_i^-$ [kJ/m <sup>2</sup> ]	-49.93	-66.09	-11.83	-79.97
$\tilde{E}_u$ [kJ/m <sup>2</sup> ]	1706.37	1497.91	717.65	351.83

The comparison between the internal steady heat flux  $\bar{\varphi}_i$  and the maximum heat flux associated with the oscillating components of the internal heat flux  $\max_{0 \leq t \leq P} (\sum_{k=1}^{10} \tilde{\varphi}_{i,k})$  shows that the heat flux entering into the environment through the walls considered present an inversion. The energy associated with the time interval in which the total heat flux is entering the environment was calculated with Eq. 26 and the exiting energy was calculated with eq. 27. Table 11 shows that the steady energy  $\bar{E}_i$  is notably reduced compared to the fluctuating energy in a semi-period  $\tilde{E}_i$ .

Wall D presents the least stored energy  $\tilde{E}_u$  and the highest peak of the internal heat flux value  $\max_{0 \leq t \leq P} (\sum_{k=1}^{10} \tilde{\varphi}_{i,k})$ , confirming that it is the least suitable wall during summer functioning.

## 6. Comparison and validation

The dynamic model for the analysis of multilayered building components was tested by means of a finite difference numerical model. This model approximates the differential equation of monodimensional transitory thermal conduction by a system of algebraic equations of nodal thermal balance solved using the implicit method [24]. Specifically, the trends of the external heat flux entering the wall were compared with the heat flux transferred to the air-conditioned environment, calculated analytically using the previously defined dynamic parameters and numerically using a nonuniform spatial discretization that involves 18 nodes and a time-step of an hour.

The comparison was made considering the wall subjected individually and simultaneously to the action of the loads  $T_{ea}$ ,  $T_{sky}$  and  $\alpha\varphi_s$ .

As a test wall reference was made to the wall B type, representative of the residential building walls, whose characteristics are shown in Table 5.

### 6.1 Analysis of the dynamic response of a hollow-wall to single loadings

The analytical evaluation of the external and internal heat fluxes was obtained considering the individual loads using the relations:

- a) external air temperature load

$$\varphi_{e,c} = \bar{\varphi}_{e,c} + \sum_{k=1}^{10} \tilde{\varphi}_{e,c_k} \quad (43)$$

$$\varphi_{i,ea} = \bar{\varphi}_{i,ea} + \sum_{k=1}^{10} \tilde{\varphi}_{i,ea_k} \quad (44)$$

The oscillating components were obtained solving the matrix equation Eq. 3 for each harmonic that supplies the expressions:

$$\hat{\varphi}_{e,c} = \frac{1}{S_{22,ea}} \hat{\varphi}_{i,ea} - \frac{S_{21,ea}}{S_{22,ea}} \hat{T}_{ea} \quad (45)$$

$$\hat{\varphi}_{i,ea} = -\frac{1}{S_{12,ea}} \hat{T}_{ea} = Y_{12,ea} \hat{T}_{ea} \quad (11)$$

for the steady components

$$\bar{\varphi}_{e,c} = \bar{\varphi}_{i,ea} = U_{ea} (\bar{T}_{ea} - \bar{T}_{ia,ea}) \quad (46)$$

with  $U_{ea}$  previously defined.

b) apparent sky temperature load

$$\varphi_{e,r} = \bar{\varphi}_{e,r} + \sum_{k=1}^{10} \tilde{\varphi}_{e,rk} \quad (47)$$

$$\varphi_{i,sky} = \bar{\varphi}_{i,sky} + \sum_{k=1}^{10} \tilde{\varphi}_{i,skyk} \quad (48)$$

by solving the matrix equation Eq. (4) the following expressions are obtained for each harmonic:

$$\hat{\varphi}_{e,r} = \frac{1}{S_{22,sky}} \hat{\varphi}_{i,sky} - \frac{S_{21,sky}}{S_{22,sky}} \hat{T}_{sky} \quad (49)$$

$$\hat{\varphi}_{i,sky} = -\frac{1}{S_{12,sky}} \hat{T}_{sky} = Y_{12,sky} \hat{T}_{sky} \quad (12)$$

for the steady components

$$\bar{\varphi}_{e,r} = \bar{\varphi}_{i,sky} = U_{sky} (\bar{T}_{sky} - \bar{T}_{ia,sky}) \quad (50)$$

with  $U_{sky}$  previously defined.

c) solar irradiation load

$$\varphi_{e,s} = \alpha \bar{\varphi}_s + \sum_{k=1}^{10} \alpha \tilde{\varphi}_{s_k} \quad (51)$$

$$\varphi_{i,s} = \bar{\varphi}_{i,s} + \sum_{k=1}^{10} \tilde{\varphi}_{i,s_k} \quad (52)$$

The matrix equation Eq. 4 supplies the following expression for each harmonic:

$$\hat{\varphi}_{i,s} = \frac{1}{S_{11,s}} \alpha \hat{\varphi}_s = Y_{11,s} \alpha \hat{\varphi}_s \quad (13)$$

The steady component  $\alpha \bar{\varphi}_s = \bar{\varphi}_{i,s}$  is the mean of the incident solar radiation absorbed by the wall.

Figures 10, 11 and 12 show the trends of the external and internal heat fluxes calculated analytically and numerically.

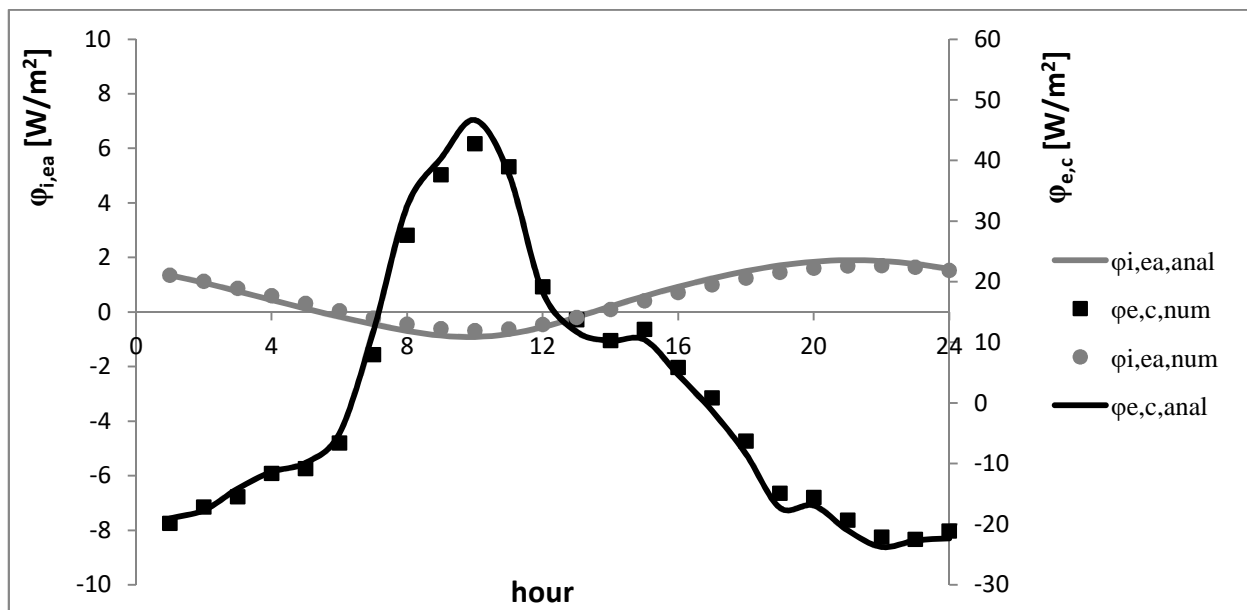


Figure 10. External air temperature load. Comparison of the trend of the external convective heat flux with the internal heat flux calculated using the analytical model and using the numerical model.

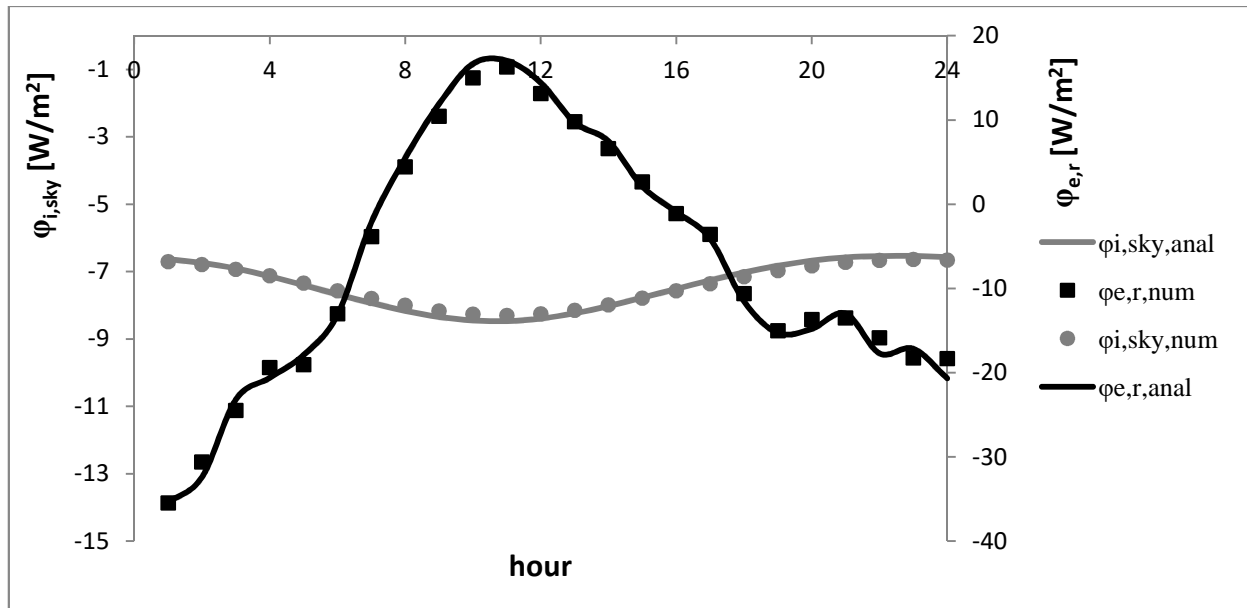


Figure 11. Apparent sky temperature load. Comparison of the trend of the external radiative heat flux with the internal heat flux calculated using the analytical model and using the numerical model.

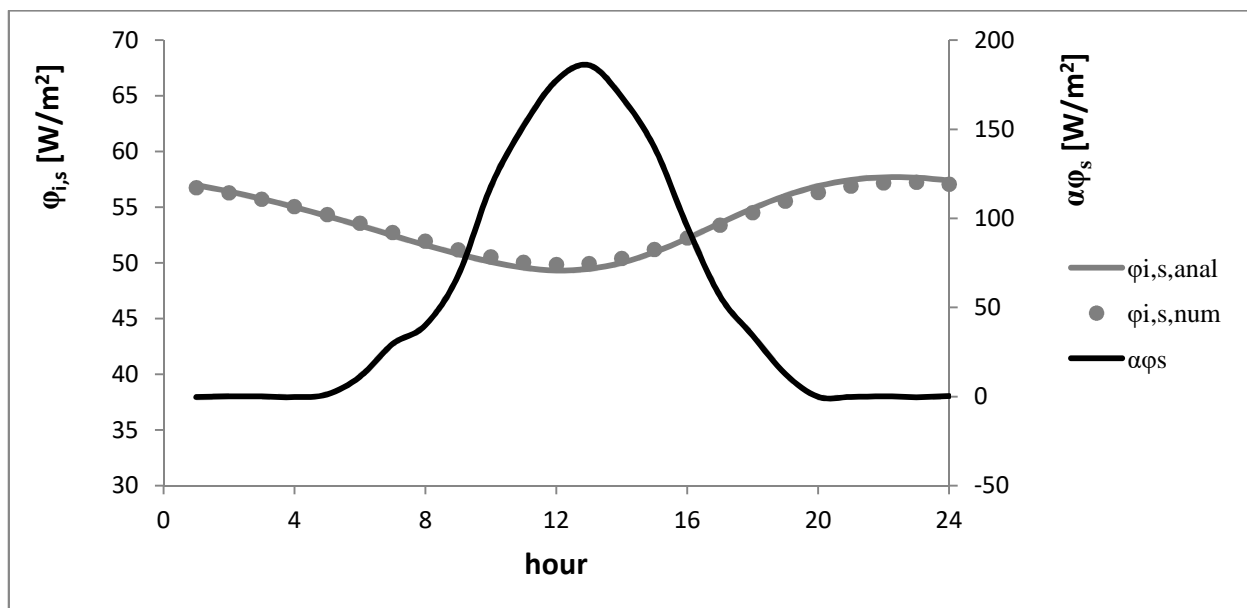


Figure 12. Solar irradiation load. Comparison of the trend of the external absorbed solar heat flux with the internal heat flux calculated using the analytical model and using the numerical model.

The numerical values follow perfectly the trends obtained analytically and the slight deviations can be reduced by increasing the number of nodes and reducing the integration step.

## 6.2 Analysis of the dynamic response of a hollow-wall under the contemporaneous action of the three loads

The relations for the calculation of the external flux  $\varphi_e$  and the internal flux  $\varphi_i$  have the form:

$$\varphi_e = \bar{\varphi}_e + \sum_{k=1}^{10} \tilde{\varphi}_{e_k} \quad (53)$$

$$\varphi_i = \bar{\varphi}_i + \sum_{k=1}^{10} \tilde{\varphi}_{i_k} \quad (54)$$

The fluctuating components  $\hat{\varphi}_e$  and  $\hat{\varphi}_i$  are obtained solving the matrix system (Eq. 19) and are obtainable respectively using Eqs. (29) and (21).

The steady heat flux is given by the relation:

$$\bar{\varphi}_e = \bar{\varphi}_i = \frac{(\bar{T}_2 - \bar{T}_1)}{\sum R} \quad (55)$$

with  $\bar{T}_1$  and  $\bar{T}_2$  mean steady internal and external surface temperatures and  $\sum R$  sum of the conductive resistances of the wall layers. The temperatures  $\bar{T}_1$  and  $\bar{T}_2$  were determined solving the electric circuit of Figure 3 without capacitors and are equal to:

$$\bar{T}_1 = \frac{\alpha \bar{\varphi}_s + h_i \bar{T}_{ia} + h_{e,c} \bar{T}_{ea} + h_{e,r} \bar{T}_{sky} + h_i \bar{T}_{ia} \sum R (h_{e,c} + h_{e,r})}{h_i + h_{e,c} + h_{e,r} + h_i \sum R (h_{e,c} + h_{e,r})} \quad (56)$$

$$\bar{T}_2 = h_i (\bar{T}_1 - \bar{T}_{ia}) \sum R + \bar{T}_1 \quad (57)$$

Figure 13 compares the trends of the entering and exiting heat fluxes of the wall calculated analytically and numerically.

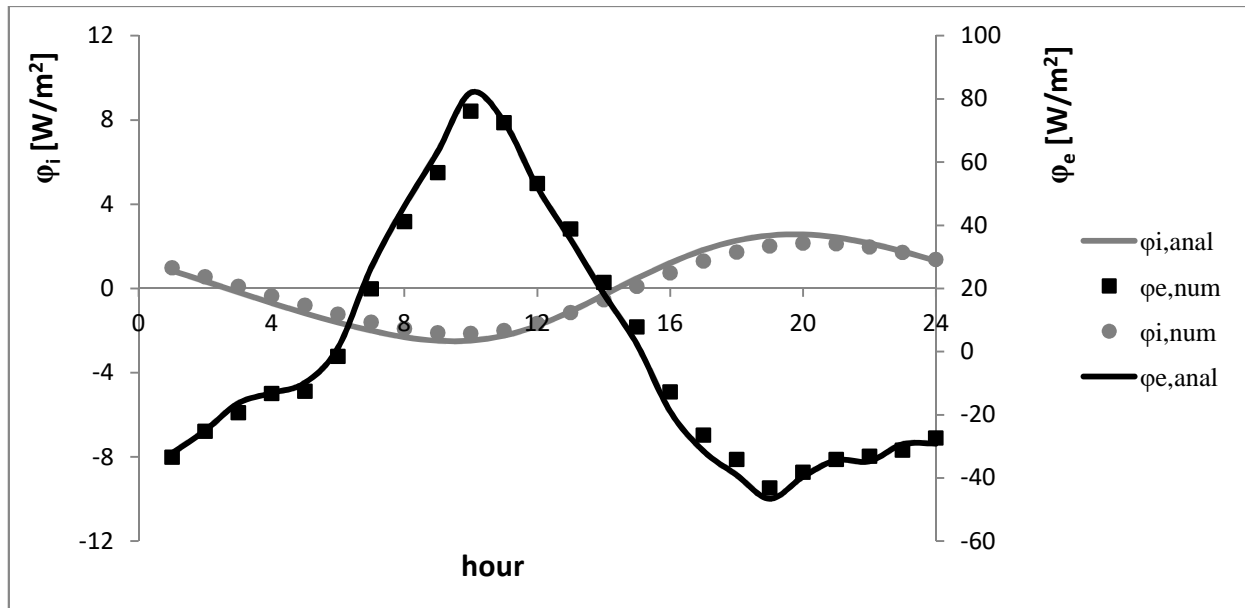


Figure 13. Contemporaneous action of the loads  $T_{ea}$ ,  $T_{sky}$ ,  $\alpha\phi_s$ . Comparison of the trend of the external and internal heat fluxes calculated using the analytical model and using the numerical model.

An excellent agreement is found also in this case between the two trends and this demonstrates that the analytical model and the relative dynamic parameters defined are suitable to describe the thermal behavior of the wall in real conditions of use.

## 7. Conclusions

An accurate analysis of the thermal behavior of external walls of buildings in a steady periodic regime by the harmonic method, considering the external air temperature, the apparent sky temperature and solar irradiation as loads, was developed.

The simplification adopted by the Standard EN ISO 13786, which provides for the schematizing of the outdoor environment by means of a temperature oscillation period equal to 24 hours, does not prove adequate for the evaluation of the dynamic characteristics of the building components. For example, the characterization of solar radiation requires the determination of the non-dimensional periodic solar thermal transmittance.

The evaluation of the conductive heat flux which penetrates the wall at the interface with the external air and of the heat flux which is transferred to the environment, by means of the simultaneous action of the three loads considered, led to the definition of the non-dimensional periodic global thermal transmittance.

This parameter allows for the calculation of the global decrement factor and time lag which is

undergone by the heat flux when it crosses the wall, the stored energy, the peak power which is transferred to the internal environment, and the energies which enter and exit the environment in the case of inversion of the heat flux at the internal air interface.

The analysis highlighted that the preceding quantities can be evaluated by means of the periodic areal thermal capacity and the periodic thermal admittance, both referring to the external side, and the periodic thermal transmittance, calculated considering only the external air temperature as load.

The non-dimensional periodic global transmittance can be used for the characterization of building components in specifications of product and as calculation parameter in dynamic regime thermal analysis.

The newly defined parameters were used to compare the thermal performance in a dynamic regime of some types of commonly used walls.

The calculation method was tested by means of a comparison of the entering and exiting heat fluxes of a typical wall calculated analytically and numerically.

## References

- [1] Directive 2002/91/EC of the European Parliament and of the Council on the energy performance of buildings, December 2002.
- [2] Directive 2010/31/UE of the European Parliament and of the Council on the energy performance of buildings (recast), May 2010.
- [3] EN ISO 13790, Energy performance of buildings - Calculation of energy use for space heating and cooling, 2008.
- [4] Youming Chen, Shengwei Wang, A new procedure for calculating periodic response factors based on frequency domain regression method, *International Journal of Thermal Sciences* 44 (2005), pp. 382-392.
- [5] Xinhua Xu, Shengwei Wang, A simplified dynamic model for existing buildings using CTF and thermal network models, *International Journal of Thermal Sciences* 47 (2008), pp. 1249-1262.
- [6] Shengwei Wang, Xinhua Xu, Simplified building model for transient thermal performance estimation using GA-based parameter identification, *International Journal of Thermal Sciences* 45 (2006), pp. 419-432.
- [7] G. Fraisse, C. Viardot, O. Lafabrie, G. Achard, Development of a simplified and accurate building model based on electrical analogy, *Energy and Buildings* 34 (2002), pp. 1017 - 1031.



- [8] M. Ciampi, F. Leccese, G. Tuoni, Multi-layered walls design to optimize building-plant interaction, *International Journal of Thermal Sciences* 43 (2004), pp. 417-429.
- [9] N. Daouas, A study on optimum insulation thickness in walls and energy savings in Tunisian buildings based on analytical calculation of cooling and heating transmission loads, *Applied Energy* 88 (2011), pp. 156-164.
- [10] H. Asan, Y.S. Sancaktar, Effect of Wall's thermophysical properties on time lag and decrement factor, *Energy and Buildings* 28 (1998), pp. 159 -166.
- [11] H. Asan, Effect of Wall's insulation thickness and position on time lag and decrement factor, *Energy and Buildings* 28 (1998), pp. 299 -305.
- [12] H. Asan, Investigation of wall's optimum insulation position from maximum time lag and minimum decrement factor point of view, *Energy and Buildings* 32 (2000), pp. 197-203.
- [13] H. Asan, Numerical computation of time lags and decrement factors for different building materials, *Building and Environment* 41 (2006), pp. 615-620.
- [14] A.D. Granja, L.C. Labaki, Influence of external surface colour on the periodic heat flow through a flat solid roof with variable thermal resistance, *Int. J. Energy Res.* 27 (2003), pp. 771-779.
- [15] J. Sykora, J. Vorel, T. Krejci, M. Sejnoha, J. Sejnoha, Analysis of coupled heat and moisture transfer in masonry structures, *Materials and Structures* 42 (2009), pp. 1153–1167.
- [16] Changhai Peng, Zhishen Wu, Thermoelectricity analogy method for computing the periodic heat transfer in external building envelopes, *Applied Energy* 85 (2008), pp. 735-754.
- [17] F. Varela, F. J. Rey, E. Velasco, S. Aroca, The harmonic method: A new procedure to obtain wall periodic cross response factors, *International Journal of Thermal Sciences* 58 (2012), pp. 20 - 28.
- [18] EN ISO 13792, Thermal performance of buildings - Calculation of internal temperatures of a room in summer without mechanical cooling - Simplified methods (2012).
- [19] EN ISO 13786, Thermal performance of buildings components - Dynamic thermal Characteristics - Calculation methods (2010).
- [20] M. G. Smart, J. A. Ballinger, Fourier-synthesized weather data for building energy use estimation, *Building and Environment* 19 (1984), pp. 41 - 48.
- [21] E. Kreyszig, *Advanced Engineering Mathematics*, John Wiley & Sons, INC, Seventh Edition, Singapore (1993).
- [22] H. S. Carslaw, J.C. Jaeger, *Conduction of Heat in Solids*, second edition, Oxford Science Publications (1988).

[23] G. Oliveti, N. Arcuri, M. De Simone, R. Bruno, Experimental evaluations of the building shell radiant exchange in clear sky conditions, *Solar Energy* 86 (2012), pp. 1785-1795.

[24] W. M. Rohsenow, J.P.Hartnett, *Handbook of heat transfer*, Mc Graw Hill Book Company, USA (1973).

## Nomenclature

a	thermal diffusivity [ $\text{m}^2/\text{s}$ ]
[A]	heat transfer matrix considering the contemporaneous action of the three loads
[B]	heat transfer matrix considering the contemporaneous action of the three loads
C	steady areal heat capacity [ $\text{J}/\text{m}^2 \text{K}$ ]
d	thickness of the layer [m]
E	thermal energy [ $\text{J}/\text{m}^2$ ]
f	decrement factor [-]
h	heat transfer coefficient [ $\text{W}/\text{m}^2\text{K}$ ]
k	harmonic order [-]
P	period of oscillation [s]
R	thermal resistance [ $\text{m}^2\text{K}/\text{W}$ ]
$S_{mn}$	element of the heat transfer matrix from environment to environment considering the individual loads
t	time [s]
T	temperature [K]
U	steady thermal transmittance [ $\text{W}/\text{m}^2\text{K}$ ]
y	thermal quantity
$Y_{22}$	periodic thermal admittance on external side wall [ $\text{W}/\text{m}^2\text{K}$ ]
$Y_{11}$	non-dimensional periodic solar thermal transmittance [-]
$Y_{12}$	periodic thermal transmittance [ $\text{W}/\text{m}^2\text{K}$ ]
[Z]	heat transfer matrix of the multilayered wall from surface to surface
$Z_{mn}$	element of the heat transfer matrix of a generic layer

### *Greek symbols*

$\alpha$	absorption coefficient [-]
$\delta$	periodic penetration depth of a heat wave in a material [m]
$\Delta t$	time lag [s]

---

$\Delta U$	instantaneous internal energy variation [W/m <sup>2</sup> ]
$\varepsilon$	periodic efficiency of thermal accumulation [-]
$\kappa$	periodic areal heat capacity [J/m <sup>2</sup> K]
$\lambda$	thermal conductivity [W/m K]
$\xi$	ratio of the thickness of the layer to the periodic penetration depth [-]
$\tau$	non-dimensional periodic thermal transmittance [-]
$\varphi$	heat flux [W/m <sup>2</sup> ]
$\psi$	argument of the thermal quantity oscillation [rad]
$\omega$	angular frequency of the variations [rad/s]

*Subscripts*

anal	analytical
A	brick wall
B	hollow wall
c	convective
C	polarized brick wall
D	prefabricated wall
e	external
ea	referring to the external air loading
G	global, referred to the three loadings
i	internal
ia	internal air
k	k-th harmonic
m	m-th row
n	n-th column
N	N-th layer
num	numerical
p	peak value
Plant	plant
r	radiative
s	referring to the solar load
sky	referring to the sky load
$\Sigma$	referring to the sum of all the harmonics
1	internal side wall

2 external side wall

*Superscripts*

+ entering  
- outgoing  
e external  
i internal  
u accumulated

*Symbols*

– mean value  
~ oscillating value in the time domain  
^ oscillating value in the complex domain  
|| amplitude of an oscillating value  
arg argument of an oscillating value

# Chapter 2

## **Influence of internal and external boundary conditions on the decrement factor and time lag heat flux of building walls in steady periodic regime**

### **Abstract**

The dynamic behaviour of opaque components of the building envelope in steady periodic regime is investigated using parameters defined by the fluctuating heat flux that is transferred in the wall. The use of the heat flux allows for the joint action of the loadings that characterise both the outdoor environment and the indoor air-conditioned environment to be taken into account.

The analysis was developed in sinusoidal conditions to determine the frequency response of the wall and in non-sinusoidal conditions to identify the actual dynamic behaviour of the wall. The use of non-dimensional periodic thermal transmittance is proposed for the sinusoidal analysis in order to evaluate the decrement factor and the time lag that the heat flux undergoes in crossing

the wall as well as the efficiency of heat storage.

In the presence of non-sinusoidal loadings, the identification of the dynamic behaviour of the wall is obtained using several dynamic parameters: the decrement factor in terms of energy, defined as the ratio between the energy in a semi-period entering and exiting the wall; the decrement factor and the time lag in terms of heat flux, considering the maximum peak and the minimum peak. These parameters allow for the identification of how the form of the heat flux trend crossing the wall is modified.

The number of harmonics to be considered for an accurate representation of heat fluxes is determined by means of the introduction of the Total Harmonic Distortion (THD), which quantifies the distortion of a non-sinusoidal periodic trend compared to a sinusoidal trend.

The methodology developed was used to evaluate the influence of external and internal loadings on the dynamic characteristics of two commonly used walls on a monthly and seasonal basis. The external loadings were changed considering two climatically different locations and different orientations of the walls, the internal loadings were changed by varying the operating mode of the plant and the shortwave radiative heat fluxes contributions on the inner surface.

Keywords: Building wall; Dynamic thermal behaviour; Non-sinusoidal periodic fluctuation; Heat flux; Time lag; Decrement factor

- Dynamic behaviour of building walls subjected to sinusoidal and actual loadings.
- The joint action of more temperature and heat flux loadings has been considered.
- Dynamic parameters were defined by the internal and external fluctuating heat flux.
- Use of the Total Harmonic Distortion to determine the number of harmonics required.
- Study of the influence of external and internal loadings on dynamic parameters.

*Non so come io appaia al mondo, ma per quel che mi riguarda, mi sembra d'essere stato soltanto come un fanciullo sulla spiaggia che si diverte nel trovare qua e là una pietra più liscia delle altre o una conchiglia più graziosa, mentre il grande oceano della verità giace del tutto inesplorato davanti a me.*

*(Isaac Newton)*

## 1. Introduction

Energy efficiency is a valuable tool to limit the use of primary energy in processes and in end use, with benefits in terms of reducing greenhouse gas emissions, of dependence on energy from abroad, as well as economic terms.

European Directive 2010/31/EU [1] on the energy performance of buildings and the subsequent 2012/27/EU [2], on measures to promote energy efficiency, reinforced studies and research for the development of innovative technological solutions to achieve a reduction in total energy consumption.

Buildings, due to their high energy needs, mainly due to winter heating and summer cooling, represent one of the sectors most involved in the reduction of energy consumption and the use of energy from renewable sources to achieve the target of nearly/net zero energy balance.

In [3] Lu et al. have presented a comprehensive review on the issues related to the design and control of the Nearly/net zero energy buildings (nZEBs), i.e. the effects of climate/site on design, design optimization methods, uncertainty and sensitivity analysis for robust design and system reliability, efficient and optimal control of high efficient generation systems and energy storage systems for alleviating/shifting the peak load, model predictive control for fast responses to the smart grid, and the adoption of advanced smart technologies.

In order to realize these buildings, the recent literature proposes innovative technological solutions that concern the stratigraphy of walls and the windows, through the use of phase change materials [4-6], of new silica aerogel-based insulating [7, 8], of green vertical system [9, 10] and of green and cool roofs [11-16], and the use of heat sources which employ solar radiation and geothermal [17-19].

The need to reduce energy consumption occurs significantly in existing buildings [20] and in historic buildings, where the necessity to preserve architectural heritage does not allow typical invasive retrofit interventions [21-25].

In particular, the thermal exchanges through the envelope contribute significantly to the determination of energy requirements that the plant must supply. Their reduction requires a correct evaluation of the dynamic characteristics of opaque envelope components considering actual boundary conditions.

The dynamic thermal characterisation of a building component is obtained by parameters that identify its thermal behaviour when it is subjected to loadings that are variable in time. The reference standard EN ISO 13786 [26] describes the thermal exchange in a steady periodic

regime between the indoor environment and the outdoor environment by means of a matrix formulation, which allows for the calculation of the periodic thermal transmittances, used to evaluate the decrement factor and time lag, the periodic thermal admittances and the areal heat capacities.

These parameters are determined by considering a sinusoidal variation of the external air temperature of unitary amplitude and period equal to 24 hours, convective-radiative heat transfer coefficients for the external and internal surface heat exchanges and the internal air temperature constant. These quantities are used by technical regulations to verify the dynamic performance of the envelope, in order to limit the energy requirements in summer air conditioning, and as product specifications.

If a cavity is considered, the thermal dynamic parameters of the walls are used, together with the surface factor, for the calculation of the summer internal temperature according to EN ISO 13792 [27], or according to the general model proposed by [28].

In recent literature, the study of the thermal dynamic properties of walls in a steady periodic regime has been the subject of increasing interest. Numerous studies have been conducted for multilayer walls in a steady periodic regime with the aim of evaluating the influence of thermophysical properties of materials, of their position, of the thickness of insulation, of the wall orientation, of the optical properties of the outer surface and of natural ventilation on decrement factor and time lag which the temperature fluctuation undergoes in crossing the wall. In particular, Asan et al. [29, 30] investigated the single and combined effects of the thermophysical properties and of the thicknesses of the wall layers on the decrement factor and time lag. Ulgen [31] experimentally investigated the thermal behaviours of opaque wall materials under the action of solar radiation. The experimental findings were compared with the results of equations derived by using an analytic methodology. Kaska et al. [32] and Yumrutas et al. [33], by using the complex finite Fourier transform technique to transform the transient heat transfer problem into a dimensionless form, found the time lag and the decrement factor values for different multilayer walls located in different Turkish cities. Aste et al. [34] conducted a parametric study on the effectiveness of thermal inertia, from the combination of two complex parameters, namely dynamic thermal transmittance and thermal admittance, in the reduction of the air-conditioning energy demand. They observed that the difference between the heating and cooling demand with a low inertia wall compared to a high inertia one might reach about 10% and 20% respectively. Al Sanea et al. [35] investigated numerically the effects of varying the amount and location of thermal mass on dynamic heat-transfer characteristics of insulated building walls, with the same nominal thermal resistance, using Riyadh climatic data. Concepts



of “thermal-mass energy-savings potential” and “critical thermal-mass thickness” were developed and utilized in order to determine thermal mass thickness required for a selected desirable percentage of energy savings. It is recommended that building walls should contain a minimum critical amount of thermal mass and that the insulation layer should be placed on the outside for applications with continuously operating AC. Kontoleon et al. [36] analyzed the influence of concrete density and concrete thermal conductivity of various multilayer walls on dynamic thermal characteristics.

In [37, 38] Asan, by using the Crank-Nicolson scheme and in [39] Bond et al., by using an electrical analogy in the frequency domain, studied the effect of the wall’s insulation thickness and position on the decrement factor and the time lag. Asan determined the optimum insulation position for the minimum decrement factor and maximum time lag. Bond et al. suggested that placing insulation on both the inside and outside layers and positioning thermal mass towards the middle of the multilayer wall will result in the best insulating performance. Al Sanea et al. [40] studied the dynamic thermal characteristics of insulated building walls with the same thermal mass, with different locations of one, two and three layers of insulation in order to achieve the best performance using the climatic data of Riyadh. The best overall performance is achieved by a wall with three layers of insulation, each 26-mm-thick, placed at the inside, the middle and the outside followed closely by a wall with two insulation layers, each 39-mm-thick, placed at the middle and the outside. Furthermore, the effects of insulation location and thickness on the heat transfer characteristics of building walls were investigated numerically by Ozel [41] in the climatic conditions of Elazig, Turkey. The maximum temperature swings and peak load in both summer and winter occur in the case that the insulation is placed at the middle of wall while the wall with outside insulation gives the smallest fluctuation.

Mavromatidis et al. [42] developed a numerical model, in which the combined conduction, radiation and convection heat transfer equation was solved explicitly via a control volume discretization, in order to analyze the influence of wall composition and orientation on the time lag and decrement factor. The wall configuration was presumed to be located in two different climatic zones (Athens and Yerevan).

Kontoleon et al. [43, 44] studied the effect of wall orientation and of the outdoor absorption coefficient on the decrement factor and the time lag by employing a dynamic thermal-network model. The investigation was carried out for representative wall formations including masonry, insulation and coatings on both surfaces during the cooling season in the Mediterranean region. Ozel et al. [45, 46] investigated the optimum insulation thickness for different wall orientations and the influence of exterior surface solar absorptivity for a south-facing wall on the thermal

dynamic characteristics using the climatic data of Elazig, Turkey. Furthermore, the author evaluated the influence of the absorption coefficient on summer thermal loads and winter heat loss. Al Sanea et al [47] also conducted these evaluations considering two insulated walls in the city of Riyadh and utilizing the concepts of “energy savings potential” and “critical thermal mass” developed in a previous study.

Gagliano et al. [48] carried out an experimental study to evaluate the thermal behavior of a massive building under the synergic combination of natural ventilation and thermal inertia in a large historical building located in Catania (Italy) in order to characterize its thermal performance under dynamic conditions by exploiting natural ventilation and by limiting both internal and solar gains. The results show that the synergic effect of the high thermal mass of the building and the nocturnal air ventilation allows comfortable indoor conditions to be maintained without the help of an AC system.

Typically, the decrement factor and time lag are determined by simplifying the actual trends of the external loadings. The outdoor environment is sometimes schematized using a sinusoidal oscillation of the external air temperature or of the sol-air temperature, while the internal air temperature is maintained constant (continuous regime). In such conditions, the dynamic behaviour of the walls depends only on the thickness, the position and the thermophysical properties of the layers.

If reference is made to the actual external loadings, the dynamic parameters also depend on their trends. In this case, many authors have proposed more parameters, in terms of decrement factor and time lag, for dynamic characterization. In particular, Sun et al. [49] correlated the dynamic properties to the Increasing Stage (IS) of the external loading in a continuous regime in order to investigate, both experimentally and numerically, how the external air temperature influences the time lags of the minimum and maximum peaks and decrement factor. The decrement factor is dependent mostly on the wall material and has little relation with the shape of the periodic external temperature wave. The time lags changed with the IS of the external temperature wave. The time lag of the maximum peak decreased with the IS, while the time lag of the minimum peak increased. Gasparella et al. [50] proposed a modification of the periodic thermal transmittance to evaluate the decrement factor and time lag of a wall subjected to the action of the sol-air temperature. In particular, the conventional periodic thermal transmittance values were corrected by a correction factor equal to the ratio between the amplitude of the fundamental harmonic and the actual amplitude of the loading sol-air temperature in order to determine the decrement factor. The equivalent time lag can be estimated summing (or subtracting) the time shift occurring between the peak of the first harmonic and the peak of the actual loading sol-air

temperature to the conventional value. This correction, however, remains an approximation since it does not take into account the effect of the harmonic terms further than the first on the internal heat flux.

The previous studies have been conducted in continuous regime conditioning and do not contemplate the presence of other loading on the inner surface.

In the air conditioning of environments, the dynamic behaviour of the walls depends on convective and radiative internal loadings, in addition to the external loadings.

The thermal response of a wall to the action of a unitary sinusoidal internal shortwave radiant loading is evaluated by the surface factor [51] while the periodic thermal admittance is used to evaluate the convective contributions produced by the unitary sinusoidal variation of the internal air temperature.

In this chapter, a more general dynamic characterisation of the opaque components of the building envelope subject to periodic sinusoidal and non-sinusoidal loadings acting on the external and internal surfaces has been developed.

The use of the heat flux allows for the joint action of all the loadings to be taken into account, to assess the peaks of thermal loads to be used for the dimensioning of the plant and, in addition, to determine the energy transferred. The use of heat flux is present in the literature and has been employed by Jin et al. [52] and by Oliveti et al. [53].

In sinusoidal conditions, the non-dimensional periodic thermal transmittance, defined as the ratio of the heat flux entering the environment and the conductive heat flux penetrating the wall at the interface with the outdoor environment, is used. This parameter is used to determine the decrement factor and time lag, which is undergone by the heat flux in crossing the wall and the efficiency of thermal storage. The non-dimensional periodic thermal transmittance was determined considering the wall subject externally to absorbed solar radiation, air temperature and the apparent sky temperature. Instead, the internal boundary conditions are those of a continuous regime conditioning with constant air temperature or a regime with nocturnal attenuation. Furthermore, eventual contributions due to shortwave radiative heat flux absorbed by the wall, to a flow rate of air infiltration and internal convective heat fluxes are considered.

For loadings with a non-sinusoidal trend, the dynamic characterisation is obtained by means of several parameters. The decrement factor is calculated as the ratio between the energy in a semi-period entering the environment and entering the wall, in order to characterize the thermal transfer properties of the component, as well as a ratio of heat fluxes considering the maximum peak and the minimum peak in a period. The time lags are calculated with reference to the maximum peak and minimum peak of heat flux. Given the heat flux transferred in steady

conditions, the maximum peak of the heat flux is employed to determine the maximum load in summer conditions and the minimum peak of the heat flux to calculate the maximum heat flux dispersed in winter.

The number of harmonics to consider for an accurate calculation is determined by the use of the Total Harmonic Distortion (THD) [54], which quantifies the distortion produced by the successive harmonics compared to the fundamental.

The methodology created was used for the calculation of the monthly and seasonal dynamic parameters of two walls with different orientations, situated in two climatically different locations, which are, indoors, subject to continuous conditioning conditions, or with nocturnal attenuation, in the absence and in the presence of a shortwave radiative heat flux absorbed on the internal surface.

## 2. Methodology

### 2.1 Mathematical formulation of the thermal transfer in the wall with internal and external loadings

A periodic thermal quantity  $y(t)$  can be expressed in an analytical form through a Fourier series expansion [55]:

$$y(t) = \bar{y} + \sum_{k=1}^n \tilde{y}_k = \bar{y} + \sum_{k=1}^n |\tilde{y}_k| \sin(k\omega t + \psi_k) \quad (1)$$

in which  $\bar{y}$  represents the mean value,  $|y|$  the amplitude,  $\omega$  the pulsation,  $\psi$  the argument of the  $k$ -th harmonic and  $n$  the number of harmonics

The wall subject to the joint action of the external and internal sinusoidal loadings was schematised by means of the equivalent electrical circuit in Figure 1. The external loadings are the air temperature, the sky temperature and the absorbed solar radiation. The internal loadings are the air temperature, the absorbed shortwave radiative heat flux, the heat flux associated with the infiltration flow rate, the convective heat fluxes contributions and the heat flux supplied by the plant. Infrared radiative exchange with the sky is linearized through the radiative heat transfer coefficient  $h_{r,e}$  while the infrared radiative exchange on the inside is incorporated in the internal surface heat transfer coefficient.

The electrical circuit refers to the periodic sinusoidal regime and represents the thermal

quantities, the temperature and heat flux, with a sinusoid described by a pulsation, an amplitude and an argument. It is possible to transform them into new variables in which time does not appear in an explicit manner. In the field of electrical engineering, such a procedure is known as the phasors method [56] and it is widely used in the study of thermal fields through the method of the complex temperature [55, 57].

The method represents each generic harmonic  $\tilde{y}_k$ , of angular frequency  $k\omega$ , as the imaginary part of the phasor written in the complex form:

$$\hat{y}_k = |\hat{y}_k| [\cos(k\omega t + \psi_k) + j\sin(k\omega t + \psi_k)] = |\hat{y}_k| \exp(j\psi_k) \exp(jk\omega t) \quad (2)$$

with  $|\hat{y}_k| = |\tilde{y}_k|$  and  $\arg(\hat{y}_k) = \arg(\tilde{y}_k) = \psi_k$ . Generally, the operator  $\exp(jk\omega t)$  in the resolution of a steady periodic problem is omitted as it is multiplicative of all the phasors and, furthermore, the sinusoidal component is reduced to a complex number.

The resolution of the equivalent electrical circuit in the complex domain gives unknown temperature and heat flux components, which are successively reported in the time domain multiplying by the operator  $\exp(jk\omega t)$ . Only the imaginary part of the product is considered. The actual trend of a thermal quantity is obtained summing the contributions of the single harmonics to the steady contribution.

The steady heat flux, which is transferred in the wall, is obtained by solving the system of equations consisting of the internal and external side heat balance and by internal air node balance. Such balances may be formulated again considering the electrical circuit in Figure 1 in which the ideal sinusoidal voltage and current sources are replaced by ideal constant sources.

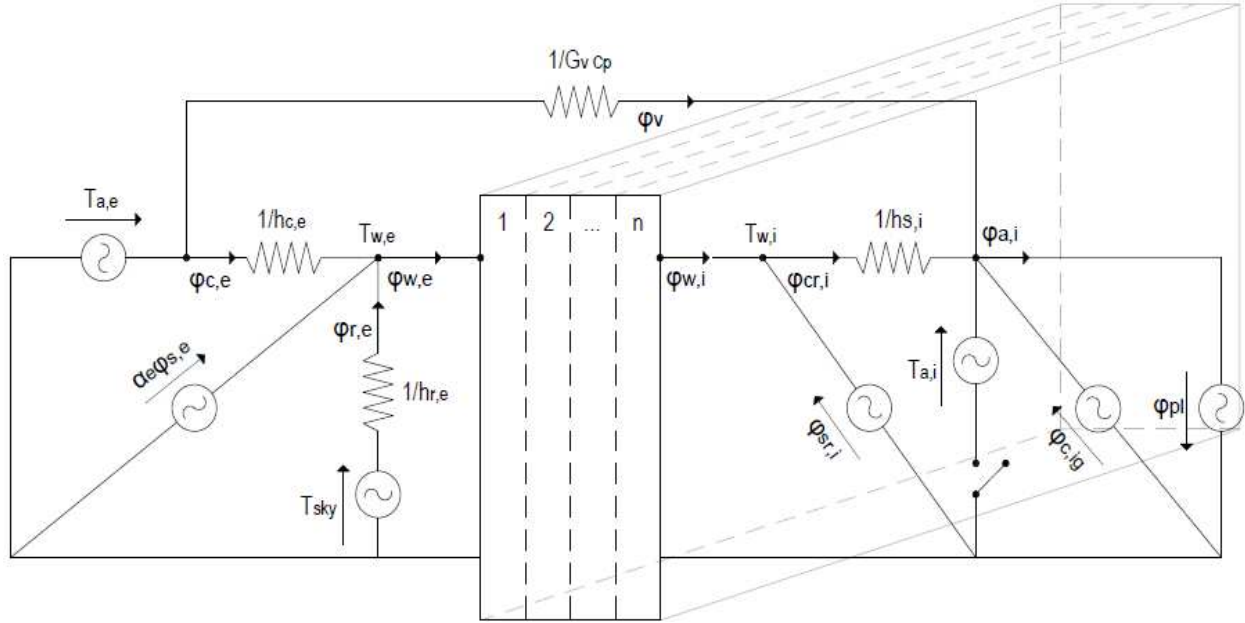


Figure 1 - Equivalent electrical circuit of a multilayer wall subject to external loadings, air temperature  $\hat{T}_{a,e}$ , sky temperature  $\hat{T}_{sky}$ , absorbed solar radiation  $\alpha_e \hat{\phi}_{s,e}$ , and to internal loadings, air temperature  $\hat{T}_{a,i}$ , absorbed shortwave radiative heat flux  $\hat{\phi}_{sr,i}$ , convective heat flux of the infiltration flow rate  $\hat{\phi}_v$ , convective heat fluxes contributions  $\hat{\phi}_{c,i,g}$  and convective heat flux supplied by the plant  $\hat{\phi}_{pl}$ .

With reference to a generic harmonic, represented by means of the associated complex phasor, the total external heat flux  $\phi_e$  assumes the form:

$$\hat{\phi}_e = \hat{\phi}_{r,e} + \hat{\phi}_{c,e} + \alpha_e \hat{\phi}_{s,e} = h_{r,e}(\hat{T}_{sky} - \hat{T}_{w,e}) + h_{c,e}(\hat{T}_{a,e} - \hat{T}_{w,e}) + \alpha_e \hat{\phi}_{s,e} \quad (3)$$

with  $\hat{\phi}_{r,e}$  sky longwave radiative heat flux,  $\hat{\phi}_{c,e}$  convective external heat flux,  $\hat{\phi}_{s,e}$  incident solar radiation heat flux,  $\alpha_e$  absorption coefficient of the external surface,  $h_{r,e}$  and  $h_{c,e}$  external radiative and convective heat transfer coefficients,  $\hat{T}_{sky}$  sky temperature,  $\hat{T}_{a,e}$  external air temperature,  $\hat{T}_{w,e}$  external surface temperature.

From Eq. (3) it is possible to obtain the equivalent temperature in function of the external loading acting from the outdoor environment:

$$\hat{T}_{eq,e} = \frac{h_{r,e}}{(h_{r,e} + h_{c,e})} \hat{T}_{sky} + \frac{h_{c,e}}{(h_{r,e} + h_{c,e})} \hat{T}_{a,e} + \frac{1}{(h_{r,e} + h_{c,e})} \alpha_e \hat{\phi}_{s,e} \quad (4)$$

The external surface balance equation is:

$$\hat{\Phi}_{w,e} = \hat{\Phi}_e \quad (5)$$

with  $\hat{\Phi}_{w,e}$  conductive heat flux that penetrates the wall at the interface with the external air.

From Eq. (3) obtaining the  $\hat{T}_{w,e}$ , it is possible to rewrite Eqs. (3) and (5) in the matrix form:

$$\begin{bmatrix} \hat{T}_{w,e} \\ \hat{\Phi}_{w,e} \end{bmatrix} = \begin{bmatrix} \frac{h_{r,e}}{h_{r,e} + h_{c,e}} & \frac{h_{c,e}}{h_{r,e} + h_{c,e}} & -\frac{1}{h_{r,e} + h_{c,e}} \\ 0 & 0 & 1 \end{bmatrix} \begin{bmatrix} \hat{T}_{sky} \\ \hat{T}_{a,e} \\ \hat{\Phi}_e \end{bmatrix} + \begin{bmatrix} 1 \\ 0 \end{bmatrix} \frac{1}{h_{r,e} + h_{c,e}} \begin{bmatrix} 0 \\ \alpha_e \hat{\Phi}_{s,e} \end{bmatrix} \quad (6)$$

Analogously, the internal surface balance is expressed by the equation:

$$\hat{\Phi}_{w,i} + \hat{\Phi}_{sr,i} = h_{s,i}(\hat{T}_{w,i} - \hat{T}_{a,i}) \quad (7)$$

with

$$\hat{\Phi}_{sr,i} = \hat{\Phi}_{sr,ts,i} + \hat{\Phi}_{sr,li} \quad (8)$$

where  $\hat{\Phi}_{w,i}$  is the conduction heat flux through the internal surface wall;  $h_{s,i}(\hat{T}_{w,i} - \hat{T}_{a,i})$  is the convective-radiative heat flux to the air zone;  $\hat{\Phi}_{sr,i}$  is the absorbed shortwave radiative heat flux to the internal surface;  $\hat{\Phi}_{sr,ts,i}$  is the absorbed shortwave radiative heat flux to the internal surface from the transmitted solar radiative heat flux;  $\hat{\Phi}_{sr,li}$  is the absorbed shortwave radiative heat flux to the internal surface from internal sources (lights).

The internal air balance equation per unit area of wall, expressed in Watt per square metre, is:

$$\hat{\Phi}_{a,i} = h_{s,i}(\hat{T}_{w,i} - \hat{T}_{a,i}) + \hat{\Phi}_v + \hat{\Phi}_{c,ig} = \hat{\Phi}_{pl} \quad (9)$$

with  $\hat{\Phi}_v$  convective heat flux of the infiltration flow rate,  $\hat{\Phi}_{c,ig}$  internal convective heat fluxes contributions and  $\hat{\Phi}_{pl}$  convective heat flux supplied by the plant.

Obtaining  $\hat{T}_{a,i}$  from Eq. (7), and substituting Eq. (7) in Eq. (9), the matrix expression that link temperature and heat flux transferred to the internal air with internal surface temperature and heat flux assume the form:

$$\begin{bmatrix} \hat{T}_{a,i} \\ \hat{\Phi}_{a,i} \end{bmatrix} = \begin{bmatrix} 1 & -\frac{1}{h_{s,i}} \\ 0 & 1 \end{bmatrix} \begin{bmatrix} \hat{T}_{w,i} \\ \hat{\Phi}_{w,i} \end{bmatrix} + \begin{bmatrix} -\frac{\hat{\Phi}_{sr,i}}{h_{s,i}} \\ \hat{\Phi}_{sr,i} + \hat{\Phi}_v + \hat{\Phi}_{c,ig} \end{bmatrix} \quad (10)$$

The heat transfer matrix of the building component from surface to surface is determined according to the procedure of the EN ISO 13786 standard with the convention that the product of the transfer matrixes is made from the most internal layer n to the most external layer 1:

$$\begin{bmatrix} \hat{T}_{w,i} \\ \hat{\Phi}_{w,i} \end{bmatrix} = \begin{bmatrix} Z_{11} & Z_{12} \\ Z_{21} & Z_{22} \end{bmatrix} \begin{bmatrix} \hat{T}_{w,e} \\ \hat{\Phi}_{w,e} \end{bmatrix} \quad (11)$$

The resolution of the electrical circuit provides a matrix expression that links, for each harmonic, the oscillating amplitudes of the temperature  $\hat{T}_{a,i}$  and of the heat flux  $\hat{\Phi}_{a,i}$  in the indoor environment with the external loadings  $\hat{T}_{sky}$ ,  $\hat{T}_{a,e}$  and  $\alpha_e \hat{\Phi}_{s,e}$  and with the internal loadings  $\hat{\Phi}_{sr,i}$ ,  $\hat{\Phi}_v$  and  $\hat{\Phi}_{c,ig}$ :

$$\begin{aligned} \begin{bmatrix} \hat{T}_{a,i} \\ \hat{\Phi}_{a,i} \end{bmatrix} &= \begin{bmatrix} 1 & -\frac{1}{h_{s,i}} \\ 0 & 1 \end{bmatrix} \begin{bmatrix} Z_{11} & Z_{12} \\ Z_{21} & Z_{22} \end{bmatrix} \left\{ \begin{bmatrix} h_{r,e} & h_{c,e} & -1 \\ h_{r,e} + h_{c,e} & h_{r,e} + h_{c,e} & h_{r,e} + h_{c,e} \\ 0 & 0 & 1 \end{bmatrix} \begin{bmatrix} \hat{T}_{sky} \\ \hat{T}_{a,e} \\ \hat{\Phi}_e \end{bmatrix} + \begin{bmatrix} \alpha_e \hat{\Phi}_{s,e} \\ h_{r,e} + h_{c,e} \\ 0 \end{bmatrix} \right\} \\ &+ \begin{bmatrix} -\frac{\hat{\Phi}_{sr,i}}{h_{s,i}} \\ \alpha_i \hat{\Phi}_{s,i} + \hat{\Phi}_v + \hat{\Phi}_{c,ig} \end{bmatrix} \\ &= \begin{bmatrix} A_{11} & A_{12} & A_{13} \\ A_{21} & A_{22} & A_{23} \end{bmatrix} \begin{bmatrix} \hat{T}_{sky} \\ \hat{T}_{a,e} \\ \hat{\Phi}_e \end{bmatrix} + \begin{bmatrix} B_{11} & B_{12} \\ B_{21} & B_{22} \end{bmatrix} \begin{bmatrix} \alpha_e \hat{\Phi}_{s,e} \\ h_{r,e} + h_{c,e} \\ 0 \end{bmatrix} + \begin{bmatrix} -\frac{\hat{\Phi}_{sr,i}}{h_{s,i}} \\ \hat{\Phi}_{sr,i} + \hat{\Phi}_v + \hat{\Phi}_{c,ig} \end{bmatrix} \\ &= [A] \begin{bmatrix} \hat{T}_{sky} \\ \hat{T}_{a,e} \\ \hat{\Phi}_e \end{bmatrix} + [B] \begin{bmatrix} \alpha_e \hat{\Phi}_{s,e} \\ h_{r,e} + h_{c,e} \\ 0 \end{bmatrix} + \begin{bmatrix} -\frac{\hat{\Phi}_{sr,i}}{h_{s,i}} \\ \hat{\Phi}_{sr,i} + \hat{\Phi}_v + \hat{\Phi}_{c,ig} \end{bmatrix} \quad (12) \end{aligned}$$

In the previous equation, matrix A represents the product between the internal surface matrix, the wall transfer matrix and the external surface matrix; B is the product of the first two.

Substituting Eq. (3) in the first equation of the matrix system (12), the expression of the external surface temperature as a function of the internal and external loadings is obtained:



$$\begin{aligned} \hat{T}_{w,e} = & \frac{A_{11} + A_{13}h_{r,e}}{A_{13}(h_{r,e} + h_{c,e})} \hat{T}_{sky} + \frac{A_{12} + A_{13}h_{c,e}}{A_{13}(h_{r,e} + h_{c,e})} \hat{T}_{a,e} + \frac{1}{A_{13}(h_{r,e} + h_{c,e})} \left( A_{13} + \frac{B_{11}}{h_{r,e} + h_{c,e}} \right) \alpha_e \hat{\Phi}_{s,e} \\ & - \frac{1}{A_{13}(h_{r,e} + h_{c,e})h_{s,i}} \hat{\Phi}_{sr,i} - \frac{1}{A_{13}(h_{r,e} + h_{c,e})} \hat{T}_{a,i} \end{aligned} \quad (13)$$

Substituting Eq. (13) in the second equation of the system (12), the relation that links the heat flux yielded to the internal air to the internal and external loadings is obtained:

$$\begin{aligned} \hat{\Phi}_{a,i} = & \left( A_{21} - \frac{A_{23}A_{11}}{A_{13}} \right) \hat{T}_{sky} + \left( A_{22} - \frac{A_{23}A_{12}}{A_{13}} + G_v c_p \right) \hat{T}_{a,e} + \frac{1}{(h_{r,e} + h_{c,e})} \left( B_{21} - \frac{A_{23}B_{11}}{A_{13}} \right) \alpha_e \hat{\Phi}_{s,e} \\ & + \left( 1 + \frac{A_{23}}{A_{13}h_{s,i}} \right) \hat{\Phi}_{sr,i} + \left( \frac{A_{23}}{A_{13}} - G_v c_p \right) \hat{T}_{a,i} + \hat{\Phi}_{c,ig} \\ = & \left( -\frac{h_{r,e}}{h_{r,e} + h_{c,e}} \frac{1}{A_{13}} \right) \hat{T}_{sky} + \left( -\frac{h_{c,e}}{h_{r,e} + h_{c,e}} \frac{1}{A_{13}} + G_v c_p \right) \hat{T}_{a,e} \\ & + \left( -\frac{h_{r,e}}{h_{r,e} + h_{c,e}} \frac{1}{A_{13}} \right) \alpha_e \hat{\Phi}_{s,e} + \left( 1 + \frac{A_{23}}{A_{13}h_{s,i}} \right) \hat{\Phi}_{sr,i} + \left( \frac{A_{23}}{A_{13}} - G_v c_p \right) \hat{T}_{a,i} \\ & + \hat{\Phi}_{c,ig} \end{aligned} \quad (14)$$

The expression of the total heat flux penetrating the wall from the external side is obtained by substituting Eq. (13) in Eq. (3).

$$\begin{aligned} \hat{\Phi}_e = & \left( -\frac{A_{11}}{A_{13}} \right) \hat{T}_{sky} + \left( -\frac{A_{12}}{A_{13}} \right) \hat{T}_{a,e} + \left( -\frac{1}{(h_{r,e} + h_{c,e})} \frac{B_{11}}{A_{13}} \right) \alpha_e \hat{\Phi}_{s,e} + \left( \frac{1}{A_{13}h_{s,i}} \right) \hat{\Phi}_{sr,i} \\ & + \left( \frac{1}{A_{13}} \right) \hat{T}_{a,i} \end{aligned} \quad (15)$$

The difference between the oscillating heat flux entering the wall (Eq. 15) and the heat flux transferred to the indoor environment (Eq. 14) provides the variation of internal energy in the wall per unit time, to which the following form can be given:

$$\begin{aligned}
\Delta\hat{U} &= \hat{\varphi}_e - \hat{\varphi}_{a,i} \\
&= \left( \frac{\frac{h_{r,e}}{h_{r,e} + h_{c,e}} - A_{11}}{A_{13}} \right) \hat{T}_{sky} + \left( \frac{\frac{h_{c,e}}{h_{r,e} + h_{c,e}} - A_{12}}{A_{13}} - G_v c_p \right) \hat{T}_{a,e} \\
&+ \left( \frac{1}{(h_{r,e} + h_{c,e})} \frac{1 - B_{11}}{A_{13}} \right) \alpha_e \hat{\varphi}_{s,e} + \left( \frac{1 - A_{13} h_{s,i} - A_{23}}{A_{13} h_{s,i}} \right) \hat{\varphi}_{sr,i} \\
&+ \left( \frac{1 - A_{23}}{A_{13}} + G_v c_p \right) \hat{T}_{a,i} - \hat{\varphi}_{c,ig} \tag{16}
\end{aligned}$$

The oscillating heat fluxes in Eq. (14) and in Eq. (15) and the variation of internal energy per unit time in Eq. (16) can be rewritten in the compact form:

$$\hat{\varphi}_{a,i} = Y_{sky}^i \hat{T}_{sky} + Y_{a,e}^i \hat{T}_{a,e} + Y_{s,e}^i \alpha_e \hat{\varphi}_{s,e} + Y_{sr,i}^i \hat{\varphi}_{sr,i} + Y_{a,i}^i \hat{T}_{a,i} + \hat{\varphi}_{c,ig} \tag{17}$$

$$\hat{\varphi}_e = Y_{sky}^e \hat{T}_{sky} + Y_{a,e}^e \hat{T}_{a,e} + Y_{s,e}^e \alpha_e \hat{\varphi}_{s,e} + Y_{sr,i}^e \hat{\varphi}_{sr,i} + Y_{a,i}^e \hat{T}_{a,i} \tag{18}$$

$$\begin{aligned}
\Delta\hat{U} &= (Y_{sky}^e - Y_{sky}^i) \hat{T}_{sky} + (Y_{a,e}^e - Y_{a,e}^i) \hat{T}_{a,e} + (Y_{s,e}^i - Y_{s,e}^e) \alpha_e \hat{\varphi}_{s,e} + (Y_{sr,i}^e - Y_{sr,i}^i) \hat{\varphi}_{sr,i} \\
&+ (Y_{a,i}^e - Y_{a,i}^i) \hat{T}_{a,i} - \hat{\varphi}_{c,ig} \tag{19}
\end{aligned}$$

The generic complex parameter  $Y$  that appears in Eqs. (17), (18) and (19) provides the contribution, in amplitude and argument, to the calculation of the heat fluxes  $\hat{\varphi}_e$  or  $\hat{\varphi}_{a,i}$  or of the variation in internal energy  $\Delta\hat{U}$ , consequent to the periodic unitary variation of the relative internal or external loading. In particular, they allow for the definition of the rates attributable to the unitary periodic variation of the incident solar heat flux on the external surface and of the incident shortwave radiant heat flux on the internal surface.

The  $Y$  parameters are correlated to the periodic thermal transmittance, to the periodic thermal admittances and to the areal heat capacities defined by EN ISO 13786. The analytical relations for the calculation of the  $Y$  parameters according to the authors' procedure and the procedure of the standard are reported in Figure 2.

	$\hat{\Phi}_{ai}$		$\hat{\Phi}_e$		$\Delta\hat{U}$	
	Methodology	EN ISO 13786	Methodology	EN ISO 13786	Methodology	EN ISO 13786
$\hat{T}_{sky}$	$Y_{sky}^i = -\frac{h_{r,e}}{(h_{r,e}+h_{c,e})} \frac{1}{A_{13}}$	$Y_{sky}^i = \frac{h_{r,e}}{(h_{r,e}+h_{c,e})} Y_{12}$	$Y_{sky}^e = -\frac{A_{11}}{A_{13}}$	$Y_{sky}^e = \frac{h_{r,e}}{(h_{r,e}+h_{c,e})} Y_{22}$	$Y_{sky}^u = \frac{h_{r,e}}{(h_{r,e}+h_{c,e})} - \frac{A_{11}}{A_{13}}$	$Y_{sky}^u = -\frac{h_{r,e}}{(h_{r,e}+h_{c,e})} \frac{2\pi}{T} k_2$
$\hat{T}_{a,e}$	$Y_{a,e}^i = -\frac{h_{c,e}}{(h_{c,e}+h_{r,e})} \frac{1}{A_{13}} + G_v c_p$	$Y_{a,e}^i = \frac{h_{c,e}}{(h_{c,e}+h_{r,e})} Y_{12} + G_v c_p$	$Y_{a,e}^e = -\frac{A_{12}}{A_{13}}$	$Y_{a,e}^e = \frac{h_{c,e}}{(h_{c,e}+h_{r,e})} Y_{22}$	$Y_{a,e}^u = \frac{h_{c,e}}{(h_{c,e}+h_{r,e})} - \frac{A_{12}}{A_{13}} - G_v c_p$	$Y_{a,e}^u = -\frac{h_{c,e}}{(h_{c,e}+h_{r,e})} \frac{2\pi}{T} k_2 - G_v c_p$
$\alpha\hat{\Phi}_{s,e}$	$Y_{s,e}^i = -\frac{1}{(h_{r,e}+h_{c,e})} \frac{1}{A_{13}}$	$Y_{s,e}^i = \frac{1}{(h_{r,e}+h_{c,e})} Y_{12}$	$Y_{s,e}^e = -\frac{B_{11}}{(h_{r,e}+h_{c,e})} \frac{1}{A_{13}}$	$Y_{s,e}^e = \frac{1}{(h_{r,e}+h_{c,e})} Y_{22}$	$Y_{s,e}^u = \frac{1}{(h_{r,e}+h_{c,e})} \frac{1-B_{11}}{A_{13}}$	$Y_{s,e}^u = -\frac{1}{(h_{r,e}+h_{c,e})} \frac{2\pi}{T} k_2$
$\hat{T}_{ai}$	$Y_{s,i}^i = \frac{A_{23}}{A_{13}} - G_v c_p$	$Y_{s,i}^i = -Y_{11} - G_v c_p$	$Y_{s,i}^e = \frac{1}{A_{13}}$	$Y_{s,i}^e = -Y_{12}$	$Y_{s,i}^u = \frac{1-A_{23}}{A_{13}} + G_v c_p$	$Y_{s,i}^u = -\frac{2\pi}{T} k_1 + G_v c_p$
$\alpha\hat{\Phi}_{sr,i}$	$Y_{a,i}^i = 1 + \frac{1}{h_{s,i}} \frac{A_{23}}{A_{13}}$	$Y_{a,i}^i = 1 - \frac{Y_{11}}{h_{s,i}}$	$Y_{a,i}^e = \frac{1}{h_{s,i}} \frac{1}{A_{13}}$	$Y_{a,i}^e = -\frac{1}{h_{s,i}} Y_{12}$	$Y_{a,i}^u = \frac{1}{h_{s,i}} \frac{1-A_{23}}{A_{13}} - 1$	$Y_{a,i}^u = -1 - \frac{2\pi}{T} \frac{1}{h_{s,i}} k_1$
$\hat{\Phi}_{c,ig}$	1		0		-1	

Figure 2 – Dynamic parameters  $Y$  calculating according to the proposed methodology and by means of the periodic thermal transmittance, the periodic thermal admittances and the areal heat capacities of EN ISO 13786.

Once the phasors associated to the thermal quantities for each harmonic have been calculated, it is then necessary to carry them to the time domain for the successive composition. The total fluctuating component of a thermal quantity is obtained by summing the oscillating contributions with different pulsations. The actual trend of the quantity is obtained by summing the relative steady component to the total fluctuating component.

## 2.2 Dynamic characterization of the wall with sinusoidal loadings

The contemporaneous presence of more temperature and heat flux loadings on the external and internal surface, differing from the schematisation provided for by EN ISO 13786, requires the use of heat fluxes entering and exiting the wall, expressed by means of Eqs. (17) and (18) for the dynamic characterisation. With reference to the generic harmonic  $k$ , in the case in which the heat flux penetrates from the outside towards the inside, the ratio between the heat flux entering the environment and the external heat flux entering the wall is the external side non-dimensional periodic thermal transmittance:

$$\tau_{ei} = \frac{\hat{\Phi}_{a,i}}{\hat{\Phi}_e} = \frac{Y_{sky}^i \hat{T}_{sky} + Y_{a,e}^i \hat{T}_{a,e} + Y_{s,e}^i \alpha_e \hat{\Phi}_{s,e} + Y_{sr,i}^i \hat{\Phi}_{sr,i} + Y_{a,i}^i \hat{T}_{a,i} + \hat{\Phi}_{c,ig}}{Y_{sky}^e \hat{T}_{sky} + Y_{a,e}^e \hat{T}_{a,e} + Y_{s,e}^e \alpha_e \hat{\Phi}_{s,e} + Y_{sr,i}^e \hat{\Phi}_{sr,i} + Y_{a,i}^e \hat{T}_{a,i}} \quad (20)$$

Such a parameter, as well as depending on the complex  $Y$  parameters, which are a function of the thermophysical properties, of the internal and external surface heat transfer coefficients and of the oscillation period, also depends on the loadings.

In the particular case of constant internal temperature, internal shortwave radiant  $\hat{\varphi}_{sr,i}$  and convective contributions  $\hat{\varphi}_{c,ig}$  equal to zero, and in the absence of infiltration flow rate, the non-dimensional periodic thermal transmittance  $\tau_{ei}$  is reduced to the ratio between the periodic thermal transmittance and the external side periodic thermal admittance calculated according to EN ISO 13786 [53].

The parameter  $\tau_{ei}$  is a phasor and it defines the decrement factor  $f_{ei}$  and the time lag  $\Delta t_{ei}$  that is undergone by the external heat flux  $\hat{\varphi}_e$ , associated with the generic harmonic in crossing the wall:

$$f_{ei} = |\tau_{ei}| \quad (21a) \quad \Delta t_{ei} = \frac{T}{2\pi} \arg(\tau_{ei}) \quad (21b)$$

The attenuation that is undergone by the energy entering the wall in a semi-period and that which are undergone by the maximum and the minimum peaks of the heat flux are described in Eq. (21a). Likewise, the time lag calculated with Eq. (21b) represents the time lag between both the maximum and minimum peaks of the heat flux.

The ratio between the energy stored per time unit and the heat flux entering the wall defines the external side instantaneous periodic efficiency of storage of the wall [53]:

$$\varepsilon_e = \frac{\Delta \hat{U}}{\hat{\varphi}_e} = \frac{\hat{\varphi}_e - \hat{\varphi}_{a,i}}{\hat{\varphi}_e} = 1 - \tau_{ei} \quad (22)$$

In the case of heat transfer from the inside towards the outside, the non-dimensional periodic transmittance relative to the internal side is:

$$\tau_{ie} = \frac{\hat{\varphi}_e}{\hat{\varphi}_{a,i}} \quad (23)$$

while the internal side instantaneous periodic efficiency of storage of the wall is:

$$\varepsilon_i = \frac{\Delta \hat{U}}{\hat{\varphi}_{a,i}} = 1 - \tau_{ie} \quad (24) \quad \text{with} \quad \Delta \hat{U} = \hat{\varphi}_{a,i} - \hat{\varphi}_e$$

### 2.3 Dynamic characterization of the wall with non-sinusoidal loadings

The loadings that act on the building walls are non-sinusoidal and can be expressed as the sum of harmonics with different pulsations, amplitudes and arguments. The total heat flux penetrating the walls and the total heat flux yielded to the indoor environment are determined composing the different harmonics. In Eq. (20), substituting the sum of the various harmonics to the phasor associated with the single harmonic, the external side non-dimensional periodic global thermal transmittance assumes the form:

$$\tau_{g,ei} = \frac{\sum_{k=1}^n \tilde{\varphi}_{a,i,k}}{\sum_{k=1}^n \tilde{\varphi}_{e,k}} = \frac{\sum_{k=1}^n \tau_{ei,k} \tilde{\varphi}_{e,k}}{\sum_{k=1}^n \tilde{\varphi}_{e,k}} = \tau_{ei,1} \frac{\tilde{\varphi}_{e,1}}{\sum_{k=1}^n \tilde{\varphi}_{e,k}} + \tau_{ei,2} \frac{\tilde{\varphi}_{e,2}}{\sum_{k=1}^n \tilde{\varphi}_{e,k}} + \dots + \tau_{ei,n} \frac{\tilde{\varphi}_{e,n}}{\sum_{k=1}^n \tilde{\varphi}_{e,k}} \quad (25)$$

In Eq. (25)  $\tau_{ei,k}$  and  $\tilde{\varphi}_{e,k}$  are sinusoidal quantities while  $\sum_{k=1}^n \tilde{\varphi}_{e,k}$  does not have a sinusoidal trend; consequently, the contributions of the single harmonics to the calculation of the global transmittance and the global transmittance  $\tau_{g,ei}$  are not phasors. Thus, the transmittance  $\tau_{g,ei}$  cannot be used to define the global decrement factor and the global time lag of the heat flux penetrating the wall.  $\tau_{g,ei}$  represents, instant by instant, the fraction of the external heat flux that penetrates to the indoor environment.

In the presence of non-sinusoidal loadings, the identification of the dynamic behaviour of the wall was obtained using several dynamic parameters, with the aim of dynamically characterising the wall in energy terms and in terms of heat flux.

In terms of energy, the decrement factor is defined as the ratio between the energy in a semi-period entering and exiting the wall. In terms of heat flux, it is necessary to consider both the decrement factor of the maximum peak and that of the minimum peak in order to identify, according to the direction of the steady heat flux, respectively the heat flux peak in summer and winter conditions. In formulae:

$$f_{g,ei} = \frac{\int_0^P \left| \sum_{k=1}^n \tilde{\varphi}_{a,i,k} \right| dt}{\int_0^P \left| \sum_{k=1}^n \tilde{\varphi}_{e,k} \right| dt} \quad (26a) \quad f_{g,ei}^{\max} = \frac{\left( \sum_{k=1}^n \tilde{\varphi}_{a,i,k} \right)_{\max}}{\left( \sum_{k=1}^n \tilde{\varphi}_{e,k} \right)_{\max}} \quad (26b) \quad f_{g,ei}^{\min} = \frac{\left( \sum_{k=1}^n \tilde{\varphi}_{a,i,k} \right)_{\min}}{\left( \sum_{k=1}^n \tilde{\varphi}_{e,k} \right)_{\min}} \quad (26c)$$

The decrement factor  $f_{g,ei}$  completes the characterisation of the wall as it allows for the evaluation of the fraction of energy transmitted in a semi-period, both in the summer and the winter period. In particular, in the summer season, the semi-period to be considered is that in

which the maximum peak of the heat flux occurs, to which a fluctuating energy entering the indoor environment in the same direction as the steady component is associated. Vice versa, in winter, the semi-period to consider is that in which the minimum peak occurs, to which a fluctuating energy exiting the indoor environment with the same direction as the steady component is associated. In a non-sinusoidal periodic regime,  $(1 - f_{g,ei})$  represents the fraction of energy that remains stored in the wall in a semi-period.

The time lag of the maximum and minimum peaks, which intervene respectively in the summer and winter behaviour of the wall, are defined by the relations:

$$\Delta t_{g,ei}^{\max} = t_{(\sum_{k=1}^n \tilde{\varphi}_{a,i,k})_{\max}} - t_{(\sum_{k=1}^n \tilde{\varphi}_{e,k})_{\max}} \quad (27a) \quad \Delta t_{g,ei}^{\min} = t_{(\sum_{k=1}^n \tilde{\varphi}_{a,i,k})_{\min}} - t_{(\sum_{k=1}^n \tilde{\varphi}_{e,k})_{\min}} \quad (27b)$$

The defined parameters, expressed by Eqs. (26a), (26b) and (26c), and (27a) and (27b), identify how the form of the external heat flux trend is modified in crossing the wall. Similar relations can be obtained for the internal side. In Figure 3 the schematic representation of the decrement factors and of the time lags are reported.

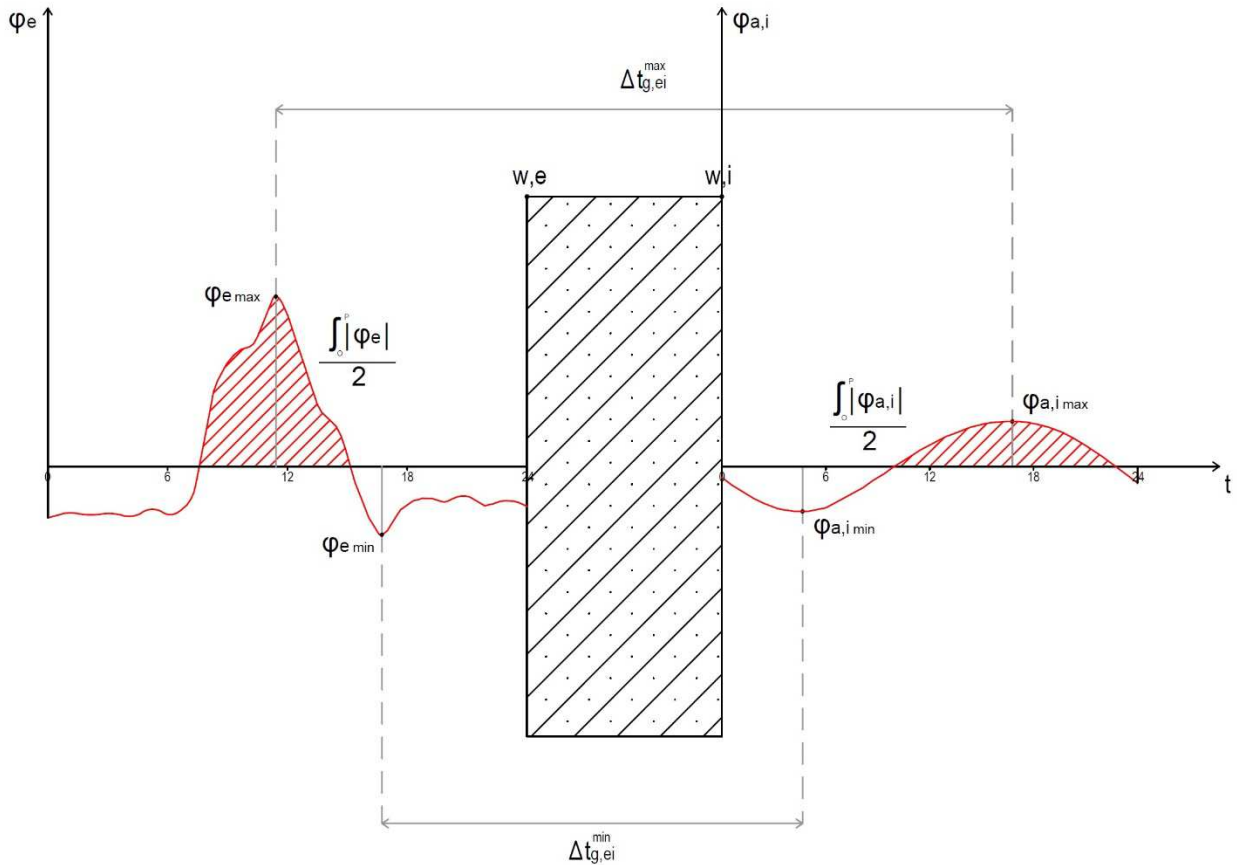


Figure 3 - Schematic representation of the decrement factors and of the time lags in non-sinusoidal conditions.

The calculation of the previous parameters requires the use of all the harmonics. A sufficiently accurate evaluation can be obtained by considering a limited number of harmonics in order to determine the internal and external heat fluxes.

A criteria that is useful in quantifying the deviation of a non-sinusoidal periodic trend from a sinusoidal trend consists in the evaluation of the Total Harmonic Distortion (THD). Such a parameter is defined as the ratio between the square root of the sum of the squares of the harmonic amplitudes that are successive to the fundamental and the fundamental sinusoid amplitude:

$$\text{THD} = \frac{(\sqrt{|\tilde{y}_2|^2 + |\tilde{y}_3|^2 + \dots + |\tilde{y}_n|^2})}{|\tilde{y}_1|} \quad (28)$$

THD is equal to zero for a sinusoid and grows with an increasing heat flux distortion compared to the trend of the fundamental, and can assume values greater than 1.

In order to determine the number of harmonics to be used, the following criteria was used. The THD parameter values for the internal and external heat flux were determined using the first two harmonics, the first three, and so on for all the harmonics. These values,  $\text{THD}_k$ , were used to evaluate the relative percentage error  $e_{\text{THD}}(k)$  compared to the  $\text{THD}_n$  value obtained considering all the harmonics. In formulae:

$$e_{\text{THD}}(k) = \frac{\text{THD}_n - \text{THD}_k}{\text{THD}_n} 100 \quad (29)$$

The number  $k$  of harmonics to be considered in the calculation of the internal and external heat flux is that which gives rise to a contained relative percentage error (2-3%) of the most distorted heat flux to which a higher THD value corresponds. In Figure 4, a typical trend of the relative percentage error, calculated with Eq. (29) as a function of the number  $k$  of harmonics used, is reported.

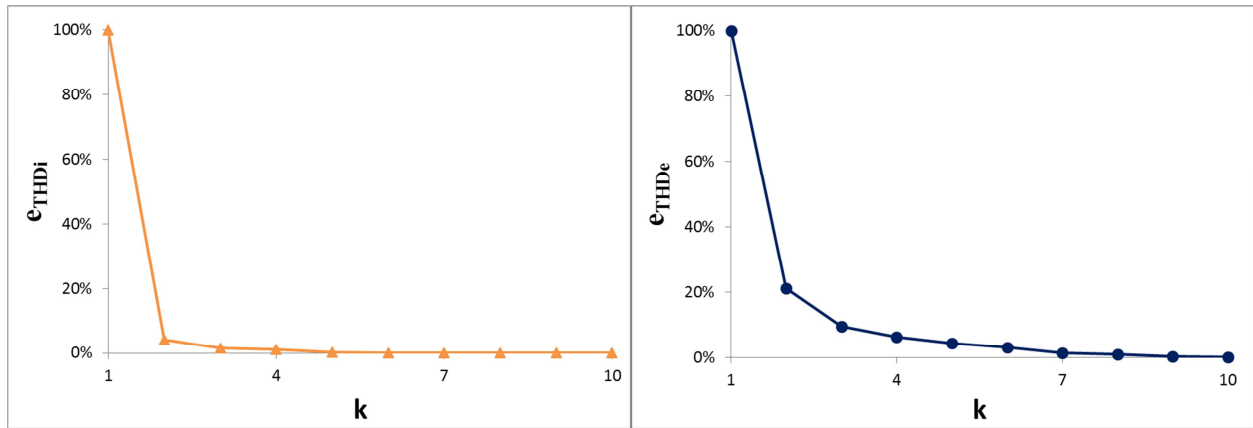


Figure 4 - Relative percentage error associated with the calculation of the THD of the internal heat flux  $e_{THDi}$  and the external heat flux  $e_{THDe}$  as a function of the number of harmonics  $k$ .

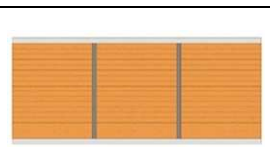
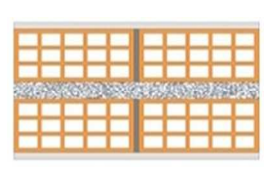
The relative percentage error  $e_{THD}(k)$  is equal to one for the first harmonic and asymptotically tends to zero with an increase in the number of harmonics.

### 3. Application of the calculation procedures

#### 3.1 Considered walls and boundary conditions

Two walls widely used in Italy [58] with different layers and thermophysical properties taken from the reference standards [59, 60] are considered, see Table 1.

Table 1. Stratigraphy of walls and thermophysical properties of layers.

<b>WALL 1: BRICK WALL</b>		$R = 1.05 \text{ m}^2 \text{ K/W};$		$U = 0.95 \text{ W}/(\text{m}^2 \text{ K});$		$C = 971.2 \text{ kJ}/(\text{m}^2 \text{ K})$	
		Material	$s$ [m]	$\lambda$ [W/(kg K)]	$c$ [J/(kg K)]	$\rho$ [kg/m <sup>3</sup> ]	
1	Internal plaster	0.02	0.70	1000	1400		
2	Brick	0.60	0.72	840	1800		
3	External plaster	0.02	0.90	1000	1800		
<b>WALL 2: HOLLOW WALL</b>		$R = 1.50 \text{ m}^2 \text{ K/W};$		$U = 0.67 \text{ W}/(\text{m}^2 \text{ K});$		$C = 328 \text{ kJ}/(\text{m}^2 \text{ K})$	
		Material	$s$ [m]	$\lambda$ [W/(kg K)]	$c$ [J/(kg K)]	$\rho$ [kg/m <sup>3</sup> ]	
1	Internal plaster	0.02	0.70	1000	1400		
2	Hollow brick	0.08	0.30	1000	800		
3	Air gap	$R = s/\lambda = 0.18 \text{ m}^2 \text{ K/W}$ [64]		-	-		
4	Hollow brick	0.25	0.30	1000	800		
5	External plaster	0.02	0.90	1000	1800		

The dynamic thermal behavior of materials similar to the ones studied, and of common use in the construction technique of buildings, has also been studied by other authors [31, 33-34, 49, 51, 61-62]. The walls were situated in two climatically different locations, Turin (TO), Lat = 45° 7',



Long = 7° 43', with a humid subtropical climate (Cfa, in accordance with the Köppen climate classification [63]) and Cosenza (CS), Lat = 37° 30', Long = 15° 05', with a warm Mediterranean climate (Csa). Wall 1 presents higher thermal capacity and steady thermal transmittance values compared to wall 2.

Climatic data were generated starting from monthly average daily values, provided by the reference national standard [65], of solar radiation on the horizontal plane and of the external air temperature using TRNSYS 17 [66] software, which with Type 54a [67] generates different hourly sequences for the different days in a month. The calculation of the hourly solar radiation on the vertical plane was obtained with Type 16 [68]. The sky temperature data were generated with Type 69b [69]. The hourly quantities calculated were used to define the type day of each month through the average hourly values. For the external surface, a solar absorption coefficient  $\alpha_e$  equal to 0.6, a convective heat transfer coefficient  $h_{c,e} = 20 \text{ W/m}^2 \text{ K}$  and a radiative heat transfer coefficient  $h_{r,e} = 5.35 \text{ W/m}^2 \text{ K}$  are employed; and on the internal side a surface heat transfer coefficient  $h_{s,i} = 7.7 \text{ W/m}^2 \text{ K}$  is used. The surface heat transfer coefficients are that reported in [64, 70].

Inside, two boundary conditions corresponding to winter heating and summer cooling, in continuous regime (cont) and with nocturnal attenuation (att), in the absence (abs) and presence (pre) of shortwave radiative heat flux on the internal surface are considered; air infiltration flow rate, nor internal convective heat fluxes contributions are not considered. According to the National regulations [58], the heating period for Cosenza is from November to March, whereas for Torino from October to April. For both localities, the remaining months were assumed as cooling period.

In the continuous regime, the internal air temperature is considered as equal to 20°C in the winter period and equal to 26°C in the summer period; in attenuated regime, the internal air temperature schedules in summer and in winter are reported in Figure 5a for Turin and in Figure 5b for Cosenza. Previous values of internal air temperature, both in continuous and attenuated regime, were chosen according to the reference standard [71].

The internal radiative shortwave heat flux was calculated taking the solar contribution and the contribution due to light sources into consideration. The solar contribution was determined starting from the solar radiation entering through a south facing glazed surface. The schedule of the contribution due to light sources is reported in Figure 5c and it was supposed to be constant in the different months for both the walls, in the two locations and for the two different plant operating regimes.

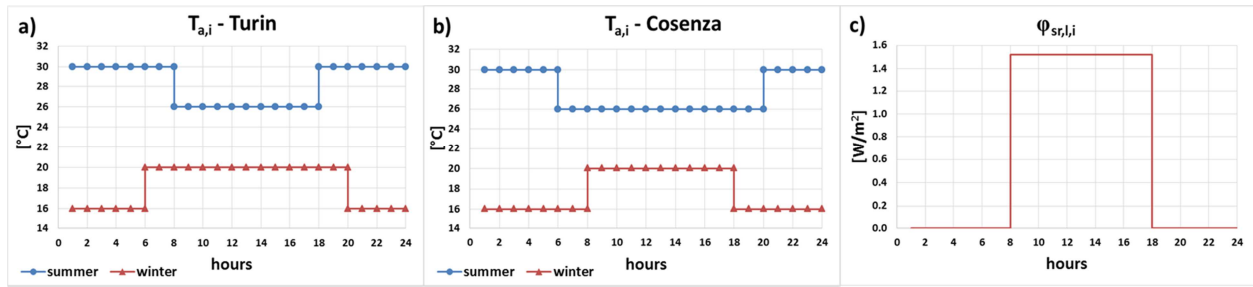


Figure 5 – Internal air temperature in attenuated regime in winter and in summer: a) Turin; b) Cosenza. c) Contribution of the light sources to the shortwave radiative heat flux absorbed by the internal surface.

The external and internal loadings trends were expressed in an analytical form by a Fourier series expansion truncated at the tenth harmonic.

The walls considered were investigated in a periodic sinusoidal and a periodic non-sinusoidal regime. In particular, in sinusoidal conditions, a frequency analysis on a monthly basis was developed considering the walls exposed to the south. A total of eight cases, relating to the two locations, to the two operating regimes of the plant in the absence and presence of internal shortwave radiant loads, were considered for each wall. In non-sinusoidal conditions, first southern orientation is considered and the dynamic parameters on a monthly basis and then average seasonal values are evaluated. Lastly, east, west and northern orientations were considered and the average seasonal dynamic parameters were evaluated. Thirty-two cases were considered for each wall, and eight for each orientation.

### 3.2 Periodic sinusoidal condition, results and discussion

The external side non-dimensional periodic thermal transmittance  $\tau_{ei}$  calculated with Eq. (20) is a phasor associated with the generic harmonic whose amplitude and argument, given by Eqs. (21a) and (21b), express, respectively, the decrement factor  $f_{ei}$  and time lag  $\Delta t_{ei}$  that the external heat flux  $\hat{\varphi}_e$  undergoes in crossing the wall. In the schematisation used, if the heat flux in the wall associated with the generic harmonic is directed from the inside to the outside, the dynamic parameters to consider are those relating to the internal side thermal transmittance  $\tau_{ie}$ , which can be calculated with Eq. (23).

The non-dimensional periodic thermal transmittance was used for the harmonic analysis in sinusoidal conditions of a south facing wall and subject to the eight heat exchange configurations identified in the previous paragraph. The analysis describes the behaviour of the wall on variation of the pulsation.

The monthly decrement factor and time lag for the different harmonics in the case of a

continuous regime in the absence of internal shortwave radiant loads, for the two walls in the two locations, are reported in Figure 6.

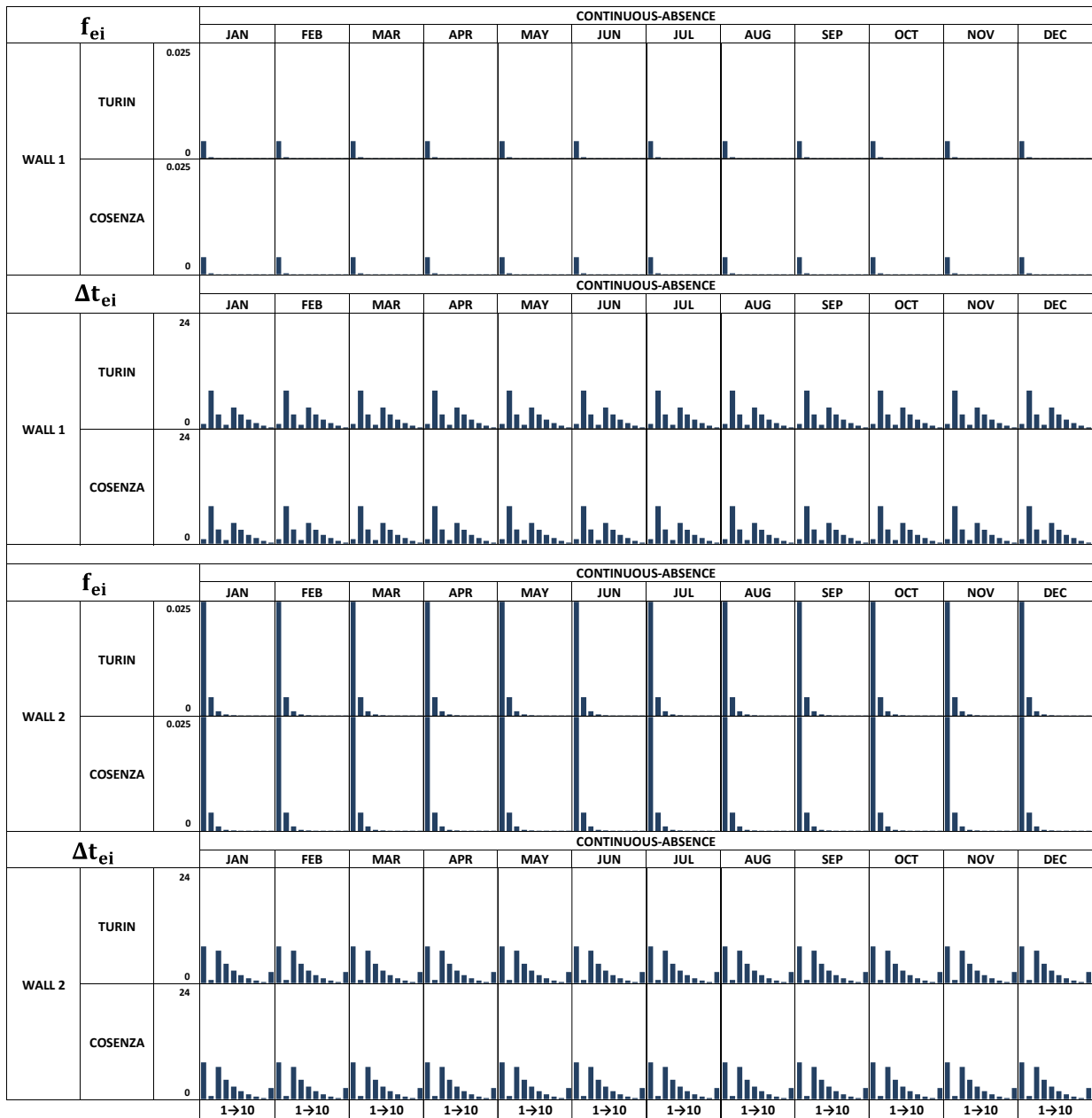


Figure 6 – Monthly decrement factor and time lag upon variation of the pulsation for the two considered walls situated in Turin and Cosenza. Continuous regime, absence of shortwave radiative heat flux on the internal surface. Southern orientation.

For a determined wall and for a determined harmonic, the decrement factor  $f_{ei}$  and the time lag  $\Delta t_{ei}$  do not depend on the location, nor on the month as they depend on periodic thermal transmittance and periodic thermal admittance defined by EN ISO 13786, function of the period of oscillation, of the stratigraphy and of the thermophysical properties of the wall. The

decrement factor reduces upon increase of the pulsation. In particular, for wall 1 only the value corresponding to the first harmonic with pulsation  $2\pi/24$  (rad/h) is appreciable. For wall 2, the values of the first two harmonics are significant. Wall 1, compared to wall 2, for the same pulsation, presents a reduced decrement factor due to the greater thermal capacity. The time lag presents values that are variable in an irregular manner, with the pulsation.

Monthly decrement factor and time lag in the case of a continuous regime in the presence of shortwave radiative heat flux on the internal surface are presented in Figure 7.

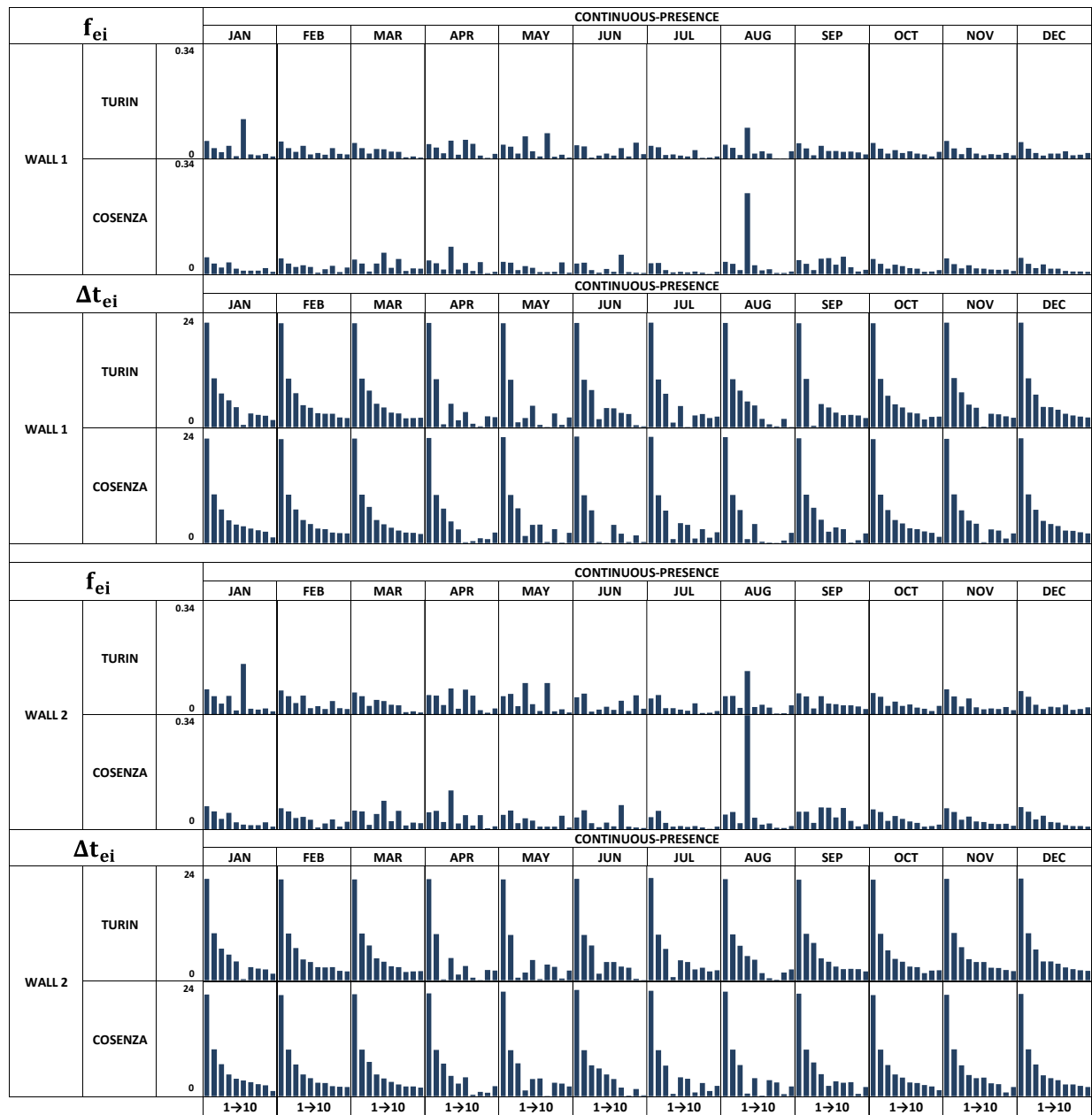


Figure 7 – Monthly decrement factor and time lag upon variation of pulsation for the two considered walls located in Turin and Cosenza. Continuous regime, presence of shortwave radiative heat flux on the internal surface. Southern orientation.

In this case, for a determined wall and for a determined harmonic, the decrement factor  $f_{ei}$  and time lag  $\Delta t_{ei}$  are different during different months; they also differ with the location. This is because the external side periodic thermal transmittance  $\tau_{ei}$  (Eq. 19) depends, not only on the periodic thermal transmittance and the external side periodic thermal admittance, but also on the internal side periodic thermal admittance and on the loadings on the internal and external surfaces. The decrement factor, compared to the previous case, varies in an irregular manner with an increase in pulsation. Concerning the time lag, during the winter period it decreases on an increase of the pulsation, unlike during the summer period when it presents a non-regular trend.

In the case of an attenuated regime in the absence of shortwave radiative heat flux on the internal surface, the results obtained in terms of decrement factor and time lag are shown in Figure 8.

The attenuated regime, varying pulsation, confers extreme variability on the dynamic parameters, which depend on the wall, on the month and on the location. This is due, with reference to Eq. (19) to the presence of the contribution of the internal air loading  $Y_{a,i}^i \hat{T}_{a,i}$  in the calculation of the internal heat flux  $\hat{\phi}_{a,i}$  and of the contribution  $Y_{a,i}^e \hat{T}_{a,i}$  in the calculation of the external heat flux  $\hat{\phi}_e$ . The amplitude of  $Y_{a,i}^i \hat{T}_{a,i}$  is greater than the amplitude of  $Y_{a,i}^e \hat{T}_{a,i}$  and thus, for some harmonics, gives rise to an amplitude of internal heat flux that is greater than the amplitude of external heat flux. In such a case, it is necessary to use the internal side periodic thermal transmittance  $\tau_{ie}$  as the fluctuating heat flux is directed from the indoor environment to the outdoor environment. In such a circumstance in Figure 8, the decrement factor and time lag are reported, for greater highlighting, in the lower half-plane with a red colour.

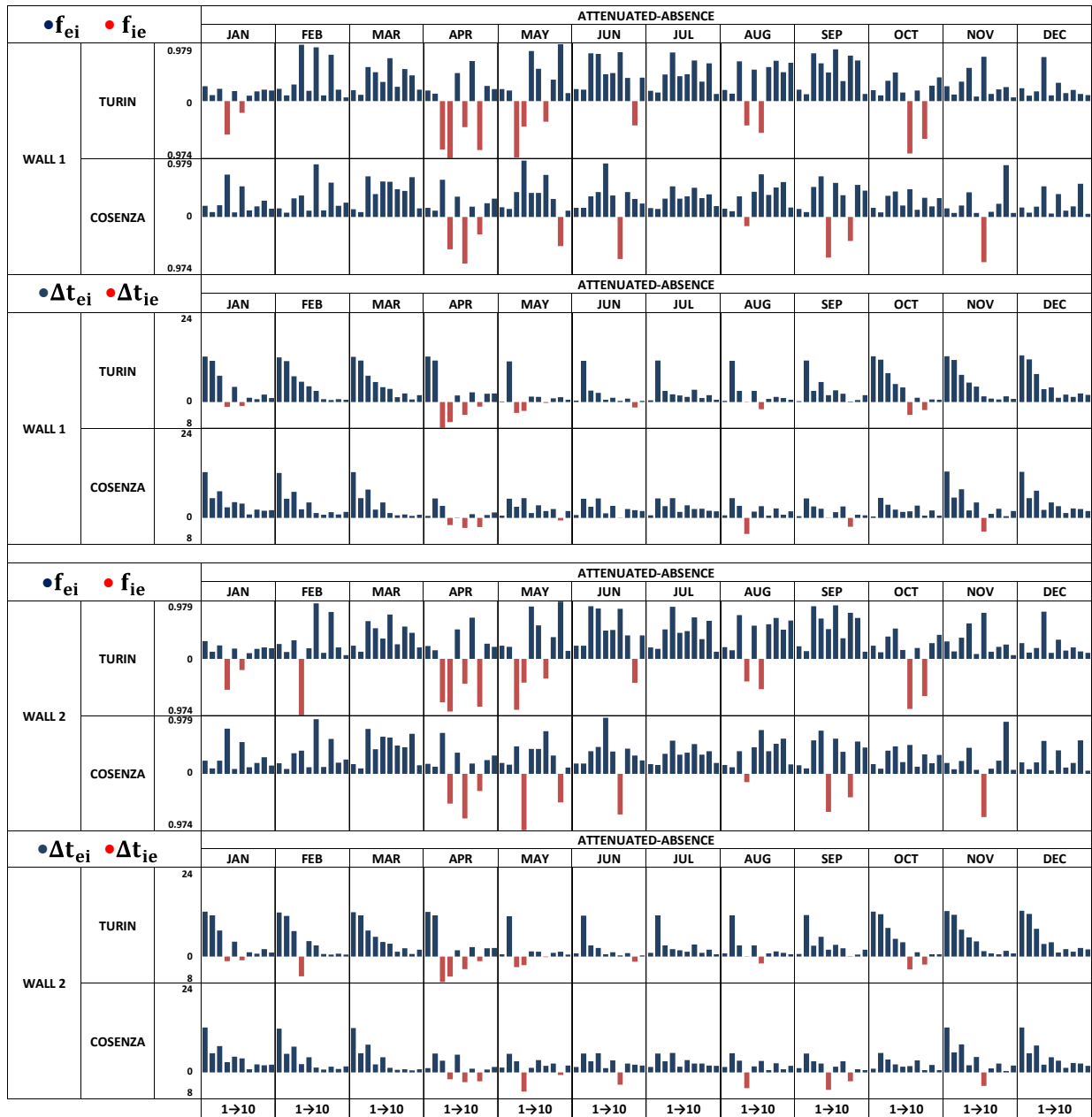


Figure 8 – Monthly decrement factor and time lag upon variation of pulsation for the two walls considered situated in Turin and Cosenza. Attenuated regime, absence of shortwave radiative heat flux on the internal surface. Southern orientation.

The presence of the shortwave radiant load on the inner surface (see Figure 9) gives rise to a slight modification of the frequency spectrum of the decrement factor only for the wall 2 in some months in Cosenza and of that of the time lag in summer. This minor change can be attributed to the small contribution of the internal shortwave radiant loading  $Y_{sr,i}^i \hat{\varphi}_{sr,i}$  compared to the internal air temperature loading contribution  $Y_{a,i}^i \hat{T}_{a,i}$ . The external heat flux is not modified as the contribution of the internal shortwave radiant loading  $Y_{sr,i}^e \hat{\varphi}_{sr,i}$  is negligible.

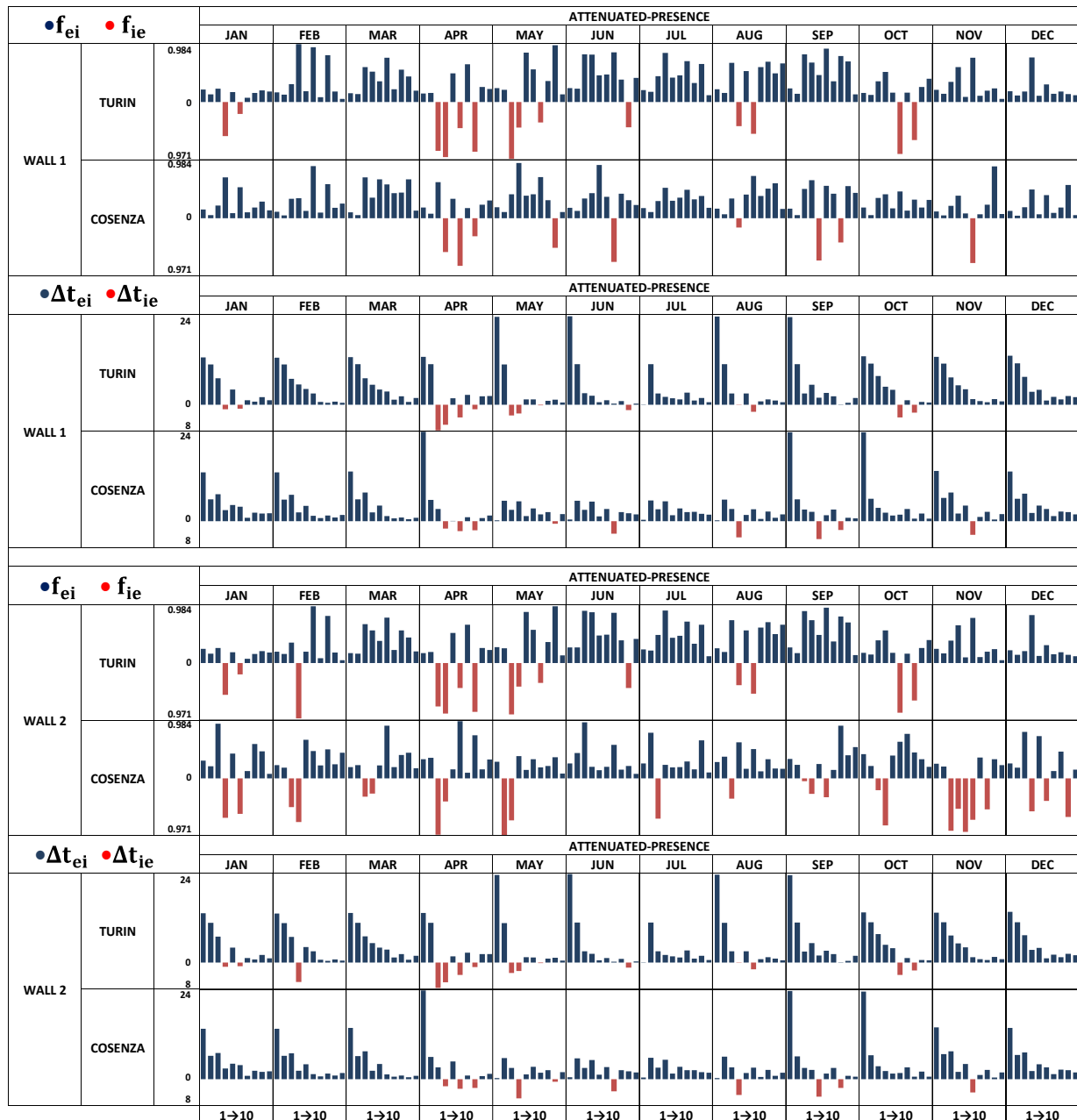


Figure 9 – Monthly decrement factor and time lag upon variation of pulsation for the two walls considered, situated in Turin and Cosenza. Attenuated regime, presence of shortwave radiative heat flux on the internal surface. Southern orientation.

### 3.3 Periodic non-sinusoidal condition, results and discussion

Summing the contributions of the single harmonics calculated with a frequency response analysis allowed us to determine the fluctuating component trends of the external and internal heat flux. Figure 10 reports the trends obtained for wall 1 situated in Turin referring to a winter month, January, (top figure) and to a summer month, August, (bottom figure). The trends are

relative to a continuous regime and to an attenuated regime in the absence and presence of shortwave radiative heat flux on the internal surface.

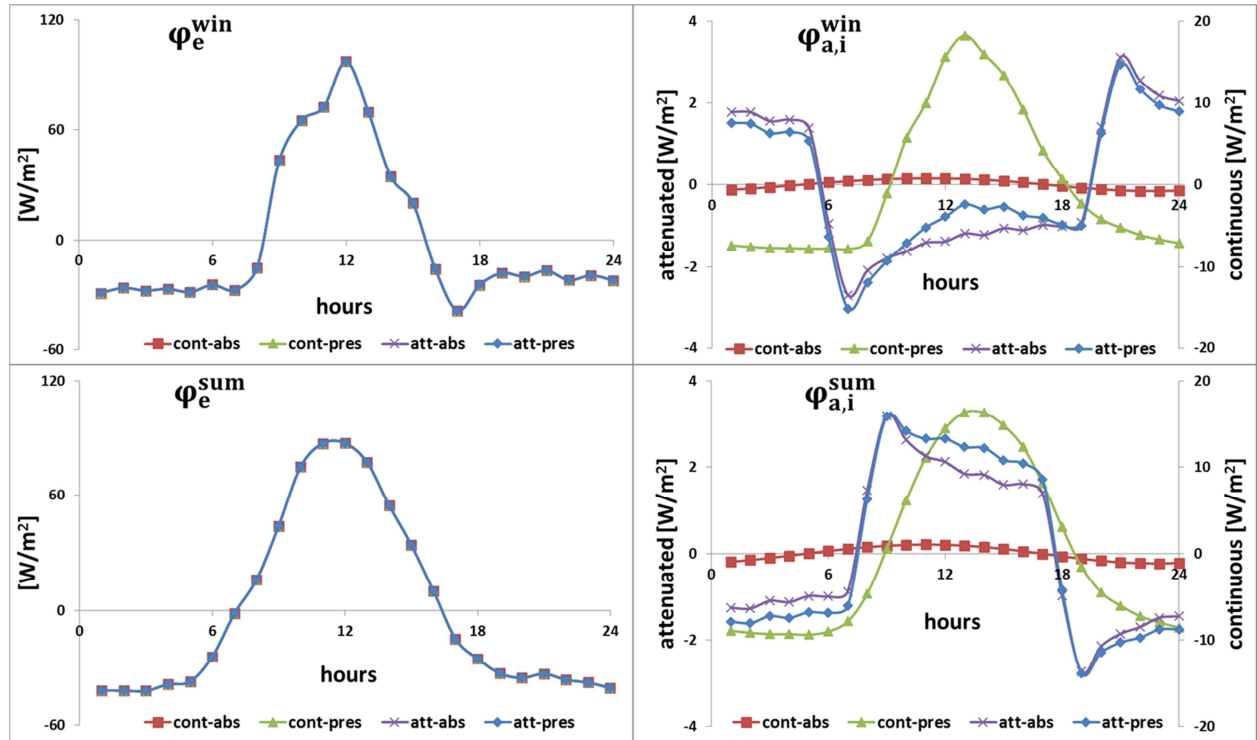


Figure 10 – Trends of the external heat flux (on the left) and of the internal heat flux (on the right) in winter (top) and in summer (bottom) in continuous (cont) and attenuated (att) regimes, in the absence (abs) and presence (pre) of shortwave radiative heat flux on the internal surface. Turin, wall 1.

The scale used to represent the fluctuating heat flux on the external surface (figure on the left) does not allow for the highlighting of marginal effects produced on the external heat flux by contributions  $Y_{sr,i}^e \hat{\varphi}_{sr,i}$  and  $Y_{a,i}^e \hat{T}_{a,i}$  due to loadings  $\hat{\varphi}_{sr,i}$  and  $\hat{T}_{a,i}$  that act on the internal surface. The figures on the right show the effects produced on the heat flux that is ceded to the indoor environment by the shortwave radiative heat flux on the internal surface, both in the continuous and the attenuated regime in the two months considered. In particular, the presence of the internal shortwave radiant load in the continuous regime increases the amplitude of the fluctuation and modifies the instant in which the heat flux peak occurs both in summer and in winter. This gives rise to an increase of the fluctuating energy transferred to the indoor environment during diurnal hours and of the fluctuating energy that is transferred in the wall to the outdoor environment during nocturnal hours.

In winter, in the attenuated regime, the shortwave radiative heat flux on the internal surface reduces the fluctuation amplitude of the internal heat flux with a consequent reduction of the fluctuating energy that is transferred in the wall to the outside during diurnal hours, and of the



fluctuating energy that is transferred to the indoor environment during at night. The opposite is the case in summer, when the fluctuation amplitude of the internal heat flux increases with a consequent increase in the fluctuating energy transferred to the indoor environment during the day, and of the fluctuating energy that is transferred in the wall, towards the outside, during nocturnal hours. The comparison between the continuous and attenuated regime shows that the internal heat flux presents a greater amplitude in the attenuated regime produced by the contribution of the internal air temperature loading fluctuation. Moreover, such a contribution modifies the instants in which the maximum and minimum peaks of the internal heat flux occur both in winter and in summer.

The monthly values of the decrement factors and of the time lags, calculated with Eqs. (26a), (26b) and (26c) and (27a) and (27b), for wall 1 in Turin, in the case of continuous heating and cooling and an absence of shortwave radiant loads on the internal surface are reported in Figure 11.

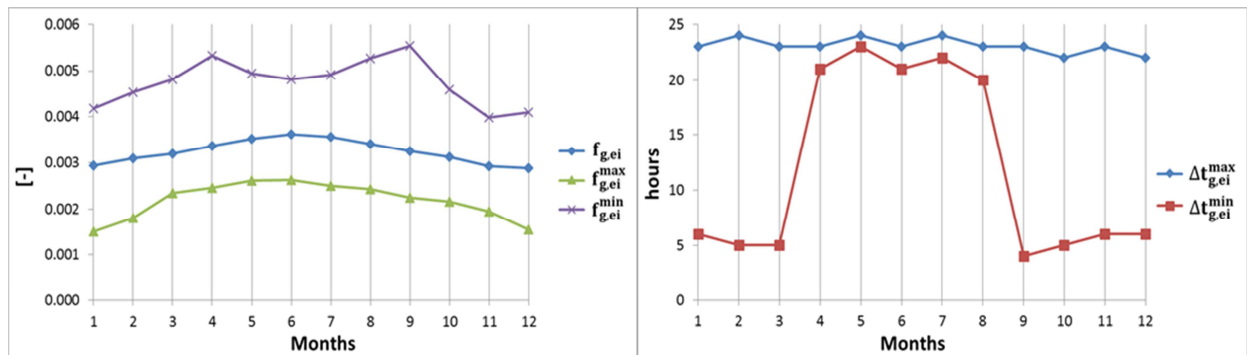


Figure 11 - Continuous regime in absence of internal shortwave radiant loads – Wall 1, Turin. Image on the left: monthly values of the energy decrement factor  $f_{g,ei}$ , of the maximum peak of the heat flux  $f_{g,ei}^{max}$  and of the minimum peak of the heat flux  $f_{g,ei}^{min}$ . Image on the right: monthly values of the time lag of the maximum peak of the heat flux  $\Delta t_{g,ei}^{max}$  and of the minimum peak of the heat flux  $\Delta t_{g,ei}^{min}$ .

The decrement factors (figure 11, left) defined in terms of maximum heat flux and energy, vary throughout the year with higher values in summer. The decrement factor of the minimum heat flux presents the same trend in summer and in winter with a minimum in the months of June and of November. A comparison of the trends highlights that the wall dampens the maximum heat flux and the energy in transit largely and, to a lesser extent, the minimum heat flux. The lower decrement factor values occur in winter months. Concerning the time lag, see Figure 11 on the right, shows that the time lag of the maximum heat flux is high and slightly variable throughout the year with values of approximately 24 hours, while the time lag of the minimum heat flux

remains high during summer and reduces notably during winter.

The presence of a shortwave radiant load on the surface in contact with the internal air modifies the dynamic behaviour of the wall. The decrement factors, see Figure 12 on the left, increase by approximately an order of magnitude, they have close values and present lesser variability throughout the year. The time lag of the maximum heat flux (see Figure 12, right) is still slightly variable throughout the year with values close to an hour, while the time lag of the minimum heat flux presents an inversion of the trend with higher values in winter.

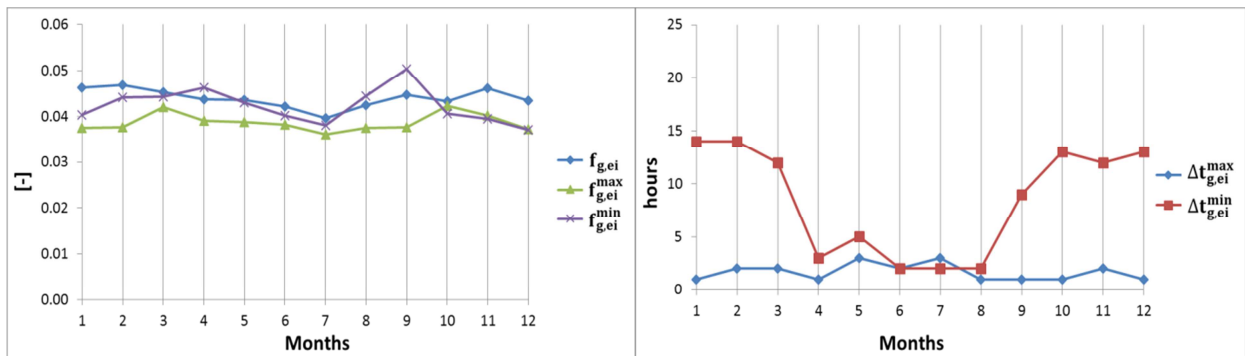


Figure 12 - Continuous regime in presence of internal shortwave radiant loads – Wall 1, Turin. Image on the left: monthly values of the energy decrement factor  $f_{g,ei}$ , of the maximum peak of the heat flux  $f_{g,ei}^{max}$  and of the minimum peak of the heat flux  $f_{g,ei}^{min}$ . Image on the right: monthly values of the time lag of the maximum peak of the heat flux  $\Delta t_{g,ei}^{max}$  and of the minimum peak of the heat flux  $\Delta t_{g,ei}^{min}$ .

The decrement factor and time lag present similar behaviour for wall 1 in Cosenza, in the absence and presence of internal shortwave radiant loads, as reported in Figures 13 and 14.

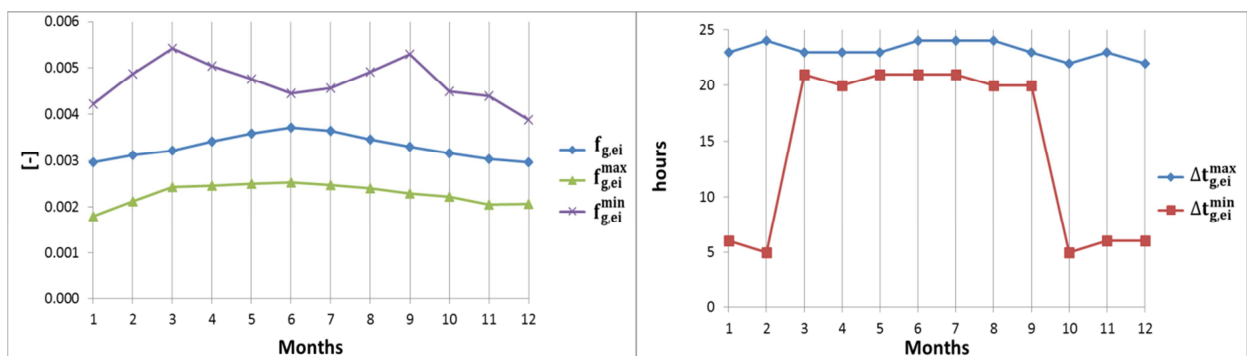


Figure 13 - Continuous regime in absence of internal shortwave radiant loads – Wall 1, Cosenza. Image on the left: monthly values of the energy decrement factor  $f_{g,ei}$ , of the maximum peak of the heat flux  $f_{g,ei}^{max}$  and of the minimum peak of the heat flux  $f_{g,ei}^{min}$ . Image on the right: monthly values of the time lag of the maximum peak of the heat flux  $\Delta t_{g,ei}^{max}$  and of the minimum peak of the heat flux  $\Delta t_{g,ei}^{min}$ .

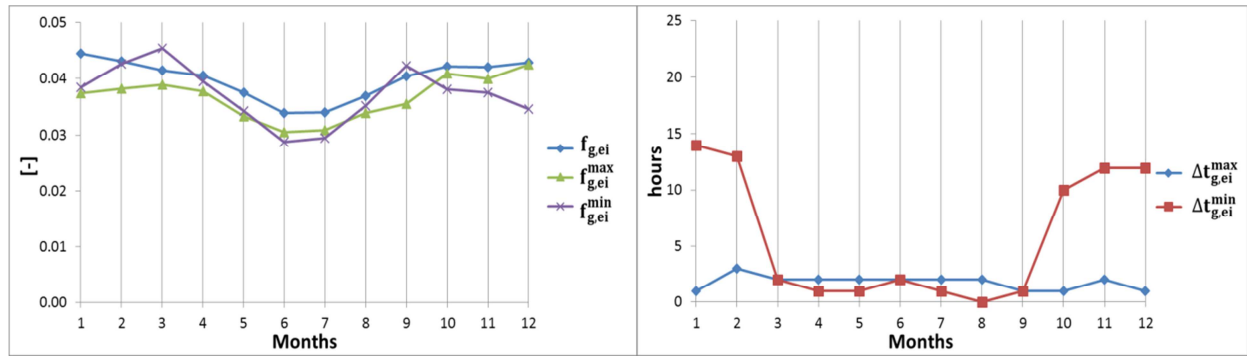


Figure 14 - Continuous regime in presence of internal shortwave radiant loads – Wall 1, Cosenza. Image on the left: monthly values of the energy decrement factor  $f_{g,ei}$ , of the maximum peak of the heat flux  $f_{g,ei}^{max}$  and of the minimum peak of the heat flux  $f_{g,ei}^{min}$ . Image on the right: monthly values of the time lag of the maximum peak of the heat flux  $\Delta t_{g,ei}^{max}$  and of the minimum peak of the heat flux  $\Delta t_{g,ei}^{min}$ .

In attenuated regime conditions in the absence of internal shortwave radiant loads (see Figure 15, left) the decrement factors, increase by approximately two orders of magnitude compared to the continuous regime; they have a trend with greater variability, which is no longer regular throughout the year. The time lag of the maximum heat flux, compared to an analogous case in a continuous regime, is significantly reduced during winter months (Figure 15, right) while the time lag of the minimum heat flux presents higher values in winter.

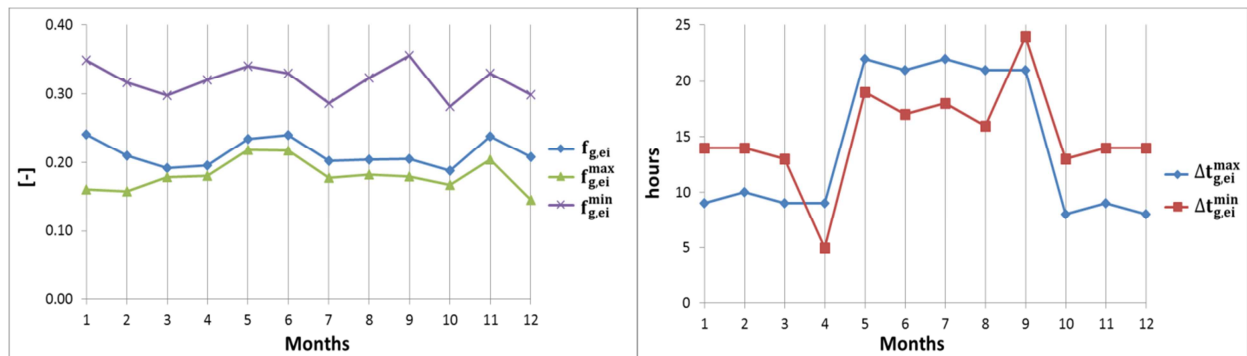


Figure 15 - Attenuated regime in the absence of internal shortwave radiant loads – Wall 1, Turin. Image on the left: monthly values of the energy decrement factor  $f_{g,ei}$ , of the maximum peak of the heat flux  $f_{g,ei}^{max}$  and of the minimum peak of the heat flux  $f_{g,ei}^{min}$ . Image on the right: monthly values of the time lag of the maximum peak of the heat flux  $\Delta t_{g,ei}^{max}$  and of the minimum peak of the heat flux  $\Delta t_{g,ei}^{min}$ .

In the presence of internal radiant loads, see Figure 16 on the left, the decrement factors increase by an order of magnitude compared to the continuous regime, and are no longer close to each other. Instead, concerning the time lag, see Figure 16 on the right, compared to an analogous case in a continuous regime, an increase in the time lag of the maximum heat flux is recorded,

which is more significant in summer. The time lag of the minimum heat flux modifies the seasonal trend with higher values during the summer period.

In the presence of internal radiant loads, compared to the case in which they are absent, the decrement factor defined in terms of minimum heat flux is higher, while that defined in terms of energy is lower in winter and greater in summer. The time lags are not subject to modifications.

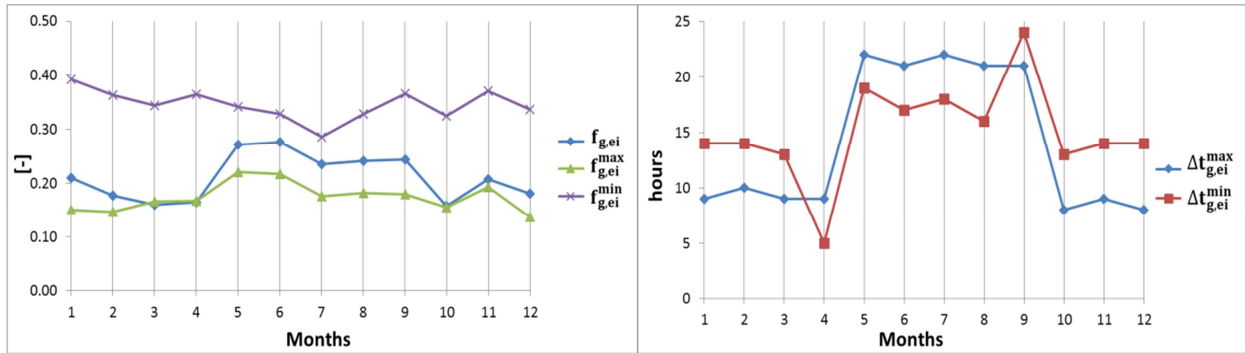


Figure 16. Attenuated regime in the presence of internal shortwave radiant loads – Wall 1, Turin. Image on the left: monthly values of the energy decrement factor  $f_{g,ei}$ , of the maximum peak of the heat flux  $f_{g,ei}^{max}$  and of the minimum peak of the heat flux  $f_{g,ei}^{min}$ . Image on the right: monthly values of the time lag of the maximum peak of the heat flux  $\Delta t_{g,ei}^{max}$  and of the minimum peak of the heat flux  $\Delta t_{g,ei}^{min}$ .

In an attenuated regime in Cosenza, both in the absence and presence of internal shortwave radiant loads, compared to Turin, the decrement factors are slightly less and the time lags record a slight reduction in the maximum heat flux in summer, see Figures 17 and 18.

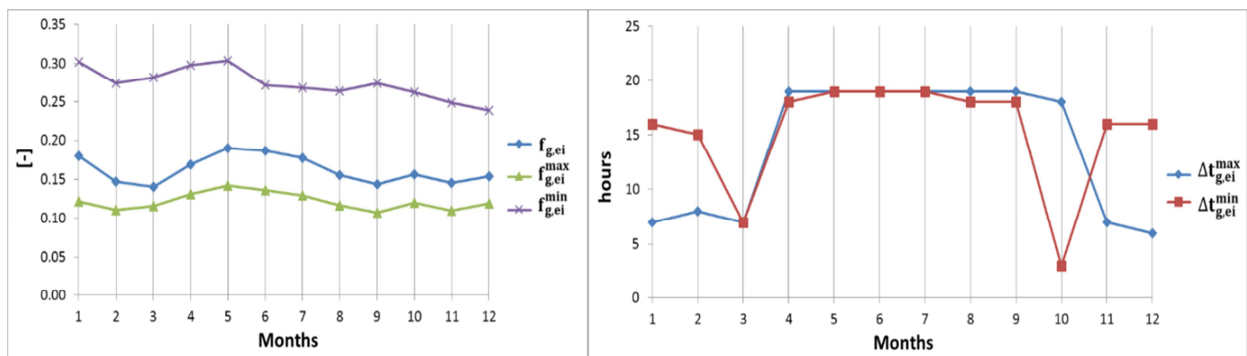


Figure 17 - Attenuated regime in the absence of internal shortwave radiant loads – Wall 1, Cosenza. Image on the left: monthly values of the energy decrement factor  $f_{g,ei}$ , of the maximum peak of the heat flux  $f_{g,ei}^{max}$  and of the minimum peak of the heat flux  $f_{g,ei}^{min}$ . Image on the right: monthly values of the time lag of the maximum peak of the heat flux  $\Delta t_{g,ei}^{max}$  and of the minimum peak of the heat flux  $\Delta t_{g,ei}^{min}$ .

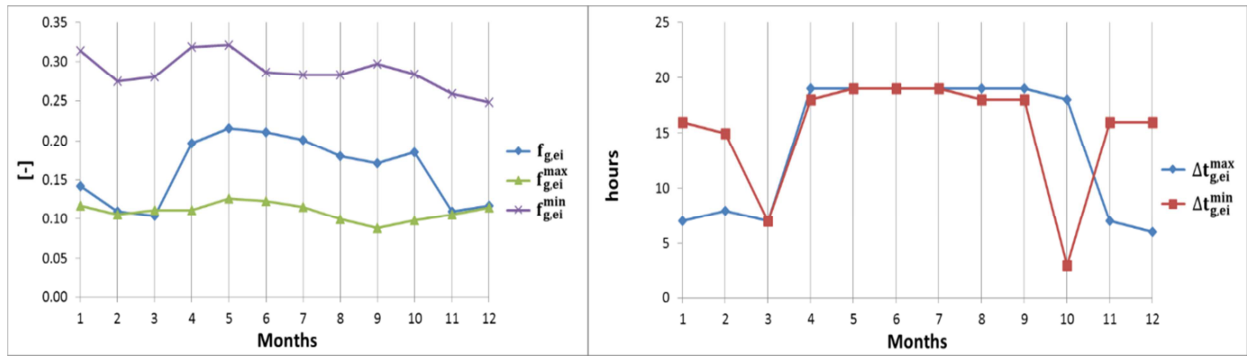


Figure 18. Attenuated regime in the presence of internal radiant loads – Wall 1, Cosenza. Image on the left: monthly values of the energy decrement factor  $f_{g,ei}$ , of the maximum peak of the heat flux  $f_{g,ei}^{max}$  and of the minimum peak of the heat flux  $f_{g,ei}^{min}$ . Image on the right: monthly values of the time lag of the maximum peak of the heat flux  $\Delta t_{g,ei}^{max}$  and of the minimum peak of the heat flux  $\Delta t_{g,ei}^{min}$ .

The previous trends show that the monthly decrement factor and time lag values can be summarised through the average summer and winter values. These results offer the possibility of distinguishing the behaviour of the wall in summer from that in winter in relation to the operating regime of the plant, to the internal side boundary conditions, to the location and to the orientation of the wall.

### 3.3.1 Decrement factor and time lag of the maximum heat flux in summer

The average values of the decrement factor of the maximum heat flux in the summer period, in relation to the relative time lag for different orientations, are reported in Figure 19. The results obtained for Southern orientation demonstrate that the sixteen cases studied, varying the location, the wall, the plant operating regime and the internal side boundary conditions, give rise to seven different dynamic behaviours, shown in the figure with symbols 1a, 1b, 2, 3a, 3b, 4a and 4b.

Each dynamic behaviour is characterised by its having close values of the decrement factor and time lag. The results can be summarised as follows:

- in a continuous regime, without internal shortwave radiant loads, the decrement factor  $f_{g,ei}^{max}$  and time lag  $\Delta t_{g,ei}^{max}$  do not vary with the location and are influenced by the type of wall (case 1a and 1b). In particular, wall 1, which is more capacitive, compared to wall 2, presents a greater time lag and a lesser decrement factor;
- in a continuous regime, in the presence of internal shortwave radiant loads, the walls present similar dynamic properties independent of the location (case 2);

- in an attenuated regime, walls 1 and 2 in Cosenza present different decrement factor values  $f_{g,ei}^{max}$  and similar time lag values  $\Delta t_{g,ei}^{max}$ ; for both the walls. The presence of internal shortwave radiant loads reduces the decrement factor (case 3a and 3b);
- in an attenuated regime, walls 1 and 2 in Turin present different decrement factor values  $f_{g,ei}^{max}$  and close time lag values  $\Delta t_{g,ei}^{max}$ . For both the wall, the decrement factor and time lag are not influenced by the internal shortwave radiant loads (case 4a and 4b).

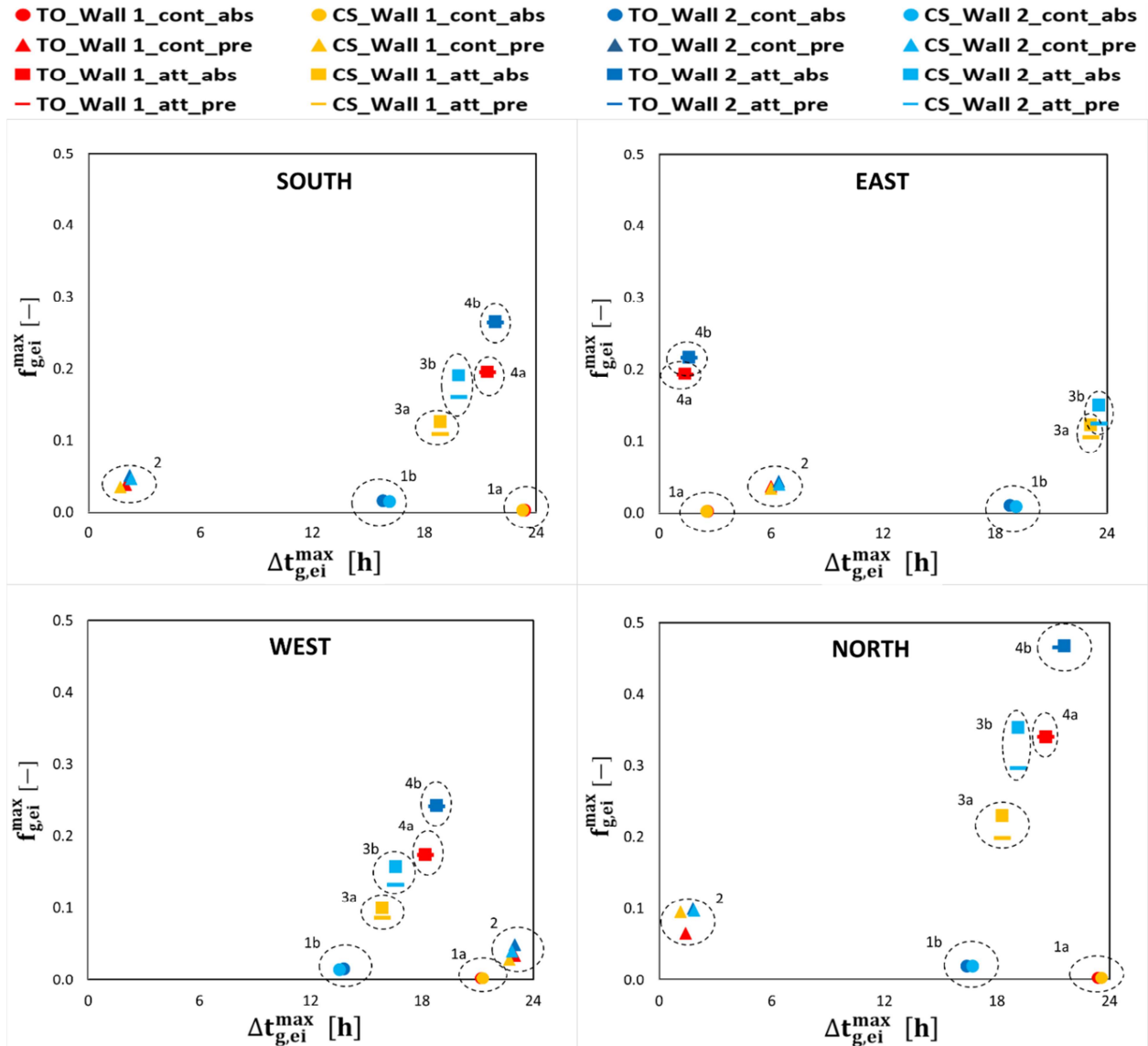


Figure 19 - Average values in summer of the decrement factor of the maximum heat flux  $f_{g,ei}^{max}$  as a function of the time lag of the maximum heat flux  $\Delta t_{g,ei}^{max}$  for the different orientations, in continuous regime and with nocturnal attenuation, in the absence and presence of internal shortwave radiant loads for walls 1 and 2 in Turin and Cosenza.

The modification of the wall's orientation gives rise to a different solar loading trend, with a

variation in the amplitude and the instant in which the maximum heat flux peak occurs. This, in turn, gives rise to a variation in the dynamic parameters, which can still be summarised by the previously identified groupings. The results relative to the walls with southern orientation are compared hereafter to those obtained varying the orientation of the walls. For each behaviour, the average summer value for the decrement factor and the time lag is considered.

The modification of the orientation in behaviours 1a and 1b gives rise, in the east, to a reduction of the decrement factor and an increase of the time lag. To the west, the decrement factor remains practically unvaried and the time lag is reduced. Finally, to the north, the decrement factor increases and the time lag remains almost identical. In particular, in the case:

**1a)**  $f_{g,ei}^{\max}$  varies from 0.0024 to the south to 0.0019 to the east, to 0.0031 to the north, and remains almost unvaried to the west.  $\Delta t_{g,ei}^{\max}$  varies from 23.3 hours for south to 26.6 hours for east, to 21.2 hours for west and remains almost unchanged for north;

**1b)**  $f_{g,ei}^{\max}$  varies from 0.015 to the south to 0.009 for east, to 0.020 for north and remains unchanged for west.  $\Delta t_{g,ei}^{\max}$  varies from 16 hours for south to 19 hours for east and 13.7 hours for west; it remains almost unaltered for north.

In behaviour **2)**, modifying orientation from south to east or west results in close decrement factor values, while the time lag increases for east and reduces for west. Instead, for northern orientation, the decrement factor increases in a different manner with a variance in location and the wall, while the time lag remains almost unvaried. In particular, for south facing walls, the decrement factor  $f_{g,ei}^{\max}$  varies between 0.035 and 0.051, and for north facing walls the corresponding values increase and are variable between 0.066 and 0.099. The time lag  $\Delta t_{g,ei}^{\max}$  varies from 2.15 hours for south to 6.2 hours for east and 22.8 hours for west.

For behaviours 3a, 3b, 4a and 4b, the decrement factor reduces for east and west, compared to south, and increases for north. The time lag increases for east, reduces for west and remains unvaried for north. In particular:

**3a)**  $f_{g,ei}^{\max}$  varies from 0.117 for south to 0.113 for the east, to 0.093 for west and to 0.214 for north.  $\Delta t_{g,ei}^{\max}$  varies from 18.9 hours for the south to 23.14 hours for east and 15.86 hours for west. It remains almost unaltered for north;

**3b)**  $f_{g,ei}^{\max}$  varies from 0.175 for south to 0.137 for east, to 0.145 for west and to 0.325 for north.  $\Delta t_{g,ei}^{\max}$  varies from 18.9 hours for the south to 23.6 hours for east, 16.6 hours for west and remains almost unvaried for the north;

**4a)**  $f_{g,ei}^{\max}$  varies from 0.195 for south to 0.193 for east, to 0.174 for west and to 0.341 for

north.  $\Delta t_{g,ei}^{\max}$  varies from 21.4 hours for south to 25.4 hours for east, to 18.2 hours for west and remains almost unaltered for north;

**4b)**  $f_{g,ei}^{\max}$  varies from 0.265 for south to 0.216 for east, to 0.242 for west and to 0.468 for north.

$\Delta t_{g,ei}^{\max}$  varies from 21.8 hours for south to 25.6 hours for east and to 18.8 hours for west; it remains almost unvaried for north.

### 3.3.2 Decrement factor and time lag of the minimum heat flux in winter

If the minimum peak of the heat flux relative to the winter season is considered, see Figure 20, the previously identified behaviours remain confirmed. A comparison with Figure 19, relating to the summer period, shows that in a continuous operating regime (cases 1a, 1b and 2), south facing walls present a dynamic behaviour that is slightly different. In an operating regime with nocturnal attenuation (cases 3a, 3b, 4a and 4b) the time lag is reduced in a significant manner while decrement factor undergoes a contained reduction.

A change in orientation, compared to south, gives rise to dynamic parameters that are different in the different cases. In particular:

**1a)** the decrement factor undergoes contained variations and goes from 0.0045 to the south to 0.0036 to the east, 0.0046 to the west and to 0.0041 to the north. The time lag increases from 8.25 hours to the south to 18.70 hours to the east, to 20.5 hours to the north. To the west, the time lag increases and also depends on the location and is equal to 12.30 hours in Turin and to 17.2 hours in Cosenza;

**1b)** western orientation gives rise to a reduction of the decrement factor from 0.0225 for a south facing wall to 0.0184. It increases for east and north facing walls and is equal to 0.0278 and 0.0302 respectively. The time lag increases from 22.4 hours to the south, to 23.86 hours to the west and reduces for east facing and north facing walls and is equal to 11.20 hours and 14.20 hours respectively;

**2)** the decrement factor increases and goes from 0.042 in the south to 0.080 in the east, to 0.054 in the west and to 0.0102 in the north. The time lag is 12.3 hours for south, 2.35 hours for east, 8.41 hours for west and 3.05 hours for north.



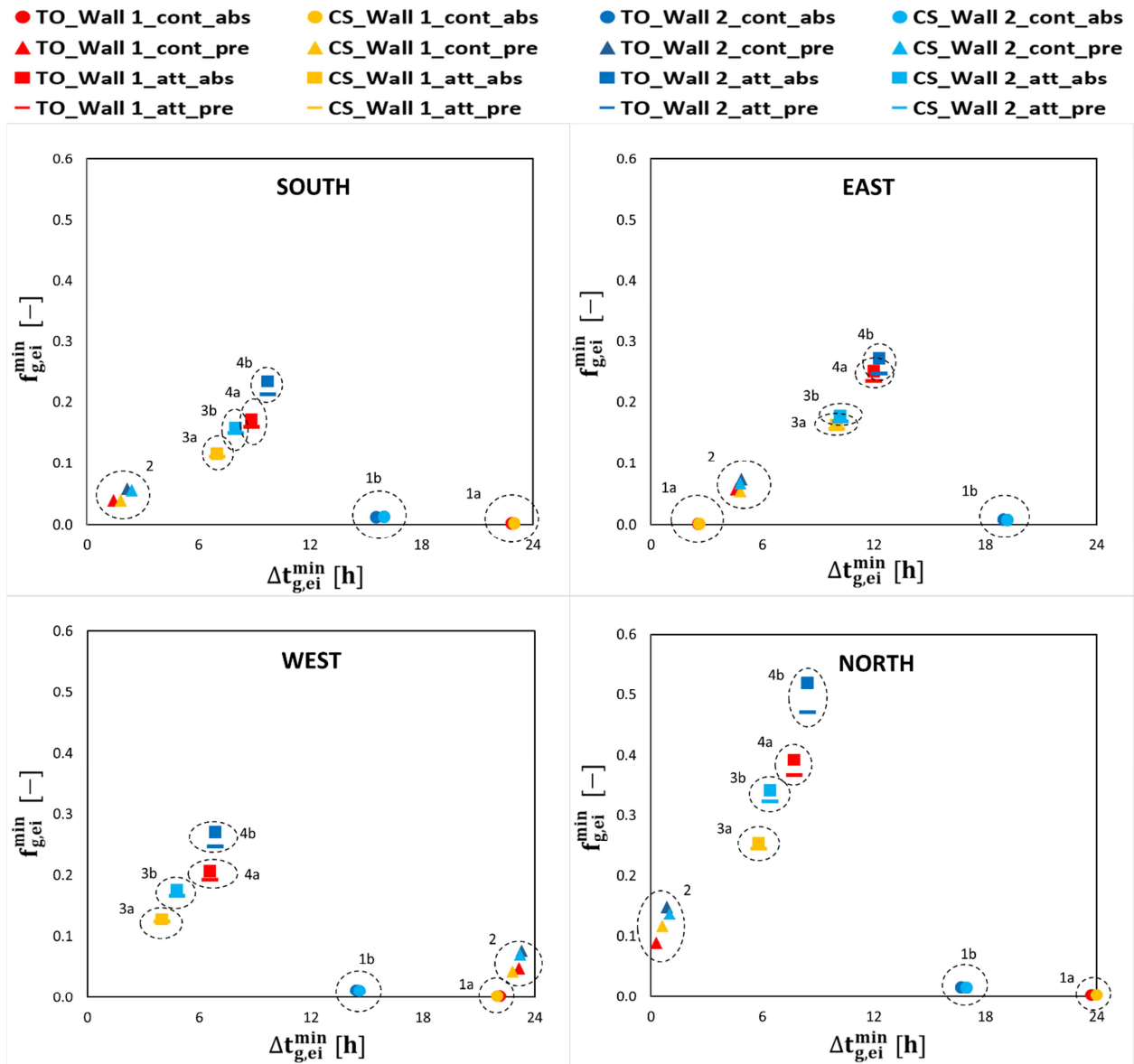


Figure 20 - Average values in winter of the decrement factor of the minimum heat flux  $f_{g,ei}^{min}$  as a function of the time lag of the minimum heat flux  $\Delta t_{g,ei}^{min}$  for the different orientations, in continuous regime and with nocturnal attenuation, in the absence and presence of internal shortwave radiant loads for walls 1 and 2 in Turin and Cosenza.

In behaviours 3a, 3b and 4a, a general trend can be seen in which the decrement factor increases, compared to south, from west to east and to north, while the time lag is reduced in an increasing manner in the order of west, north, and east. In particular:

**3a)** the decrement factor increases from 0.272 for south to 0.402 for east and west and to 0.470 for north. The time lag reduces from 14 hours for south to 4.6 hours for east and north and to 6.4 hours in the west.

**3b)** the decrement factor ranges from 0.271 for south to 0.321 for west, to 0.604 for east and to 0.688 for north. The time lag of 15.6 hours for south becomes 15.5 hours for west, 6 hours for north and 4.8 hours for east.

**4a)** the decrement factor is 0.335 for south, 0.459 for west, 0.489 for east and 0.574 for north. The south time lag of 12.43 hours becomes 8.57 hours for west, 2.71 hours for north and 2.43 hours for east;

**4b)** the decrement factor increases from 0.271 for south to 0.414 for west, to 0.758 for east, and to 0.876 for north; the time lag for south of 15.6 hours becomes 13.43 hours for west, 4.43 hours for north and 3.14 hours for east.

### **3.3.3 Decrement factor in terms of energy in the summer and winter period**

The average decrement factor in the summer period in relation to the winter decrement factor for the different orientations is reported in Figure 21. In order to facilitate reading, the bisector has also been traced to highlight the season in which the decrement factor is lower.

In a continuous operating regime in the absence of internal shortwave radiant loads (cases 1a and 1b), the summer decrement factor differs slightly from the winter decrement factor regardless of the orientation. The presence of internal shortwave radiant loads (case 2) increases the decrement factor both in summer and in winter. For southern orientation the increase is almost equal in both seasons and for the other orientations the winter increase prevails over the summer one.

In an attenuated regime, the classification of the previous behaviours is no longer valid. In particular, the two decrement factors for southern orientation are close in the absence of internal shortwave radiant loads. For the other orientations, compared to the south, the decrement factors are modified: for western orientation the winter one increase while the summer one decreases; while for northern and eastern orientations both winter and summer decrement factors increase. In the presence of internal shortwave radiant loads, compared to the case in which they are absent, for all the orientations, the decrement factor in winter is reduced and it increases during the summer period. In the west, the two decrement factors are close.

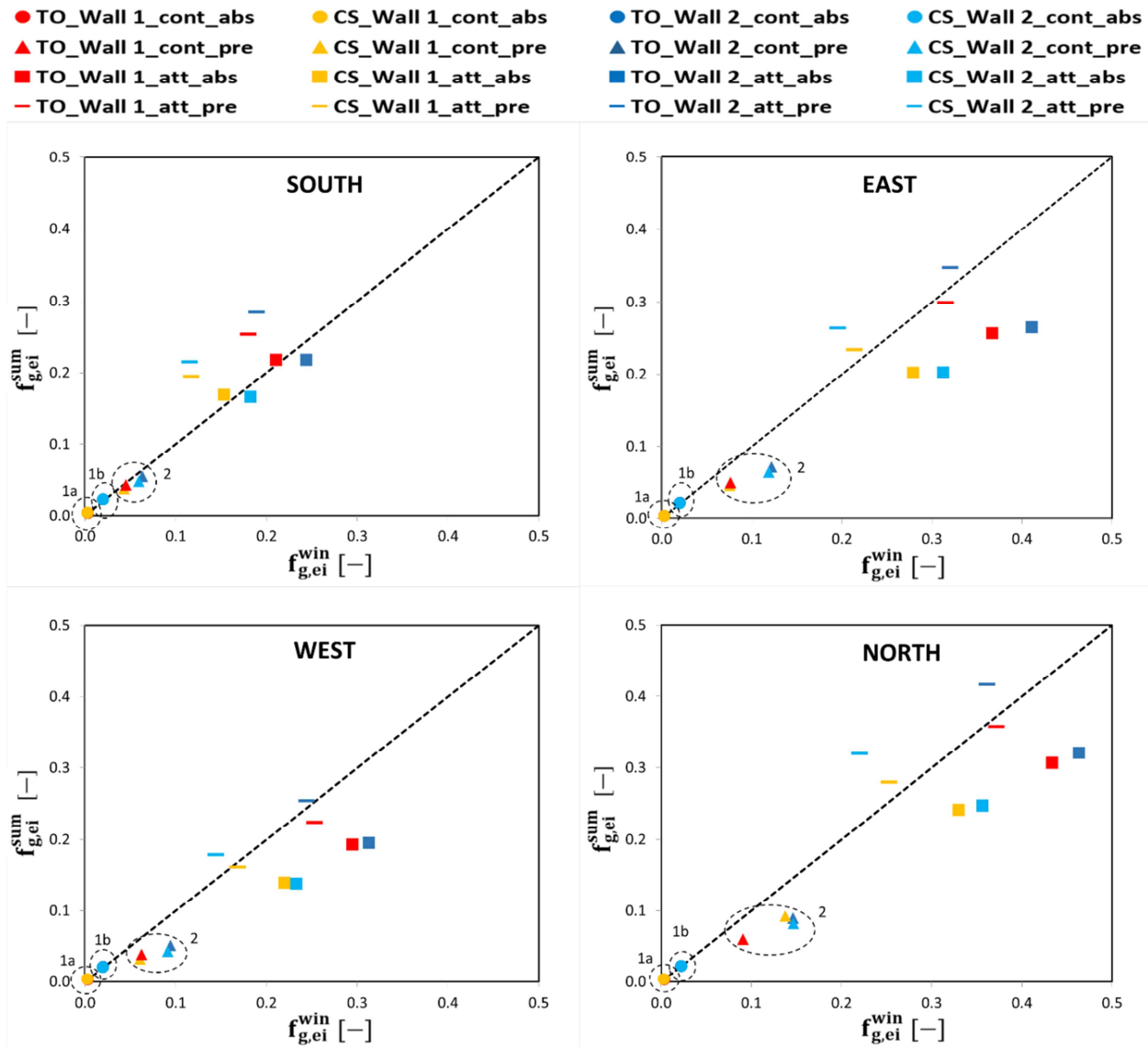


Figure 21 – Average values of the decrement factor in terms of energy in the summer and winter period for the different orientations, in continuous regime and with nocturnal attenuation, in the absence and presence of internal shortwave radiant loads for walls 1 and 2 in Turin and Cosenza.

### 3.3.4 Determination of the number of harmonics required by means of the THD criterion

For all the cases considered relating to southern orientation, the distortion of the external heat flux THDe and of the heat flux that penetrates the indoor environment THDi was determined by Eq. (28) considering all the harmonics ( $n=10$ ). The average seasonal values, calculated as the average of the relative monthly values, are reported in Table 2. The table shows that in a continuous operation regime, both in summer and in winter, the most distorted heat flux is the external heat flux, in both the presence and absence of a shortwave radiant heat flux on the internal surface. In particular, in the absence of a shortwave radiant heat flux on the internal

surface, the internal heat flux does not deviate greatly from a sinusoidal trend. The presence of the internal shortwave radiant heat flux increases distortion of the internal heat flux. In an attenuated regime, the distortion of the internal heat flux is approximate to that of the external heat flux and the presence of the internal shortwave radiant heat flux does not significantly modify distortion.

*Table 2 – Winter and summer seasonal average value of the external heat flux  $THD_e$  and of the internal heat flux  $THD_i$  for  $n=10$  harmonics for the two walls varying the location and the plant operating regime, in the absence and presence of internal shortwave radiant loads. Southern orientation.*

$THD_e$		cont-abs		cont-pres		att-abs		att-pres	
		win	sum	win	sum	win	sum	win	sum
Wall 1	TU	0.6918	0.4012	0.6920	0.4013	0.6925	0.4008	0.6927	0.4009
	CS	0.6769	0.4318	0.6771	0.4319	0.6775	0.4316	0.6777	0.4316
Wall 2	TU	0.8028	0.4617	0.8012	0.4609	0.7982	0.4647	0.7966	0.4638
	CS	0.7830	0.4974	0.7815	0.4965	0.7791	0.4993	0.7776	0.4984
$THD_i$		cont-abs		cont-pres		att-abs		att-pres	
		win	sum	win	sum	win	sum	win	sum
Wall 1	TU	0.0499	0.0303	0.4174	0.3130	0.5469	0.5277	0.7360	0.4827
	CS	0.0495	0.0322	0.4249	0.3453	0.5506	0.5247	0.6489	0.4030
Wall 2	TU	0.1155	0.0700	0.5748	0.4620	0.6122	0.656	0.8725	0.5776
	CS	0.1145	0.0744	0.5982	0.5392	0.5947	0.6464	0.7473	0.4743

The percentage relative error, evaluated with Eq. (29) was used to determine the number of harmonics  $n$  necessary to calculate the most distorted heat flux with a THD error of no more than 2%. Table 3 reports the average number of harmonics required during summer and winter for the different cases.

*Table 3 – Winter and summer seasonal average value of the number of harmonics necessary for the calculation of the most distorted heat flux with a percentage relative error less than 2%. Southern orientation.*

Number of harmonics		cont-abs		cont-pres		att-abs		att-pres	
		win	sum	win	sum	win	sum	win	sum
WALL 1	TU	5.43	5.00	5.43	5.00	8.00	8.00	6.86	7.00
	CS	4.60	4.43	4.60	4.43	8.00	8.00	8.00	8.00
WALL 2	TU	6.14	5.80	6.14	5.80	8.00	8.00	7.57	8.00
	CS	5.60	5.00	5.60	5.00	8.00	8.00	8.00	8.00

In a continuous regime, the average number of harmonics to consider for the calculation of the external heat flux is greater during winter and varies between four and six. Instead, in an

attenuated regime, the number of harmonics is between seven and eight. For example, in Figure 22, in the case of wall 1 situated in Turin and in an attenuated regime in the absence of internal shortwave radiant loads, monthly values of the decrement factors and of the time lags calculated considering all the harmonics and a number of harmonics identified with the THD criterion are compared.

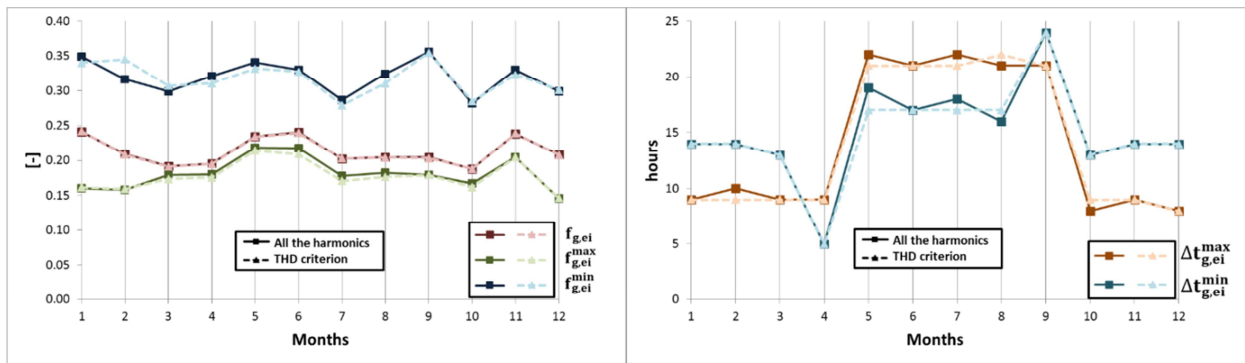


Figure 22 - Comparison between the decrement factors and the time lags calculated considering all the harmonics and a reduced number of harmonics determined with the THD criterion. Wall 1, south facing, Turin, attenuated regime in the absence of internal shortwave radiant loads.

#### 4. Conclusions

The dynamic analysis in a sinusoidal periodic regime has shown that the internal and external side non-dimensional periodic thermal transmittances are the reference parameters to define the decrement factor and time lag that is undergone by the heat flux and the heat storage capacity of the wall. Such parameters can be calculated by means of the periodic thermal transmittance, the periodic thermal admittances and the areal heat capacities determined according to the EN ISO 13786 procedure.

The analysis of the frequency response has highlighted how, in general, the dynamic properties of a wall depend on the pulsation, on the amplitude and on the argument of the sinusoids associated with the different loadings, which vary with the month and the location, and on the plant operating regime.

In a continuous regime and in the absence of shortwave radiative heat flux on the internal surface, the parameter to be considered is the external side non-dimensional periodic thermal transmittance, whose decrement factor and time lag, for a generic harmonic, are not dependent on the location and do not present monthly variability. The decrement factor decreases upon an increase of the pulsation, while the time lag varies in a way that is not regular with the pulsation.

In the presence of internal shortwave radiant loads, the decrement factor and time lag of the external side non-dimensional periodic thermal transmittance of a generic harmonic vary with the location and month. The decrement factor, compared to the previous case, varies in an irregular manner upon pulsation increase; the time lag decreases with an increase in the pulsations in winter while it varies in an irregular manner during the summer months.

In an attenuated regime, the dynamic parameters present extreme variability to the different pulsations and still depend on the location and the month. In these conditions, since the direction of the fluctuating heat flux is reversed in some cases, the use of both the external side and internal side non-dimensional periodic thermal transmittance is necessary. The presence of the internal shortwave radiant load on the inner surface slightly modifies the frequency spectrum of the decrement factor and of the time lag.

Ultimately, the frequency analysis allows for the dynamic qualification of building components with identical boundary conditions and, for a defined component, consents the evaluation of the dynamic properties under changing boundary conditions.

The dynamic behaviour of the walls in actual operating conditions requires an analysis under a periodic non-sinusoidal regime, as the loadings that operate both inside and outside of the wall are non-sinusoidal. In such conditions, the decrement factor and the time lag of the maximum and minimum peak of the heat flux do not coincide, unlike the sinusoidal regime. The parameters necessary to describe the dynamic response fully are the decrement factor in terms of energy, the decrement factor of the maximum and minimum peak of the heat flux and the relative time lags. The calculation of dynamic parameters is achieved by means of non-dimensional periodic thermal transmittance at different pulsations. The sum of the heat flux transferred in steady conditions and the maximum peak of the fluctuating heat flux provides the maximum peak of the heat flux in the summer period; the sum calculated with the minimum peak of the fluctuating heat flux determines the maximum peak of the heat flux in the winter period.

The results of the analysis show that the operating mode of the plant and the possible presence of internal shortwave radiant loads, even in this case, modify the dynamic properties of the wall in a significant manner.

In a continuous regime, the presence of internal shortwave radiant loads increases the decrement factor by an order of magnitude, evaluated both in terms of heat flux and of energy. The internal radiant shortwave load gives rise to a time lag of the maximum heat flux which is still slightly variable during the year; furthermore, such loads increases during winter and in reduces summer the time lag of minimum heat flux.

In attenuated regime conditions and in the absence of internal shortwave radiant loads, the decrement factors, compared to a continuous regime, increase by approximately two orders of magnitude. The time lag of the maximum heat flux is reduced during winter months, while that of the minimum heat flux increases in winter. The presence of internal shortwave radiant loads, compared to the case in which they are absent, gives rise to an increase in the decrement factor of the minimum heat flux, and to a reduction in winter, and an increase in summer, of the decrement factor defined in terms of energy. The time lag does not change. Compared to the analogue case in a continuous regime, the decrement factors increase by an order of magnitude, while the time lag of the maximum heat flux increases largely in summer and the minimum heat flux presents higher values in summer.

The analysis conducted considering two walls with different thermophysical properties located in two climatically different locations has highlighted that the dynamic parameters, in terms of heat flux, in a continuous regime and in the absence of internal shortwave radiant loads, do not depend on the location and, instead, depend on the type of wall. In the presence of internal shortwave radiant loads, the previous considerations remain confirmed and the dependence of the type of wall is manifested only on the decrement factor and not on the time lag. In attenuated regime, the dynamic parameters depend on the location and on the wall. The presence of internal shortwave radiant loads modifies the decrement factor of the maximum and minimum heat flux and leaves the relative time lags unchanged.

The dynamic characteristics, as well as depending on the previously highlighted parameters, also depend on the trend of the loadings that vary with the orientation of the wall. Such dependence can be summarised thus.

The decrement factor of the maximum heat flux is higher to the north, regardless of the operating regime, the internal surface boundary conditions, the location and the wall. In a continuous regime and in the absence of internal shortwave radiant loads, the minimum value is found to the east, independent of the wall and the location. In all the other cases, east, west and south orientations present similar values. In all cases, the relative time lag presents the lowest value to the west and the highest to the east. North and south have similar values.

In addition, the decrement factor of the minimum heat flux presents, in general, higher values to the north. The most contained values can be observed in the eastern orientation in a continuous regime in the absence of internal shortwave radiant loads, in the west in the presence of internal shortwave radiant loads and in the south in an attenuated regime. The time lag of the minimum heat flux has higher values in the north in a continuous regime in the absence of internal shortwave radiant loads, in the west in a continuous regime in the presence of internal shortwave

radiant loads ad in the south in an attenuated regime. The lowest value is generally recorded in the east.

In terms of energy, the decrement factor, both during summer and winter, assumes higher values to the north. The orientation in which lower values are present depends upon the boundary conditions. In particular, in attenuated regime, they are recorded in the southern orientation in winter and in the western orientation in summer.

This study offers the possibility of distinguishing the summer and winter behaviour of the wall. Moreover, it can be useful in the thermal design of the wall in order to reduce power peaks and energy requirements during summer and winter conditioning.

## References

- [1] Directive 2010/31/EU. European Parliament and of the Council of 19 May 2010 on the Energy Performance of Buildings (recast). Official Journal of the European Union (2010), L 153, pp. 13-35.
- [2] Directive 2012/27/EU. European Parliament and of the Council of 25 October 2012 on energy efficiency, amending Directives 2009/125/EC and 2010/30/EU and repealing Directives 2004/8/EC and 2006/32/EC. Official Journal of the European Union (2012), L 315/1, pp. 1-56.
- [3] Lu Y, Wang S, Shan K. Design optimization and optimal control of grid-connected and standalone nearly/net zero energy buildings. *Applied Energy* 2015; 155:463-477. 10.1016/j.apenergy.2015.06.007.
- [4] Ascione F, Bianco N, De Masi RF, de Rossi F, Vanoli GP. Energy refurbishment of existing buildings through the use of phase change materials: Energy savings and indoor comfort in the cooling season. *Applied Energy* 2014; 113:990-1007. j.apenergy.2013.08.045.
- [5] Lee OL, Medina MA, Raith E, Sun X. Assessing the integration of a thin phase change material (PCM) layer in a residential building wall for heat transfer reduction and management. *Applied Energy* 2015; 137:699-706. 10.1016/j.apenergy.2014.09.003.
- [6] Goia F, Perino M, Haase M. A numerical model to evaluate the thermal behaviour of PCM glazing system configurations. *Energy and Buildings* 2012; 54:141-153. 10.1016/j.enbuild.2012.07.036.
- [7] Ibrahim M, Biwole PH, Achard P, Wurtz E, Ansart G. Building envelope with a new aerogel-based insulating rendering: Experimental and numerical study, cost analysis, and thickness optimization. *Applied Energy* 2015; 159:490-501. 10.1016/j.apenergy.2015.08.090.



- [8] Berardi U. The development of a monolithic aerogel glazed window for an energy retrofitting project. *Applied Energy* 2015; 154:603-615. 10.1016/j.apenergy.2015.05.059.
- [9] Pérez G, Coma J, Martorell I, Cabeza LF. Vertical Greenery Systems (VGS) for energy saving in buildings: A review. *Renewable and Sustainable Energy Reviews* 2014; 39:139-165. 10.1016/j.rser.2014.07.055.
- [10] Pérez G, Rincón L, Vila A, González JM, Cabeza LF. Green vertical systems for buildings as passive systems for energy savings, *Applied Energy* 2011; 88:4854-4859. 10.1016/j.apenergy.2011.06.032.
- [11] Bevilacqua P, Coma J, Pérez G, Chocarro C, Juárez A, Solé C, De Simone M, Cabeza LF. Plant cover and floristic composition effect on thermal behaviour of extensive green roofs. *Building and Environment* 2015; 92: 305-316. 10.1016/j.buildenv.2015.04.026.
- [12] Ascione F, Bianco N, de Rossi F, Turni G, Vanoli GP. Green roofs in European climates. Are effective solutions for the energy savings in air-conditioning?. *Applied Energy* 2013; 104:845-859. 10.1016/j.apenergy.2012.11.068.
- [13] Jim CY. Air-conditioning energy consumption due to green roofs with different building thermal insulation. *Applied Energy* 2014; 128:49-59. 10.1016/j.apenergy.2014.04.055.
- [14] Pisello AL, Piselli C, Cotana F. Thermal-physics and energy performance of an innovative green roof system: The Cool-Green Roof. *Solar Energy* 2015; 116:337-356. 10.1016/j.solener.2015.03.049.
- [15] Romeo C, Zinzi M, Impact of a cool roof application on the energy and comfort performance in an existing non-residential building. A Sicilian case study. *Energy and Buildings* 2013; 67:647-657. 10.1016/j.enbuild.2011.07.023.
- [16] Kolokotroni M, Gowreesunker BL, Giridharan R. Cool roof technology in London: An experimental and modelling study. *Energy and Buildings* 2013; 67:658-667. 10.1016/j.enbuild.2011.07.011.
- [17] Reda F, Arcuri N, Loiacono P, Mazzeo D. Energy assessment of solar technologies coupled with a ground source heat pump system for residential energy supply in Southern European climates. *Energy* 2015; 91:294-305. 10.1016/j.energy.2015.08.040
- [18] Reda F. Long term performance of different SAGSHP solutions for residential energy supply in Finland. *Applied Energy* 2015; 144:31-50. 10.1016/j.apenergy.2015.01.059.
- [19] Chen X, Yang H. Performance analysis of a proposed solar assisted ground coupled heat pump system. *Applied Energy* 2012; 97:888-896. 10.1016/j.apenergy.2011.11.073.
- [20] Hong T, Koo C, Kim J, Lee M, Jeong K. A review on sustainable construction management strategies for monitoring, diagnosing, and retrofitting the building's dynamic energy

- performance: Focused on the operation and maintenance phase. *Applied Energy* 2015; 155:671-707. 10.1016/j.apenergy.2015.06.043.
- [21] Pisello AL, Petrozzi A, Castaldo VL, Cotana F. On an innovative integrated technique for energy refurbishment of historical buildings: Thermal-energy, economic and environmental analysis of a case study. *Applied Energy* 2015; In Press, Corrected Proof - Note to users. 10.1016/j.apenergy.2015.05.061.
- [22] Ascione F, de Rossi F, Vanoli GP. Energy retrofit of historical buildings: theoretical and experimental investigations for the modelling of reliable performance scenarios. *Energy and Buildings* 2011; 43(8):1925-1936. 10.1016/j.enbuild.2011.03.040.
- [23] Fabbri K, Zuppiroli M, Ambrogio K. Heritage buildings and energy performance: Mapping with GIS tools. *Energy and Buildings* 2012; 48:137-145. 10.1016/j.enbuild.2012.01.018.
- [24] Arumägi E, Kalamees T. Analysis of energy economic renovation for historic wooden apartment buildings in cold climates. *Applied Energy* 2014; 115:540-548. 10.1016/j.apenergy.2013.10.041.
- [25] Kramer RP, Maas MPE, Martens MHJ, van Schijndel AWM, Schellen HL. Energy conservation in museums using different setpoint strategies: A case study for a state-of-the-art museum using building simulations. *Applied Energy* 2015; 158:446-458. 10.1016/j.apenergy.2015.08.044.
- [26] EN ISO 13786, Thermal Performance of Buildings Components e Dynamic Thermal Characteristics e Calculation Methods, 2010.
- [27] EN ISO 13792, Thermal Performance of Buildings e Calculation of Internal Temperatures of a Room in Summer Without Mechanical Cooling e Simplified Methods, 2012.
- [28] Marletta L, Evola G, Giuga M. Using the dynamic thermal properties to assess the internal temperature swings in free running buildings. A general model and its validation according to ISO 13792. *Energy and Buildings* 2015; 87:57-65. 10.1016/j.enbuild.2014.11.025.
- [29] Asan H, Sancaktar YS. Effects of wall's thermophysical properties on time lag and decrement factor. *Energy and Building* 1998; 28:159-66. 10.1016/S0378-7788(98)00007-3.
- [30] Asan H. Numerical computation of time lags and decrement factors for different building materials. *Building and Environment* 2006; 41:615-20. 10.1016/j.buildenv.2005.02.020.
- [31] Ulgen K. Experimental and theoretical investigation of effects of wall's thermophysical properties on time lag and decrement factor. *Energy and Buildings* 2002; 34(3):273-8. 10.1016/S0378-7788(01)00087-1.

- [32] Yumrutas R, Kaska O, Yildirim E. Estimation of total equivalent temperature difference values for multilayer walls and flat roofs by using periodic solution. *Building and Environment* 2007; 42:1878-85. DOI:10.1016/j.buildenv.2006.02.020.
- [33] Kaska O., R. Yumrutas, O. Arpa, Theoretical and experimental investigation of total equivalent temperature difference (TETD) values for building walls and flat roofs in Turkey. *Applied Energy* 2009; 86:737-747. 10.1016/j.apenergy.2008.09.010.
- [34] Aste N, Angelotti A, Buzzetti M. The influence of the external walls thermal inertia on the energy performance of well insulated buildings. *Energy and Buildings* 2009; 41:1181-87. 10.1016/j.enbuild.2009.06.005.
- [35] Al-Sanea SA, Zedan MF, Al-Hussain SN. Effect of thermal mass on performance of insulated building walls and the concept of energy savings potential. *Applied Energy* 2012; 89:430-42. 10.1016/j.apenergy.2011.08.009.
- [36] Kontoleon K J, Theodosiou Th G, Tsikaloudaki K G. The influence of concrete density and conductivity on walls' thermal inertia parameters under a variety of masonry and insulation placements. *Applied Energy* 2013; 112:325-37. 10.1016/j.apenergy.2013.06.029.
- [37] Asan H. Effects of wall's insulation thickness and position on time lag and decrement factor. *Energy and Buildings* 1998; 28(3):299–305. 10.1016/S0378-7788(98)00030-9.
- [38] Asan H. Investigation of wall's optimum insulation position from maximum time lag and minimum decrement factor point of view. *Energy and Buildings* 2000; 32(2):197–203. 10.1016/S0378-7788(00)00044-X.
- [39] Bond DEM, Clark WW, Kimber M. Configuring wall layers for improved insulation performance. *Applied Energy* 2013; 112:235-45. 10.1016/j.apenergy.2013.06.024.
- [40] Al-Sanea SA, Zedan MF. Improving thermal performance of building walls by optimizing insulation layer distribution and thickness for same thermal mass. *Applied Energy* 2011; 88:3113-24. DOI:10.1016/j.apenergy.2011.02.036. 10.1016/j.apenergy.2011.02.036.
- [41] Ozel M. Effect of insulation location on dynamic heat-transfer characteristics of building external walls and optimization of insulation thickness. *Energy and Buildings* 2014; 72:288-95. 10.1016/j.enbuild.2013.11.015.
- [42] Kontoleon KJ, Bikas DK. The effect of south wall's outdoor absorption coefficient on time lag, decrement factor and temperature variations. *Energy and Buildings* 2007; 39:1011-18. 10.1016/j.enbuild.2006.11.006.
- [43] Kontoleon KJ, Eumorfopoulou EA. The influence of wall orientation and exterior surface solar absorptivity on time lag and decrement factor in the Greek region. *Renewable Energy* 2008; 33:1652-64. 10.1016/j.renene.2007.09.008.

- [44] M. Ozel, Effect of wall orientation on the optimum insulation thickness by using a dynamic method. *Applied Energy* 2011; 88:2429-2435. 10.1016/j.apenergy.2011.01.049.
- [45] M. Ozel, The influence of exterior surface solar absorptivity on thermal characteristics and optimum insulation thickness. *Renewable Energy* 2012; 39:347-355. 10.1016/j.renene.2011.08.039.
- [46] Mavromatidis LE, Mankibi MEL, Michel P, Santamouris M. Numerical estimation of time lags and decrement factors for wall complexes including multilayer thermal Insulation, in two different climatic zones. *Applied Energy* 2012; 92:480-91. 10.1016/j.apenergy.2011.10.007.
- [47] Al-Sanea SA, Zedan MF, Al-Hussain SN. Effect of masonry material and surface absorptivity on critical thermal mass in insulated building walls. *Applied Energy* 2013; 102:1063-1070. 10.1016/j.apenergy.2012.06.016.
- [48] Gagliano A, Patania F, Nocera F, Signorello C. Assessment of the dynamic thermal performance of massive buildings. *Energy and Buildings* 2014; 72:361-70. 10.1016/j.enbuild.2013.12.060.
- [49] Sun C, Shu S, Ding G, Zhang X, Hu X. Investigation of time lags and decrement factors for different building outside temperatures. *Energy and Buildings* 2013; 61:1-7. 10.1016/j.enbuild.2013.02.003.
- [50] Gasparella A, Pernigotto G, Baratieri M, Baggio P. Thermal dynamic transfer properties of the opaque envelope: Analytical and numerical tools for the assessment of the response to summer outdoor conditions. *Energy and Buildings* 2011; 43:2509-17. 10.1016/j.enbuild.2011.06.004.
- [51] Evola G, Marletta L. A dynamic parameter to describe the thermal response of buildings to radiant heat gains. *Energy and Buildings* 2013; 65:448-57. DOI:10.1016/j.enbuild.2013.06.026.
- [52] Jin X, Zhang X, Cao Y, Wang G. Thermal performance evaluation of the wall using heat flux time lag and decrement factor. *Energy and Buildings* 2012; 47:369-74. 10.1016/j.enbuild.2011.12.010.
- [53] Oliveti G, Arcuri N, Mazzeo D, De Simone M. A new parameter for the dynamic analysis of building walls using the harmonic method. *International Journal of Thermal Sciences* 2015; 88:96-109. 10.1016/j.ijthermalsci.2014.09.006.
- [54] Shmilovitz D. On the Definition of Total Harmonic Distortion and Its Effect on Measurement Interpretation. *IEEE TRANSACTION ON POWER DELIVERY* 2005;20(1):526-8. 10.1109/TPWRD.2004.839744.
- [55] H. S. Carslaw, J. C. Jaeger, *Conduction of Heat in Solids*, second edition, Oxford Science Publications, 1988.

- [56] V. S. Arpaci, Conduction Heat Transfer, Addison – Wesley Publishing Company, Inc., Reading Mass., 1966.
- [57] Basic Circuit Theory, McGraw-Hill, Inc., New York, New York, USA.
- [58] UNI TS 11300-1:2008. Energy performance of buildings. Part 1: Evaluation of energy need for space heating and cooling.
- [59] UNI 10351:1994. Building materials. Thermal conductivities and vapour permeabilities.
- [60] ISO EN 10456:2007. Building materials and products - Hygrothermal properties - Tabulated design values and procedures for determining declared and design thermal values.
- [61] Arendt K, Krzaczek M, Florczuk J. Numerical analysis by FEM and analytical study of the dynamic thermal behavior of hollow bricks with different cavity concentration. International Journal of Thermal Sciences 2011; 50(8):1543-1553. 10.1016/j.ijthermalsci.2011.02.027.
- [62] de Gracia A, Castell A, Medrano M, Cabeza LF. Dynamic thermal performance of alveolar brick construction system. Energy Conversion and Management, 2011; 52(7):2495-2500. 10.1016/j.enconman.2011.01.022.
- [63] Köppen climate classification, Wikipedia, last access September 2015, [http://en.wikipedia.org/wiki/K%C3%B6ppen\\_climate\\_classification](http://en.wikipedia.org/wiki/K%C3%B6ppen_climate_classification).
- [64] BS EN ISO 6946:1997. Building components and building elements – thermal resistance and thermal transmittance – calculation method.
- [65] UNI 10349:1994. Heating and cooling of buildings. Climatic data.
- [66] Solar Energy Laboratory University of Wisconsin-Madison, TRNSYS, Version 17, 2012.
- [67, 68, 69] Mathematical Reference, TRNSYS, 2012; pp. 291-294, pp. 284, pp. 309-310.
- [70] Oliveti G, Arcuri N, De Simone M, Bruno R. Experimental evaluations of the building shell radiant exchange in clear sky conditions. Solar Energy 2012; 86:1785-1795. 10.1016/j.solener.2012.03.009.
- [71] EN ISO 13790:2008. Energy performance of buildings – calculation of energy use for space heating and cooling.

## **Nomenclature**

- [A], [B] heat transfer matrix
- c specific heat capacity [J/kg K]
- C steady areal heat capacity [J/m<sup>2</sup> K]
- e relative percentage error [%]
- f decrement factor [-]

---

G	specific air flow rate [ $\text{kg}/(\text{m}^2 \text{ s})$ ]
h	heat transfer coefficient [ $\text{W}/(\text{m}^2 \text{ K})$ ]
k	harmonic order [-]
n	n-th harmonic
P	period of oscillation [s]
R	thermal resistance [ $\text{m}^2\text{K}/\text{W}$ ]
s	layer thickness [m]
t	time [s]
T	temperature [K]
THD	Total Harmonic Distortion
U	steady thermal transmittance [ $\text{W}/(\text{m}^2 \text{ K})$ ]
y	thermal quantity
Y	generic complex thermal parameter
[Z]	heat transfer matrix of the multilayered wall from surface to surface

*Greek symbols*

$\alpha$	absorption coefficient [-]
$\Delta t$	time lag [s]
$\Delta U$	instantaneous internal energy variation [ $\text{W}/\text{m}^2$ ]
$\varepsilon$	periodic thermal storage efficiency [-]
$\lambda$	thermal conductivity [ $\text{W}/\text{m K}$ ]
$\rho$	density [ $\text{kg}/\text{m}^3$ ]
$\tau$	non-dimensional periodic thermal transmittance [-]
$\varphi$	heat flux [ $\text{W}/\text{m}^2$ ]
$\psi$	argument of the thermal quantity oscillation [rad]
$\omega$	angular frequency of the variations [rad/s]

*Subscripts*

a	air
c	convective
e	external
ei	from outdoor to indoor environment
eq	equivalent
g	global, referring to the joint action of external and internal loadings
i	internal

---

ie	from indoor to outdoor environment
ig	internal heat gain
k	k-th harmonic
l	light
max	max value
min	min value
n	n-th harmonic
pl	plant
r	radiative
s	surface
s,e	referring to the solar load
sky	referring to the sky load
sr	shortwave radiation
ts	referring to the transmitted solar radiative heat flux
v	ventilation
w	wall
$\Sigma$	referring to the sum of all the harmonics

*Superscripts*

e	referring to the external heat flux
i	referring to the internal heat flux
max	referring to the maximum peak of the heat flux
min	referring to the minimum peak of the heat flux
sum	referring to the summer period
u	referring to the instantaneous internal energy variation
win	referring to the winter period

*Symbols*

–	mean value
~	oscillating value in the time domain
^	oscillating value in the complex domain
	amplitude of an oscillating value
arg	argument of an oscillating value

# Chapter 3

## Mapping of the seasonal dynamic properties of building walls in actual periodic conditions and effects produced by solar radiation incident on the outer and inner surfaces of the wall

### Abstract

In this chapter, the dynamic characteristics of the external walls of air-conditioned buildings subject to the joint action of periodic non-sinusoidal external and internal loadings are determined. The dynamic parameters used are the energy decrement factor, which is evaluated by means of the fluctuating heat flux in a semi-period exiting and entering the wall, the decrement factor of the maximum peak and minimum peak of the heat flux in a period and the relative time lags. The fluctuating heat flux in the wall in steady periodic regime conditions is determined with an analytical model obtained by resolving the equivalent electrical circuit. The



preceding parameters are used for a study of the influence of solar radiation on the dynamic characteristics of the walls in summer and winter air-conditioning. Solar radiation is considered as operating on the external surface and on the internal surface due to the presence in the indoor environments of a shortwave radiant field. The absorbed solar heat flux by the external surface varies, modifying the solar absorption coefficient and wall orientation. Indoors, a continuous operating regime of the plant and a regime with nocturnal attenuation are considered.

The results obtained, relating to 1152 different boundary conditions, are used for the construction of maps of dynamic characteristics, different on variation of the plant functioning regime and of the shortwave radiant load on the internal surface. The maps show the dependence of the decrement factors and of the time lags on variation of the season, of the external surface absorption coefficient, of the orientation and the type of wall, and of the locations. This representation allows a comparison of the dynamic behaviour of the wall in the two air conditioning seasons and, for defined boundary conditions, to quickly determine the dynamic characteristics.

Keywords: building wall; dynamic thermal characteristics; fluctuating heat flux; actual loadings; solar radiation; seasonal thermal behaviour.

- Dynamic behaviour of building walls subjected to sinusoidal and actual loadings.
- The joint action of more temperature and heat flux loadings has been considered.
- Dynamic parameters were defined by the internal and external fluctuating heat flux.
- Use of the Total Harmonic Distortion to determine the number of harmonics required.
- Study of the influence of external and internal loadings on dynamic parameters.

*Una ricerca comincia sempre con la fortuna del principiante. E finisce sempre con la prova del conquistatore.*

*(Paulo Coelho)*

## 1. Introduction

The study of the dynamic thermal properties of building components has been of growing interest related to European Directive 2010/31/EU (EPBD) [1] that requires member states to achieve a significant reduction of energy requirements in building air conditioning. These requirements should be met through appropriate thermal characteristics of building components and through systems located in-situ, which mainly employ renewable energy with the aim of achieving building energy independence (nZEB). The thermal characteristics describe the dynamic response of a system to variable loadings in time. Their study in building energetics mainly regards the external walls through the development of stratigraphic solutions and surface optical properties, which ensure a limitation of energy requirements, a reduction of heat flux peaks and convenient time lags. The fulfilment of these requirements are especially necessary in summer air conditioning in the Mediterranean area due to the important action of the solar loading.

The dynamic thermal characterisation of a building component is currently obtained by means of EN ISO 13786 [2]. It employs a matrix formulation in which the outdoor environment is schematized with a sinusoidal temperature oscillation, the indoor environment with a constant temperature and the external and internal surface heat exchanges with the heat transfer coefficients for the calculation of heat transfer in a steady periodic regime. The periodic thermal transmittances, used to evaluate the decrement factor and time lag, define the heat transfer properties, while the periodic thermal transmittance and admittances are used to calculate the areal heat capacities. In sinusoidal conditions, all these parameters depend only on the pulsation of the oscillation of the loadings, on the thickness, on the thermophysical properties of the layers and on their disposal in the wall.

In the air-conditioning of buildings, the external walls are subjected to combined boundary conditions, the trend of which is periodic but not sinusoidal. In this case, the actual loadings acting on the walls of the buildings are expressible as sums of harmonics of different pulsation, amplitude and argument. Such procedure, mostly based on Fourier series analysis, has been widely used for dynamic thermal analysis of composite walls subjected to time-dependent outdoor and indoor conditions [3, 4]. External loadings are the air temperature, the sky temperature and the absorbed solar radiation. Internal loadings are the air temperature, the absorbed shortwave radiant heat flux, the heat flux associated with the infiltration flow rate, the internal convective gain and the heat flux provided by the plant. In non-sinusoidal conditions, the

dynamic behaviour of the wall is much more complex and also depends on the trend of the loadings [5]. In order to take into account the joint action of the external and internal loadings, the thermal quantity to be considered is the heat flux that is transferred in the wall. The use of the heat flux to dynamically characterise walls has been used by Jin et al. [6] and by Oliveti et al. [7, 8]. These latter authors defined the different parameters necessary to identify how the form of the heat flux trend crossing the wall can be modified.

In scientific literature, little research has been conducted in order to study the influence of the solar radiation on dynamic characteristics. The available results were obtained using only numerical mathematical models in non-sinusoidal periodic conditions and considering the wall subject to simplified boundary conditions. Usually, the wall is subjected to the action of sol-air temperature in the outdoor environment and the air temperature is kept constant in the indoor environment. In actual outdoor conditions, Ruivo et al. concluded that the decrement factor and the time lag depend on the outer surface colour and on the orientation of walls and they showed that simplified methods using constant decrement factor and time lag values have poor accuracy in a significant number of cases [9]. Kontoleon et al. [10-11] evaluated the dependence of the decrement factor of the daily maximum excursion of the temperature, and of the time lag of the maximum and minimum temperature peak, from the absorption coefficient for some insulated walls exposed differently and located in Greece during the summer season. A similar study was conducted by Ozel [12], which, with the variation of the absorption coefficient, determined the annual average values of the decrement factor of the daily maximum excursion of the temperature and the time lag of the maximum peak of two walls, a non-isolated and isolated wall, exposed to the south in the city of Elizig, Turkey. Furthermore, the results showed that solar absorptivity has very small effect on the optimum insulation thickness and highlighted the influence of the absorption coefficient on summer thermal loads and winter heat loss. These latter evaluations were conducted by Al Sanea et al. [13] considering two insulated walls in the city of Riyadh and introducing the concepts of “energy savings potential” and “critical thermal mass”. Granja and Labaki [14], using the analytical solution of the heat conduction in steady periodic regime, determined, for different values of the absorption coefficient, the heat flux transmitted to the indoor environment through different roof coverings, on a summer day in São Paulo, Brazil. Cheng et al. [15] presented the results of two different experiments conducted in Hong Kong, with a hot and humid climate: the first to study the effects of the outer surfaces colour of light and heavy walls on the internal air temperature of two small sized test cells; the second to investigate the effects of the external walls orientation of one large test cell, constituted by 4 rooms, on the internal air temperature. The authors demonstrate the possibility

of developing predictive equations for the evaluation of the daily maximum value of the internal air temperature. In the same locality, Han et al. [16] evaluated the effect of various roofing structures with different colour on the corresponding space cooling load. Cooling load reduction ratio for white painted surface could be 9.3%, 8.8% for off-white painted, 2.5% for brown painted and 1.3% for green painted surface when same roof structure with different colour are used for this comparison. Furthermore, they found that the type of insulation materials used for roof construction has significant effect than the effect from the roof exterior surface colour. Bansal et al. [17] conducted experimental and analytical analyses, based on the periodic solution of the heat conduction equation, to evaluate the effect of outer surface colour on the thermal behaviour of the walls in scaled down units of 1 m<sup>3</sup> volume. The analytical model was then use to evaluate the dynamic behaviour of a normal sized heavy structure. Finally, Marino et al. [18] analysed the energy saving obtainable by applying innovative surface finishes on interior and exterior surfaces of opaque envelope components of existing buildings considering various Italian and European cities.

This chapter is a follow up on the chapter 2 in which a more general dynamic characterisation of the opaque components of the building envelope, subject to the joint action of periodic sinusoidal or non-sinusoidal loadings on the external and internal surfaces, has been developed. Such methodology was used to evaluate the influence of external and internal loadings on the dynamic characteristics. In the present study such analytical methodology, based on the harmonic and phasors methods, is used to study the influence of the solar radiation, which varies with the absorptivity (colour) and the orientation of the external surface, on the dynamic characteristics of walls. Solar radiation was considered as operating on the outer and inner surface of the wall, and the latter is also caused by solar radiation penetrating through the glass surfaces. The dynamic characteristics are identified by the decrement factor in terms of energy, the ratio between the integral of the fluctuating heat flux in a semi-period entering the indoor environment and entering the wall, the decrement factor of the maximum and the minimum peaks of the heat flux and the time lags undergone by the maximum and minimum peaks of the heat flux. These parameters are determined considering different external and internal boundary conditions. The external ones are changed by assigning different values to the solar absorption coefficient and varying wall orientation while the internal ones considering the plant operating regime as continuous or with nocturnal attenuation, with the absence or presence of an absorbed shortwave radiant heat flux. Seasonal analyses are developed considering two commonly used walls located in two locations characteristics of the European continental climate and the Mediterranean climate.

In the first part of the chapter, the authors present the analytical model and the various dynamic parameters defined in non-sinusoidal conditions. Successively, with reference to the two external walls and to the locality of Turin, the dependence and range of variability of dynamic parameters varying the external surface solar absorption coefficient and the orientation of the wall, the plant operating regime and the radiant loads on the internal surface is described. Finally, maps created to employ for the comparison between the winter and summer dynamic characteristics of the two walls are reported, varying external and internal boundary conditions, for the two locations.

## 2. Methodology

The external wall of a building subject to the joint action of external and internal loadings was schematized through the equivalent electrical circuit of Figure 1. The circuit refers to the sinusoidal periodic regime and represents all the thermal quantities, temperature and heat flux, by means of a sinusoid described by a pulsation, an amplitude and an argument. It is possible to transform the sinusoidal thermal quantities in complex numbers in which time does not appear explicitly. In the field of electrical engineering, this procedure is known as the phasor method [19], while in the context of heat transmission it is known as the complex temperature method [20]. Recently, this procedure has been used in order to provide the exact analytical solution of the heat transfer in a finite layer subject to phase change in steady periodic regime [21].

The external loadings are the air temperature  $T_{a,e}$ , the sky temperature  $T_{sky}$  and the absorbed solar radiation  $\alpha_e \varphi_{s,e}$ . Instead, the internal loadings are the air temperature  $T_{a,i}$ , the absorbed shortwave radiant heat flux  $\varphi_{sr,i}$ , the infiltration heat flux  $\varphi_v$ , the internal convective heat gains  $\varphi_{c,ig}$  and the heat flux supplied by the plant  $\varphi_{pl}$ . The latter heat flux is that which must be provided or subtracted, for a square meter of opaque wall, to an air-conditioned environment to maintain the desired operating temperature conditions during a given period of time.

The radiative infrared exchange with the sky is linearized through the radiative heat transfer coefficient  $h_{r,e}$ , while the radiative exchange on the internal side is incorporated in the internal surface heat transfer coefficient  $h_{s,i}$ .

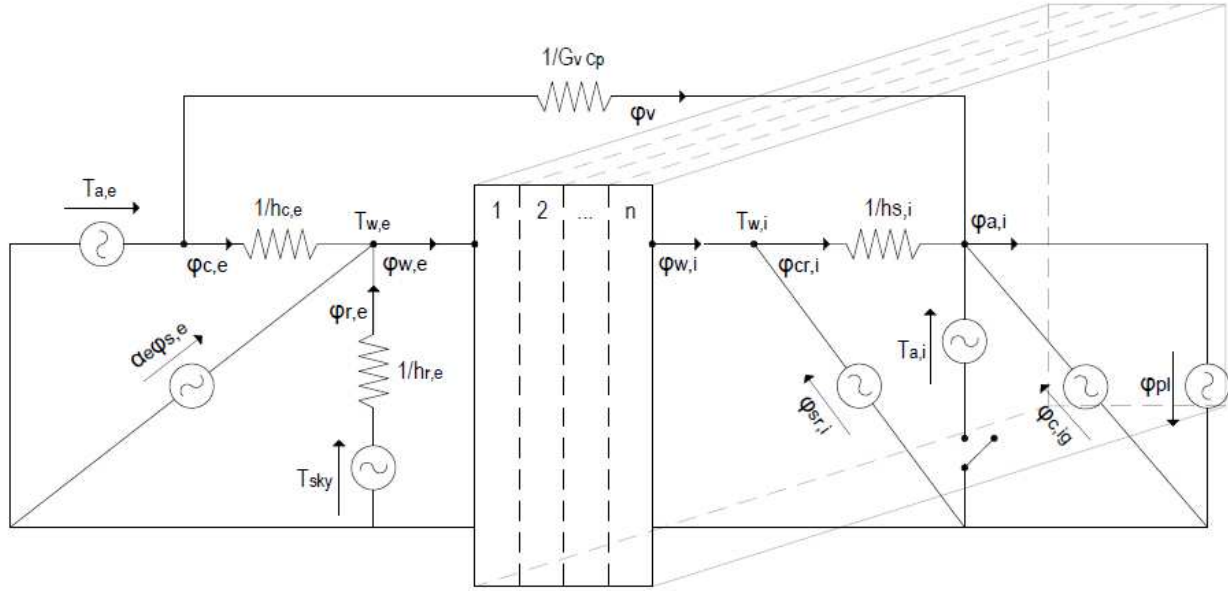


Figure 1. Equivalent electric circuit of a multilayer wall subject to external loadings, air temperature  $\hat{T}_{a,e}$ , sky temperature  $\hat{T}_{sky}$ , absorbed solar radiation  $\alpha_e \hat{\phi}_{s,e}$ , and to internal loadings, air temperature  $\hat{T}_{a,i}$ , shortwave radiant heat flux  $\hat{\phi}_{sr,i}$ , convective heat flux of the infiltration flow rate  $\hat{\phi}_v$ , internal convective heat flux  $\hat{\phi}_{c,ig}$  and convective heat flux supplied by the plant  $\hat{\phi}_{pl}$ .

The electric circuit was solved by the method of superposition of causes and effects. The matrix expression, that connects for each harmonic the amplitudes of the oscillating temperature  $\hat{T}_{a,i}$  and of the oscillating heat flux in the indoor environment  $\hat{\phi}_{a,i}$  with external loadings  $\hat{T}_{sky}$ ,  $\hat{T}_{a,e}$  and  $\alpha_e \hat{\phi}_{s,e}$ , and with internal loadings  $\hat{\phi}_{sr,i}$ ,  $\hat{\phi}_v$  and  $\hat{\phi}_{c,ig}$ , assumes the form:

$$\begin{aligned}
 \begin{bmatrix} \hat{T}_{a,i} \\ \hat{\phi}_{a,i} \end{bmatrix} &= \begin{bmatrix} 1 & -\frac{1}{h_{s,i}} \\ 0 & 1 \end{bmatrix} \begin{bmatrix} Z_{11} & Z_{12} \\ Z_{21} & Z_{22} \end{bmatrix} \left\{ \begin{bmatrix} h_{r,e} & h_{c,e} & -1 \\ h_{r,e} + h_{c,e} & h_{r,e} + h_{c,e} & h_{r,e} + h_{c,e} \\ 0 & 0 & 1 \end{bmatrix} \begin{bmatrix} \hat{T}_{sky} \\ \hat{T}_{a,e} \\ \hat{\phi}_e \end{bmatrix} + \begin{bmatrix} \alpha_e \hat{\phi}_{s,e} \\ 0 \end{bmatrix} \right\} \\
 &+ \begin{bmatrix} -\frac{\hat{\phi}_{sr,i}}{h_{s,i}} \\ \hat{\phi}_{sr,i} + \hat{\phi}_v + \hat{\phi}_{c,ig} \end{bmatrix} \\
 &= \begin{bmatrix} A_{11} & A_{12} & A_{13} \\ A_{21} & A_{22} & A_{23} \end{bmatrix} \begin{bmatrix} \hat{T}_{sky} \\ \hat{T}_{a,e} \\ \hat{\phi}_e \end{bmatrix} + \begin{bmatrix} B_{11} & B_{12} \\ B_{21} & B_{22} \end{bmatrix} \begin{bmatrix} \alpha_e \hat{\phi}_{s,e} \\ 0 \end{bmatrix} + \begin{bmatrix} -\frac{\hat{\phi}_{sr,i}}{h_{s,i}} \\ \hat{\phi}_{sr,i} + \hat{\phi}_v + \hat{\phi}_{c,ig} \end{bmatrix} \\
 &= [A] \begin{bmatrix} \hat{T}_{sky} \\ \hat{T}_{a,e} \\ \hat{\phi}_e \end{bmatrix} + [B] \begin{bmatrix} \alpha_e \hat{\phi}_{s,e} \\ 0 \end{bmatrix} + \begin{bmatrix} -\frac{\hat{\phi}_{sr,i}}{h_{s,i}} \\ \hat{\phi}_{sr,i} + \hat{\phi}_v + \hat{\phi}_{c,ig} \end{bmatrix} \quad (1)
 \end{aligned}$$

In Eq. (1), matrix A represents the product between the internal surface matrix, that of wall transfer [Z] and that of external surface; B is the product of the internal surface matrix and the

wall transfer matrix. The wall transfer matrix from surface to surface [Z] is determined according to the procedure of the EN ISO 13786 standard [2] with the convention that the product of the transfer matrixes is made from the most internal layer n to the most external layer 1.

The heat flux transferred to the indoor environment in function of the internal and external loadings is given by the relation:

$$\begin{aligned}
\hat{\varphi}_{a,i} &= \left( A_{21} - \frac{A_{23}A_{11}}{A_{13}} \right) \hat{T}_{sky} + \left( A_{22} - \frac{A_{23}A_{12}}{A_{13}} + G_v c_p \right) \hat{T}_{a,e} + \frac{1}{(h_{r,e} + h_{c,e})} \left( B_{21} - \frac{A_{23}B_{11}}{A_{13}} \right) \alpha_e \hat{\varphi}_{s,e} \\
&\quad + \left( 1 + \frac{A_{23}}{A_{13}h_{s,i}} \right) \hat{\varphi}_{sr,i} + \left( \frac{A_{23}}{A_{13}} - G_v c_p \right) \hat{T}_{a,i} + \hat{\varphi}_{c,ig} \\
&= -\frac{h_{r,e}}{h_{r,e} + h_{c,e}} \frac{1}{A_{13}} \hat{T}_{sky} + \left( -\frac{h_{c,e}}{h_{r,e} + h_{c,e}} \frac{1}{A_{13}} + G_v c_p \right) \hat{T}_{a,e} - \frac{h_{r,e}}{h_{r,e} + h_{c,e}} \frac{1}{A_{13}} \alpha_e \hat{\varphi}_{s,e} \\
&\quad + \left( 1 + \frac{A_{23}}{A_{13}h_{s,i}} \right) \hat{\varphi}_{sr,i} + \left( \frac{A_{23}}{A_{13}} - G_v c_p \right) \hat{T}_{a,i} + \hat{\varphi}_{c,ig} \tag{2}
\end{aligned}$$

The heat flux penetrating the wall from the external side is equal to:

$$\hat{\varphi}_e = \left( -\frac{A_{11}}{A_{13}} \right) \hat{T}_{sky} + \left( -\frac{A_{12}}{A_{13}} \right) \hat{T}_{a,e} + \left( -\frac{1}{(h_{r,e} + h_{c,e})} \frac{B_{11}}{A_{13}} \right) \alpha_e \hat{\varphi}_{s,e} + \left( \frac{1}{A_{13}h_{s,i}} \right) \hat{\varphi}_{sr,i} + \left( \frac{1}{A_{13}} \right) \hat{T}_{a,i} \tag{3}$$

The variation of internal energy in the wall per unit time can be calculated with the relation:

$$\Delta \hat{U} = \hat{\varphi}_e - \hat{\varphi}_{a,i} \tag{4}$$

Oscillating heat fluxes (2) and (3) and the variation of internal energy (4) can be rewritten in the compact form:

$$\hat{\varphi}_{a,i} = Y_{sky}^i \hat{T}_{sky} + Y_{a,e}^i \hat{T}_{a,e} + Y_{s,e}^i \alpha_e \hat{\varphi}_{s,e} + Y_{sr,i}^i \hat{\varphi}_{sr,i} + Y_{a,i}^i \hat{T}_{a,i} + \hat{\varphi}_{c,ig} \tag{5}$$

$$\hat{\varphi}_e = Y_{sky}^e \hat{T}_{sky} + Y_{a,e}^e \hat{T}_{a,e} + Y_{s,e}^e \alpha_e \hat{\varphi}_{s,e} + Y_{sr,i}^e \hat{\varphi}_{sr,i} + Y_{a,i}^e \hat{T}_{a,i} \tag{6}$$

$$\begin{aligned}
\Delta \hat{U} &= (Y_{sky}^e - Y_{sky}^i) \hat{T}_{sky} + (Y_{a,e}^e - Y_{a,e}^i) \hat{T}_{a,e} + (Y_{s,e}^e - Y_{s,e}^i) \alpha_e \hat{\varphi}_{s,e} + (Y_{sr,i}^e - Y_{sr,i}^i) \hat{\varphi}_{sr,i} \\
&\quad + (Y_{a,i}^e - Y_{a,i}^i) \hat{T}_{a,i} - \hat{\varphi}_{c,ig} \tag{7}
\end{aligned}$$

The generic complex parameter  $Y$ , appearing in the previous relations, provides the contribution, in amplitude and argument, to the calculation of the heat flux  $\hat{\varphi}_e$  or  $\hat{\varphi}_{a,i}$  or of the variation of internal energy  $\Delta\hat{U}$ , consequent to the periodic unitary variation of the relative internal or external loading. In particular, they allow definition of the aliquots attributable to the unitary periodic variation of the solar radiation incident on the external surface and of the shortwave radiant heat flux incident on the internal surface. The parameters  $Y$  are related to the periodic thermal transmittances, to the periodic thermal admittance and the areal heat capacities defined in standard EN ISO 13786 [2,7-8].

### 3. Dynamic characterisation of the wall in non-sinusoidal conditions

The actual loadings acting on the walls of the buildings are expressible as sums of sinusoidal harmonics of different pulsation, amplitude and argument:

$$y(t) = \bar{y} + \sum_{k=1}^n \tilde{y}_k = \bar{y} + \sum_{k=1}^n |\tilde{y}_k| \text{sen}(k\omega t + \psi_k) \quad (8)$$

in which  $\bar{y}$  represents the mean value,  $k\omega$  the pulsation,  $|\tilde{y}|$  the amplitude,  $\psi$  the argument of the  $k$ -th harmonic and  $n$  the number of harmonics.

The actual heat flux transferred to the internal air and the actual heat flux that penetrates the wall are determined by composing the contributions of individual harmonics. These heat fluxes determined thus are not sinusoidal quantities and their ratio, which represents the non-dimensional periodic global thermal transmittance [7, 8], cannot be used to define the decrement factor and time lag that the heat flux undergoes. In such conditions, the dynamic behaviour of the wall is defined considering the energy transferred and the maximum and minimum peak of the fluctuating heat flux.

Assuming that the fluctuating heat flux is directed from the outside inwards, the ratio between the energy in a semi-period exiting and entering the wall defines the decrement factor in terms of energy. In order to define the decrement factor in terms of heat flux, it is necessary to consider both that relating to the maximum peak and that relating to the minimum peak. In formulae:

$$f_e = \frac{\int_0^P |\sum_{k=1}^n \tilde{\varphi}_{a,i,k}| dt}{\int_0^P |\sum_{k=1}^n \tilde{\varphi}_{e,k}| dt} \quad (9a) \quad f_{\max} = \frac{(\sum_{k=1}^n \tilde{\varphi}_{a,i,k})_{\max}}{(\sum_{k=1}^n \tilde{\varphi}_{e,k})_{\max}} \quad (9b) \quad f_{\min} = \frac{(\sum_{k=1}^n \tilde{\varphi}_{a,i,k})_{\min}}{(\sum_{k=1}^n \tilde{\varphi}_{e,k})_{\min}} \quad (9c)$$



with P period of the fluctuation and n number of harmonics.

The decrement factor  $f_e$  provides the fraction of energy transmitted in a semi-period both in the summer and winter period. In particular, in the summer season the half-period to consider is the one in which the maximum heat flux occurs, to which a fluctuating energy entering the indoor environment, in the same direction as the steady component, is associated. Conversely, in winter, the semi-period to consider is that in which the minimum peak occurs, which is associated with a fluctuating energy exiting the environment, with the same direction of the steady component. The fraction of energy that remains accumulated in the wall in a semi-period is equal to  $(1 - f_e)$ . The time lags of the maximum and minimum heat flux, occurring respectively in the summer and winter behaviour of the wall, are defined by the relations:

$$\Delta t_{\max} = t_{(\sum_{k=1}^n \tilde{\varphi}_{a,i,k})_{\max}} - t_{(\sum_{k=1}^n \tilde{\varphi}_{e,k})_{\max}} \quad (10a) \quad \Delta t_{\min} = t_{(\sum_{k=1}^n \tilde{\varphi}_{a,i,k})_{\min}} - t_{(\sum_{k=1}^n \tilde{\varphi}_{e,k})_{\min}} \quad (10b)$$

Similar relations can be written in the case that the fluctuating flux in the wall is directed from the inside towards the outside.

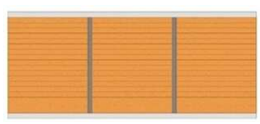
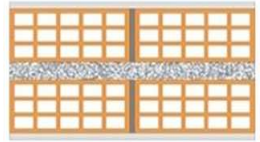
The previous relations, with oscillating heat fluxes exiting and entering the wall calculated for each harmonic respectively by means Eqs. (5) and (6), allow to for dynamic characterisation of the wall taking account of all the loadings acting on the boundary.

To reduce energy requirements in air conditioning, a low decrement factor of the energy in transit in the wall, a low decrement factor of the maximum heat flux in summer and of the minimum heat flux in winter are required; furthermore convenient time lags of the heat flux peaks, in relation with the orientation of the wall, are also required.

#### 4. Walls considered and boundary conditions

Two walls located in two climatically different locations, Turin (TO, Lat. = 45° 7', Long. = 7° 43') with a continental climate and Cosenza (CS, Lat. = 37° 30', Long. = 15 ° 05') with a Mediterranean climate, are examined. Stratigraphy of walls and thermal properties of layers, provided from the reference standards [22-24], are reported in Table 1. Wall 1 has higher thermal capacity and steady thermal transmittance values compared to Wall 2.

Table 1. Stratigraphy of walls and thermophysical properties of layers.

WALL 1: BRICK WALL		R = 1.05 m <sup>2</sup> K/W;		U = 0.95 W/(m <sup>2</sup> K);		C = 971.2 kJ/(m <sup>2</sup> K)	
Material		s [m]	λ [W/(m K)]	c [J/(kg K)]	ρ [kg/m <sup>3</sup> ]		
	1	Internal plaster	0.02	0.70	1000	1400	
	2	Brick	0.60	0.72	840	1800	
	3	External plaster	0.02	0.90	1000	1800	
WALL 2: HOLLOW WALL		R = 1.50 m <sup>2</sup> K/W;		U = 0.67 W/(m <sup>2</sup> K);		C = 328 kJ/(m <sup>2</sup> K)	
Material		s [m]	λ [W/(m K)]	c [J/(kg K)]	ρ [kg/m <sup>3</sup> ]		
	1	Internal plaster	0.02	0.70	1000	1400	
	2	Hollow brick	0.08	0.30	1000	800	
	3	Air gap	R = s/λ = 0.18 m <sup>2</sup> K/W		-	-	
	4	Hollow brick	0.25	0.30	1000	800	
	5	External plaster	0.02	0.90	1000	1800	

Climate data are generated from the monthly average daily values, provided by the reference national standard [25], of solar radiation on the horizontal plane and the external air temperature with the software TRNSYS 17 [26], which with Type 54a [27] generates different hourly sequences for different days of the month. The solar radiation per hour on the vertical plane was obtained with the Type 16 [28]. The data of apparent temperature of the sky are generated by Type 69b [29]. The hourly thermal quantities calculated are used to define the day type for each month through the hourly average values. Figure 2 shows, for the monthly average day of January and August, on the top the trends of the absorbed solar radiation calculated with different values of the absorption coefficient in the southern exposure and on the bottom the trends of the absorbed solar radiation calculated varying exposure for  $\alpha_e=0.6$ .

As regards the surface heat exchanges, in the outdoor environment are considered a convective and radiative heat transfer coefficients, respectively,  $h_{c,e} = 20 \text{ W}/(\text{m}^2\text{K})$  and  $h_{r,e} = 5.35 \text{ W}/(\text{m}^2 \text{K})$  while in the indoor environment a surface heat transfer coefficient  $h_{s,i} = 7.7 \text{ W}/(\text{m}^2 \text{K})$ . The surface heat transfer coefficients are that reported in [30, 31].

In the indoor environment, two boundary conditions, corresponding to winter heating and summer cooling in continuous regime and with nocturnal attenuation, in the absence and presence of shortwave radiant contributions on the inner surface are considered; internal convective contributions are not considered. According to the National regulations [32], the heating period for Cosenza is from November to March, whereas for Torino from October to April. For both localities, the remaining months are assumed as cooling period.

In continuous regime, during the winter period, the plant supplies heat flux in the indoor environment to maintain the air temperature equal to 20 °C, while in summer the plant subtracts the heat flux from the indoor environment to maintain the air temperature equal to 26 °C. In

attenuated regime, during nocturnal hours, the plant supplies in winter and extracts in summer, a lower heat flux to keep the internal air temperature at a reduced value in winter and higher value in summer. Schedule in attenuated regime of the internal air temperature in summer and winter are shown in Figure 3a for Turin and in Figure 3b for Cosenza. Previous values of internal air temperature, both in continuous and attenuated regime, are chosen according to the reference standard [33].

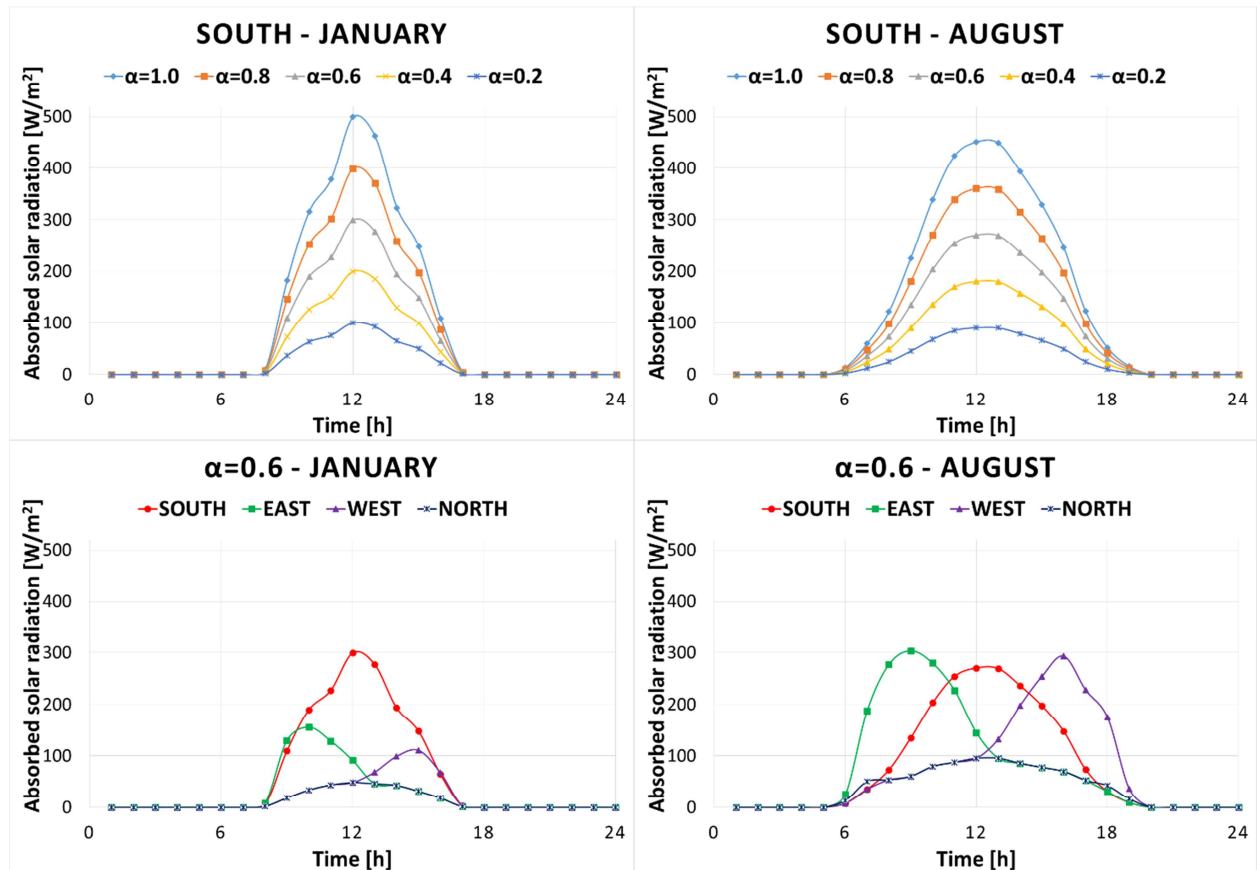


Figure 2 – Monthly average hourly trends in January and August of absorbed solar radiation for different absorption coefficient values in the southern exposure (on the top) and varying exposure for  $\alpha=0.6$  (on the bottom).

The internal shortwave radiant contributions  $\varphi_{sr,i}$  are calculated as the sum of the solar contribution and the contribution due to light sources. In particular, the solar contribution was determined from the solar radiation entering through a glazed area facing south, variable on an hourly basis in different months of the year for the two localities. An environment, with plan dimensions of 4 m x 4 m and a height of 3 m, with a 1.8 m<sup>2</sup> glass surface having a transmission coefficient in the solar band equal to 0.80 was considered. The solar absorption coefficient of the internal opaque surfaces was set equal to 0.20. Solar radiation actually absorbed by the cavity was calculated with a calculation correlation, developed by two of the authors in a previous work

[34]. In the considered conditions, the absorption coefficient of the cavity is close to 1. The solar radiation absorbed by the cavity was supposed as being uniformly distributed on the walls of the same cavity. The contribution due to light sources is shown in the schedule of Figure 3c and it has been assumed constant in the different months, for both walls, in the two locations, and for the two different plant-operating regimes.

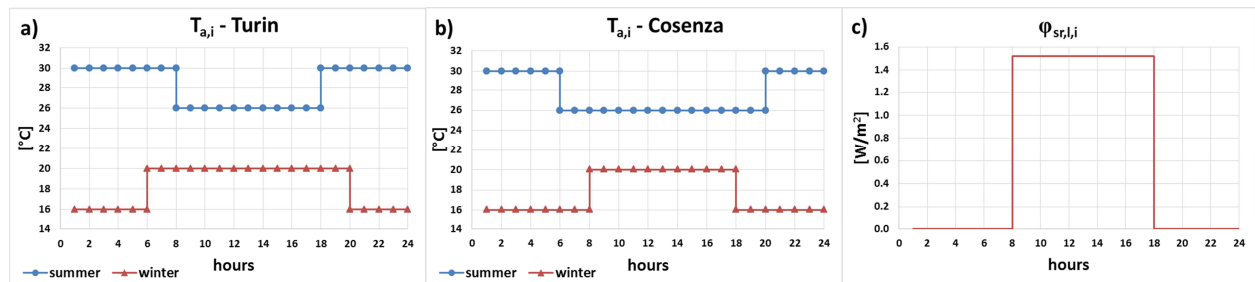


Figure 3 – Internal air temperature in attenuated regime in winter and in summer: a) Turin; b) Cosenza; c) Contribution of light sources to the shortwave heat flux absorbed by the internal surface.

The trends in time of the external and internal loadings are expressed in an analytical form by means of a Fourier series expansion truncated at the tenth harmonic. The walls are oriented to the South, East, West and North and the solar absorption coefficient  $\alpha_e$  of the external surface varied between zero and one. For each wall, 192 cases are considered.

## 5. Results and discussion

In each case, the dynamic parameters relating to the monthly average day for all months of the year are determined. Following are the results of analyses by means of the seasonal average values related to summer and winter air-conditioning, calculated as the average of the values in the corresponding months. The seasonal average value is representative of monthly values as they result as being only slightly variable. In particular, sections 5.1, 5.2, 5.3 and 5.4 show the dependence and range of variability of dynamic parameters in summer and winter air-conditioning for Turin varying the plant operating regime, the radiant loads on the internal surface, the solar absorption coefficient of the external surface and the orientation of the wall. In section 5.5, the winter and summer behaviour of the two walls, varying external and internal boundary conditions, is compared for the two locations. This analysis required a detailed presentation of the results, by means maps, to highlight the effect of various parameters on the dynamic characteristics. In general, a different boundary condition on the inner surface or on the

outer surface gives rise to a change in the trend of the fluctuating heat fluxes on both surfaces. For both heat fluxes, the time instants when the maximum heat flux and the minimum heat flux occur and their amplitude vary with a consequent change in the dynamic properties of the wall. In particular, for defined boundary conditions, the modification of the solar absorption coefficient on the outer surface gives rise to very contained variations of the fluctuating heat flux on the inner surface compared to that on the outer surface. On such a surface, for low values of  $\alpha_e$ , generally, the convective contribution and the radiative contribution determine the time instant and the amplitude of the maximum and the minimum heat flux. The increase in the solar absorption coefficient results in the prevalence of solar contribution over other contributions with a consequent modification of the time instants and the amplitude of the maximum and minimum heat flux. For this reason, in some cases, for certain values of the solar absorption coefficient, the decrement factors have a maximum or minimum value and the time lags present abrupt variations.

### 5.1 Continuous regime and absence of internal radiant loads

Figure 4, in the case of continuous air conditioning and of absence of internal radiant loads, reports the trend varying the absorption coefficient of the decrement factors (left) and time lags (right) for South, East, West and North exposures. The figures on the left show the trends in summer of the energy decrement factor ( $f_{e,sum}$ ) and of the maximum heat flux ( $f_{max,sum}$ ), and the trends in winter of the energy decrement factor ( $f_{e,win}$ ) and of the minimum heat flux ( $f_{min,win}$ ). The figures on the right show the trends of the time lag of the maximum heat flux in summer ( $\Delta t_{max,sum}$ ) and of the minimum heat flux in winter ( $\Delta t_{min,win}$ ).

For southern exposure on an increase in  $\alpha_e$ , the decrement factor of the energy and of the maximum heat flux decrease with values between 0.0036 ( $f_{e,sum}$ ) and 0.0023 ( $f_{max,sum}$ ) for Wall 1, and between 0.024 ( $f_{e,sum}$ ) and 0.015 ( $f_{max,sum}$ ) for Wall 2. The decrement factor of the minimum heat flux, increases before reaching a maximum value and subsequently decreases. For Wall 1, the maximum value is obtained for  $\alpha_e = 0.2$  and is equal to 0.005 while for Wall 2 it is equal to 0.032 for  $\alpha_e = 0.4$ . The minimum values, for  $\alpha_e = 1$ , are equal, respectively, to 0.0037 and 0.019. The comparison between the two walls shows that Wall 1, which is more capacitive, presents decrement factors of about one order of magnitude lower than those of Wall 2. Regarding the time lag, that of the maximum heat flux is little influenced by the variation of  $\alpha_e$  and is equal to about 24 hours for Wall 1 and 16 hours for Wall 2; that of the minimum heat flux presents different trends for the two walls on variation of  $\alpha_e$ . In particular, for the Wall 1, it is slightly

variable for  $\alpha_e < 0.4$  and equal to approximately 20 hours, while for  $\alpha_e > 0.4$  the time lag undergoes a drastic reduction and becomes equal to 4.5 hours for  $\alpha_e = 1$ ; for Wall 2, for  $\alpha_e < 0.2$  and for  $\alpha_e > 0.4$  it is almost constant and from  $\alpha_e = 0.2$  to 0.4 it increases from 14 hours to 22.5 hours.

For eastern exposure, the variation of  $\alpha_e$  has a significant effect on the decrement factor of the maximum heat flux, which first grows reaching a maximum for  $\alpha_e = 0.2$ , equal to 0.004 for Wall 1 and to 0.022 for Wall 2, and then decreases until a minimum value for  $\alpha_e = 1$ , equal to 0.0016 for Wall 1 and to 0.0082 for Wall 2. The decrement factor of the minimum heat flux presents a range of contained variation between 0.0036 and 0.0040 for Wall 1, with a minimum value for  $\alpha_e = 0.4$ , and between 0.026 and 0.030 for Wall 2, with a minimum value for  $\alpha_e = 0.2$ . The energy decrement factors upon an increase of  $\alpha_e$  are reduced in a contained manner for values of  $\alpha_e < 0.4$  and for greater values they are almost constant. The trend of the time lag of the maximum heat flux presents a limited variation for both walls, with a maximum value that is equal to 3 hours for  $\alpha_e = 0.4$  for Wall 1, and to 20.5 hours for  $\alpha_e = 0.2$  for Wall 2. That of the minimum heat flux, for Wall 1 decreases upon the increase of  $\alpha_e$  with values between 21.5 and 16.5 hours, for Wall 2 decreases from 15 hours for  $\alpha_e = 0$  to a minimum value equal to 10 hours for  $\alpha_e = 0.8$ .

The decrement factors for western exposure present trends and values very close to those obtained for the southern exposure. Only the decrement factor of the minimum heat flux for Wall 1 presents higher values in southern exposure for  $\alpha_e$  of between 0.2 and 0.6. The time lag of the maximum heat flux undergoes a slight reduction on the increase of  $\alpha_e$  with values between 24.5 and 21 hours for Wall 1, and between 17 and 13 hours for Wall 2. The time lag of the minimum heat flux for Wall 2 is approximate to that recorded for southern exposure, while for Wall 1 it is slightly variable and equal to approximately -3 hours (corresponding to 21 hours) for  $\alpha_e < 0.4$ ; for greater values of  $\alpha_e$  it increases and for  $\alpha_e = 1$  becomes equal to 6.3 hours.

Finally, for the northern exposure, for both walls the decrement factors of energy and of the maximum heat flux are reduced almost linearly with an increasing  $\alpha_e$ ; instead, that of the minimum heat flux increases with the increase of  $\alpha_e$ . For both walls the energy decrement factors in winter and summer are very close, while the decrement factor of the minimum heat flux is higher than that of the maximum heat flux. The variation of  $\alpha_e$  has a slight influence on the time lags of the maximum and minimum heat flux. The first presents values equal to approximately 24.5 hours for Wall 1 and to 17.5 hours for Wall 2, while for the second they result as being respectively equal to 21 hours and 15 hours.

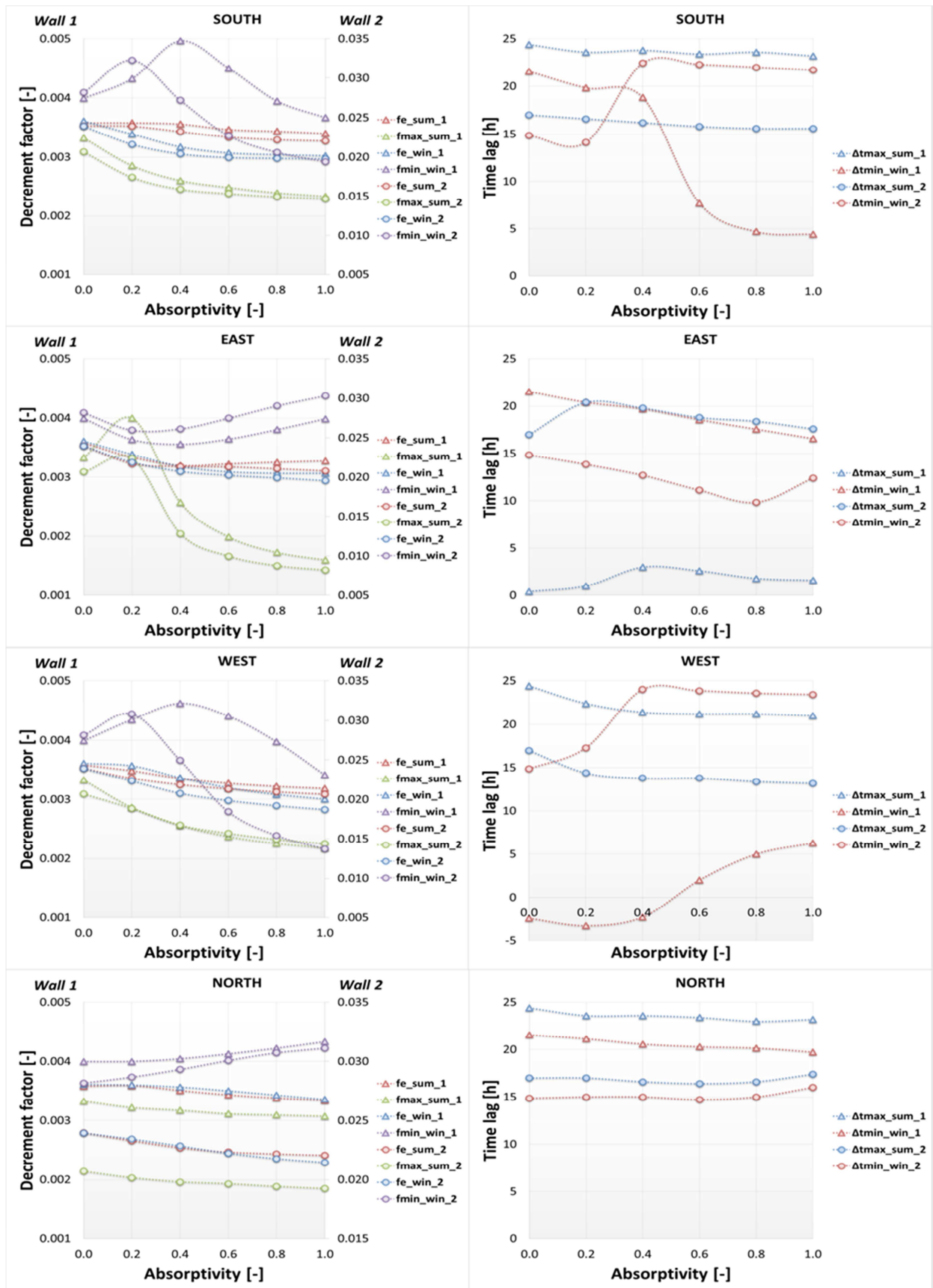


Figure 4 – Image on the left: for the different exposures, trend varying the absorption coefficient  $\alpha_e$  of the energy decrement factor in the summer period  $f_{e,sum}$  and in the winter period  $f_{e,win}$ , of the decrement factor of the maximum heat flux in summer  $f_{max,sum}$  and of the decrement factor of the minimum heat flux in winter  $f_{min,win}$ ; image on the

*right: for the different exposures, trend varying the absorption coefficient  $\alpha_e$  of the time lag of the maximum heat flux in the summer period  $\Delta t_{\max, \text{sum}}$  and of the time lag of the minimum heat flux in the winter period  $\Delta t_{\min, \text{win}}$ . Continuous regime and absence of internal radiant loads, Turin.*

## 5.2 Continuous regime and presence of radiant internal loads

The decrement factors and time lags of the two walls, in the case that a shortwave radiant load is present on the internal surface, are reported for the various exposures in Figure 5. The presence of the radiant load gives rise to a modification of the dynamic parameters trends with an increase of the decrement factors of two orders of magnitude for Wall 1, which is more capacitive, and of one order of magnitude for Wall 2. The two walls have close decrement factor values with higher values for Wall 2. The increase is attributable to the greater amplitude of the heat flux transferred to the indoor environment compared to that of the heat flux occurring in the absence of internal radiant loads.

The energy decrement factors, with an increase of  $\alpha_e$ , for both walls decrease to different extents for the different exposures, with winter period values always higher than summer period values. Similar trends upon variation of exposure are recorded by the decrement factor of the minimum and maximum heat flux. For the latter parameter, the eastern exposure records a different profile for the presence of a maximum of  $f_{\max, \text{sum}}$  for  $\alpha_e = 0.4$  for Wall 1, and for a value of  $\alpha_e$  slightly lower than 0.2 for Wall 2. The increase  $\alpha_e$  gives rise to a reduction of the decrement factors that is more significant for Wall 2, which is less capacitive, compared to Wall 1. For each wall there is a value of  $\alpha_e$  below which  $f_{\max, \text{sum}}$  is greater than  $f_{\min, \text{win}}$  and vice versa for greater values of  $\alpha_e$ .

The ranges of variation of the decrement factors, calculated for  $\alpha_e = 0$  and  $\alpha_e = 1$ , show that the maximum reduction of the fluctuating energy transferred in summer and of the minimum heat flux in winter occurs, in order, for southern and western exposures. The highest reduction of the maximum heat flux in summer occurs for west and, to a lesser extent, south. Lastly, the reduction of the energy decrement factor in winter is higher, in the order, in south, west and east. For walls with north exposure, the increase of  $\alpha_e$  gives rise to more contained reductions.



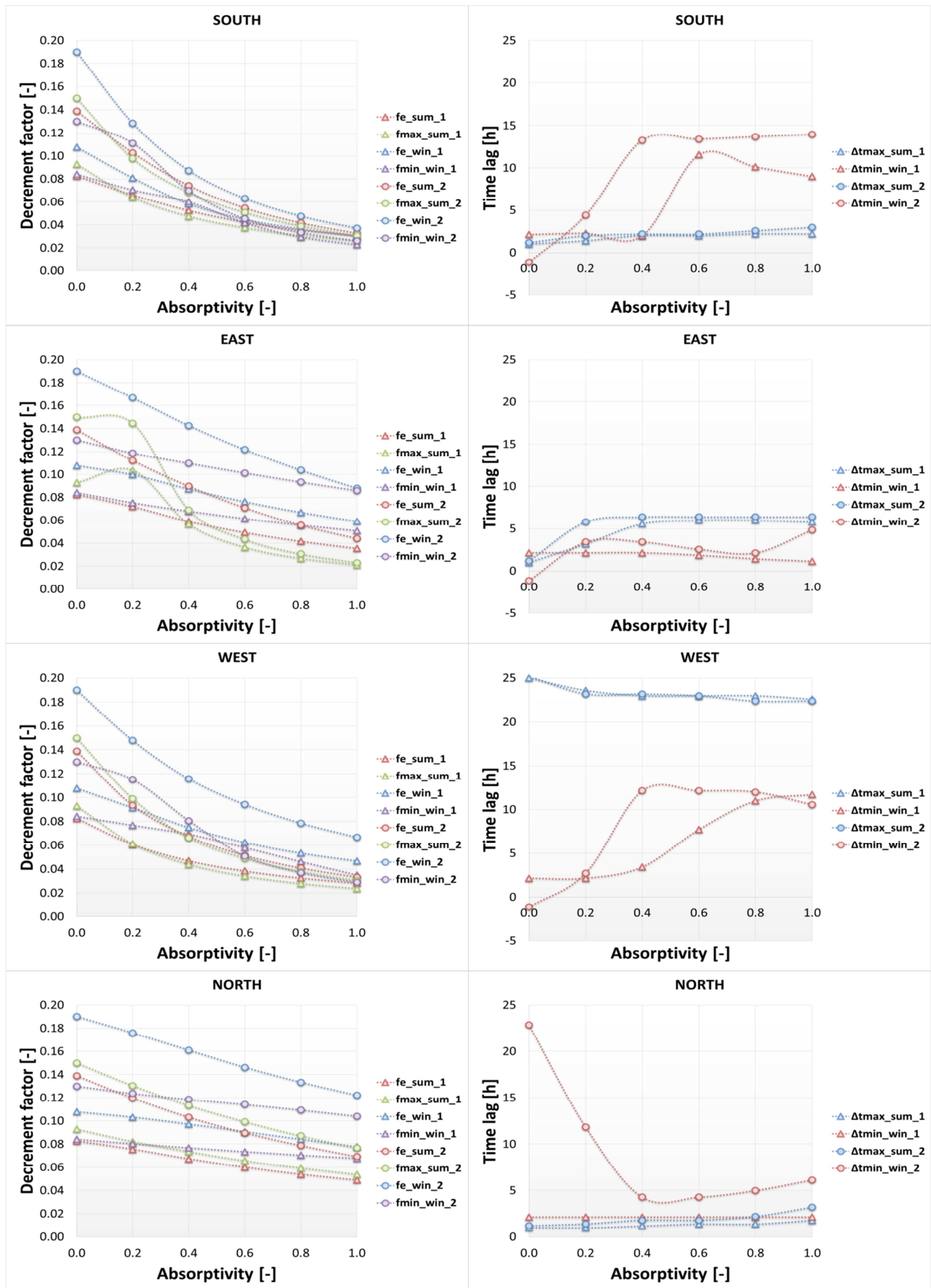


Figure 5 – Image on the left: for the different exposures, trend varying the absorption coefficient  $\alpha_e$  of the energy decrement factor in the summer period  $f_{e,sum}$  and in the winter period  $f_{e,win}$ , of the decrement factor of the maximum heat flux in summer  $f_{max,sum}$  and of the decrement factor of the minimum heat flux in winter  $f_{min,win}$ ; image on the

*right: for the different exposures, trend varying the absorption coefficient  $\alpha_e$  of the time lag of the maximum heat flux in the summer period  $\Delta t_{max, sum}$  and of the time lag of the minimum heat flux in the winter period  $\Delta t_{min, win}$ . Continuous regime and presence of internal radiant loads, Turin.*

As regards the time lag of the maximum heat flux, upon the increase of  $\alpha_e$ , the two walls present very close trends and values. In particular: the time lag is slightly variable between 1 hour and 3 hours for walls with northern and southern exposure; for exposure to the east, the time lag of the maximum heat flux grows from 1 hour to 6 hours for  $\alpha_e < 0.4$ , while for higher values it remains constant; finally, for exposure to the west, it decreases from 25 hours to 23.2 hours for  $\alpha_e < 0.2$  and is constant for greater values.

For all exposures, the trend of the time lag of the minimum heat flux with increasing of  $\alpha_e$  is different for the two walls. In particular, in the south: Wall 1 operates a time lag of about 2.3 hours for  $\alpha_e > 0.4$ , for higher values it grows and reaches a maximum value of 11.5 hours for  $\alpha_e = 0.6$ , and finally decreases and for  $\alpha_e = 1$  is equal to 9 hours; Wall 2 presents increasing values from -1 hour (corresponding to 23 hours) to 13 hours for  $\alpha_e < 0.4$  and is constant for higher values. To the east, for Wall 1, the time lag of the minimum heat flux is approximately constant and equal to 2 hours, while for Wall 2 it increases from -1 hour to 3 hours for  $\alpha_e < 0.2$ , remains approximately constant for  $0.2 < \alpha_e < 0.8$  and increases to 5 hours for  $\alpha_e = 1$ . To the west, the increase of  $\alpha_e$ , significantly affects  $\Delta t_{min, win}$ : for Wall 1 it increases from 2 hours, for  $\alpha_e = 0$ , to 12 hours, for  $\alpha_e = 1$ ; for Wall 2 there is an abrupt increase from -1 hour to 12 hours for  $\alpha_e < 0.4$ , while for higher values it decreases until it reaches, for  $\alpha_e = 1$ , a value of 11 hours. Finally, to the north, the time lag of the minimum heat flux operated by the Wall 1 does not depend on  $\alpha_e$ , while that operated by Wall 2, upon an increase of  $\alpha_e$ , it first decreases from 23 hours up to a minimum value of 4 hours for  $\alpha_e = 0.4$ , and for greater values it increases and becomes equal to 6 hours for  $\alpha_e = 1$ .

### 5.3 Attenuated regime in the absence of internal radiant loads

Figure 6 reports, for the different exposures, the decrement factors and time lags on variation of  $\alpha_e$  in the case of air conditioning attenuated during the night and the absence of internal radiant loads.

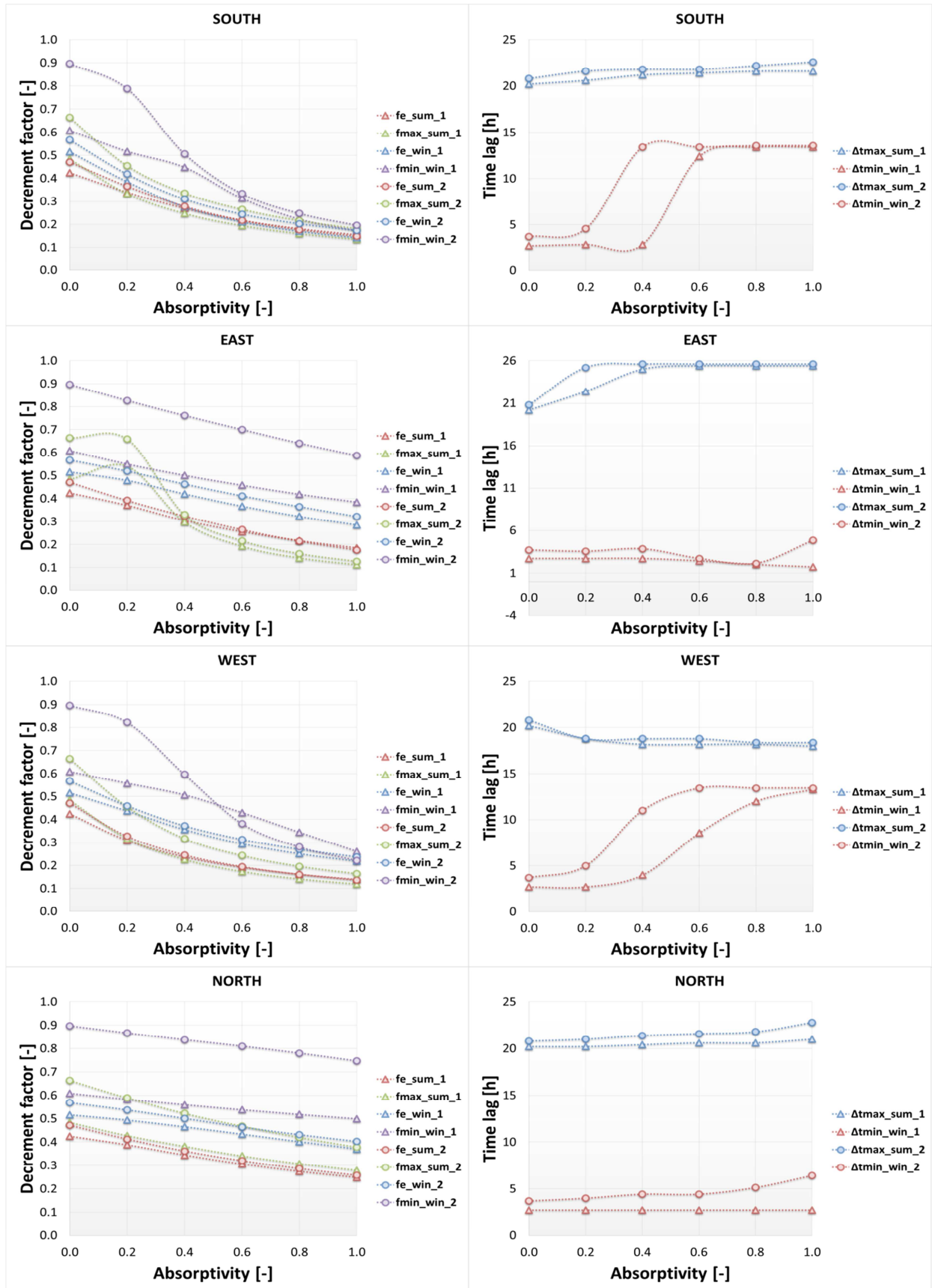


Figure 6 – Image on the left: for the different exposures, trend varying the absorption coefficient  $\alpha_e$  of the energy decrement factor in the summer period  $f_{e,sum}$  and in the winter period  $f_{e,win}$ , of the decrement factor of the maximum heat flux in summer  $f_{max,sum}$  and of the decrement factor of the minimum heat flux in winter  $f_{min,win}$ ; image on the

*right: for the different exposures, trend varying the absorption coefficient  $\alpha_e$  of the time lag of the maximum heat flux in the summer period  $\Delta t_{max,sum}$  and of the time lag of the minimum heat flux in the winter period  $\Delta t_{min,win}$ . Attenuated regime and absence of internal radiant loads, Turin.*

Compared to a similar case in a continuous regime, the decrement factors increase, by two orders of magnitude for Wall 1 and of one order of magnitude for Wall 2, and time lags are less influenced by the type of wall.

The energy decrement factors, for all exposures, are reduced with an increase of  $\alpha_e$ , with higher values in the winter period than in the summer period; they are little affected by the type of wall, and for high values of  $\alpha_e$  are almost coincident for both walls. Similar trends are presented by the decrement factors of the maximum and minimum heat flux. Only the decrement factor  $f_{max,sum}$  to the east presents a different trend, with a maximum for both walls for  $\alpha_e$  equal to about 0.2.

Whatever the orientation and for both walls, the decrement factor of the maximum heat flux is always less than that of the minimum heat flux. The comparison between the two walls in terms of the decrement factor of the maximum and the minimum heat flux shows that Wall 1 has smaller values for all exposures, except  $f_{min,win}$  to the west, which for  $\alpha_e > 0.5$  is lower for Wall 2. In particular, the different behaviour between the two walls in terms of  $f_{min,win}$  is significant to the south and west for  $\alpha_e < 0.4$ , and in the east and north for any value of  $\alpha_e$ .

The time lag of the maximum heat flux, for all exposures is little influenced by  $\alpha_e$  and by the type of wall, with values between 18 hours and 25 hours. Upon variation of exposure, the time lag of the minimum heat flux presents different trends and different values. In particular, for eastern and northern exposure, the two walls have close values and are slightly variable with  $\alpha_e$ , while in the south and west there are similar trends with higher values for Wall 2 to the south in the range of  $0.2 < \alpha_e < 0.6$ , and to the west in the range of  $0.2 < \alpha_e < 0.8$ .

#### **5.4 Attenuated regime in the presence of internal radiant loads**

In the regime with nocturnal attenuation, the presence of radiant loads on the internal surface of the wall, compared to the case in which they are absent, gives rise to a significant change of the heat flux that is transferred to the indoor environment, while the overall external heat flux remains almost unchanged.

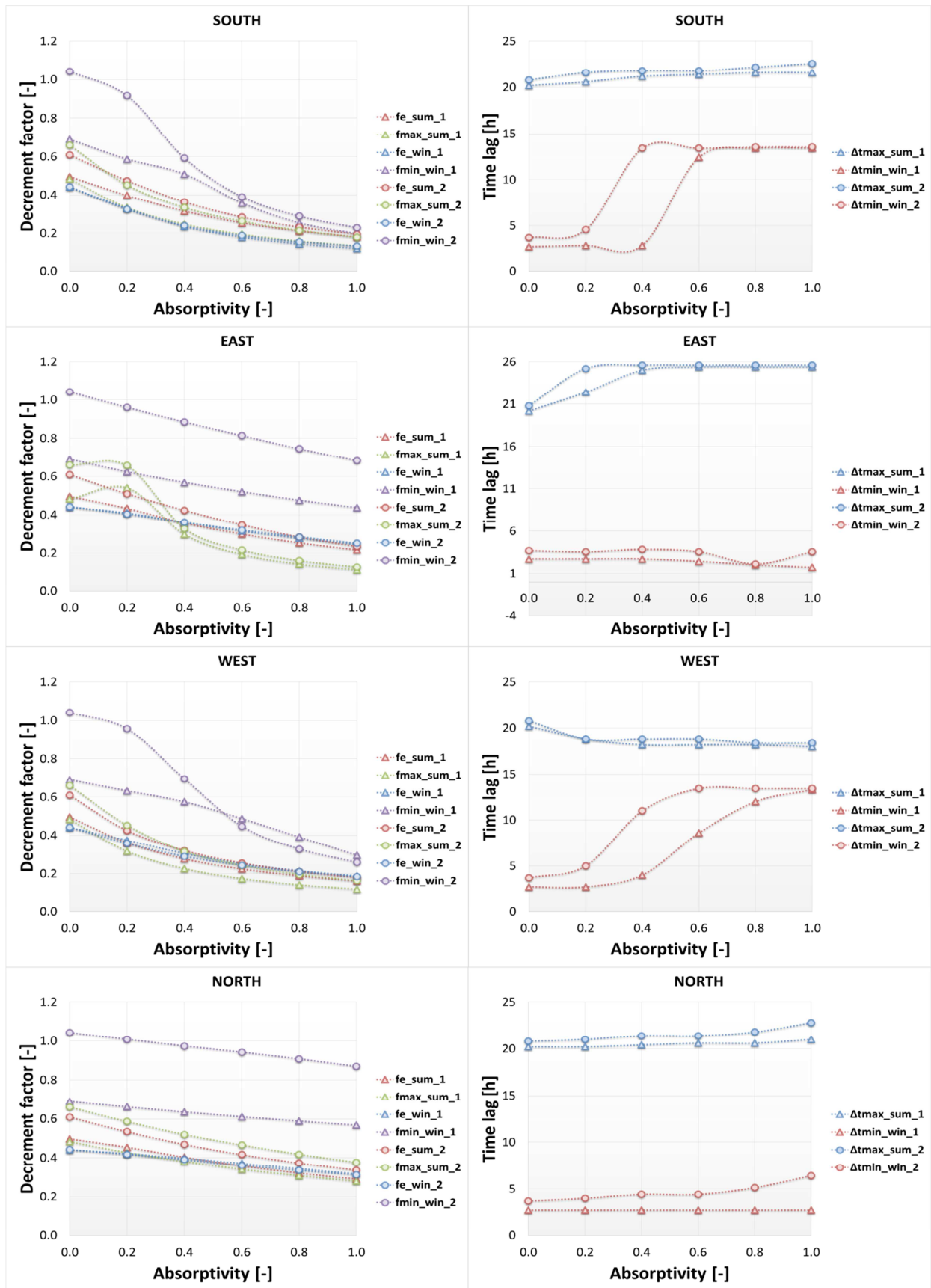


Figure 7 – Image on the left: for the different exposures, trend varying the absorption coefficient  $\alpha_e$  of the energy decrement factor in the summer period  $f_{e, \text{sum}}$  and in the winter period  $f_{e, \text{win}}$ , of the decrement factor of the maximum heat flux in summer  $f_{\text{max, sum}}$  and of the decrement factor of the minimum heat flux in winter  $f_{\text{min, win}}$ ; image on the

*right: for the different exposures, trend varying the absorption coefficient  $\alpha_e$  of the time lag of the maximum heat flux in the summer period  $\Delta t_{max, sum}$  and of the time lag of the minimum heat flux in the winter period  $\Delta t_{min, win}$ . Attenuated regime and presence of internal radiant loads, Turin.*

In particular, the radiant contribution on the internal surface, due to solar radiation through a glazed area facing south and light sources, determines: in summer during the day an increase of the fluctuating energy transferred within the indoor environment with a maximum heat flux that is reduced; in winter during the daytime, a reduction of the fluctuating energy exiting the indoor environment with a higher minimum heat flux. This gives rise to an increase in summer of the energy decrement factor and a reduction of the decrement factor of the maximum heat flux, while in winter the energy decrement factor is reduced and that of the minimum heat flux increases. Such considerations do not depend on the absorption coefficient, the orientation or on the type of wall.

The trends of the decrement factors (Figure 7 left) on variation of  $\alpha_e$ , for the different exposures, do not undergo significant changes compared to the corresponding trends shown in Figure 6, while the value range varies as shown above. For this reason, the values of the energy decrement factor in the summer season are higher than those in winter for any absorption coefficient value, orientation and type of wall, unlike that shown in a regime in the absence of radiant loads.

As for the time lags, in the present case in an attenuated regime, the presence of a radiant heat flux on the internal surface does not give rise to any change because the external heat flux remains almost unchanged while the time instants at which the maximum and minimum internal heat flux occur are determined by the internal air temperature loading, which determines a fluctuation of the convective heat flux greater than the radiant fluctuating component.

### **5.5 Maps for the comparison of the summer and winter dynamic properties**

In order to highlight the behaviour of the walls in the summer and winter season in the two locations, upon variation of the solar absorption coefficient, of the orientation and of the type of wall, the results of the analyses are mapped and summarised for the continuous regime in Figures 8 and 9, respectively in the absence and presence of radiant internal loads, and similarly for the attenuated regime in Figures 10 and 11.

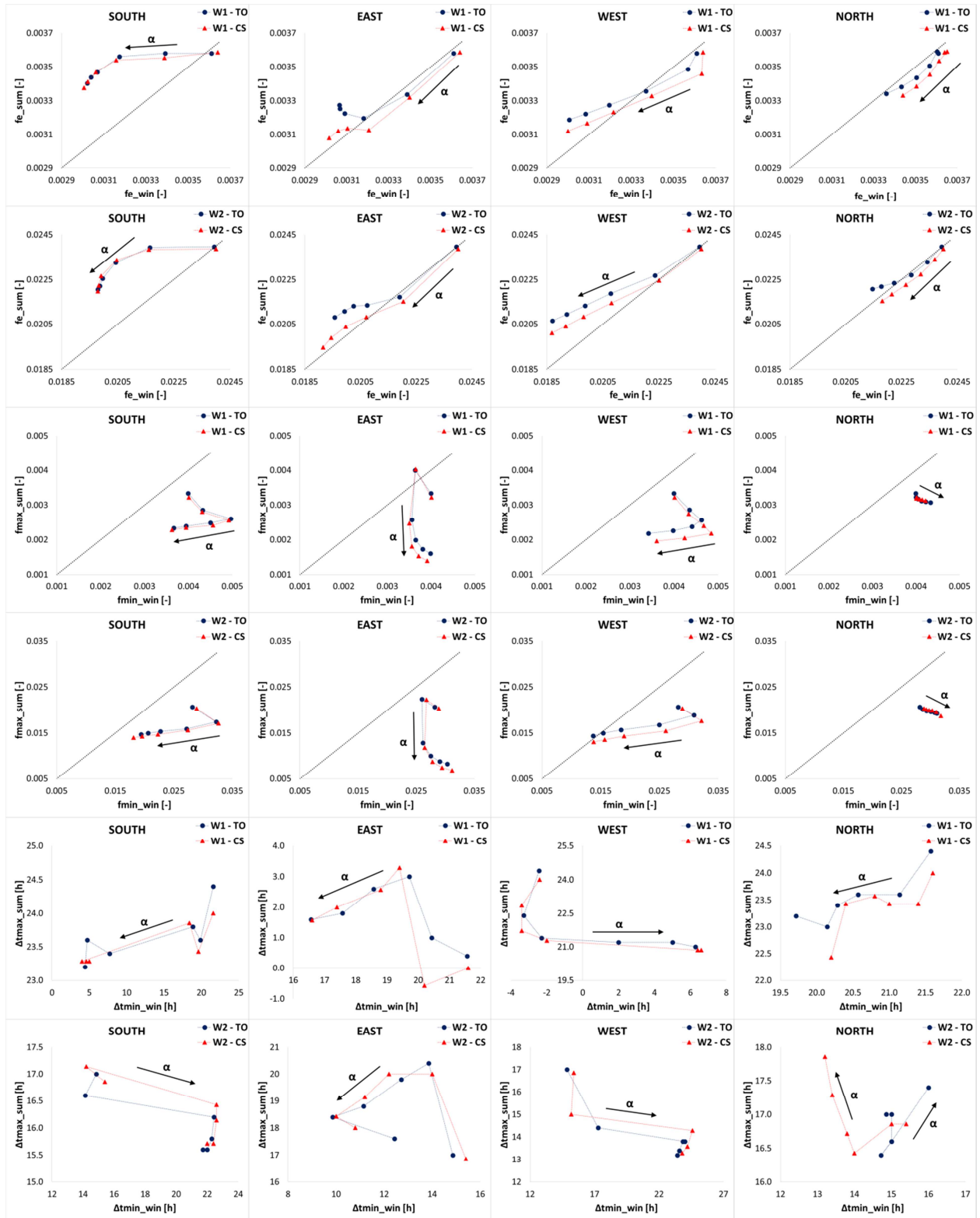


Figure 8 – Comparison between the energy decrement factors in summer and winter (first and second line), between the decrement factor of the maximum heat flux in summer and that of the minimum heat flux in winter (third and fourth line) and between the time lag of the maximum heat flux and that of the minimum heat flux (fifth and sixth line) varying the location, the absorption coefficient, the orientation and the type of wall. Continuous regime in the absence of internal radiant loads.

Each figure contains 24 maps arranged in six rows and four columns. In the maps, the energy decrement factor in summer and winter is compared in the first two rows, in the third and fourth line the decrement factor of the maximum heat flux in summer is compared with that of the minimum heat flux in winter and in the last two lines the relative time lags. All comparisons are reported on two lines, the first relating to Wall 1 (W1) for the different exposures, the second relates to Wall 2 (W2). In each map, for the locations of Turin (TO) and Cosenza (CS), the dynamic parameters are compared in two seasons with a variation of the absorption coefficient. In order to analyse the different behaviour of the wall in the summer and winter season, a bisector and an arrow indicating the increasing values of  $\alpha_e$  are traced.

Figure 8 shows that the change of location does not alter the trends of the energy decrement factors and of the maximum and minimum heat flux in the two seasons upon variation of  $\alpha_e$ . Between the two localities slightly different values are recorded, both in terms of energy and heat flux, for eastern and western exposures, and only in terms of energy for the northern exposure.

The seasonal behaviour differs with the exposure. The energy decrement factor to the south in winter is less than that in the summer period irrespective of the absorption coefficient  $\alpha_e$ ; to east and to west only for high values of  $\alpha_e$ , whereas to the north they are close. The decrement factor of the maximum heat flux, for any exposure, is less than that of the minimum heat flux.

As for the time lags, the change of location changes the values, to a different extent for the two walls and for the different exposures, and also the trend for northern exposure for Wall 2.

In the case in which there is a radiant load on the internal surface, see Figure 9, the different locations does not involve a modification of the trends of the decrement factor on variation of  $\alpha_e$ . Unlike the case in which radiant loads are absent, for all exposures and for both the walls, the range of variation of the decrement factors on variation of  $\alpha_e$  is slightly more contained in Cosenza. In the two locations, the energy decrement factors differ for reduced values of  $\alpha_e$ , while the decrement factors of the heat flux peaks only to the east and west.



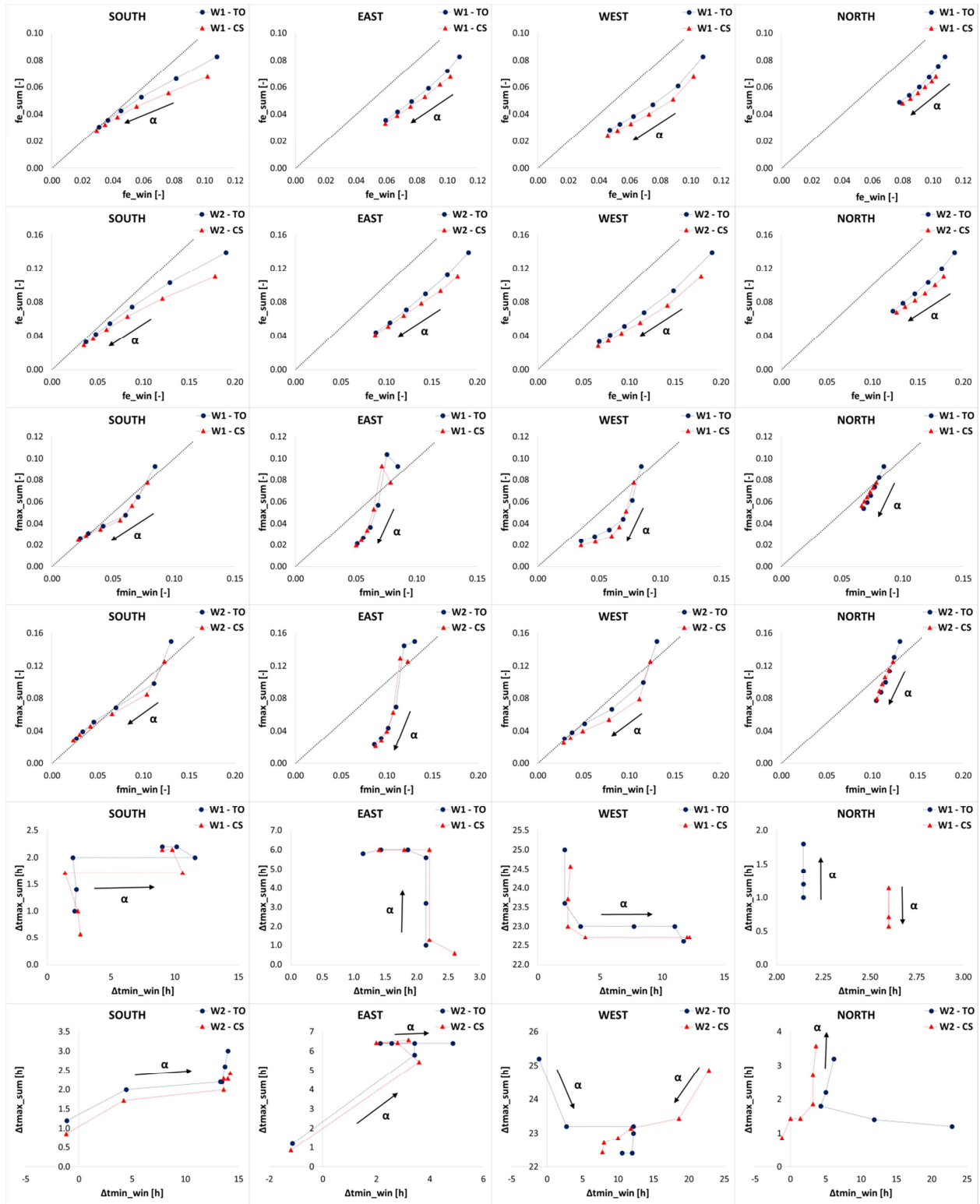


Figure 9 – Comparison between the energy decrement factors in summer and winter (first and second line), between the decrement factor of the maximum heat flux in summer and that of the minimum heat flux in winter (third and fourth line) and between the time lag of the maximum heat flux and that of the minimum heat flux (fifth and sixth line) varying the location, the absorption coefficient, the orientation and the type of wall. Continuous regime in the presence of internal radiant loads.

The dynamic behaviour of the walls in the two seasons is characterised by more reduced energy decrement factor values in summer compared to those in winter, with the exception of southern exposure for which are close for high values of  $\alpha_e$ . The decrement factor of the maximum heat flux in summer and of the minimum heat flux in winter present close values in the two seasons for southern and northern exposure; to the east and for high values of  $\alpha_e$  the decrement factor in summer is smaller than that in winter; to the west the latter consideration is valid only for  $\alpha_e$  between 0.2 and 0.6 for Wall 1, and between 0.2 and 0.4 for Wall 2.

With regard to the time lag trends in the two locations: for Wall 1 they are similar for all exposures; for Wall 2 are similar for only southern and eastern exposure, while to the west and north trends are different. In all cases in which the trends are similar, numerical values of the time lags in the two locations are close. In other cases, the numerical values differ significantly on variation of the location due to the significant variation of the time lag of the minimum heat flux.

Figure 10, relating to the attenuated regime in the absence of radiant loads, shows that for both walls the pattern of decrement factors are similar for the two locations, with lower values for Cosenza both in summer and winter. The increase of  $\alpha_e$  gives rise to a variation of the decrement factors that is much more contained in Cosenza than in Turin and, furthermore, the decrement factors in the summer season, both in terms of energy and of maximum heat flux, are always lower than those relating to winter. To the south and west, with an increasing  $\alpha_e$ , the decrement factors in the two seasons are increasingly closer.

As for the time lags, trends are identical for the two locations and those of Cosenza are shifted in the plane compared to those of Turin. In particular, the shift gives rise to smaller values of the time lag of the maximum heat flux and to higher values of the time lag of the minimum heat flux. Only Wall 2 in the north presents different trends for the two locations with time lag of the maximum heat flux values in Cosenza smaller than those of Turin.

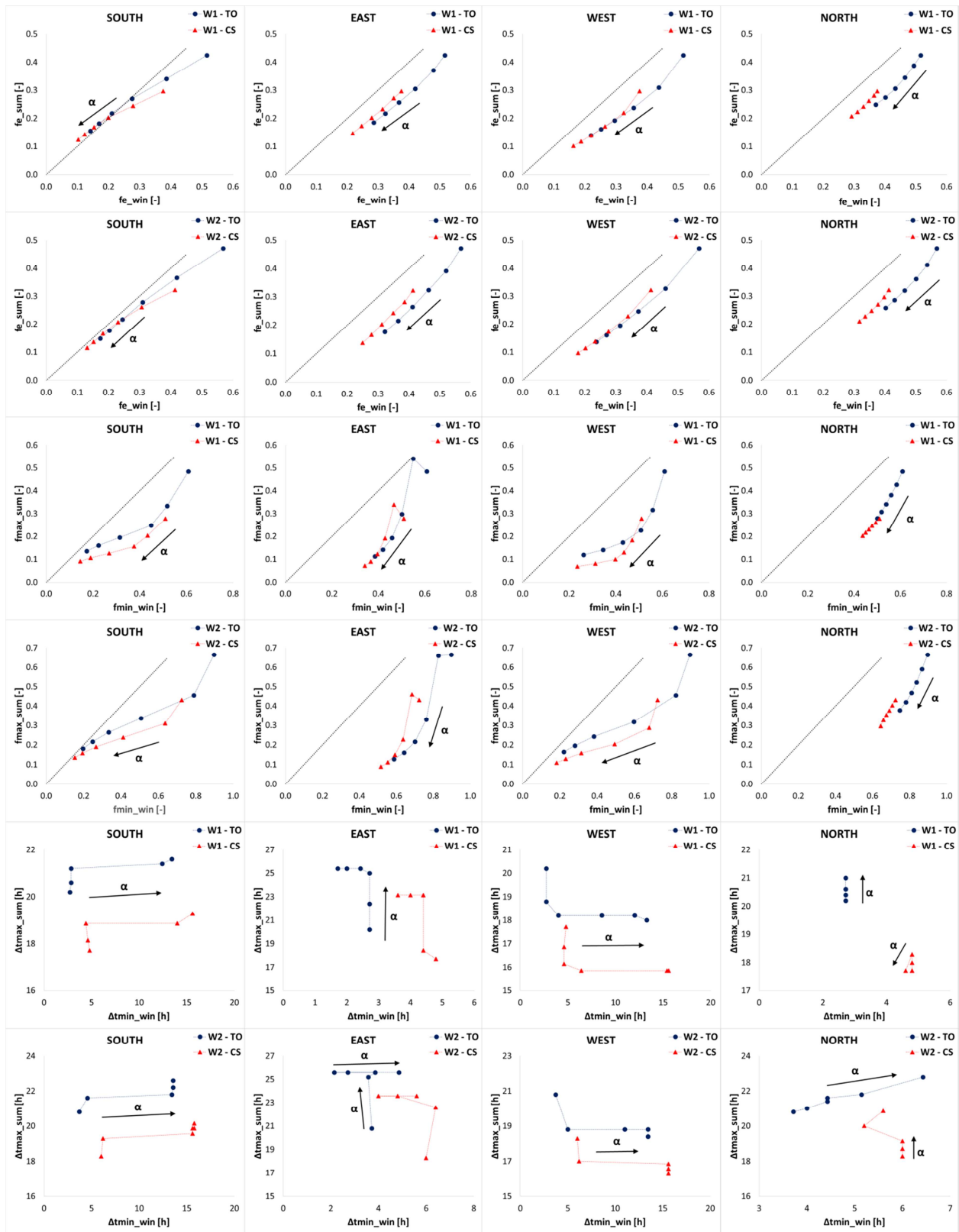


Figure 10 – Comparison between the energy decrement factors in summer and winter (first and second line), between the decrement factor of the maximum heat flux in summer and that of the minimum heat flux in winter (third and fourth line) and between the time lag of the maximum heat flux and that of the minimum heat flux (fifth and sixth line) varying the location, the absorption coefficient, the orientation and the type of wall. Attenuated regime in the absence of internal radiant loads.

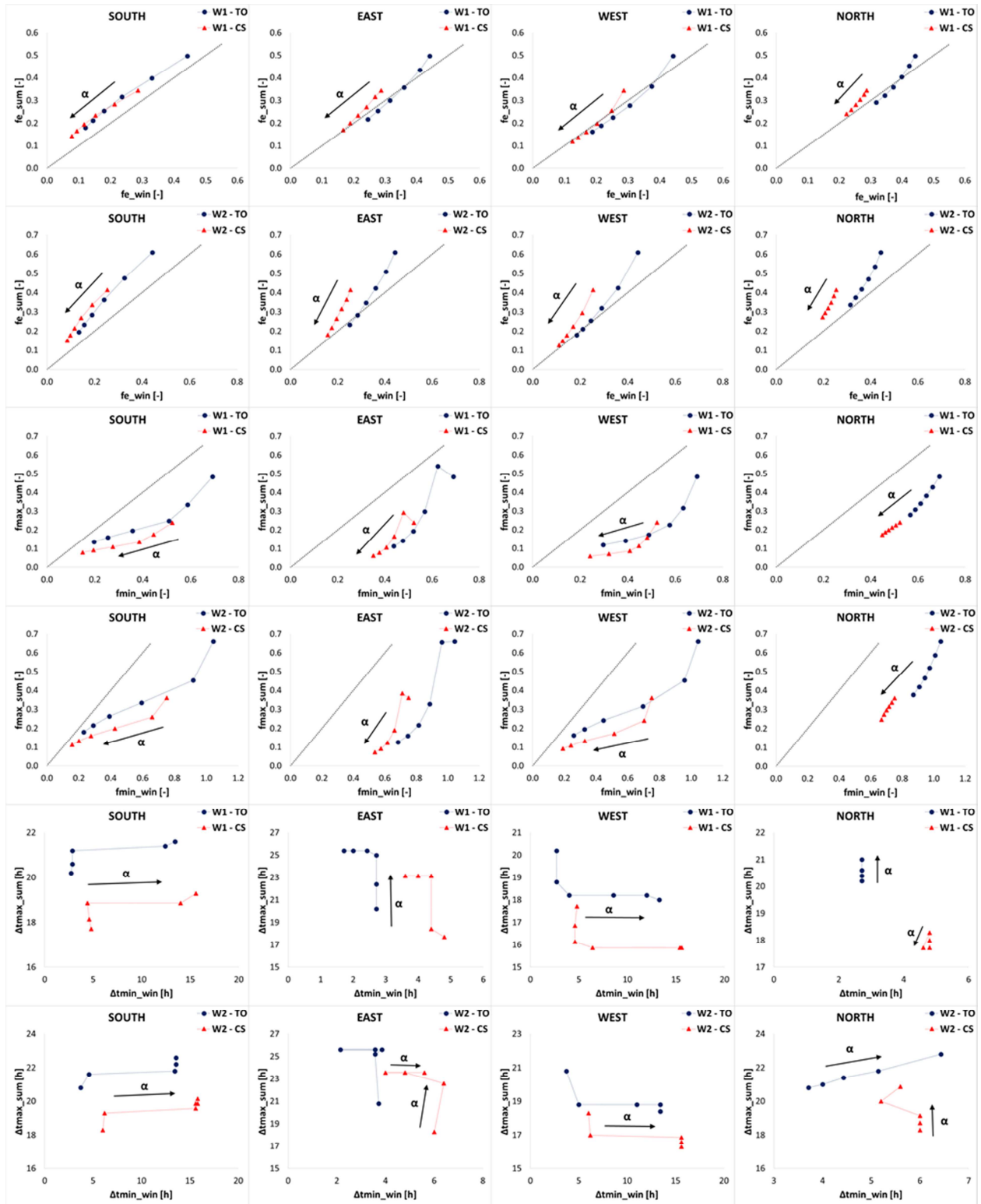


Figure 11 – Comparison between the energy decrement factors in summer and winter (first and second line), between the decrement factor of the maximum heat flux in summer and that of the minimum heat flux in winter (third and fourth line) and between the time lag of the maximum heat flux and that of the minimum heat flux (fifth and sixth line) varying the location, the absorption coefficient, the orientation and the type of wall. Attenuated regime in the presence of internal radiant loads.

Also in the presence of radiant loads, the trends of decrement factors for the two locations are similar with lower values in both the summer and winter in Cosenza, as shown in Figure 11. The presence of the radiant load changes the seasonal behaviour of the energy decrement factor. In winter, it is lower than in the summer season in the south, while in the other exposures only for Wall 2 for reduced values of  $\alpha_e$ . In all other cases, the summer and winter decrement factors are close. In terms of heat flux, the decrement factors are still lower in the summer season.

Finally, the time lags, as highlighted in the previous section, do not undergo modifications compared to the case where radiant loads are absent.

## 6. Conclusions

The dynamic analysis of the external walls of buildings in a non-sinusoidal periodic regime, developed by means of an analytical model formulated by an equivalent electrical circuit and solved by the harmonic method and the phasor method, has allowed for the identification of dynamic characteristics. The survey refers to two commonly used walls located in two climatically different locations.

The analyses showed that the dynamic characteristics are strongly dependent on the solar absorption coefficient of the outer surface of the wall. This dependence varies with the type and orientation of the wall, with the plant operating regime and with the possible presence of shortwave radiant loads on the internal surface. In particular:

- the energy decrement factor decreases with the increasing of the absorption coefficient for any exposure;
- the decrement factor of the maximum heat flux decreases with the increasing of the absorption coefficient only for south, west and north exposures, while in the east before it increases, reaching a maximum and then decreases;
- the decrement factor of the minimum heat flux decreases with an increase of the absorption coefficient in the attenuated regime and in the continuous regime in the presence of radiant interior loads. In a continuous regime, in the absence of radiant loads, it presents a maximum value to the south and west, a minimum value in the east and is always higher with an increasing absorption coefficient in the north.
- in general, in the north more contained variations of the decrement factors are recorded on variation of the absorption coefficient.

- the variation of the absorption coefficient has a significant influence on the time lag of the minimum heat flux, while the time lag of the maximum heat flux undergoes changes that are more contained.

The results, obtained considering 1152 different boundary conditions and summarised using maps, show that the walls have a different dynamic behaviour in summer and winter air conditioning since, for defined boundary conditions, the energy decrement factors are different in the two seasons, and the decrement factor and time lag of the maximum heat flux in summer are different from those of the minimum heat flux in winter.

In the case of air conditioning in summer or winter, the results allow definition of the most suitable value of the absorption coefficient to reduce the energy requirements and contain the power required of the system. If the air conditioning is annual, the choice of the absorption coefficient must lead to an overall reduction in energy and power needed in the two seasons or in the more energetically expensive season.

The modification of the absorption coefficient of the external surfaces of the walls can be used effectively in building energy retrofit to obtain favourable dynamic characteristics. This solution is feasible and economically sustainable.

## References

- [1] Directive 2010/31/EU. European Parliament and of the Council of 19 May 2010 on the Energy Performance of Buildings (recast), Off. J. Eur. Union (2010), pp. 13–35
- [2] EN ISO 13786, Thermal Performance of Buildings Components e Dynamic Thermal Characteristics e Calculation Methods, 2010.
- [3] Daouas N, Hassen Z, Aissia HB. Analytical periodic solution for the study of thermal performance and optimum insulation thickness of building walls in Tunisia, *Applied Thermal Engineering* 2010;30(4):319-26.
- [4] Lü X, Lu T, Viljanen M. A new analytical method to simulate heat transfer process in buildings, *Applied Thermal Engineering* 2006;26(16):1901-9.
- [5] Sun C, Shu S, Ding G, Zhang X, Hu X. Investigation of time lags and decrement factors for different building outside temperatures, *Energy and Buildings* 2013;61:1-7.
- [6] Jin X, Zhang X, Cao Y, Wang G. Thermal performance evaluation of the wall using heat flux time lag and decrement factor, *Energy and Buildings* 2012;47:369-74.
- [7] Oliveti G, Arcuri N, Mazzeo D, De Simone M. A new parameter for the dynamic analysis of building walls using the harmonic method, *International Journal of Thermal Sciences* 2015;88:96-109.

- [8] Mazzeo D, Oliveti G, Arcuri N. Influence of internal and external boundary conditions on the decrement factor and time lag heat flux of building walls in steady periodic regime, *Applied Energy* 2016;164:509-31.
- [9] Ruivo CR, Ferreira PM, Vaz DC. On the error of calculation of heat gains through walls by methods using constant decrement factor and time lag values, *Energy and Buildings* 2013;60:252-61.
- [10] Kontoleon KJ, Bikas DK. The effect of south wall's outdoor absorption coefficient on time lag, decrement factor and temperature variations, *Energy and Buildings* 2007;39:1011-18.
- [11] Kontoleon KJ, Eumorfopoulou EA. The influence of wall orientation and exterior surface solar absorptivity on time lag and decrement factor in the Greek region, *Renewable Energy* 2008;33:1652-64.
- [12] Ozel M. The influence of exterior surface solar absorptivity on thermal characteristics and optimum insulation thickness, *Renewable Energy* 2012;39(1):347-55.
- [13] Al-Sanea SA, Zedan MF, Al-Hussain SN. Effect of masonry material and surface absorptivity on critical thermal mass in insulated building walls, *Applied Energy* 2013;102:1063-70.
- [14] Granja AD, Labaki LC, Influence of external surface colour on the periodic heat flow through a flat solid roof with variable thermal resistance, *International Journal of Energy Research* 2003;27:771-9.
- [15] Cheng V, Ng E, Givoni B. Effect of envelope colour and thermal mass on indoor temperatures in hot humid climate, *Solar Energy* 2005;78(4):528-34.
- [16] Han J, Lu L, Yang H. Investigation on the thermal performance of different lightweight roofing structures and its effect on space cooling load, *Applied Thermal Engineering* 2009;29(11-12):2491-99.
- [17] Bansal NK, Garg SN, Kothari S. Effect of exterior surface colour on the thermal performance of buildings, *Building and Environment* 1992;27(1):31-7.
- [18] Marino C, Minichiello F, Bahnfleth W. The influence of surface finishes on the energy demand of HVAC systems for existing buildings, *Energy and Buildings* 2015;95:70-79.
- [19] Desoer CA, Kuh ES, *Basic Circuit Theory*, 1969, McGraw-Hill Inc, New York, USA.
- [20] Arpaci VS, *Conduction Heat Transfer*, Addison - Wesley Publishing Company, Inc., Reading Mass., 1966.
- [21] Mazzeo D, Oliveti G, De Simone M, Arcuri N. Analytical model for solidification and melting in a finite PCM in steady periodic regime, *International Journal of Heat and Mass Transfer*, 2015;88:844-861.

- [22] UNI 10351:1994. Building materials. Thermal conductivities and vapour permeabilities.
- [23] ISO EN 10456:2007. Building materials and products - Hygrothermal properties - Tabulated design values and procedures for determining declared and design thermal values.
- [24] UNI 10355:1994. Walls and floors - Thermal resistance values and calculation method
- [25] UNI 10349:1994. Heating and cooling of buildings. Climatic data.
- [26] Solar Energy Laboratory University of Wisconsin-Madison, TRNSYS, Version 17, 2012.
- [27] Mathematical Reference, TRNSYS, 2012; pp. 291-294.
- [28] Mathematical Reference, TRNSYS, 2012; pp. 284.
- [29] Mathematical Reference, TRNSYS, 2012; pp. 309-310.
- [30] EN ISO 6946:1997. Building components and building elements – Thermal resistance and thermal transmittance – Calculation method.
- [31] Oliveti G, Arcuri N, De Simone M, Bruno R. Experimental evaluations of the building shell radiant exchange in clear sky conditions. *Solar Energy* 2012; 86:1785-1795.
- [32] UNI TS 11300-1:2014. Energy performance of buildings - Part 1: Evaluation of energy need for space heating and cooling.
- [33] EN ISO 13790:2008. Energy performance of buildings – Calculation of energy use for space heating and cooling.
- [34] Oliveti G, Arcuri N, Bruno R, De Simone M. An accurate calculation model of solar heat gain through glazed surfaces, *Energy and Buildings* 2011; 43(2-3):269-74.

## Nomenclature

[A], [B]	heat transfer matrix
c	specific heat capacity [J/(kg K)]
C	steady areal heat capacity [J/(m <sup>2</sup> K)]
fe	energy decrement factor [-]
f <sub>max</sub>	decrement factor of the maximum heat flux [-]
f <sub>min</sub>	decrement factor of the minimum heat flux [-]
G	specific air flow rate [kg/(m <sup>2</sup> s)]
h	heat transfer coefficient [W/(m <sup>2</sup> K)]
n	number of harmonics
P	period of oscillation [s]
R	thermal resistance [m <sup>2</sup> K/W]
s	layer thickness [m]



---

t	time [s]
T	temperature [K]
U	steady thermal transmittance [ $\text{W}/(\text{m}^2 \text{K})$ ]
y	thermal quantity
Y	generic complex thermal parameter
[Z]	heat transfer matrix of the multilayered wall from surface to surface

*Greek symbols*

$\alpha$	absorption coefficient [-]
$\Delta t_{\max}$	time lag of the maximum heat flux [s]
$\Delta t_{\min}$	time lag of the minimum heat flux [s]
$\Delta U$	instantaneous internal energy variation [ $\text{W}/\text{m}^2$ ]
$\lambda$	thermal conductivity [ $\text{W}/(\text{m K})$ ]
$\rho$	density [ $\text{kg}/\text{m}^3$ ]
$\varphi$	heat flux [ $\text{W}/\text{m}^2$ ]
$\psi$	argument of the sinusoidal thermal quantity [rad]
$\omega$	pulsation of the sinusoid [rad/s]

*Subscripts*

1	Wall 1
2	Wall 2
a	air
c	convective
e	external
i	internal
ig	internal heat gain
k	k-th harmonic
l	light source
max	max value
min	min value
p	at constant pressure
pl	plant
r	radiative
s	surface
s,e	referring to the solar load
sky	referring to the sky load

sr	shortwave radiative
sum	summer period
v	ventilation
w	wall
wint	winter period
$\Sigma$	referring to the sum of all the harmonics

*Superscripts*

e	external
i	internal

*Symbols*

–	mean value
~	oscillating value in the time domain
^	oscillating value in the complex domain
	amplitude of an oscillating value

# **Latent heat storage materials (PCM)**

# Chapter 4

## Analytical model for solidification and melting in a finite PCM in steady periodic regime

### Abstract

An analytical solution of the phase change problem, known as the Stefan or Moving Boundary Problem, in a PCM layer (Phase Change Materials) subject to boundary conditions that are variable in time, is presented, in steady periodic regime. The two-phase Stefan Problem is resolved considering periodic boundary conditions of temperature or of heat flux, or even mixed conditions.

This phenomenon is present in air-conditioned buildings, the walls of which use PCM layers to reduce thermal loads and energy requirements to be compensated by the plant.

The resolution method used is one in which phasors allow the transformation of partial differential equations, describing conduction in the solid and liquid phase, into ordinary differential equations; furthermore the phasors allow transformation of the thermal balance

equation at the bi-phase interface into algebraic equations. The Moving Boundary Problem is then reduced to a system of algebraic equations, the solution of which provides the position in time of the bi-phase interface and the thermal field of the layer. The solution obtained provides for different thermodynamic configurations that the layer can assume and makes the position of the bi-phase interface and the thermal field depend on the Fourier number and on the Stefan number calculated in the solid phase and in the liquid phase.

In the case of two boundary conditions represented by a single sinusoidal oscillation, a general analysis, addressed in different thermodynamic configurations obtained by varying the Fourier and Stefan number, shows the calculation procedure of the steady and of the oscillating component of the position of the bi-phase interface, of the temperature field and of the heat flux field. In addition, we considered the particular case of a PCM layer with an oscillating temperature boundary condition on one face and a constant temperature on the other face.

The analytical procedure was also used for an analysis dedicated to the thermal behaviour of Glauber's salt subject to independent multi harmonic boundary conditions. This salt hydrate is one of the most studied, having a high latent fusion heat and a melting temperature that is suited for use in the walls of buildings.

Keywords: Moving Boundary Problem; Stefan Problem; PCM; Analytical model; Steady periodic regime; Wall.

- An analytical solution of the Stefan Problem is presented
- The thermal regime considered is the steady periodic
- The resolution method used is that of phasors
- The equations that describes the thermal field have been rendered dimensionless
- The solution was used to determine the thermal behaviour of a Glauber's Salt layer

*Sollevare nuove domande, nuove possibilità, riguardo a vecchi problemi da un nuovo punto di vista, richiede immaginazione creativa e segna un reale avanzamento della scienza.*

*(Albert Einstein)*

## 1. Introduction

Among the technologies available to improve thermal performance of the walls in air-conditioned buildings, the use of PCM has attracted notable attention. These materials, due to the variability of the boundary conditions, undergo phase changes with storage of latent heat in the wall and successive releasing, and consequent modification of the thermal exchanges between the air-conditioned environment and the outdoor environment. Storage of latent heat is preferable to the storage of sensible heat due to its isothermal properties and the high energetic contribution.

In the winter heating of the environments, a part of the energy lost through an opaque element of the external envelope is used for the solid-liquid phase change of the PCM layer. This process gives rise to a storage of latent heat in the wall, which, in part, can be returned to the internal environment if the opposite liquid-solid phase change occurs subsequently. In this way, the energy lost from the environment to the outside is reduced.

In summer cooling, the presence of a PCM layer drastically reduces the solar loads entering through opaque walls; the energy stored in the wall is returned in part to the outdoor environment during nocturnal hours, prevalently following radiant exchange with the sky. The advantage is the net reduction in the loads to be removed by the air-conditioning plant, the time lag of the entering heat flux and the attenuation of temperature oscillations.

If the internal walls are considered, the presence of a PCM layer increases thermal storage with a consequent reduction of internal air temperature oscillations.

In order for the benefits to be continuous over time, the variability of the boundary conditions must be such as to cause a fusion cycle in the layer and successive solidification in a period of 24 h.

This chapter addresses the problem of heat transfer in a PCM layer subject to phase changes due to the variability of the loadings, which act on the two faces delimiting it. The external loadings, which are variable in time, are the air temperature, solar irradiance, and infrared radiation from the sky. While internal loadings are solar radiation entering through the glazed surfaces, internal loads and the power supplied by the plant. Since the obtainable benefits in terms of energy are linked to the realisation of continuous phase change cycles, and considering that the loadings have trends that can always be expressed through the sum of periodic functions, the analysis was conducted considering the steady periodic thermal regime. This regime is representative of the thermal behaviour of the building walls, especially in summer and is used for the dynamic

thermal characterisation of building walls in EN ISO 13786 [1] and in [2]. The technical Standard uses harmonic analysis in a steady periodic regime for the dynamic characterization of finite monophasic layers of building components with only sensible thermal storage. The boundary conditions on the two faces delimiting the wall are temperature or heat flux that vary sinusoidally.

In a PCM layer subject to phase changes, the transfer regime of the heat flux is modified due to the discontinuity of the heat flux at the bi-phase interface due to the latent heat storage. This phenomenon determines variability in time of the position of the bi-phase interface in the layer and the modification of the thickness of both the solid phase and the liquid phase. The thermal field in the two phases, which present different thermophysical properties, is a function of the position of the bi-phase interface that is variable in time, as well as the relative boundary conditions.

From a historical survey, several authors have given exact analytical solutions only in monodimensional semi-infinite or infinite domains with simple initial and boundary conditions. However, they neglected convection in the liquid phase and the variation of the thermophysical properties in the two phases. The Stefan Problem is divided into a one-phase Stefan Problem and a two-phase Stefan Problem. The term ‘one-phase’ designates one of the phases being active, the other phase staying at its melting temperature, while the term ‘two phase’ indicates that the thermal field varies in both phases. In particular, the following one-phase problems have been solved, by using similarity variable [3-8]: (1) conduction in a semi-infinite phase change material with a constant temperature greater than zero at the initial time. In the subsequent instants a constant temperature less than zero at abscissa  $x = 0$  causes a solidification which occurs at a temperature equal to zero; (2) conduction in an infinite phase change material with, at the initial time, a liquid phase placed in the abscissae  $0 < x < +\infty$  at a temperature greater than zero and the solid phase placed in the abscissae  $-\infty < x < 0$  at a temperature less than zero. Analogously to the first problem, a constant temperature less than zero at abscissa  $x = 0$  causes a solidification which occurs at a temperature equal to zero. In these Stefan Problems the liquid phase stays at melting temperature during the solidification process.

The extension of the one-phase problem solution to the two-phase problem is known as Neumann’s solution [3-8]. Such a Moving Boundary Problem concerns conduction in a monodimensional and semi-infinite domain assumed to be solid, at the initial time, at a uniform temperature less than the melting temperature. In the subsequent instants on face  $x = 0$  a constant temperature, greater than the melting temperature, causes the melting process. In this case, during melting both liquid and solid phases present a temperature distribution. There is also an

exact Neumann solution for a particular prescribed heat flux at the face  $x = 0$ , and for a particular prescribed convective condition at the face  $x = 0$  [9].

The cases considered regard the thermal transient in an infinite or semi-infinite layer subject to phase change with an initial temperature constant in the domain and with constant temperature assigned on the boundary. Instead, no analytical solution in a finite domain is available as self-similarity cannot be applied when the PCM layer has a characteristic length and is subjected to boundary conditions that are variable in time.

However, approximate methods for a one-dimensional Moving Boundary Problem in finite and semi-infinite domain with various boundary conditions [5-8] are available. These include the integral method, the variational formulation, the moving heat source, the perturbation method, the embedding technique, the variable eigenvalue approach, the electrical network analog method, the quasi-stationary approximation and the Megerlin method.

From an examination of scientific literature, it has emerged that an analytical solution to the Moving Boundary Problem in steady periodic regime is not available. Instead, the solutions available regard thermal transients whose boundary conditions do not vary in time and cannot be expressed through the sum of periodic functions.

Several authors, through numerical models used to solve the ‘one-phase’ or the ‘two phase’ Stefan Problem and through experimental investigations, have addressed the problem of the thermal behaviour of a PCM layer in a steady periodic regime.

In a PCM layer, Savovic et al. [10] evaluated the position and the velocity of the bi-phase interface and the temperature field through a ‘one-phase’ numerical model. Hasan et al. [11] have determined the thermal field and the position of the bi-phase interface by using a ‘two phase’ approach and a boundary condition cycling above and below the melting point. Subsequently, the work of Hasan et al. was extended by Voller et al. [12] also considering convection in the liquid phase and by Casano and Piva [13] who formulated a numerical model in dimensionless form considering a sinusoidal heat flux boundary condition.

In a multilayer wall containing a PCM layer, the influence of the melting temperature and the latent heat capacity on the energy that can be passively absorbed and released during a diurnal cycle have been investigated by Neeper [14]. While Halford [15] examined the influence of the layer thickness and of the outdoor climatic conditions on the time lag and on the attenuation of the peak load. Instead, the influence of the position and the melting temperature of the PCM layer on the annual energy requirement has been studied by Mathieu-Potvin et al. [16].

In order to provide a new mathematical model of the thermal problem in a finite layer subject to phase change in steady periodic regime, an exact analytical solution is presented in this chapter;



it was obtained by reformulating the equations that describe the phenomenon using the phasors method, which is widely used in electrical engineering.

## 2. Methodology

### 2.1. Formulation of physical model

The study of thermal exchange in a phase change system subjected to boundary conditions that are variable in time is usually developed by simultaneously solving the general equation of conduction in the solid phase, the conservation of mass, of momentum and of energy equation in liquid phase, coupled by bi-phase interface boundary conditions.

The physical model can be simplified if one takes into consideration that the geometry of the system is flat with reduced thicknesses. The boundary conditions on the two external faces, expressed in terms of temperature or of heat flux, are such that they do not generate a flow field in the liquid phase. In the formulation of the mathematical model, which is representative of the physical system, classical simplifications were adopted: the conductive and monodirectional heat transfer in the liquid phase and in the solid phase; the flat bi-phase interface and the reversible and isothermal phase change if supercooling and phase segregation phenomena are excluded [17, 18]; PCM physical properties constant with temperature, but different in the solid and liquid phases; the difference in density between the solid phase and the liquid phase is negligible.

The PCM layer can be either in a totally solid or liquid phase, at a temperature that is respectively lower or higher than the melting temperature. Both phases can be present occupying different layers and are separated by a bi-phase interface, at the melting temperature; the bi-phase interface is in motion, with transformation of one phase to another. The PCM portion involved in the phase change can be lesser than the layer thickness and differently arranged. The general heat conduction equation in the solid or liquid phase of a layer subjected to a phase change has the form:

$$\frac{\partial^2 T}{\partial x^2} - \frac{1}{\alpha} \frac{\partial T}{\partial t} = 0 \quad (1)$$

with  $T$  temperature at the abscissa  $x$  and time  $t$ ,  $\alpha = \lambda/(\rho c)$  thermal diffusivity,  $\lambda$  thermal conductivity,  $\rho$  density and  $c$  specific heat capacity of the phase.

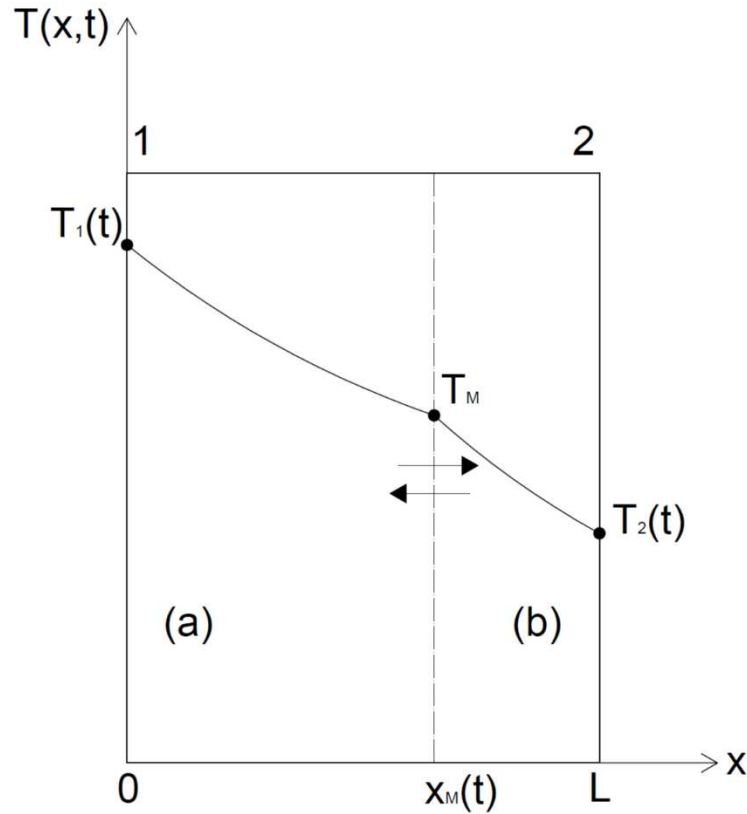


Figure 1 - Temperature field in a bi-phase layer. (a) liquid phase, (b) solid phase,  $T_M$  melting temperature,  $X_M(t)$  position of the bi-phase interface and boundary conditions  $T_1(t)$  and  $T_2(t)$ .

For boundary conditions on face 1 of abscissa  $x = 0$  of the layer (a) and on face 2 of abscissa  $x = L$  of the layer (b) see Figure 1. The boundary condition temperatures are:

$$T_a(0, t) = T_1(t) \quad (2)$$

$$T_b(L, t) = T_2(t)$$

with (a) liquid phase and (b) solid phase if  $T_2(t) < T_M < T_1(t)$  and with (a) solid phase and (b) liquid phase if  $T_1(t) < T_M < T_2(t)$ .

Considering, for example, the fusion process, two conditions, known as Stefan conditions, must be met at the liquid-solid interface:

$$\left[ \lambda_a \frac{\partial T_a}{\partial x} - \lambda_b \frac{\partial T_b}{\partial x} \right]_{x=X_M} = \rho H \frac{dX_M}{dt} \quad (3)$$

$$T_a(X_M, t) = T_b(X_M, t) = T_M \quad (4)$$

Eq. (3) expresses the thermal balance at the bi-phase interface, which requires that the difference in heat fluxes between the liquid phase and the solid phase is equal to the heat needed for the fusion process per unit time. The equivalence of the melting temperature  $T_M$  at the abscissa  $X_M$  for the two phases is expressed by Eq. (4). In Eq. (3)  $H$  is the latent fusion heat and  $dX_M/dt$  is the velocity of the bi-phase interface.

Interface conditions (3) and (4) introduce complexity in the resolution of the temperature field given that the position of  $X_M$  in various instants, which is determined in relation to the conductive heat flux entity in the two layers, is unknown.

In this chapter, a two-phase Stefan Problem is addressed in a cyclic process, in a steady periodic regime, in which the two phases are active since the boundary conditions regard a temperature oscillation above the melting temperature on one face and an oscillating temperature below the melting temperature on the other face.

The temperature and heat flux fields and the bi-phase interface movement, generated following the periodic action of the temperature loadings  $T_1(t)$  and  $T_2(t)$  on the two external surfaces, are expressed through a Fourier series expansion [4] as the sum of a steady value and of a fluctuating value, which can be expressed as sum of sinusoidal variations.

For the temperature and the heat flux, it can be supposed that:

$$T(x, t) = \bar{\vartheta}(x) + \vartheta(x, t) = \bar{\vartheta}(x) + \sum_{k=1}^n \tilde{\vartheta}_k(x, t) = \bar{\vartheta} + \sum_{k=1}^n |\tilde{\vartheta}_k| \sin(k\omega t + \varphi_k) \quad (5)$$

$$F(x, t) = \bar{\phi} + \phi(x, t) = \bar{\phi} + \sum_{k=1}^n \tilde{\phi}_k(x, t) = \bar{\phi} + \sum_{k=1}^n |\tilde{\phi}_k| \sin(k\omega t + \psi_k) \quad (6)$$

with  $\bar{\vartheta}(x)$  and  $\bar{\phi}$  steady temperature at abscissa  $x$  and steady heat flux,  $\vartheta(x, t)$  and  $\phi(x, t)$  fluctuations with mean value equal to zero calculated as the sum of harmonics,  $k$  order and  $n$  number of the harmonics  $\tilde{\vartheta}_k(x, t)$  and  $\tilde{\phi}_k(x, t)$ ,  $\omega$  angular frequency,  $|\tilde{\vartheta}_k|$  and  $|\tilde{\phi}_k|$  sinusoid amplitudes,  $\varphi_k$  and  $\psi_k$  arguments evaluated compared to a reference axis. In these conditions, even the position of the bi-phase interface can be expressed as the sum of a steady value and of a fluctuating value:

$$X_M(t) = \bar{\chi}_M + \chi_M(t) = \bar{\chi}_M + \sum_{k=1}^n \tilde{\chi}_{Mk}(t) = \bar{\chi}_M + \sum_{k=1}^n |\tilde{\chi}_{Mk}| \sin(k\omega t + \zeta_k) \quad (7)$$

with  $\bar{\chi}_M$  steady component,  $\chi_M(t)$  fluctuation component, expressed as the sum of n harmonics  $\tilde{\chi}_{Mk}(t)$  of amplitude  $|\tilde{\chi}_{Mk}|$  and of argument  $\zeta_k$ , of the position of bi-phase interface.

Using Eqs. (5) and (6), the boundary conditions (2) assume the form:

$$T_1(t) = \bar{\vartheta}_1 + \vartheta_1(t) = \bar{\vartheta}_1 + \sum_{k=1}^n \tilde{\vartheta}_{1k}(t) \quad (8)$$

$$T_2(t) = \bar{\vartheta}_2 + \vartheta_2(t) = \bar{\vartheta}_2 + \sum_{k=1}^n \tilde{\vartheta}_{2k}(t) \quad (9)$$

Since the phase change occurs at a constant temperature, the fluctuating component of the temperature at the abscissa  $X_M(t)$  is equal to zero.

The steady thermal field and the fluctuating field in the two phases are obtained separately. Summing the term relative to the harmonic component of oscillation equal to zero (steady condition) and adding the solutions obtained for the successive harmonics it is possible to determine the temperature field  $T(x,t)$ , the heat flux field  $F(x,t)$  and the position of bi-phase interface  $X_M(t)$ .

In order that the position of the bi-phase interface  $X_M(t)$  falls within the physical domain, once the steady component has been calculated, the fluctuating component of the position of the bi-phase interface must satisfy some conditions. In particular, at each instant, the sum of the steady component and of the fluctuating component must not be less than zero nor greater than L. Such conditions exclude overheating and supercooling of the entire layer.

Considering the maximum and minimum value of the fluctuating component, obtained as the sum of the n harmonics, the preceding condition leads to the relations:

if  $\bar{\chi}_M \leq \frac{L}{2}$  then

$$\min_{0 \leq t \leq P} [\chi_M(t)] \leq \bar{\chi}_M \quad (10.1)$$

if  $\bar{\chi}_M \geq \frac{L}{2}$  then

$$\max_{0 \leq t \leq P} [\chi_M(t)] \leq L - \bar{\chi}_M \quad (10.2)$$

with P fundamental oscillation period and L thickness of the layer.

It is also possible that the preceding conditions are not satisfied; in such a case, the position of the bi-phase interface  $X_M(t)$  in some instants during a period is outside the physical domain and this can occur if it is greater than the thickness L or lower than zero. In the hypothesis that  $\bar{\vartheta}_1 > T_M > \bar{\vartheta}_2$ , in the first case all the layer is liquid and it overheats while in the other case the layer is solid and it subcools. In the successive instants, the position of the bi-phase interface is within the physical domain and this could lead to a partial or full phase change of the layer.

Another condition that can occur is that the  $X_M(t)$  assumes values both greater than L and lower than zero, therefore during a period the entire layer is subjected to phase change and it overheats and subcools. In the case that the sole fundamental harmonic is considered, the maximum and minimum value of the fluctuating component is equal to the amplitude and Eq. (10) becomes:

$$\text{if } \bar{\chi}_M \leq \frac{L}{2} \quad \text{then} \quad |\tilde{\chi}_M| \leq \bar{\chi}_M \quad (11.1)$$

$$\text{if } \bar{\chi}_M \geq \frac{L}{2} \quad \text{then} \quad |\tilde{\chi}_M| \leq L - \bar{\chi}_M \quad (11.2)$$

With reference to the fundamental harmonic, all the possible thermodynamic configurations (from A to H) which can be realised in the layer, with  $\bar{\vartheta}_1 > T_M > \bar{\vartheta}_2$ , are reported in Figure 2:

- A) The condition of equality in Eq. (11.1) or Eq. (11.2) ensures that a part of the layer, of a thickness equal to  $(L - 2|\tilde{\chi}_M|)$ , is not subjected to phase change. Such a layer is adjacent to face 2 and is in a solid phase if  $\bar{\chi}_M < L/2$ , while it is adjacent to face 1 and is in a liquid phase in other configurations. The figure relative to case A regards the condition  $\bar{\chi}_M < L/2$ .
- B) In the particular case in which  $\bar{\chi}_M = |\tilde{\chi}_M| = L/2$  the entire layer is subjected to phase change and cyclically passes from solid phase to liquid phase and vice versa.
- C) In the case that in Eq. (11.1) or in Eq. (11.2) a condition of inequality occurs, the part of the layer involved in the phase change lies within the layer, and gives origin to a layer with a thickness equal to  $(\bar{\chi}_M - |\tilde{\chi}_M|)$  that is always in a liquid phase adjacent to face 1, and another with a thickness equal to  $(L - \bar{\chi}_M - |\tilde{\chi}_M|)$  which is always in a

solid state adjacent to face 2. The figure relative to case C, regards the condition  $\bar{\chi}_M < L/2$ .

- D) If Eq. (11.1) is not satisfied, or rather  $|\tilde{\chi}_M| > \bar{\chi}_M$ , and  $|\tilde{\chi}_M| < L - \bar{\chi}_M$ , with  $\bar{\chi}_M < L/2$ , the layer is partially subjected to a phase change with the formation of a layer with a thickness equal to  $(L - \bar{\chi}_M - |\tilde{\chi}_M|)$  which is always in a solid phase adjacent to face 2. After changing from a liquid phase to a solid phase the entire layer is subjected to subcooling.
- E) Similarly, if Eq. (11.2) is not satisfied, or rather  $|\tilde{\chi}_M| > L - \bar{\chi}_M$ , and  $|\tilde{\chi}_M| < \bar{\chi}_M$ , with  $\bar{\chi}_M > L/2$ , a layer with a thickness equal to  $(\bar{\chi}_M - |\tilde{\chi}_M|)$  is formed, that is always in the liquid phase adjacent to face 1 and after the solid-liquid phase change the entire layer overheats.
- F) If Eq. (11.1) is not satisfied and  $|\tilde{\chi}_M| = L - \bar{\chi}_M$ , with  $\bar{\chi}_M < L/2$ , the whole layer is subject to phase change. After the change from liquid to solid phase, the entire layer is subjected to subcooling.
- G) Similarly, if Eq. (11.2) is not satisfied and  $|\tilde{\chi}_M| = \bar{\chi}_M$ , with  $\bar{\chi}_M > L/2$ , the entire layer undergoes a phase change and, after the solid-liquid phase change, the entire layer overheats.
- H) If Eq. (11.1) or Eq. (11.2) are not satisfied and, respectively,  $|\tilde{\chi}_M| > L - \bar{\chi}_M$  or  $|\tilde{\chi}_M| > \bar{\chi}_M$ , the entire layer changes phase. After the solid-liquid phase change, the entire layer overheats and in the successive change from liquid to solid, the whole layer is subjected to subcooling. The figure relative to case H regards the condition  $\bar{\chi}_M < L/2$ .

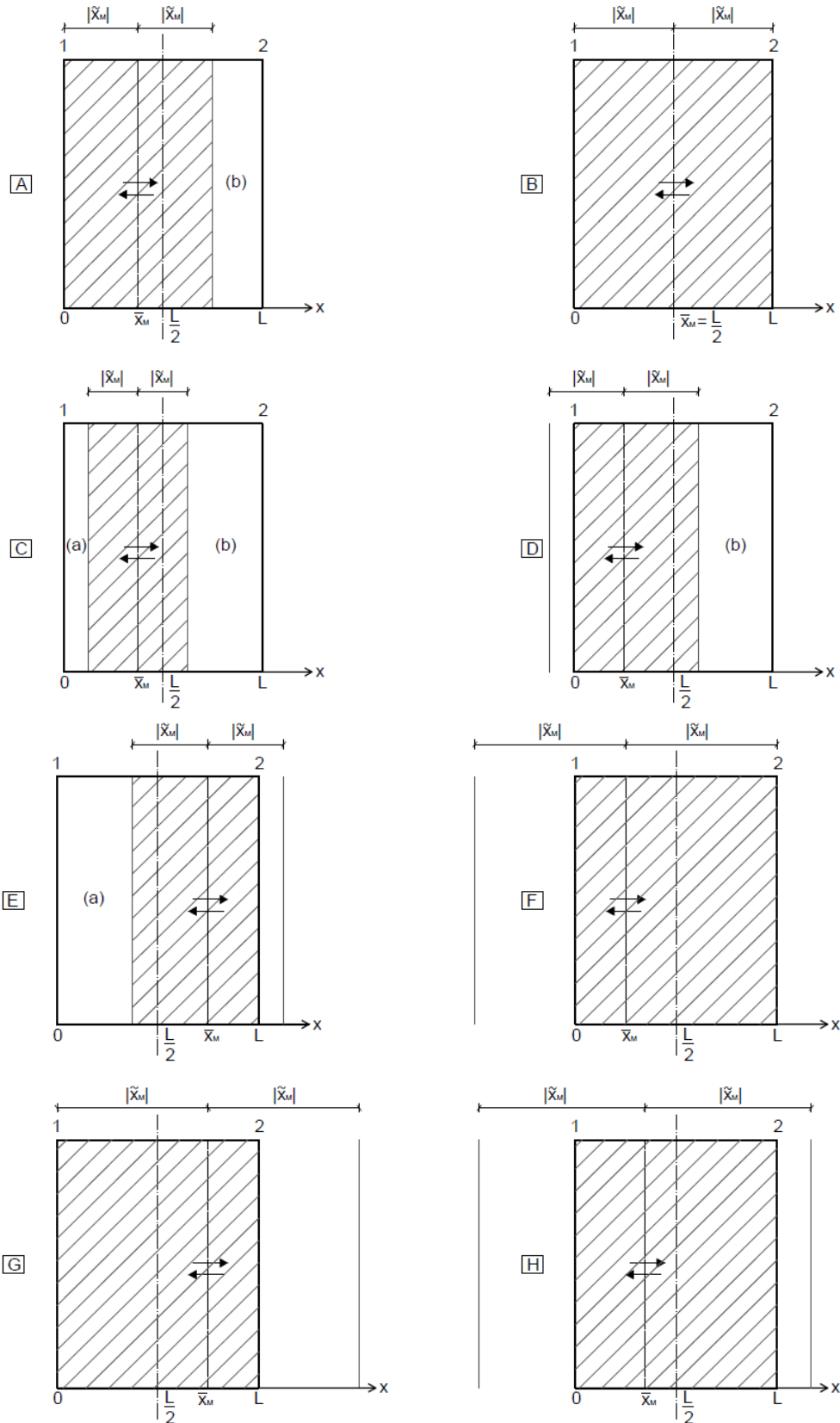


Figure 2 - Configuration of the thermodynamic state of the layer varying the steady position  $\bar{\chi}_M$  and the amplitude of the bi-phase interface oscillation  $|\tilde{\chi}_M|$ .

As a general comment, the condition  $T_2(t) < T_M < T_1(t)$  or  $T_1(t) < T_M < T_2(t)$  guarantees that the position of the bi-phase interface  $X_M(t)$  falls, at each instant, in the physical domain. Such a condition is respected only when the boundary conditions and the thermophysical properties of the layer are such as to give rise to configuration C from those reported in Figure 2. In such a configuration, the system operates a damping effect in that the thermal oscillations that propagate in a phase reach the bi-phase interface. The thermal oscillations are entirely converted in stored latent energy and do not remerge in the other phase. In the other cases, in correspondence with the bi-phase interface, the two heat fluxes originating from the liquid phase and from the solid phase penetrate in the other phase thus reducing the damping effect of the layer. In such conditions, given the steady component and the amplitude of the oscillating component of the bi-phase interface, identification of the geometrical configuration allows for the tracing of the temperature field in the layer. Moreover, identification consents the establishing of the portions of the layer on which the thermal field depends, as well as the periodic condition acting on one face, also on the thermal oscillation reemerging from the bi-phase interface.

## 2.2. Steady thermal field

The equation to be considered in the material is that of monodimensional steady conduction with a bi-phase interface at melting temperature  $T_M$  of abscissa  $\bar{\chi}_M$ , which is not dependent on time, and with boundary conditions (see Figure 3):

$$\bar{\vartheta}_a(0) = \bar{\vartheta}_1 \tag{12}$$

$$\bar{\vartheta}_b(L) = \bar{\vartheta}_2$$

Stefan conditions (3) and (4) in steady conditions become:

$$\left[ \lambda_a \frac{d\bar{\vartheta}_a}{dx} - \lambda_b \frac{d\bar{\vartheta}_b}{dx} \right]_{x=\bar{\chi}_M} = 0 \tag{13}$$

$$\bar{\vartheta}_a(\bar{\chi}_M) = \bar{\vartheta}_b(\bar{\chi}_M) = T_M \tag{14}$$



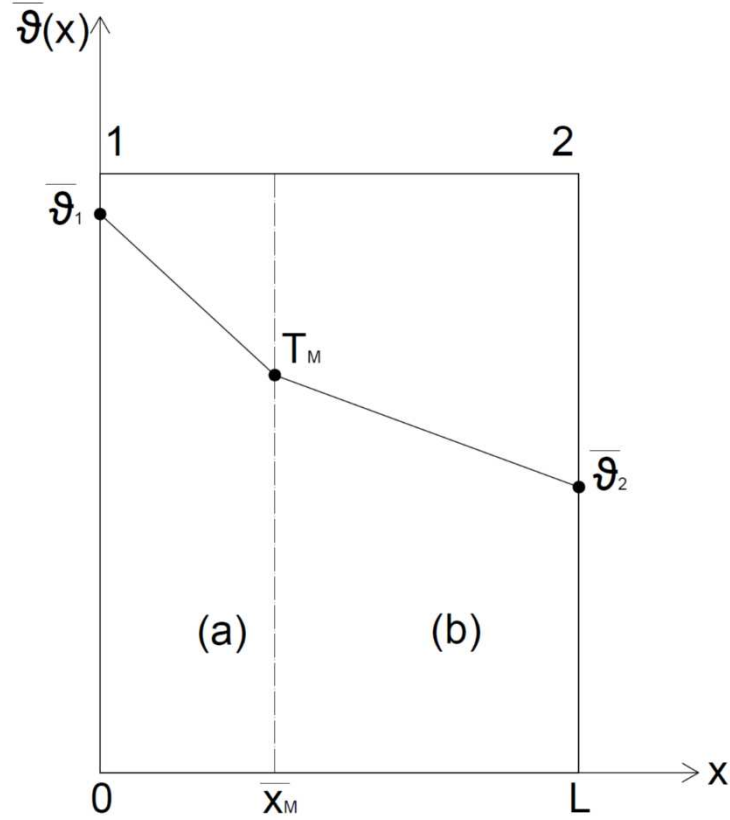


Figure 3 - Steady temperature field in a bi-phase layer  $\bar{\vartheta}(x)$ . (a) liquid phase, (b) solid phase,  $T_M$  melting temperature,  $\bar{x}_M$  steady component of the position of the bi-phase interface and steady boundary conditions  $\bar{\vartheta}_1$  and  $\bar{\vartheta}_2$ .

The steady component of  $X_M(t)$  has the expression:

$$\bar{x}_M = \frac{\lambda_a(\bar{\vartheta}_1 - T_M)}{\lambda_a(\bar{\vartheta}_1 - T_M) + \lambda_b(T_M - \bar{\vartheta}_2)} L \quad (15)$$

In order that  $\bar{x}_M$  falls in physical domain, the melting temperature  $T_M$  must be between  $\bar{\vartheta}_1$  and  $\bar{\vartheta}_2$ .

Steady heat flux  $\bar{\Phi}$  is the heat flux in the multilayer wall in part in the solid phase and in part in the liquid phase produced by the temperature difference  $(\bar{\vartheta}_1 - \bar{\vartheta}_2)$ .

$$\bar{\Phi} = \frac{\bar{\vartheta}_1 - \bar{\vartheta}_2}{\frac{\bar{x}_M}{\lambda_a} + \frac{L - \bar{x}_M}{\lambda_b}} \quad (16)$$

Such a heat flux is used for the calculation of the temperature linear profile through the relations:

$$0 \leq x \leq \bar{\chi}_M$$

$$\bar{\vartheta}_a(x) = T_M + \frac{\bar{\chi}_M - x}{\lambda_a} \bar{\phi} \quad (17a)$$

$$\bar{\chi}_M \leq x \leq L$$

$$\bar{\vartheta}_b(x) = T_M - \frac{x - \bar{\chi}_M}{\lambda_b} \bar{\phi} \quad (17b)$$

### 2.3. Steady periodic thermal field

The coordinate reference system of the oscillating component, with origins in correspondence with the steady position of the bi-phase interface, is defined in Figure 4.

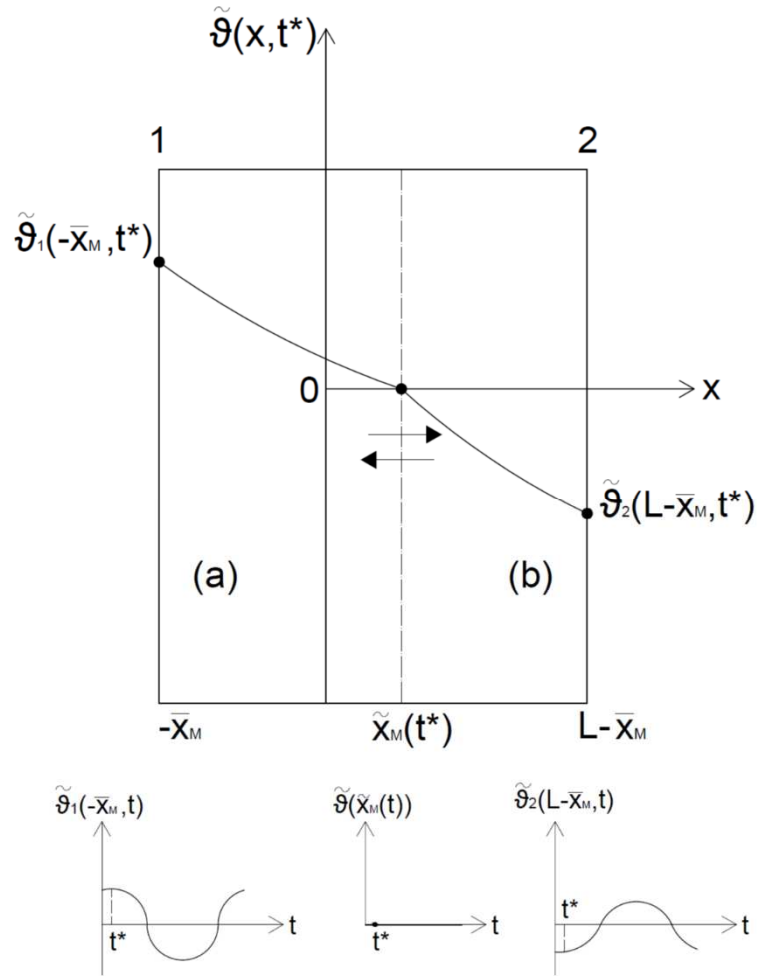


Figure 4 - Coordinate reference system for the oscillating component  $\tilde{\chi}_M$  of the position of the bi-phase interface, boundary conditions  $\tilde{\vartheta}_1$  and  $\tilde{\vartheta}_2$  and oscillating temperature field  $\tilde{\vartheta}(x, t)$  at the instant  $t=t^*$ .

Since the reference coordinate system used for the calculation of the periodic thermal field is shifted compared to the coordinate reference system used for the steady thermal field, the temperature and heat flux in a point of the layer is calculated with the relation:

$$T(x, t) = \bar{\vartheta}(x) + \tilde{\vartheta}(x - \bar{\chi}_M, t) \quad (18)$$

$$F(x, t) = \bar{\Phi} + \tilde{\Phi}(x - \bar{\chi}_M, t)$$

with  $x$  abscissa referred to the reference coordinate system of the steady thermal field.

The equation to be considered for a generic harmonic is:

$$\frac{\partial^2 \tilde{\vartheta}}{\partial x^2} - \frac{1}{\alpha} \frac{\partial \tilde{\vartheta}}{\partial t} = 0 \quad (19)$$

With boundary conditions:

$$\begin{aligned} \tilde{\vartheta}_a(-\bar{\chi}_M, t) &= \tilde{\vartheta}_1 \\ \tilde{\vartheta}_b(L - \bar{\chi}_M, t) &= \tilde{\vartheta}_2 \end{aligned} \quad (20)$$

The conditions to be satisfied at abscissa  $x = \tilde{\chi}_M$ , at the bi-phase interface are:

$$\left[ \lambda_a \frac{\partial \tilde{\vartheta}_a}{\partial x} - \lambda_b \frac{\partial \tilde{\vartheta}_b}{\partial x} \right]_{x=\tilde{\chi}_M} = \rho H \frac{d\tilde{\chi}_M}{dt} \quad (21)$$

$$\tilde{\vartheta}_a(\tilde{\chi}_M, t) = \tilde{\vartheta}_b(\tilde{\chi}_M, t) = 0 \quad (22)$$

Since the oscillating variables  $\tilde{\vartheta}(x, t)$ ,  $\tilde{\Phi}(x, t)$  and  $\tilde{\chi}_M(t)$  for a determined harmonic all have the same temporal dependence, it is possible to transform them into new variables in which time does not appear in an explicit manner. Such a procedure is known in the field of electrical engineering as the phasors method [19]; it is widely used through the complex temperature method in the study of thermal fields [4, 6].

The method represents each generic harmonic  $\tilde{\vartheta}_k$ , of angular frequency  $k\omega$ , as the imaginary part of the phasor written in the complex form:

$$\hat{\vartheta}_k = |\hat{\vartheta}_k| [\cos(k\omega t + \varphi_k) + j \sin(k\omega t + \varphi_k)] = |\hat{\vartheta}_k| \exp(j\varphi_k) \exp(jk\omega t) \quad (23)$$

with  $|\hat{\vartheta}_k| = |\tilde{\vartheta}_k|$  and  $\arg(\hat{\vartheta}_k) = \arg(\tilde{\vartheta}_k) = \varphi_k$ . Generally, the operator  $\exp(jk\omega t)$  in the resolution of a steady periodic problem is omitted in that it is multiplicative of all the phasors. Furthermore, the sinusoidal component is reduced to a complex number. Therefore, the use of phasors allows for the resolution of the problem in the domain of space separating it from the time domain.

The resolution of the thermal field in the complex domain gives unknown components  $\hat{\vartheta}_k(x)$ ,  $\hat{\varphi}_k(x)$  and  $\hat{\chi}_{Mk}$ , which are successively reported in the time domain by multiplying the operator  $\exp(jk\omega t)$ . Only the imaginary part of the product is considered.

The solution of the oscillating thermal field in a PCM layer, with reference to generic harmonic angular frequency  $\omega$  is reported hereafter. Taking Eq. (23) into consideration, Eq. (19) becomes:

$$\frac{d^2 \hat{\vartheta}}{dx^2} - \frac{j\omega}{\alpha} \hat{\vartheta} = 0 \quad (24)$$

Applying the phasor method, Eqs. (20) - (22) become:

$$\hat{\vartheta}_a(-\bar{\chi}_M) = \hat{\vartheta}_1 \quad (25)$$

$$\hat{\vartheta}_b(L - \bar{\chi}_M) = \hat{\vartheta}_2$$

$$\left[ \lambda_a \frac{d\hat{\vartheta}_a}{dx} - \lambda_b \frac{d\hat{\vartheta}_b}{dx} \right]_{x=\hat{\chi}_M} = j\omega \rho H \hat{\chi}_M \quad (26)$$

$$\hat{\vartheta}_a(\hat{\chi}_M) = \hat{\vartheta}_b(\hat{\chi}_M) = 0 \quad (27)$$

Eqs. (24) and (26) are ordinary differential equations in which the temperature phasor appears as a function only of the space.

The solution to differential equation (23) is given by the relation:

$$\hat{\vartheta}(x) = \vartheta_p \exp(-\gamma x) + \vartheta_r \exp(\gamma x) \quad (28)$$

and is the sum of two temperature oscillations: the first attenuates when  $x$  increases, the second attenuates when  $x$  diminishes.  $\vartheta_p$  and  $\vartheta_r$  are constants of integration and  $\gamma = (1+j)(\omega/2\alpha)^{1/2}$  is the propagation constant of such waves.

The phasor associated to the oscillating component of the heat flux  $\tilde{\phi}$  at abscissa  $x$  is:

$$\hat{\phi}(x) = -\lambda \frac{d\hat{\vartheta}}{dx} \quad (29)$$

which, taking Eq. (28) into consideration, becomes:

$$\hat{\phi}(x) = \lambda \gamma \vartheta_p \exp(-\gamma x) - \lambda \gamma \vartheta_r \exp(\gamma x) \quad (30)$$

Eqs. (28) and (30) calculated on face 1 of the abscissa  $x = -\bar{\chi}_M$  and on face 2 of abscissa  $x = L - \bar{\chi}_M$  become:

$$\hat{\vartheta}_1 = \vartheta_{p_a} \exp(\gamma_a \bar{\chi}_M) + \vartheta_{r_a} \exp(-\gamma_a \bar{\chi}_M) \quad (31)$$

$$\hat{\phi}_1 = \lambda_a \gamma_a \vartheta_{p_a} \exp(\gamma_a \bar{\chi}_M) - \lambda_a \gamma_a \vartheta_{r_a} \exp(-\gamma_a \bar{\chi}_M) \quad (32)$$

$$\hat{\vartheta}_2 = \vartheta_{p_b} \exp[-\gamma_b (L - \bar{\chi}_M)] + \vartheta_{r_b} \exp[\gamma_b (L - \bar{\chi}_M)] \quad (33)$$

$$\hat{\phi}_2 = \lambda_b \gamma_b \vartheta_{p_b} \exp[-\gamma_b (L - \bar{\chi}_M)] - \lambda_b \gamma_b \vartheta_{r_b} \exp[\gamma_b (L - \bar{\chi}_M)] \quad (34)$$

At abscissa  $x = \hat{\chi}_M$ , the annullment of the temperature oscillating component is expressed by relations:

$$\vartheta_{p_a} \exp(-\gamma_a \hat{\chi}_M) + \vartheta_{r_a} \exp(\gamma_a \hat{\chi}_M) = \vartheta_{p_b} \exp(-\gamma_b \hat{\chi}_M) + \vartheta_{r_b} \exp(\gamma_b \hat{\chi}_M) = 0 \quad (35)$$

Finally, Eq. (26) of bi-phase interface balance assumes the form:

$$\left[ \lambda_a \gamma_a \vartheta_{p_a} \exp(-\gamma_a \hat{\chi}_M) - \lambda_a \gamma_a \vartheta_{r_a} \exp(\gamma_a \hat{\chi}_M) \right] - \left[ \lambda_b \gamma_b \vartheta_{p_b} \exp(-\gamma_b \hat{\chi}_M) - \lambda_b \gamma_b \vartheta_{r_b} \exp(\gamma_b \hat{\chi}_M) \right] = j\omega\rho H \hat{\chi}_M \quad (36)$$

The system of Eqs. (31) - (36) permits the resolution of the thermal field in the PCM layer. The expressions of the constants of integration  $\vartheta_{p_a}$  and  $\vartheta_{r_a}$  obtained from Eqs. (31) and (32), and of the constants  $\vartheta_{p_b}$  and  $\vartheta_{r_b}$  obtained from Eqs. (33) and (34) are:

$$(37) \quad \vartheta_{p_a} = \frac{\lambda_a \gamma_a \hat{\vartheta}_1 + \hat{\Phi}_1}{2\lambda_a \gamma_a \exp(\gamma_a \bar{\chi}_M)} \quad \vartheta_{r_a} = \frac{\lambda_a \gamma_a \hat{\vartheta}_1 - \hat{\Phi}_1}{2\lambda_a \gamma_a \exp(-\gamma_a \bar{\chi}_M)}$$

$$\vartheta_{p_b} = \frac{\lambda_b \gamma_b \hat{\vartheta}_2 + \hat{\Phi}_2}{2\lambda_b \gamma_b \exp[-\gamma_b (L - \bar{\chi}_M)]} \quad \vartheta_{r_b} = \frac{\lambda_b \gamma_b \hat{\vartheta}_2 - \hat{\Phi}_2}{2\lambda_b \gamma_b \exp[\gamma_b (L - \bar{\chi}_M)]}$$

Substituting the constants of integration respectively in Eq. (28) and in Eq. (30), expressions of the temperature and of the oscillating heat flux in layer (a) and in layer (b) at each time are:

layer a ( $-\bar{\chi}_M \leq x \leq -|\hat{\chi}_M|$ ):

$$\hat{\vartheta}_a(x) = \hat{\vartheta}_1 \cosh[\gamma_a (x + \bar{\chi}_M)] - \frac{\hat{\Phi}_1}{\lambda_a \gamma_a} \sinh[\gamma_a (x + \bar{\chi}_M)] \quad (38)$$

$$\hat{\Phi}_a(x) = -\lambda_a \gamma_a \hat{\vartheta}_1 \sinh[\gamma_a (x + \bar{\chi}_M)] + \hat{\Phi}_1 \cosh[\gamma_a (x + \bar{\chi}_M)] \quad (39)$$

layer b ( $|\hat{\chi}_M| \leq x \leq L - \bar{\chi}_M$ ):

$$\hat{\vartheta}_b(x) = \hat{\vartheta}_2 \cosh[\gamma_b (L - x - \bar{\chi}_M)] + \frac{\hat{\Phi}_2}{\lambda_b \gamma_b} \sinh[\gamma_b (L - x - \bar{\chi}_M)] \quad (40)$$

$$\hat{\Phi}_b(x) = \lambda_b \gamma_b \hat{\vartheta}_2 \sinh[\gamma_b (L - x - \bar{\chi}_M)] + \hat{\Phi}_2 \cosh[\gamma_b (L - x - \bar{\chi}_M)] \quad (41)$$

For layer (a) Eqs. (38) and (39) provide the temperature and heat flux, as a function of the temperature and heat flux at abscissa  $x = -\bar{\chi}_M$ , and of the thermophysical properties of layer (a).

For layer (b) the boundary conditions are those concerning the abscissa  $x = L - \bar{\chi}_M$ .

Through the substitution of constants  $\vartheta_{p_a}$ ,  $\vartheta_{r_a}$  and  $\vartheta_{p_b}$ ,  $\vartheta_{r_b}$  in Eq. (35), the expressions of heat flux on face 1 and face 2, as a function of the position of the bi-phase interface and relative boundary condition, are obtained and are as follows:

$$\hat{\Phi}_1 = \frac{\lambda_a \gamma_a}{\tanh[\gamma_a (\hat{\chi}_M + \bar{\chi}_M)]} \hat{\vartheta}_1 \quad (42)$$

$$\hat{\Phi}_2 = -\frac{\lambda_b \gamma_b}{\tanh[\gamma_b(L - \hat{\chi}_M - \bar{\chi}_M)]} \hat{\vartheta}_2 \quad (43)$$

Eqs. (38)-(41) of the temperature and heat flux in layer (a) and in layer (b) can be rewritten in relation to the boundary temperature and the position of the bi-phase interface if Eqs. (42) and (43) are taken into consideration. The relations obtained are:

layer a ( $-\bar{\chi}_M \leq x \leq -|\hat{\chi}_M|$ ):

$$\hat{\vartheta}_a(x) = \hat{\vartheta}_1 \left\{ \cosh[\gamma_a(x + \bar{\chi}_M)] - \frac{\sinh[\gamma_a(x + \bar{\chi}_M)]}{\tanh[\gamma_a(\bar{\chi}_M + \hat{\chi}_M)]} \right\} \quad (44)$$

$$\hat{\Phi}_a(x) = -\lambda_a \gamma_a \hat{\vartheta}_1 \left\{ \sinh[\gamma_a(x + \bar{\chi}_M)] - \frac{\cosh[\gamma_a(x + \bar{\chi}_M)]}{\tanh[\gamma_a(\bar{\chi}_M + \hat{\chi}_M)]} \right\} \quad (45)$$

layer b ( $|\hat{\chi}_M| \leq x \leq L - \bar{\chi}_M$ ):

$$\hat{\vartheta}_b(x) = \hat{\vartheta}_2 \left\{ \cosh[\gamma_b(L - \bar{\chi}_M - x)] - \frac{\sinh[\gamma_b(L - \bar{\chi}_M - x)]}{\tanh[\gamma_b(L - \bar{\chi}_M - \hat{\chi}_M)]} \right\} \quad (46)$$

$$\hat{\Phi}_b(x) = \lambda_b \gamma_b \hat{\vartheta}_2 \left\{ \sinh[\gamma_b(L - \bar{\chi}_M - x)] - \frac{\cosh[\gamma_b(L - \bar{\chi}_M - x)]}{\tanh[\gamma_b(L - \bar{\chi}_M - \hat{\chi}_M)]} \right\} \quad (47)$$

In the portion of material, included between the abscissae  $-|\hat{\chi}_M| \leq x/L \leq |\hat{\chi}_M|$ , in which both the thermal oscillations that act on the boundary penetrate, the two trends of temperature and heat flux are intersected through a linear combination, weighted with respect to the distance from the boundary faces:

( $-|\hat{\chi}_M| \leq x \leq |\hat{\chi}_M|$ ):

$$\tilde{\vartheta}(x) = \frac{(L - x) \tilde{\vartheta}_a(x) + x \tilde{\vartheta}_b(x)}{L} \quad (48)$$

$$\tilde{\Phi}(x) = \frac{(L - x) \tilde{\Phi}_a(x) + x \tilde{\Phi}_b(x)}{L} \quad (49)$$

Finally, the equation to determine oscillating component  $\hat{\chi}_M$  is obtained by substituting the expressions of the constants of integration in balance Eq. (36):

$$\frac{\lambda_a \gamma_a}{\sinh[\gamma_a(\bar{\chi}_M + \hat{\chi}_M)]} \hat{\theta}_1 + \frac{\lambda_b \gamma_b}{\sinh[\gamma_b(L - \bar{\chi}_M - \hat{\chi}_M)]} \hat{\theta}_2 = j\omega\rho H \hat{\chi}_M \quad (50)$$

Equations (44-47) and Eq. (49), taking Eqs. (42) and (43) into account, can be formulated considering the heat flux as loadings on face 1 and on face 2, or mixed boundary conditions on the two faces.

Equation (50) is a transcendental equation with complex parameters and a complex variable. In order to carry the solution  $\hat{\chi}_M$  in the time domain, it is necessary to multiply the phasors by  $\exp(j\omega t)$  and consider the imaginary part.

$$\tilde{\chi}_M = \text{Im}[\hat{\chi}_M \exp(j\omega t)] = \text{Im}[|\hat{\chi}_M| \exp(j\zeta) \exp(j\omega t)] = |\hat{\chi}_M| \sin(\omega t + \zeta) \quad (51)$$

The amplitude of  $\hat{\chi}_M$  represents the maximum variation of the abscissa where the phase change occurs compared to the steady component  $\bar{\chi}_M$ . Argument  $\zeta$  determines the position of the bi-phase interface at the initial instant.

The velocity of the bi-phase interface  $\tilde{v}_M$ , with reference to a harmonic, is obtained deriving the  $\tilde{\chi}_M$ :

$$\tilde{v}_M = \frac{d\tilde{\chi}_M}{dt} = \text{Im}[j\omega \hat{\chi}_M \exp(j\omega t)] = \omega |\hat{\chi}_M| \cos(\omega t + \zeta) \quad (52)$$

with a steady component equal to zero. The latent heat stored or released per unit time can be calculated, with reference to Eq. (26), with the expression:

$$\tilde{\Phi}_H = \rho H \tilde{v}_M \quad (53)$$

Equations (44)-(47), that describe the oscillating temperature and heat flux fields, and the balance Eq. (50) can be rendered dimensionless by introducing abscissa  $x/L$ , the Fourier number and the Stefan number calculated in layer (a) and in layer (b). The latter is evaluated considering temperature oscillations on face 1 and face 2:

$$Fo_a = \frac{\alpha_a P}{L^2} ; Fo_b = \frac{\alpha_b P}{L^2} ; \widehat{Ste}_{a1} = \frac{c_a \hat{\theta}_1}{H} ; \widehat{Ste}_{b2} = \frac{c_b \hat{\theta}_2}{H} \quad (54)$$



with  $P=2\pi/\omega$  oscillation period. The Stefan number amplitude represents the ratio between the sensible heat corresponding to temperature variation  $|\hat{\theta}|$  in the solid or liquid phase (J/kg) and the latent heat in the phase change at the interface.

Eqs. (44)-(47) become:

layer a  $\left(-\frac{\bar{\chi}_M}{L} \leq \frac{x}{L} \leq -\frac{|\hat{\chi}_M|}{L}\right)$ :

$$\frac{\hat{\theta}_a(x)}{\hat{\theta}_1} = \cosh \left[ (1+j) \sqrt{\frac{\pi}{Fo_a}} \left( \frac{x}{L} + \frac{\bar{\chi}_M}{L} \right) \right] - \frac{\sinh \left[ (1+j) \sqrt{\frac{\pi}{Fo_a}} \left( \frac{x}{L} + \frac{\bar{\chi}_M}{L} \right) \right]}{\tanh \left[ (1+j) \sqrt{\frac{\pi}{Fo_a}} \left( \frac{\hat{\chi}_M}{L} + \frac{\bar{\chi}_M}{L} \right) \right]} \quad (55)$$

$$\frac{\hat{\Phi}_a(x)}{(1+j) \sqrt{\frac{\pi}{Fo_a}} \frac{\lambda_a}{L} \hat{\theta}_1} = -\sinh \left[ (1+j) \sqrt{\frac{\pi}{Fo_a}} \left( \frac{x}{L} + \frac{\bar{\chi}_M}{L} \right) \right] + \frac{\cosh \left[ (1+j) \sqrt{\frac{\pi}{Fo_a}} \left( \frac{x}{L} + \frac{\bar{\chi}_M}{L} \right) \right]}{\tanh \left[ (1+j) \sqrt{\frac{\pi}{Fo_a}} \left( \frac{\hat{\chi}_M}{L} + \frac{\bar{\chi}_M}{L} \right) \right]} \quad (56)$$

layer b  $\left(\frac{|\hat{\chi}_M|}{L} \leq \frac{x}{L} \leq 1 - \frac{\bar{\chi}_M}{L}\right)$ :

$$\frac{\hat{\theta}_b(x)}{\hat{\theta}_2} = \cosh \left[ (1+j) \sqrt{\frac{\pi}{Fo_b}} \left( 1 - \frac{\bar{\chi}_M}{L} - \frac{x}{L} \right) \right] - \frac{\sinh \left[ (1+j) \sqrt{\frac{\pi}{Fo_b}} \left( 1 - \frac{\bar{\chi}_M}{L} - \frac{x}{L} \right) \right]}{\tanh \left[ (1+j) \sqrt{\frac{\pi}{Fo_b}} \left( 1 - \frac{\bar{\chi}_M}{L} - \frac{\hat{\chi}_M}{L} \right) \right]} \quad (57)$$

$$\frac{\hat{\Phi}_b(x)}{(1+j) \sqrt{\frac{\pi}{Fo_b}} \frac{\lambda_b}{L} \hat{\theta}_2} = \sinh \left[ (1+j) \sqrt{\frac{\pi}{Fo_b}} \left( 1 - \frac{\bar{\chi}_M}{L} - \frac{x}{L} \right) \right] - \frac{\cosh \left[ (1+j) \sqrt{\frac{\pi}{Fo_b}} \left( 1 - \frac{\bar{\chi}_M}{L} - \frac{x}{L} \right) \right]}{\tanh \left[ (1+j) \sqrt{\frac{\pi}{Fo_b}} \left( 1 - \frac{\bar{\chi}_M}{L} - \frac{\hat{\chi}_M}{L} \right) \right]} \quad (58)$$

Moreover, Eqs. (55)-(58) describe the thermal field in an abscissa  $\hat{x}/L = (|\hat{x}|/L) \exp(j\varsigma)$  that is in motion with amplitude  $|\hat{x}|/L$  and argument  $\varsigma$ .

Balance Eq. (50) becomes:

$$\frac{1+j}{2\sqrt{\pi}} \left\{ \frac{\sqrt{Fo_a}}{\sinh \left[ (1+j) \sqrt{\frac{\pi}{Fo_a}} \left( \frac{\bar{\chi}_M}{L} + \frac{\hat{\chi}_M}{L} \right) \right]} \widehat{Ste}_{a1} + \frac{\sqrt{Fo_b}}{\sinh \left[ (1+j) \sqrt{\frac{\pi}{Fo_b}} \left( 1 - \frac{\bar{\chi}_M}{L} - \frac{\hat{\chi}_M}{L} \right) \right]} \widehat{Ste}_{b2} \right\} = j \frac{\hat{\chi}_M}{L} \quad (59)$$

Eqs. (55)-(59) have a transcendental structure that is very similar to the Neumann solution of the ‘two-phase’ Stefan Problem obtained in a semi-infinite layer with the face maintained at a constant temperature. The same dimensionless parameters are present in the equations. The two solutions differ because the error function and exponential function appear in the Neumann solution, as well as the real Stefan number linked to the step boundary condition. Instead, in the case under examination, hyperbolic functions and the phasor of the Stefan number that represent the sinusoidal boundary conditions appear.

The resolution of Eq. (59) provides abscissa  $\hat{\chi}_M/L$ , and therefore the amplitude and argument of the bi-phase interface. Eqs. (55)-(58) provide the temperature field and heat flux field in layer (a) and in layer (b). The solution of Eq. (59) cannot be obtained in a symbolic explicit form since the unknown variable  $\hat{\chi}_M/L$  appears in transcendental functions. A solution that satisfies Eq. (59) can be found, by using numerical algorithms, once the complex and real parameter values have been set. The Neumann solution presents a similar problem and the solution is obtained through analytical approximation or numerical algorithms, such as the Newton algorithm.

The solution is also valid when either the temperature or the heat flux on one of the boundary faces is constant and equal to the steady component. Consequently, it is possible to study the behaviour of the layer with oscillating heat flux or oscillating temperature on a face and a constant temperature or heat flux on the other face.

In the particular case in which the PCM layer is subjected to a sinusoidal temperature that oscillates around a mean steady temperature on the face of abscissa  $x = 0$  and at a constant temperature on face of abscissa  $x = L$  the calculation procedure of the steady thermal field to be considered is identical to that shown in Paragraph 2.2. Annulling the oscillating component of the temperature on the face of abscissa  $x = L$  in Eq. (59), the equation to determine oscillating component  $\hat{\chi}_M$  becomes:

$$\frac{1 + j}{2\sqrt{\pi}} \frac{\sqrt{Fo_a}}{\sinh \left[ (1 + j) \sqrt{\frac{\pi}{Fo_a}} \left( \frac{\bar{\chi}_M}{L} + \frac{\hat{\chi}_M}{L} \right) \right]} \widehat{Ste}_{a1} = j \frac{\hat{\chi}_M}{L} \quad (60)$$

The oscillating component of the temperature and of the heat flux in layer (a) are described again by Eqs. (55) and (56) and in layer (b) is equal to zero.

### 3. Application of the model

The solution obtained was used for the general analysis of the configurations that can be made in the PCM layer upon variation of the thermophysical properties and the boundary conditions acting on the two faces of the layer, represented by a temperature oscillation. Furthermore, an application is shown in the particular case in which a PCM layer is subjected to an oscillating temperature on one face and a constant temperature on the other face.

The analytical procedure was also applied to a layer comprising of a Glauber's salt, with boundary temperature conditions expressed through a Fourier series expansion. In such an application the temperature field, the heat flux field and the thermal energy stored per unit time were determined.

#### 3.1. General analysis of the basic cases considered

The solution obtained was used to address a general theoretical analysis to study the temperature field and heat fluxes entering and exiting a PCM layer upon varying the configurations identified in Figure 2 with letters A-H, in the case of two boundary conditions represented by a single sinusoidal oscillation.

Reference is made to a layer with a length of  $L=0.05$  m, a melting temperature equal to  $25$  °C and at a temperature oscillation period  $P=24$  h.

The different configurations were obtained varying the steady component of  $X_M(t)$ , modifying the steady temperature values on the two faces, and the oscillating component of  $X_M(t)$ , through the variation of the Fourier number and the Stefan number in the liquid phase and the solid phase.

Since constant layer thickness has been assumed, in order to vary the Fourier number and the Stefan number in the two phases, it was necessary to modify the thermophysical properties of the PCM and the temperature amplitudes on the two boundary faces.

For each case considered, Table 1 reports the thermophysical properties of the PCM considered, the boundary conditions on the two faces, the values relating to the dimensionless parameter, the steady component  $\bar{\chi}_M$  calculated with Eq. 15 and the oscillating component  $\tilde{\chi}_M$  calculated with Eq. (59) that were used to realise the different configurations.

In Figures 5-8, the images on the left show the oscillating temperature field  $\tilde{\theta}(x,t)$ , the oscillating heat fluxes entering  $\tilde{\phi}_1$  and exiting  $\tilde{\phi}_2$  the layer and the variation of energy per unit

time of the layer, sensible plus latent, obtained as the difference of the preceding heat fluxes. Instead, the images on the right show the temperature field  $T(x, t)$ , the steady heat flux  $\bar{\phi}$  and the heat fluxes entering  $F_1(t)$  and exiting  $F_2(t)$  the wall, sum of the steady and the oscillating components.

The determination of the temperature field in the layer requires the calculation of the steady component  $\bar{\chi}_M$  of the position of the biphasic interface through Eq. (15), of the steady temperature field  $\bar{\vartheta}(x)$  by means of Eqs. (17a) and (17b) and of the phasors associated with the oscillating component of the two boundary conditions  $\tilde{\vartheta}_1$  and  $\tilde{\vartheta}_2$  (Eq. (23)) and with the oscillating component  $\tilde{\chi}_M$  of the position of the bi-phase interface (Eq. (59)).

When the steady component  $\bar{\chi}_M$  and the phasor  $\hat{\chi}_M$  are known, it is possible to identify the range of variation of abscissa  $x$  for the application of Eqs. (44), (46) and (48) that supply the phasor  $\hat{\vartheta}(x)$  associated with the oscillating component of the temperature field. The oscillating heat flux entering  $\hat{\phi}_1$  and exiting  $\hat{\phi}_2$  the layer are calculated by means of Eqs. (42) and (43).

Table 1 - Thermophysical properties of the PCM, boundary conditions on the two faces, dimensionless parameter values, steady component  $\bar{\chi}_M$  and oscillating component  $\tilde{\chi}_M$  values and  $|\tilde{\phi}_1 - \tilde{\phi}_2|/[F_1(t)]_{max}$  in the different configurations identified with letters A-H.

	L m	$\lambda_a$ W/(m <sup>2</sup> K)	$\lambda_b$ W/(m <sup>2</sup> K)	$c_a$ J/(kg K)	$c_b$ J/(kg K)	$\rho$ kg/m <sup>3</sup>	H J/kg	$T_M$ °C	$\bar{\vartheta}_1$ °C	$\bar{\vartheta}_2$ °C	$\tilde{\vartheta}_1$ °C	$\tilde{\vartheta}_2$ °C	Fo <sub>a</sub> -	Fo <sub>b</sub> -	$\widehat{Ste}_{a1}$ -	$\widehat{Ste}_{b2}$ -	$\bar{\chi}_M/L$ -	$\tilde{\chi}_M/L$ -	$\bar{\chi}_M$ m	$\tilde{\chi}_M$ m	$\frac{ \tilde{\phi}_1 - \tilde{\phi}_2 }{[F_1(t)]_{max}}$ -
<b>CONFIGURATION A</b>																					
<b>Amp.</b>	0.05	2.80	2.80	3310	1760	700	254000	25	35	10	6.00	2.50	41.76	78.55	0.078	0.017	0.40	0.40	0.020	0.020	0.130
<b>Arg.</b>											2.62	0.79			2.62	0.79		-0.39		-0.39	
<b>CONFIGURATION B</b>																					
<b>Amp.</b>	0.05	2.80	2.80	3310	1760	700	85770	25	35	15	6.00	2.50	41.76	78.55	0.231	0.051	0.50	0.50	0.025	0.025	0.086
<b>Arg.</b>											0.00	-1.57			0.00	-1.57		-1.07		-1.07	
<b>CONFIGURATION C</b>																					
<b>Ampl.</b>	0.05	0.20	0.20	3310	1760	1464	254000	25	35	10	6.00	2.50	1.43	2.68	0.078	0.017	0.40	0.04	0.0206	0.002	0.353
<b>Arg.</b>											2.62	0.79			2.62	0.79		0.54		0.54	
<b>CONFIGURATION D</b>																					
<b>Amp.</b>	0.05	1.50	1.50	3310	1760	700	85770	25	35	10	6.00	2.50	22.37	42.08	0.231	0.051	0.40	0.48	0.020	0.024	0.126
<b>Arg.</b>											0.00	-1.57			0.00	-1.57		-1.11		-1.11	
<b>CONFIGURATION E</b>																					
<b>Amp.</b>	0.05	1.50	1.50	3310	1760	700	85770	25	40	20	6.00	2.50	22.37	42.08	0.231	0.051	0.75	0.35	0.0375	0.018	0.104
<b>Arg.</b>											0.00	-1.57			0.00	-1.57		4.58		4.58	
<b>CONFIGURATION F</b>																					
<b>Amp.</b>	0.05	10.00	10.00	13240	7040	700	85770	25	35	10	6.00	2.30	37.29	70.13	0.926	0.189	0.40	0.60	0.020	0.030	0.0366
<b>Arg.</b>											0.00	-1.57			0.00	-1.57		-0.69		-0.69	
<b>CONFIGURATION G</b>																					
<b>Amp.</b>	0.05	3.552	3.552	3310	7040	700	85770	25	40	20	2.80	0.15	52.98	24.91	0.108	0.012	0.75	0.75	0.0375	0.0375	0.093
<b>Arg.</b>											0.00	1.57			0.00	1.57		-1.10		-1.10	
<b>CONFIGURATION H</b>																					
<b>Amp.</b>	0.05	10.00	10.00	13240	7040	700	85770	25	35	10	5.00	1.20	37.29	70.13	0.772	0.098	0.40	0.63	0.020	0.031	0.0367
<b>Arg.</b>											0.00	-1.57			0.00	-1.57		-0.43		-0.43	

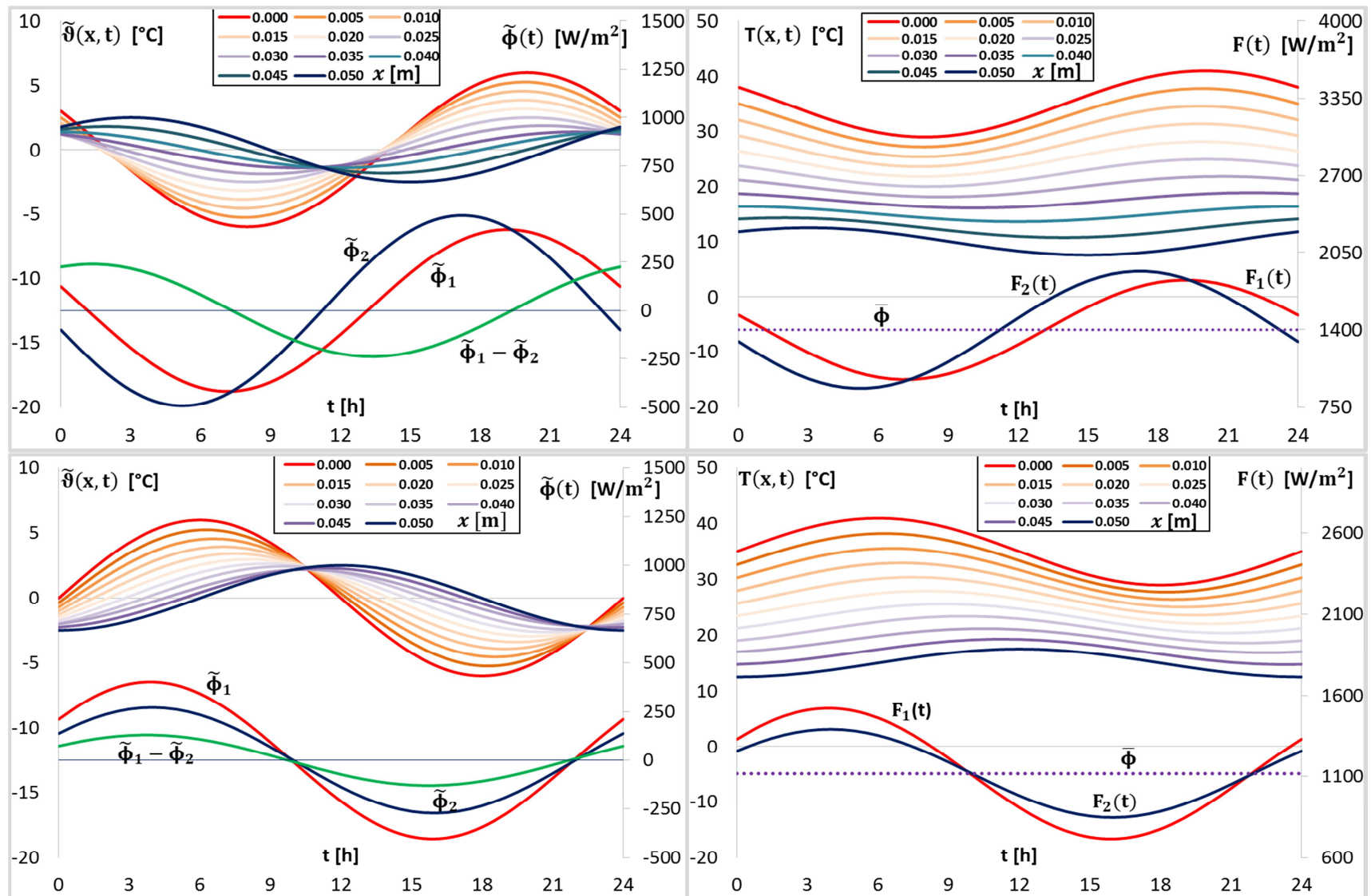


Figure 5 - Configurations A (Top) and B (Bottom). Images on the left: oscillating temperature field, oscillating heat fluxes entering and exiting the layer and variation of energy per unit time of the layer. Images on the right: temperature field, steady heat flux and heat fluxes entering and exiting the wall.

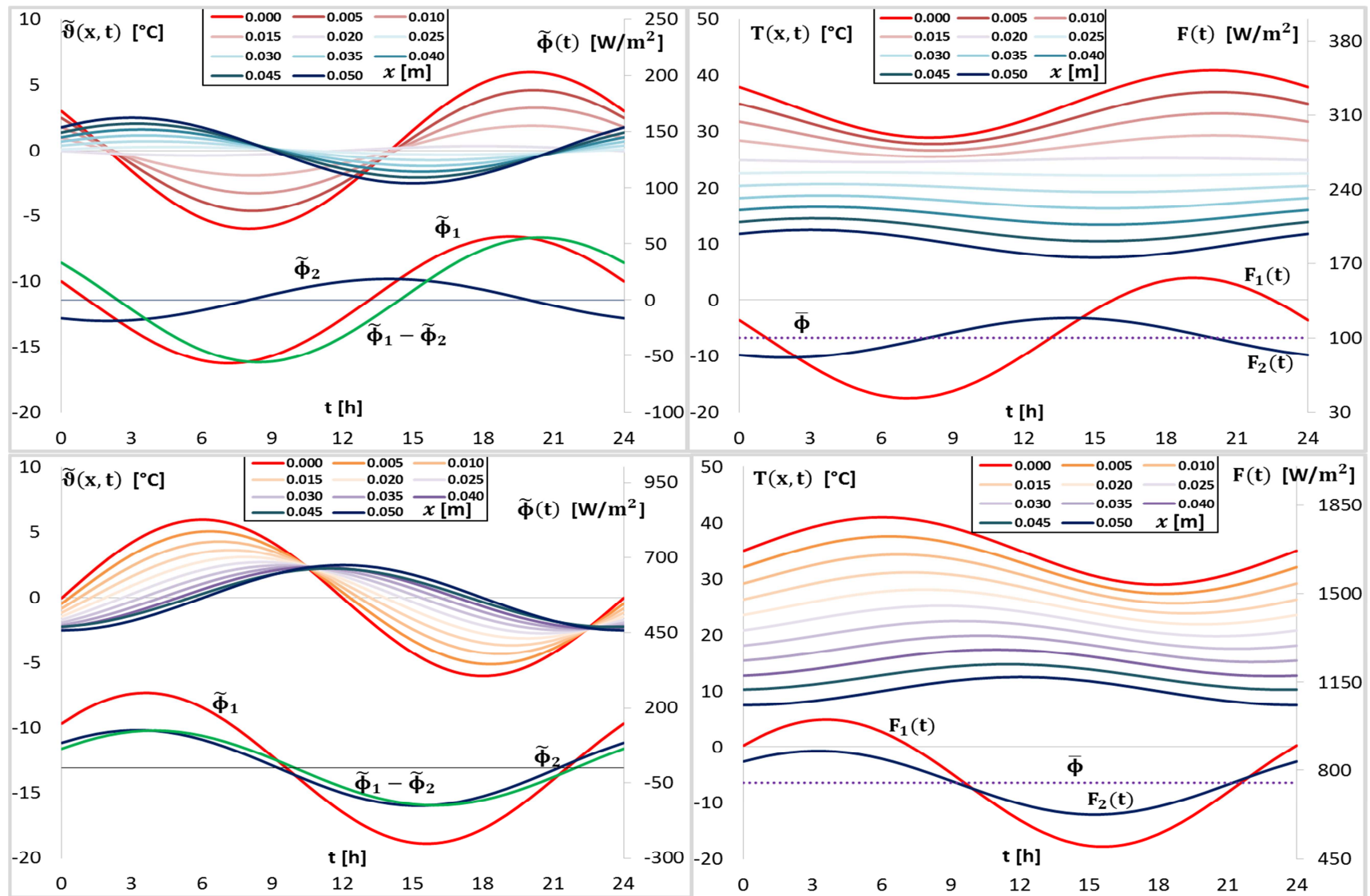


Figure 6 - Configurations C (Top) and D (Bottom). Images on the left: oscillating temperature field, oscillating heat fluxes entering and exiting the layer and variation of energy per unit time of the layer. Images on the right: temperature field, steady heat flux and heat fluxes entering and exiting the wall.

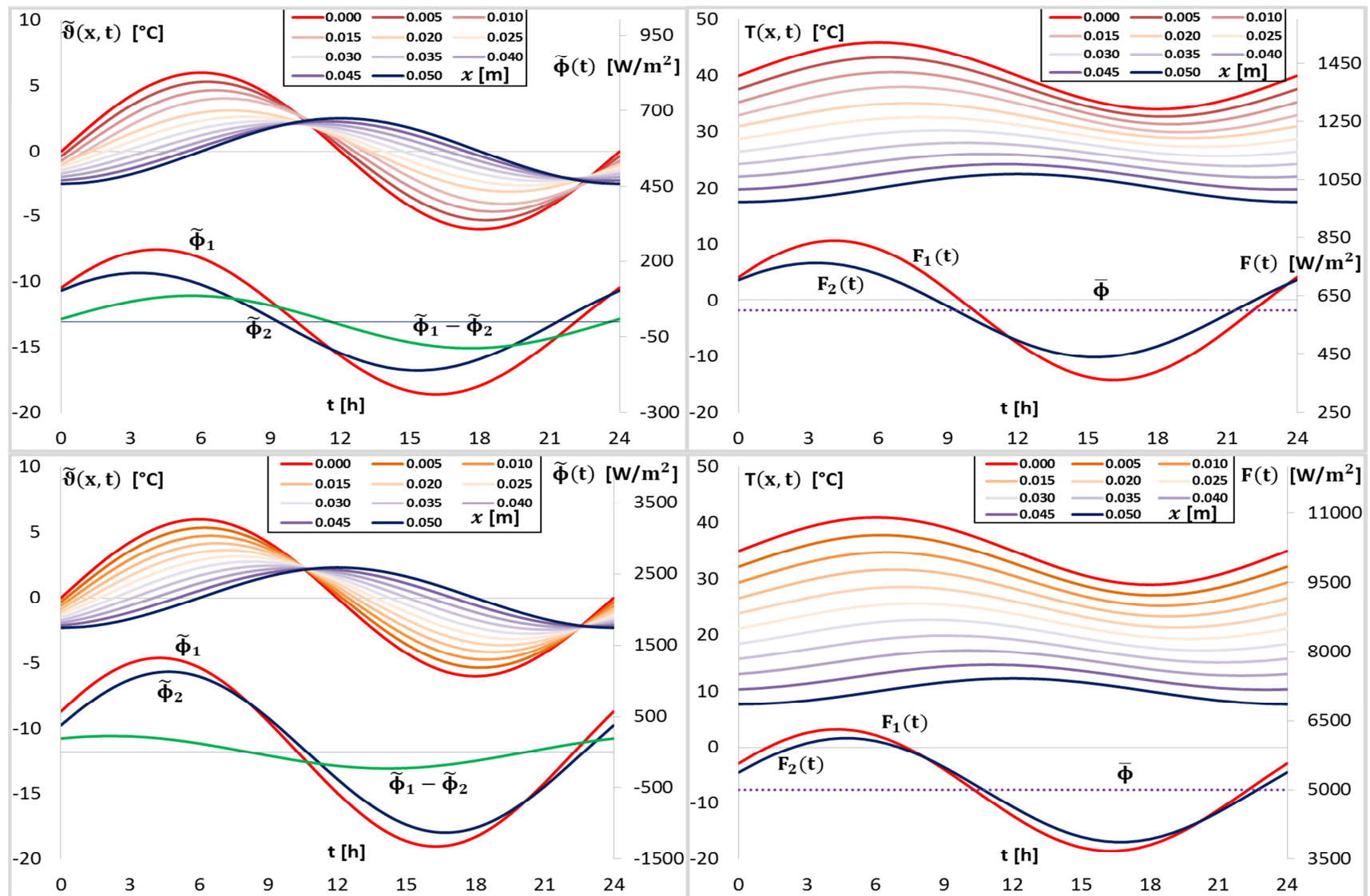


Figure 7 - Configurations E (Top) and F (Bottom): Images on the left: oscillating temperature field, oscillating heat fluxes entering and exiting the layer and variation of energy per unit time of the layer. Images on the right: temperature field, steady heat flux and heat fluxes entering and exiting the wall.



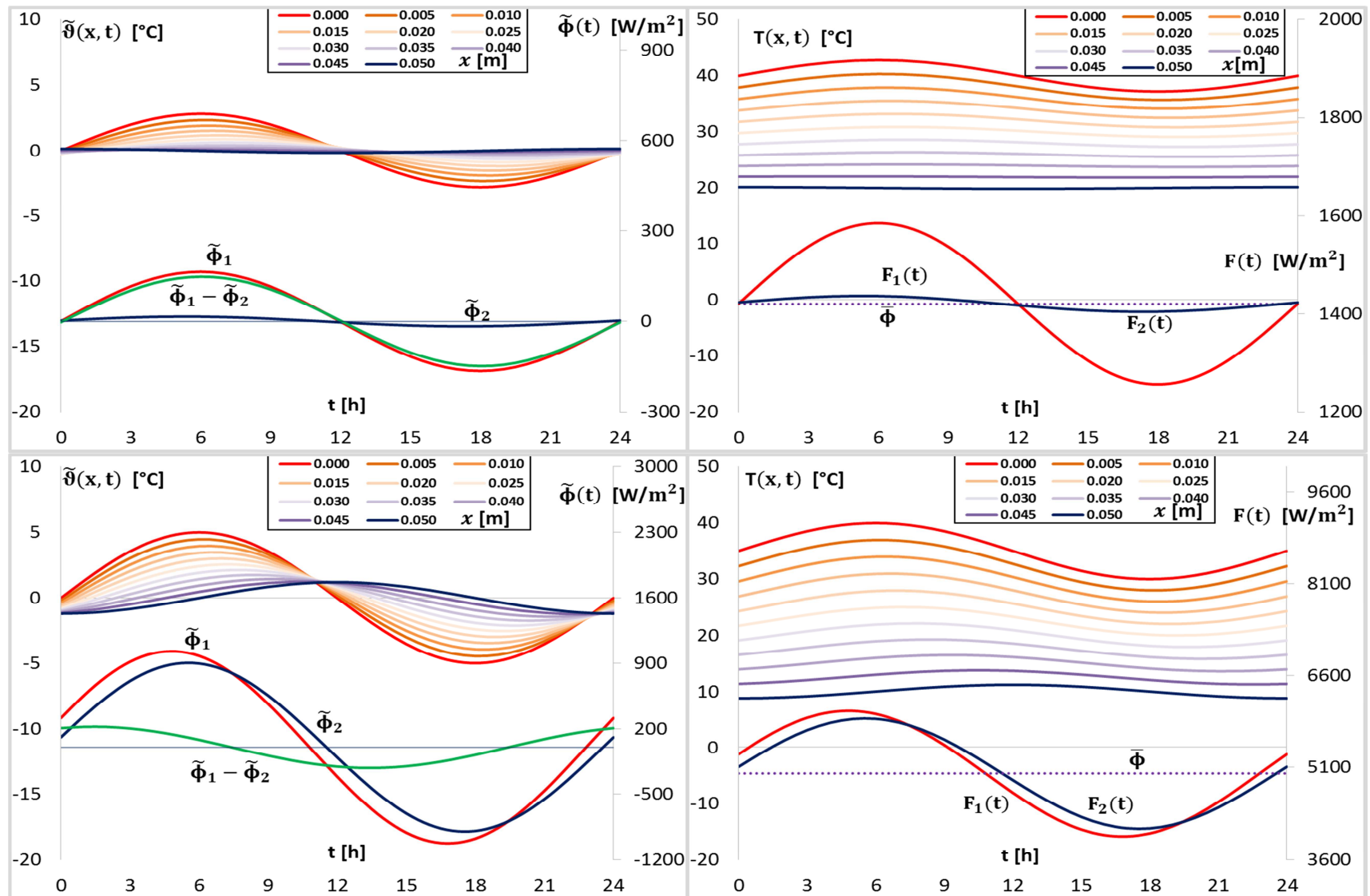


Figure 8 - Configurations G (Top) and H (Bottom). Images on the left: oscillating temperature field, oscillating heat fluxes entering and exiting the layer and variation of energy per unit time of the layer. Images on the right: temperature field, steady heat flux and heat fluxes entering and exiting the wall.

The configurations C, A, D, F and H, in this order, present an identical value for the steady component ( $\bar{\chi}_M/L = 0.4$ ), obtained assigning the same value in different cases to the steady temperatures  $\bar{\vartheta}_1$  and  $\bar{\vartheta}_2$ , and increasing values of the oscillating component amplitude  $\tilde{\chi}_M/L$ .

The latter are obtained, starting from case C, in case A increasing  $Fo_a$  and  $Fo_b$  and in the other cases modifying the argument of  $\widehat{Ste}_{a1}$  and  $\widehat{Ste}_{b2}$  and increasing, in addition to  $Fo_a$  and  $Fo_b$ , also the amplitude of  $\widehat{Ste}_{a1}$  and of  $\widehat{Ste}_{b2}$ . Configurations E and G, compared to the previous cases, have a value of  $\bar{\chi}_M/L$  greater than 1/2, obtained increasing the values of  $\bar{\vartheta}_1$  and  $\bar{\vartheta}_2$  and the increase of the oscillating component amplitude  $\hat{\chi}_M/L$  is obtained assigning higher values to  $Fo_a$  and  $Fo_b$ , reduced values to the amplitudes  $\widehat{Ste}_{a1}$  and  $\widehat{Ste}_{b2}$  and varying the argument of  $\widehat{Ste}_{b2}$ . Case B, with  $\bar{\chi}_M/L = |\hat{\chi}_M|/L = 1/2$ , compared to case A presents an increase of  $\hat{\chi}_M/L$  amplitude, obtained increasing the amplitude and modifying the argument of  $\widehat{Ste}_{a1}$  and  $\widehat{Ste}_{b2}$ .

If one considers the ratio  $|\tilde{\Phi}_1 - \tilde{\Phi}_2|/[F_1(t)]_{\max}$ , between the energy stored per unit time in a semi-period, calculated starting from the maximum amplitude of  $(\tilde{\Phi}_1 - \tilde{\Phi}_2)$ , and the energy entering face 1, calculated by means of the maximum value of  $F_1(t)$ , it highlights that such a parameter increases upon diminishment of oscillating component amplitude  $|\hat{\chi}_M|/L$  and can be assumed as an index of the thermal storage capacity of the layer. If such a parameter assumes a high value, the thermal oscillations from the boundary faces give rise to a greater value of stored energy and, therefore, to a higher reduction of the heat flux transferred to the bi-phase interface from one phase to the other, with a consequent more complete transformation of thermal oscillations in stored latent energy. In the borderline case that the heat flux transferred through the bi-phase interface is nil, the thermal fields in the two phases are only influenced by the relative boundary condition.

In particular, configuration C, which is characterised for having the highest value of the ratio between energy stored and the energy entering face 1 in a semi-period, presents oscillating temperature fields in both liquid and solid phases that present higher attenuation and time lag until they cancel themselves on the bi-phase interface giving rise to the complete conversion of the energy entering the layer in stored energy (see Figure 6, image on the left). In configuration B, it is vice versa, the oscillation of the heat flux originating from a boundary face penetrates the layer, through the bi-phase interface that has not been entirely converted into stored energy until it reaches the opposite face (see Figure 5, image on the left). Identical behaviour is encountered for the oscillation from the other face. This occurs when the heat flux in the layer is higher than the latent storage capacity of the layer. Analogously, the configurations F, G and H show a small value of the ratio  $|\tilde{\Phi}_1 - \tilde{\Phi}_2|/[F_1(t)]_{\max}$ .

Such behaviour of the layer has already been shown in literature through an experimental and numerical investigation of the steady periodic solid–liquid phase-change heat transfer [13].

The procedure was applied in the particular case of a PCM layer subject on face 1 at a sinusoidal temperature  $\tilde{\vartheta}_1$ , oscillating around a mean steady value  $\bar{\vartheta}_a(0) = \bar{\vartheta}_1$ , and on face 2 at a constant temperature equal to the steady value  $\bar{\vartheta}_b(L) = \bar{\vartheta}_2$ . The steady thermal field can be calculated by means of the procedure shown in Paragraph 2.2. The temperature fluctuation operating on face 1 and the thermophysical properties of the layer (see Table 2) are those used in case C, considered previously.

Oscillating temperature fields, the oscillating heat flux on face 1 and on face 2, the temperature field and the heat flux entering and exiting the layer are shown in Figure 9.

Table 2 - PCM layer with oscillating boundary temperature condition on the face 1 and constant boundary temperature on the face 2. Thermophysical properties of the PCM, boundary conditions on the two faces, dimensionless parameter values, steady component  $\bar{\chi}_M$  and oscillating component  $\tilde{\chi}_M$  values and  $|\tilde{\phi}_1 - \tilde{\phi}_2|/[F_1(t)]_{max}$ .

	L m	$\lambda_a$ W/(m <sup>2</sup> K)	$\lambda_b$ W/(m <sup>2</sup> K)	$c_a$ J/(kg K)	$c_b$ J/(kg K)	$\rho$ kg/m <sup>3</sup>	H J/kg	$T_M$ °C	$\bar{\theta}_1$ °C	$\bar{\theta}_2$ °C	$\tilde{\theta}_1$ °C	$\tilde{\theta}_2$ °C	Fo <sub>a</sub> -	Fo <sub>b</sub> -	$\widehat{Ste}_{a1}$ -	$\widehat{Ste}_{b2}$ -	$\bar{\chi}_M/L$ -	$\tilde{\chi}_M/L$ -	$\bar{\chi}_M$ m	$\tilde{\chi}_M$ m	$\frac{ \tilde{\phi}_1 - \tilde{\phi}_2 }{[F_1(t)]_{max}}$ -
Ampl.	0.05	0.2	0.2	3310	1760	1464	254000	25	35	10	6	0	1.43	2.68	0.078	0	0.4	0.042	0.02	0.0021	0.361
Arg.											2.62	0			2.618	0		0.84		0.84	

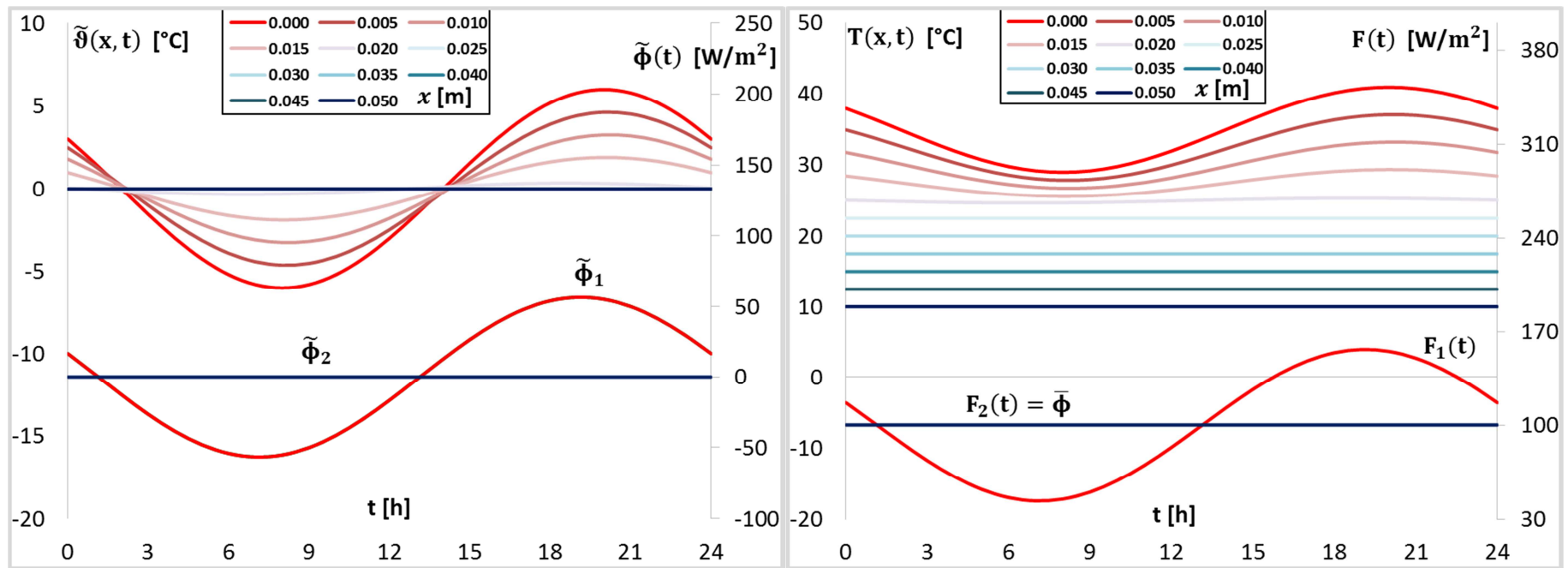


Figure 9 - PCM layer with oscillating boundary temperature condition on the face 1 and constant boundary temperature on the face 2. Top image: oscillating temperature field, oscillating heat fluxes entering and exiting the layer and variation of energy per unit time of the layer. Bottom Image: temperature field, steady heat flux and heat fluxes entering and exiting the wall.

The trends show that the layer gives rise to a complete damping of the thermal oscillations, which, on the bi-phase interface, are entirely converted into latent energy.

### 3.2. An example of resolution of a multi-harmonic thermal field

The determination of  $\hat{\chi}_M/L$  through Eq. (59) allows for the temperature and heat flux fields in the PCM layer to be resolved by means of the Eqs. (55) - (58). A PCM layer, made with a Glauber's salt ( $\text{Na}_2\text{SO}_4 \cdot 10\text{H}_2\text{O}$ ), of a thickness equal to 10 cm was considered. In Table 3 the thermophysical properties of the liquid phase (a) and of the solid phase (b), the steady value and the amplitude and the argument of the two sinusoidal temperature oscillations, with a period equal respectively to 24 h and 12 h, on the two boundary faces of the layer, and the dimensionless numbers that appear in Eq. (59), for the first and second harmonic are reported.

Table 3 - Thermophysical properties of the liquid phase (a) and of the solid phase (b) of Glauber's salt, steady value and amplitude and argument of the two sinusoidal temperature oscillations on the two boundary faces, and dimensionless numbers.

$\lambda_a = 0.554 \text{ W/(m K)}$ [20]	$\lambda_b = 0.554 \text{ W/(m K)}$ [20]
$c_a = 3310 \text{ J/(kg K)}$ [21]	$c_b = 1760 \text{ J/(kg K)}$ [21]
$\rho = 1463.50 \text{ kg/m}^3$ [20]	
$H = 254 \text{ kJ/kg}$ [20]	
$T_M = 32.4 \text{ }^\circ\text{C}$ [20]	
$T_1(t) = \bar{\vartheta}_1 + \vartheta_1(t) = 50 + 7\sin\left(\frac{2\pi}{24}t + \frac{3\pi}{2}\right) + 2.5\sin\left(\frac{2\pi}{12}t + \frac{\pi}{3}\right)$	
$T_2(t) = \bar{\vartheta}_2 + \vartheta_2(t) = 10 + 1.7\sin\left(\frac{2\pi}{24}t + \frac{3\pi}{4}\right) + 0.6\sin\left(\frac{2\pi}{12}t + \frac{\pi}{5}\right)$	
$\text{Fo}_{a_1} = 0.988$	$\text{Fo}_{b_1} = 1.858$
$\widehat{\text{Ste}}_{a_{11}} = 0.091\exp\left(j\frac{3\pi}{2}\right)$	$\widehat{\text{Ste}}_{b_{21}} = 0.012\exp\left(j\frac{3\pi}{4}\right)$
$\text{Fo}_{a_2} = 0.494$	$\text{Fo}_{b_2} = 0.929$
$\widehat{\text{Ste}}_{a_{12}} = 0.033\exp\left(j\frac{\pi}{3}\right)$	$\widehat{\text{Ste}}_{b_{22}} = 0.0042\exp\left(j\frac{\pi}{5}\right)$

Carrying the solution of Eq. (59) for the first and second harmonic in the domain of time, arranging the harmonics through Eqs. (7) and (51), and taking into account the steady solution calculated with Eq. (15), the following is obtained:

$$\begin{aligned} \frac{X_M(t)}{L} &= \frac{\bar{\chi}_M}{L} + \frac{\chi_M(t)}{L} = \frac{\bar{\chi}_M}{L} + \sum_{k=1}^2 \frac{\tilde{\chi}_{Mk}}{L}(t) \\ &= 0.44 + 0.031\sin\left(\frac{2\pi}{24}t + 2.8021\right) + 0.006\sin\left(\frac{2\pi}{12}t - 0.9826\right) \end{aligned}$$

Figure 10 reports the trends of loadings  $T_1(t)$  and  $T_2(t)$ , of the position of the bi-phase interface  $X_M(t)/L$ , of the relative steady values and the melting temperature.

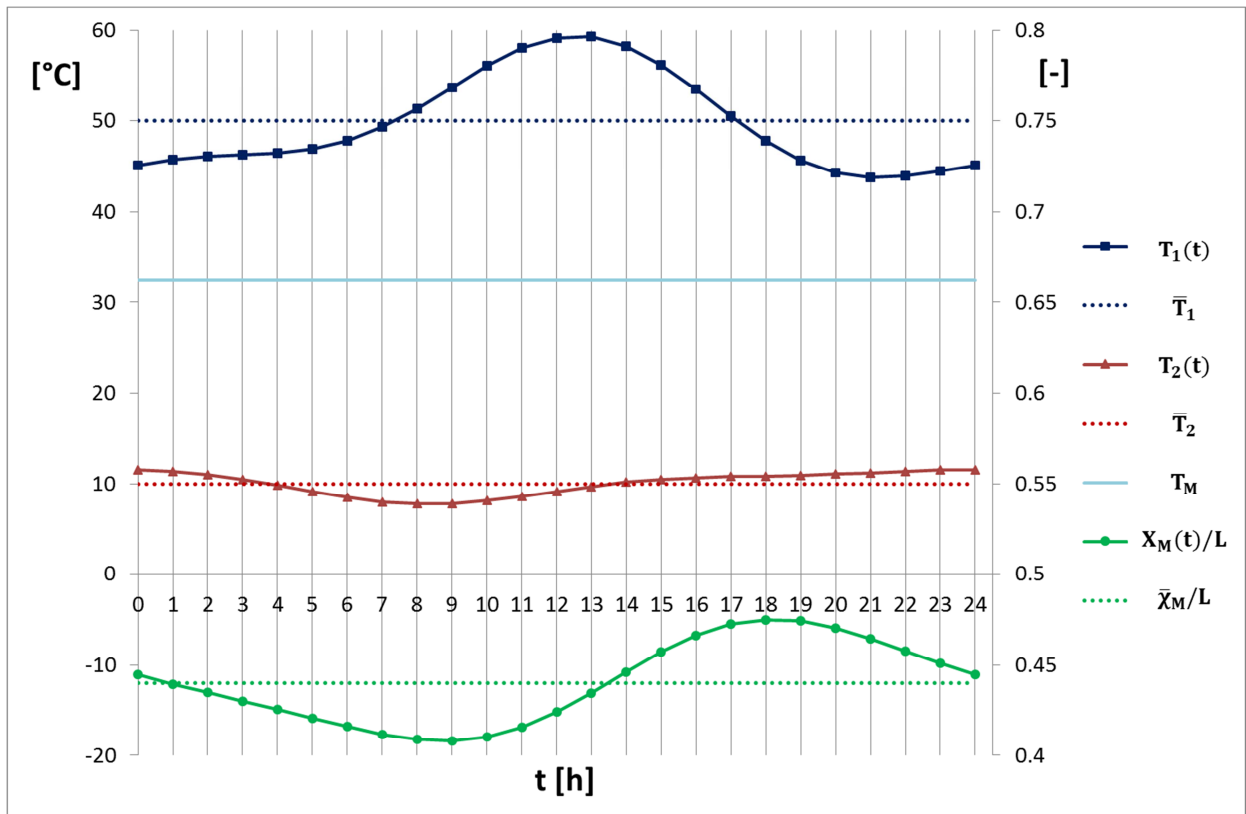


Figure 10 - Trends of loadings  $T_1(t)$  and  $T_2(t)$  and of the position of the bi-phase interface  $X_M(t)/L$ , relative steady values and melting temperatures.

Given the steady component  $\bar{\chi}_M/L$  and the maximum value of fluctuating component  $\chi_M(t)/L$ , Eq. (10) indicates that not all the layer is involved in the phase change and the configuration that occurs is that corresponding to letter C in Figure 2. The fluctuating temperature fields obtained in the two layers  $\vartheta_a(x/L, t)$  and  $\vartheta_b(x/L, t)$ , always in the liquid phase and solid phase, respectively, are reported in Figure 11.

The figure shows that the fluctuation of the temperature starting from abscissa  $x/L = -\bar{\chi}_M/L$  and  $x/L = 1 - \bar{\chi}_M/L$  attenuates and presents a higher time lag until it is annulled in correspondence with the bi-phase interface. The oscillations are more contained in the solid phase since the

amplitude of the oscillating component of the temperature boundary condition on face 2 is lower than the oscillating component of the temperature boundary condition on face 1.

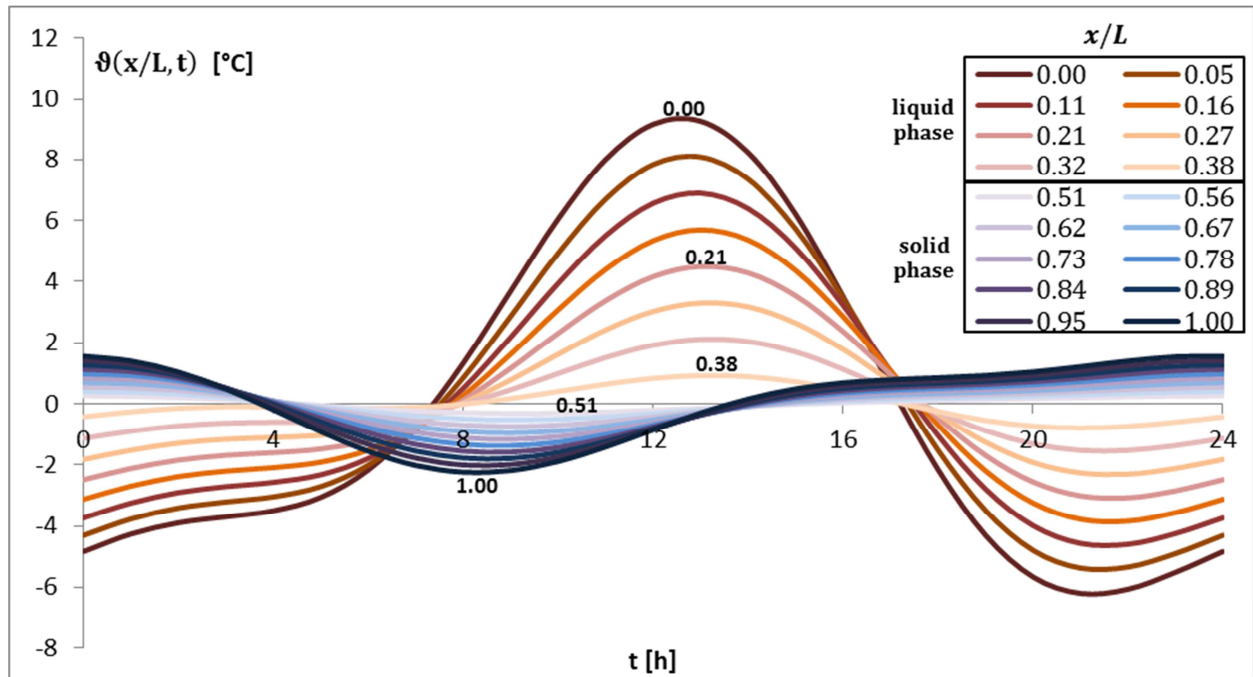


Figure 11 - Fluctuating temperature field in the liquid and solid portions not subject to phase change  $\vartheta_a(x/L, t)$  and  $\vartheta_b(x/L, t)$  as a function of time for different abscissae  $x/L$ .

The trend in time of the fluctuating components  $\phi_a(x/L, t)$  and  $\phi_b(x/L, t)$  of the heat fluxes in the portions of materials not subject to phase change, for some values of  $x/L$ , are reported in Figure 12.

Starting from faces 1 and 2, on the boundary of the layer, the heat flux attenuates and presents a higher time lag proceeding towards the bi-phase interface in a greater measure in the liquid phase compared to the solid phase. The figure shows the different values of the amplitude of the heat flux fluctuations in the liquid phase compared to the solid phase. The oscillation of heat flux transferred in the liquid phase and which arrives at the bi-phase interface is completely used for the phase change. This makes the heat flux field in the solid phase dependent on the boundary condition which acts on the face of abscissa  $x = L$ ; it is also dependent on the position of the bi-phase interface to the melting temperature. The situation is similar for the heat flux field in the liquid phase. Furthermore, the fluctuating heat flux in the liquid phase assumes the same value at the different abscissae in two characteristic instants, that have a half-period time lag. Such instants correspond to the condition of annulment of sensible stored energy per unit time in the

liquid phase, the latter being fluctuant with a mean value equal to zero. Similar considerations are also valid for the solid phase.

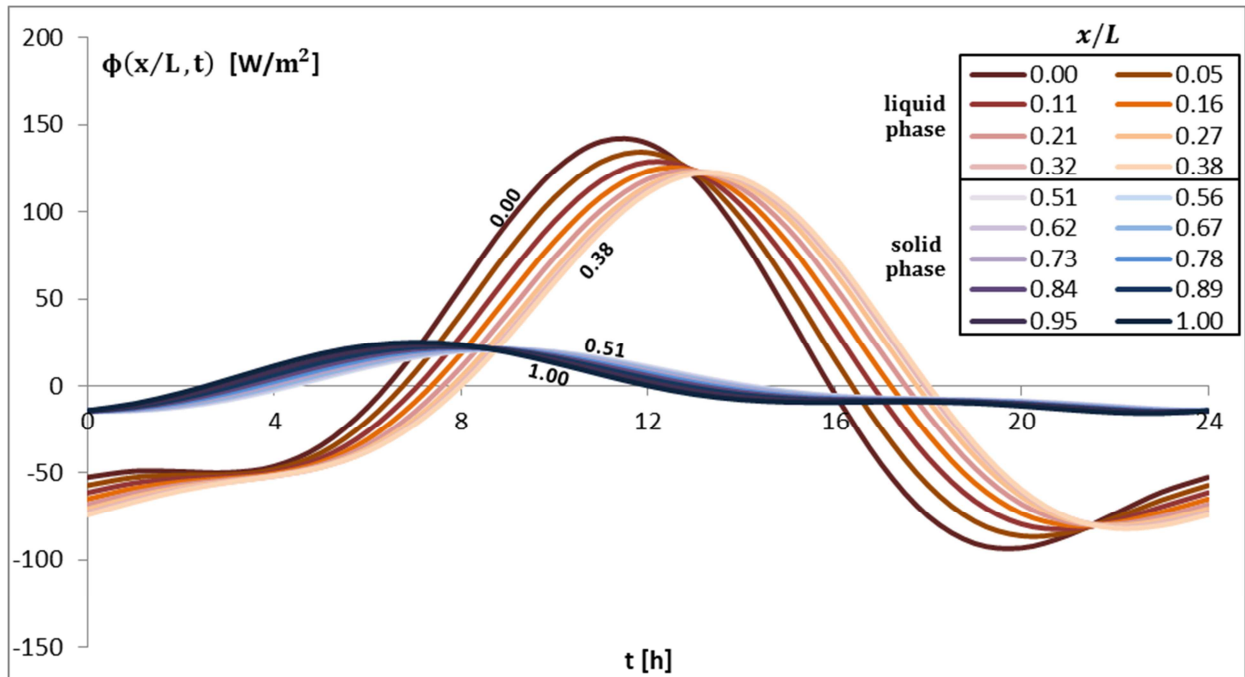


Figure 12 - Fluctuating heat flux field in the liquid and solid portions not subject to phase change  $\phi_a(x/L, t)$  and  $\phi_b(x/L, t)$  as a function of time for different abscissae  $x/L$ .

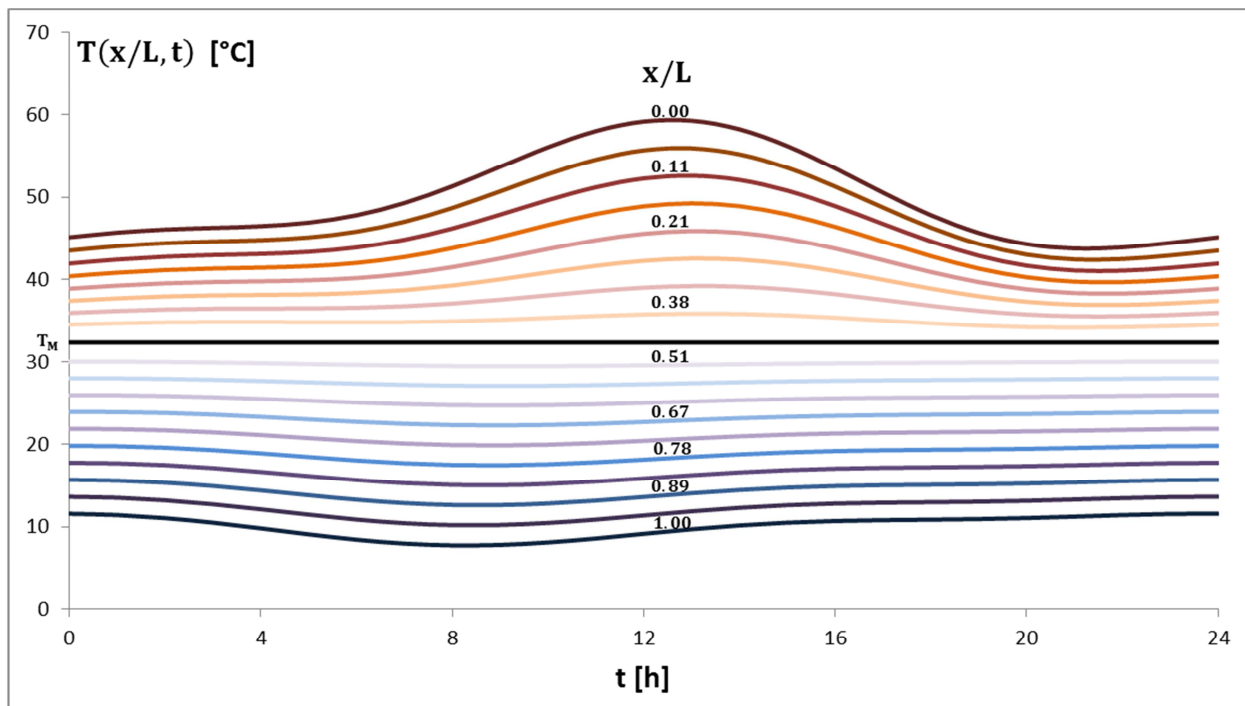


Figure 13 - Temperature field  $T(x, t)$  in the portions which are not subject to phase change as a function of time for some values of  $x/L$ .



The temperature trend in the two phases  $T_a(x/L, t)$  and  $T_b(x/L, t)$  as a function of time for some values of the ratio  $x/L$  is reported in Figure 13.

The heat flux  $F_a(x, t)$  and  $F_b(x, t)$  in the two portions that are not subjected to phase change is obtained by summing the steady component  $\bar{\phi}$ , equal to  $221.6 \text{ W/m}^2$ , and the fluctuating component  $\phi$ .

The heat flux field in the entire layer at different instants is reported in Figure 14.

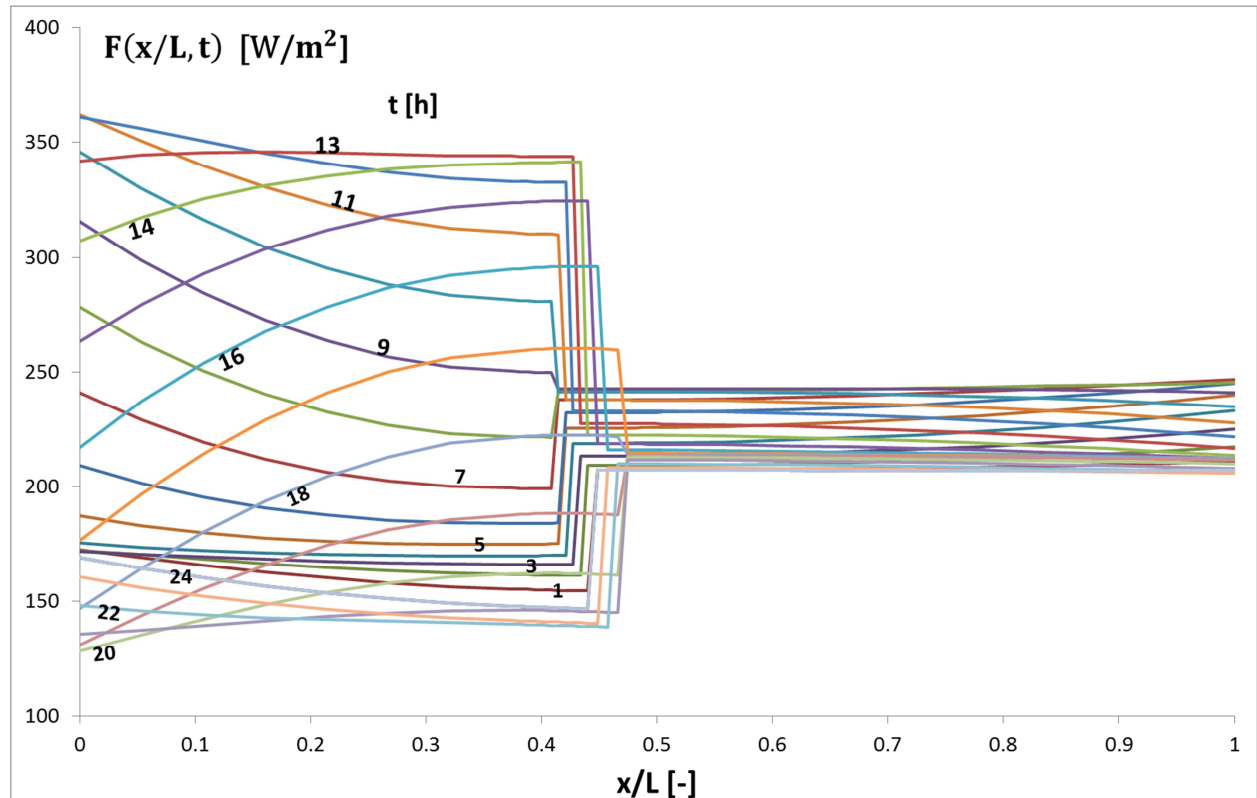


Figure 14 - Heat flux field  $F(x/L, t)$  as a function of  $x/L$  at different hours.

The constancy of the heat flux in the liquid phase occurs at the 13th hour and at the 22nd hour; such instants define two temporal intervals with different heat flux trends. From the 22nd hour to the 13th hour the heat flux decreases with an increase in abscissa  $x/L$  indicating a storage of sensible heat, while in the successive time interval the heat flux increases with a release of energy. Similar considerations are valid for the solid phase. In correspondence with the bi-phase interface, the discontinuity of the heat flux required for the phase change depends linearly, as shown by Eq. (3), on the velocity of the bi-phase interface  $dX_M/dt$ , which can be calculated deriving the expression of  $X_M(t)/L$ . Figure 15 reports the trend of the velocity  $v_M$  and of the latent heat per unit time  $\phi_H$  as a function of time determined with Eqs. (51) and (52) for each harmonic. Such velocity presents a maximum in the 13th hour corresponding to the maximum of

latent energy stored per unit time, and values equal to zero at the 9th and 18th hour due to inversion of the latent energy stored per unit time.

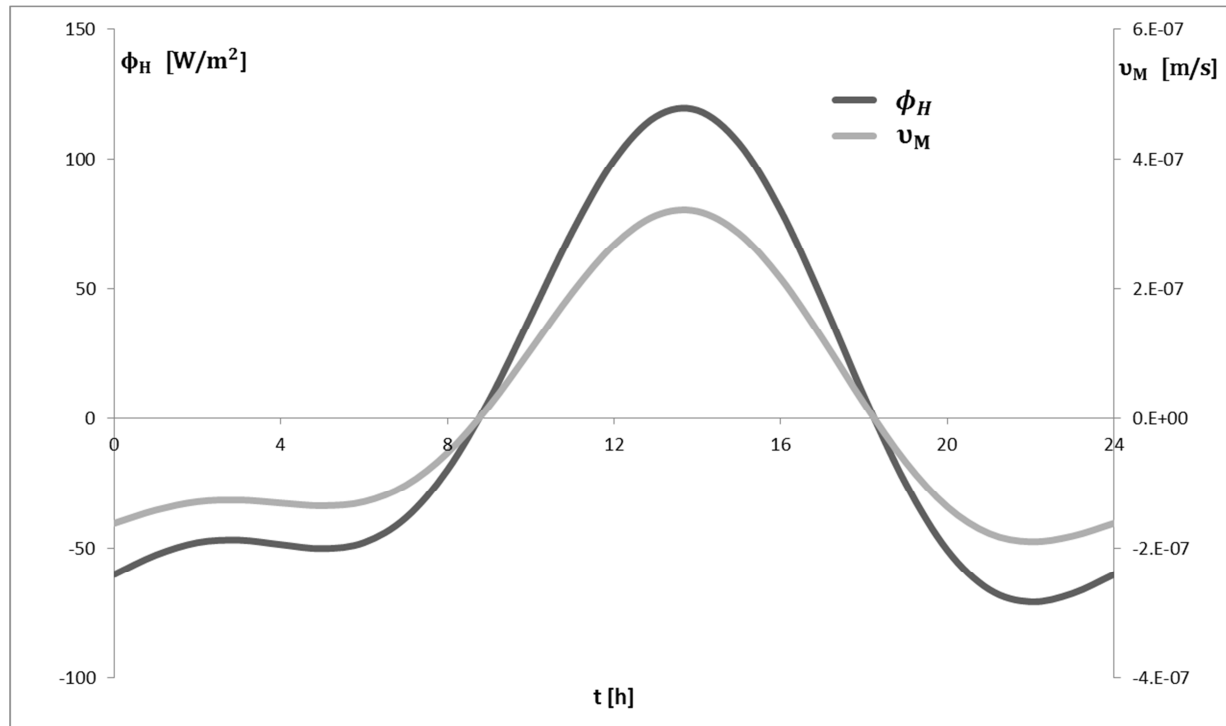


Figure 15 - Trends of velocity of the bi-phase interface  $v_M$  and of the latent heat stored or released per unit time  $\phi_H$  as a function of time.

#### 4. Comparison between analytical and numerical solution

The analytical solution can be used to check a numerical approach. Therefore, in all the sample cases reported, a numerical solution was used, by means of a comparison, to verify that it constitutes an approximation of the analytical solution. From the different numerical models available in the literature, we considered that used by Halford et al. [15], which is based on an explicit time-variant scheme, in which the thermal balance equation at the bi-phase interface is formulated in a manner that is more adherent to the physical phenomenon. In particular, the discontinuity of the heat flux at the interface is considered substituting the relative incremental ratio  $\Delta X_M/\Delta t$  at the derivative  $dX_M/dt$ . The numerical profile was obtained: in the case of two sinusoidal boundary conditions, discretising the layer with a thickness equal to 5 cm with 11 nodes; in the case of 2 multi-harmonic boundary conditions, discretising the layer with a thickness equal to 10 cm with 18 nodes. In every sample case the finite difference time step is  $\Delta t = 15$  s. The sinusoidal temperature fields calculated analytically and numerically for the

different configuration (A-H) are reported in Figure 16 while the multi-harmonic temperature field is shown in Figure 17.

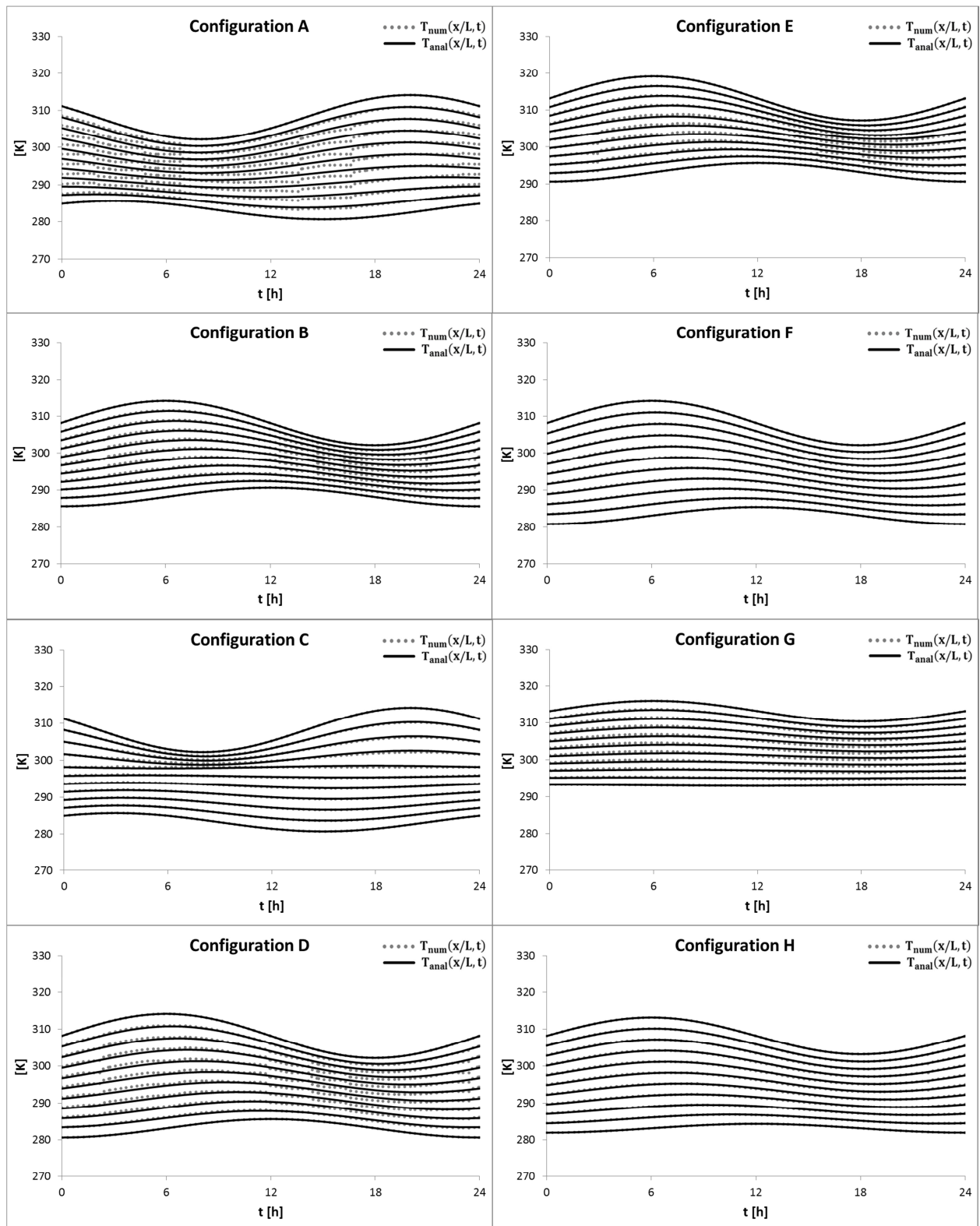


Figure 16 – Sinusoidal boundary conditions. Analytical and numerical temperature field as a function of time at different abscissae.

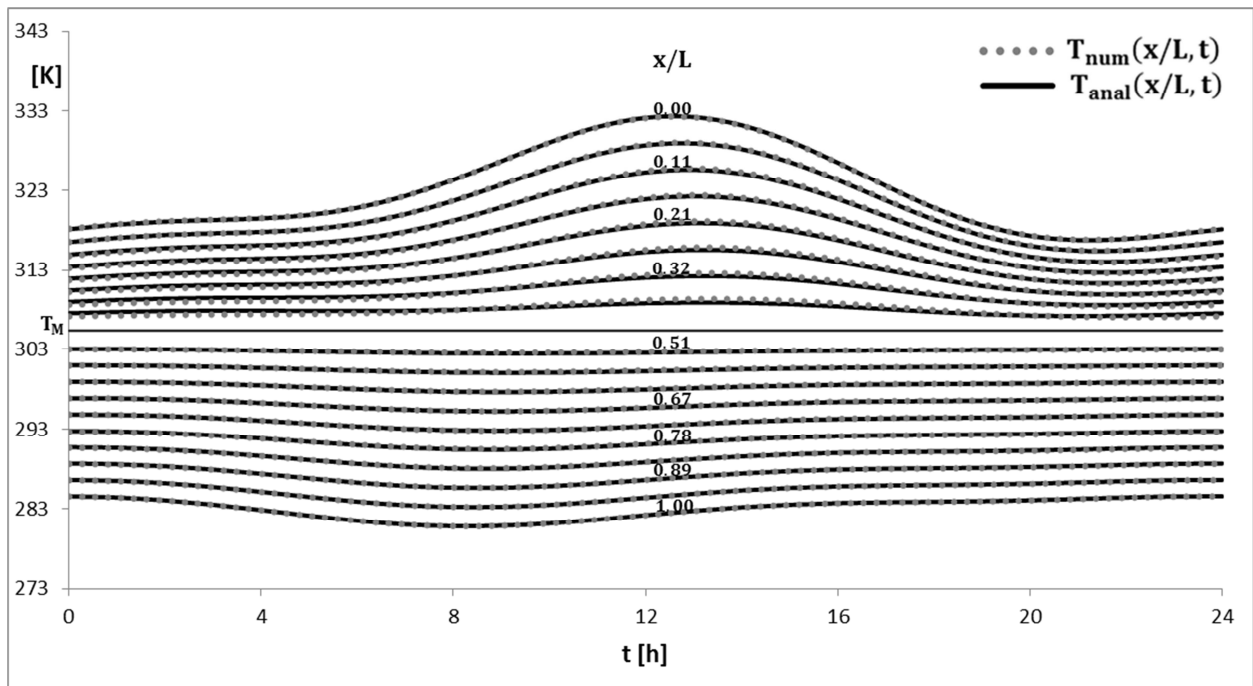


Figure 17 – Multi harmonic boundary conditions. Analytical and numerical temperature field as a function of time at different abscissae.

In all the considered cases, the two profiles are in excellent agreement and the irrelevant displacements, in proximity of the bi-phase interface, can be reduced by means of a denser spatial discretization.

## 5. Conclusions

An analytical approach is used to solve the one-dimensional Stefan Problem with periodic boundary conditions. In the model, the temperature and the heat flux fields, and the position of the bi-phase interface were calculated as the sum of a steady component and a fluctuating component, of mean value equal to zero, expressed as the sum of sinusoidal variations represented by means of phasors.

The oscillating component of the position of the bi-phase interface, for a determined angular frequency, is the solution of a transcendental equation with real and complex parameters. The parameters are: the steady dimensionless position of the bi-phase interface, the Fourier number root evaluated in the two phases and the Stefan number in the two phases.

The evaluation of the oscillating component of the bi-phase interface determines: the portion of the layer involved in the phase change and, by means of the steady value, its position in the layer; the position of the bi-phase interface and its velocity at each instant; the temperature and

heat flux field in the portions of the layer which do not change phase and in the portion of layer subjected to the phase change and the latent energy stored per unit time consequent to the phase change.

The solution of the model was used to carry out a thermal analysis in different thermodynamic configurations of the PCM layer subject to sinusoidal temperature boundary conditions and to determine the thermal behaviour of a PCM layer (Glauber's salt) subject to periodic multi-harmonic temperature boundary conditions.

The analyses conducted have highlighted the conditions necessary to obtain a complete transformation of the oscillating heat fluxes coming from the boundary faces of the layer into stored latent heat. The results obtained also show how behaviour of the layer alters up on varying of the dimensionless parameters.

## References

- [1] EN ISO 13786, Thermal performance of buildings components - Dynamic thermal Characteristics - Calculation methods, 2010.
- [2] G. Oliveti, N. Arcuri, D. Mazzeo, M. De Simone, A new parameter for the dynamic analysis of building walls using the harmonic method, *International Journal of Thermal Sciences* 88 (2015), pp. 96–109.
- [3] L. I. Rubinstein, *The Stefan Problem*, Translations of Mathematical Monographs, Vol. 27, American Mathematical Society, Providence, Rhode Island, 1971.
- [4] H. S. Carslaw, J. C. Jaeger, *Conduction of Heat in Solids*, second edition, Oxford Science Publications, 1988.
- [5] J. Crank, *Free and Moving Boundary Problems*, Oxford University Press, 1987.
- [6] V. S. Arpaci, *Conduction Heat Transfer*, Addison – Wesley Publishing Company, Inc., Reading Mass., 1966.
- [7] V. Alexiades, A. Solomon, *Mathematical modelling of melting and freezing processes*, Hemisphere Publishing Corporation, Washington, 1993.
- [8] M. N. Ozisik, *Heat conduction*, J. Wiley & Sons, New York, 1980.
- [9] D.A. Tarzia, Explicit and Approximated Solutions for Heat and Mass Transfer Problems with a Moving Interface, Chapter 20, in *Advanced Topics in Mass Transfer*, Ed. Mohamed El-Amin, InTech Open Access Publisher, Rijeka, 2011, pp. 439-484.
- [10] S. Savovic, J. Caldwell, Numerical solution of Stefan problem with time-dependent boundary conditions by variable space grid method, *Thermal Science* 13 (2009), pp. 165-174.

- [11] M. Hasan, A. S. Mujumdar, M. E. Weber, Cyclic melting and freezing, *Chemical Engineering Science* 46 (1991), pp. 1573-1587.
- [12] V. R. Voller, P. Felix, C. R. Swaminathan, Cyclic phase change with fluid flow, *International Journal of Numerical Methods for Heat & Fluid Flow* 6 (1996), pp. 57-64.
- [13] G. Casano, S. Piva, Experimental and numerical investigation of the steady periodic solid-liquid phase-change heat transfer, *International Journal of Heat and Mass Transfer* 45 (2002), pp. 4181-4190.
- [14] D. A. Neeper, Thermal dynamics of wallboard with latent heat storage, *Solar Energy* 68(5) (2000), pp. 393-403.
- [15] C. K. Halford, R. F. Boehm, Modeling of phase change material peak load shifting, *Energy and Buildings* 39 (2007), pp. 298-305.
- [16] F. Mathieu-Potvin, L. Gosselin, Thermal shielding of multilayer walls with phase change materials under different transient boundary conditions, *International Journal of Thermal Sciences* 48 (2009), pp. 1707-1717.
- [17] M. M. Farid, A. M. Khudhair, S. A. K. Razack, S. Al-Hallaj, A review on phase change energy storage: materials and applications, *Energy Conversion and Management* 45, 2004, 1597-1615.
- [18] L.F. Cabeza, A. Castell, C. Barreneche, A. de Gracia, A.I. Fernández, Materials used as PCM in thermal energy storage in buildings: A review, *Renewable and Sustainable Energy Reviews* 15 (2011), pp. 1675-1695.
- [19] C. A. Desoer, E. S. Kuh, *Basic Circuit Theory*, 1969, McGraw-Hill Inc, New York, USA.
- [20] B. Zalba, J. M. Marin, L. F. Cabeza, H. Mehling, Review on thermal energy storage with phase change: materials, heat transfer analysis and applications, *Applied Thermal Engineering* 23 (2003), pp. 251-283.
- [21] S. Canbazoglu, A. Sahinaslan, A. Ekmekyapar, Y. G. Aksoy, F. Akarsu, Enhancement of solar thermal energy storage performance using sodium thiosulfate pentahydrate of a conventional solar water-heating system, *Energy and Buildings* 37 (2005), pp. 235-242.

## Nomenclature

- (a) portion of the layer in phase a  
(b) portion of the layer in phase b  
c specific heat capacity [J/(kg K)]  
F heat flux [W/m<sup>2</sup>]

---

Fo	Fourier number [-]
H	latent heat of fusion [J/kg]
k	harmonic order [-]
L	thickness of the PCM layer [m]
n	harmonic number [-]
P	period of oscillation [s]
Ste	Stefan number [-]
t	time [s]
T	temperature [K]
t*	a particular instant [s]
x	spatial Cartesian coordinates [m]
X	position of the bi-phase interface [m]

*Greek symbols*

$\alpha$	thermal diffusivity [ $\text{m}^2/\text{s}$ ]
$\gamma$	propagation constant [ $\text{m}^{-1}$ ]
$\Delta t$	finite difference time step [s]
$\Delta X$	finite difference of the variation of the position of the bi-phase interface [m]
$\zeta$	argument of the oscillating component of the position of bi-phase interface [rad]
$\vartheta$	generic component of the temperature Fourier series expansion [K]
$\vartheta_p, \vartheta_r$	constants of integration [K]
$\lambda$	thermal conductivity [ $\text{W}/(\text{m K})$ ]
$\rho$	density [ $\text{kg}/\text{m}^3$ ]
$\varsigma$	argument of the abscissa in motion [rad]
$u$	velocity of the bi-phase interface [m/s]
$\varphi$	argument of the oscillating component of the temperature [rad]
$\Phi$	generic component of the heat flux Fourier series expansion [ $\text{W}/\text{m}^2$ ]
$\chi$	generic component of the position of bi-phase interface Fourier series expansion [m]
$\psi$	argument of the oscillating component of the heat flux [rad]
$\omega$	angular frequency [rad/s]

*Subscripts*

1	face 1
2	face 2
a	phase a

a1	oscillation on face 1 in a-phase
anal	analytical
b	phase b
b2	oscillation on face 2 in b-phase
H	latent heat stored per unit time
k	k-th harmonic
M	melting
num	numerical

*Symbols*

–	mean value
~	oscillating value in the time domain
^	oscillating value in the complex domain
	amplitude of an oscillating value
arg	argument of an oscillating value



# Chapter 5

## Parametric study and approximation of the exact analytical solution of the Stefan problem in a finite PCM layer in a steady periodic regime

### Abstract

In this chapter a parametric study and an approximation of the exact analytical solution of the Stefan problem in steady periodic regime conditions (Mazzeo et al., 2015) is presented. The physical model describes the thermal behaviour of a PCM (Phase Change Material) layer subject to phase transition, and the considered thermal regime ensures continuous cycles of phase changes under the action of the periodic boundary conditions. The exact analytical solution determines, through implicit transcendental equation with complex thermal parameters and unknowns, the bi-phase interface position, the thermal field and the sensible and latent stored energy in the layer. The dimensionless solution is a function of the Fourier and Stefan numbers

calculated in the two phases, and of the dimensionless bi-phase interface position corresponding to the steady regime.

For the parametric study, the thermophysical properties of the most commonly used PCMs and the variation range of attenuation and time lag between the temperature loadings operating on the internal and external surfaces were considered. This study has allowed for the identification of the thermal parameters that mainly influence the dynamic thermal behaviour of the PCM layer and the mathematical structure of the frequency response of the layer.

Since an analytical expression in an explicit form of the position of the bi-phase interface in the layer is not available, an approximate analytical solution was obtained, which makes the bi-phase interface position depends on the product between the Fourier number and the Stefan number calculated in the two phases. The limits of validity of such a solution were determined evaluating the relative error, which is committed in the determination of the amplitude and of the argument of the oscillating component of the bi-phase interface position. Finally, the fields of variation of the thermal parameters that ensure a relative error value lower than 3 % and the corresponding values of the maximum errors of the amplitude or the argument are determined. In PCM layer thermal analysis it is useful to have an expression in an explicit form of the oscillating component of the bi-phase interface position to obtain the mathematical expression of the temperature and heat flux field as a function of only dimensionless thermal parameters and boundary loadings.

**Keywords:** Moving Boundary Problem; Stefan Problem; PCM; Analytical model; Steady periodic regime; Parametric study; Frequency response; Approximate solution.

- A parametric study of the exact solution of the steady periodic Stefan Problem is presented
- The thermophysical properties of the most commonly used PCMs were considered
- The structure of the transfer function of the layer has been identified
- An approximate analytical solution and errors arising were obtained
- The approximate solution can be used to evaluate the thermal field in the layer

*Quelli che s'innamoran di pratica senza scienza, son come il nocchiere ch'entra in navilio senza timone o bussola, che mai ha certezza dove si vada.*

*(Leonardo da Vinci)*

## 1. Introduction

Compared to the dynamic thermal behaviour of layers of traditional materials, which can be studied with several mathematical methods [1-8], the several applications and the diffusion of phase change materials (PCMs) have required studies and researches with the formulation of models with differing complexity that, in almost all of the cases, have been resolved numerically. Generally, the treatment is simplified considering the general equation of monodimensional heat conduction in the solid phase and in the liquid phase, the equation of thermal balance and of equality of the temperature at the bi-phase interface. The equations at the bi-phase interface are called Stefan conditions while the system of differential equations is known as the Stefan or Moving Boundary Problem. Heat flux discontinuity at the bi-phase interface introduces a non-linearity to the problem rendering its resolution complex.

Several authors have proposed analytical solutions of the model obtained introducing approximations and numerical solutions that use mathematical artifice to describe the phase change and the relative heat latent storage once the melting temperature has been met [9-12].

The heat balance integral method, one of the analytical approximation techniques, is frequently used; it considers a polynomial thermal field both in the solid phase and in the liquid phase and the transformation of the differential equations in a system of algebraic equations that are resolved considering the boundary conditions [13-15].

Instead, the most widespread numerical methods require a spatial discretization of the physical domain and a temporal discretization. The discretization of the PCM layer is executed by means of the use of a nodalisation that is fixed [16-20] or variable in time [21-27] with the aim of following the process of fusion. In the time instants in which a generic node is subject to phase transition, the thermal balance can be discretized at the bi-phase interface assessing in explicitly manner the position of the bi-phase interface [28] or can be employed a mathematical artifice to describe the high heat storage capacity, through a function of state or a variation of a thermophysical property [8]. The apparent heat capacity method utilizes a piecewise function upon temperature variation to describe the heat capacity of the layer [29-31]. In proximity of the melting temperature, such a capacity is evaluated as the sum of the sensible heat capacity of the layer and of an equivalent latent heat capacity. Instead, the effective heat capacity method utilizes a continuous analytical function on temperature variation or an experimental curve obtained through calorimetric techniques [32-34]. The enthalpy method uses the state function of enthalpy instead of temperature [35-38]. Similarly, around the melting temperature, such a function assumes a value that is equal to latent heat of fusion.

All these calculation methodologies have not led to a model, that can correctly interpret in a general manner the effective dynamic response of the layer to internal and external loadings that are variable in time.

With regard to the analytical resolution of the Stefan Problem the case of the infinite and semi-infinite layer with constant temperature boundary conditions is present in the scientific literature [11, 12, 39-43].

In chapter 4, the analytical solution of the phase change problem in a PCM layer subject to boundary conditions that are variable in time, in the hypothesis that the thermal regime is a steady periodic [44], is presented. The problem was resolved supposing heat transfer conductive in the two phases, with different thermophysical properties; through the Fourier series expansion of the temperature, of the heat flux and of the position of the bi-phase interface; through the phasors method. Such formulation permitted the reduction of the system of partial differential equations in a system of algebraic equations whose solution provides the bi-phase interface position at different time instants. Such a position resulted as a function of the square root of the Fourier number, referred to the length of the PCM layer, and of the Stefan number, calculated in the two phases; it cannot be expressed in an explicit form but can be obtained through dedicated algorithms once thermal parameter values are set. The determination of the bi-phase interface position allows for the thermal field in the liquid phase and in the solid phase to be resolved, to determine the advancement velocity of the bi-phase interface and of evaluating the latent heat that is stored or released per unit time. The unavailability in an explicit form of the function that provides the bi-phase interface position does not allow for the analytical description of variations in the dynamic behaviour of the layer upon variation of thermal parameters.

In this chapter are presented: a parametric study of the exact solution to determine the dynamic behaviour of a PCM layer, upon the variation of the thermal parameters, subject to boundary temperature conditions that are periodic in time; an analysis of the frequency influence on the oscillating component of the bi-phase interface position to identify the mathematical structure of the frequency response of the PCM layer; the formulation of an explicit approximate solution and the field of variation of the thermal parameters that ensure its validity with negligible errors.

## **2. The exact analytical solution of the Stefan problem in steady periodic regime**

The determination of the bi-phase interface position and of the thermal field in a PCM layer, with reference to Figure 1, was obtained by the authors [44] resolving a system of equations

formed by the general equation of monodimensional heat conduction in the solid phase and the liquid phase, by the thermal balance equation that describes the discontinuity of the heat flux and the temperature continuity on the interface, and by the boundary conditions on the two faces that delimit the layer.

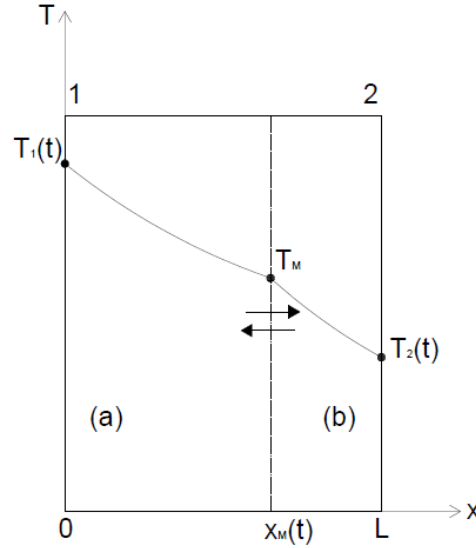


Figure 1 – Temperature field in a bi-phase layer. (a) liquid phase, (b) solid phase,  $T_M$  melting temperature.

The temperature and the heat flux in an abscissa  $x$  of the domain, upon reaching the steady periodic regime, were expressed as sum of the steady component and the fluctuating component, by means a Fourier series expansion [11]:

$$T(x, t) = \bar{\vartheta}(x) + \vartheta(x, t) = \bar{\vartheta}(x) + \sum_{k=1}^n \tilde{\vartheta}_k(x, t) = \bar{\vartheta} + \sum_{k=1}^n |\tilde{\vartheta}_k| \sin(k\omega t + \varphi_k) \quad (1)$$

$$F(x, t) = \bar{\phi} + \phi(x, t) = \bar{\phi} + \sum_{k=1}^n \tilde{\phi}_k(x, t) = \bar{\phi} + \sum_{k=1}^n |\tilde{\phi}_k| \sin(k\omega t + \psi_k) \quad (2)$$

$\bar{\vartheta}(x)$  and  $\bar{\phi}$  are the steady temperature at abscissa  $x$  and the steady heat flux;  $\vartheta(x, t)$  and  $\phi(x, t)$  are the fluctuations of mean value equal to zero calculated as the sum of harmonics;  $k$  is the order,  $\omega$  the angular frequency and  $n$  the number of the harmonics  $\tilde{\vartheta}_k(x, t)$  and  $\tilde{\phi}_k(x, t)$ ;  $|\tilde{\vartheta}_k|$  and  $|\tilde{\phi}_k|$  are the amplitudes of the sinusoids;  $\varphi_k$  and  $\psi_k$  are the arguments.

In these conditions, also the bi-phase interface position presents a periodic fluctuating trend around a mean value:

$$X_M(t) = \bar{\chi}_M + \chi_M(t) = \bar{\chi}_M + \sum_{k=1}^n \tilde{\chi}_{M_k}(t) = \bar{\chi}_M + \sum_{k=1}^n |\tilde{\chi}_{M_k}| \sin(k\omega t + \zeta_k) \quad (3)$$

with  $\bar{\chi}_M$  steady component of the bi-phase interface position around which oscillates the fluctuation  $\chi_M(t)$ , expressed as the sum of  $n$  harmonics  $\tilde{\chi}_{M_k}(t)$  of amplitude  $|\tilde{\chi}_{M_k}|$  and of argument  $\zeta_k$ .

The steady component of  $X_M(t)$  is expressed as a function of the melting temperature  $T_M$ :

$$\bar{\chi}_M = \frac{\lambda_a(\bar{\vartheta}_1 - T_M)}{\lambda_a(\bar{\vartheta}_1 - T_M) + \lambda_b(T_M - \bar{\vartheta}_2)} L \quad (4)$$

and allows for the determination of the linear steady temperature field in the two phases and the steady heat flux, constant in the layer.

In Figure 2, the reference system of the oscillating component, with origin in correspondence of the steady position, of the bi-phase interface is defined.

The oscillating temperature field was determined with the symbolic or phasors method [45] that represent each generic harmonic  $\tilde{\vartheta}_k$ , of angular frequency  $k\omega$ , like the imaginary part of the phasor written in the complex form:

$$\hat{\vartheta}_k = |\hat{\vartheta}_k| [\cos(k\omega t + \varphi_k) + j\sin(k\omega t + \varphi_k)] = |\hat{\vartheta}_k| \exp(j\varphi_k) \exp(jk\omega t) \quad (5)$$

with  $|\hat{\vartheta}_k| = |\tilde{\vartheta}_k|$  and  $\arg(\hat{\vartheta}_k) = \arg(\tilde{\vartheta}_k)$ .

The resolution of the oscillating thermal field in the complex domain provided the phasors associated with the temperature  $\hat{\vartheta}_k(x)$ , with the heat flux  $\hat{\varphi}_k(x)$  and with the bi-phase interface position  $\hat{\chi}_{M_k}$ .

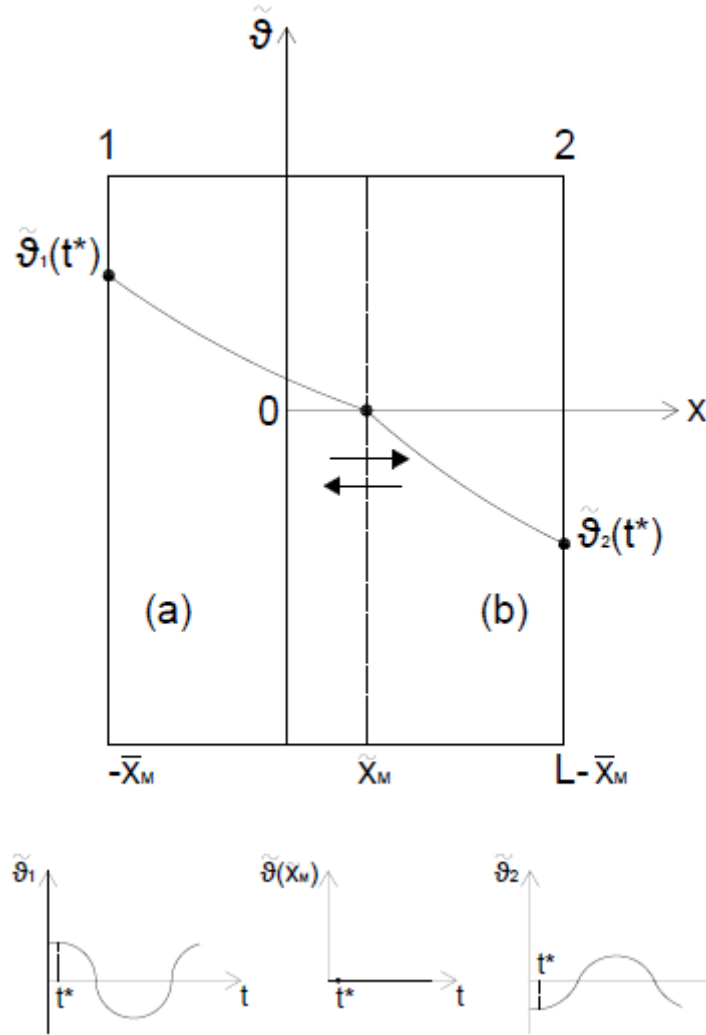


Figure 2 – Reference system for the oscillating component of the bi-phase interface position, boundary conditions and oscillating temperature field in a generic time instant  $t^*$ .

The equations that describes the oscillating temperature and heat flux fields in the phase (a) and (b) are:

layer (a)  $\left(-\frac{\bar{x}_M}{L} \leq \frac{x}{L} \leq -\frac{|\hat{x}_M|}{L}\right)$ :

$$\frac{\hat{\theta}_a(x)}{\hat{\theta}_1} = \cosh \left[ (1+j) \sqrt{\frac{\pi}{Fo_a}} \left( \frac{x}{L} + \frac{\bar{x}_M}{L} \right) \right] - \frac{\sinh \left[ (1+j) \sqrt{\frac{\pi}{Fo_a}} \left( \frac{x}{L} + \frac{\bar{x}_M}{L} \right) \right]}{\tanh \left[ (1+j) \sqrt{\frac{\pi}{Fo_a}} \left( \frac{\hat{x}_M}{L} + \frac{\bar{x}_M}{L} \right) \right]} \quad (6)$$

$$\frac{\hat{\phi}_a(x)}{(1+j) \sqrt{\frac{\pi}{Fo_a}} \frac{\lambda_a}{L} \hat{\theta}_1} = -\sinh \left[ (1+j) \sqrt{\frac{\pi}{Fo_a}} \left( \frac{x}{L} + \frac{\bar{x}_M}{L} \right) \right] + \frac{\cosh \left[ (1+j) \sqrt{\frac{\pi}{Fo_a}} \left( \frac{x}{L} + \frac{\bar{x}_M}{L} \right) \right]}{\tanh \left[ (1+j) \sqrt{\frac{\pi}{Fo_a}} \left( \frac{\hat{x}_M}{L} + \frac{\bar{x}_M}{L} \right) \right]} \quad (7)$$

layer (b)  $\left(\frac{|\hat{\chi}_M|}{L} \leq \frac{x}{L} \geq 1 - \frac{\bar{\chi}_M}{L}\right)$ :

$$\frac{\hat{\theta}_b(x)}{\hat{\theta}_2} = \cosh \left[ (1+j) \sqrt{\frac{\pi}{Fo_b}} \left(1 - \frac{\bar{\chi}_M}{L} - \frac{x}{L}\right) \right] - \frac{\sinh \left[ (1+j) \sqrt{\frac{\pi}{Fo_b}} \left(1 - \frac{\bar{\chi}_M}{L} - \frac{x}{L}\right) \right]}{\tanh \left[ (1+j) \sqrt{\frac{\pi}{Fo_b}} \left(1 - \frac{\bar{\chi}_M}{L} - \frac{\hat{\chi}_M}{L}\right) \right]} \quad (8)$$

$$\frac{\hat{\Phi}_b(x)}{(1+j) \sqrt{\frac{\pi}{Fo_b}} \frac{\lambda_b}{L} \hat{\theta}_2} = \sinh \left[ (1+j) \sqrt{\frac{\pi}{Fo_b}} \left(1 - \frac{\bar{\chi}_M}{L} - \frac{x}{L}\right) \right] - \frac{\cosh \left[ (1+j) \sqrt{\frac{\pi}{Fo_b}} \left(1 - \frac{\bar{\chi}_M}{L} - \frac{x}{L}\right) \right]}{\tanh \left[ (1+j) \sqrt{\frac{\pi}{Fo_b}} \left(1 - \frac{\bar{\chi}_M}{L} - \frac{\hat{\chi}_M}{L}\right) \right]} \quad (9)$$

The oscillating component of the bi-phase interface position is the solution of the equation:

$$\frac{1+j}{2\sqrt{\pi}} \left\{ \frac{\sqrt{Fo_a}}{\sinh \left[ (1+j) \sqrt{\frac{\pi}{Fo_a}} \left(\frac{\bar{\chi}_M}{L} + \frac{\hat{\chi}_M}{L}\right) \right]} \widehat{Ste}_{a1} + \frac{\sqrt{Fo_b}}{\sinh \left[ (1+j) \sqrt{\frac{\pi}{Fo_b}} \left(1 - \frac{\bar{\chi}_M}{L} - \frac{\hat{\chi}_M}{L}\right) \right]} \widehat{Ste}_{b2} \right\} = j \frac{\hat{\chi}_M}{L} \quad (10)$$

Such a solution makes the oscillating component of the bi-phase interface position and the oscillating thermal field depend on the square root of the Fourier number and the Stefan number calculated in the solid phase and in the liquid phase.

$$Fo_a = \frac{\alpha_a P}{L^2} ; Fo_b = \frac{\alpha_b P}{L^2} ; \widehat{Ste}_{a1} = \frac{c_a \hat{\theta}_1}{\lambda} ; \widehat{Ste}_{b2} = \frac{c_b \hat{\theta}_2}{\lambda} \quad (11)$$

with  $P = 2\pi/\omega$  period of oscillation.

### 3. Parametric study of the exact analytical solution

Despite the use of software with dedicated algorithms [46-47], the solution of Eq. (10) cannot be expressed in a symbolic form. However, these algorithms provide the solution to the equation once the thermal parameter values have been set. With the aim to carry out a parametric study, Eq. (10) was rewritten in the form:

$$\frac{1+j}{2\sqrt{\pi}} \sqrt{Fo_a} \widehat{Ste}_{a1} \left\{ \frac{1}{\sinh \left[ (1+j) \sqrt{\frac{\pi}{Fo_a}} \left(\frac{\bar{\chi}_M}{L} + \frac{\hat{\chi}_M}{L}\right) \right]} + \frac{\sqrt{\frac{Fo_b}{Fo_a}} \frac{\widehat{Ste}_{b2}}{\widehat{Ste}_{a1}}}{\sinh \left[ (1+j) \sqrt{\frac{\pi}{Fo_a}} \frac{1}{\sqrt{\frac{Fo_b}{Fo_a}}} \left(1 - \frac{\bar{\chi}_M}{L} - \frac{\hat{\chi}_M}{L}\right) \right]} \right\} = j \frac{\hat{\chi}_M}{L} \quad (12)$$



and was studied considering the dependence on the thermal parameters:

$$\sqrt{Fo_a}, \quad \widehat{Ste}_{a1}, \quad \sqrt{\frac{Fo_b}{Fo_a}}, \quad \sqrt{\frac{Fo_b}{Fo_a}} \frac{\widehat{Ste}_{b2}}{\widehat{Ste}_{a1}}, \quad \frac{\bar{\chi}_M}{L}$$

The dimensionless number  $\sqrt{Fo_b}/\sqrt{Fo_a}$  represents the ratio between the thermal diffusivity of the two phases, while  $(\sqrt{Fo_b}|\widehat{Ste}_{b2}|)/(\sqrt{Fo_a}|\widehat{Ste}_{a1}|)$  also takes into consideration the attenuation and time lag between the temperature loadings applied on the boundary of the layer.

The amplitude and the argument of the oscillating component of the bi-phase interface position were studied considering the variability of the real and complex thermal parameters of Table 1. In the study, such variability was determined with reference to the thermophysical properties of the most commonly used PCMs in building walls [48]. Moreover, temperature oscillation amplitudes  $|\hat{\vartheta}_1|$  between 1 °C and 30 °C, attenuations  $|\hat{\vartheta}_2|/|\hat{\vartheta}_1|$  between 0.1 and 0.9, and characteristic values of the argument of  $|\hat{\vartheta}_1|$  and of the time lag between  $|\hat{\vartheta}_2|$  and  $|\hat{\vartheta}_1|$ , were considered.

Table 1 - Field of variability of the dimensionless thermal parameters of Eq. (12).

Amplitude	Argument
$\sqrt{Fo_a} = (0.3162, 14.1421)$	
$ \widehat{Ste}_{a1}  = (0.001, 1.0)$	$\arg(\widehat{Ste}_{a1}) = \varphi_1 = (0, 2\pi)$
$\sqrt{\frac{Fo_b}{Fo_a}} = (0.7071, 1.4142)$	
$\sqrt{\frac{Fo_b}{Fo_a}} \frac{ \widehat{Ste}_{b2} }{ \widehat{Ste}_{a1} } = (0.0707, 1.2728)$	$\arg\left(\frac{\widehat{Ste}_{b2}}{\widehat{Ste}_{a1}}\right) = (\varphi_2 - \varphi_1) = \left(\frac{\pi}{2}, \frac{3}{2}\pi\right)$

The trends of the oscillating component  $\hat{\chi}_M/L$  are reported in terms of the amplitude in Figure 3 and of the argument in Figure 4. Figure 3 provides the amplitude trend as a function of  $\sqrt{Fo_a}$  for different values of  $\sqrt{Fo_b}/\sqrt{Fo_a}$  and  $(\sqrt{Fo_b}|\widehat{Ste}_{b2}|)/(\sqrt{Fo_a}|\widehat{Ste}_{a1}|)$  and for some characteristic values of  $|\widehat{Ste}_{a1}|$ . The figure was obtained assuming  $\bar{\chi}_M/L = 0.5$ ,  $\varphi_1 = 0$  and  $(\varphi_2 - \varphi_1) = \pi/2$ .

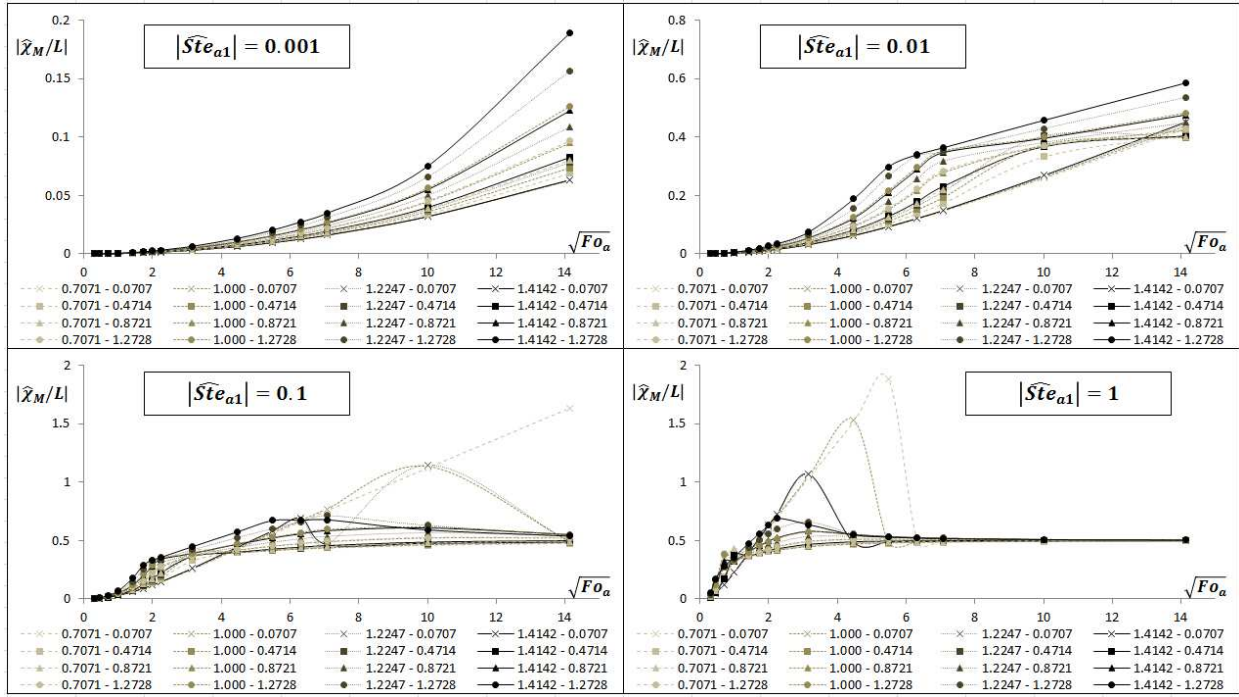


Figure 3. Trend of  $|\hat{\chi}_M/L|$  as a function of  $\sqrt{Fo_a}$  for different values of  $\sqrt{Fo_b}/\sqrt{Fo_a}$  and  $(\sqrt{Fo_b}|\hat{St}_{e_{b2}}|)/(\sqrt{Fo_a}|\hat{St}_{e_{a1}}|)$  and for some characteristic values of  $|\hat{St}_{e_{a1}}|$ .  $\bar{\chi}_M/L = 0.5$ ;  $\varphi_1 = 0$ ;  $(\varphi_2 - \varphi_1) = \pi/2$ . In the legend, the value of  $\sqrt{Fo_b}/\sqrt{Fo_a}$  and of  $(\sqrt{Fo_b}|\hat{St}_{e_{b2}}|)/(\sqrt{Fo_a}|\hat{St}_{e_{a1}}|)$  is reported for each curve in order.

Figure 3 shows that the period of oscillation, contained in  $Fo_a$ , and therefore the velocity with which the PCM is subjected to repeated cycles of heating and cooling, is a quantity that significantly influences the thermal performance of the layer. In particular, for a determined layer of the higher value of the oscillation amplitude of the bi-phase interface in period  $P$ , and therefore to the largest velocity of bi-phase interface. Such maximum overshoot is highlighted in the figures for  $\hat{St}_{e_{a1}} = 0.1$  and  $\hat{St}_{e_{a1}} = 1$ .

Furthermore, the trends in the figure show that a value of  $\sqrt{Fo_a}$  exists, below which the oscillating component amplitude does not vary, namely settling value. Such value, necessary to attain regime conditions, is mainly influenced by  $\hat{St}_{e_{a1}}$  and decreases with the increase of this thermal parameter. For  $\hat{St}_{e_{a1}} = 1$ , irrespective of the values of other thermal parameters, such a condition is obtained for  $\sqrt{Fo_a} \approx 7$ , while for  $\hat{St}_{e_{a1}} = 0.001$  a much higher value is required. Furthermore, the settling value of  $\sqrt{Fo_a}$  increases upon the decrease of  $(\sqrt{Fo_b}|\hat{St}_{e_{b2}}|)/(\sqrt{Fo_a}|\hat{St}_{e_{a1}}|)$  and, fixing the value of this latter thermal parameter, on the decrease of  $\sqrt{Fo_b}/\sqrt{Fo_a}$ .

The settling value of  $\sqrt{Fo_a}$ , for a determined harmonic of period  $P$ , can be employed to determine a corresponding characteristic length of the PCM layer.

The regime value of  $\hat{\chi}_M/L$ , can be analytically obtained considering the limit for  $\sqrt{Fo_a} \rightarrow +\infty$  in Eq. (12), (see Appendix A). Such a limit, for any value of  $\widehat{Ste}_{a1}$ , is:

$$\left(\frac{\hat{\chi}_M}{L}\right)_{\text{reg}} = \frac{1}{1 - \left(\sqrt{\frac{Fo_b}{Fo_a}}\right) \cdot \left(\sqrt{\frac{Fo_b}{Fo_a}} \frac{\widehat{Ste}_{b2}}{\widehat{Ste}_{a1}}\right)} - \frac{\bar{\chi}_M}{L} \quad (13)$$

In the variation field of the thermal parameters highlighted in Figure 3, the regime value of  $|\hat{\chi}_M/L|$ , calculated with the preceding equation, is equal to 0.5, for any value of  $\sqrt{Fo_b}/\sqrt{Fo_a}$  and  $(\sqrt{Fo_b}\widehat{Ste}_{b2})/(\sqrt{Fo_a}\widehat{Ste}_{a1})$ .

The maximum overshoot of  $|\hat{\chi}_M/L|$  and the correspondent value of  $\sqrt{Fo_a}$  increase on the decrease of  $(\sqrt{Fo_b}|\widehat{Ste}_{b2}|)/(\sqrt{Fo_a}|\widehat{Ste}_{a1}|)$ , and fixing the value of this latter thermal parameter, upon a decrease of  $\sqrt{Fo_b}/\sqrt{Fo_a}$ .

The argument  $\zeta$  of  $\hat{\chi}_M/L$  as a function of  $\sqrt{Fo_a}$  for different values of  $\sqrt{Fo_b}/\sqrt{Fo_a}$  and  $(\sqrt{Fo_b}|\widehat{Ste}_{b2}|)/(\sqrt{Fo_a}|\widehat{Ste}_{a1}|)$ , and for some characteristic values of  $|\widehat{Ste}_{a1}|$ , is reported in Figure 4. The figure is obtained for  $\bar{\chi}_M/L = 0.5$ ,  $\varphi_1 = 0$  and  $(\varphi_2 - \varphi_1) = \pi/2$ . The procedure for the calculation of a phasor argument is reported in Appendix B.

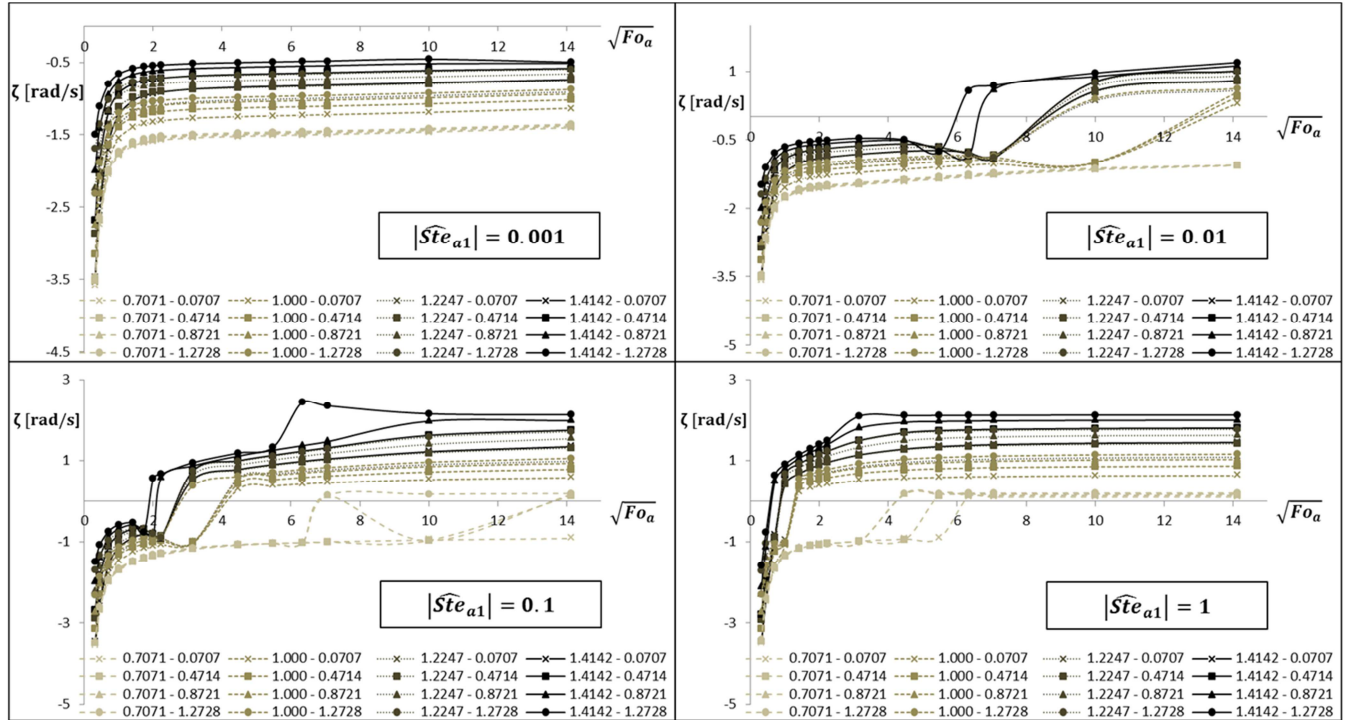


Figure 4. Trend of  $\zeta = \arg(\hat{\chi}_M/L)$  as a function of  $\sqrt{Fo_a}$  for different values of  $\sqrt{Fo_b}/\sqrt{Fo_a}$  and  $(\sqrt{Fo_b}|\widehat{Ste}_{b2}|)/(\sqrt{Fo_a}|\widehat{Ste}_{a1}|)$  and for some characteristic values of  $|\widehat{Ste}_{a1}|$ .  $\bar{\chi}_M/L = 0.5$ ;  $\varphi_1 = 0$ ;  $(\varphi_2 - \varphi_1) = \pi/2$ . In the legend, the value of  $\sqrt{Fo_b}/\sqrt{Fo_a}$  and of  $(\sqrt{Fo_b}|\widehat{Ste}_{b2}|)/(\sqrt{Fo_a}|\widehat{Ste}_{a1}|)$  is reported for each curve in order.

Argument  $\zeta$  increases with  $\sqrt{Fo_a}$  and reaches a regime value that can be evaluated with Eq. (13) which depends on thermal parameters  $\sqrt{Fo_b}/\sqrt{Fo_a}$  and  $(\sqrt{Fo_b}|\widehat{Ste}_{b2}|)/(\sqrt{Fo_a}|\widehat{Ste}_{a1}|)$ . In particular,  $\zeta$  increases with a growing  $(\sqrt{Fo_b}|\widehat{Ste}_{b2}|)/(\sqrt{Fo_a}|\widehat{Ste}_{a1}|)$  and, fixing the value of this latter thermal parameter, increasing  $\sqrt{Fo_b}/\sqrt{Fo_a}$ . The value of  $\sqrt{Fo_a}$  necessary in order to attain regime conditions, or the settling value, is mainly influenced by  $\widehat{Ste}_{a1}$  and decreases when this thermal parameter increases. All the curves present an abrupt variation of  $\zeta$  which occurs for a value of  $\sqrt{Fo_a}$  equal to that corresponding to the maximum overshoot of  $|\hat{\chi}_M/L|$ .

The influence of argument  $\varphi_1$  relative to  $\widehat{Ste}_{a1}$ , and of the time lag  $(\varphi_2 - \varphi_1)$ , which appears in the ratio  $\widehat{Ste}_{b2}/\widehat{Ste}_{a1}$ , on the amplitude of  $\hat{\chi}_M/L$ , upon variation of  $\sqrt{Fo_a}$  and for different values of  $|\widehat{Ste}_{a1}|$  is shown in Figures 5a and 5b. Figure 5a was obtained for  $\sqrt{Fo_b}/\sqrt{Fo_a}$  and  $(\sqrt{Fo_b}|\widehat{Ste}_{b2}|)/(\sqrt{Fo_a}|\widehat{Ste}_{a1}|)$  equal respectively to 0.7071 and 0.0707, while in figure 5b such values are 1.4142 and 1.2728.

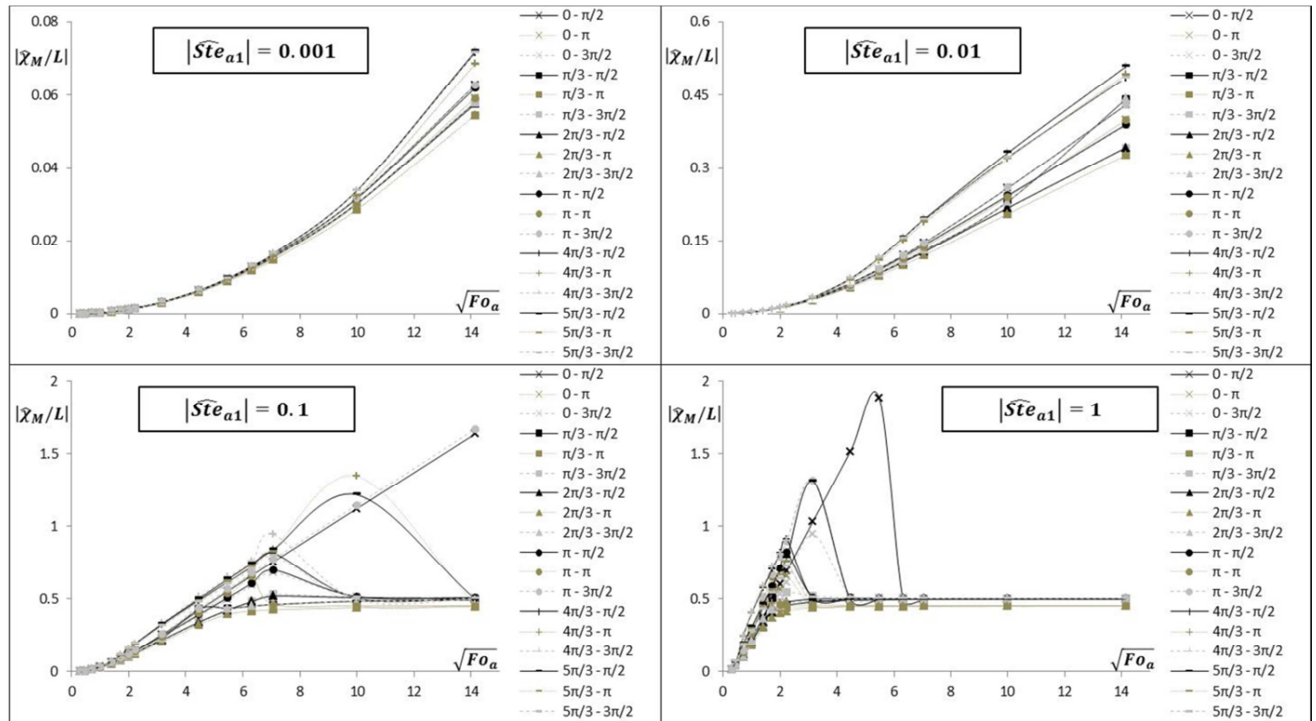


Figure 5a. Trend of  $|\hat{\chi}_M/L|$  as a function of  $\sqrt{Fo_a}$  for different values of the argument  $\varphi_1$  and time lag  $(\varphi_2 - \varphi_1)$  and for some characteristic values of  $|\widehat{Ste}_{a1}|$ .  $\bar{\chi}_M/L = 0.5$ ;  $\sqrt{Fo_b}/\sqrt{Fo_a} = 0.7071$ ;  $\sqrt{Fo_b}|\widehat{Ste}_{b2}|/\sqrt{Fo_a}|\widehat{Ste}_{a1}| = 0.0707$ . In the legend, the value of  $\varphi_1$  and of  $(\varphi_2 - \varphi_1)$  is reported for each curve in order.

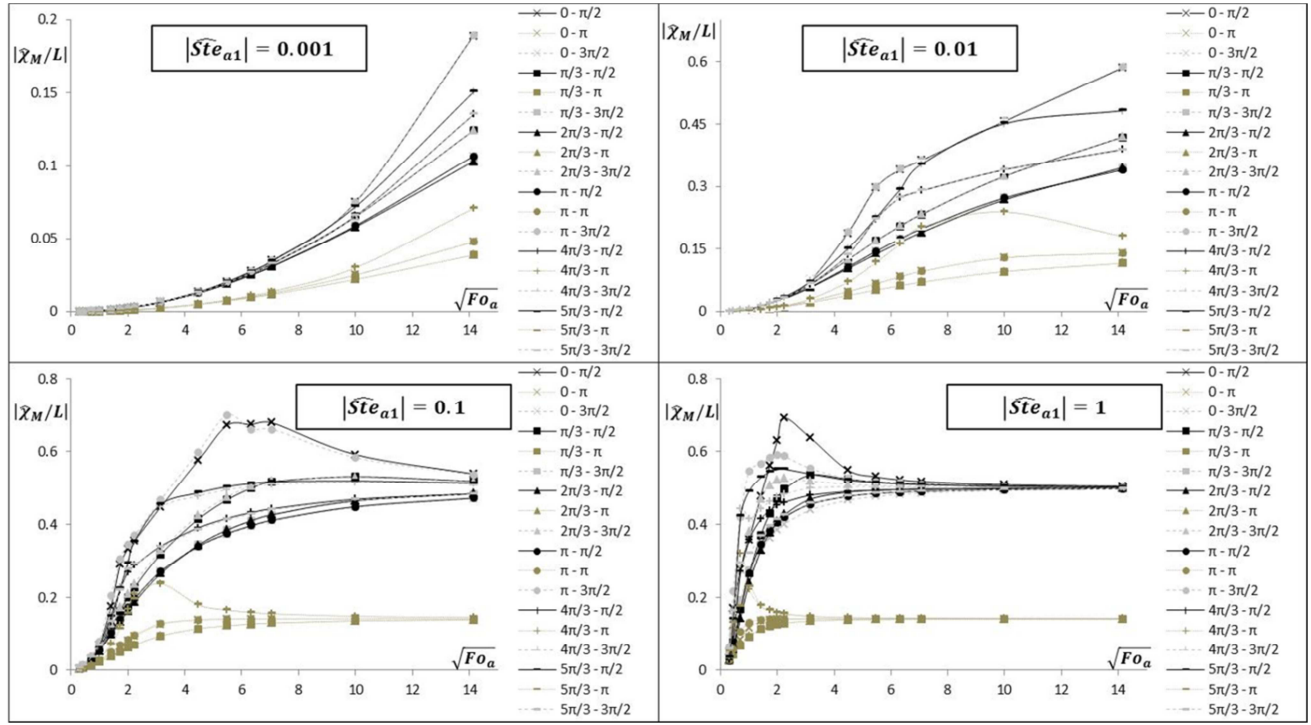


Figure 5b. Trend of  $|\hat{\chi}_M/L|$  as a function of  $\sqrt{Fo_a}$  for different values of the argument  $\varphi_1$  and time lag  $(\varphi_2 - \varphi_1)$  and for some characteristic values of  $|\hat{Ste}_{a1}|$ .  $\bar{\chi}_M/L = 0.5$ ;  $\sqrt{Fo_b}/\sqrt{Fo_a} = 1.4142$ ;  $\sqrt{Fo_b}|\hat{Ste}_{b2}|/\sqrt{Fo_a}|\hat{Ste}_{a1}| = 1.2728$ . In the legend, the value of  $\varphi_1$  and of  $(\varphi_2 - \varphi_1)$  is reported for each curve in order.

The two figures highlight that the variation of argument  $\varphi_1$  and of the time lag  $(\varphi_2 - \varphi_1)$  do not modify the dependence of the amplitude of  $\hat{\chi}_M/L$  on  $\sqrt{Fo_a}$  nor on  $|\hat{Ste}_{a1}|$ , presented in Figure 3. In particular, the regime value can still be evaluated with Eq. (13), and is a function of the time lag  $(\varphi_2 - \varphi_1)$ . Furthermore, the maximum overshoot and the corresponding value of  $\sqrt{Fo_a}$ , and the settling value of  $\sqrt{Fo_a}$  depend on  $\varphi_1$  and on  $(\varphi_2 - \varphi_1)$ . The increase of  $\sqrt{Fo_b}/\sqrt{Fo_a}$  and  $(\sqrt{Fo_b}|\hat{Ste}_{b2}|)/(\sqrt{Fo_a}|\hat{Ste}_{a1}|)$  gives rise to a reduction of the maximum overshoot, of the corresponding value of  $\sqrt{Fo_a}$ , and of the settling value of  $\sqrt{Fo_a}$ . For time lags equal to  $180^\circ$  the regime value of  $|\hat{\chi}_M/L|$  is the lowest and is equal to 0.1429 for  $\sqrt{Fo_b}/\sqrt{Fo_a} = 1.4142$  and  $(\sqrt{Fo_b}|\hat{Ste}_{b2}|)/(\sqrt{Fo_a}|\hat{Ste}_{a1}|) = 1.2728$ , while it is equal to 0.4524 for  $\sqrt{Fo_b}/\sqrt{Fo_a} = 0.7071$  and  $(\sqrt{Fo_b}|\hat{Ste}_{b2}|)/(\sqrt{Fo_a}|\hat{Ste}_{a1}|) = 0.0707$ .

Figures 6a and 6b show the dependence of the argument  $\zeta$  of  $\hat{\chi}_M/L$  on  $\sqrt{Fo_a}$  and on  $|\hat{Ste}_{a1}|$  upon the variation of the time lag  $(\varphi_2 - \varphi_1)$  for different values of argument  $\varphi_1$  and for constant values of  $\sqrt{Fo_b}/\sqrt{Fo_a}$  and of  $(\sqrt{Fo_b}|\hat{Ste}_{b2}|)/(\sqrt{Fo_a}|\hat{Ste}_{a1}|)$ . Such dependence is identical to that already shown in Figure 4.

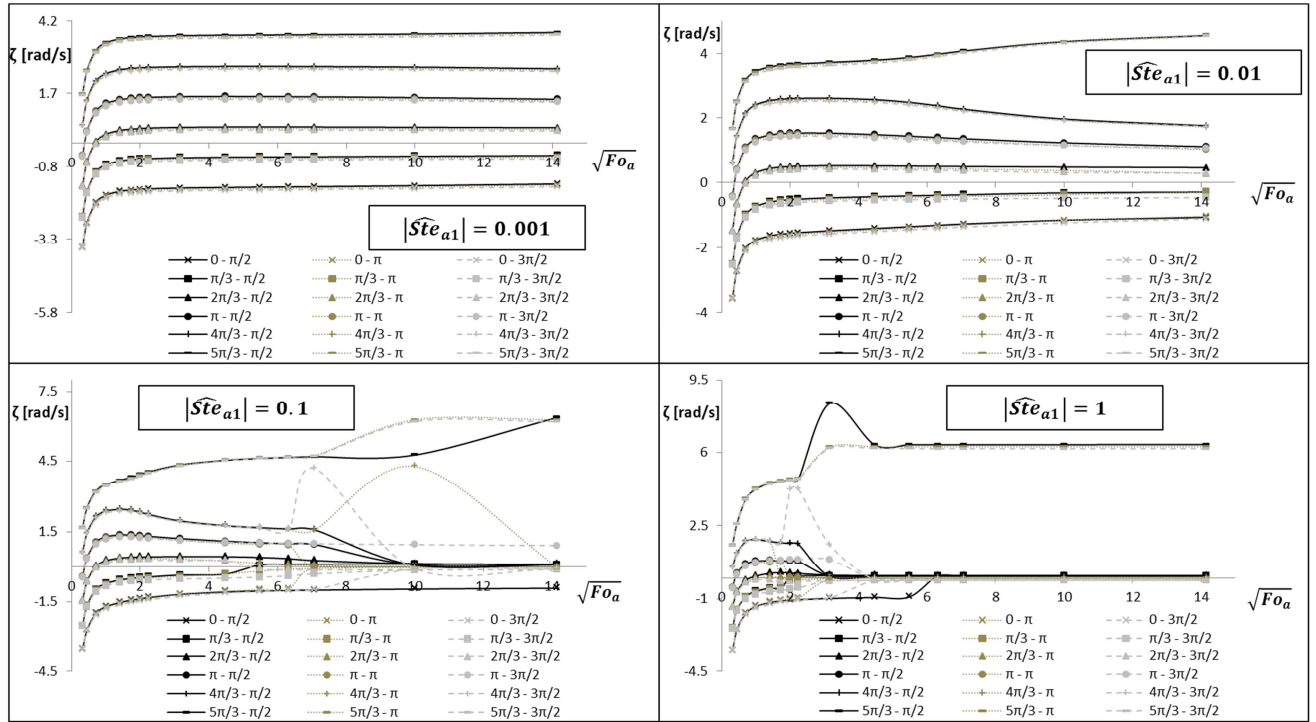


Figure 6a. Trend of  $\zeta = \arg(\hat{\chi}_M/L)$  as a function of  $\sqrt{Fo_a}$  for different values of the argument  $\varphi_1$  and time lag  $(\varphi_2 - \varphi_1)$  and for some characteristic values of  $|\widehat{Ste}_{a1}|$ .

$\bar{\chi}_M/L = 0.5$ ;  $\sqrt{Fo_b}/\sqrt{Fo_a} = 0.7071$ ;  $\sqrt{Fo_b}|\widehat{Ste}_{b2}|/\sqrt{Fo_a}|\widehat{Ste}_{a1}| = 0.0707$ . In the legend, the value of  $\varphi_1$  and  $(\varphi_2 - \varphi_1)$  is reported for each curve in order.

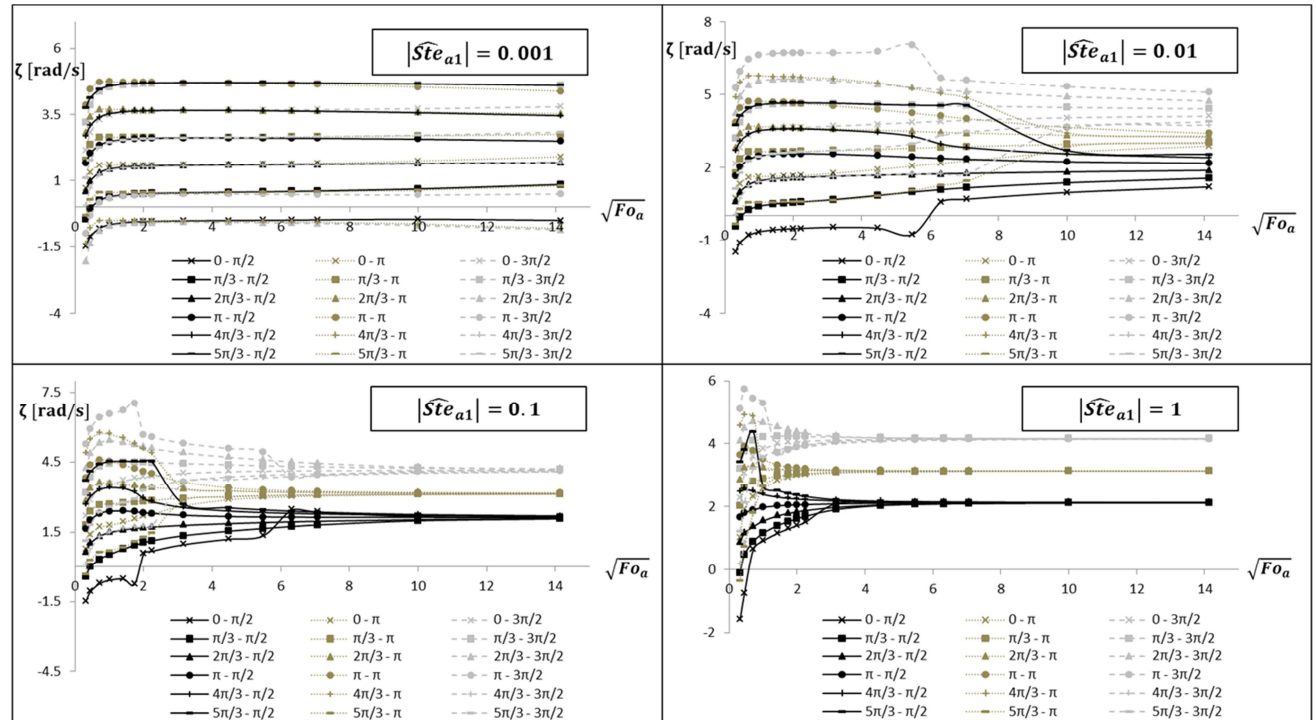


Figure 6b. Trend of  $\zeta = \arg(\hat{\chi}_M/L)$  as a function of  $\sqrt{Fo_a}$  for different values of the argument  $\varphi_1$  and time lag  $(\varphi_2 - \varphi_1)$  and for some characteristic values of  $|\widehat{Ste}_{a1}|$ .

$\bar{\chi}_M/L = 0.5$ ;  $\sqrt{Fo_b}/\sqrt{Fo_a} = 1.4142$ ;  $\sqrt{Fo_b}|\widehat{Ste}_{b2}|/\sqrt{Fo_a}|\widehat{Ste}_{a1}| = 1.2728$ . In the legend, the value of  $\varphi_1$  and  $(\varphi_2 - \varphi_1)$  is reported for each curve in order.

The regime value is independent of time lag  $(\varphi_2 - \varphi_1)$  and of argument  $\varphi_1$ ; it is equal to 0, or to  $2\pi$  for a greater graphic evidence, for the lower values of  $\sqrt{Fo_b}/\sqrt{Fo_a}$  and  $(\sqrt{Fo_b}|\widehat{Ste}_{b2}|)/(\sqrt{Fo_a}|\widehat{Ste}_{a1}|)$ . Instead, time lag  $(\varphi_2 - \varphi_1)$  and argument  $\varphi_1$  influence the abrupt variation in the argument and the corresponding value of  $\sqrt{Fo_a}$ . The increase in the thermal parameters  $\sqrt{Fo_b}/\sqrt{Fo_a}$  and  $(\sqrt{Fo_b}|\widehat{Ste}_{b2}|)/(\sqrt{Fo_a}|\widehat{Ste}_{a1}|)$  determines a dependence of the regime value of  $\zeta$  on the time lag  $(\varphi_2 - \varphi_1)$ .

The influence of the steady component on the amplitude of  $\widehat{\chi}_M/L$ , upon variation of  $\sqrt{Fo_a}$  for different values of  $|\widehat{Ste}_{a1}|$  is shown in Figure 7. The figure is relative to constant values of  $\sqrt{Fo_b}/\sqrt{Fo_a}$  and  $(\sqrt{Fo_b}|\widehat{Ste}_{b2}|)/(\sqrt{Fo_a}|\widehat{Ste}_{a1}|)$ , and of  $\varphi_1$  and  $(\varphi_2 - \varphi_1)$ .

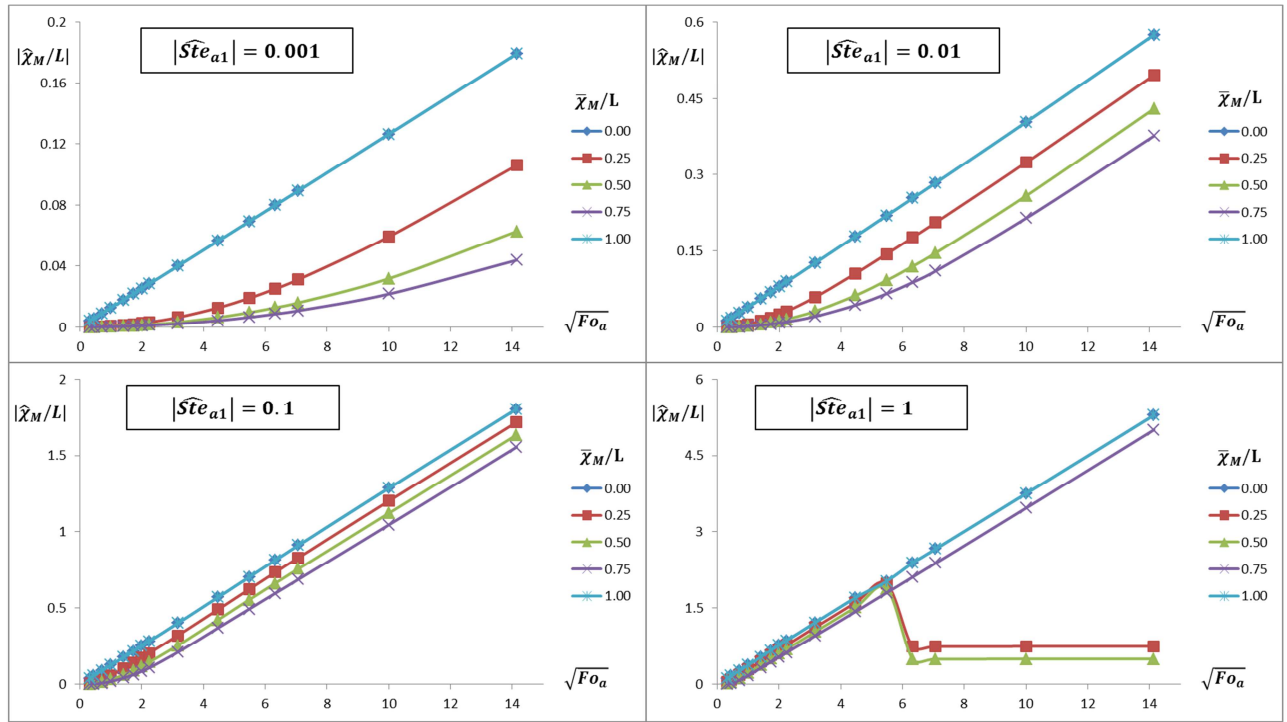


Figure 7. Trend of  $|\widehat{\chi}_M/L|$  as a function of  $\sqrt{Fo_a}$  on variation of  $\bar{\chi}_M/L$  and for some characteristic values of  $|\widehat{Ste}_{a1}|$ .  $\sqrt{Fo_b}/\sqrt{Fo_a} = 0.7071$  and  $(\sqrt{Fo_b}|\widehat{Ste}_{b2}|)/(\sqrt{Fo_a}|\widehat{Ste}_{a1}|) = 0.0707$ ,  $\varphi_1 = 0$  and  $(\varphi_2 - \varphi_1) = \pi/2$ .

For values of  $\sqrt{Fo_a}$  lesser than that corresponding to the maximum overshoot, the amplitude of  $\widehat{\chi}_M/L$  increases with a decrease of  $\bar{\chi}_M/L$ . In the considered variation interval of the thermal parameter  $\sqrt{Fo_a}$ , only the curves with  $\bar{\chi}_M/L = 0.5$  and  $\bar{\chi}_M/L = 0.25$  attain the regime value which is equal to 0.5 and 0.75 respectively; higher values of  $\sqrt{Fo_a}$  are required for other values of  $\bar{\chi}_M/L$ . Furthermore, the trends of the amplitude of  $\widehat{\chi}_M/L$  on variation of  $\sqrt{Fo_a}$  calculated for  $\bar{\chi}_M/L = 0$  and for  $\bar{\chi}_M/L = 1$  result as coinciding.

Figure 8 shows the dependence of argument  $\zeta$  of  $\hat{\chi}_M/L$  on  $\sqrt{Fo_a}$  and on  $|\widehat{Ste}_{a1}|$  upon the variation of the steady component  $\bar{\chi}_M/L$ , for constant values of  $\sqrt{Fo_b}/\sqrt{Fo_a}$  and  $(\sqrt{Fo_b}|\widehat{Ste}_{b2}|)/(\sqrt{Fo_a}|\widehat{Ste}_{a1}|)$ , and of  $\varphi_1$  and  $(\varphi_2 - \varphi_1)$ .

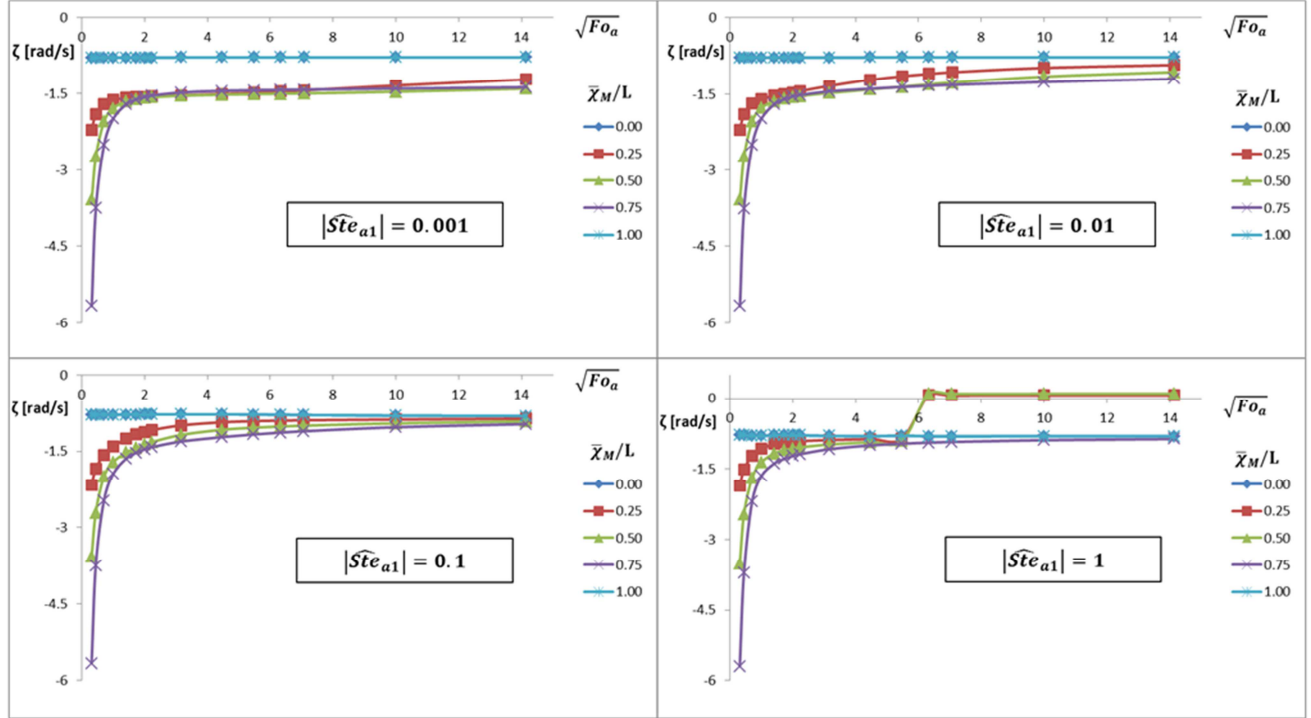


Figure 8. Trend of  $\zeta = \arg(\hat{\chi}_M/L)$  as a function of  $\sqrt{Fo_a}$  for some characteristic values of  $\bar{\chi}_M/L$  on variation of  $|\widehat{Ste}_{a1}|$ .  $\sqrt{Fo_b}/\sqrt{Fo_a} = 0.7071$  and  $(\sqrt{Fo_b}|\widehat{Ste}_{b2}|)/(\sqrt{Fo_a}|\widehat{Ste}_{a1}|) = 0.0707$ ,  $\varphi_1 = 0$  and  $(\varphi_2 - \varphi_1) = \pi/2$ .

For values of  $\sqrt{Fo_a}$  lesser than that corresponding to the abrupt variation, the argument  $\zeta$  increases if  $\bar{\chi}_M/L$  decreases. In the considered field of variability of the thermal parameters, only for  $\bar{\chi}_M/L = 0.5$  and for  $\bar{\chi}_M/L = 0.25$  is the regime value attained, and the abrupt variation in  $\zeta$  occurs for a value of  $\sqrt{Fo_a}$  equal to that corresponding to the maximum overshoot of  $|\hat{\chi}_M/L|$ . Also in this case, for the other values of  $\bar{\chi}_M/L$  the variability interval of  $\sqrt{Fo_a}$  is not sufficient to attain the regime value. Moreover, the argument  $\zeta$  is constant upon variation of  $\sqrt{Fo_a}$  and of  $|\widehat{Ste}_{a1}|$  for  $\bar{\chi}_M/L = 0$  and for  $\bar{\chi}_M/L = 1$ .

#### 4. Frequency response of the Stefan Problem

The analysis reported in Section 3 can be reformulated in the frequency domain since the Fourier number, which is reported on the horizontal axis in the previous representations, contains the oscillation period. The amplitude in decibel and argument  $\hat{\chi}_M/L$  in degrees as a function of the logarithm of the reciprocal of the Fourier number, namely dimensionless angular frequency



$\omega^* = 1/Fo_a = (L^2/(2\pi\alpha)\omega)$  is represented in Figure 9. Such representation is used in the theory of dynamic systems to study the frequency response of a system subject to periodic signals and it is known as Bode diagram [49, 50]. The curves reported in figure 9 relate to  $\bar{\chi}_M/L = 0.5$ ,  $|\widehat{Ste}_{a1}| = 1$ ,  $\sqrt{Fo_b}/\sqrt{Fo_a} = 0.7071$ ,  $(\sqrt{Fo_b}|\widehat{Ste}_{b2}|)/(\sqrt{Fo_a}|\widehat{Ste}_{a1}|) = 0.0707$ ,  $(\varphi_2 - \varphi_1) = \pi$ , and for some values of  $\varphi_1$ .

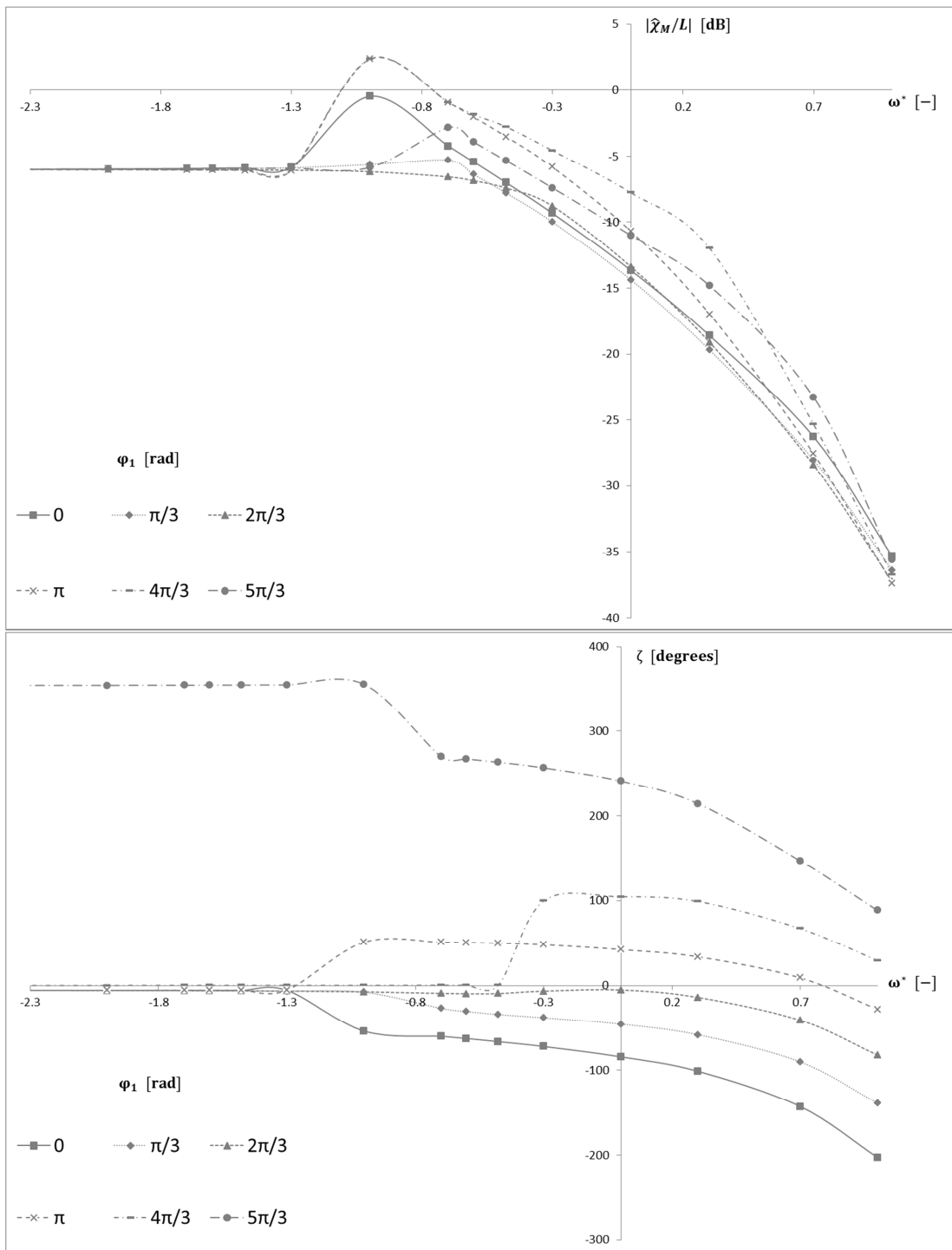


Figure 9. Bode diagram of  $\hat{\chi}_M/L$  as a function of the dimensionless angular frequency  $\omega^*$ .  $\bar{\chi}_M/L = 0.5$ ,  $|\widehat{Ste}_{a1}| = 1$ ,  $\sqrt{Fo_b}/\sqrt{Fo_a} = 0.7071$ ,  $(\sqrt{Fo_b}|\widehat{Ste}_{b2}|)/(\sqrt{Fo_a}|\widehat{Ste}_{a1}|) = 0.0707$ ,  $(\varphi_2 - \varphi_1) = \pi$  and for some characteristic values of  $\varphi_1$ .

Such trends show that the oscillating component  $\hat{\chi}_M/L$ , in terms of amplitude and argument, has a trend that is very similar to a frequency response that in the Laplace domain is equal to the transfer function of a dynamic linear system of the third order with a finite time-delay [49, 50]:

$$G(s) = \frac{K}{(s^2 + 2\delta\omega_n s + \omega_n^2)} \frac{(s + z)}{(s + p)} \exp(-s\tau) \quad (14)$$

which rewritten in the domain of the frequencies represents the frequency response:

$$G(j\omega^*) = \frac{K}{(\omega_n^2 + 2j\delta\omega_n\omega^* - \omega^{*2})} \frac{(j\omega^* + z)}{(j\omega^* + p)} \exp(-j\omega^*\tau) \quad (15)$$

The function  $G(s)$  is represented by the gain constant  $K$ , by a couple of real or complex conjugates poles  $p_{1,2} = -\omega_n\delta \pm \omega_n\sqrt{(\delta^2 - 1)}$ , by a pole  $-p$ , by a zero  $-z$  and by a finite time-delay  $\tau$ . The gain constant  $K$  represents the value of the frequency response for  $\omega^* = 0$  or the regime value. The couple of poles, characterised by natural angular frequency  $\omega_n$  and by the damping factor  $\delta$ , for values of  $\delta < 1$  are complex conjugates and for  $\delta \geq 1$  are real.

At low frequencies, this couple of poles for values of  $\delta < \sqrt{2}/2$  determine maximum overshoot of the amplitude and an abrupt reduction or increase of the argument in correspondence of the dimensionless resonance angular frequency. For values of  $\delta \geq \sqrt{2}/2$ , the maximum overshoot of the amplitude and the discontinuity of the argument are no longer present.

At high frequencies, the couple of poles considered, gives rise to a variation in the slope of the amplitude of  $-40$  dB/decade.

At medium frequencies, zero and the pole determine a variation in the slope of the amplitude of  $\pm 20$  dB/decade starting from the relative break point and a variation of the argument of  $\pm \pi/2$  around the relative break point.

The finite time-delay represents the sole contribution which influences the argument at high frequencies. In fact, the response function of the time-delay presents a unitary amplitude on all frequencies and an argument delay which grows linearly, with slope  $\tau$ , on the increase in frequency.

All these parameters are correlated with the thermal parameters reported in Table 1, whose variations determine a different dynamic behaviour of the PCM layer.

Figures 10 and 11 show the comparison between the analytically plotted Bode diagram and that obtained with the frequency response function Eq. (15) in the case in which the argument of the loading temperature on face 1 is equal respectively to  $\varphi_1 = 0$  and  $\varphi_1 = 4\pi/3$ .

Such approximate functions respectively have the form:

$$G(j\omega^*) = \frac{1.836}{(0.053 + j0.299\omega^* - \omega^{*2})} \frac{(j\omega^* + 0.13)}{(j\omega^* + 8)} \exp(-j0.1\omega^*) \quad (16)$$

with  $K = 1.836$ ,  $\omega_n = 0.23$ ,  $\delta = 0.65$ ,  $p = 8$ ,  $z = 0.13$  and  $\tau = 0.1$

and

$$G(j\omega^*) = \frac{1.721}{(0.490 - j0.280\omega^* - \omega^{*2})} \frac{(j\omega^* + 1)}{(j\omega^* + 8)} \exp(-j0.2\omega^*) \quad (17)$$

with  $K = 1.721$ ,  $\omega_n = 0.7$ ,  $\delta = -0.2$ ,  $p = -8$ ,  $z = -1$  and  $\tau = 0.2$ .

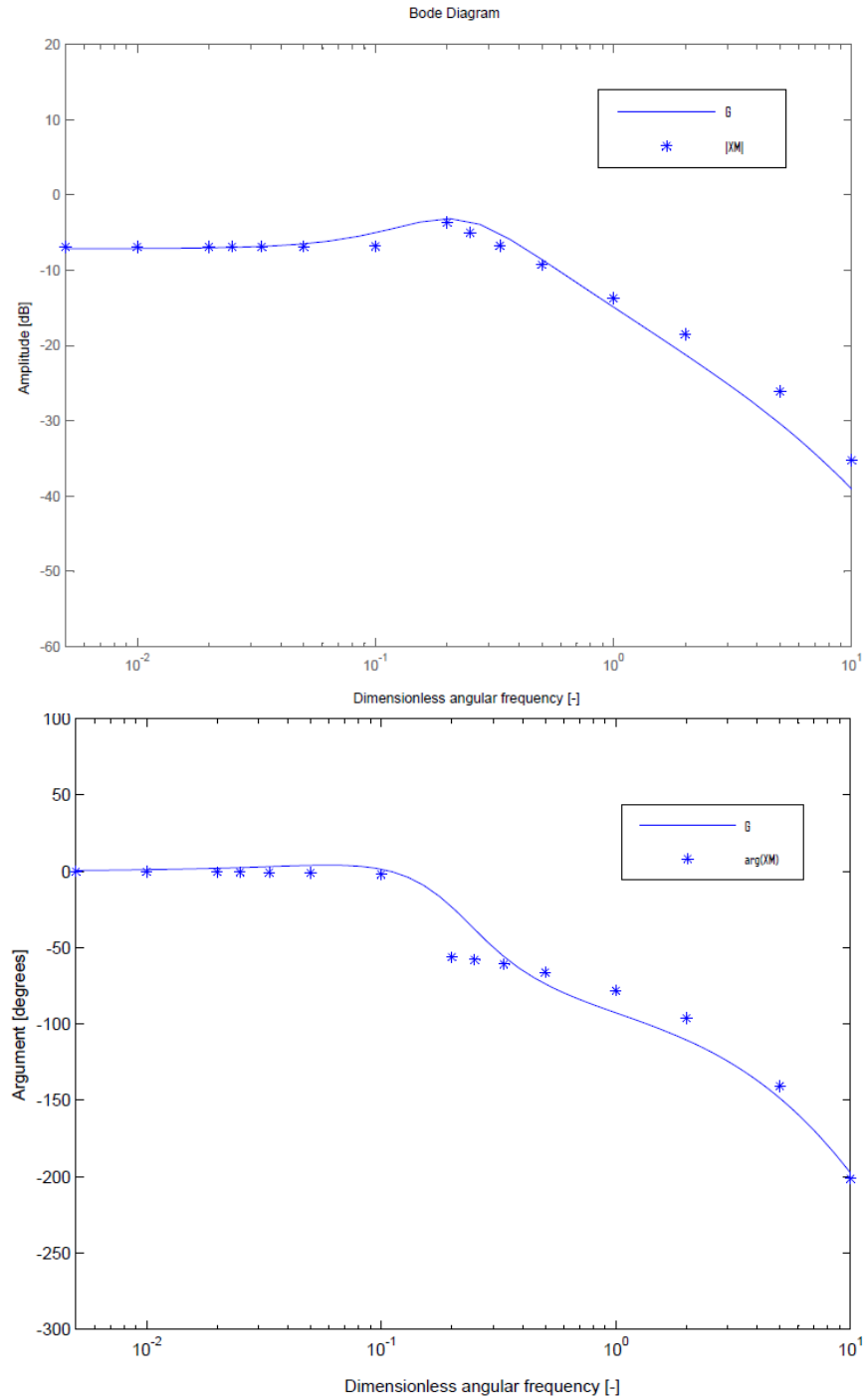


Figure 10. Comparison between the analytically determined Bode diagram of  $\hat{\chi}_M/L$  and that obtained with the frequency response function Eq. (16), as a function of the dimensionless angular frequency  $\omega^*$ .  $\bar{\chi}_M/L = 0.5$ ,  $|\widehat{Ste}_{a1}| = 1$ ,  $\sqrt{Fo_b}/\sqrt{Fo_a} = 0.7071$ ,  $(\sqrt{Fo_b}|\widehat{Ste}_{b2}|)/(\sqrt{Fo_a}|\widehat{Ste}_{a1}|) = 0.0707$ ,  $(\varphi_2 - \varphi_1) = \pi$  and  $\varphi_1 = 0$ .

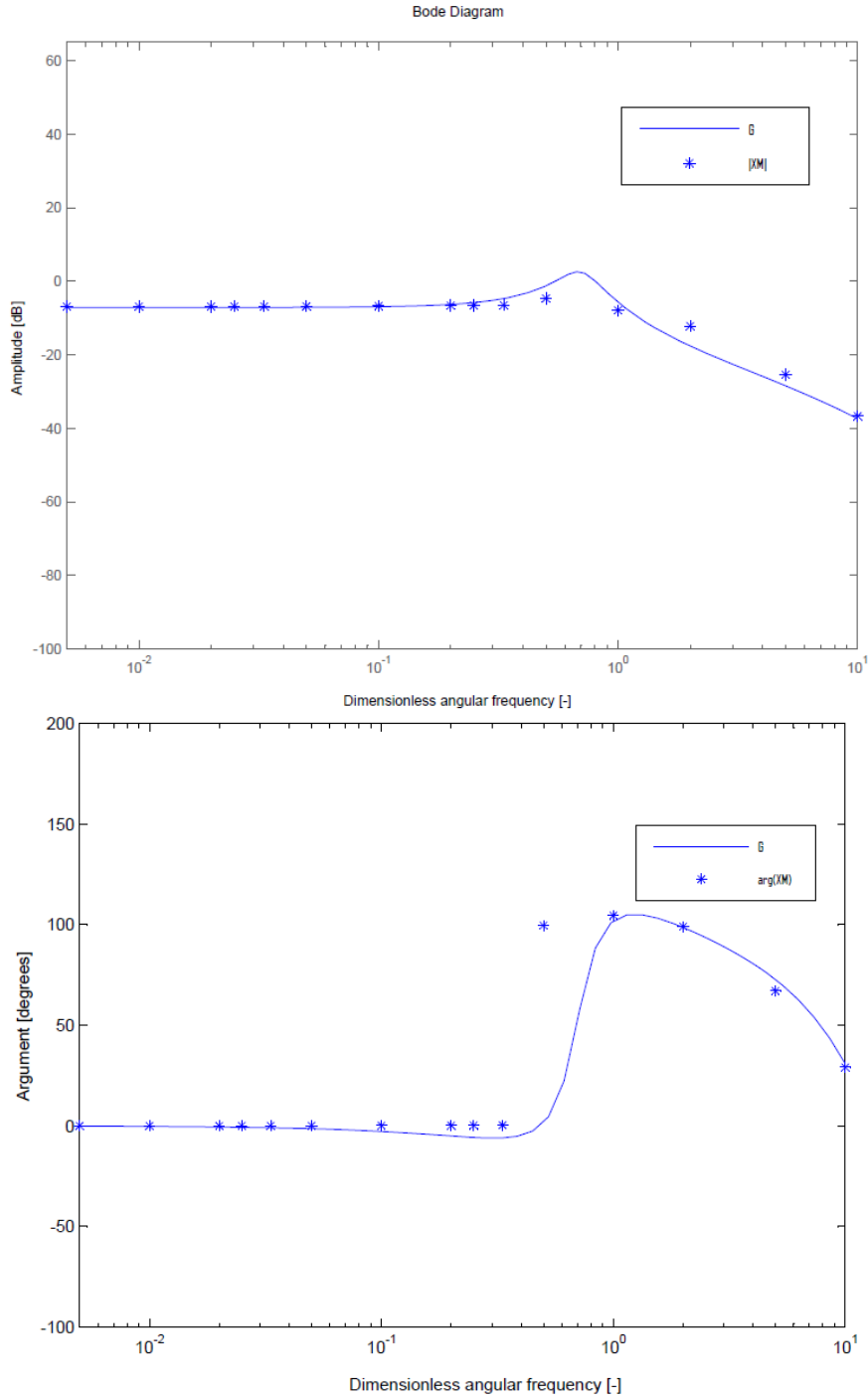


Figure 11. Comparison between the analytically determined Bode diagram  $\hat{\chi}_M/L$  and that obtained with the frequency response function (17), as a function of the dimensionless angular frequency  $\omega^*$ .  $\bar{\chi}_M/L = 0.5$ ,  $|\widehat{Ste}_{a1}| = 1$ ,  $\sqrt{Fo_b}/\sqrt{Fo_a} = 0.7071$ ,  $(\sqrt{Fo_b}|\widehat{Ste}_{b2}|)/(\sqrt{Fo_a}|\widehat{Ste}_{a1}|) = 0.0707$ ,  $(\varphi_2 - \varphi_1) = \pi$  and  $\varphi_1 = 4\pi/3$ .

The comparison highlights a high accuracy of the frequency response and a greater adherence between the two profiles can be obtained with a transfer function  $G(s)$  of an order greater than the third order, which is obtainable adding, in the same number, further poles and zeros.

## 5. An approximate solution of the Stefan problem in steady periodic regime

### 5.1. Mathematical formulation

In the thermal analysis of a PCM layer it is useful to have an expression in an explicit form of the oscillating component of the bi-phase interface position  $\hat{\chi}_M/L$  to be substituted in Eqs. (6)-(9) to obtain the mathematical expression of the temperature and heat flux field as a function of only dimensionless thermal parameters and boundary loadings. This was obtained approximating hyperbolic functions in Eq. (12) with a MacLaurin series expansion, truncated to first order [51]:

$$\sinh \left[ (1+j) \sqrt{\frac{\pi}{\text{Fo}_a}} \left( \frac{\bar{\chi}_M}{L} + \frac{\hat{\chi}_M}{L} \right) \right] \approx \left[ (1+j) \sqrt{\frac{\pi}{\text{Fo}_a}} \left( \frac{\bar{\chi}_M}{L} + \frac{\hat{\chi}_M}{L} \right) \right] \quad (18)$$

$$\sinh \left[ (1+j) \sqrt{\frac{\pi}{\text{Fo}_a}} \frac{1}{\sqrt{\frac{\text{Fo}_b}{\text{Fo}_a}}} \left( 1 - \frac{\bar{\chi}_M}{L} - \frac{\hat{\chi}_M}{L} \right) \right] \approx \left[ (1+j) \sqrt{\frac{\pi}{\text{Fo}_a}} \frac{1}{\sqrt{\frac{\text{Fo}_b}{\text{Fo}_a}}} \left( 1 - \frac{\bar{\chi}_M}{L} - \frac{\hat{\chi}_M}{L} \right) \right]$$

Taking the previous relations into account, Eq. (12) becomes:

$$\frac{1}{2\pi} \text{Fo}_a \widehat{\text{Ste}}_{a1} \left\{ \frac{1}{\frac{\bar{\chi}_M}{L} + \frac{\hat{\chi}_M}{L}} + \frac{\frac{\text{Fo}_b \widehat{\text{Ste}}_{b2}}{\text{Fo}_a \widehat{\text{Ste}}_{a1}}}{1 - \frac{\bar{\chi}_M}{L} - \frac{\hat{\chi}_M}{L}} \right\} = j \frac{\hat{\chi}_M}{L} \quad (19)$$

which can be rewritten in the form:

$$\left( \frac{\bar{\chi}_M}{L} + \frac{\hat{\chi}_M}{L} \right)^3 - \left( 1 + \frac{\bar{\chi}_M}{L} \right) \left( \frac{\bar{\chi}_M}{L} + \frac{\hat{\chi}_M}{L} \right)^2 + \left[ \frac{\bar{\chi}_M}{L} + \frac{j}{2\pi} \text{Fo}_a \widehat{\text{Ste}}_{a1} \left( 1 - \frac{\text{Fo}_b \widehat{\text{Ste}}_{b2}}{\text{Fo}_a \widehat{\text{Ste}}_{a1}} \right) \right] \left( \frac{\bar{\chi}_M}{L} + \frac{\hat{\chi}_M}{L} \right) - \frac{j}{2\pi} \text{Fo}_a \widehat{\text{Ste}}_{a1} = 0 \quad (20)$$

Eq. (20) is an algebraic equation of the third degree with coefficients that are in part real and in part complex, which admit three roots, of which only one is the solution to the Eq. (12). The three roots are expressed by Eqs. (21).

$$\frac{\hat{\chi}_M^I}{L} = C_I - \frac{C_{III}}{C_I} - C_{II} \quad (21. a)$$

$$\frac{\hat{\chi}_M^{II}}{L} = - \left( \frac{C_I}{2} + \frac{C_{III}}{2C_I} + C_{II} \right) + j \frac{\sqrt{3}}{2} \left( \frac{C_{III}}{C_I} + C_I \right) \quad (21. b)$$

$$\frac{\hat{\chi}_M^{III}}{L} = -\left(\frac{C_I}{2} + \frac{C_{III}}{2C_I} + C_{II}\right) - j\frac{\sqrt{3}}{2}\left(\frac{C_{III}}{C_I} + C_I\right) \quad (21.c)$$

with  $C_I$ ,  $C_{II}$  and  $C_{III}$  given by relations:

$$C_I = \left\{ \left[ \left( \frac{jFo_a\widehat{Ste}_{a1}\left(1 - \frac{\bar{\chi}_M}{L} + \frac{Fo_b\widehat{Ste}_{b2}\bar{\chi}_M}{Fo_a\widehat{Ste}_{a1}L}\right)}{4\pi} - C_{II}^3 + \frac{jC_{II}\left[2\pi j\frac{\bar{\chi}_M}{L}\left(1 - \frac{\bar{\chi}_M}{L}\right) + Fo_a\widehat{Ste}_{a1}\left(1 - \frac{Fo_b\widehat{Ste}_{b2}}{Fo_a\widehat{Ste}_{a1}}\right)\right]}{4\pi} \right)^2 \right. \right. \\ \left. \left. + C_{III}^3 \right]^{\frac{1}{2}} + \frac{jFo_a\widehat{Ste}_{a1}\left(1 - \frac{\bar{\chi}_M}{L} + \frac{Fo_b\widehat{Ste}_{b2}\bar{\chi}_M}{Fo_a\widehat{Ste}_{a1}L}\right)}{4\pi} - C_{II}^3 \right. \\ \left. + \frac{jC_{II}\left[2\pi j\frac{\bar{\chi}_M}{L}\left(1 - \frac{\bar{\chi}_M}{L}\right) + Fo_a\widehat{Ste}_{a1}\left(1 - \frac{Fo_b\widehat{Ste}_{b2}}{Fo_a\widehat{Ste}_{a1}}\right)\right]}{4\pi} \right]^{\frac{1}{3}} \right\} \quad (22a)$$

$$C_{II} = \frac{2\frac{\bar{\chi}_M}{L} - 1}{3} \quad (22b)$$

$$C_{III} = \frac{\left[2\pi j\frac{\bar{\chi}_M}{L}\left(1 - \frac{\bar{\chi}_M}{L}\right) + Fo_a\widehat{Ste}_{a1}\left(1 - \frac{Fo_b\widehat{Ste}_{b2}}{Fo_a\widehat{Ste}_{a1}}\right)\right]j}{6\pi} - C_{II}^2 \quad (22c)$$

Eqs. (21) and (22) demonstrate that  $\hat{\chi}_M/L$  is a function of the product of the Fourier number and the Stefan number for phase (a) and for phase (b). The amplitude of such a product assumes the form:

$$Fo|\widehat{Ste}| = \left(\frac{\lambda}{L}|\hat{\vartheta}|P\right)\left(\frac{1}{\rho HL}\right) \quad (23)$$

and represents the ratio between the specific energy ( $J/m^2$ ), that is transferred for conduction in time  $t=P$ , oscillation period, in the layer of thickness  $L$  due to the difference in temperature  $|\hat{\vartheta}|$ , and the specific energy required for the phase change of the entire layer. It is necessary to highlight that in Eq. (23) no sensible heat capacity term in relation to the two phases is present, demonstrating that Eq. (18) gives rise to the linearisation at each time instant of the trend of the amplitude of the temperature oscillating component  $|\hat{\vartheta}_a(x)|$  and  $|\hat{\vartheta}_b(x)|$  in the two phases.

Substituting the complex expression  $\hat{\chi}_M/L$  in Eqs. (6)-(9), the phasors associated to the oscillating components of the temperature,  $\hat{\vartheta}_a(x)$  and  $\hat{\vartheta}_b(x)$ , and of the heat flux,  $\hat{\Phi}_a(x)$  and  $\hat{\Phi}_b(x)$ , in phase (a) and phase (b), as a function of the sole dimensionless thermal parameters and boundary loadings  $\hat{\vartheta}_1$  and  $\hat{\vartheta}_2$  are obtained.

The criteria for the selection of the solution root consists in the verification of the exact Eq. (12). According to the values that are assumed by the complex coefficients of the approximate Eq. (20) the root solution changes. In particular, comparing the trend of the amplitude and of the argument of the exact solution and the trend of the three roots of the approximate equation as a function of the thermal parameter  $Fo_a|\widehat{Ste}_{a1}|$ , it can be stated that the exact solution constitutes an envelope of the three roots, which modify upon variation of  $Fo_b\widehat{Ste}_{b2}/Fo_a\widehat{Ste}_{a1}$ . The latter thermal parameter, with reference to the boundary temperatures, has an amplitude proportional to attenuation and the argument equal to the time lag. The establishing of a criterion for the identification of the solution root, starting from the values assumed by the thermal parameters, appears complex.

Considering the field of variation of the thermal parameters reported in Table 1, applying the previous criterion, of 1680 solutions of the exact equation, 14.76% of the cases admit as root of the approximate Eq. (21.a), 65.42 % admit Eq. (21.b) and 19.82 % Eq. (21.c).

The trends of the amplitude and argument of  $\hat{\chi}_M/L$  obtained with approximate solution Eq. (21) and with exact solution Eq. (12) as a function of the new thermal parameters  $Fo_a|\widehat{Ste}_{a1}|$  and  $(Fo_b|\widehat{Ste}_{b2}|)/(Fo_a|\widehat{Ste}_{a1}|)$  are almost identical.

## 5.2. Accuracy

Only three thermal parameters appear in the approximate equation, namely  $Fo_a\widehat{Ste}_{a1}$ ,  $(Fo_b|\widehat{Ste}_{b2}|)/(Fo_a|\widehat{Ste}_{a1}|)$  and  $\bar{\chi}_M/L$ . The limits of validity of such a solution were determined evaluating the relative error  $\varepsilon = [(\hat{\chi}_M/L)_{\text{exac}} - (\hat{\chi}_M/L)_{\text{appr}}]/(\hat{\chi}_M/L)_{\text{exac}}$  which is committed in the determination of the amplitude and of the argument of  $\hat{\chi}_M/L$ . The trend of the relative error of the amplitude  $|\hat{\chi}_M/L|$ , for  $\bar{\chi}_M/L = 0.5$ , upon the variation of  $\sqrt{Fo_a}$  and of thermal parameters  $(\sqrt{Fo_b}|\widehat{Ste}_{b2}|)/(\sqrt{Fo_a}|\widehat{Ste}_{a1}|)$  and  $\sqrt{Fo_b}/\sqrt{Fo_a}$ , for some characteristic values of  $|\widehat{Ste}_{a1}|$  are reported in Figure 12.



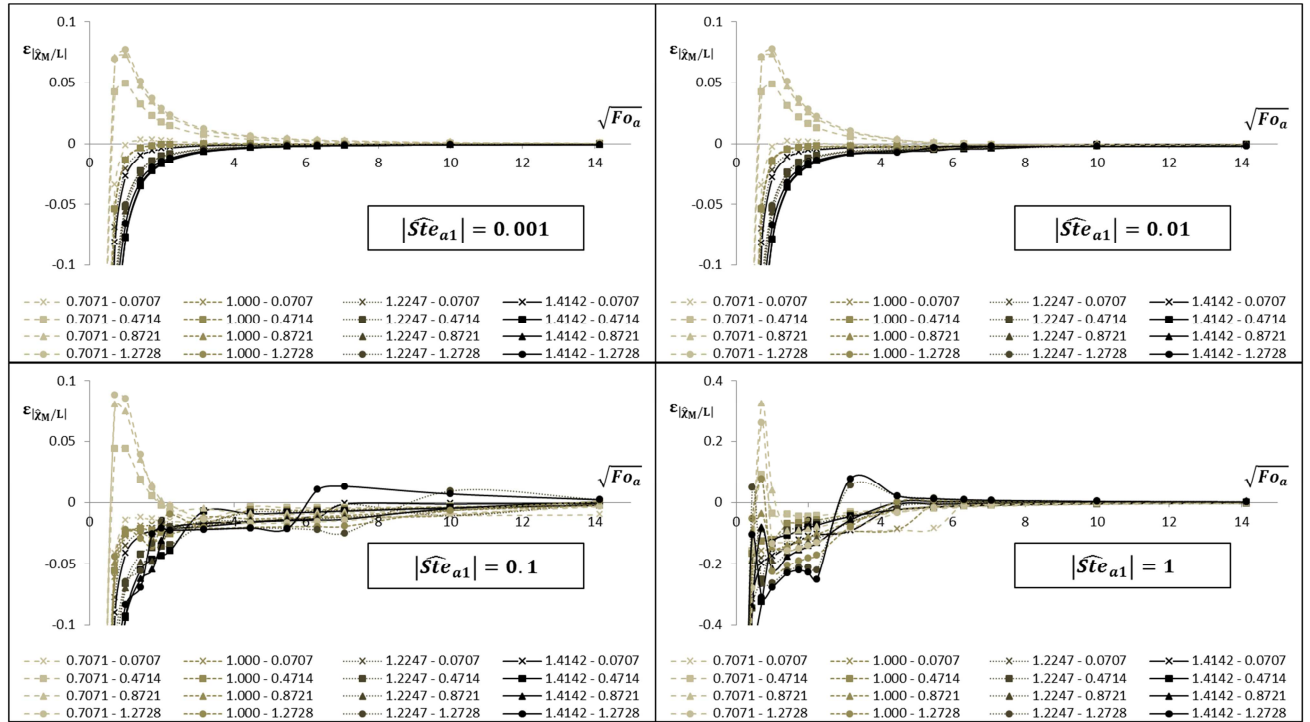


Figure 12. Trend of the relative error on the amplitude  $|\hat{\chi}_M/L|$  as a function of  $\sqrt{Fo_a}$  for different values of the thermal parameters  $\sqrt{Fo_b}/\sqrt{Fo_a}$  and  $(\sqrt{Fo_b}|\widehat{Ste}_{b2}|)/(\sqrt{Fo_a}|\widehat{Ste}_{a1}|)$  and for some characteristic values of  $|\widehat{Ste}_{a1}|$ .  $\bar{\chi}_M/L = 0.5$ . In the legend, the value of  $\sqrt{Fo_b}/\sqrt{Fo_a}$  and of  $(\sqrt{Fo_b}|\widehat{Ste}_{b2}|)/(\sqrt{Fo_a}|\widehat{Ste}_{a1}|)$  is reported for each curve in order.

Figure 12 highlights that for any value of the thermal parameters  $(Fo_b|\widehat{Ste}_{b2}|)/(Fo_a|\widehat{Ste}_{a1}|)$ ,  $\sqrt{Fo_b}/\sqrt{Fo_a}$  and of  $|\widehat{Ste}_{a1}|$  the relative error of the amplitude  $|\hat{\chi}_M/L|$  has an asymptotic trend, tending to zero with an increase in  $\sqrt{Fo_a}$ , as also shown by Eqs. (18). For reduced values of  $\sqrt{Fo_a}$  the error increases for low values of the thermal parameters  $(Fo_b|\widehat{Ste}_{b2}|)/(Fo_a|\widehat{Ste}_{a1}|)$  and  $\sqrt{Fo_b}/\sqrt{Fo_a}$ . Analogously, in Figure 13, the corresponding values of the error relative on the argument  $\zeta$  of  $\hat{\chi}_M/L$  are reported.

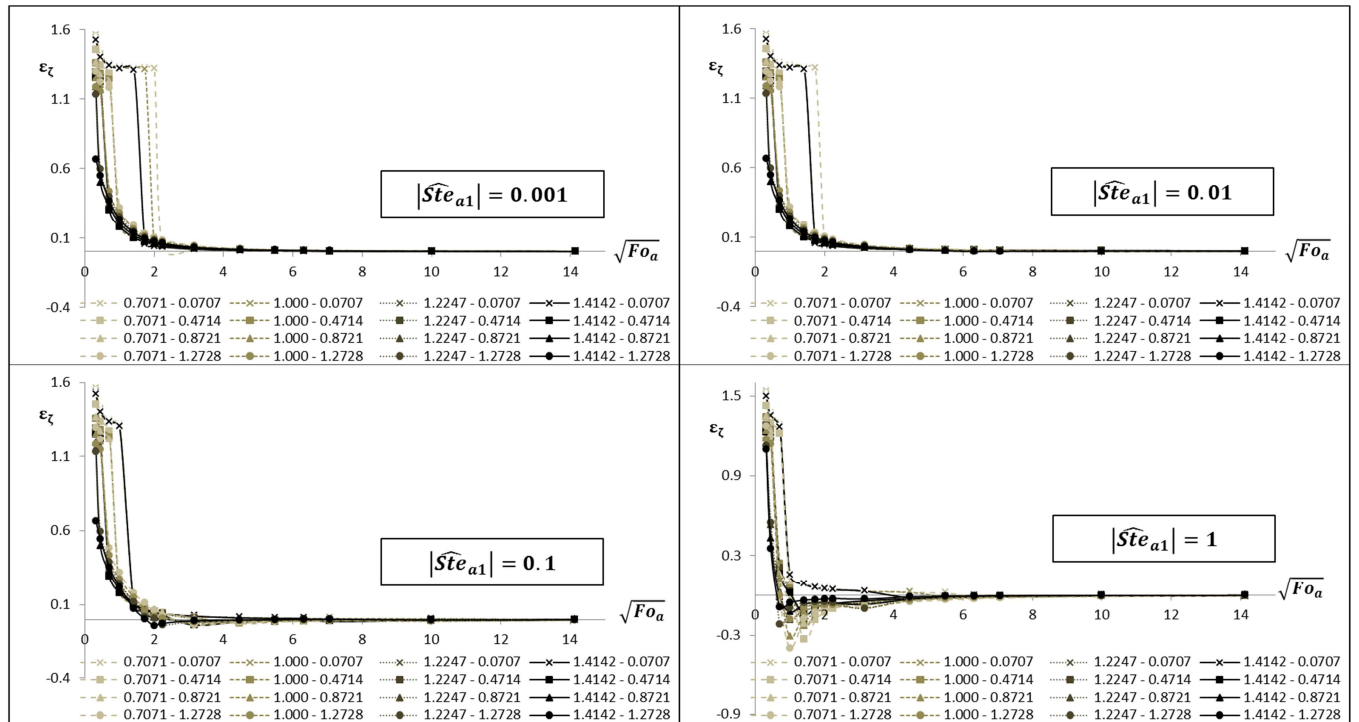


Figure 13. Trend of the error relative on the argument  $\zeta$  as a function of  $\sqrt{Fo_a}$  for different values of the thermal parameters  $\sqrt{Fo_b}/\sqrt{Fo_a}$  and  $(\sqrt{Fo_b}|\widehat{Ste}_{b2}|)/(\sqrt{Fo_a}|\widehat{Ste}_{a1}|)$  and for some characteristic values of  $|\widehat{Ste}_{a1}|$ .  $\bar{\chi}_M/L = 0.5$ . In the legend, the value of  $\sqrt{Fo_b}/\sqrt{Fo_a}$  and of  $(\sqrt{Fo_b}|\widehat{Ste}_{b2}|)/(\sqrt{Fo_a}|\widehat{Ste}_{a1}|)$  is reported for each curve in order.

The dependence of the error on the thermal parameters is analogous to the former.

The investigation of the error estimation has highlighted that the more restrictive conditions are imposed by the error of the argument  $\epsilon_\zeta$  for values of  $|\widehat{Ste}_{a1}| \leq 0.1$ , while for greater values of  $|\widehat{Ste}_{a1}|$  the error of the amplitude  $\epsilon_{|\hat{\chi}_M/L|}$  prevails. Table 2 reports, for some values of  $|\widehat{Ste}_{a1}|$ , the fields of variation of the other thermal parameters which ensure an relative error of argument  $\epsilon_\zeta$  or of the amplitude  $\epsilon_{|\hat{\chi}_M/L|}$  lower than 3% and the corresponding values of the maximum relative errors of the amplitude  $\epsilon_{|\hat{\chi}_M/L|,max}$  or of the argument  $\epsilon_{\zeta,max}$ .

Table 2 – Fields of variation of the thermal parameters which ensure a relative error of argument  $\varepsilon_\zeta$  or of the amplitude  $\varepsilon_{|\bar{\chi}_{M/L}|}$  lower than 3 % and the corresponding values of the maximum relative errors of the amplitude  $\varepsilon_{|\bar{\chi}_{M/L}|,max}$  or of the argument  $\varepsilon_{\zeta,max}$ .

		$\varepsilon_\zeta \leq 3 \%$	$\varepsilon_{ \bar{\chi}_{M/L} ,max}$
$0.001 \leq  \widehat{Ste}_{a1}  < 0.01$	$\sqrt{Fo_a}$	$\geq 3.9$	0.8 %
	$\sqrt{Fo_b}/\sqrt{Fo_a}$	$\forall$	
	$(Fo_b \widehat{Ste}_{b2} )/(Fo_a \widehat{Ste}_{a1} )$	$\forall$	
$0.01 <  \widehat{Ste}_{a1}  \leq 0.1$	$\sqrt{Fo_a}$	$\geq 3.0$	2.6 %
	$\sqrt{Fo_b}/\sqrt{Fo_a}$	$\forall$	
	$(Fo_b \widehat{Ste}_{b2} )/(Fo_a \widehat{Ste}_{a1} )$	$\forall$	
		$\varepsilon_{ \bar{\chi}_{M/L} } \leq 3 \%$	$\varepsilon_{\zeta,max}$
$ \widehat{Ste}_{a1}  = 0.5$	$\sqrt{Fo_a}$	$\geq 8.0$	1.8 %
	$\sqrt{Fo_b}/\sqrt{Fo_a}$	$\forall$	
	$(Fo_b \widehat{Ste}_{b2} )/(Fo_a \widehat{Ste}_{a1} )$	$\forall$	
$ \widehat{Ste}_{a1}  = 1.0$	$\sqrt{Fo_a}$	$\geq 6.0$	2.6 %
	$\sqrt{Fo_b}/\sqrt{Fo_a}$	$\forall$	
	$(Fo_b \widehat{Ste}_{b2} )/(Fo_a \widehat{Ste}_{a1} )$	$\forall$	

## 6. Conclusions

The parametric analysis of the exact solution of the equation that provides the bi-phase interface position in a PCM layer in steady periodic regime allowed for the identification of the dynamic behaviour of the layer. The study has highlighted that the bi-phase interface position depends mainly on the Fourier and Stefan numbers in a phase, and to a lesser extent by the ratio between the Fourier numbers calculated in the two phases  $\sqrt{Fo_b/Fo_a}$ , the product between the previous thermal parameter and the the ratio between the Stefan numbers calculated in the two phases  $\sqrt{Fo_b/Fo_a} * \widehat{Ste}_{b2}/\widehat{Ste}_{a1}$  and the dimensionless steady component of the bi-phase interface position  $\bar{\chi}_{M/L}$ .

The study of the phasor that describes the oscillating component of the bi-phase interface position, as a function of the square root of the Fourier number, and upon variation of the other thermal parameters, has highlighted how the trends of the amplitude and the argument are very similar to a frequency response that in the Laplace domain is equal to the transfer function of a dynamic linear system of the third order with a finite time-delay. This system is represented in the Laplace domain by a transfer function whose parameters can be correlated with the

dimensionless parameters used in the thermal analysis. This similarity allows for the identification of the main quantity that determine the dynamic behaviour of the PCM layer, in particular:

- the regime value of the amplitude and of the argument;
- the Fourier number corresponding to the regime conditions of the amplitude and the argument;
- the maximum overshoot of the amplitude and the discontinuity of the argument, consequent to the resonance phenomenon;
- the Fourier number for which the resonance phenomenon occurs.

Furthermore, an explicit expression of the oscillating component of the bi-phase interface position was obtained through a simplification obtained by neglecting sensible heat stored in the two phases. Such an approximate solution, acceptable for wide intervals of variation in thermal parameters, is only a function, of the dimensionless steady component of the bi-phase interface position  $\bar{\chi}_M/L$  and of two new dimensionless thermal parameters:

- the product between the Fourier number and the Stefan number calculated in a phase  $Fo_a \widehat{Ste}_{a1}$ ;
- the ratio between the previous products calculated considering both the phases  $(Fo_b \widehat{Ste}_{b2}) / (Fo_a \widehat{Ste}_{a1})$ .

The limits of validity of such a solution were determined evaluating the relative error which is committed in the determination of the amplitude and of the argument of the oscillating component of the bi-phase interface position, and the fields of variation of the thermal parameters which ensure a relative error value lower than 3 %.

This solution allows also to directly obtain the thermal field in the two phases as a function of only dimensionless thermal parameters and boundary loadings.

## Appendix A

### Regime value of the oscillating component of the bi-phase interface position

Such a value is evaluated considering the limit for  $Fo_a \rightarrow +\infty$  of Eq. (12):

$$\lim_{Fo_a \rightarrow +\infty} \left\{ \frac{1+j}{\sqrt{\pi}} \left[ \frac{1}{\sinh \left[ (1+j) \sqrt{\frac{\pi}{Fo_a}} \left( \frac{\bar{\chi}_M}{L} + \frac{\hat{\chi}_M}{L} \right) \right]} + \frac{\sqrt{\frac{Fo_b}{Fo_a}} \frac{\widehat{Ste}_{b2}}{\widehat{Ste}_{a1}}}{\sinh \left[ (1+j) \sqrt{\frac{\pi}{Fo_a}} \frac{1}{\sqrt{\frac{Fo_b}{Fo_a}}} \left( 1 - \frac{\bar{\chi}_M}{L} - \frac{\hat{\chi}_M}{L} \right) \right]} \right] = 2 \frac{j \frac{\hat{\chi}_M}{L}}{\sqrt{Fo_a \widehat{Ste}_{a1}}} \right\} \quad (A.1)$$

Taking into consideration that for  $FO_a \rightarrow +\infty$  the hyperbolic sine tends towards the hyperbolic sine argument, and that the second member of the equation tends to zero, the following equation is obtained:

$$\frac{1}{\left(\frac{\bar{\chi}_M}{L} + \frac{\hat{\chi}_M}{L}\right)} + \frac{\sqrt{\frac{FO_b}{FO_a}} \sqrt{\frac{FO_b}{FO_a}} \frac{\widehat{Ste}_{b2}}{\widehat{Ste}_{a1}}}{\left(1 - \frac{\bar{\chi}_M}{L} - \frac{\hat{\chi}_M}{L}\right)} = 0 \quad (A.2)$$

Therefore, the regime value of the phasor associated with the oscillating component of the bi-phase interface position is:

$$\left(\frac{\hat{\chi}_M}{L}\right)_{\text{reg}} = \frac{1}{1 - \sqrt{\frac{FO_b}{FO_a}} \cdot \sqrt{\frac{FO_b}{FO_a}} \frac{\widehat{Ste}_{b2}}{\widehat{Ste}_{a1}}} - \frac{\bar{\chi}_M}{L} \quad (A.3)$$

## Appendix B

### Argument of a complex number

$$Cx = \text{Re} + j\text{Im}$$

$$\arg(Cx) = \begin{cases} \text{arctg}\left(\frac{\text{Im}}{\text{Re}}\right) & \text{if Re} > 0 \\ \text{arctg}\left(\frac{\text{Im}}{\text{Re}}\right) + \pi & \text{if Re} < 0 \\ \text{sgn}(\text{Im}) + \frac{\pi}{2} & \text{if Re} = 0 \end{cases}$$

## References

- [1] Y. Chen, S. Wang, A new procedure for calculating periodic response factors based on frequency domain regression method, *International Journal of Thermal Sciences* 44 (2005), pp. 382-392.
- [2] G. Oliveti, N. Arcuri, D. Mazzeo, M. De Simone. A new parameter for the dynamic analysis of building walls using the harmonic method, *International Journal of Thermal Sciences* 2015;88:96-109.

- [3] D. Mazzeo, G. Oliveti, N. Arcuri, Influence of internal and external boundary conditions on the decrement factor and time lag heat flux of building walls in steady periodic regime, *Applied Energy* 2016;164:509-31.
- [4] D. Mazzeo, G. Oliveti, N. Arcuri, Mapping of the seasonal dynamic properties of building walls in actual periodic conditions and effects produced by solar radiation incident on the outer and inner surfaces of the wall, *Applied Thermal Engineering*, Volume 102, 5 June 2016, Pages 1157-1174, ISSN 1359-4311, <http://dx.doi.org/10.1016/j.applthermaleng.2016.04.039>.
- [5] C. Baglivo and P. M. Congedo, High performance precast external walls for cold climate by a multi-criteria methodology, *Energy* 115 (Part 1), November 15 2016, 561–576, <http://dx.doi.org/10.1016/j.energy.2016.09.018>, (ISSN 0360-5442).
- [6] X. Xu, S. Wang, A simplified dynamic model for existing buildings using CTF and thermal network models, *International Journal of Thermal Sciences* 47 (2008), pp. 1249-1262.
- [7] S. Wang, X. Xu, Simplified building model for transient thermal performance estimation using GA-based parameter identification, *International Journal of Thermal Sciences* 45 (2006), pp. 419-432.
- [8] G. Fraisse, C. Viardot, O. Lafabrie, G. Achard, Development of a simplified and accurate building model based on electrical analogy, *Energy and Buildings* 34 (2002), pp. 1017-1031.
- [9] H. Huy, S. A. Argyropoulosz, *Modelling Simul. Mater. Sci. Eng.* 4 (1996), pp. 371-396. Printed in the UK Mathematical modelling of solidification and melting: a review.
- [10] E. R. G. Eckert, R. J. Goldstein, W. E. Ibele, S. V. Patankar, T. W. Simon, P. J. Strykowski, K. K. Tamma, T.H. Kuehn, A. Bar-Cohen, J. V. R. Heberlein, D.L. Hofeldt, J. H. Davidson, J. Bischof, F. Kulacki, Heat transfer-a review of 1994 literature, *Int. J. Heat Transfer* 40 (1997), pp. 3729-3804.
- [11] H. S. Carslaw, J.C. Jaeger, *Conduction of Heat in Solids*, second edition, Oxford Science Publications, 1988.
- [12] J. Crank, *Free and Moving Boundary Problems*, Oxford: Clarendon, 1984.
- [13] T. R. Goodman, The heat balance integral and its application in problems involving a change, *Trans ASME* 80 (1958), pp. 335-342.
- [14] T. R. Goodman, J. J. Shea, The melting of finite slabs, *J. Appl. Mech.* 27 (1960), pp. 16-27.
- [15] G. E. Bell, A refinement of heat balance integral methods applied to a melting problem, *Int. J. Heat Mass Transfer* 21 (1978), pp. 1357-1361.
- [16] A. Lazaridis, A numerical solution of the multidimensional solidification (or melting) problem, *Int. J. Heat Mass Transfer* 13 (1970), pp. 1459-1477.

- [17] V. R. Voller, C. R. Swaminathan, B. G. Thomas, Fixed grid techniques for phase change problems: a review, *Int. J. Numer. Meth. Eng.* 30 (1990), pp. 875-898.
- [18] S. E. Hibbert, N. C. Markatos, V. R. Voller, Computer simulation of moving interface, convective, phase change process, *Int J Heat Mass Transfer* 31 (1988), 1785-1795.
- [19] A. Laoud, M. Lacroix, Thermal performance of a latent heat energy storage ventilated panel for electric load management, *Int J Heat Mass Transfer* 42 (1999), pp. 275-286.
- [20] P. Lamberg, K. Siren, Analytical model for melting in semi-infinite PCM storage with an internal fin, *Heat Mass Transfer* 39 (2003), pp. 167-176.
- [21] S. Savovic, J. Caldwell, Numerical solution of Stefan problem with time-dependent boundary conditions by variable space grid method, *Therm. Sci.* 13 (2009), pp. 165-174.
- [22] R. S. Gupta, D. Kumar, A modified variable time step method for the one-dimensional Stefan problem, *Comput. Meth. Appl. Mech. Eng.* 23 (1980), pp. 101-109.
- [23] J. S. Goodling, M. S. Khader, Inward solidification with radiation-convection boundary condition, *J. Heat Transfer* 96 (1974), pp. 114-115.
- [24] R. S. Gupta, D. Kumar, Variable time step methods for one-dimensional Stefan problem with mixed boundary condition, *Int. J. Mass Heat Transfer* 24 (1981), pp. 251-259.
- [25] J. Crank, R. S. Gupta, A method for solving moving boundary problems in heat flow using cubic splines or polynomials, *J. Inst. Math. Appl.* 10 (1972), pp. 296-304.
- [26] R. S. Gupta, Moving grid method without interpolations, *Comput. Meth. Appl. Mech. Eng.* 4 (1974), pp. 143-152.
- [27] J. Yoo, B. Rubinsky, Numerical computation using finite elements for the moving interface in heat transfer problems with phase change transformation, *Numer Heat Transfer* 6 (1983), pp. 209-222.
- [28] C.K. Halford, R.F. Boehm, Modeling of phase change material peak load shifting, *Energy and Buildings*, Volume 39, Issue 3, March 2007, Pages 298-305, ISSN 0378-7788, <http://dx.doi.org/10.1016/j.enbuild.2006.07.005>.
- [29] C. Chen, H. Guo, Y. Liu, H. Yue, C. Wang, A new kind of phase change material (PCM) for energy-storing wallboard, *Energy and Buildings*, Volume 40, Issue 5, 2008, Pages 882-890, ISSN 0378-7788, <http://dx.doi.org/10.1016/j.enbuild.2007.07.002>.
- [30] B. M. Diaconu, Thermal energy savings in buildings with PCM-enhanced envelope: Influence of occupancy pattern and ventilation, *Energy and Buildings*, Volume 43, Issue 1, January 2011, Pages 101-107, ISSN 0378-7788, <http://dx.doi.org/10.1016/j.enbuild.2010.08.019>.
- [31] G. Evola, L. Marletta, F. Sicurella, A methodology for investigating the effectiveness of PCM wallboards for summer thermal comfort in buildings, *Building and Environment*, Volume

- 59, January 2013, Pages 517-527, ISSN 0360-1323, <http://dx.doi.org/10.1016/j.buildenv.2012.09.021>.
- [32] A. M. Thiele, A. Jamet, G. Sant, L. Pilon, Annual energy analysis of concrete containing phase change materials for building envelopes, *Energy Conversion and Management*, Volume 103, October 2015, Pages 374-386, ISSN 0196-8904, <http://dx.doi.org/10.1016/j.enconman.2015.06.068>.
- [33] D. Zhou, G.S.F. Shire, Y. Tian, Parametric analysis of influencing factors in Phase Change Material Wallboard (PCMW), *Applied Energy*, Volume 119, 15 April 2014, Pages 33-42, ISSN 0306-2619, <http://dx.doi.org/10.1016/j.apenergy.2013.12.059>.
- [34] S. N. Al-Saadi, Z. (J.) Zhai, A new validated TRNSYS module for simulating latent heat storage walls, *Energy and Buildings*, Volume 109, 15 December 2015, Pages 274-290, ISSN 0378-7788, <http://dx.doi.org/10.1016/j.enbuild.2015.10.013>.
- [35] H. Ling, C. Chen, S. Wei, Y. Guan, C. Ma, G. Xie, N. Li, Z. Chen, Effect of phase change materials on indoor thermal environment under different weather conditions and over a long time, *Applied Energy*, Volume 140, 15 February 2015, Pages 329-337, ISSN 0306-2619, <http://dx.doi.org/10.1016/j.apenergy.2014.11.078>.
- [36] D. Zhou, Y. Tian, Y. Qu, Y.K. Chen, Thermal analysis of phase change material board (PCMB) under weather conditions in the summer, *Applied Thermal Engineering*, Volume 99, 25 April 2016, Pages 690-702, ISSN 1359-4311, <http://dx.doi.org/10.1016/j.applthermaleng.2016.01.121>.
- [37] J. Lei, J. Yang, E.-H. Yang, Energy performance of building envelopes integrated with phase change materials for cooling load reduction in tropical Singapore, *Applied Energy*, Volume 162, 15 January 2016, Pages 207-217, ISSN 0306-2619, <http://dx.doi.org/10.1016/j.apenergy.2015.10.031>.
- [38] M. Saffari, A. de Gracia, S. Ushak, L. F. Cabeza, Economic impact of integrating PCM as passive system in buildings using Fanger comfort model, *Energy and Buildings*, Volume 112, 15 January 2016, Pages 159-172, ISSN 0378-7788, <http://dx.doi.org/10.1016/j.enbuild.2015.12.006>.
- [39] L. I. Rubinstein, *The Stefan Problem*, Translations of Mathematical Monographs, Vol. 27, American Mathematical Society, Providence, Rhode Island, 1971.
- [40] J. Crank, *Free and Moving Boundary Problems*, Oxford University Press, 1987.
- [41] V. S. Arpaci, *Conduction Heat Transfer*, Addison – Wesley Publishing Company, Inc., Reading Mass., 1966.
- [42] M. N. Ozisik, *Heat conduction*, J. Wiley & Sons, New York, 1980



- [43] V. Alexiades, A. Solomon, Mathematical modelling of melting and freezing processes, Hemisphere Publishing Corporation, Washington, 1993.
- [44] D. Mazzeo, G. Oliveti, M. De Simone, N. Arcuri, Analytical model for solidification and melting in a finite PCM in steady periodic regime, International Journal of Heat and Mass Transfer, 88, 2015, Pages 844-861, <http://dx.doi.org/10.1016/j.ijheatmasstransfer.2015.04.109>
- [45] Basic Circuit Theory, McGraw-Hill, Inc., New York, N. Y., USA.
- [46] Stephen Wolfram, The Mathematica Book, 5th ed. (Wolfram Media, 2003).
- [47] The MathWorks, Inc., MATLAB User's Guide Symbolic Math Toolbox™, Natick, MA. © COPYRIGHT 1993-2014.
- [48] L. F. Cabeza, A. Castell, C. Barreneche, A. de Gracia, A.I. Fernández, Materials used as PCM in thermal energy storage in buildings: A review, Renewable and Sustainable Energy Reviews, Renewable and Sustainable Energy Reviews 15 (2011), pp. 1675-1695.
- [49] B. C. Kuo, Automatic Control Systems, 5th Edition Prentice-Hall, Englewood Cliffs, N. J., 1996.
- [50] K. Ogata, Modern Control Engineering. 5th Edition, Prentice-Hall, Upper Saddle River, N. J. 2010.
- [51] E. Kreyszig, Advanced Engineering Mathematics, John Wiley & Sons, INC, Seventh Edition, Singapore 1993.

## Nomenclature

- (a) portion of layer in phase a
- (b) portion of layer in phase b
- c specific heat capacity [J/(kg K)]
- C coefficient in the root solution of the approximate equation [-]
- Cx complex number
- F heat flux [W/m<sup>2</sup>]
- Fo Fourier number [-]
- G(s) Laplace transform of a generic system transfer function
- H latent heat of fusion [J/kg]
- Im imaginary part of the complex number
- k harmonic order [-]
- K gain of the transfer function
- L thickness of the PCM layer [m]
- n harmonic number [-]

p	poles of the transfer function
P	period of oscillation [s]
Re	real part of the complex number
Ste	Stefan number [-]
t	time [s]
T	temperature [K]
t*	a particular time instant [s]
x	spatial Cartesian coordinate [m]
X	position of the bi-phase interface [m]
z	zeros of the transfer function

*Greek symbols*

$\alpha$	thermal diffusivity [ $\text{m}^2/\text{s}$ ]
$\gamma$	propagation constant [1/m]
$\delta$	damping factor
$\varepsilon$	relative error [-]
$\zeta$	argument of the oscillating component of the position of the bi-phase interface [rad]
$\vartheta$	generic component of the temperature Fourier series expansion [K]
$\lambda$	thermal conductivity [ $\text{W}/(\text{m K})$ ]
$\rho$	density [ $\text{kg}/\text{m}^3$ ]
$\tau$	finite time-delay of the transfer function [s]
$\varphi$	argument of the temperature oscillation [rad]
$\Phi$	generic component of the heat flux Fourier series expansion [ $\text{W}/\text{m}^2$ ]
$\chi$	generic component of the position of bi-phase interface Fourier series expansion [m]
$\psi$	argument of the heat flux oscillation [rad]
$\omega$	angular frequency [rad/s]
$\omega^*$	dimensionless angular frequency [-]
$\omega_n$	natural angular frequency [rad/s]

*Subscripts*

1	face 1
2	face 2
1,2	couple of poles of the transfer function
I	first coefficient of the root solution of the approximate equation
II	second coefficient of the root solution of the approximate equation
III	third coefficient of the root solution of the approximate equation

a	phase a
a1	oscillation on face 1 in a-phase
appr	approximate
b	phase b
b2	oscillation on face 2 in phase (b)
exa	exact
H	latent heat stored per unit time
k	k-th harmonic
M	melting
max	maximum
reg	regime value
$\zeta$	argument of the oscillating component of the position of the bi-phase interface
$ \hat{\chi}_M/L $	amplitude of the oscillating component of the position of the bi-phase interface

*Superscripts*

I	first root solution of the approximate equation
II	second root solution of the approximate equation
III	third root solution of the approximate equation

*Symbols*

–	mean value
~	oscillating value in the time domain
^	oscillating value in the complex domain
	amplitude of an oscillating value
arg	argument of an oscillating value

# Chapter 6

## Thermal field and heat storage in PCM walls with multiple bi-phase interfaces under actual periodic boundary conditions

### Abstract

This work determines the effective thermal fields in a non-sinusoidal periodic regime, which form in a layer of phase change material (PCM) within which multiple solidification and melting bi-phase interfaces are present. The thermal loadings considered are typical of those operating on the external walls of air-conditioned buildings. In particular, in the outdoor environment the non-sinusoidal periodic action of the absorbed solar radiation, of the external air and of the sky temperature is considered, while in the indoor environment the air temperature is supposed as constant.

The physical model used describes heat conduction in the solid phase and the liquid phase and the phase change at the melting temperature with the equation of thermal balance at the bi-phase

interface. The resolution of the physical model is obtained by means of the finite difference numerical model, in which the advancement velocity of the bi-phase interface is calculated with the relative incremental ratio; unknown thermal quantities are the temperature in the nodes in the solid phase and in the liquid phase, and the liquid fraction in the nodes in phase change at the melting temperature. The numerical model and the resolution algorithm were obtained by extending those proposed by Halford et al. (2009). In particular, some simplifications, such as the uniformity of the spatial discretization of the subvolumes of the layer, the invariance in space and time of the thermal resistances and the areal heat capacities, were removed in order to obtain a more accurate representation of heat flux discontinuity in the subvolumes involved in the phase change. The numerical model and the resolution algorithm foresee the presence of one or more bi-phase interfaces in the layer and it is validated by means of a comparison with an analytical model, which resolves the Stefan problem in a finite layer in a steady periodic regime.

The calculation procedure is employed for the study of the thermal behaviour of PCM layers, with different melting temperatures and thermophysical properties, with boundary conditions characteristic of two localities with a continental climate and a mediterranean climate. Such a procedure allows for the determination, at different time instants of the period  $P=24$  hours, of the positions of the bi-phase interfaces present in the layer, the field of temperature and of the heat flux and the energy released and stored per unit time of each interface. The PCM layer has different configurations in the various months of the year and the thermal fields depend upon the advancement velocity of the eventual bi-phase interfaces, which define the law of storage and release of latent energy at the melting temperature in the portion of the layer involved. The numerical results reveal interesting phenomena that for such boundary conditions and in such detail have never previously been reported in the literature. In the literature, in this regime, this problem is addressed exclusively by considering a sinusoidal periodic forcing that acts on the external surface.

The calculation procedure created and the phenomena described in the paper provide an instrument, which can be validly used for the thermal dimensioning of the layer, or rather the choice of the PCM and its thickness, as well as for a dynamic thermal characterisation of the layer through the thermal fluctuations entering and exiting the layer.

**Keywords:** Moving Boundary Problem; Stefan Problem; PCM; Mutiple bi-phase interfaces; Building external wall; Periodic heat transfer

- Thermal fields in a PCM layer with multiple bi-phase interfaces are presented
- Periodic boundary conditions characteristic of building external walls are imposed
- Finite difference model used has been validated with an available analytical model
- Various PCM layers with different melting temperatures are considered
- The analysis regard a continental and a mediterranean climate

Le verità scientifiche non si decidono a maggioranza.

(Galileo Galilei)

## 1. Introduction

The phase transition in a PCM layer situated within the external wall of an air-conditioned building modifies the trend of the temperature and of the heat flux with consequent reduction of the thermal power peaks and of the energy transferred in the wall. The use of this technology for the reduction of energy requirements has led to studies and research on the thermal behaviour of PCM [1], which have produced models of differing complexity that, in almost all cases, have been resolved numerically.

The mathematical formulation of the heat exchange in a PCM layer is known as the Stefan problem and its analytical solution is available only for semi-finite or infinite monodirectional geometries and temperature or heat flux boundary conditions that are constant in time [2-8]. The exact solution recently obtained by a source and sink technique associated with the Laplace transform approach concerns only problems with a bi-phase interface travelling at a constant velocity in a fixed direction [9]. The complexity of the resolution is due to the discontinuity of the heat flux at the bi-phase interface whose position is variable in time with consequent variation of the solid and liquid phase domain.

Several authors have proposed analytical solutions of the model obtained introducing approximations and numerical solutions to describe the phase change and the relative latent storage once the melting temperature has been reached.

The heat balance integral method, one of the analytical approximation techniques, is frequently used [10-12]; it considers a polynomial thermal field both in the solid phase and in the liquid phase and the reduction of the differential equations in a system of algebraic equations that are resolved considering the boundary conditions.

Instead, the most widespread numerical methods require the integration of a spatial and temporal discretization of the physical domain and the use of a function of state or a modification of the thermophysical property to describe the high storage capacity in the time instants in which a generic node is subject to phase transition. The discretization of the PCM layer is executed by means of the use of a nodalisation that is fixed or variable in time [13-16]. The mathematical stratagem consists of considering an equivalent monophasic layer and an increase in specific heat capacity or enthalpy, variable with the temperature, in the vicinity of melting temperature. Such methods, known as the effective thermal capacity method [17-21], the apparent heat capacity method [22-28] and the enthalpy method [29-39], allow for the obtainment of a numerical solution to the thermal exchange problem without directly resolving the equation of discontinuity

of the heat flux at the bi-phase interface on which the Stefan problem is based. The apparent heat capacity method utilizes a piecewise function upon temperature variation to describe the heat capacity of the layer. In proximity of the melting temperature, such a capacity is evaluated as the sum of the sensible heat capacity of the layer and of an equivalent latent heat capacity. Instead, the effective heat capacity method utilizes a continuous analytical function on temperature variation or an experimental curve obtained through calorimetric techniques. The enthalpy method uses the function of the state of enthalpy instead of temperature. Similarly, in the vicinity of melting temperature, such a function assumes a value that is equal to fusion latent heat.

A comprehensive review of mathematical and numerical methods applied to the solutions of phase change problems is presented in [4, 6-8].

The previous methodologies have mainly been used to study the thermal transient in a PCM layer while there are few studies related to their use in steady periodic regime. The problem of the determination of the thermal field in PCM layers subject to boundary conditions variable in time in the case of a steady periodic regime is of particular interest. Such a regime, due to the daily periodicity of the loadings that act on the external surface of the walls, such as solar radiation, is representative of the behaviour of building walls. The analytical solution of the Stefan problem in a finite layer subject to periodic boundary conditions was recently provided by Mazzeo et al. [40]. Such a solution is valid in the case in which the boundary conditions of temperature or heat flux ensure, during the period, a temperature oscillation on a face that is always less than the melting temperature and which is always greater on the other face. In such conditions, a sole bi-phase interface originates which oscillates within the layer with the same frequency of the thermal oscillations on the boundary of the layer. A numerical study of the periodic phase change in a layer, initially in solid phase, subject to a sinusoidal surface temperature, in all times above the melting temperature of the PCM, on one face while the other face is kept isothermal below the melting temperature, was reported by Ho and Chu [41], who adopted the enthalpy method. They studied the influence of the amplitude of the imposed enthalpy sinusoidal oscillation, of the period of the imposed wall temperature oscillation and of the Rayleigh number on the heat transfer rates and the melting rate. The periodic mean values of the heat transfer rates at the vertical hot and cold walls, as well as the melting rate, are strongly affected by the Rayleigh number, but are rather insensitive to the amplitude or the period of the imposed wall temperature oscillation. Moreover, the oscillation of the heat transfer rates, as well as the melting rate, respond differently to the variation of amplitude and period of imposed wall temperature oscillation, the Rayleigh number and the Stefan number. Furthermore, the authors



found that the heat transfer rates and the melting rate exhibit a regular temporal oscillation at a frequency equal to the imposed wall temperature oscillation but with different argument. Casano and Piva [42] presented a numerical and experimental investigation of a phase-change process in a plane slab of PCM periodically heated from above, while the bottom is kept at a temperature lower than the melting point of the test material by means of a refrigeration system. Having demonstrated the numerical validity of the code by comparison with results for an analytical solution, the physical validity of the mathematical model may be studied by comparing predictions with the data of three experimental tests, which differ according to the period of the sinusoidal power dissipated in the heater. For all the tests, the presence of an interface separating an upper zone, where the material is liquid, from a lower zone in solid phase, is clearly evidenced. The liquid zone is characterized by wide oscillations of temperature, reaching the maximum amplitude at the heated surface while the solid region is characterized by moderate oscillations of temperature, practically negligible in a test and increasing with the period. This is because the greater part of the heat flux introduced in the sample via the heater is used for the advancement of the interface and only a limited part of this heat flux is still available for the heating of the remaining solid phase. From a qualitative point of view, the numerical model gives temperature trends that are very similar to experimental ones, both in the solid and in the liquid phase.

In the building walls, the boundary conditions characterising the outdoor environment and the indoor air-conditioned environment give rise, generally, to more bi-phase interfaces in the layer and this renders the problem even more complex. The multiple bi-phase interfaces originate when the periodic temperature oscillation on the boundary face varies around the melting temperature. The presence of multiple bi-phase interfaces in materials subject to phase change with sinusoidal periodic temperature and heat flux boundary conditions, such as to originate an oscillation of temperature around the melting temperature, on one face and constant temperature, below the melting temperature, on the other face, by using source and sink methods, has been highlighted in the literature by Choi et al. [43]. They found that during the heating process, the layer melts and the melting bi-phase interface moves from the boundary surface to the interior of the layer, while during the cooling process a solidification bi-phase interface appears on the same surface, which does not reach the first bi-phase interface, dividing the layer into three regions. Analysing only one cycle, the results of this analysis do not constitute the steady periodic regime solution, determining at the end of the cycle a gap between the two bi-phase interfaces and a stored energy different from that released. Similar result was also reported by Ho and Chu [44]

who have highlighted that there might coexist three solid-liquid interfaces, dividing the layer into four regions, during the periodic solid-liquid phase change process inside the layer depending on the periodic amplitude oscillating boundary temperature. These authors found that for high values of the amplitude of the periodic temperature oscillation on the boundary surface, the steady periodic heat transfer rates at the wall as well as the melting rate assume a very complicated cyclic variation in comparison with that found in the absence of the re-solidification and re-melting phenomena. The effect of the increase in the period appears to be similar to the observations in [41]: a marked amplification of the induced steady oscillation amplitudes of both the melting rate and heat transfer rate at the cold wall arises; while an adverse effect occurs for the heat transfer rate at the hot wall. This implies that the effect of varying time period on the melting rate and the heat transfer rate has little or no bearing on whether the imposed wall-temperature oscillation amplitude is greater or not. The steady periodic melting behaviour and the heat transfer characteristics, when the amplitude of the wall temperature oscillation is high, show a dependence on the Rayleigh number generally similar to that found for low amplitude of the wall temperature oscillation, as reported in [41]. In a recent work, Mazzeo et al. [45] have highlighted that in a PCM layer, with reference to boundary conditions characteristic of the building external wall, the thermodynamic state is variable over the course of the year. The layer can be completely solid or liquid, there may be one bi-phase interface or there might coexist two or three solid-liquid bi-phase interfaces.

From the literature it appears that a detailed study of the thermal field and the heat storage in a PCM layer, in presence of multiple bi-phase interfaces, subjected to the joint action of more non-sinusoidal periodic thermal loadings has not been addressed.

In this work, we studied the problem of the determination of the thermal field in PCM layers subject to periodically variable boundary conditions that describe the actual trends of the loadings that operate within the outdoor environment. The behaviour of the layer is schematised with a physical model that describes heat conduction in the solid phase and in the liquid phase, having different thermophysical properties, and the phase change by means of the thermal balance equation at the bi-phase interface at the melting temperature. The finite difference numerical model and the resolution algorithm were obtained by modifying those proposed by Halford et al. [46], which allow for the position for the bi-phase interface to be evaluated explicitly. In particular, some simplifications, such as the uniformity of the spatial discretization of the subvolumes of the layer, the invariance in space and time of the thermal resistances and the areal heat capacities, were removed in order to obtain a more accurate representation of heat

flux discontinuity in the sublayer involved in the phase change. The model and algorithm developed contemplate the contemporaneous presence in the layer of several bi-phase interfaces. Validation was obtained by a comparison with the results obtained with an analytical model available in literature [40] that resolves the Stefan problem in a finite layer subject to periodic temperature or heat flux fluctuations on both boundary faces of the layer. The calculation procedure created was used to study the thermal behaviour in different PCM layers available on the market, with melting temperatures ranging between 15°C and 32 °C, subject to boundary conditions typical of building walls. The external loadings considered, relating to two climatically different locations and representative of the continental climate and of the mediterranean climate, are the hourly values of the monthly average day of the air temperature, of the solar irradiation and of the apparent sky temperature. The air temperature, supposed as constant, was considered as internal loading.

In the first part of the paper, the authors present the numerical model, the resolution algorithm used, and the validation of the numerical procedure. Successively, with reference to a particular PCM and to the locality of Turin, for each month of the year, we present the trends in the layer relative to the monthly average daily of the temperature, of the position of eventual solidification and fusion bi-phase interfaces present, of the latent energy stored per unit time associated with the single bi-phase interfaces and of the heat flux. Finally, for the different PCM considered and for the two localities, we present a comparison of the temperature and heat flux.

## 2. Methodology

### 2.1. Calculation model

The equations describing heat exchange in a layer subject to phase change are the general equation of heat conduction in the solid phase and in the liquid phase, Eq. (1), and the Stefan conditions, Eqs. (2) and (3), expressed by the thermal balance equation at the bi-phase interface which is at the melting temperature.

$$\frac{\partial^2 T}{\partial x^2} - \frac{1}{a} \frac{\partial T}{\partial t} = 0 \quad (1)$$

$$\left[ k_l \frac{\partial T_l}{\partial x} - k_s \frac{\partial T_s}{\partial x} \right]_{x=X_M} = \rho H \frac{dX_M}{dt} \quad (2)$$

$$T_l(X_M, t) = T_s(X_M, t) = T_M \quad (3)$$

with  $H$  latent heat of fusion,  $T_M$  melting temperature,  $X_M$  position of the bi-phase interface,  $\rho$  density,  $T_l$  and  $T_s$  temperature in the portion of the layer in liquid and solid phase, and  $k_l$  and  $k_s$  thermal conductivity in the liquid phase and in the solid phase.

The boundary conditions, on the external surface of the PCM layer are defined by the convective and shortwave and longwave radiative heat exchanges and, on the internal surface by the heat exchanges calculated by the surface heat transfer coefficient. The corresponding equations are:

$$\Phi_e = \Phi_{r,e} + \Phi_{c,e} + \alpha \Phi_s = h_{r,e}(T_{sky} - T_1) + h_{c,e}(T_{ea} - T_1) + \alpha_e \Phi_{s,e} = -k \frac{\partial T}{\partial x} \Big|_{x=0} \quad (4)$$

$$\Phi_{ia} = h_{s,i}(T_N - T_{ia}) = -k \frac{\partial T}{\partial x} \Big|_{x=L} \quad (5)$$

with  $\Phi_e$  total heat flux from the outdoor environment,  $\Phi_{r,e}$  longwave radiative heat flux exchanged with the sky,  $\Phi_{c,e}$  convective heat flux exchanged with the external air,  $\alpha_e$  absorption coefficient,  $\Phi_{s,e}$  solar radiation,  $h_{r,e}$  and  $h_{c,e}$  radiative and convective heat transfer coefficients,  $T_{sky}$  sky temperature,  $T_{ea}$  external air temperature,  $T_1$  external surface temperature,  $\Phi_{ia}$  heat flux transferred in the indoor environment,  $h_{s,i}$  internal surface heat transfer coefficient,  $T_N$  internal surface temperature,  $T_{ia}$  internal air temperature and  $L$  thickness of the layer.

Since the boundary surface temperatures of the PCM layer can fluctuate around the melting temperature, it is possible that more bi-phase interfaces form in the layer in the considered period. In such conditions, Eqs. (2) and (3) must be formulated for each bi-phase interface. For example, in the presence of two bi-phase interfaces with a succession of liquid-solid-liquid or solid-liquid-solid phases, the system of differential equations will be constituted by the heat conduction equation (1), written for each of the phases, and by the Stefan conditions (2) and (3) written for each interface. To such equations, it is necessary to add the boundary conditions expressed by relations (4) and (5).

The numerical discretization of the system of differential equations according to an explicit finite difference scheme, with the time derivative evaluated with the relative incremental ratio, leads to a system of algebraic equations representing the heat balance of all the subvolumes (see Figure 1). With subvolume the authors intend the volume associated to the single node. Such equations provide the temperatures of the nodes that are not subject to phase change and liquid fractions  $\lambda$  in the nodes at the melting temperature at the successive time instant through thermal quantities calculated at the preceding time instant.

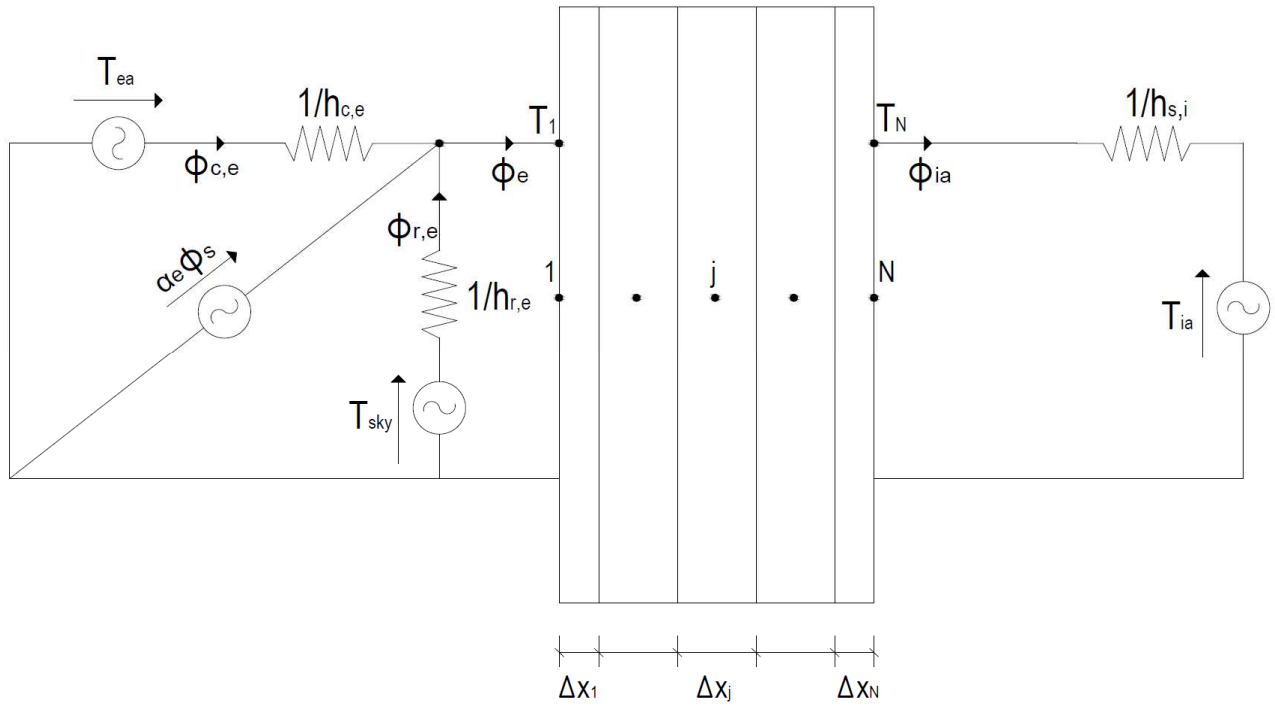


Figure 1 – Equivalent electrical circuit of a PCM layer, discretized with  $N$  subvolumes, subject to the external air temperature loading  $T_{ea}$ , sky temperature loading  $T_{sky}$  and absorbed solar radiation loading  $\alpha_e \Phi_{s,e}$ , and to the internal air temperature loading  $T_{ia}$ .

The relations obtained for the calculation of the temperature and the liquid fraction  $\lambda$ , which assumes values of between 0 and 1, in surface node 1 in contact with the external air are:

$$T_1^{n+1} = T_1^n + \frac{\Delta t}{C_1^n} \left( \frac{T_{ea}^n - T_1^n}{R_{c,e}} + \frac{T_{sky}^n - T_1^n}{R_{r,e}} + \alpha_e \Phi_{s,e}^n + \frac{T_2^n - T_1^n}{R_{1,2}^n} \right) \quad (6)$$

$$\lambda_1^{n+1} = \lambda_1^n + \frac{\Delta t}{\rho H \Delta x_1} \left( \frac{T_{ea}^n - T_M}{R_{c,e}} + \frac{T_{sky}^n - T_M}{R_{r,e}} + \alpha_e \Phi_{s,e}^n + \frac{T_2^n - T_M}{R_{1,2}^n} \right) \quad (7)$$

For the internal nodes  $j$ :

$$T_j^{n+1} = T_j^n + \frac{\Delta t}{C_j^n} \left( \frac{T_{j-1}^n - T_j^n}{R_{j-1,j}^n} + \frac{T_{j+1}^n - T_j^n}{R_{j,j+1}^n} \right) \quad (8)$$

$$\lambda_j^{n+1} = \lambda_j^n + \frac{\Delta t}{\rho H \Delta x_j} \left( \frac{T_{j-1}^n - T_M}{R_{j-1,j}^n} + \frac{T_{j+1}^n - T_M}{R_{j,j+1}^n} \right) \quad (9)$$

For node  $N$  in contact with the internal air:

$$T_N^{n+1} = T_N^n + \frac{\Delta t}{C_N^n} \left( \frac{T_{N-1}^n - T_N^n}{R_{N-1,N}^n} + \frac{T_{ia}^n - T_N^n}{R_{c,r_i}} \right) \quad (10)$$

$$\lambda_N^{n+1} = \lambda_N^n + \frac{\Delta t}{\rho H \Delta x_N} \left( \frac{T_{N-1}^n - T_M}{R_{N-1,N}^n} + \frac{T_{ia}^n - T_M}{R_{c,r_i}} \right) \quad (11)$$

with  $T_2$  temperature in the volume of node 2 adjacent to the volume of the external surface node,  $R_{c,e}$  external convective thermal resistance,  $R_{r,e}$  external radiative thermal resistance,  $C_j$  areal heat capacity of the node  $j$ ,  $R_{c,r_i}$  internal surface convective-radiative thermal resistance,  $\Delta x_j$  thickness of the volume of the node  $j$ ,  $\Delta t$  temporal discretization interval,  $T_{j-1}$  temperature of node  $j-1$ ,  $T_j$  temperature of node  $j$ ,  $T_{j+1}$  temperature of node  $j+1$ ,  $R_{j-1,j}$  thermal resistance between nodes  $j-1$  and  $j$ ,  $R_{j,j+1}$  thermal resistance between nodes  $j$  and  $j+1$ ,  $n$  current time instant and  $n + 1$  successive time instant.

In the previous equations, the thermal resistances  $R$  between the nodes and the areal heat capacities  $C$  of the nodes, different in the liquid phase and in the solid phase, are updated at each time instant taking into account the positions of the melting or solidification bi-phase interfaces in the layer. For the calculation of the thermal resistances between generic node  $j$  and the two nodes  $j-1$  e  $j+1$  adjacent, it is necessary to take into account the position of the bi-phase interfaces present in the three subvolumes (Appendix A).

At time instant  $n$ , if the bi-phase interface is of melting, the position of the  $k$ -th bi-phase interface  $X_{M,k}^n$  present in subvolume  $jk$  is calculated summing the thicknesses of the subvolumes  $\Delta x_i$  preceding the node  $jk$  to the portion of the subvolume  $jk$  in liquid phase  $\Delta x_{jk} \lambda_{jk}^n$ . If it is a

solidification interface (see Eq. 13), the position of the k-th bi-phase interface  $X_{M,k}^n$  present in subvolume jk is calculated summing the thicknesses of the subvolumes  $\Delta x_i$  preceding the node jk to the portion of the subvolume jk in solid phase  $\Delta x_{jk}(1 - \lambda_{jk}^n)$ .

$$X_{M,k}^n = \sum_{i=1}^{j_k-1} \Delta x_i + \Delta x_{j_k} \lambda_{j_k}^n \quad (12)$$

$$X_{M,k}^n = \sum_{i=1}^{j_k-1} \Delta x_i + \Delta x_{j_k} (1 - \lambda_{j_k}^n) \quad (13)$$

The created algorithm determines the configuration of the phases in the nodes of the layer at different time instants and consists of three subprogrammes for the calculation of the temperature and of the liquid fraction present in the node. In a node, at each time instant, according to whether it is in a solid phase, a liquid phase or in phase change the corresponding subprogramme is used.

As the time in the numerical model is discretized, it is not possible to precisely identify: the instant in which the temperature in the node becomes equal to the melting temperature with a the start of the melting or solidification interface; the instant in which the liquid fraction becomes unitary with the end of the melting process or becomes equal to zero with the end of the solidification process. For this reason, each subprogramme uses values of temperature and the liquid fraction in a node in the preceding two time instants to determine correctly the thermodynamic state and the temporal instants in which the phase change completes or starts. In particular, Figure 2 reports the flow chart of the calculation algorithm that provides for, at each time instant, three possible decisions:

- the generic node j at time n+1 is in the solid phase if the temperature in the two previous time instants n-1 and n is less than the melting temperature, or if the liquid fraction in the node at the time instant n-1 is between zero and one, and at the time instant n becomes less than zero to indicate completion of the solid-liquid phase change. In this case, at the time instant n+1 the liquid fraction is set equal to zero and the temperature is calculated with one of the three Eqs. (6), (8) and (10) depending on the position of the node in the layer.
- the generic node j at time n+1 is in the liquid phase if the temperature in the two previous time instants n-1 and n is greater than the melting temperature, or if the liquid fraction in the node at the time instant n-1 is between zero and one, and at time instant n becomes greater than one to indicate completion of the solid-liquid phase change. In this case, at

the time instant  $n + 1$  the liquid fraction is set equal to one and the temperature is calculated with one of the three Eqs (6), (8) and (10) depending on the position of the node in the layer.

- the generic node  $j$  at time instant  $n+1$  is subject to the phase change if the temperature in the two time instants  $n-1$  and  $n$  is less than the melting temperature and in the time instant  $n+1$  is greater than the melting temperature; or if the temperature in the two time instants  $n-1$  and  $n$  is greater than the melting temperature and in the time instant  $n+1$  is less than the melting temperature; or if the liquid fraction at time instant  $n$  is between zero and one. In the first case the melting process begins, in the second case solidification begins, while in the third case a phase change occurs. If one of the three conditions is verified, the temperature is set equal to the melting temperature and the liquid fraction is calculated with one of the three Eqs (7), (9) and (11) depending on the position of the node.

The thermal resistances and the areal heat capacity to be used in the equations for the calculation of the temperature and of the liquid fraction in a node in the successive time instant  $n+1$  are calculated as a function of the position of the bi-phase interfaces as described previously.

The developed model and algorithm differ from those used by Halford and Boehm [46] to determine the temperature field within a PCM layer interposed between two insulating layers. They adopt some simplifications in the numerical model, namely:

- uniform nodal discretization of the layer;
- identical thermophysical properties in the solid phase and in the liquid phase;
- thermal resistances between the nodes affected by the phase change that are not dependent on the location of the bi-phase interface;
- the algorithm uses the values of temperature and of the liquid fraction in a node at the previous time instant  $n$  to determine the thermodynamic state at the successive time instant  $n+1$ ;
- presence of a sole bi-phase interface in the layer.



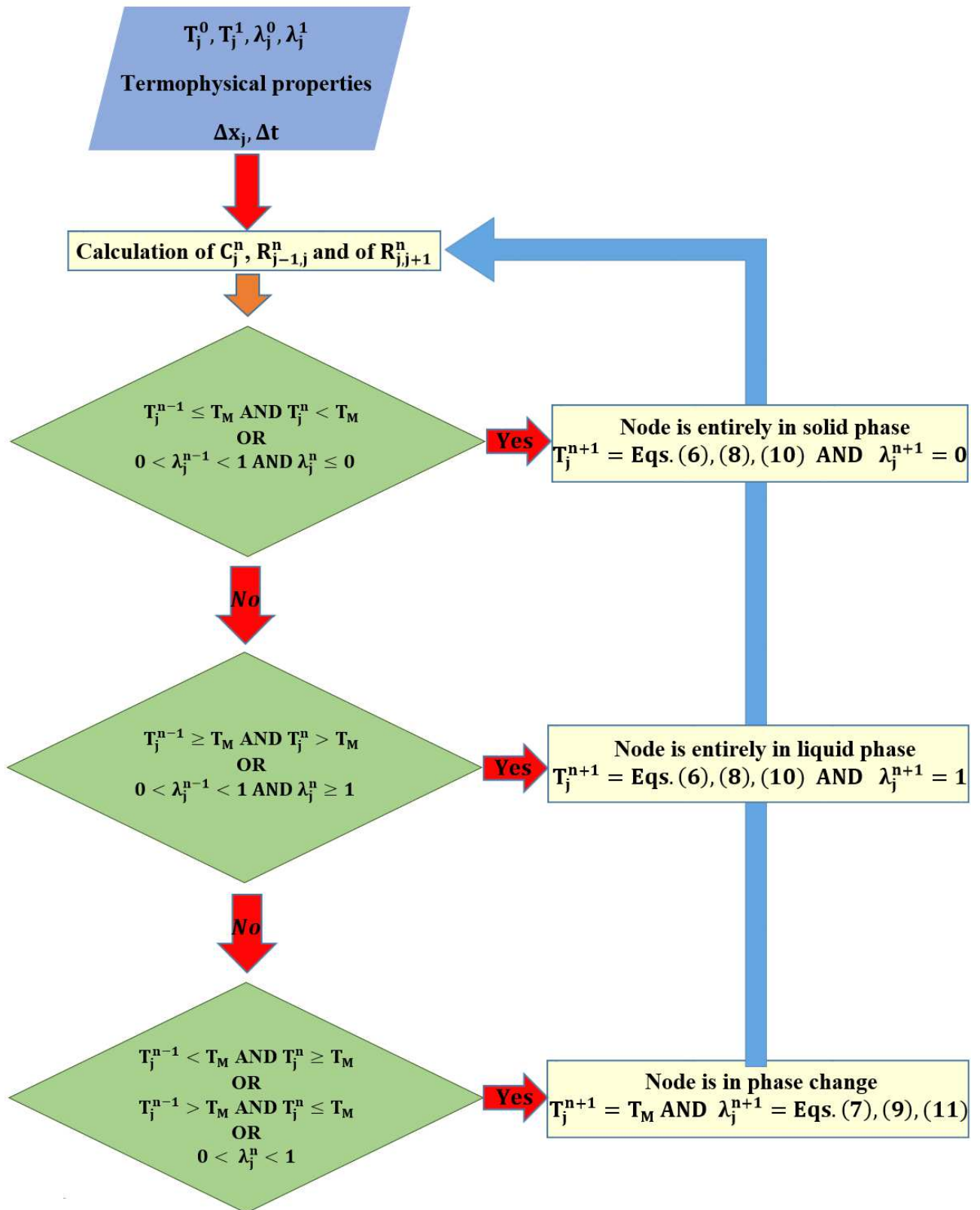


Figure 2 - Algorithm flowchart

## 2.2. Validation of the numerical code

The results obtained with the numerical code were compared with those determined by using the exact analytical solution of the Stefan problem, in a steady periodic regime, of a finite PCM layer subject on both faces to periodic boundary conditions [40]. The analytical solutions regards the fluctuating boundary conditions to ensure surface temperature values on a face that are always greater than the melting temperature and that are always lower than the melting temperature on the other face. In these conditions, only one bi-phase interface originates the position of which oscillates within the layer around a mean steady value.

Verification was obtained by considering 6 cm of PCM layer, S15 in Table 1, subject on the two boundary faces to non-sinusoidal periodic temperature. Such conditions are expressed as a sum of the steady component and the fluctuating component, the latter evaluated as a sum of sinusoids of a different period, amplitude and argument:

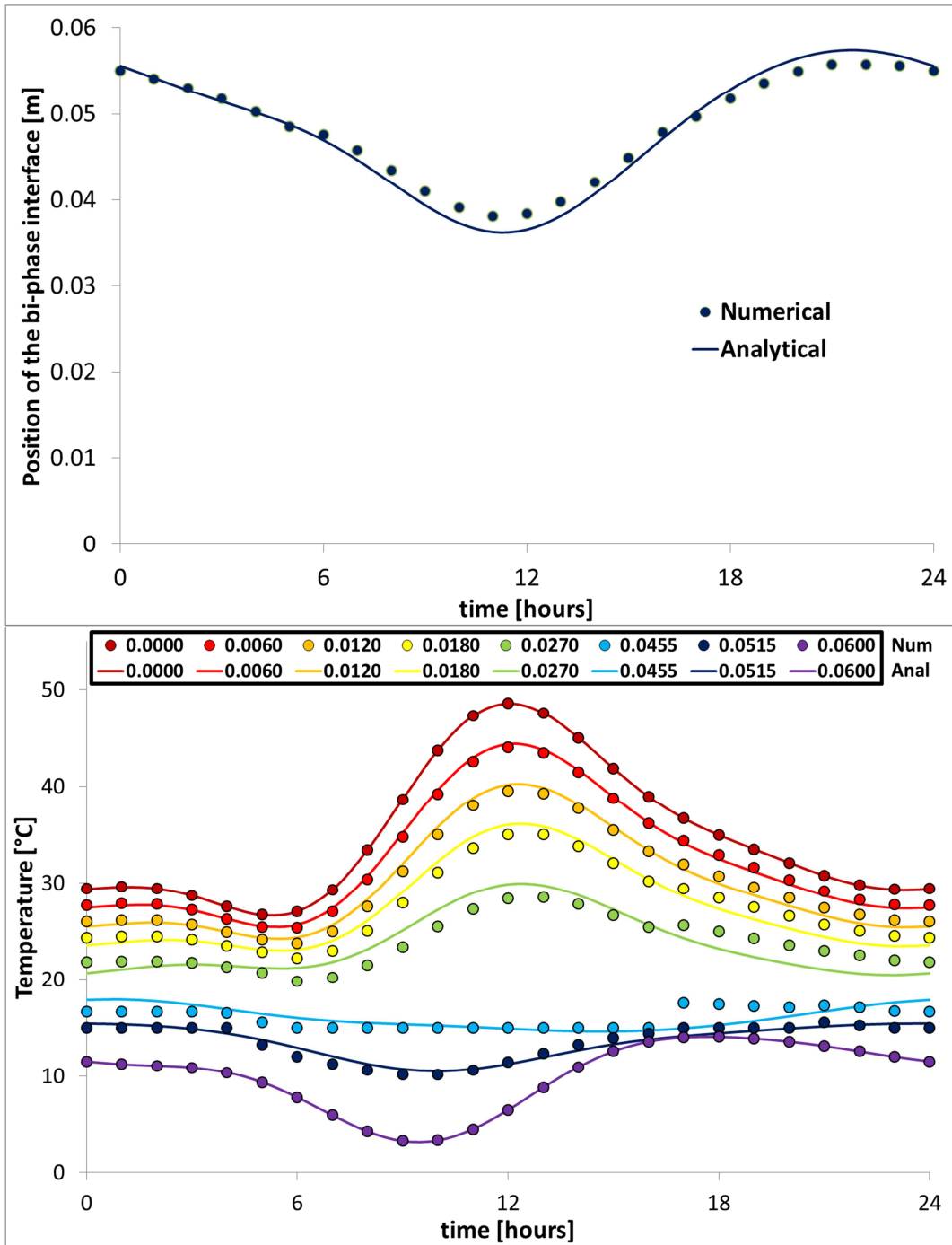
$$T_1(t) = \bar{\vartheta}_1 + \tilde{\vartheta}_1(t) = 35 + 9 \sin\left(\frac{2\pi}{24}t - 1.90\right) + 4 \sin\left(\frac{2\pi}{12}t + 1.50\right) + 1.5 \sin\left(\frac{2\pi}{8}t - 0.80\right)$$

$$T_N(t) = \bar{\vartheta}_N + \tilde{\vartheta}_N(t) = 10 + 4.5 \sin\left(\frac{2\pi}{8}t + 2.50\right) + 2 \sin\left(\frac{2\pi}{24}t - 0.50\right) + 0.5 \sin\left(\frac{2\pi}{12}t + 3.50\right)$$

The layer was modelled with 19 nodes in the numerical solution, and a temporal discretization interval  $\Delta t = 5$  s was used to ensure stability and convergence of the solution.

The comparison between the trends calculated with the analytical solution and with the numerical code is reported in terms of position of the bi-phase interface, temperature and heat flux at different abscissae in the layer in Figure 3.

The excellent agreement between the trends obtained justify use of the numerical code. The slight deviations of the temperature and the heat flux obtained using the numerical model to those calculated analytically, in the vicinity of the portion subject to phase change, they are due, as will be explained in detail in the next section, to the arrest and the next restart of the advancement of the bi-phase interface in the transition from a subvolume to the adjacent one.



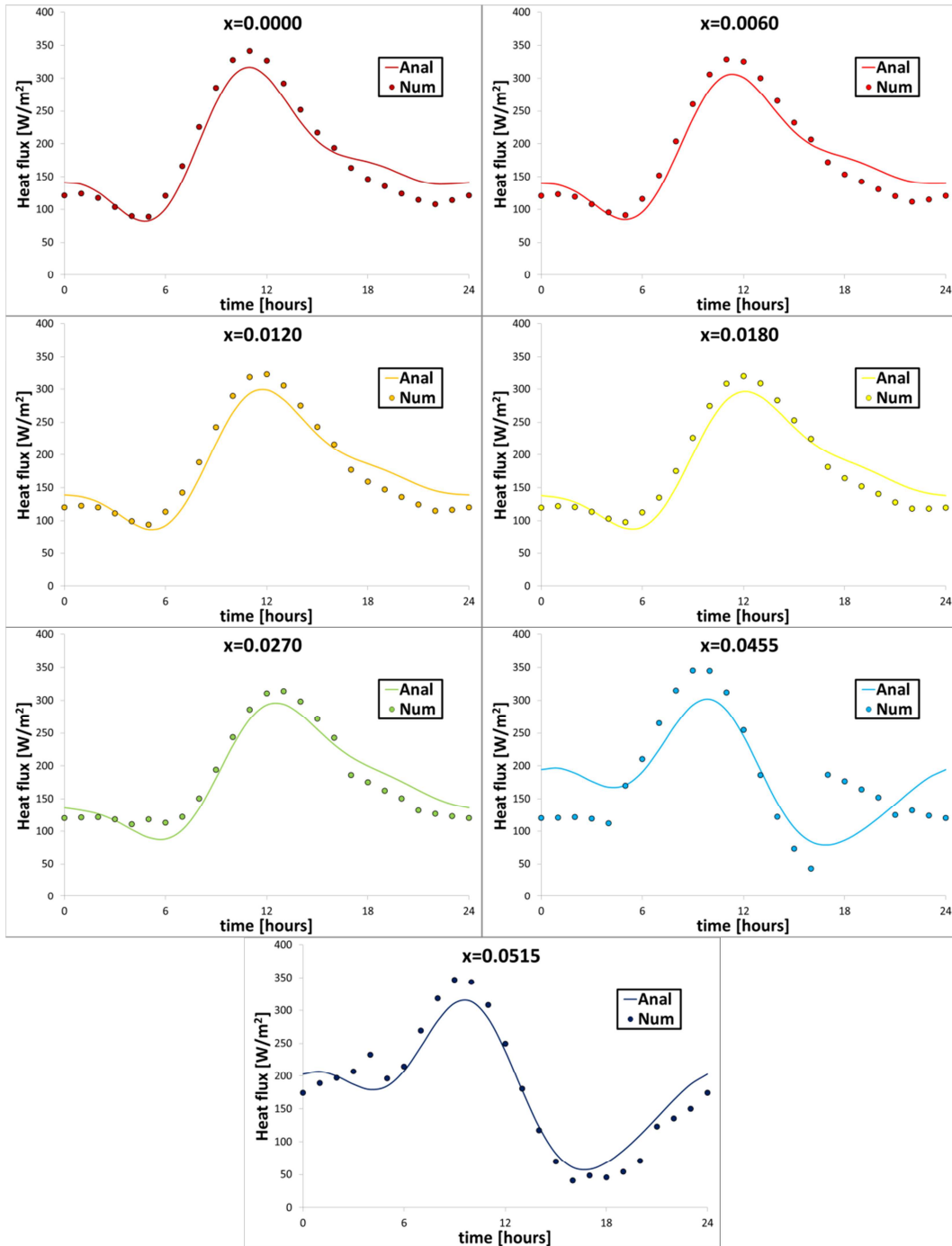


Figure 3 - Comparison between the trends calculated with the analytical solution and with the numerical code in terms of position of the bi-phase interface (top image), temperature (image in the center) and heat flux (bottom images) at different abscissae in the layer.

### 3. Results and discussion

#### 3.1. PCM considered and boundary conditions

The calculation model developed was used for a thermal analysis in steady periodic regime conditions of five different types of PCM (see Table 1), commercially available, of a thickness equal to 0.06 m. The PCM have different thermophysical properties and a variable melting temperature between 15 °C and 32 °C.

Table 1 – Thermophysical properties of the different types of PCM

Company	PCM	T <sub>M</sub> [K]	H [kJ/kg]	ρ [kg/m <sup>3</sup> ]	k [W/(m K)]	c <sub>p</sub> [kJ/(kg K)]
EPS [47]	S15	15	160	1510	0.43	1.90
TEAP [48]	LATEST 20T	20	175	1490	1	2.00
savENRG [49]	HS22P	23	185	1690	0.815	3.06
RUBITHERM [50]	SP26E	26	190	1450	0.6	2.00
CLIMATOR [51]	C32	32	162	1420	0.6	3.60

The hourly data of the external air temperature, the sky temperature and solar irradiation are for the monthly average days in Turin (Lat = 45° 7', Long = 7° 43') and Cosenza (Lat = 37° 30', Long = 15° 05'). The two locations are climatically different, the first is representative of a continental climate and the second is representative of a Mediterranean climate. The external air temperature and solar irradiation on the horizontal plane data utilised, relative to the monthly average days are those from the reference national standard [52] and are shown in Table 2.

Table 2 - Monthly average daily values of the external air temperature and solar irradiation on the horizontal plane in Turin and Cosenza.

COSENZA												
Months	Jan	Feb	Mar	Apr	May	Jun	Jul	Aug	Sep	Oct	Nov	Dec
G [MJ/m <sup>2</sup> ]	7.7	11.8	17.3	21.8	25.7	29.6	28.9	26	20	12.9	9.4	7.7
T <sub>ea</sub> [°C]	8.1	8.8	11.3	14.4	18.1	23.1	26	25.8	22.7	17.8	13.4	9.4
TURIN												
Months	Jan	Feb	Mar	Apr	May	Jun	Jul	Aug	Sep	Oct	Nov	Dec
G [MJ/m <sup>2</sup> ]	5	7.8	12.2	17	19.6	21.5	23.5	18.5	13.5	9.3	5.5	4.7
T <sub>ea</sub> [°C]	0.4	3.2	8.2	12.5	16.7	21.1	23.3	22.6	18.8	12.6	6.8	2

The type day of each month, represented through the monthly average hourly values of solar radiation on the vertical plane exposed to the South, of the sky temperature and of the external air temperature, were generated starting from monthly average daily values using TRNSYS 17 [53] software. The steps to obtain the monthly average hourly trend of the three loadings used in the simulations are as follows:

- use of Type 54a to obtain, from the monthly average daily values of the solar radiation on the horizontal plane and of the external air, the relative hourly values for all the days of the year;
- use of Type 16 to report the hourly solar radiation from the horizontal plane to the vertical plane exposed to the south;
- use of Type 69b, which implements Martin and Berdahl's model [54] to obtain the hourly temperature values of the sky temperature starting from the hourly values of the external air temperature, the saturation temperature corresponding to the ambient conditions, the atmospheric pressure and the cloudiness factor;
- for each month the relative average day was built, represented with 24 hourly values. Each hourly value was obtained as the average of the corresponding hourly values relative to all the days of the month.

For the external surface, we considered a solar absorption coefficient  $\alpha$  equal to 0.60, a convective heat transfer coefficient  $h_{c,e} = 20 \text{ W/m}^2 \text{ K}$  and a radiative heat transfer coefficient  $h_{r,e} = 5.35 \text{ W/m}^2 \text{ K}$  and on the internal side, a surface heat transfer coefficient  $h_{s,i} = 7.7 \text{ W/m}^2 \text{ K}$ . The value of the radiative heat transfer coefficient on the external surface was obtained from an previous experimental work by the authors [55], while, for the others the reference regulation [56] was applied.

In the indoor environment, the air temperature is constant and is equal to  $20^\circ\text{C}$  during the heating period,  $26^\circ\text{C}$  during the cooling period and  $23^\circ\text{C}$  in intermediate months. Previous values of internal air temperature in continuous regime were chosen according to the reference standard [57]. According to the national regulations [58], the heating period for Cosenza is from November to March and the cooling period from June to September. For Turin, the heating period is from October to April and the cooling period from June to August. For both localities, the remaining months were assumed as the intermediate period.

In all the simulations conducted in the present study, we modelled the layer with 19 nodes and used a time step  $\Delta t = 5 \text{ s}$ . Such values give rise to negligible errors in the determination of the liquid fractions and of the nodal temperature and ensure stability of the explicit solution. This result was obtained by means of parametrical simulations obtained by varying the number of

nodes and, for each nodalization, using a lower time step than the limit one to ensure stability of the numerical simulation. The space step used satisfies the condition of grid independence of the spatial discretization.

A steady periodic regime at a frequency of the imposed periodic temperature perturbation emerges following an initial transient oscillatory regime.

### 3.2. Configuration of phases in the layer and thermal fields

The calculation algorithm developed was used to determine, for each PCM and for the two locations considered, the position of any bi-phase interfaces and temperature field in the layer in the different months of the year. These results were used to define the configuration of the phases in the layer and to calculate the heat flux field and the energy stored per unit time, sum of the latent contribution and sensible contribution. In the successive sections, we report, for the location of Turin and for the PCM S15, upon variation of time in a period  $P = 24$  hours, the thermal configurations obtained in the layer in the case of the absence of a bi-phase interface (Section 3.2.1), of formation of a bi-phase interface (Section 3.2.2), of two bi-phase interfaces (Section 3.2.3) and of three bi-phase interfaces (Section 3.2.4). In the figures present in these sections the following are reported: on the top the temperature trends in the nodes and, for completeness, the trend of the equivalent external temperature  $T_{e,eq}$  [59-60], representative of the three loadings, of the internal air temperature  $T_{ai}$  and of the melting temperature  $T_M$ ; in the centre, for configurations with more phases, the corresponding trends of the bi-phase interfaces positions  $X_{M,k}$  and of the respective latent energies stored per unit time; lastly, at the bottom, the trends of the heat flux deriving from the outdoor environment  $\Phi_e$ , in the different nodes of the layer, and that which is transferred in the indoor environment  $\Phi_{ia}$ . The vertical lines indicate the beginning and the end of the phase change associated with each bi-phase interface and the time instants at which the process is reversed. A summary of the results obtained, using different PCMs for the two locations of Turin and Cosenza are reported in Section 3.2.5.

The analysis of the trends has shown that, whatever the configuration of the phases in the layer, the average temperature value in time, corresponding to the steady condition, varies linearly in the layer and the relative heat flux is constant.

It is to be pointed out that, due to the different velocity of variation of the external loadings in time, the velocity of advancement of the bi-phase interface is not constant. Therefore, the duration of the melting process, which gives rise to the storage of latent energy, is different from

that of the solidification process, with release of the stored energy. In the case of periodic occurrence of multiple bi-phase interfaces, according to that is reported in [44], a complex periodic variation of the heat transfer and of the heat storage arises.

### 3.2.1. Absence of phase change

In January, the boundary conditions of the layer provide surface temperatures that are always lower than the melting temperature, equal to 15°C, and the layer is always in a solid phase. Conversely, in the months of June, July and August surface temperatures that occur are always above the melting temperature and the layer is always in a liquid phase. The corresponding temperature and heat flux fields are shown for January and June in Figure 4, and for the months of July and August in Figure 5.

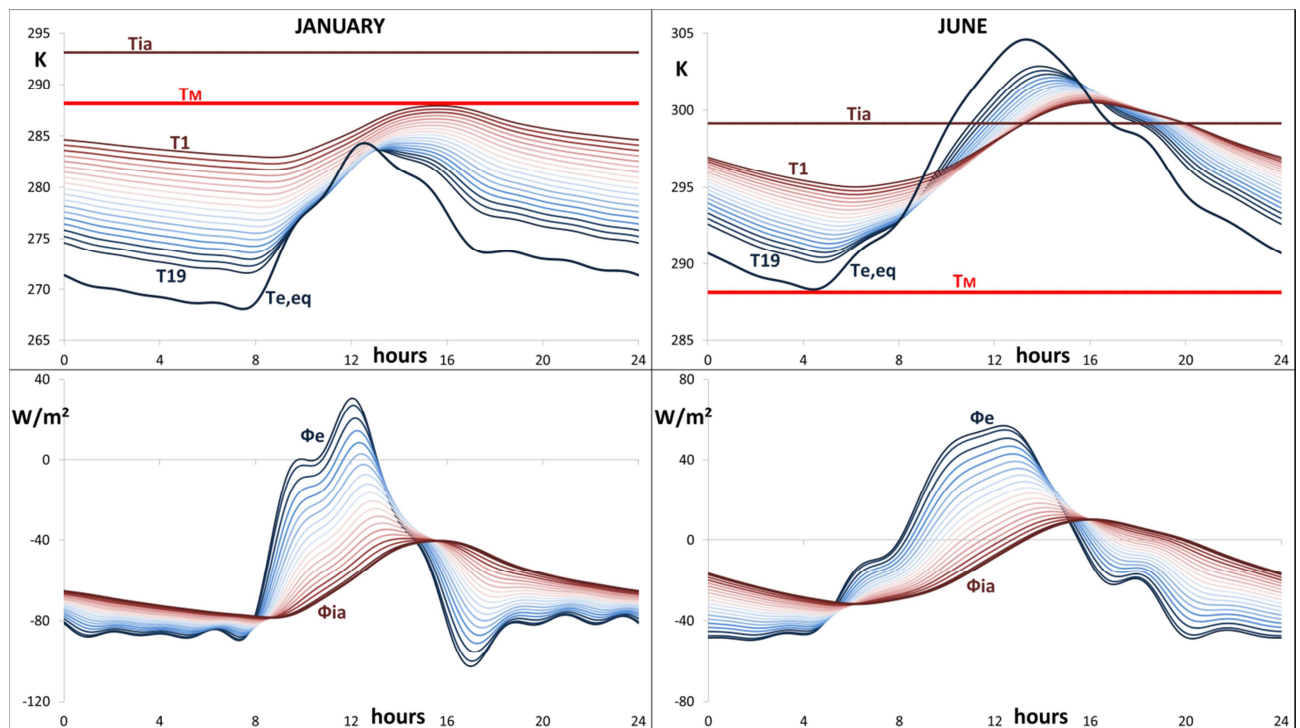


Figure 4 - Temperature field, external and internal loadings and melting temperature (top images), and heat flux field (bottom images) as a function of time in a PCM always solid (January) and always liquid (June).

In all the cases, the daily maximum excursion of the temperature fluctuation is reduced from the external surface towards the internal surface and the maximum peak and the minimum peak undergo a time lag. The heat flux presents a similar behaviour. It is necessary to highlight the inversion of the direction of heat flux in the layer between the diurnal and nocturnal hours, which is mainly produced by solar irradiation. In particular, in January, with the layer entirely in the



solid phase, during nocturnal hours the heat flux in all the nodes is directed towards the outdoor environment, while in the daytime the heating produced by solar absorption gives rise to the reversal of the heat flux in the more external nodes and a reduction in the heat flux dispersed in the other nodes.

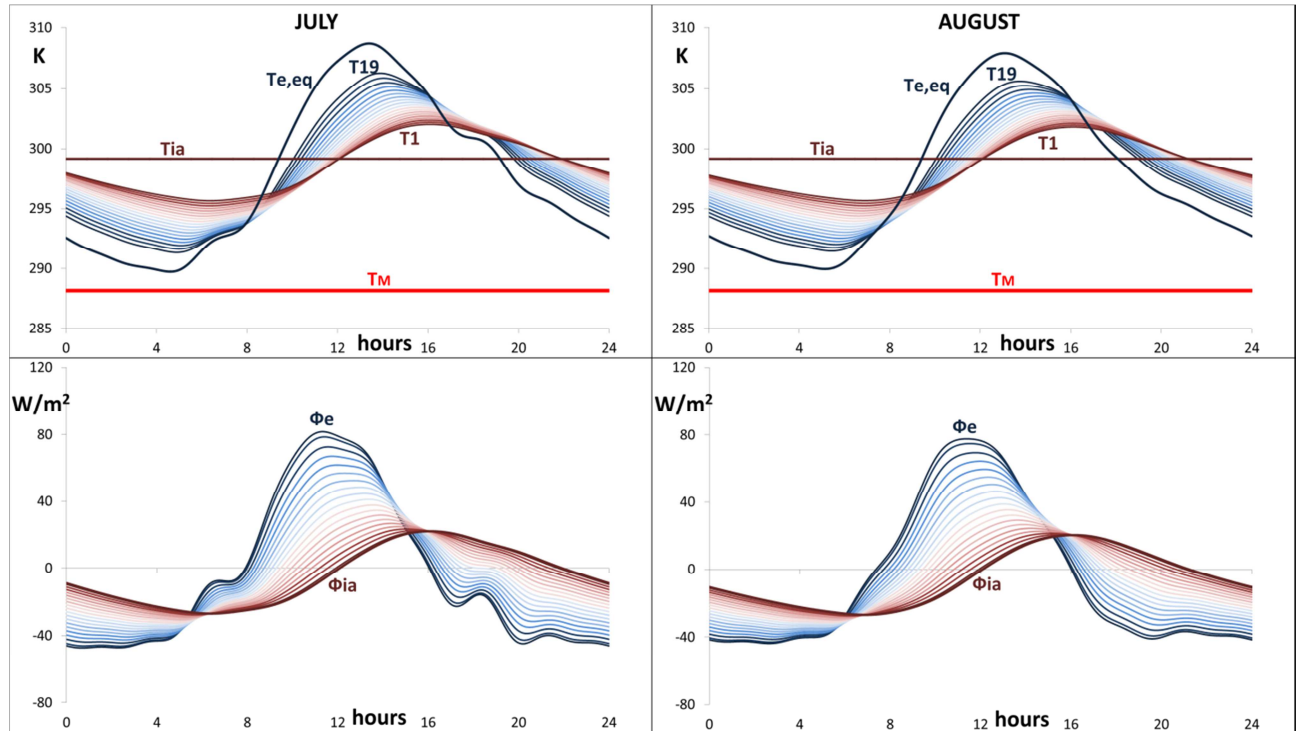


Figure 5 - Temperature field, external and internal loadings and melting temperature (top images), and heat flux field (bottom images) as a function of time in a PCM always liquid (July and August).

A similar behaviour is recorded in summer months (June, July and August), with the layer in a liquid phase. In these months, compared to January, the dispersed heat flux in nocturnal hours is less and, during diurnal hours, the inversion of the heat flux interests all the nodes of the layer and presents greater values. Such a behaviour is produced by the higher values of the three loadings during summer months.

### 3.2.2. Presence of a bi-phase interface

Figure 6 is for the months of February and December while Figure 7 regards the month of September. In such cases, there is only one bi-phase interface present in the layer. If the temperature of one of the boundary faces of the layer, at a given time instant of the period, becomes equal to the melting temperature a bi-phase interface originates that penetrates into the

layer, reaches a maximum depth, and then reverses direction and reconstitutes the initial monophasic layer. Only a part of the layer undergoes the phase change.

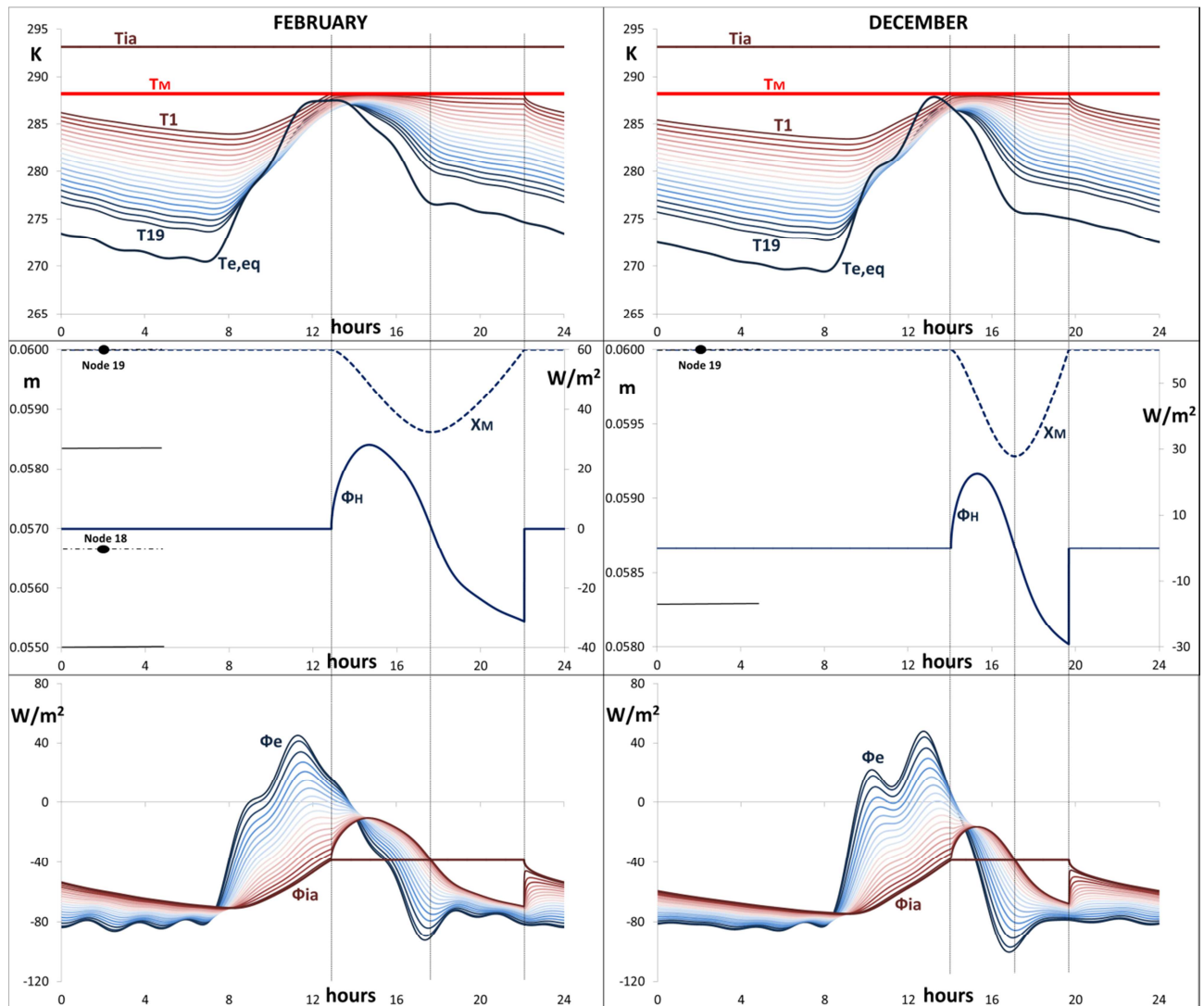


Figure 6. Temperature field, external and internal loadings and melting temperature (top images), position of the bi-phase interfaces and latent heat stored (images in the centre) and heat flux field (bottom images) as a function of time in a PCM layer in presence of one bi-phase interface (February and December).

In particular, in February and December, during nocturnal hours the layer is in the solid phase, with internal surface temperatures that are always greater than those recorded on the external surfaces. During the daytime, due to the prevalent effect of the solar irradiation absorbed by the external surface and of the surface heat exchange with the internal air, the layer heats and, even given the greater increases on the external surface, surface node 19 in contact with the internal air first reaches the melting temperature. The solar gain is not sufficient to heat the external

surface to 15°C due to the greater convective-radiative losses on the external surface compared to the losses recorded on the internal surface.

The solid-liquid phase change involves almost the entire volume of surface node 19 in February and only a portion of this in December. The temperature remains constant with a variation of slope at the start and at the end of the process (Images on the top in Figure 6). The extension of the volume involved in the phase change and the portions in a solid and liquid phase at different time instants are reported in the images in the centre. Also reported in the same image is the latent stored energy per unit time, which is proportional to the velocity of advancement of the bi-phase interface (Eq. 2). The latent energy stored first increases, reaches a maximum value and then decreases to zero at the time instant in which the bi-phase interface reverses direction and the solidification process begins. During this process, the energy released per unit time always increases and reaches the maximum value in the time instant in which the phase change stops with the recovery of the solid phase in all the volume of node 19. At the end of the solidification process, the bi-phase interface, reaching the internal surface, gives rise to an instantaneous annulment of the advancement speed with consequent discontinuity of the latent energy release trend per unit time.

The latent storage changes the thermal exchanges in node 19 subject to the phase change and, consequently, those of the other nodes. In particular, in the bottom images in Figure 6, during the melting process, the convective-radiative heat flux exchanged with the indoor environment  $\Phi_{ia}$  is constant as the temperature difference between the node surface, at the melting temperature, and the internal environment is constant.

Thus, the variation of latent energy stored per unit time determines the reduction of the conductive heat flux between surface node 19 and the adjacent node 18 and, subsequently, in the other nodes in the layer, attenuating moving outwards. In the time instant in which the melting process stops, the conductive heat flux exiting from the node 19 becomes equal to the convective-radiative heat flux entering the node. In the subsequent solidification process, the latent energy released per unit time determines the increase in the heat flux exiting from the surface node 19 towards the other internal nodes, while the convective-radiative heat flux remains constant. Also in this case, such a change is propagated in the internal nodes attenuating. It is necessary to highlight that in February, when compared to December, the bi-phase interface reaches a greater depth in the layer (1.4 mm compared to 0.7 mm) and uses a higher time interval to recover the initial phase (9.18 hours compared to 5.64 hours). In such a time interval, the melting process uses 4.70 hours in February and 3.15 hours in December, while the solidification

process occurs in 4.48 hours in February and 2.49 hours in December. The latent energy stored in February, equal to  $92.85 \text{ Wh/m}^2$ , is greater than that stored in December, which is equal to  $47.97 \text{ Wh/m}^2$ .

Behaviour in September is different in that, starting from the liquid phase during diurnal hours, due to the effect of convective-radiative heat exchange on the external surface during nocturnal hours, the layer cools and surface node 1, in contact with the outdoor environment, reaches the melting temperature at 5.36 hours.

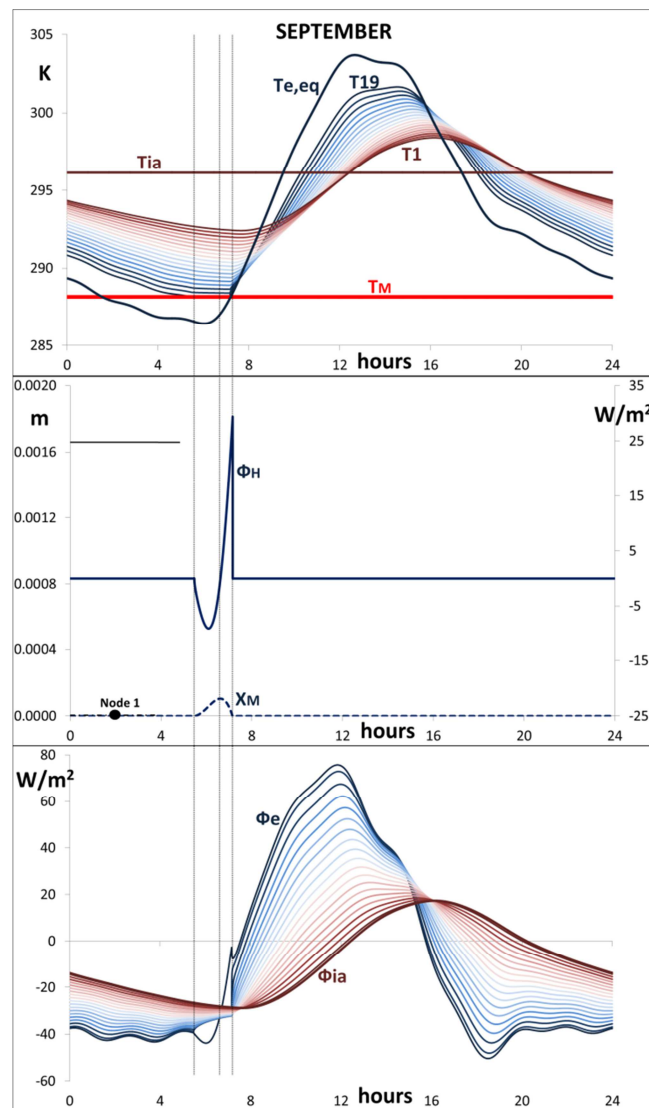


Figure 7. Temperature field, external and internal loadings and melting temperature (top image), position of the bi-phase interfaces and latent heat stored (image in the centre) and heat flux field (bottom image) as a function of time in a PCM layer in presence of one bi-phase interface (September).

The liquid-solid phase change involves only a portion of the volume of surface node 1, the temperature of which remains constant with a variation of slope both at the start and at the end of the process (top image in Figure 7). The solidification bi-phase interface penetrates into the layer, reaches a maximum depth at 6.61 and reverses the process by restoring the initial liquid phase at 7.16 due to the presence of solar irradiation. Due to the latent energy released during the solidification process, the surface heat flux of node 1 undergoes an increase, while in the successive melting process it undergoes a net reduction. In all the other nodes, the heat flux reduces slightly during the phase change.

The maximum depth reached by the bi-phase interface in the layer is equal to 0.1 mm and the process requires 1.80 hours. In such a time interval, the solidification process occurs in 1.25 hours while the melting process uses 0.55 hours. The latent energy stored is equal to 7.13 Wh/m<sup>2</sup>.

### 3.2.3. Presence of two bi-phase interfaces

Figure 8 regards May and October, while Figure 9 regards November. In these months, there are two bi-phase interfaces in the layer. When the temperature on one of the boundary faces of the layer in two successive time instants in the period, become equal to the melting temperature, it gives rise to two bi-phase interfaces: a solidification one and the other a melting one, that penetrate in the layer and reunite again to reform the initial monophasic layer. It may also occur that one of the interfaces originates on the internal surface and the other on the external surface and can both be of melting if the initial layer is solid or, they can both be of solidification if the initial layer is liquid.

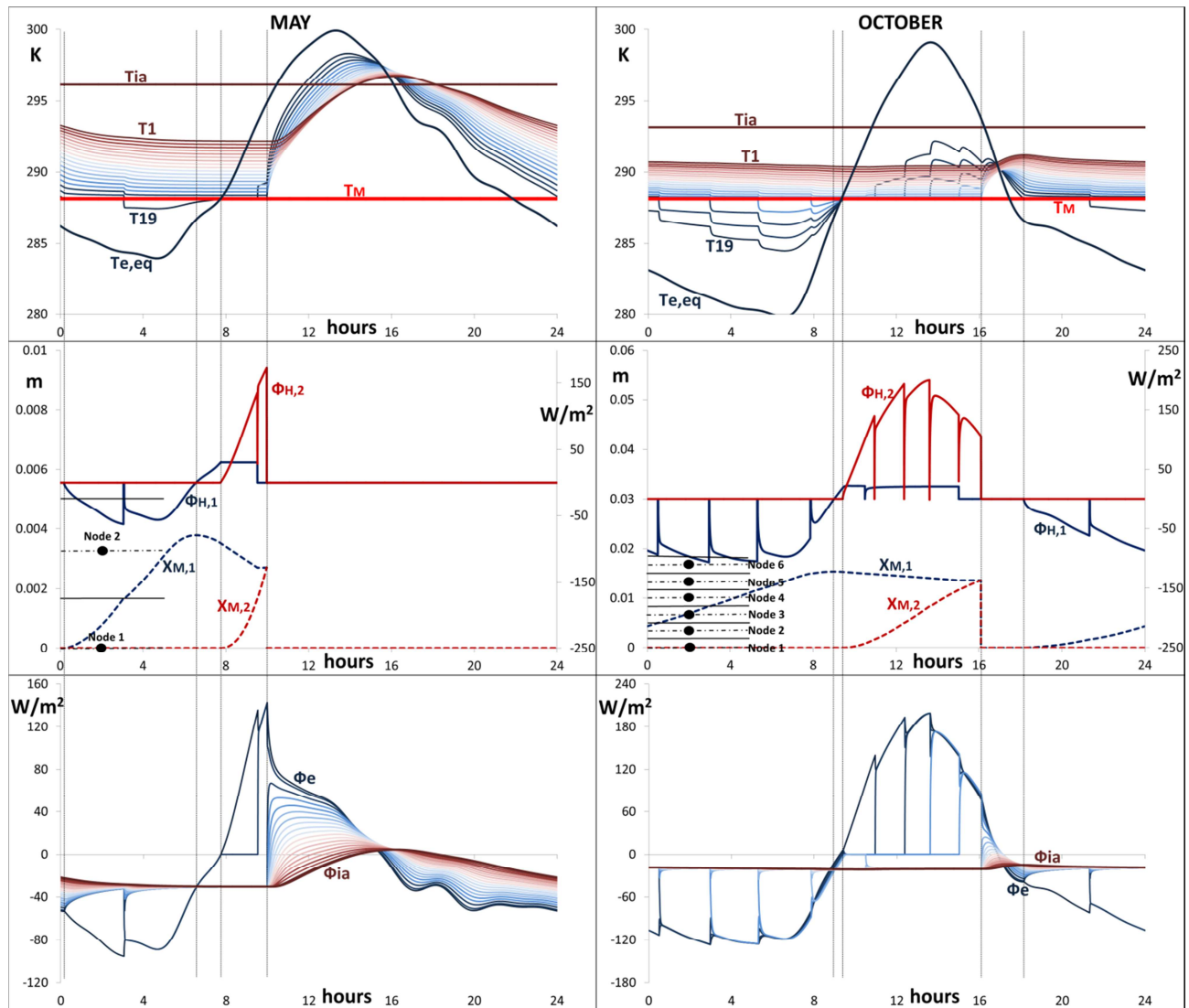


Figure 8. Temperature field, external and internal loadings and melting temperature (top images), position of the bi-phase interfaces and latent heat stored (images in the centre) and heat flux field (bottom images) as a function of time in a PCM layer in presence of two bi-phase interfaces (May and October).

In May the layer is affected by two bi-phase interfaces, a melting and a solidification interface, generated by oscillation of the equivalent temperature, representative of the external loadings, around the melting temperature. Starting from a layer completely in the liquid phase, at 0.31 hours a first solidification bi-phase interface is generated on the outer face; it penetrates into the layer and affects the volume of node 1, and only partly affects the volume of node 2. Once the maximum depth is reached, this interface inverts direction and it changes into a melting interface due to the presence of solar radiation. Subsequently, starting again from the outer face, at 7.69 hours a second melting bi-phase interface originates which, after having determined the variation of the phase in the volume of node 1, reaches the first bi-phase interface in the volume

of node 2, and restores the starting liquid phase in the whole layer (image in the center in the Figure 8). Figure 8 also reports the trend of the latent energy stored per unit time associated to the formation of the first and second bi-phase interface.

During the solidification process, the energy released per unit time at first increases, then reaches a maximum value and subsequently decreases to zero at the time instant in which the bi-phase interface reverses direction. At this time instant, the melting process begins with a storage of latent energy that increases and which is then constant following the formation of the second bi-phase interface. The second melting bi-phase interface gives rise to a trend of the stored energy per unit time that increases and then annuls itself in the time instant in which the bi-phase interface reaches the first melting interface.

It ought to be highlighted that the spatial discretization of a layer subject to phase change requires a very dense nodalization to render the advancement of the bi-phase interface continuous in transition of the volume from one node to the next. Thus, once the phase change in a node has completed, a very dense nodalization reduces the time taken for the next node to reach the melting temperature thus avoiding stopping and then restarting the bi-phase interface. In this transition, the latent energy stored per time unit is cancelled, creating perturbation that is extinguished in the time instant in which the next node reaches the melting temperature. Such perturbation, on the first solidification bi-phase interface and the second melting bi-phase interface in the transition between the node 1 and node 2, is also highlighted by heat flux trends in the layer, which are in the bottom image of Figure 8. The image highlights that the formation of the solid-liquid interface on the external surface of the wall, with the release of the stored latent heat, determines the increase of the heat flux dispersed by node 1 to the outdoor environment and a reduction of heat fluxes exiting the other nodes. The phase change in node 2 gives rise to an increase of the heat flux exiting node 2, which becomes very close to the heat flux dispersed from node 1, while in the other nodes the heat flux is approximately constant. In the following time instants, the heat fluxes exiting node 1 and 2 decrease following the reduction of the velocity of advancement of the bi-phase interface until it equals the heat fluxes in the successive nodes in the time instant when the process inverts. In the time instant in which the second melting bi-phase interface is formed on the external surface, with the first bi-phase interface which is also of melting that interests the second node, the external heat flux in node 1 is used entirely for the advancement of the second melting bi-phase interface while the first melting bi-phase interface, which has an opposite direction, only uses the conductive heat flux from the internal surface of the layer. In such conditions, the conductive heat flux in node 2 from

the adjacent nodes is null, that in node 1 equals the latent energy stored per unit time, and the heat flux in the subsequent nodes is equal to the energy stored per unit time of the first bi-phase interface. At the time instant of phase change completion, the fluctuating heat flux from the outdoor environment penetrates the layer and subsequently is attenuated and undergoes a time lag. The maximum depth reached by the first bi-phase interface in the layer is equal to 3.79 mm and the recovery of the liquid phase in the entire layer occurs at a depth equal to 2.68 mm. The solidification process produced by the first bi-phase interface has a duration of 6.34 hours while that of the melting is 3.28 hours. The recovery of the liquid phase achieved by means of the second bi-phase interface, requires 2.34 hours. The latent energy stored by the two bi-phase interfaces is equal to  $254.56 \text{ Wh/m}^2$  and this energy is released solely by the first solidification bi-phase interface.

In October, the layer is also affected by two bi-phase interfaces, one of melting and the other of solidification, since the external loadings give rise to a fluctuation of the equivalent external temperature around the melting temperature. Starting from a layer that is completely in a liquid phase, on the external face at 18.06 hours a first solidification bi-phase interface is generated, penetrating the layer and affecting the volume of the first five nodes and only part of the volume of the sixth node. This interface, once the maximum depth is reached at 8.94 hours, it inverts direction and transforms into a melting interface. Subsequently, starting again from the external face, at 9.34 hours a second melting interface originates which, after having determined the variation in the phase of the volume of the first five nodes, reaches the first interface in the volume of node 5 and recovers the starting liquid phase at 16.04 hours in the entire layer (image in the center of Figure 8). Compared to the month of May both the duration, equal to 21.98 hours, and the total volume affected by the phase change, equal to 15.40 mm, are greater.

Also in this case, during the solidification process, the energy released per unit time increases, reaches a maximum value and subsequently decreases until it annuls itself in the time instant in which the bi-phase interface inverts direction. In this time instant, the melting process starts with a storage of energy that, at first increases and subsequently is constant following the modest velocity of advancement of the bi-phase interface. The reduced velocity of advancement is due to the formation of the second bi-phase interface. The second melting bi-phase interface gives rise to a growing trend of the energy stored per unit time, reaches a maximum value and subsequently reduces and annuls itself in the time instant in which the interface reaches the first melting interface.



The heat flux trends highlight that the formation of the solid-liquid interface on the external face of the wall, with the release of stored latent heat, determine the increase of the heat flux dispersed by surface node 1 towards the outdoor environment and a reduction of the heat fluxes exiting the other nodes. The phase change in node 2 gives rise to an increase of the heat flux exiting node 2 which becomes very close to the heat flux dispersed by node 1 while, in all subsequent nodes it is identical and almost constant. The heat flux records a similar behaviour in nodes 3, 4, 5 and 6, when they are reached by the bi-phase interface. For example, when the bi-phase interface reaches node 3, the heat flux dispersed by the node becomes close to the heat flux dispersed by preceding nodes 2 and 1 while in successive nodes, the heat flux assumes identical values and remains constant.

Once node 6 is reached, the last node affected by the phase change, the heat fluxes exiting the first six nodes assumes near values and, following a reduction of the advancement velocity of the bi-phase interface, decrease. Subsequently, at the time instant of inversion of the process, the heat flux in the first six nodes becomes equal to the subsequent nodes.

The second melting interface that is formed on the external face, with the first interface which is also of melting and interests the sixth node, entirely uses the external heat flux for advancement in the volume of node 1. At the same time, the first melting interface, which has an opposite direction, uses all the conductive heat flux from the inner side of the layer for the phase change. In such conditions: the conductive heat fluxes in nodes 2, 3, 4, 5 and 6, interposed between the two bi-phase interfaces, are null; that of node 1 is equal to the latent energy stored per unit time of the second bi-phase interface; the heat flux in the subsequent nodes (7-19) is equal to the latent energy stored per time unit from the first bi-phase interface.

Successively, with the second bi-phase interface still in node 1, the first bi-phase interface, after having recovered the liquid phase in node 6, reaches the volume of node 5. Starting from this time instant, the trend of the heat fluxes changes: the conductive heat fluxes in nodes 2, 3, 4 and 5, interposed between the two bi-phase interfaces, are still nil; instead, that of node 1 is equal to the latent energy stored per unit time of the second bi-phase interface; the heat flux in the successive nodes (6-19) is equal to the energy stored per unit time of the first bi-phase interface. The first bi-phase interface, in the successive time instants, and until reunion with the second bi-phase interface, solely affects the volume associated to node 5 given the reduced advancement velocity. Instead, the second bi-phase interface penetrates in the layer and reaches the first bi-phase interface in node 5. In this time interval: the heat flux in the node affected by the advancement of the second bi-phase interface and in the preceding nodes is equal to the latent

energy stored per unit time; the conductive heat fluxes in the nodes interposed between the two bi-phase interfaces are nil; the heat flux in nodes 6-19 is equal to the energy stored per unit time from the first bi-phase interface. For example, with the melting interface in the volume of node 2, the heat flux in nodes 1 and 2 increases in the same way as the latent energy stored per unit time, while that in nodes 3, 4 and 5 is nil. In all the successive nodes it is constant and equal to the latent energy stored per unit time from the first bi-phase interface. Once the two melting bi-phase interfaces have been reunited and, the liquid phase recovered in the layer, the heat flux from the external environment penetrates the layer attenuating and undergoing a time lag until formation of the first solidification interface in the successive period.

The solidification process produced by the first bi-phase interface has a duration of 14.88 hours while the melting process lasts 7.10 hours. The restoration of the liquid phase, accomplished by the second bi-phase interface takes 6.70 hours. The latent energy stored by the two bi-phase interfaces is equal to  $1034.56 \text{ Wh/m}^2$ ; this energy is only released by the first solidification interface.

In November, two melting interfaces originate; one starts from the inner surface and the other from the outer surface.

Starting from a layer completely in solid phase, a first melting bi-phase interface is generated on the outer face at 12.87 hours which penetrates into the layer and in part affects the volume of node 1. The interface reaches the maximum depth at 15.27 hours, then inverts direction and turns into a melting interface until the initial solid phase is restored at 16.45 hours. At the same time, a second melting interface originates on the inner surface starting at 11.85 hours which, after having determined the phase variation in the whole volume of node 19 and in a portion of the node 18, reverses direction at 18.83 hours and restores the starting solid phase at 6.13 hours (image in the center of Figure 9).

Compared to the months of May and October, the bi-phase interfaces arise on the two opposite faces. It arises on the outer surface due to solar irradiation, while on the inner surface due to the effect of heat exchange with the internal air, which is at higher temperature. For both bi-phase interfaces, during the melting process the latent energy stored per unit time first increases, then reaches a maximum value and subsequently decreases to zero at the time instant in which the bi-phase interface inverts direction. During the solidification process, associated with both the bi-phase interfaces, the latent energy released per unit time is always increasing and annuls in the time instant in which the phase change stops.

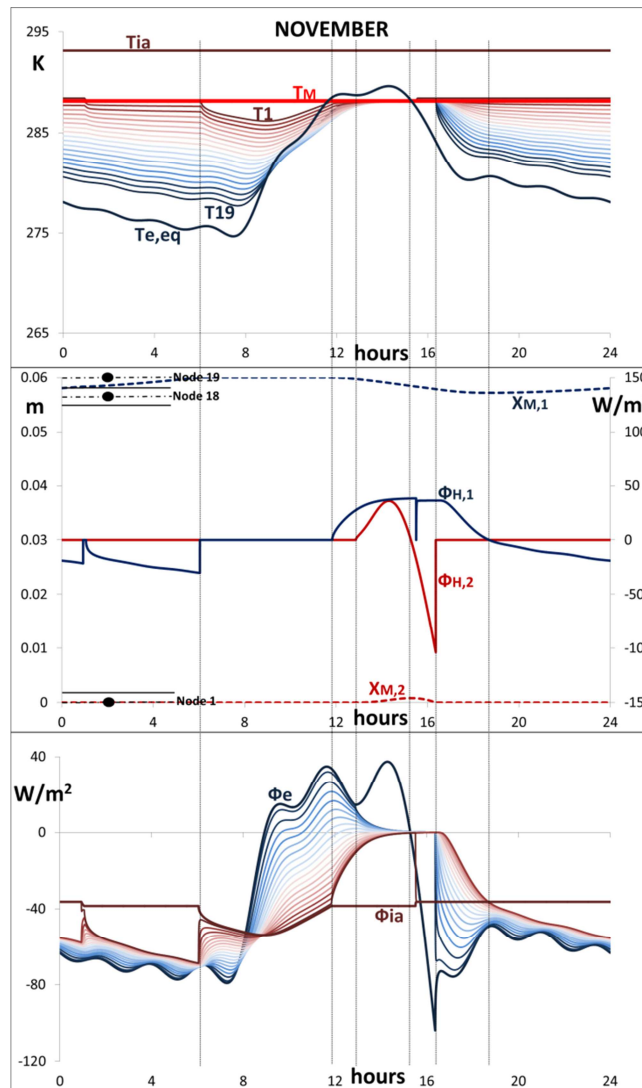


Figure 9. Temperature field, external and internal loadings and melting temperature (top image), position of the bi-phase interfaces and latent heat stored (image in the centre) and heat flux field (bottom image) as a function of time in a PCM layer in presence of two bi-phase interfaces (November).

The formation of the interface on the internal surface modifies the trends of the heat fluxes in the nodes affected in a similar way to that described in February and December. In particular, the internal convective-radiative internal heat flux is constant during the phase change. The heat flux dispersed in node 19 is constant when the bi-phase interface is in node 18, it increases by a quantity equal to the latent energy released per unit time when it is in node 19 and the process is of melting; it reduces by a quantity equal to the latent energy released per unit time when it is in node 19 and the process is of solidification. The heat flux dispersed in node 18, regardless of the position of the bi-phase interface, increments when the process is of solidification and decreases when it is of melting.

Regarding the formation of the interface on the external surface, the changes undergone by the heat flux trend in node 1 are similar to those recorded in September. In particular, during the melting process in that node, the heat flux is equal to that entering the layer through the outer surface and is entirely stored in latent form, while it decreases in the subsequent nodes. During the solidification process, the heat flux in node 1 is equal to the energy released per unit time and in the successive nodes, interposed between the two bi-phase interfaces, is null.

In the time instants in which there are no bi-phase interfaces in the layer, the heat flux from the outdoor environment penetrates the layer, attenuating and undergoing a time lag.

The maximum depth reached by the bi-phase interfaces that originate on the internal and external surfaces are equal, respectively, to 3 mm and 0.78 mm. The solidification processes produced by the external and internal side bi-phase interfaces have a duration respectively of 1.18 hours and of 11.30 hours while those of melting has a duration of 2.40 hours and 6.98 hours. The latent energy stored by the two bi-phase interfaces is equal to 209.86 Wh/m<sup>2</sup>.

#### 3.2.4. Presence of three bi-phase interfaces

The boundary conditions in the layer in March and April determine three bi-phase interfaces as shown in Figure 10.

In March one bi-phase interface forms close to the internal surface and two form on the external surface. The liquid-solid bi-phase interface close to the internal surface is always present in period P and affects the volumes in nodes 16, 17 and 18 and not surface node 19, which is always in a liquid phase. On the external surface, the second melting interface and the third solidification interface originate respectively at 10.78 and 16.33 hours and affect both the volumes of nodes 1 and 2 and, in part, the volume of node 3, in which the recovery of the solid phase at 20.25 hours occurs. With reference to the first interface, during the solidification process, the release of latent heat stored per unit time increases, reaching a maximum and is annulled in correspondence with the inversion of the bi-phase interface with the start of the melting process. During such a process, the trend of the stored latent heat per unit time is similar to the previous and in the time instant in which it is nil the process inverts. Considering the external surface, the latent energy stored per unit time of the second melting bi-phase interface trend at first increases, then reaches a maximum value and subsequently decreases annulling itself in the time instant in which the third solidification bi-phase interface originates on the external surface. The energy released through the advancement of such interface increases in time and is annulled in the time instant in which the third bi-phase interface reaches the second.

As regards the heat flux field during the solidification process, with the first bi-phase interface in node 16, in nodes 17 and subsequent nodes (18 and 19) does not vary by presenting identical values, in that the temperature is constant in both node 16 and the successive nodes. Similar temperature and heat flux trends are recorded in the subsequent nodes when the bi-phase interface affects node 17 or node 18. For this reason, the heat flux exiting the indoor environment and the conductive heat flux between nodes 18 and 19 are equal and constant. The heat flux, in the time interval during which the second melting interface moves towards the inside of the layer, is reduced in the nodes subsequent to the bi-phase interface since the heat flux entering from the external surface is used for the phase change. In the nodes that precede the bi-phase interface, the heat flux increases by a quantity equal to the corresponding latent energy stored per unit time. In the time interval in which the third solidification bi-phase interface also operates, in the nodes that precede the bi-phase interface the heat flux exiting towards the outdoor environment increases by a quantity equal to the latent energy released per unit time. In all the successive nodes in liquid phase, including those between the third and second bi-phase interface, the heat flux is annulled.

In the time interval in which there are no bi-phase interfaces on the external surface, during the latent energy storage process, consequent to the melting produced by the first bi-phase interface, the heat flux exiting towards the outdoor environment in the nodes preceding such an interface are reduced while in the successive nodes it increases. In the successive process of latent energy release, the heat flux exiting the layer increases in all the nodes that precede the solidification interface.

The maximum depth reached by the internal side bi-phase interface is equal to 9.0 mm and that of the two external side bi-phase interfaces is identical and equal to 5.9 mm, abscissa in which the reunification of the two interfaces occurs. The melting process associated to the second bi-phase interface and that of solidification associated to the third bi-phase interface, have a duration of respectively 9.47 hours and 3.92 hours. The latent energy stored by the three bi-phase interfaces is equal to  $610.55 \text{ Wh/m}^2$ .

In April, two bi-phase interfaces originate on the external surface; one is a solidification interface affecting the first 5 nodes and partially affecting node 6 and the other is a melting interface reaching the first bi-phase interface in the fifth node to recover the initial liquid phase. The solidification bi-phase interface originates at 18.28 hours, the melting bi-phase interface occurs at 9.46 hours of the successive period, and recovery occurs at 21.61 hours of the successive period. Therefore the solidification interface remains in the layer for a time interval

greater than the period  $P=24$  hours. From 21.61 hours to 9.46 hours, only a solidification bi-phase interface is present in the layer, from 9.46 hours to 18.28 hours there are two bi-phase interfaces and, finally, from 18.28 hours to 21.61 hours there are three bi-phase interfaces.

The trend of the temperatures in the nodes, of the positions of the bi-phase interfaces, of the energy stored and released consequent to the phenomena of melting and solidification, of the heat fluxes in the nodes, and the nodes interested in the phase change are similar to those described in October. In such a month, the duration of the phase changes is different, as they all complete in a time interval less than the period. Consequently, in April compared to October, the heat flux trend is different only in the time interval in which no phase changes are present.

The solidification process produced by the first bi-phase interface has a duration of 14.74 hours while the melting process has a duration of 12.59 hours. The recovery of the liquid phase, achieved with the second bi-phase interface, requires 12.15 hours. The latent energy stored consequent to the phase changes is, overall, equal to  $1093.94 \text{ Wh/m}^2$  and is only released by the first solidification interface.

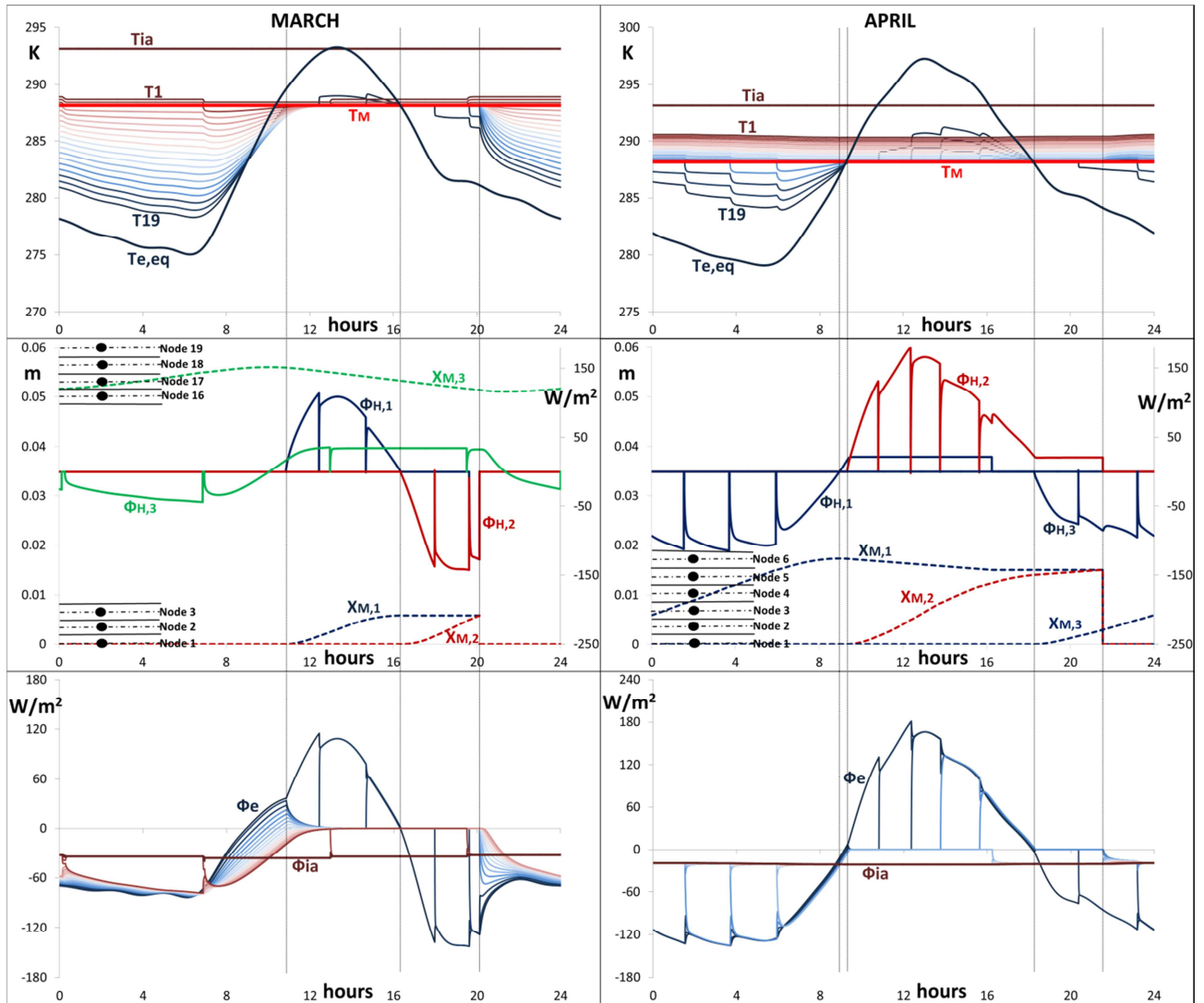


Figure 10. Temperature field, external and internal loadings and melting temperature (top images), position of the bi-phase interfaces and latent heat stored (images in the centre) and heat flux field (bottom images) as a function of time in a PCM layer in presence of three bi-phase interfaces (March and April).

### 3.2.5. Phases configurations in the different PCM for the two considered locations

For the PCM previously defined in Section 3.1, Figure 11 for Turin and Figure 12 for Cosenza report the number of bi-phase interfaces that form in the layer and the disposal of the phases, proceeding from the external surface towards the internal surface, for each month of the year. The number of the bi-phase interfaces is the maximum which is contemporaneously present in the layer in a defined time interval belonging to period  $P = 24$  hours.

S15			LATEST20			HS22P			SP26E			C32		
	N° interface	Phases configuration in the layer		N° interface	Phases configuration in the layer		N° interface	Phases configuration in the layer		N° interface	Phases configuration in the layer		N° interface	Phases configuration in the layer
JAN	0	sol	JAN	0	sol	JAN	0	sol	JAN	0	sol	JAN	0	sol
FEB	1	sol liq	FEB	0	sol	FEB	0	sol	FEB	0	sol	FEB	0	sol
MAR	3	sol liq sol liq	MAR	0	sol	MAR	0	sol	MAR	0	sol	MAR	0	sol
APR	3	sol liq sol liq	APR	2	sol liq sol	APR	0	sol	APR	0	sol	APR	0	sol
MAY	2	liq sol liq	MAY	3	sol liq sol liq	MAY	1	liq sol	MAY	0	sol	MAY	0	sol
JUN	0	liq	JUN	2	liq sol liq	JUN	2	liq sol liq	JUN	2	sol liq sol	JUN	0	sol
JUL	0	liq	JUL	1	sol liq	JUL	2	liq sol liq	JUL	2	sol liq sol	JUL	0	sol
AUG	0	liq	AUG	2	liq sol liq	AUG	2	liq sol liq	AUG	2	sol liq sol	AUG	0	sol
SEP	1	liq sol	SEP	2	liq sol liq	SEP	2	sol liq sol	SEP	2	sol liq sol	SEP	0	sol
OCT	2	liq sol liq	OCT	2	sol liq sol	OCT	0	sol	OCT	0	sol	OCT	0	sol
NOV	2	liq sol liq	NOV	0	sol	NOV	0	sol	NOV	0	sol	NOV	0	sol
DEC	1	sol liq	DEC	0	sol	DEC	0	sol	DEC	0	sol	DEC	0	sol

Figure 11 – Number of bi-phase interfaces present in the layer and arrangement of the phases from the outside to the inside in the various months of the year and for different PCM. Turin.

S15			LATEST20			HS22P			SP26E			C32		
	N° interface	Phases configuration in the layer		N° interface	Phases configuration in the layer		N° interface	Phases configuration in the layer		N° interface	Phases configuration in the layer		N° interface	Phases configuration in the layer
JAN	3	sol liq sol liq	JAN	0	sol	JAN	0	sol	JAN	0	sol	JAN	0	sol
FEB	3	sol liq sol liq	FEB	2	sol liq sol	FEB	0	sol	FEB	0	sol	FEB	0	sol
MAR	3	sol liq sol liq	MAR	2	sol liq sol	MAR	0	sol	MAR	0	sol	MAR	0	sol
APR	2	liq sol liq	APR	3	sol liq sol	APR	2	sol liq sol	APR	0	sol	APR	0	sol
MAY	2	liq sol liq	MAY	3	sol liq sol liq	MAY	2	sol liq sol	MAY	2	sol liq sol	MAY	0	sol
JUN	0	liq	JUN	2	liq sol liq	JUN	2	liq sol liq	JUN	2	sol liq sol	JUN	0	sol
JUL	0	liq	JUL	1	sol liq	JUL	2	liq sol liq	JUL	2	liq sol liq	JUL	2	sol liq sol
AUG	0	liq	AUG	1	sol liq	AUG	2	liq sol liq	AUG	2	liq sol liq	AUG	2	sol liq sol
SEP	0	liq	SEP	2	liq sol liq	SEP	2	liq sol liq	SEP	2	sol liq sol	SEP	2	sol liq sol
OCT	2	liq sol liq	OCT	3	sol liq sol liq	OCT	2	sol liq sol	OCT	2	sol liq sol	OCT	0	sol
NOV	2	liq sol liq	NOV	2	sol liq sol	NOV	2	sol liq sol	NOV	1	liq sol	NOV	0	sol
DEC	3	sol liq sol liq	DEC	2	sol liq sol	DEC	0	sol	DEC	0	sol	DEC	0	sol

Figure 12 - Number of interfaces present in the layer and arrangement of the phases from the outside to the inside in the various months of the year and for different PCM. Cosenza.



The tables show the variability of the configurations of the phases in the layer varying the melting temperature and the external climatic conditions. In general, upon an increase of the melting temperature, the number of months in which only the solid phase is present increases; first, the intermediate months are added to the winter months and then the summer months are added. The months in which there is only the liquid phase, however, increase with a decreasing melting temperature. In the other months, there are one, two or three bi-phase interfaces in the layer. For the same melting temperature, the higher external air temperature and solar radiation values in Cosenza give rise to more months in which the phase is only liquid and, in the months in which there is phase change, a higher portion of liquid phase material. In the presence of a phase change, the formation dynamics and the type of bi-phase interface are attributable to those described in the preceding Sections; the portion of the layer affected by the phase change, the duration of melting or solidification processes and the relative energy stored and successively released in latent form change.

The comparison between the distributions of temperature and heat flux in the layer for different PCM in the different months of the year are reported respectively in Figures 14 and 15 for Turin and in Figures 16 and 17 for Cosenza.

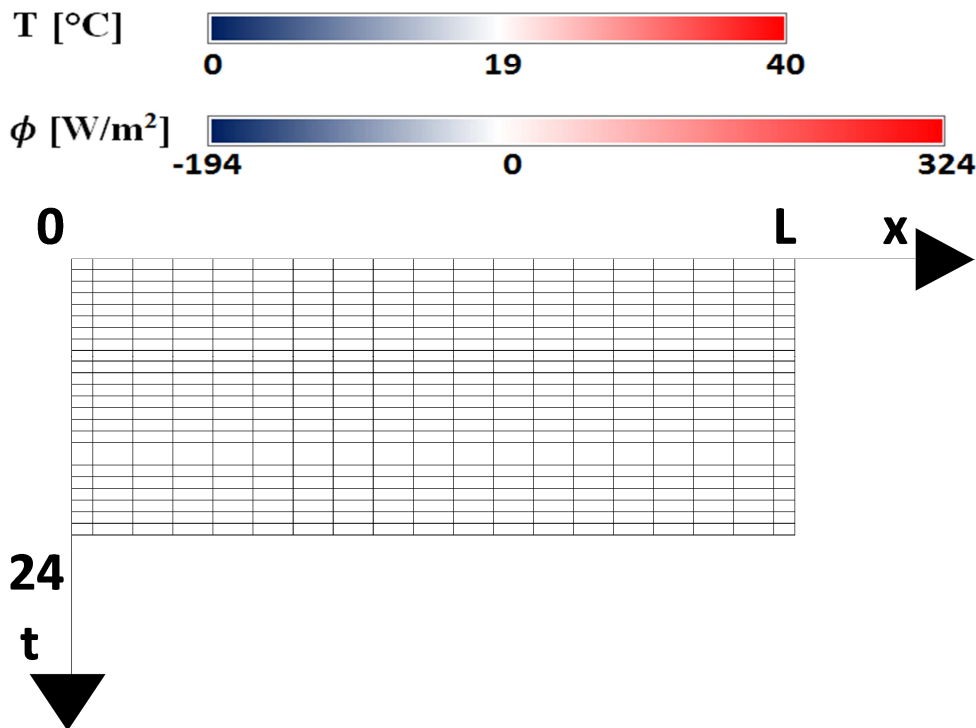


Figure 13 – Spatio-temporal grid for the identification, according to a colour scale from blue to red, of the temperature and heat flux of the nodes in the PCM layer.

With reference to Figure 13, in each image, relative to a particular month and PCM, along direction  $x$ , the volumes associated with the single nodes are reported, starting from the external surface ( $x=0$ ) to the internal surface ( $x=L$ ). Instead, along direction  $t$ , all the hours relative to the period  $P=24$  h are reported. A cell of the table represents the volume associated to a node at a particular instant in time. In each cell, a colour whose scale is variable from blue (minimum value) and red (maximum value) represents the temperature and the heat flux. In particular, a heat flux directed towards the outdoor environment (numerically negative) is associated to the blue graduation heat flux, while a heat flux directed towards the indoor environment (numerically positive) is associated with the red graduation heat flux. The colour white highlights the annulment of the heat flux.

In the absence of a phase change or for reduced latent energy values, the excursions of temperature and of heat flux in the period  $P$ , produced mainly by the external loadings, remain highlighted both on the external surface as well as on the internal surface; they denote the reduced phenomena of storage and release of energy. Furthermore, the images allow for identification of the attenuation and time lag that are undergone by such excursions when they proceed in the layer from the external surface to the internal surface.

In the presence of a phase change, the temperature field images do not directly highlight the number and position of the bi-phase interfaces at different temporal instants, but indicate in which months and for which PCM the latent energy stored and successively released is higher. A greater total volume involved in the phase change in period  $P$  corresponds to high levels of such energy, determining a greater advancement velocity of the bi-phase interface. To this, a larger region whose temperature is uniform corresponds, as in the case of S15 in the months of April and October, of LATEST20 in the months of May and September, of HS22P in June and of SP26E in July and August in Turin and, in the case of S15 in March, April, November and December, of LATEST20 in April, May and October, of HS22P in June and September and of SP26E in the months between June and September in Cosenza. The different melting temperature gives rise, in the months in which the temperature is almost uniform, to different colours.

The images of the heat flux fields highlight the number, the typology, the position and the evolution in time of the bi-phase interfaces. In particular, at a given time instant, the presence in the layer of bi-phase interfaces is highlighted by the sudden variation in colour; this also allows for the identification of the bi-phase interface type: proceeding from the external surface towards the internal surface, the change from the colour blue to white and red denotes a melting bi-phase

interface; instead, the change from the colour red to white and blue indicates the presence of a solidification bi-phase interface. For example, for S15 in Turin in March: on the external surface during diurnal hours the change from red to white indicates the evolution in time of the melting bi-phase interface which penetrates within the layer involving the first three nodes, while during nocturnal hours the change from blue to white identifies the presence of a solidification bi-phase interface which is also directed towards the inside of the layer; a third bi-phase interface is always present in period P in proximity to the internal surface which is a melting interface in the hours in which the colour varies from white to light blue and is a solidification interface in the hours in which the colour varies from blue to light blue.

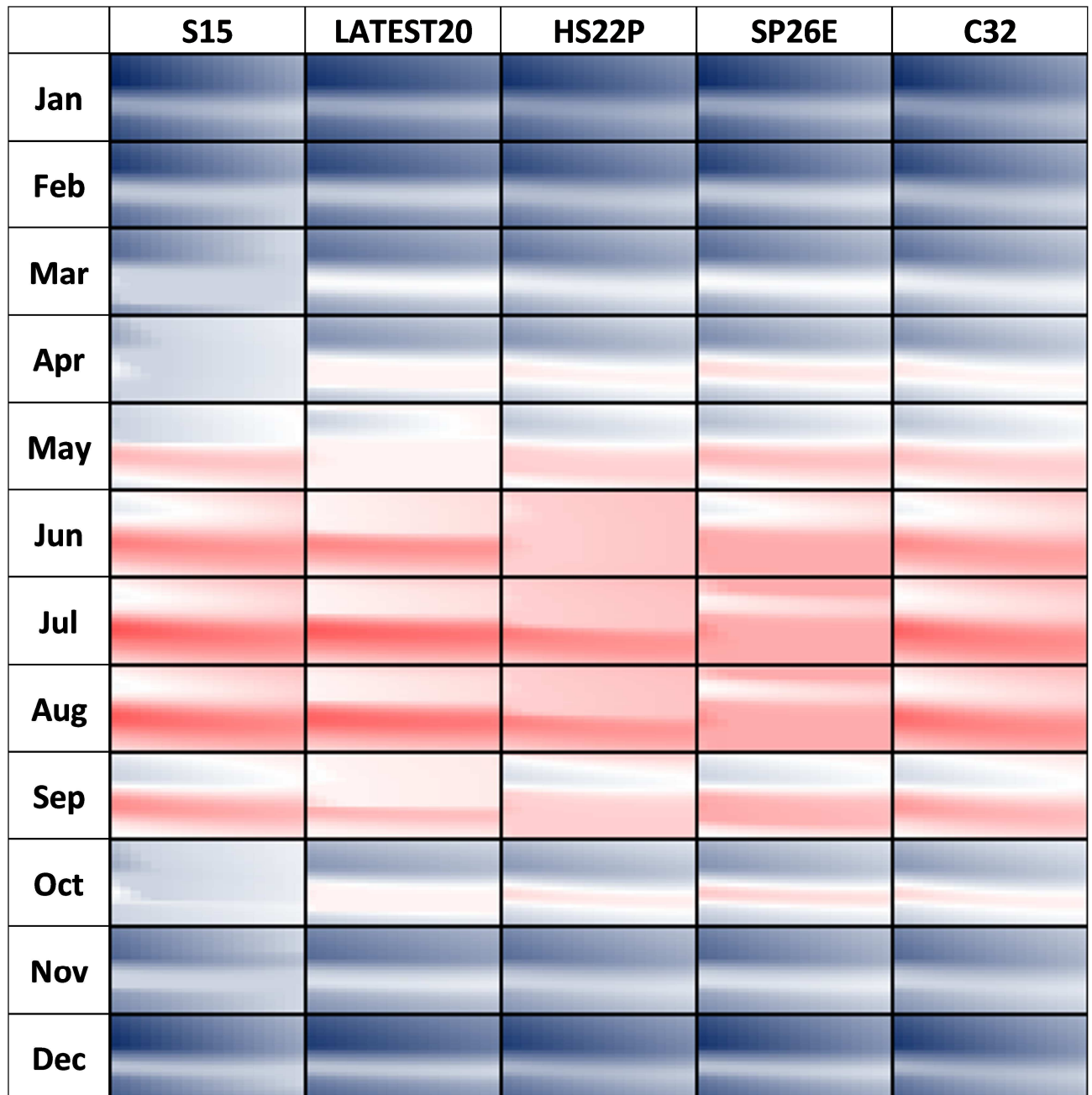


Figure 14 – Temperature in the nodes of the layer in all the hours of the period for different PCM, varying the month. Turin.

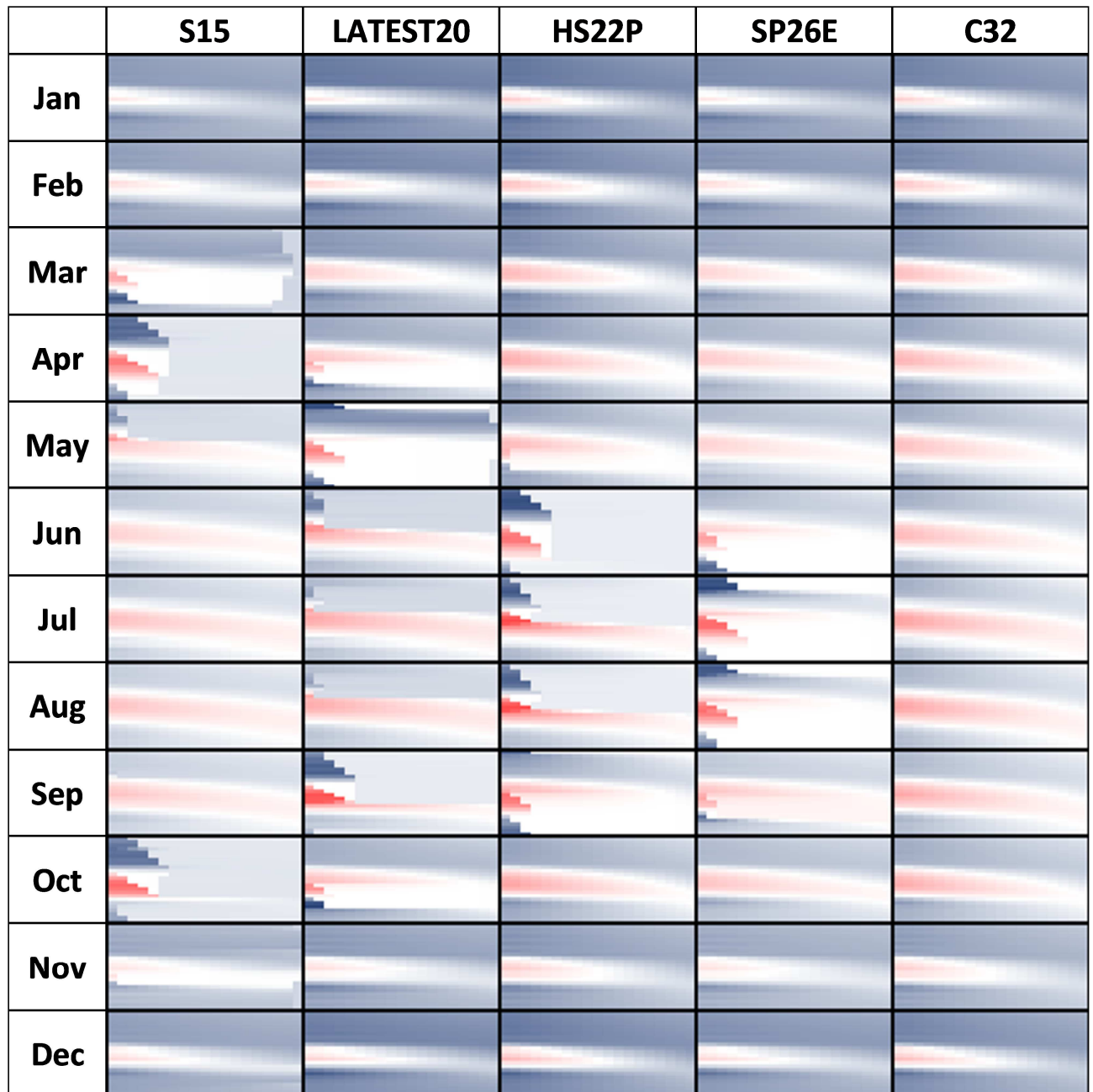


Figure 15 – Heat flux in the nodes of the layer in all the hours of the period for different PCM varying the month. Turin.

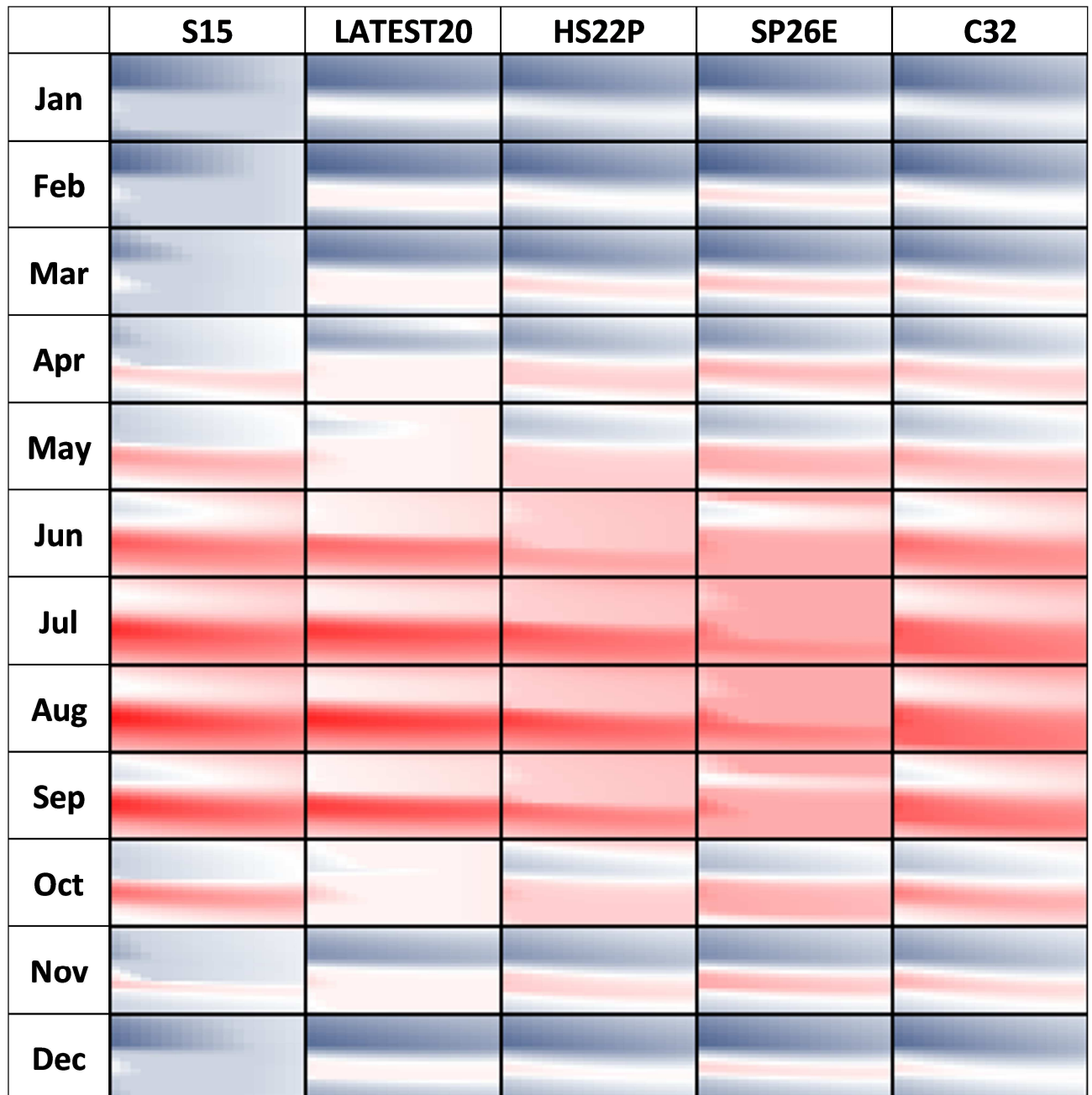


Figure 16 – Temperature in the nodes of the layer in all the hours of the period for different PCM, varying the month. Cosenza.

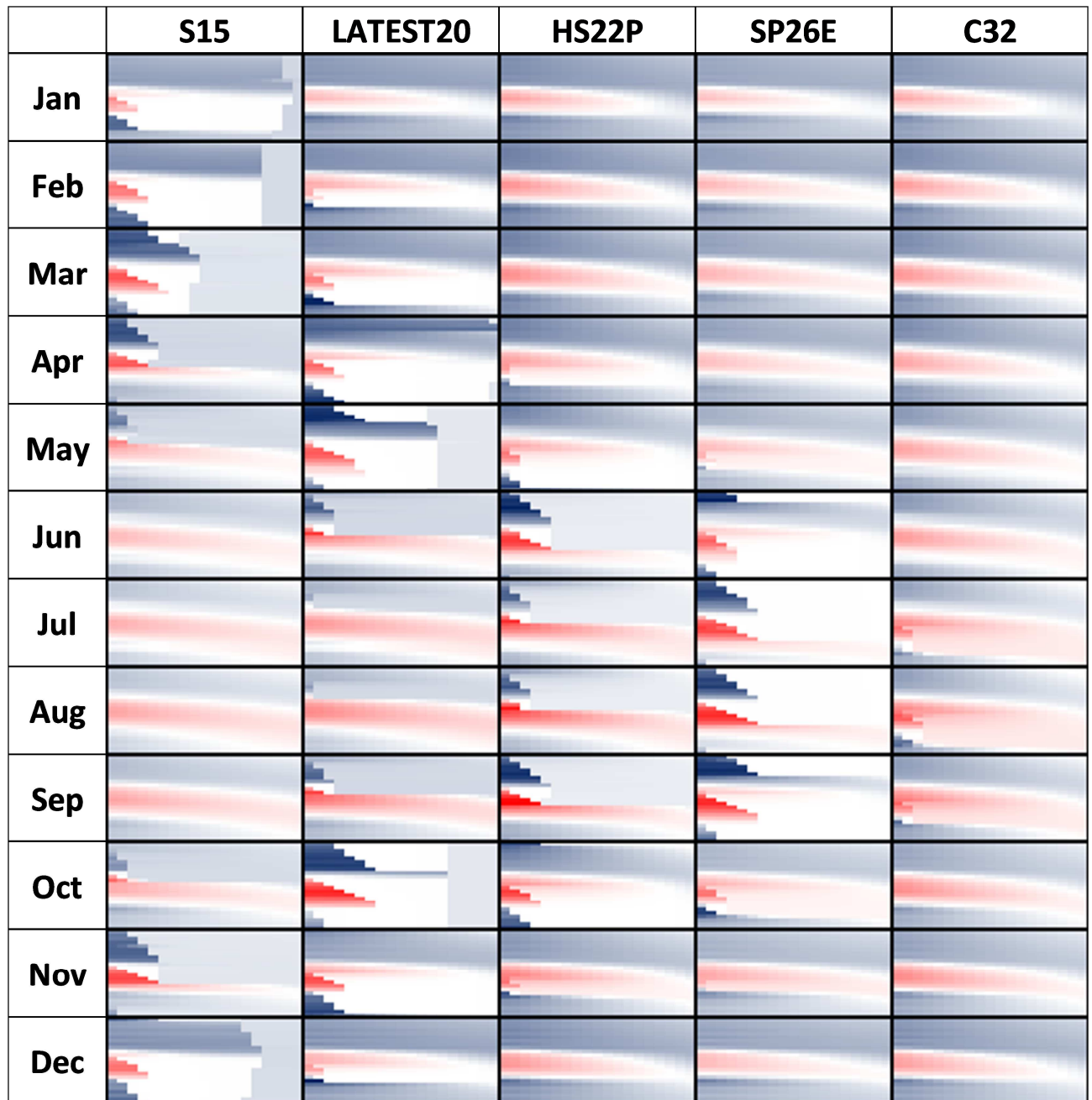


Figure 17 – Heat flux in the nodes of the layer in all the hours of the period for different PCM varying the month. Cosenza.

#### 4. Conclusions

The paper presents advancements and new findings compared to the existing literature in that it provides a detailed description of the phenomena that occur in a PCM layer, location of several bi-phase interfaces when it is subject to the typical loadings that operate on the building envelope. The boundary conditions considered were modelled with non-sinusoidal trends. In the

literature, this problem has been dealt with exclusively by considering a sole ideal sinusoidal loading that acts on the external surface.

Furthermore, the model and algorithm developed form an extension of those of Halford and Boehm, and allow to take into account the contemporaneous presence of several bi-phase interfaces and the variability of the nodal thermal capacities and thermal resistances, which are different in the two phases, as a function of the position and type of bi-phase interfaces present in the layer.

Analyses of PCM layers have permitted clarification of the dynamics of formation, evolution and extinction of the bi-phase interfaces in the layer and the corresponding thermal fields. The considered PCM layers have different melting temperatures and thermo-physical properties; the external boundary conditions are characteristic of a continental climate (Turin) and of a Mediterranean climate (Cosenza).

In the absence of a phase change, the layer is homogenous and has a temperature field with values greater or lesser than the melting temperature. The periodic fluctuations of the temperature and the heat flux are attenuated and undergo a time lag proceeding from the external surface to the internal surface.

In the presence of a phase change, the variability of the external and internal surface temperature compared to the melting temperature determines the abscissae of the formation of the phase change (on the boundary surfaces or within the layer) and the number, typology (melting or solidification) and the advancement velocity of the bi-phase interface within the layer. Such velocity, which is moreover influenced by the eventual presence of other bi-phase interfaces within the layer, determines the law of storage and release of latent energy at the melting temperature, in definite time intervals of the period, with the different duration of the storage process compared to the release process. In particular:

- if the temperature on one of the layer boundary surfaces, at a given time instant in the period, becomes equal to the melting temperature, a bi-phase interface originates on such a surface which, penetrating in the layer, reaches a maximum depth, and then inverts its direction and reconstitutes the initial monophasic layer. Only one part of the layer undergoes a phase change. During the process of penetrating the layer, the latent energy per unit time first increases, reaches a maximum value and then decreases until it annuls itself in the time instant in which the bi-phase interface inverts direction. During the opposite process, the latent energy per unit time is ever increasing and annuls itself in the time instant in which the phase change stops. In the time instants in which there are no



bi-phase interfaces present in the layer, the heat flux from the outside penetrates the layer undergoing an attenuation and a time lag.

- if the temperature of the external surface of the layer, in two successive time instants in the period, become equal to the melting temperature, two bi-phase interfaces, one a solidification interface and the other a melting one, originate in the layer and penetrate the layer with different velocities, and re-join within the layer to reform the initial monophasic layer. The process of storage of latent energy is principally associated with a bi-phase interface while the release process is associated with the other bi-phase interface. It is even possible that the two bi-phase interfaces originate and extinguish one on the internal surface and the other on the external surface and they can both be of melting if the initial layer is solid or both can be of solidification if the initial layer is liquid. It is necessary to highlight that the dynamics of the two bi-phase interfaces are not simultaneous and both contribute to the storage and release process of latent energy.
- the variability of the boundary conditions in the layer can determine three bi-phase interfaces, one close to the internal surface and two originating on the external surface, or which interest only the external surface.

In the first case, the first bi-phase interface is always present in period  $P$  and interests an internal portion of the layer in proximity to the internal surface. On the external surface, the two bi-phase interfaces re-join together within the layer. With reference to the first interface, the stored energy is successively released by the same bi-phase interface with similar trend; for the other two bi-phase interfaces, the latent energy storage process is mainly associated to a bi-phase interface while the other bi-phase interface is associated to the release process.

In the second case, with the formation of three interfaces on the external surface, it is necessary to highlight that two bi-phase interfaces originate, a solidification one and a melting one, which re-join together in order to recover the initial phase. One of the two bi-phase interfaces that remains in the layer with a duration greater than period  $P = 24$  ore, and, therefore, in a definite time interval of the period, in the layer there are three bi-phase interfaces. In the rest of the period, there are either two or one bi-phase interfaces present. Also in this case, the latent energy stored in an interface is completely returned by the other.

The storage and release of latent energy during the phase change of the volumes interested gives rise to significant changes of the field of temperature and heat flux in the layer. In the nodes in phase change, the constancy of the temperature and the abrupt variation of the heat flux lead, in relation to the number and position of the bi-phase interfaces present in the layer, to a net

reduction of the excursions of the temperature and heat flux fluctuations on the external surface, or on the internal surface, or on both surfaces.

The analyses conducted have shown that upon an increase of the melting temperature, the number of months in which only the solid phase is present grows. The months in which only the liquid phase is present, instead, increase upon a decrease of the melting temperature. In the other months in the layer, one, two and three bi-phase interfaces are present. The months in which the phase is only liquid result as being greater in Cosenza compared to Turin for the same melting temperature and, in the months in which phase change occurs, the portion of the material in a liquid phase is greater. A colour scale was used to effectively represent the fields of temperature and heat flux in the layer, allowing for the highlighting of the isothermal behaviour of the layer and the discontinuities of the heat flux generated by the presence of bi-phase interfaces in the layer.

The numerical model and the calculation algorithm can be validly used for the thermal dimensioning of the layer, or rather the choice of PCM and its thickness. The objective is to obtain a reduction of both the thermal loads and the energy requirements in the two air conditioning seasons, and to improve the thermal comfort within the environment through control of the surface temperature. Furthermore, the created procedure allows for a dynamic thermal characterisation by means of the study of the modifications undergone by the surface thermal fluctuations in transit through the layer.

## Appendix A

In the hypothesis in which two bi-phase interfaces  $X_{M,1}$  and  $X_{M,2}$ , are present in the volumes of the three nodes  $j-1$ ,  $j$  and  $j+1$  for the calculation of the resistances, it is possible to identify four cases a, b, c and d upon variation of the liquid fraction in generic node  $j$ , see Figure A1. The calculation of the thermal resistances in the four cases is reported in Figures A2, A3, A4 and A5.

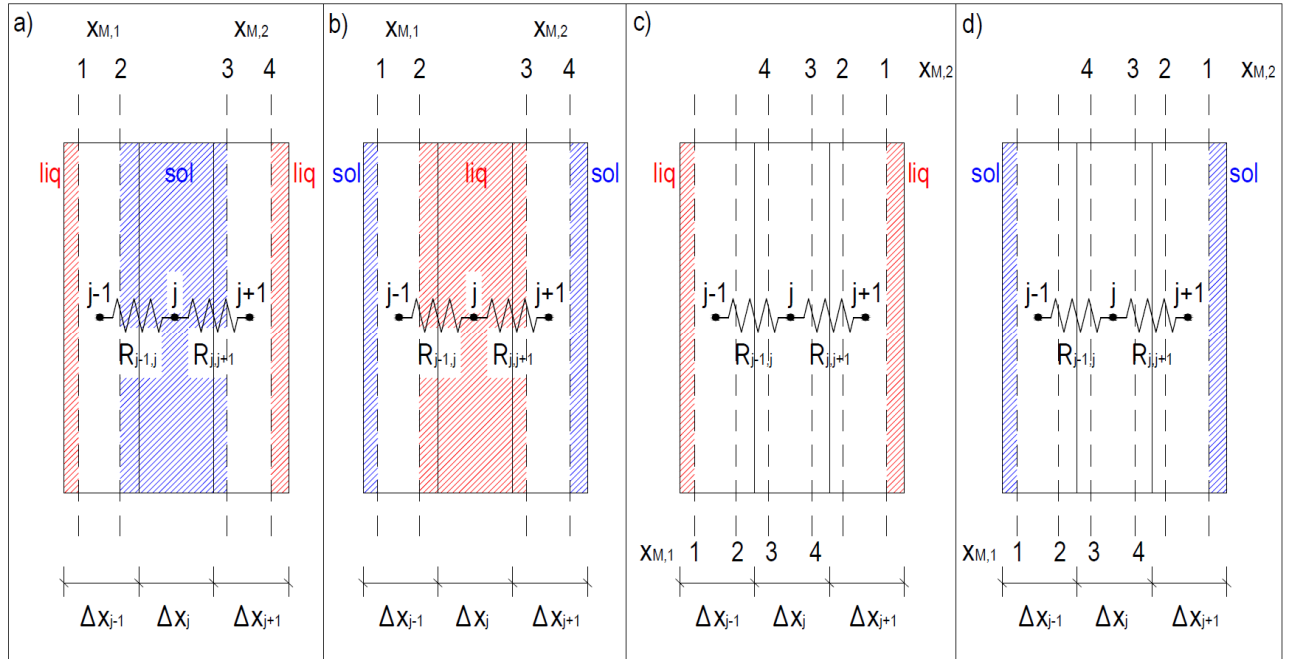


Figure A1 – Scheme for the calculation of the thermal resistances between the  $j$  node and the adjacent nodes as a function of the position of the bi-phase interfaces. a) the node  $j$ -th is completely solid; a) the node  $j$ -th is completely liquid; c) the node  $j$ -th is involved in the phase change and the phases follow a liquid-solid-liquid order; d) the  $j$ -th node is involved in the phase change and the phases follow a solid-liquid-solid order.

<p>The <math>j</math>-th node is completely solid: <math>\lambda_j^n = 0</math></p>	<p>if <math>\lambda_{j-1}^n \leq 0.5</math> and <math>\lambda_{j+1}^n \leq 0.5</math></p>	<p><math>X_{M,1}</math> falls to the left of the node <math>j-1</math> (position 1 in Figure A1a). <math>X_{M,2}</math> falls to the right of the node <math>j+1</math> (position 4 in Figure A1a)</p>	<p>The thermal resistances do not depend on the liquid fraction.</p> $R_{j-1,j}^n = \frac{\Delta x_{j-1}}{2k_s} + \frac{\Delta x_j}{2k_s}$ $R_{j,j+1}^n = \frac{\Delta x_j}{2k_s} + \frac{\Delta x_{j+1}}{2k_s}$
	<p>if <math>\lambda_{j-1}^n \geq 0.5</math> and <math>\lambda_{j+1}^n \leq 0.5</math></p>	<p><math>X_{M,1}</math> falls to the right of the node <math>j-1</math> (position 2 in Figure A1a). <math>X_{M,2}</math> falls to the right of the node <math>j+1</math> (position 4 in Figure A1a).</p>	<p>The thermal resistances depend on the liquid fraction in the volume <math>j-1</math>.</p> $R_{j-1,j}^n = (1 - \lambda_{j-1}^n) \frac{\Delta x_{j-1}}{k_s} + \left( \lambda_{j-1}^n - \frac{1}{2} \right) \frac{\Delta x_{j-1}}{k_l} + \frac{\Delta x_j}{2k_s}$ $R_{j,j+1}^n = \frac{\Delta x_j}{2k_s} + \frac{\Delta x_{j+1}}{2k_s}$
	<p>if <math>\lambda_{j-1}^n \leq 0.5</math> and <math>\lambda_{j+1}^n \geq 0.5</math></p>	<p><math>X_{M,1}</math> falls to the left of the node <math>j-1</math> (position 1 in Figure A1a). <math>X_{M,2}</math> falls to the left of the node <math>j+1</math> (position 3 in Figure A1a)</p>	<p>The thermal resistances depend on the liquid fraction in the volume <math>j-1</math> and in the volume <math>j+1</math>.</p> $R_{j-1,j}^n = \frac{\Delta x_{j-1}}{2k_s} + \frac{\Delta x_j}{2k_s}$ $R_{j,j+1}^n = (1 - \lambda_{j+1}^n) \frac{\Delta x_{j+1}}{k_s} + \left( \lambda_{j+1}^n - \frac{1}{2} \right) \frac{\Delta x_{j+1}}{k_l} + \frac{\Delta x_j}{2k_s}$
	<p>if <math>\lambda_{j-1}^n \geq 0.5</math> and <math>\lambda_{j+1}^n \geq 0.5</math></p>	<p><math>X_{M,1}</math> falls to the right of the node <math>j-1</math> (position 2 in Figure A1a). <math>X_{M,2}</math> falls to the left of the node <math>j+1</math> (position 3 in Figure A1a)</p>	<p>The thermal resistances depend on the liquid fraction in the volume <math>j-1</math> and in the volume <math>j+1</math>.</p> $R_{j-1,j}^n = (1 - \lambda_{j-1}^n) \frac{\Delta x_{j-1}}{k_s} + \left( \lambda_{j-1}^n - \frac{1}{2} \right) \frac{\Delta x_{j-1}}{k_l} + \frac{\Delta x_j}{2k_s}$ $R_{j,j+1}^n = (1 - \lambda_{j+1}^n) \frac{\Delta x_{j+1}}{k_s} + \left( \lambda_{j+1}^n - \frac{1}{2} \right) \frac{\Delta x_{j+1}}{k_l} + \frac{\Delta x_j}{2k_s}$

Figure A2 – Calculation of the thermal resistances between the  $j$  node and the adjacent nodes in the case in which node  $j$ -th is completely solid.

The $j$ -th node is completely liquid: $\lambda_j^n = 1$	if $\lambda_{j-1}^n \geq 0.5$ and $\lambda_{j+1}^n \geq 0.5$	$X_{M,1}$ falls to the left of the node $j-1$ (position 1 in Figure A1b). $X_{M,2}$ falls to the right of the node $j+1$ (position 4 in Figure A1b)	The thermal resistances do not depend on the liquid fraction. $R_{j-1,j}^n = \frac{\Delta x_{j-1}}{2k_1} + \frac{\Delta x_j}{2k_1}$ $R_{j,j+1}^n = \frac{\Delta x_j}{2k_1} + \frac{\Delta x_{j+1}}{2k_1}$
	if $\lambda_{j-1}^n \leq 0.5$ and $\lambda_{j+1}^n \geq 0.5$	$X_{M,1}$ falls to the right of the node $j-1$ (position 2 in Figure A1b). $X_{M,2}$ falls to the right of the node $j+1$ (position 4 in Figure A1b).	The thermal resistances depend on the liquid fraction in the volume $j-1$ . $R_{j-1,j}^n = \lambda_{j-1}^n \frac{\Delta x_{j-1}}{k_1} + \left(\frac{1}{2} - \lambda_{j-1}^n\right) \frac{\Delta x_{j-1}}{k_s} + \frac{\Delta x_j}{2k_1}$ $R_{j,j+1}^n = \frac{\Delta x_j}{2k_1} + \frac{\Delta x_{j+1}}{2k_1}$
	if $\lambda_{j-1}^n \geq 0.5$ and $\lambda_{j+1}^n \leq 0.5$	$X_{M,1}$ falls to the left of the node $j-1$ (position 1 in Figure A1b). $X_{M,2}$ falls to the left of the node $j+1$ (position 3 in Figure A1b)	The thermal resistances depend on the liquid fraction in the volume $j-1$ and in the volume $j+1$ . $R_{j-1,j}^n = \frac{\Delta x_{j-1}}{2k_1} + \frac{\Delta x_j}{2k_1}$ $R_{j,j+1}^n = \lambda_{j+1}^n \frac{\Delta x_{j+1}}{k_1} + \left(\frac{1}{2} - \lambda_{j+1}^n\right) \frac{\Delta x_{j+1}}{k_s} + \frac{\Delta x_j}{2k_1}$
	if $\lambda_{j-1}^n \leq 0.5$ and $\lambda_{j+1}^n \leq 0.5$	$X_{M,1}$ falls to the right of the node $j-1$ (position 2 in Figure A1b). $X_{M,2}$ falls to the left of the node $j+1$ (position 3 in Figure A1b)	The thermal resistances depend on the liquid fraction in the volume $j-1$ and in the volume $j+1$ . $R_{j-1,j}^n = \lambda_{j-1}^n \frac{\Delta x_{j-1}}{k_1} + \left(\frac{1}{2} - \lambda_{j-1}^n\right) \frac{\Delta x_{j-1}}{k_s} + \frac{\Delta x_j}{2k_1}$ $R_{j,j+1}^n = \lambda_{j+1}^n \frac{\Delta x_{j+1}}{k_1} + \left(\frac{1}{2} - \lambda_{j+1}^n\right) \frac{\Delta x_{j+1}}{k_s} + \frac{\Delta x_j}{2k_1}$

Figure A3 – Calculation of the thermal resistances between the  $j$  node and the adjacent nodes in the case in which the node  $j$ -th is completely liquid.

b) The $j$ -th node is involved in the phase change with $0 < \lambda_j^n < 1$ and the phases are in the order liquid-solid-liquid	if $\lambda_j^n \leq 0.5$ , $\lambda_{j-1}^n \leq 0.5$ and $\lambda_{j+1}^n = 1$	$X_{M,1}$ falls to the left of the node $j-1$ (position 1 in Figure A1c). $X_{M,2}$ falls to the right of the node $j$ (position 3 in Figure A1c).	The thermal resistances depend on the liquid fraction in the volume $j$ . $R_{j-1,j}^n = \frac{\Delta x_{j-1}}{2k_s} + \frac{\Delta x_j}{2k_s}$ $R_{j,j+1}^n = \lambda_j^n \frac{\Delta x_j}{k_1} + \left(\frac{1}{2} - \lambda_j^n\right) \frac{\Delta x_j}{k_s} + \frac{\Delta x_{j+1}}{2k_1}$
	if $\lambda_j^n \geq 0.5$ , $\lambda_{j-1}^n \leq 0.5$ and $\lambda_{j+1}^n = 1$	$X_{M,1}$ falls to the left of the node $j-1$ (position 1 in Figure A1c). $X_{M,2}$ falls to the left of the node $j$ (position 4 in Figure A1c).	The thermal resistances depend on the liquid fraction in the volume $j$ . $R_{j-1,j}^n = (1 - \lambda_j^n) \frac{\Delta x_j}{k_s} + \left(\lambda_j^n - \frac{1}{2}\right) \frac{\Delta x_j}{k_1} + \frac{\Delta x_{j-1}}{2k_s}$ $R_{j,j+1}^n = \frac{\Delta x_j}{2k_1} + \frac{\Delta x_{j+1}}{2k_1}$
	if $\lambda_j^n \leq 0.5$ , $\lambda_{j-1}^n \geq 0.5$ and $\lambda_{j+1}^n = 1$	$X_{M,1}$ falls to the right of the node $j-1$ (position 2 in Figure A1c). $X_{M,2}$ falls to the right of the node $j$ (position 3 in Figure A1c).	The thermal resistances depend on the liquid fraction in the volume $j-1$ and in the volume $j$ . $R_{j-1,j}^n = (1 - \lambda_{j-1}^n) \frac{\Delta x_{j-1}}{k_s} + \left(\lambda_{j-1}^n - \frac{1}{2}\right) \frac{\Delta x_{j-1}}{k_1} + \frac{\Delta x_j}{2k_s}$ $R_{j,j+1}^n = \lambda_j^n \frac{\Delta x_j}{k_1} + \left(\frac{1}{2} - \lambda_j^n\right) \frac{\Delta x_j}{k_s} + \frac{\Delta x_{j+1}}{2k_1}$
	if $\lambda_j^n \geq 0.5$ , $\lambda_{j-1}^n \geq 0.5$ and $\lambda_{j+1}^n = 1$	$X_{M,1}$ falls to the right of the node $j-1$ (position 2 in Figure A1c). $X_{M,2}$ falls to the left of the node $j$ (position 4 in Figure A1c)	The thermal resistances depend on the liquid fraction in the volume $j-1$ and in the volume $j$ . $R_{j-1,j}^n = (1 - \lambda_{j-1}^n) \frac{\Delta x_{j-1}}{k_s} + \left(\lambda_{j-1}^n - \frac{1}{2}\right) \frac{\Delta x_{j-1}}{k_1} + (1 - \lambda_j^n) \frac{\Delta x_j}{k_s} + \left(\lambda_j^n - \frac{1}{2}\right) \frac{\Delta x_j}{k_1}$ $R_{j,j+1}^n = \frac{\Delta x_j}{2k_1} + \frac{\Delta x_{j+1}}{2k_1}$
	if $\lambda_j^n \leq 0.5$ , $\lambda_{j-1}^n = 1$ and $\lambda_{j+1}^n \leq 0.5$	$X_{M,1}$ falls to the left of the node $j$ (position 3 in Figure A1c). $X_{M,2}$ falls to the right of the node $j+1$ (position 1 in Figure A1c).	The thermal resistances depend on the liquid fraction in the volume $j$ . $R_{j-1,j}^n = \lambda_j^n \frac{\Delta x_j}{k_1} + \left(\frac{1}{2} - \lambda_j^n\right) \frac{\Delta x_j}{k_s} + \frac{\Delta x_{j-1}}{2k_1}$ $R_{j,j+1}^n = \frac{\Delta x_j}{2k_s} + \frac{\Delta x_{j+1}}{2k_s}$
	if $\lambda_j^n \leq 0.5$ , $\lambda_{j-1}^n = 1$ and $\lambda_{j+1}^n \geq 0.5$	$X_{M,1}$ falls to the left of the node $j$ (position 3 in Figure A1c). $X_{M,2}$ falls to the left of the node $j+1$ (position 2 in Figure A1c).	The thermal resistances depend on the liquid fraction in the volume $j$ and in the volume $j+1$ . $R_{j-1,j}^n = \lambda_j^n \frac{\Delta x_j}{k_1} + \left(\frac{1}{2} - \lambda_j^n\right) \frac{\Delta x_j}{k_s} + \frac{\Delta x_{j-1}}{2k_1}$ $R_{j,j+1}^n = (1 - \lambda_{j+1}^n) \frac{\Delta x_{j+1}}{k_s} + \left(\lambda_{j+1}^n - \frac{1}{2}\right) \frac{\Delta x_{j+1}}{k_1} + \frac{\Delta x_j}{2k_s}$
	if $\lambda_j^n \geq 0.5$ , $\lambda_{j-1}^n = 1$ and $\lambda_{j+1}^n \leq 0.5$	$X_{M,1}$ falls to the right of the node $j$ (position 4 in Figure A1c). $X_{M,2}$ falls to the right of the node $j+1$ (position 1 in Figure A1c)	The thermal resistances depend on the liquid fraction in the volume $j$ . $R_{j-1,j}^n = \frac{\Delta x_{j-1}}{2k_1} + \frac{\Delta x_j}{2k_1}$ $R_{j,j+1}^n = (1 - \lambda_j^n) \frac{\Delta x_j}{k_s} + \left(\lambda_j^n - \frac{1}{2}\right) \frac{\Delta x_j}{k_1} + \frac{\Delta x_{j+1}}{2k_s}$
	if $\lambda_j^n \geq 0.5$ , $\lambda_{j-1}^n = 1$ and $\lambda_{j+1}^n \geq 0.5$	$X_{M,1}$ falls to the right of the node $j$ (position 4 in Figure A1c). $X_{M,2}$ falls to the left of the node $j+1$ (position 2 in Figure A1c).	The thermal resistances depend on the liquid fraction in the volume $j$ and in the volume $j+1$ . $R_{j-1,j}^n = \frac{\Delta x_{j-1}}{2k_1} + \frac{\Delta x_j}{2k_1}$ $R_{j,j+1}^n = (1 - \lambda_j^n) \frac{\Delta x_j}{k_s} + \left(\lambda_j^n - \frac{1}{2}\right) \frac{\Delta x_j}{k_1} + (1 - \lambda_{j+1}^n) \frac{\Delta x_{j+1}}{k_s} + \left(\lambda_{j+1}^n - \frac{1}{2}\right) \frac{\Delta x_{j+1}}{k_1}$

Figure A4 – Calculation of the thermal resistances between the  $j$  node and the adjacent nodes in the case in which the node  $j$ -th is involved in the phase change and the phases follow a liquid-solid-liquid order.

<p>The <i>j</i>-th node is involved in the phase change with <math>0 &lt; \lambda_j^n &lt; 1</math> and the phases are in the order solid-liquid-solid</p>	<p>if <math>\lambda_j^n \geq 0.5</math>, <math>\lambda_{j-1}^n \geq 0.5</math> and <math>\lambda_{j+1}^n = 0</math></p>	<p><math>X_{M,1}</math> falls to the left of the node <i>j</i>-1 (position 1 in Figure A1d). <math>X_{M,2}</math> falls to the right of the node <i>j</i> (position 3 in Figure A1d).</p>	<p>The thermal resistances depend on the liquid fraction in the volume <i>j</i>. <math>R_{j-1,j}^n = \frac{\Delta x_{j-1}}{2k_1} + \frac{\Delta x_j}{2k_1}</math> <math>R_{j,j+1}^n = (1 - \lambda_j^n) \frac{\Delta x_j}{k_s} + \left(\lambda_j^n - \frac{1}{2}\right) \frac{\Delta x_j}{k_1} + \frac{\Delta x_{j+1}}{2k_s}</math></p>
	<p>if <math>\lambda_j^n \leq 0.5</math>, <math>\lambda_{j-1}^n \geq 0.5</math> and <math>\lambda_{j+1}^n = 0</math></p>	<p><math>X_{M,1}</math> falls to the left of the node <i>j</i>-1 (position 1 in Figure A1d). <math>X_{M,2}</math> falls to the left of the node <i>j</i> (position 4 in Figure A1d).</p>	<p>The thermal resistances depend on the liquid fraction in the volume <i>j</i>. <math>R_{j-1,j}^n = \lambda_j^n \frac{\Delta x_j}{k_1} + \left(\frac{1}{2} - \lambda_j^n\right) \frac{\Delta x_j}{k_s} + \frac{\Delta x_{j-1}}{2k_1}</math> <math>R_{j,j+1}^n = \frac{\Delta x_j}{2k_s} + \frac{\Delta x_{j+1}}{2k_s}</math></p>
	<p>if <math>\lambda_j^n \geq 0.5</math>, <math>\lambda_{j-1}^n \leq 0.5</math> and <math>\lambda_{j+1}^n = 0</math></p>	<p><math>X_{M,1}</math> falls to the right of the node <i>j</i>-1 (position 2 in Figure A1d). <math>X_{M,2}</math> falls to the right of the node <i>j</i> (position 3 in Figure A1d).</p>	<p>The thermal resistances depend on the liquid fraction in the volume <i>j</i>-1 and in the volume <i>j</i>. <math>R_{j-1,j}^n = \lambda_{j-1}^n \frac{\Delta x_{j-1}}{k_1} + \left(\frac{1}{2} - \lambda_{j-1}^n\right) \frac{\Delta x_{j-1}}{k_s} + \frac{\Delta x_j}{2k_1}</math> <math>R_{j,j+1}^n = (1 - \lambda_j^n) \frac{\Delta x_j}{k_s} + \left(\lambda_j^n - \frac{1}{2}\right) \frac{\Delta x_j}{k_1} + \frac{\Delta x_{j+1}}{2k_s}</math></p>
	<p>if <math>\lambda_j^n \leq 0.5</math>, <math>\lambda_{j-1}^n \leq 0.5</math> and <math>\lambda_{j+1}^n = 0</math></p>	<p><math>X_{M,1}</math> falls to the right of the node <i>j</i>-1 (position 2 in Figure A1d). <math>X_{M,2}</math> falls to the left of the node <i>j</i> (position 4 in Figure A1d).</p>	<p>The thermal resistances depend on the liquid fraction in the volume <i>j</i>-1 and in the volume <i>j</i>. <math>R_{j-1,j}^n = \lambda_{j-1}^n \frac{\Delta x_{j-1}}{k_1} + \left(\frac{1}{2} - \lambda_{j-1}^n\right) \frac{\Delta x_{j-1}}{k_s} + \lambda_j^n \frac{\Delta x_j}{k_1} + \left(\frac{1}{2} - \lambda_j^n\right) \frac{\Delta x_j}{k_s}</math> <math>R_{j,j+1}^n = \frac{\Delta x_j}{2k_s} + \frac{\Delta x_{j+1}}{2k_s}</math></p>
	<p>if <math>\lambda_j^n \geq 0.5</math>, <math>\lambda_{j-1}^n = 0</math> and <math>\lambda_{j+1}^n \geq 0.5</math></p>	<p><math>X_{M,1}</math> falls to the left of the node <i>j</i> (position 3 in Figure A1d). <math>X_{M,2}</math> falls to the right of the node <i>j</i>+1 (position 1 in Figure A1d).</p>	<p>The thermal resistances depend on the liquid fraction in the volume <i>j</i>. <math>R_{j-1,j}^n = (1 - \lambda_j^n) \frac{\Delta x_j}{k_s} + \left(\lambda_j^n - \frac{1}{2}\right) \frac{\Delta x_j}{k_1} + \frac{\Delta x_{j-1}}{2k_s}</math> <math>R_{j,j+1}^n = \frac{\Delta x_j}{2k_1} + \frac{\Delta x_{j+1}}{2k_1}</math></p>
	<p>if <math>\lambda_j^n \geq 0.5</math>, <math>\lambda_{j-1}^n = 0</math> and <math>\lambda_{j+1}^n \leq 0.5</math></p>	<p><math>X_{M,1}</math> falls to the left of the node <i>j</i> (position 3 in Figure A1d). <math>X_{M,2}</math> falls to the left of the node <i>j</i>+1 (position 2 in Figure A1d).</p>	<p>The thermal resistances depend on the liquid fraction in the volume <i>j</i> and in the volume <i>j</i>+1. <math>R_{j-1,j}^n = (1 - \lambda_j^n) \frac{\Delta x_j}{k_s} + \left(\lambda_j^n - \frac{1}{2}\right) \frac{\Delta x_j}{k_1} + \frac{\Delta x_{j-1}}{2k_s}</math> <math>R_{j,j+1}^n = \lambda_{j+1}^n \frac{\Delta x_{j+1}}{k_1} + \left(\frac{1}{2} - \lambda_{j+1}^n\right) \frac{\Delta x_{j+1}}{k_s} + \frac{\Delta x_j}{2k_1}</math></p>
	<p>if <math>\lambda_j^n \leq 0.5</math>, <math>\lambda_{j-1}^n = 0</math> and <math>\lambda_{j+1}^n \geq 0.5</math></p>	<p><math>X_{M,1}</math> falls to the right of the node <i>j</i> (position 4 in Figure A1d). <math>X_{M,2}</math> falls to the right of the node <i>j</i>+1 (position 1 in Figure A1d).</p>	<p>The thermal resistances depend on the liquid fraction in the volume <i>j</i>. <math>R_{j-1,j}^n = \frac{\Delta x_{j-1}}{2k_s} + \frac{\Delta x_j}{2k_s}</math> <math>R_{j,j+1}^n = \lambda_j^n \frac{\Delta x_j}{k_1} + \left(\frac{1}{2} - \lambda_j^n\right) \frac{\Delta x_j}{k_s} + \frac{\Delta x_{j+1}}{2k_1}</math></p>
	<p>if <math>\lambda_j^n \leq 0.5</math>, <math>\lambda_{j-1}^n = 0</math> and <math>\lambda_{j+1}^n \leq 0.5</math></p>	<p><math>X_{M,1}</math> falls to the right of the node <i>j</i> (position 4 in Figure A1d). <math>X_{M,2}</math> falls to the left of the node <i>j</i>+1 (position 2 in Figure A1d).</p>	<p>The thermal resistances depend on the liquid fraction in the volume <i>j</i> and in the volume <i>j</i>+1. <math>R_{j-1,j}^n = \frac{\Delta x_{j-1}}{2k_s} + \frac{\Delta x_j}{2k_s}</math> <math>R_{j,j+1}^n = \lambda_j^n \frac{\Delta x_j}{k_1} + \left(\frac{1}{2} - \lambda_j^n\right) \frac{\Delta x_j}{k_s} + \lambda_{j+1}^n \frac{\Delta x_{j+1}}{k_1} + \left(\frac{1}{2} - \lambda_{j+1}^n\right) \frac{\Delta x_{j+1}}{k_s}</math></p>

Figure A5 – Calculation of the thermal resistances between the *j* node and the adjacent nodes in the case in which the node *j*-th is involved in the phase change and the phases follow a solid-liquid-solid order.

References

[1] Hussein Akeiber, Payam Nejat, Muhd Zaimi Abd. Majid, Mazlan A. Wahid, Fatemeh Jomehzadeh, Iman Zeynali Famileh, John Kaiser Calautit, Ben Richard Hughes, Sheikh Ahmad Zaki, A review on phase change material (PCM) for sustainable passive cooling in building envelopes, Renewable and Sustainable Energy Reviews, Volume 60, July 2016, Pages 1470-1497, ISSN 1364-0321, <http://dx.doi.org/10.1016/j.rser.2016.03.036>.

[2] L.I. Rubinstein, The Stefan Problem, Translations of Mathematical Monographs, vol. 27 American, Mathematical Society, Providence, Rhode Island (1971)

[3] M.N. Ozisik, Heat Conduction, J. Wiley & Sons, New York (1980)

[4] J. Crank, Free and Moving Boundary Problems, Oxford: Clarendon, 1984.

[5] H. S. Carslaw, J.C. Jaeger, Conduction of Heat in Solids, second edition, Oxford Science Publications, 1988.

[6] V. Alexiades, A. Solomon, Mathematical Modelling of Melting and Freezing Processes, Hemisphere Publishing Corporation, Washington (1993)

[7] Hu H, Argyropoulos SA. Mathematical modelling of solidification and melting: a review. Modelling and Simulation in Materials Science and Engineering 1996;4:4:371-396.

- [8] Shuli Liu, Yongcai Li, Yaqin Zhang, Mathematical solutions and numerical models employed for the investigations of PCMs' phase transformations, *Renewable and Sustainable Energy Reviews*, Volume 33, May 2014, Pages 659-674, ISSN 1364-0321, <http://dx.doi.org/10.1016/j.rser.2014.02.032>.
- [9] C.K. Hsieh, Exact solutions of Stefan problems for a heat front moving at constant velocity in a quasi-steady state, *International Journal of Heat and Mass Transfer*, Volume 38, Issue 1, January 1995, Pages 71-79, ISSN 0017-9310, [http://dx.doi.org/10.1016/0017-9310\(94\)00140-Q](http://dx.doi.org/10.1016/0017-9310(94)00140-Q).
- [10] T.R. Goodman, The heat-balance integral and its application to problems involving a change of phase, *Transactions of the ASME*, vol. 80, pp. 335–342, 1958.
- [11] Goodman TR, Shea JJ. The Melting of Finite Slabs. *ASME. J. Appl. Mech.* 1960;27(1):16-24. doi:10.1115/1.3643893.
- [12] G.E. Bell, A refinement of the heat balance integral method applied to a melting problem, *International Journal of Heat and Mass Transfer*, Volume 21, Issue 11, 1978, Pages 1357-1362, ISSN 0017-9310, [http://dx.doi.org/10.1016/0017-9310\(78\)90198-9](http://dx.doi.org/10.1016/0017-9310(78)90198-9).
- [13] Voller, V. R., Swaminathan, C. R. and Thomas, B. G. (1990), Fixed grid techniques for phase change problems: A review. *Int. J. Numer. Meth. Engng.*, 30: 875–898. doi:10.1002/nme.1620300419
- [14] Y.C. Lam, J.C. Chai, P. Rath, H. Zheng, V.M. Murukeshan, A fixed-grid method for chemical etching, *International Communications in Heat and Mass Transfer*, Volume 31, Issue 8, 2004, Pages 1123-1131, ISSN 0735-1933, <http://dx.doi.org/10.1016/j.icheatmasstransfer.2004.08.010>.
- [15] Savovic, Svetislav, and James Caldwell. "Numerical solution of Stefan problem with time-dependent boundary conditions by variable space grid method." *Therm. Sci* 13 (2009): 165-174.
- [16] Radhey S. Gupta, Moving grid method without interpolations, *Computer Methods in Applied Mechanics and Engineering*, Volume 4, Issue 2, 1974, Pages 143-152, ISSN 0045-7825, [http://dx.doi.org/10.1016/0045-7825\(74\)90031-0](http://dx.doi.org/10.1016/0045-7825(74)90031-0).
- [17] Frédéric Kuznik, Joseph Virgone, Kevyn Johannes, Development and validation of a new TRNSYS type for the simulation of external building walls containing PCM, *Energy and Buildings*, Volume 42, Issue 7, July 2010, Pages 1004-1009, ISSN 0378-7788, <http://dx.doi.org/10.1016/j.enbuild.2010.01.012>.
- [18] K. Darkwa, P.W. O'Callaghan, Simulation of phase change drywalls in a passive solar building, *Applied Thermal Engineering*, Volume 26, Issues 8–9, June 2006, Pages 853-858, ISSN 1359-4311, <http://dx.doi.org/10.1016/j.applthermaleng.2005.10.007>.

- [19] Chao Chen, Haifeng Guo, Yuning Liu, Hailin Yue, Chendong Wang, A new kind of phase change material (PCM) for energy-storing wallboard, *Energy and Buildings*, Volume 40, Issue 5, 2008, Pages 882-890, ISSN 0378-7788, <http://dx.doi.org/10.1016/j.enbuild.2007.07.002>.
- [20] Bogdan M. Diaconu, Thermal energy savings in buildings with PCM-enhanced envelope: Influence of occupancy pattern and ventilation, *Energy and Buildings*, Volume 43, Issue 1, January 2011, Pages 101-107, ISSN 0378-7788, <http://dx.doi.org/10.1016/j.enbuild.2010.08.019>.
- [21] G. Evola, L. Marletta, F. Sicurella, A methodology for investigating the effectiveness of PCM wallboards for summer thermal comfort in buildings, *Building and Environment*, Volume 59, January 2013, Pages 517-527, ISSN 0360-1323, <http://dx.doi.org/10.1016/j.buildenv.2012.09.021>.
- [22] Peter W. Egolf, Heinrich Manz, Theory and modeling of phase change materials with and without mushy regions, *International Journal of Heat and Mass Transfer*, Volume 37, Issue 18, 1994, Pages 2917-2924, ISSN 0017-9310, [http://dx.doi.org/10.1016/0017-9310\(94\)90346-8](http://dx.doi.org/10.1016/0017-9310(94)90346-8).
- [23] Alexander M. Thiele, Astrid Jamet, Gaurav Sant, Laurent Pilon, Annual energy analysis of concrete containing phase change materials for building envelopes, *Energy Conversion and Management*, Volume 103, October 2015, Pages 374-386, ISSN 0196-8904, <http://dx.doi.org/10.1016/j.enconman.2015.06.068>.
- [24] A. Pasupathy, R. Velraj, Effect of double layer phase change material in building roof for year round thermal management, *Energy and Buildings*, Volume 40, Issue 3, 2008, Pages 193-203, ISSN 0378-7788, <http://dx.doi.org/10.1016/j.enbuild.2007.02.016>.
- [25] Esam M. Alawadhi, Hashem J. Alqallaf, Building roof with conical holes containing PCM to reduce the cooling load: Numerical study, *Energy Conversion and Management*, Volume 52, Issues 8-9, August 2011, Pages 2958-2964, ISSN 0196-8904, <http://dx.doi.org/10.1016/j.enconman.2011.04.004>.
- [26] Servando Álvarez, Luisa F. Cabeza, Alvaro Ruiz-Pardo, Albert Castell, José Antonio Tenorio, Building integration of PCM for natural cooling of buildings, *Applied Energy*, Volume 109, September 2013, Pages 514-522, ISSN 0306-2619, <http://dx.doi.org/10.1016/j.apenergy.2013.01.080>.
- [27] D. Zhou, G.S.F. Shire, Y. Tian, Parametric analysis of influencing factors in Phase Change Material Wallboard (PCMW), *Applied Energy*, Volume 119, 15 April 2014, Pages 33-42, ISSN 0306-2619, <http://dx.doi.org/10.1016/j.apenergy.2013.12.059>.

- [28] Saleh Nasser Al-Saadi, Zhiqiang (John) Zhai, A new validated TRNSYS module for simulating latent heat storage walls, *Energy and Buildings*, Volume 109, 15 December 2015, Pages 274-290, ISSN 0378-7788, <http://dx.doi.org/10.1016/j.enbuild.2015.10.013>.
- [29] Fabrizio Ascione, Nicola Bianco, Rosa Francesca De Masi, Filippo de' Rossi, Giuseppe Peter Vanoli, Energy refurbishment of existing buildings through the use of phase change materials: Energy savings and indoor comfort in the cooling season, *Applied Energy*, Volume 113, January 2014, Pages 990-1007, ISSN 0306-2619, <http://dx.doi.org/10.1016/j.apenergy.2013.08.045>.
- [30] Guobing Zhou, Yongping Yang, Xin Wang, Shaoxiang Zhou, Numerical analysis of effect of shape-stabilized phase change material plates in a building combined with night ventilation, *Applied Energy*, Volume 86, Issue 1, January 2009, Pages 52-59, ISSN 0306-2619, <http://dx.doi.org/10.1016/j.apenergy.2008.03.020>.
- [31] Guobing Zhou, Yongping Yang, Hong Xu, Performance of shape-stabilized phase change material wallboard with periodical outside heat flux waves, *Applied Energy*, Volume 88, Issue 6, June 2011, Pages 2113-2121, ISSN 0306-2619, <http://dx.doi.org/10.1016/j.apenergy.2011.01.016>.
- [32] Guobing Zhou, Yongping Yang, Xin Wang, Jinming Cheng, Thermal characteristics of shape-stabilized phase change material wallboard with periodical outside temperature waves, *Applied Energy*, Volume 87, Issue 8, August 2010, Pages 2666-2672, ISSN 0306-2619, <http://dx.doi.org/10.1016/j.apenergy.2010.02.001>.
- [33] Bogdan M. Diaconu, Mihai Cruceru, Novel concept of composite phase change material wall system for year-round thermal energy savings, *Energy and Buildings*, Volume 42, Issue 10, October 2010, Pages 1759-1772, ISSN 0378-7788, <http://dx.doi.org/10.1016/j.enbuild.2010.05.012>.
- [34] Paulo Cesar Tabares-Velasco, Craig Christensen, Marcus Bianchi, Verification and validation of EnergyPlus phase change material model for opaque wall assemblies, *Building and Environment*, Volume 54, August 2012, Pages 186-196, ISSN 0360-1323, <http://dx.doi.org/10.1016/j.buildenv.2012.02.019>.
- [35] Haoshu Ling, Chao Chen, Shen Wei, Yong Guan, Caiwen Ma, Guangya Xie, Na Li, Ziguang Chen, Effect of phase change materials on indoor thermal environment under different weather conditions and over a long time, *Applied Energy*, Volume 140, 15 February 2015, Pages 329-337, ISSN 0306-2619, <http://dx.doi.org/10.1016/j.apenergy.2014.11.078>.



- [36] D. Zhou, Y. Tian, Y. Qu, Y.K. Chen, Thermal analysis of phase change material board (PCMB) under weather conditions in the summer, *Applied Thermal Engineering*, Volume 99, 25 April 2016, Pages 690-702, ISSN 1359-4311, <http://dx.doi.org/10.1016/j.applthermaleng.2016.01.121>.
- [37] Kaushik Biswas, Jue Lu, Parviz Soroushian, Som Shrestha, Combined experimental and numerical evaluation of a prototype nano-PCM enhanced wallboard, *Applied Energy*, Volume 131, 15 October 2014, Pages 517-529, ISSN 0306-2619, <http://dx.doi.org/10.1016/j.apenergy.2014.02.047>.
- [38] Jiawei Lei, Jinglei Yang, En-Hua Yang, Energy performance of building envelopes integrated with phase change materials for cooling load reduction in tropical Singapore, *Applied Energy*, Volume 162, 15 January 2016, Pages 207-217, ISSN 0306-2619, <http://dx.doi.org/10.1016/j.apenergy.2015.10.031>.
- [39] Mohammad Saffari, Alvaro de Gracia, Svetlana Ushak, Luisa F. Cabeza, Economic impact of integrating PCM as passive system in buildings using Fanger comfort model, *Energy and Buildings*, Volume 112, 15 January 2016, Pages 159-172, ISSN 0378-7788, <http://dx.doi.org/10.1016/j.enbuild.2015.12.006>.
- [40] D. Mazzeo, G. Oliveti, M. De Simone, N. Arcuri, Analytical model for solidification and melting in a finite PCM in steady periodic regime, *International Journal of Heat and Mass Transfer*, Volume 88, September 2015, Pages 844-861, ISSN 0017-9310, <http://dx.doi.org/10.1016/j.ijheatmasstransfer.2015.04.109>.
- [41] C.J. Ho, C.H. Chu, Periodic melting within a square enclosure with an oscillatory surface temperature, *International Journal of Heat and Mass Transfer*, Volume 36, Issue 3, February 1993, Pages 725-733, ISSN 0017-9310, [http://dx.doi.org/10.1016/0017-9310\(93\)80048-Y](http://dx.doi.org/10.1016/0017-9310(93)80048-Y).
- [42] Giovanni Casano, Stefano Piva, Experimental and numerical investigation of the steady periodic solid-liquid phase-change heat transfer, *International Journal of Heat and Mass Transfer*, Volume 45, Issue 20, September 2002, Pages 4181-4190, ISSN 0017-9310, [http://dx.doi.org/10.1016/S0017-9310\(02\)00122-9](http://dx.doi.org/10.1016/S0017-9310(02)00122-9).
- [43] Choi Chang-Yong, C.K. Hsieh, Solution of Stefan problems imposed with cyclic temperature and flux boundary conditions, *International Journal of Heat and Mass Transfer*, Volume 35, Issue 5, 1992, Pages 1181-1195, ISSN 0017-9310, [http://dx.doi.org/10.1016/0017-9310\(92\)90178-U](http://dx.doi.org/10.1016/0017-9310(92)90178-U).
- [44] C.J. Ho, C.H. Chu, A simulation for multiple moving boundaries during melting inside an enclosure imposed with cyclic wall temperature, *International Journal of Heat and Mass*

Transfer, Volume 37, Issue 16, November 1994, Pages 2505-2516, ISSN 0017-9310, [http://dx.doi.org/10.1016/0017-9310\(94\)90288-7](http://dx.doi.org/10.1016/0017-9310(94)90288-7).

[45] Domenico Mazzeo, Giuseppe Oliveti, Natale Arcuri, Multiple Bi-phase Interfaces in a PCM Layer Subject to Periodic Boundary Conditions Characteristic of Building External Walls, Energy Procedia, Volume 82, December 2015, Pages 472-479, ISSN 1876-6102, <http://dx.doi.org/10.1016/j.egypro.2015.11.846>.

[46] C.K. Halford, R.F. Boehm, Modeling of phase change material peak load shifting, Energy and Buildings, Volume 39, Issue 3, March 2007, Pages 298-305, ISSN 0378-7788, <http://dx.doi.org/10.1016/j.enbuild.2006.07.005>.

[47] Environmental Process Systems Ltd (EPS). <http://www.epsltd.co.uk>. Last access: February 2016.

[48] Teappcm. <http://www.teappcm.com>. Last access: February 2016.

[49] savENRGTM phase change materials. <http://www.rgees.com>. Last access: February 2016.

[50] Rubitherm® Technologies GmbH. <http://www.rubitherm.eu>. Last access: February 2016.

[51] Climator Sweden AB. <http://www.climator.com>. Last access: February 2016.

[52] UNI 10349:1994. Heating and cooling of buildings. Climatic data.

[53] Solar Energy Laboratory University of Wisconsin-Madison, TRNSYS, Version 17, 2012.

[54] M. Martin, P. Berdahl, Characteristics of Infrared Sky Radiation in the United States, Lawrence Berkeley Laboratory, University of California - Berkeley, Solar Energy Vol. 33, No. 3/4, pp. 321-336, 1984.

[55] Giuseppe Oliveti, Natale Arcuri, Marilena De Simone, Roberto Bruno, Experimental evaluations of the building shell radiant exchange in clear sky conditions, Solar Energy, Volume 86, Issue 6, June 2012, Pages 1785-1795, ISSN 0038-092X, <http://dx.doi.org/10.1016/j.solener.2012.03.009>.

[56] EN ISO 6946:1997. Building components and building elements - Thermal resistance and thermal transmittance – Calculation method.

[57] EN ISO 13790:2008. Energy performance of buildings – calculation of energy use for space heating and cooling

[58] UNI TS 11300-1:2008. Energy performance of buildings. Part 1: Evaluation of energy need for space heating and cooling.

[59] G. Oliveti, N. Arcuri, D. Mazzeo, M. De Simone, A new parameter for the dynamic analysis of building walls using the harmonic method, International Journal of Thermal Sciences, Volume

88, February 2015, Pages 96-109, ISSN 1290-0729,  
<http://dx.doi.org/10.1016/j.ijthermalsci.2014.09.006>.

[60] D. Mazzeo, G. Oliveti, N. Arcuri, Influence of internal and external boundary conditions on the decrement factor and time lag heat flux of building walls in steady periodic regime, Applied Energy, Volume 164, 15 February 2016, Pages 509-531, ISSN 0306-2619,  
<http://dx.doi.org/10.1016/j.apenergy.2015.11.076>.

## Nomenclature

a	thermal diffusivity [ $\text{m}^2/\text{s}$ ]
c	specific heat capacity [ $\text{J}/\text{kg K}$ ]
C	areal heat capacity [ $\text{J}/\text{m}^2 \text{K}$ ]
G	monthly average daily solar irradiation on the horizontal plane
h	heat transfer coefficient [ $\text{W}/(\text{m}^2 \text{K})$ ]
H	latent heat of fusion [ $\text{J}/\text{kg}$ ]
$j_k$	j-th subvolume including the k-th bi-phase interface [-]
k	thermal conductivity [ $\text{W}/\text{m K}$ ]
L	layer thickness [m]
R	thermal resistance [ $\text{m}^2 \text{K}/\text{W}$ ]
t	time [s]
T	Temperature [K]
x	spatial coordinate [m]
$X_M$	position of the bi-phase interface [m]

### *Greek symbols*

$\alpha$	solar absorption coefficient [-]
$\Delta t$	finite difference time step [s]
$\Delta x$	thickness of the subvolume [m]
$\varphi$	heat flux [ $\text{W}/\text{m}^2$ ]
$\lambda$	liquid fraction [-]
$\rho$	density [ $\text{kg}/\text{m}^3$ ]
$\vartheta$	generic component of the temperature Fourier series expansion [K]

### *Subscripts*

l	external surface
c	convective

---

e	external
eq	equivalent
ea	referring to the external air load
H	referring to the latent energy stored
i	i-th subvolume preceding the subvolume in phase change
ia	internal air
j	referring to the j-th node
j-1	referring to the (j-1)-th node
j+1	referring to the (j+1)-th node
j-1, j	between (j-1)-th node and j-th node
j, j+1	between j-th node and (j+1)-th node
$j_k$	referring to the j-th subvolume including the k-th bi-phase interface
k	k-th bi-phase interface
l	liquid
M	melting
N	internal surface
p	at constant pressure
r	radiative
s	solid
s,e	referring to the solar load
s,i	referring to the internal surface
sky	referring to the sky load

*Superscripts*

n	current time instant
n-1	previous time instant
n+1	successive time instant

*Symbols*

-	steady value
~	fluctuating value

# Chapter 7

## **Definition of a new set of parameters for the dynamic thermal characterization and energy behavior evaluation of PCM layers in the presence of one or more liquid-solid interfaces**

### **Abstract**

This chapter addresses the problem of the definition of the energetic and dynamic behavior of a layer subject to phase change (PCM) with periodic non-sinusoidal boundary conditions, characterizing the external walls of air conditioned buildings. In such conditions, the layer is the site of the formation of one or more bi-phase interfaces, which originate on the boundary surfaces, or are always present and fluctuate within the layer. It is also possible that the layer does not undergo any phase change. The study has been developed by a finite difference numeric calculation model which explicitly determines the number and the position of the bi-phase

interfaces that originate in the layer and the temperature and the heat flux fields. The surface heat fluxes are used to evaluate the PCM layer energetic behavior in terms of energy transferred through the boundary surfaces and of stored energy in sensible and latent form.

Furthermore, the trends of surface temperatures and heat fluxes, the fluctuating energy transferred and stored in sensible and latent form, are used in order to define the parameters necessary to the complete dynamic characterization of the layer. Such parameters are: the latent storage efficiency; the fraction of latent energy stored in respect to the total energy stored; the decrement factor of the maximum excursion of the temperature and heat flux; the energy decrement factor; the maximum peak and minimum peak time lags of the temperature and heat flux; the fraction of the period in which the maximum or minimum peak of the temperature and heat flux on the internal surface are constant in time. Defined parameters are to be used for the thermal design of innovative walls of air conditioned buildings, targeting the reduction of power peaks entering the environment, in order to reduce the energy requirements and even to improve the indoor thermal comfort.

The proposed method employs the characteristic day that it is periodically repeated for all the days of the considered month. The use of the characteristic days drastically reduces the computational burden of the numerical calculation and it allows to obtain guidance on the behaviour of the PCM throughout the year, in accordance with the variability of external climatic conditions, in order to select the PCM with the most suitable thermophysical properties.

The methodology developed is applied to PCM layers with different melting temperatures and thermo-physical properties and subject to climatic conditions of two locations, one with a continental climate and the second one with a Mediterranean climate. The results obtained allowed to identify which PCM is more suitable in improving the energetic performances in the heating or cooling period and to determine the dynamic characteristics during the year.

In particular, the energy analysis highlighted that, in both localities, during the winter period: the lowest energy exiting from the indoor environment is ensured by a PCM with a melting temperature of 15°C; the highest contribution of energy entering the indoor environment, mainly due to solar radiation, is recorded for a PCM with a melting temperature of 26°C. During the summer period: the lowest value of energy entering the indoor environment is obtained by a PCM with a melting temperature of 26°C; the highest value of energy exiting from the indoor environment is ensured by a melting temperature equal to 20°C. In both locations, a PCM with a melting temperature intermediate between those of the winter and summer set points of the indoor environment is the best compromise between winter and summer energy needs for an air-

conditioned environment, as it allows obtainment of the highest values of the yearly total stored energy.

The dynamic analysis highlighted that all defined dynamic parameters, irrespective of locality and of PCM type, are related to the latent storage efficiency. Furthermore, the results show that it was sufficient to reach the phase change in a portion of the layer of about 35% to obtain: complete attenuation of the maximum excursion of the temperature and heat flux on the internal surface; an annulment of the fluctuating energy transferred in the indoor environment; unitary values of the latent energy fraction; a higher increase of the time lag of maximum peak of the temperature and heat flux, of the minimum peak of the temperature and of the minimum peak of the heat flux in the summer time; a high reduction of the minimum peak of the heat flux in the winter period.

Finally, a strict correlation between the decrement factor of the maximum excursion of the heat flux and the decrement factor of the energy was found, and as well as between the time lag of the maximum peak of the temperature and the time lag of the maximum peak of the heat flux.

Keywords: Phase change material; Building wall; Energy behavior; Dynamic Thermal behavior; Dynamic parameters

- Thermal fields in a PCM layer with multiple bi-phase interfaces are presented
- An accurate thermal and energetic analysis of PCM layers has been developed
- A set of parameters for a complete thermal characterization of PCM layers are defined
- Various PCM layers with different melting temperatures are considered
- The analysis regard a continental and a mediterranean climate
- Phase change in a portion of the layer equal to 35% is sufficient to reach high thermal performances

Nessuno si impegna in una ricerca in fisica con l'intenzione di vincere un premio. È la gioia di scoprire qualcosa che nessuno conosceva prima.

(Stephen Hawking)

## 1. Introduction

### 1.1. Research background

Phase change material (PCM) has been widely employed in building envelopes with the aim of reducing and shifting the heating and cooling load peak, allowing for smaller dimensions of air-conditioning plants, to reduce energy requirements, and to maintain a more comfortable indoor environment due to smaller temperature fluctuations [1-13]. In recent decades, different passive and active technology systems with PCM were realized to improve the energy efficiency in the building envelope and to contain the temperature fluctuations in the indoor environment within a specific comfort range. Passive systems include PCM in building envelopes i.e. walls, roofs, floors and windows as part of the building materials or as a building component. In the first case, PCM are incorporated in a building construction material such as plaster, gypsum plasterboards, bricks, concrete and panels, or are blended with thermal insulations. Some other panels, such as PVC panels, CSM panels, plastic and aluminium foils are also used to encapsulate PCMs. In the second case, the component can be manufactured before the building being constructed and have a particular design. In contrast to previous passive systems, PCM active systems lead to a better heat transfer coefficient by replacing free convection by forced convection, with the help of small fans, to complete the solidification of the PCM. PCMs integrated in an external building envelope accumulate solar heating and melt during the daytime, and release the heat stored and solidifies during nighttime, due to the external infrared radiative heat exchange and the reduction of the external air temperature. This prevents overheating during the daytime in warm months and may also reduce heating needs during nighttime in the winter [14]. An effective passive PCM system is able to fully release the accumulated heat during nighttime in warm periods. Ascione et al. [15] found that during the summer, the period where the PCM solidifies would not always be sufficient for the PCM to fully solidify and that during the winter, the heat available during the day would not be enough to completely melt the PCM. Also Halford et al. [16] predict that the fraction of the mass melting is relatively low, maximum 5–11%, through most of the expected range of temperatures (307–314 K).

The presence of a phase change material (PCM) layer in an air conditioned building wall, due to the effect of storage and release of latent energy phenomena, modifies the thermal and dynamic behavior, both during the summer and winter periods.



The building external walls are subject, on the outside surface, to the action of solar radiation, as well as that of air temperature and apparent sky temperature. On the internal surface they are subject to the thermal exchanges, convective with the air and, infrared radiative with other walls and to the absorbed solar radiation that penetrates through the glazed surfaces. The variability of such loadings can be schematized by non-sinusoidal periodical fluctuations, which in the outdoor environment are representative of the average monthly day of the thermal quantities, and which cause a steady periodic thermal regime in the layer after an initial thermal transient. In such a regime, upon variability of the boundary conditions in relation to the PCM melting temperature, one or more bi-phase interfaces can originate, which are formed on the external surface or also on the internal surface, and that involve a part of the layer or the entire layer. It may occur that the layer is not subject to phase change and it remains in a solid or liquid phase. The storage and the release processes of latent energy at the melting temperature, compared to the monophasic layer, modifies the fluctuant field of the temperature and of the heat flux. The heat flux shows a sharp variation at the beginning and at the end of the phase change at the interested abscissas, and the temperature, in the correspondent time period, stays constant. During the process, such modifications propagate also to the adjacent abscissas not interested by phase change.

The thermal field in the layer is modified according to the number, typology and formation position of the bi-phase interfaces. In particular, on the external and internal surface of the layer, the daily maximum excursions change, maximum and minimum peaks undergo a time lag, and in some cases it can even happen that, in a fraction of the period, they are constant. Also the fluctuating energy, associated with the fluctuations of the surface heat fluxes, varies.

### 1.1.1. Literature investigation on the dynamic characterization

In order to take into consideration the above described events, the dynamic characterization of a PCM layer, unlike a monophasic layer, requires the definition of new parameters that identify dynamic thermal and energetic behavior.

In a monophasic layer in periodic sinusoidal conditions, the dynamic characterization is obtained by: the periodic thermal transmittance, the thermal admittances, the areal heat capacities, the decrement factor and the time lag of the periodic thermal transmittance, determined by the consideration of the air temperature as external loading and the temperature of the environment, supposed as constant, as the internal loading [17]; the surface factor evaluated in the presence of a heat flux oscillation on the internal surface and with the air temperature on both faces of the wall maintained constant [18]; the non-dimensional periodic thermal

transmittance and the periodic heat storage efficiency in the presence of more loadings which act on the external and internal face [19, 20].

In non-sinusoidal periodic conditions, the dynamic parameters considered are:

- the decrement factor of energy, the decrement factor and the time lag of the maximum and the minimum peak of the heat flux calculated in the presence of more loadings which act on the external and internal surface [19-21];
- the decrement factor of the daily maximum excursion and the time lag of the maximum peak and the minimum peak of the temperature considering the actual sol-air temperature as the external loading and considering constant the indoor air temperature [22];
- the conventional periodic thermal transmittance corrected by a factor evaluated considering the actual sol-air temperature as the external loading and considering constant the indoor air temperature [23].

For the dynamic characterization of a PCM, new parameters have been proposed in the scientific literature. In a sinusoidal periodic regime, Zhou et al. [24, 25] have studied the effects of PCM thermophysical properties, inner surface convective heat transfer coefficient and thickness of a PCM wallboard on the time lag, decrement factor and phase transition keeping time of the inner surface when the layer is subjected to the action of a periodic sinusoidal temperature or heat flux on the outer surface. Sharifi et al. [26] have used the decrement factor and the time lag, in sinusoidal temperature conditions, and the duration of being in the comfort zone and the energy required to keep the inside temperature in the comfort zone, in a dynamic regime, to evaluate the dynamic behavior of a based PCM-impregnated gypsum board. Ling et al. [27] have proposed and evaluated three indicators, namely, thermal storage coefficient, thermal resistance and thermal inertia index of PCM useful in evaluating the thermal inertia performance of a building component with PCM heated with periodic fluctuation. Evola et al. [28] have introduced a series of indicators in dynamic regime that allow a precise description of both the PCM behavior (frequency of melting, storage efficiency) and the intensity and duration of the thermal comfort perceived by occupants.

In the same thermal regime, Ye et al. [29] have evaluated the ESI, the ratio of a particular material or component's energy saving equivalent (ESE) to the corresponding value of the ideal material or component that can maintain the room at an ideal thermal state in passive mode, where the ESE represents the hypothetical energy to be supplied to maintain a passive room at the same thermal state as that when a particular material or component is adopted. Sun et al. [30] have proposed the energy and mass efficiency (EME), an index which considers the melting temperature, PCM layer thickness and the outdoor and indoor air temperature, to evaluate the

energy efficiency of PCM walls in office buildings located in various climatic regions in China for cooling. In the summer period, Lei et al. [31] have used the envelope heat gain reduction rate, which is a percentage reduction of the heat gains through the envelope due to the addition of PCM layer. In the work of Zwanzig et al. [32] PCM performance was evaluated according to three metrics: seasonal peak load shifting, seasonal peak load reduction, and total annual cooling and heating load reduction. Kuznik et al. [33], have experimentally investigated, in a full scale controlled test room, a PCM wall on a summer day, a winter day and a mid-season day. The results have shown that for all the cases tested, the decrement factor varies between 0.73 and 0.78. Mandilaras et al. [34] have presented the monthly average decrement factor and time lag values for a typical, two-storey, family house built in the mid-western part of Greece. Its walls consist of multiple layers of insulation materials and gypsum plasterboard panels containing PCMs. A decrease of the decrement factor by a further 30-40% and an increase on the time lag of approximately 100 min during late spring, early summer and autumn, attributed to the PCM implementation, are shown. Furthermore, in order to study the nonlinear behavior for PCM the “mean-effective” specific heat capacity has been calculated. The abrupt increase of the “mean-effective” specific heat capacity during spring, early summer and autumn is an indication of the enhanced thermal mass of the walling system, when PCMs are activated. In [35] the authors have presented an experimental installation of real size, concrete cubicles with PCM, constructed in the locality of Puigverd of Lleida (Spain), that can reduce the fluctuation of the external surface temperature of walls and obtain a time lag around + 2 h, compared to the base wall without PCM. In another investigation, by means of the use of PCM in the roof, numerically, Dong et al. have obtained a time delay of the temperature peak 3 h higher than a common roof in the cold area of China [36]. In the experiment of Guarino et al. [37] a building-integrated thermal storage system in a cold climate has allowed solar radiation to be stored and released up to 6–8 hours. Thiele et al. [38] have evaluated the effects of adding PCM on the reduction and delay of thermal load through composite walls subjected to diurnal sinusoidal outdoor temperature and solar radiation heat flux. They concluded that increasing the latent heat of fusion both substantially reduced and delayed the thermal load on the building and that, in order to achieve the maximum time delay, the optimum phase change temperature rose by increasing average outdoor temperature.

### 1.1.2. Literature investigation on the energy performance

In energetic terms, the phase change within the layer causes a reduction of the lost energy towards the outdoor environment in the winter period and of the energy that the outdoor

environment transfers to the indoor environment during the summer period. For example, studies have reported that PCMs can potentially save 10-30% of the annual cooling and heating loads for buildings in various climate zones in the world. By means of a year-round simulation, Diaconu and Cruceru [39] have studied the annual energy request in Bechar (Algeria) of a room built using a three-layer sandwich-type insulating panel with outer layers consisting of PCM wallboards and a middle layer of conventional thermal insulation. They have found that the reductions of the peak heating and cooling loads are both around 35.4%. The annual energy savings for space heating and cooling are respectively around 12.8% and 1.0%. Wang et al. [40] have evaluated the thermal behavior of a full-scale room with PCM wall in three seasons. The results show: for the summer cases, a reduction of about 0.2 °C and a time delay of about 1-2 h for the maximum interior surface temperature, and a reduction of 24.32% of the cooling load; for the midseason cases, a lower amplitude of the fluctuation of the interior surface temperature; for the winter cases, a reduction respectively of 10-19%, and 10-30% of the heating load in continuous and in intermittent regime and of 9-72% of the heat lost in free floating.

Chen et al. [41] have demonstrated that using PCM, when the phase change temperature is set at 23 °C, the thickness at 30 mm, the phase change enthalpy at 60 kJ/kg and the heating temperature at 20 °C, the energy saving rate of heating season can reach up to 17% or higher during a whole winter in Beijing, China. Qureshi et al. [42] have monitored a test facility at the University of Auckland (New Zealand) consisting of two identical offices; the first one has walls and ceilings finished with gypsum boards impregnated with PCM. The authors have concluded that, during the days characterized by lower average ambient temperatures and high solar radiation, the energy requirement for heating decreases to around 31%. Peippo et al. [43] have found that, through the use of passive solar heating with a PCM wall in a room of a residential building, direct energy savings of 5-20% could be expected, in Helsinki, Finland and Madison, Wisconsin. Athienitis et al. [44] have obtained a total heating load reduction of approximately 15% in Montreal in a passive solar test-room in which gypsum board is impregnated with a PCM. In the same locality, by means of a system that can simultaneously and efficiently store and manage heat from solar and electric sources, Hammou and Lacroix [45] have attained an electricity consumption for space heating during four consecutive winter months reduced by 32%. Castell et al. [46] have tested macro-encapsulated PCMs in typical Mediterranean building technologies. The authors, with reference to the cooling season, have concluded that the “RT27 - Polyurethane cubicle” implied a reduction of 15% compared to the simple Polyurethane one, while the “SP25 - Alveolar cubicle” obtained 17% of energy savings compared to the Alveolar solution. Lei et al. [31] have addressed the energy performance of building envelopes integrated

with PCM for cooling load reduction in Singapore, with a tropical climate. For the cubic model integrated with 10mm PCM layer (melting temperature 28 °C) and with an ideal heating, ventilating and air conditioning system (HVAC), they have found that the PCM can effectively reduce heat gains through building envelopes in a range of 21-32% throughout the whole year. Kosny et al. [47] have numerically analyzed a southern-oriented wall for the hot summer period between June 30th and July 3rd in three climatic locations: Warsaw (Poland), Marseille (France) and Cairo (Egypt). They have obtained that for an internal air temperature of 24 °C, hourly peaks of heat gains were reduced by 23-37% for Marseille and 21-25% for Cairo; similar effects were observed for Warsaw.

## **1.2. Objectives of this chapter**

The studies analyzed reveal that it is indispensable to select the correct phase change temperature in order to optimize the PCM thermal performance when it is integrated in the external walls of the buildings. The optimal phase change temperature in the cooling period is different from that in the heating period. This temperature has been studied by different researchers who have obtained very useful results. From the literature it emerges that, in order to minimize the thermal load of the building or maximize the heat storage, a phase change temperature roughly equal or 1-3 °C higher than the average indoor air temperature is necessary [43,48-51]. Jiang et al. [52] have proposed a simple analytical method which has been used to estimate in a passive solar room the optimal phase change temperature, that is 1.1-3.3 °C higher than the lower limit of thermal comfort range. Ye et al. [29] have concluded that, in order to maximize the parameter ESI, the melting temperatures in Beijing and Shanghai are about 16 °C and 10 °C, respectively. Diaconu et al. [39] have found that the melting temperature for which the peak of the cooling load reached a minimum is approximately 33.2 °C, while that for which the lowest peak of the heating load and minimum annual energy requirement for heating are, respectively, 19.0 and 19.8 °C. Arnault et al. [53] have obtained an optimal melting temperature to reduce energy cooling consumption of 33.9 °C and to reduce the yearly energy consumed of 26.1 °C. Sun et al. [54] have carried out, for a time period of three summer months in five different climate regions in China, a selection of the optimum melting temperatures of the PCMs, employing both energy and economic criteria, evaluating the energy savings ratio (ESR) and the simple payback period (SPP). Subsequently, the same authors [30] have concluded that the optimal melting temperatures, which resulted in the maximum EME in a office building, are 24.1 °C in Shenyang, 25.0 °C in Kunming, 25.3 °C in Zhengzhou and 25.5 °C Changsha, respectively.

Thiele et al. [38] have found that: the phase change temperature leading to the maximum energy reduction was equal to the desired indoor temperature regardless of the climate conditions; to achieve the maximum time delay, the optimum phase change temperature rose by increasing the average outdoor temperature. Zhou et al. [55] have stated that the optimal melting temperature depends on both the average outside temperature and the average room temperature.

As evidenced by the scientific literature, the choice of the most appropriate PCM for a given location in the two seasons of air-conditioning requires in-situ experimental testing or dynamic numerical simulations. In the first case, experimental equipment and high monitoring times and costs are required, while in the second case a high computational burden of calculation is required. Furthermore, the aforementioned studies are not generalizable since the choice of the PCM is made for a given building and given weather conditions. The effects produced by a particular PCM vary by varying the locality and, for a given locality, varying the climate conditions over the year. The selection of a PCM based on a specific melting temperature in one climate region will not be appropriate for another. Another critical point is that the PCM behaviour should be evaluated under realistic conditions over a long period (on an annual basis), not just over a few days or weeks. Actually, the PCM could work improperly during very hot and sunny days, if solidification is not effectively performed; it could also become useless during cool and cloudy days, if melting is not produced. A study based on a few days of observation might not tackle these issues properly. All these points induced the authors to elaborate a general methodology for the evaluation of the actual thermal performance of the PCM layer for the improvement of seasonal or annual thermal behaviour in buildings. Such a methodology is general, based on a series of dynamic parameters and thermal quantities evaluated in the monthly average day for every month through the year, and summarized on a seasonal and yearly level. It represents a simplified method of thermal dimensioning of the PCM layer that regards the choice of the melting temperature, of the thermophysical properties and of the most appropriate thickness for a given location and season.

This chapter addresses the issue of the thermal energy exchange and of the dynamic characterization of a PCM layer in which one or more bi-phase interfaces are formed, in the hypothesis that the thermal regime is a steady periodic regime. The boundary conditions of the layer are those which characterize the external walls of air conditioned buildings. The analyses are developed as an explicit finite difference numerical model, which resolves the equation of conduction in solid phase and liquid phase and the equation of thermal balance at the bi-phase interfaces at the melting temperature.

The temperature and heat flux trends on the external and internal surface, energy entering and exiting from the layer, and the stored energy in the layer in the sensible and latent form, are employed in order to define new parameters necessary to dynamically characterize the layer. Defined parameters are: latent storage efficiency; the fraction of latent energy stored compared to the total energy stored; decrement factor of the maximum excursion of the temperature and of the heat flux; the energy decrement factor; the time lag of the maximum and minimum peak of the temperature and heat flux; the fraction of the period during which the temperature and the heat flux maximum peak or minimum peak are constant in time on the internal surface.

The procedure is used in order to evaluate energy performances and dynamic characteristics of a PCM layer, with different melting temperatures and thermophysical properties. The climatic conditions taken into consideration, relating to two locations, one with a continental climate and the other one with a Mediterranean climate, are represented through the monthly average day and modeled with periodical non-sinusoidal fluctuations.

In the first part of this chapter, the authors present the numeric model, an analysis of the surface temperatures and heat fluxes in the event that one or more bi-phase interfaces are present in the layer, the calculation procedure of the exchanged and stored energy, and the definition of dynamic characteristics. In the second part of the chapter, referring to five different types of PCM and two locations, the configurations of the phases in the layer, monthly and seasonal energy transferred and stored, monthly trends of dynamic characteristics are shown for each month of the year. Finally, the authors present a study on the influence of the latent storage on the dynamic characteristics and some calculation correlations amongst dynamic parameters. In a previous work [56] by the same authors, more complete examples of temperature and heat flux fields in the presence of one or more bi-phase interfaces, the evolution in time of the bi-phase interface and the related trends of latent energies stored or released per unit time are described.

## **2. Methodology**

### **2.1. Calculation model**

The model constitutive equations are the general equation of heat conduction in the solid phase and in the liquid phase (1) and the balance equation at the bi-phase interface at the melting temperature (2) and (3):

$$\frac{\partial^2 T}{\partial x^2} - \frac{1}{a} \frac{\partial T}{\partial t} = 0 \quad (1) \quad \left[ k_l \frac{\partial T_l}{\partial x} - k_s \frac{\partial T_s}{\partial x} \right]_{x=X_M} = \rho H \frac{dX_M}{dt} \quad (2) \quad T_l(X_M, t) = T_s(X_M, t) = T_M \quad (3)$$

With  $H$  representing latent heat of fusion,  $T_M$  melting temperature and  $X_M$  position of the bi-phase interface. Boundary conditions on the external surface of PCM layer are represented by the convective and radiative, at short and long wavelength, thermal exchanges with the outdoor environment, and on the internal surface by thermal exchanges with the indoor environment evaluated through the surface heat transfer coefficient. The corresponding equations are:

$$\Phi_e = \Phi_{r,e} + \Phi_{c,e} + \alpha \Phi_{sol} = h_{r,e}(T_{sky} - T_{s,e}) + h_{c,e}(T_{ea} - T_{s,e}) + \alpha \Phi_{sol} = -k \left. \frac{\partial T}{\partial x} \right|_{x=0} \quad (4)$$

$$\Phi_{ia} = h_{s,i}(T_{s,i} - T_{ia}) = -k \left. \frac{\partial T}{\partial x} \right|_{x=L} \quad (5)$$

with  $\Phi_e$  signifying total heat flux from the outdoor environment,  $\Phi_{r,e}$  longwave radiative heat flux exchanged with the sky,  $\Phi_{c,e}$  convective heat flux exchanged with the external air,  $\alpha_e$  absorption coefficient,  $\Phi_{sol}$  solar radiation,  $h_{r,e}$  and  $h_{c,e}$  radiative and convective heat transfer coefficients,  $T_{sky}$  sky temperature,  $T_{ea}$  external air temperature,  $T_{s,e}$  external surface temperature,  $\Phi_{ia}$  heat flux transferred in the indoor environment,  $h_{s,i}$  internal surface heat transfer coefficient,  $T_{s,i}$  internal surface temperature,  $T_{ia}$  internal air temperature and  $L$  thickness of the layer.

A sketch of the thermal exchanges between the PCM layer and the outdoor and indoor environments is shown in Figure 1.

An explicit finite difference numeric model has solved the equations system (1)-(5). The discretization of the equation, obtained by evaluating the time derivative with its related incremental ratio, leads to the relations for the calculation of the temperatures in the nodes not subject to a phase change and of the liquid fractions  $\lambda$  present in the subvolume of nodes at the melting temperature. Such equations and the employed calculation algorithm, validated by means of a comparison with the results determined by an analytical model that resolves the heat transfer in a PCM layer in a steady periodic regime [57], are reported in [56]. In detail, the algorithm provides for:

- the possibility that one or more bi-phase interfaces form in the layer, when the temperatures on the PCM boundary surfaces fluctuate around the melting temperature;
- a non-uniform spatial discretization;



- different thermo-physical properties in the solid phase and in the liquid phase
- the update at every time instant of the thermal resistances among nodes and of nodal heat capacities according to the position and typology of the bi-phase interfaces.

The model does not contemplate phenomena of phase segregation, of subcooling and of hysteresis.

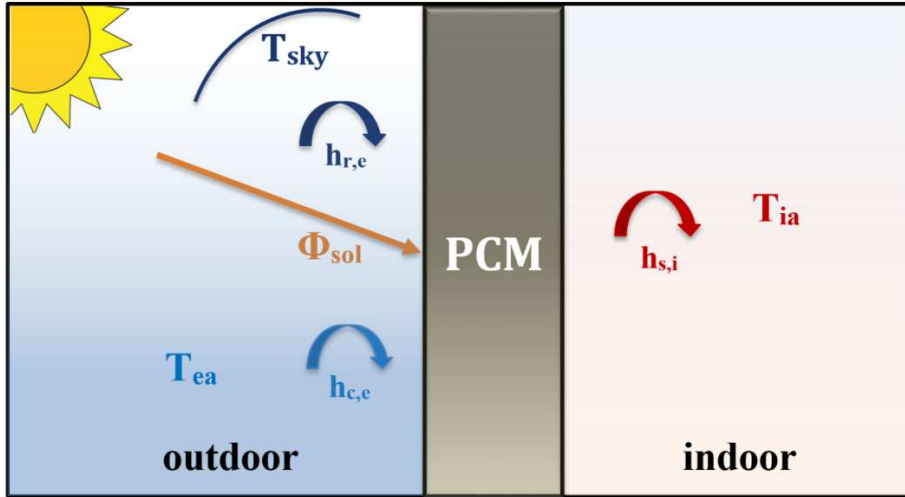


Figure 1 – Thermal exchanges schematization on the external and internal surface of the PCM layer.

The position of the bi-phase interfaces is determined depending on the thickness and the liquid fractions  $\lambda_{jk}$  present in subvolumes, with the relations:

$$X_{M,k} = \sum_{i=1}^{j_k-1} \Delta x_i + \Delta x_{j_k} \lambda_{j_k} \quad (6)$$

$$X_{M,k} = \sum_{i=1}^{j_k-1} \Delta x_i + \Delta x_{j_k} (1 - \lambda_{j_k}) \quad (7)$$

In the previous equations, if the bi-phase interface is of melting (see Eq. 6), the position of the k-th bi-phase interface  $X_{M,k}$  present in subvolume  $jk$  is calculated summing the thicknesses of the subvolumes  $\Delta x_i$  preceding the node  $jk$  to the portion of the subvolume  $jk$  in liquid phase  $\Delta x_{j_k} \lambda_{j_k}$ . If it is a solidification interface (see Eq. 7), the position of the k-th bi-phase interface  $X_{M,k}$  present in subvolume  $jk$  is calculated summing the thicknesses of the subvolumes  $\Delta x_i$  preceding the node  $jk$  to the portion of the subvolume  $jk$  in solid phase  $\Delta x_{j_k} (1 - \lambda_{j_k})$ . For example, if the bi-phase interface is of melting and falls within the volume associated with the fourth node ( $j_k = 4$ ), Eq. (6) provides  $X_{M,k} = \Delta x_1 + \Delta x_2 + \Delta x_3 + \Delta x_4 \lambda_4$ , with  $\lambda_4$  fraction of volume 4 in liquid phase. Viceversa, if the bi-phase interface is of solidification, Eq. (7) provides

$\Delta x_1 + \Delta x_2 + \Delta x_3 + \Delta x_4(1 - \lambda_4)$ , with  $(1 - \lambda_4)$  fraction of volume 4 in solid phase. All the equations and the algorithm have been implemented in our own MATLAB program code. Such a code allows us to determine the number and the position of eventual bi-phase interfaces in the layer, the configuration of the phases, the temperature and heat flux fields and the stored energy per unit time, the sum of latent and sensible contribution. In each point of the layer, the temperature and heat flux trends can be considered as the sum of a steady component and a fluctuating component. The steady component is calculated as an average of the instant values in the time period, and the fluctuating component is obtained by subtracting the steady component from the overall trend.

## 2.2. Configuration of the phases in the layer and surface temperatures and heat fluxes

Whichever is the configuration of the phases in the layer, the temperature steady component varies linearly in the layer, and the respective heat flux is constant. Instead, the temperature and heat flux fluctuating component, change according to the latent contributions, proportionate to the bi-phase interface advancing speed.

Figs. 2-5 show examples of temperature and heat flux trends on the layer external and internal surface. Such trends have been obtained considering the PCM S15, whose thermophysical properties are reported in Table 2 with reference to the boundary conditions, defined in Section 3, related to Turin. In order to be complete, the images also show the PCM melting temperature  $T_M$ , the trends of the internal air temperature  $T_{ia}$  and also of the equivalent temperature of the outdoor environment  $T_{e,eq}$  [20] which are representative of the three external loadings. In every image, the upper curves represent temperatures, whose scales are reported on the left axes, while the lower curves represent heat fluxes, whose scales are reported on the right axes. The vertical lines allow us to identify the time instants when the phase change process associated to each single bi-phase interface starts and ends, while the horizontal arrows indicate the duration of the phase change process associated with each single bi-phase interface. Figure 2 refers to the case of the absence of bi-phase interfaces and the layer is entirely in a solid phase (a) or in a liquid phase (b). Figure 3 shows the trends in the case of a bi-phase interface formation on the external surface (a) or on the internal surface (b). While, figure 4 relates to the formation of two bi-phase interfaces, both on the external surface (a) or one on the internal surface and the other one on the external surface (b); figure 5 relates to the case of the presence of three bi-phase interfaces all of them on the external surface (a) or two on the external surface and one on the internal surface (b).

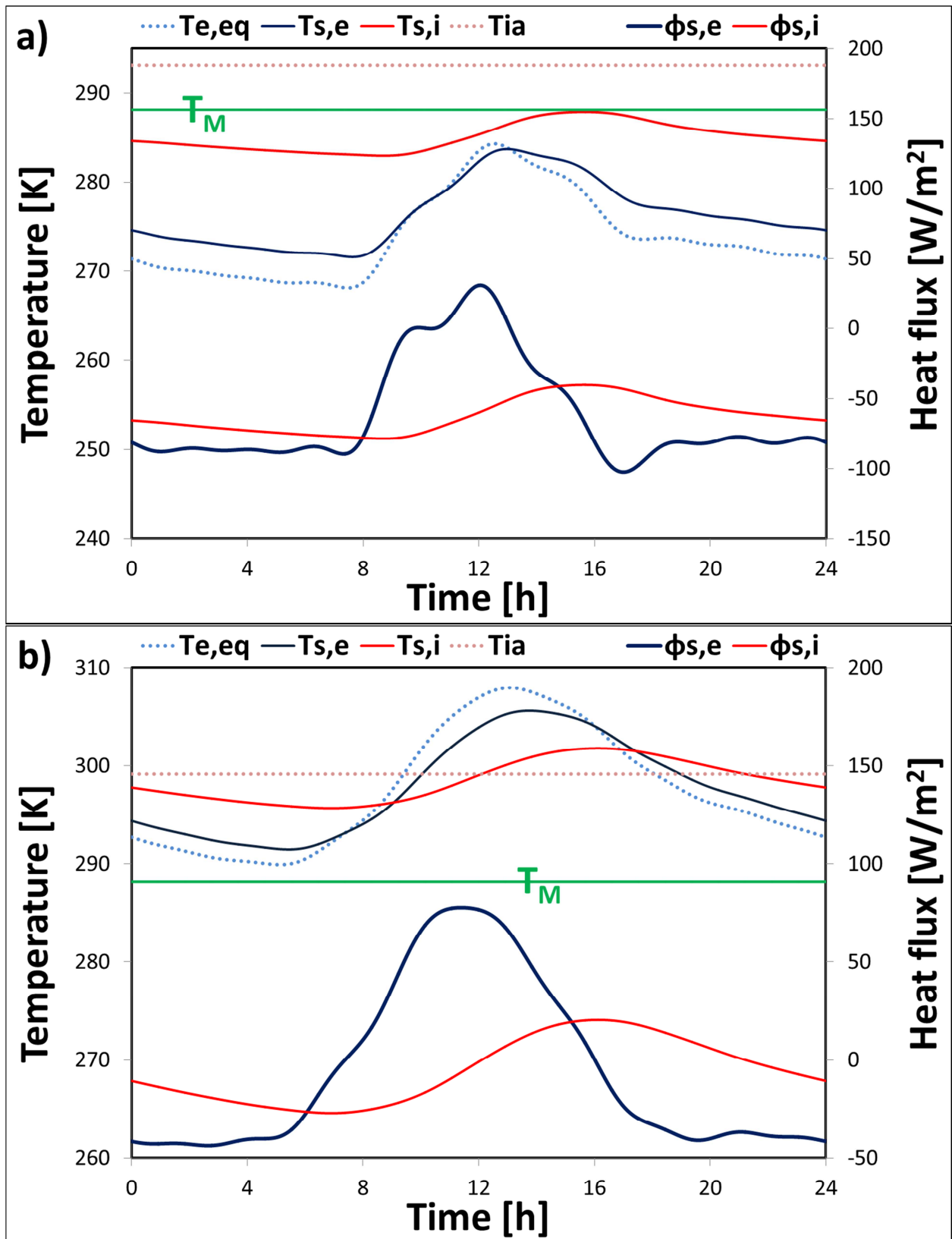


Figure 2 – Absence of phase change a) solid phase b) liquid phase. Temperatures,  $T_{s,e}$  and  $T_{s,i}$ , and heat fluxes,  $\phi_{s,e}$  and  $\phi_{s,i}$ , on the external surface and on the internal surface; melting temperature  $T_M$ ; internal air temperature  $T_{ia}$ ; equivalent outdoor temperature  $T_{e,eq}$ .

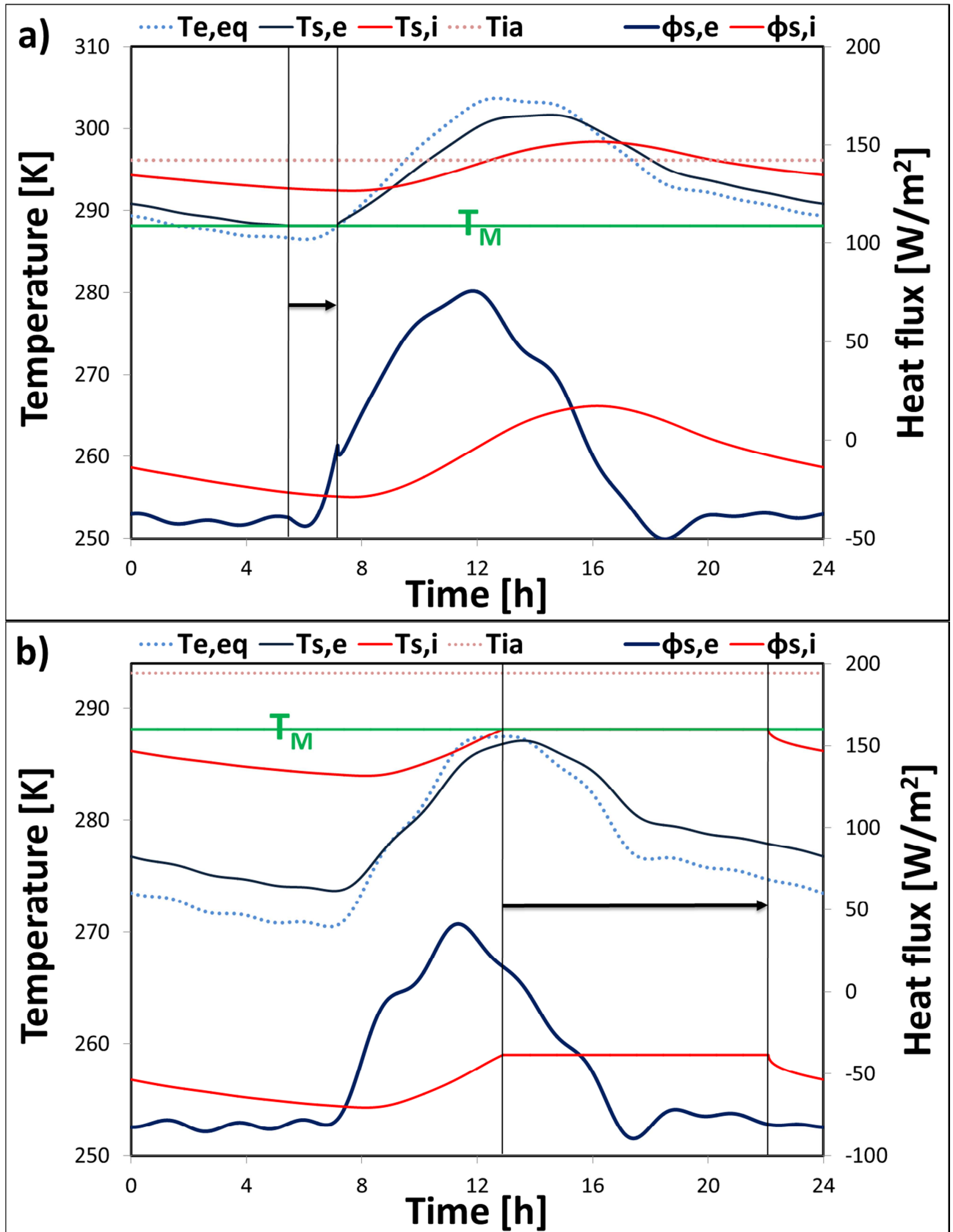


Figure 3 – Presence of a bi-phase interface originating on the external surface a) or on the internal surface b). Temperatures,  $T_{s,e}$  and  $T_{s,i}$ , and heat fluxes,  $\Phi_{s,e}$  and  $\Phi_{s,i}$ , on the external surface and on the internal surface; melting temperature  $T_M$ ; internal air temperature  $T_{ia}$ ; equivalent outdoor temperature  $T_{e,eq}$ .

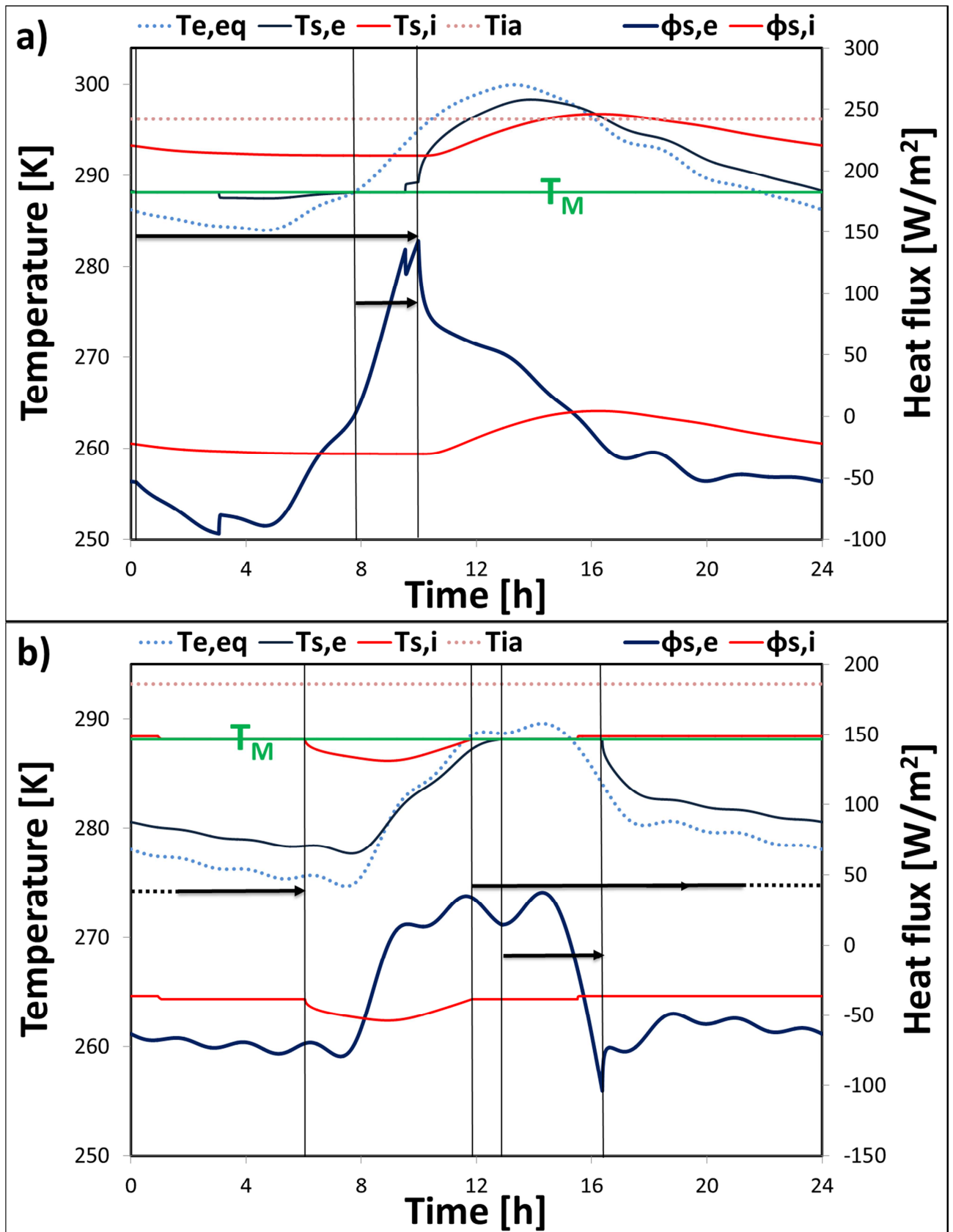


Figure 4 – Presence of two bi-phase interfaces both originating on the external surface a) or one on the external surface and the other on the internal surface b). Temperatures,  $T_{s,e}$  and  $T_{s,i}$ , and heat fluxes,  $\phi_{s,e}$  and  $\phi_{s,i}$ , on the

external surface and on the internal surface; melting temperature  $T_M$ ; internal air temperature  $T_{ia}$ ; equivalent outdoor temperature  $T_{e,eq}$ .

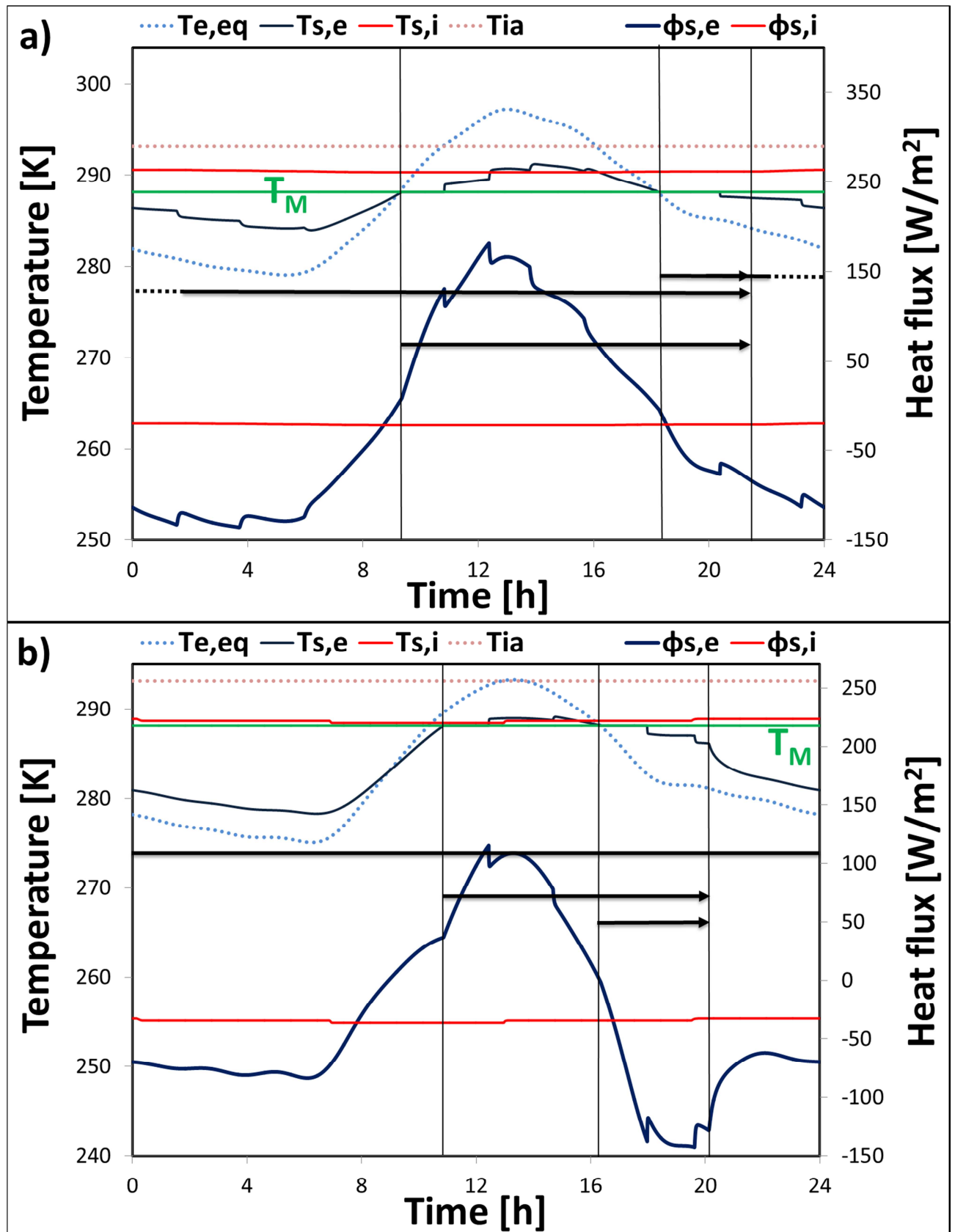


Figure 5 – Presence of three bi-phase interfaces all originating on the external surface a) or two on the external surface and the other on the internal surface b). Temperatures,  $T_{s,e}$  and  $T_{s,i}$ , and heat fluxes,  $\Phi_{s,e}$  and  $\Phi_{s,i}$ , on the external surface and on the internal surface; melting temperature  $T_M$ ; internal air temperature  $T_{ia}$ ; equivalent outdoor temperature  $T_{e,eq}$ .

If the PCM layer is monophasic, see figures 2a and 2b, the temperature in the entire layer is always higher than the melting temperature if the layer is in liquid phase, and is always lower than the melting temperature if the layer is in solid phase. The periodic temperature and heat flux fluctuations on the internal surface present a lower amplitude and are shifted, compared to these on the external surface.

The temperature variability on the external and internal surfaces of the layer in respect to the melting temperature determines the phase change formation abscissa (on the boundary surfaces or in the layer) and the number, the typology (of fusion or solidification), and the advancing speed of the bi-phase interfaces in the layer.

When the temperature on the external surface, see figure 3a, or on the internal surface of the layer, see figure 3b, during the period, becomes equal to the melting temperature, a bi-phase interface forms. Such an interface penetrates the layer, it reaches maximum depth, then it reverts direction and restores the initial monophasic layer. Usually, during the winter season, at night time, the layer is totally in a solid phase; in the day time, due to the prevailing effect of solar radiation absorbed by the external surface and also due to the surfacel thermal exchange with the indoor environment, the layer heats up and the internal surface or the external surface reaches the melting temperature, starting the fusion process. The behavior is different during the months when the layer is entirely in a liquid phase in the day time. In fact, during nocturnal hours, due to the convective-radiative thermal exchange with the outdoor environment, the layer starts the solidification process. The interface penetrates the layer, and once a given depth is reached, during daytime hours, it reverts direction mainly due to the absorbed solar radiation, and it restores the liquid phase in the whole layer. In both cases, during the phase change, the latent energy per unit time, proportional to the advancing velocity of the bi-phase interface, at the beginning increases, it reaches a certain maximum value and afterwards decreases until it is annulled at the instant when the bi-phase interface reverts direction and starts the opposite process. During this process, the latent energy per unit time always increases and it is at its maximum value at the time instant when the phase change stops restoring the initial phase. Due to the effect of the velocity variation in the different time instants of the external loadings, the advancing velocity of the bi-phase interface is not constant in time. Because of this, the duration

of the fusion process, which gives rise to a the latent energy storage, is different from that of the solidification process, releasing the stored energy.

When the temperature on the external surface and on the internal surface of the layer become equal to the melting temperature, see Figure 4b, two bi-phase interfaces originated, and they can be both fusion interfaces if the initial layer is solid, or solidification interfaces if the initial layer is liquid. Both interfaces penetrate the layer, and reach a maximum depth to finally be extinguished on the surface of origin. The two interfaces do not develop simultaneously and they both contribute to the latent energy storage and release process.

When the temperature on the external surface of the layer, in two successive time instants in the period, becomes equal to the melting temperature, two bi-phase interfaces originate on this surface, see Figure 4a. For instance, if the layer is totally in the liquid phase, the first bi-phase interface is a solidification one during nocturnal hours, and the other is a fusion one during diurnal hours, mainly produced by solar radiation. Such interfaces penetrate the layer at different velocities, and rejoin internally to re-establish the original monophase layer. The latent energy storage process is mainly connected to a bi-phase interface while the release process is connected to the other interface.

It can also happen that one of the two interfaces stays in the layer with a time length longer than the period  $P = 24$  h, see Figure 5a, so that, in a defined interval of time in the period, three bi-phase interfaces are present in the layer. Also in this case, the latent energy stored by one interface is completely returned by the other one. It is also possible that, in the case when three bi-phase interfaces are present, two originate on the external surface, while a third one is always present in period  $P$  and fluctuates concerning a portion of the layer near to the internal surface, see figure 5b. Also in this case, the two interfaces originating on the external face, rejoin in the inner part of the layer and the stored latent energy is completely returned by the other one. The energy stored by the third interface is then released by the same one with a similar trend.

The phase change effects within the layer on the surface temperature and heat flux trends can be summarized as follows. Regarding the temperature trend on the surface where the bi-phase interfaces originate, see Figures 3 and 4, unlike a monophase material, it is revealed that:

- a) for a fraction of the period the related maximum or minimum peaks are constant and approximate to the melting temperature;
- b) the maximum or the minimum peak persists in time;
- c) the maximum excursion in the period is reduced due to decrement of the maximum peak amplitude, if the interface is one of fusion, or that of the minimum peak, if the interface is one of solidification;



Concerning the heat flux trend:

- if the bi-phase interfaces originate on the external surface, on this surface it is highlighted that:
  - d) at the beginning and at the end of the phase change there is discontinuity;
  - e) the daily maximum excursion increases;
  - f) the instant when the maximum or the minimum peak occur changes;
  - g) the fluctuant energy changes.
- if the bi-phase interfaces originate on the internal surface, on this surface it is noticed that:
  - h) at the beginning and at the end of the phase change there is a discontinuity;
  - i) for a fraction of the period, the related maximum or minimum peak can be considered constant;
  - j) the daily maximum excursion decreases;
  - k) the instant when the maximum or the minimum peak occur changes;
  - l) the fluctuant energy decreases.

On the surface that is not the site of bi-phase interface formation, if it is the internal one, the maximum excursions decrease and the fluctuating temperature and heat flux maximum and minimum peaks undergo a time lag. Whereas, if it is the external one, the fluctuations of temperature and heat flux stay basically unchanged. Furthermore, increasing the number of the bi-phase interfaces on the external surface, the thermal fluctuations on the internal surface result as being damped until a complete attenuation with three bi-phase interfaces is reached, see Figure 5a.

Finally, the contemporary presence of bi-phase interfaces on the internal and external surfaces, see Figures 4b and 5b, causes analogous behavior on the external surfaces to those described in the previous a) - g) points, while on the internal surface the maximum temperature and heat flux excursions are almost completely damped.

The above described trends show that, for the complete dynamic characterization of the PCM layer, the employment of more parameters is necessary, as defined in section 2.4, in order to identify fully the transformation that the form of the fluctuating thermal quantity undergoes when passing through the layer.

### 2.3. Fluctuanting transferred energy and stored energy

The temperature and heat flux trends on the external and internal surface are used to evaluate the energy behaviour of the PCM layer in terms of transferred energy and of stored energy in the

layer in the sensible and latent form. The temperature and heat flux trends can be considered as a sum of a steady component and a fluctuant component.

The monthly average daily fluctuant energy on the internal surface  $\tilde{E}_i$  and external surface  $\tilde{E}_e$  of the layer calculated taking into account that, for a fluctuating quantity around a mean value, the area subtended the trend in the time interval in which the quantity is greater than the average value is equal to the area subtended the trend in the time interval in which the quantity is less than the average value. For this reason,  $\tilde{E}_i$  e  $\tilde{E}_e$  are determined by half of the numeric integral in time, extended to the period, of the absolute value of the surface fluctuant heat fluxes  $\tilde{\Phi}_{s,i}$  and  $\tilde{\Phi}_{s,e}$  (Eqs. 8 - 9). The surface fluctuant heat fluxes  $\tilde{\Phi}_{s,i}$  and  $\tilde{\Phi}_{s,e}$  are equal to the difference between the relative total value and the steady mean value.

$$\tilde{E}_i = \frac{1}{2} \sum_{n=0}^P |\tilde{\Phi}_{s,i}^{n+1}| \Delta t \quad (8) \quad \tilde{E}_e = \frac{1}{2} \sum_{n=0}^P |\tilde{\Phi}_{s,e}^{n+1}| \Delta t \quad (9)$$

The total energy stored  $E_T$  is calculated by half of the numeric integral in time, extended to the period, of the difference in absolute value of the heat flux entering the layer and exiting from the layer (Eq. 10). Likewise, the advancing velocity of the k-th bi-phase interface, given by the ratio  $(X_{M,k}^{n+1} - X_{M,k}^n)/\Delta t$ , is used to evaluate the latent energy stored, by the Eq. (11).

$$E_T = \frac{1}{2} \sum_{n=0}^P |\Phi_T^{n+1}| \Delta t = \frac{1}{2} \sum_{n=0}^P |\Phi_{s,i}^{n+1} - \Phi_{s,e}^{n+1}| \Delta t \quad (10)$$

$$E_{L,k} = \frac{1}{2} \sum_{n=0}^P |\Phi_{L,k}^{n+1}| \Delta t = \frac{1}{2} \sum_{n=0}^P \left| \rho H \frac{(X_{M,k}^{n+1} - X_{M,k}^n)}{\Delta t} \right| \Delta t \quad (11)$$

The sensible energy  $E_S$  is given by half of the numeric integral in time of the difference, in absolute value, between the total stored energy per unit time and the latent stored energy per unit time, (Eq. 12).

$$E_S = \frac{1}{2} \sum_{n=0}^P |\Phi_S^{n+1}| \Delta t = \frac{1}{2} \sum_{n=0}^P |(\Phi_{s,i}^{n+1} - \Phi_{s,e}^{n+1}) - \Phi_L^{n+1}| \Delta t \quad (12)$$

Furthermore, the surface heat fluxes are used to calculate the energy through the inner surface, entering the indoor environment  $E_i^+$  and exiting from the indoor environment  $E_i^-$ , and through the external surface, entering the layer  $E_e^+$  and exiting the layer  $E_e^-$  (Figure 6). The superscripts + and – indicate the energy associated to the time interval in which the heat flux is respectively positive and negative.

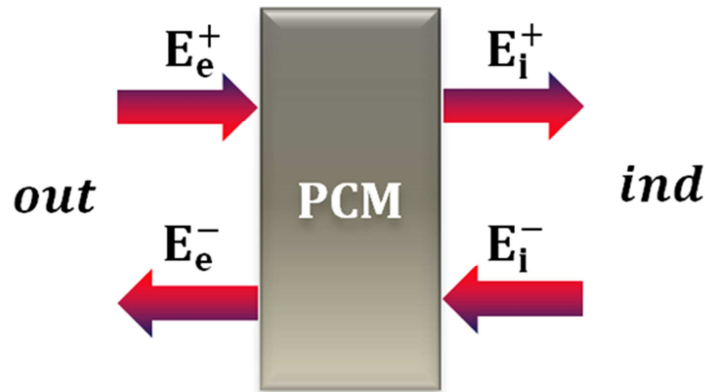


Figure 6 – Energy entering and energy exiting through the external surface,  $E_e^+$  and  $E_e^-$ , and internal surface,  $E_i^+$  and  $E_i^-$ , of the PCM layer.

The monthly average daily values of the energy transferred through the layer and the stored energy values in the various months have been used for the calculation of the related seasonal and yearly values.

#### 2.4. Definition of the dynamic parameters

With reference to a period  $P=24$  hours, the temperature and heat flux trends on the external surface and on the internal surface, the fluctuant energy entering in the layer  $\tilde{E}_e$  and exiting from the layer  $\tilde{E}_i$ , and the stored energy in the form of sensible energy  $E_S$  and latent energy  $E_L$ , are used in order to define the parameters necessary to dynamically characterize the PCM layer.

With reference to Figure 7, such parameters are:

- a) the latent storage efficiency  $\varepsilon_L$ , ratio between the latent energy stored  $E_L$  and the maximum storable latent energy  $E_{L,max}$ , evaluated on the basis of the assumption that the whole layer changes phase; the fraction of latent energy  $\Lambda_L$  with respect to total energy stored in the layer, see Figure 7d:

$$\varepsilon_L = \frac{E_L}{E_{L,\max}} = \frac{\rho H \Delta x_{PC}}{\rho H L} \quad (13)$$

$$\Lambda_L = \frac{E_L}{E_T} \quad (14)$$

- b) the decrement factor of the maximum excursion of the temperature  $f_T$  (Eq. 15), see figure 7a, and of the heat flux  $f_\Phi$  (Eq. 16), see Figure 7b, and the decrement factor of the fluctuating energy transferred  $f_E$  (Eq. 17), see Figure 7c:

$$f_T = \frac{(T_i^{\max} - T_i^{\min})}{(T_e^{\max} - T_e^{\min})} \quad (15)$$

$$f_\Phi = \frac{(\Phi_i^{\max} - \Phi_i^{\min})}{(\Phi_e^{\max} - \Phi_e^{\min})} \quad (16)$$

$$f_E = \frac{\tilde{E}_i}{\tilde{E}_e} \quad (17)$$

- c) the time lag of the maximum and the minimum peak of the temperature  $\Delta t_{T^{\max}}$  and  $\Delta t_{T^{\min}}$  (Eqs. 18-19), see Figure 7a, and of the heat flux  $\Delta t_{\Phi^{\max}}$  and  $\Delta t_{\Phi^{\min}}$  (Eqs. 20-21), see Figure 7b:

$$\Delta t_{T^{\max}} = (t_{T_i^{\max}} - t_{T_e^{\max}}) \quad (18)$$

$$\Delta t_{T^{\min}} = (t_{T_i^{\min}} - t_{T_e^{\min}}) \quad (19)$$

$$\Delta t_{\Phi^{\max}} = (t_{\Phi_i^{\max}} - t_{\Phi_e^{\max}}) \quad (20)$$

$$\Delta t_{\Phi^{\min}} = (t_{\Phi_i^{\min}} - t_{\Phi_e^{\min}}) \quad (21)$$

- d) the constant peak time fraction of the temperature or of the heat flux, namely the fraction of period  $P$  in which the maximum or the minimum peak of temperature  $\Pi_{T_i}$  (Eq. 22), see Figure 7a, and of heat flux  $\Pi_{\Phi_i}$  (Eq. 23), see figure 7b, on the internal surface are constant.

$$\Pi_{T_i} = \frac{\Delta P_{T_i^p = \text{const}}}{P} \quad (22)$$

$$\Pi_{\Phi_i} = \frac{\Delta P_{\Phi_i^p = \text{const}}}{P} \quad (23)$$

In the previous equations the subscripts  $i$  and  $e$  respectively indicate the internal and external surface of the layer, while the superscripts  $p$ ,  $max$  and  $min$  identify the generic peak value, the maximum value and minimum value of the considered thermal quantity.

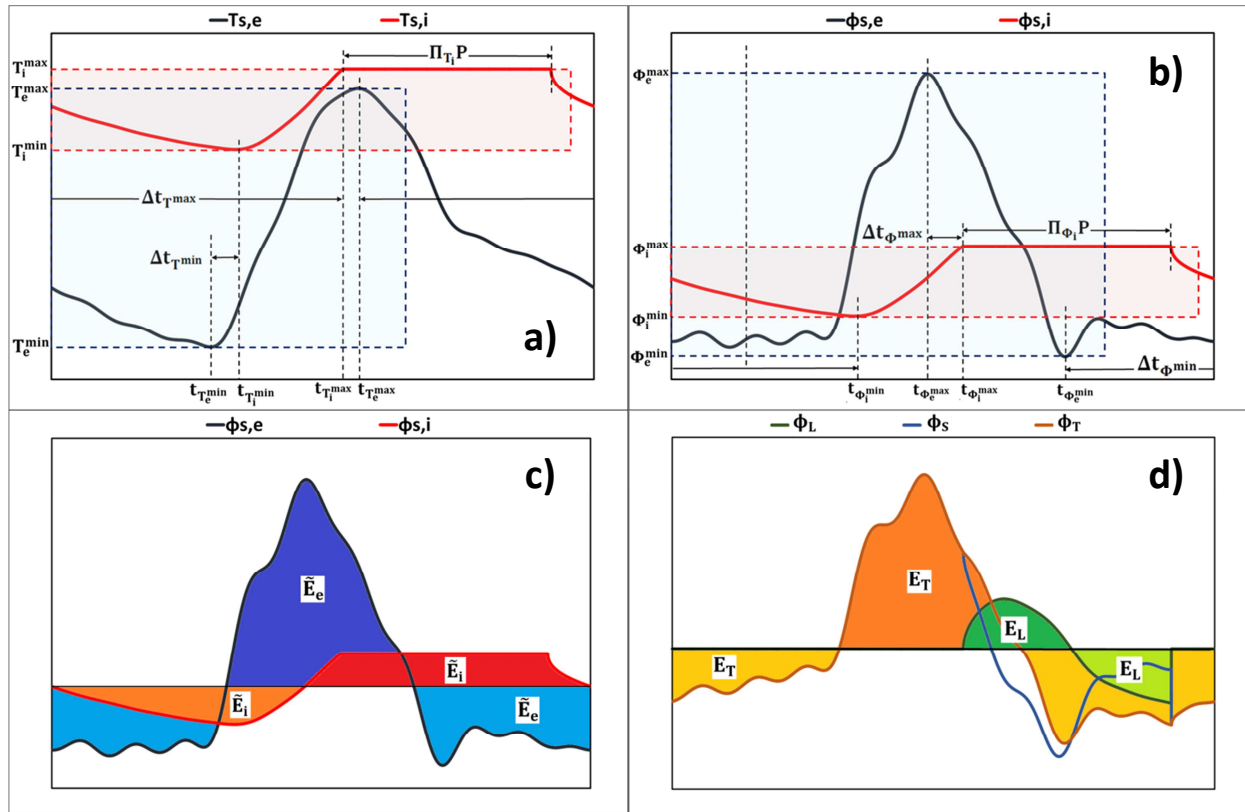


Figure 7 – Representation of the thermal quantities used for the definition of the dynamic parameters of the PCM layer. a) temperature trends on the external surface  $T_{s,e}$  and on the internal surface  $T_{s,i}$ ; b) heat flux trend on the external surface  $\Phi_{s,e}$  and on the internal surface  $\Phi_{s,i}$ ; c) fluctuating energy on the external surface  $\tilde{E}_e$  and on the internal surface  $\tilde{E}_i$ ; d) sensible  $E_S$ , latent  $E_L$  and total  $E_T$  energy stored.

If the parameter  $\Pi$  is different to zero, for the evaluation of the time lag (Eqs. 18-21), the time  $t$  to be considered is that at the beginning of the fraction of the period in which the maximum or minimum peak of the thermal quantity is constant, see Figures 7a and 7b.

The defined dynamic parameters allow us to quantify the attenuation and the time lag which temperature and heat flux fluctuations undergo when passing through the layer and the extent of the latent thermal storage in the layer. These parameters are to be used for the thermal sizing of the layer, which is related to the choice of PCM and of its thickness, and also for identifying the thermal behavior of the layer when working.

In particular, concerning the temperature fluctuation, the decrement factor of the maximum excursion  $f_T$ , the time lag of the maximum peak  $\Delta t_{T,max}$  and the minimum peak  $\Delta t_{T,min}$ , and the constant peak time fractions on the internal surface  $\Pi_{T_i}$  are to be used in order to quantify the thermal discomfort as a consequence of the internal surface temperature variation, in the winter as well as in the summer.

If the heat flux is considered, analogous parameters  $f_\phi$ ,  $\Delta t_{\phi \max}$ ,  $\Delta t_{\phi \min}$  and  $\Pi_{\phi_i}$  provide the extent of the attenuation and of the time lag of the power peak, entering in the summer period and exiting during the winter period, in order to evaluate the maximum loads which operate indoors.

If, on the other hand, the fluctuating energy passing through the layer is considered, the decrement factor  $f_E$  allows us to estimate the fraction of energy transferred indoors in summer and winter air conditioning, in order to determine energy requirements.

Finally, the latent storage efficiency  $\varepsilon_L$  and the fraction of stored latent energy  $\Lambda_L$  allow us to assess the correct use of the layer as a system of latent thermal storage.

All the parameters defined are to be used both in the absence of and in the presence of phase change. In Table 1 some special cases of combinations of the parameters are reported and for each case an indication to thermally size the layer well. In the absence of phase change  $\Pi_{T_i}$ ,  $\Pi_{\phi_i}$ ,  $\varepsilon_L$  and  $\Lambda_L$  are nil and the dynamic parameters are reduced to those characteristics of a monophase layer. In the presence of phase change, parameters  $\Pi_{T_i}$ ,  $\Pi_{\phi_i}$ ,  $\varepsilon_L$  and  $\Lambda_L$  identify the behavior of the layer both in energetic terms and as damping of thermal fluctuations. In fact, from the analysis of Eqs. (13), (14), (22) and (23), with an increase of  $\Pi_{T_i}$  and  $\Pi_{\phi_i}$  the fraction of the period in which the thermal fluctuations on the internal surface are completely damped increases, while with a growth of  $\varepsilon_L$  and  $\Lambda_L$ , the portion of the layer interested by the phase change and the fraction of latent energy stored compared to sensible one, respectively, increase.

In the absence of phase change  $\Pi_{T_i}$ ,  $\Pi_{\phi_i}$ ,  $\varepsilon_L$  and  $\Lambda_L$  are nil and the dynamic parameters are reduced to those characteristics of a monophase layer. In the presence of phase change, parameters  $\Pi_{T_i}$ ,  $\Pi_{\phi_i}$ ,  $\varepsilon_L$  and  $\Lambda_L$  identify the behavior of the layer both in energetic terms and as damping of thermal fluctuations. In fact, from the analysis of Eqs. (12), (13), (21) and (22), with an increase of  $\Pi_{T_i}$  and  $\Pi_{\phi_i}$  the fraction of the period in which the thermal fluctuations on the internal surface are completely damped increases, while with a growth of  $\varepsilon_L$  and  $\Lambda_L$ , the portion of the layer interested by the phase change and the fraction of latent energy stored compared to sensible one, respectively, increase.

Table 1 - Description of the dynamic behavior of a PCM layer in some special cases and related latent storage parameter values,  $\varepsilon_L$  and  $\Lambda_L$  and of the constant peak time fractions  $\Pi_{T_i}$  and  $\Pi_{\Phi_i}$ .

Case 1	$\varepsilon_L = 0$	$\Lambda_L = 0$	$\Pi_{T_i} = 0$	$\Pi_{\Phi_i} = 0$
Since	The layer is not subject to phase change	The thermal storage is of only sensible energy	The temperature and heat flux are fluctuating on the internal surface	
Then	In order to have phase change, a PCM with a melting temperature higher is required if the layer is in a liquid phase and lower if it is in a solid phase.			
Case 2	$\varepsilon_L = 1$	$\Lambda_L = 1$	$\Pi_{T_i} = 1$	$\Pi_{\Phi_i} = 1$
Since	The whole layer is subject to phase change	The thermal storage is of only latent energy	The thermal fluctuations appear completely damped on the internal surface	
Then	The layer is thermally well sized.			
Case 3	$0 < \varepsilon_L < 1$	$0 < \Lambda_L < 1$	$\Pi_{T_i} = 1$	$\Pi_{\Phi_i} = 1$
Since	A portion of the layer is subject to phase change and it stores latent energy	The remaining part of the layer is in excess and it only stores sensible energy	The thermal fluctuations appear completely damped on the internal surface	
Then	A lower PCM thickness is required.			
Case 4	$\varepsilon_L = 1$	$\Lambda_L = 1$	$0 < \Pi_{T_i} < 1$	$0 < \Pi_{\Phi_i} < 1$
Since	The whole layer is subject to phase change	The thermal storage is of only latent energy	The thermal fluctuations appear not to be completely damped on the internal surface	
Then	A higher layer thickness is required.			
Case 5	$0 < \varepsilon_L < 1$	$\Lambda_L \approx 1$	$0 < \Pi_{T_i} < 1$	$0 < \Pi_{\Phi_i} < 1$
Since	A portion of the layer is subject to a phase change and it stores latent energy	The thermal storage is mainly of the latent energy	The thermal fluctuations appear not to be completely damped on the internal surface	
Then	The PCM shows a high latent heat of fusion and a reduced volumetric heat capacity $\rho c_p$ .			
Case 6	$\varepsilon_L = 1$	$0 < \Lambda_L < 1$	$0 < \Pi_{T_i} < 1$	$0 < \Pi_{\Phi_i} < 1$
Since	The whole layer is subject to phase change	The thermal storage is partly sensible and partly latent	The thermal fluctuations appear not to be completely damped on the internal surface	
Then	The PCM shows a reduced latent heat of fusion and a high volumetric heat capacity $\rho c_p$ .			

### 3. Case study description

The calculation procedure for the determination of the thermal fields and of the stored energy was used in order to evaluate, on a monthly basis, the energetic and dynamic

characteristics of five different PCM typologies (see Table 2), all of a thickness equal to 6 cm. Melting temperatures ranging from 15°C to 32°C were chosen in relation to the set point temperatures of air-conditioned environments in summer and winter periods.

Table 2 – Thermophysical properties of the different types of PCM.

Company	PCM	Melting temperature $T_M$ [°C]	Heat latent of fusion H [kJ/kg]	Density $\rho$ [kg/m <sup>3</sup> ]	Thermal conductivity k [W/(m K)]	Specific heat capacity $c_p$ [J/(kg K)]
EPS	S15	15	160	1510	0.43	1900
TEAP	LATEST20T	20	175	1490	1	2000
savENRG	HS22P	23	185	1690	0.815	3060
RUBITHERM	SP26E	26	190	1450	0.6	2000
CLIMATOR	C32	32	162	1420	0.6	3600

In the analysis, two locations with quite different climatic conditions, Turin (TO) and Cosenza (CS) were considered. In particular, the Mediterranean climate of Cosenza, identified as Csa in the Köppen climate classification [31], has moderate temperatures with changeable and rainy weather in winter, while summers are hot and dry. The continental climate of Turin, classified as Dfb, is characterized by hot and humid summers, and winters that are cold with little rainfall, typical of the interior of a continent. The solar irradiation on the horizontal plane G and external air temperature  $T_{ea}$  data employed, relative to the monthly average days of a whole year, are those from the national standard reference [58] and are shown in Table 3, respectively, in the first and in the second row for each location.

Table 3 - Monthly average daily values of a whole year of the external air temperature  $T_{ea}$  and of the solar irradiation on the horizontal plane G in Turin and Cosenza.

TURIN (Lat = 45° 7', Long = 7° 43', TO)												
Months	Jan	Feb	Mar	Apr	May	Jun	Jul	Aug	Sep	Oct	Nov	Dec
G [MJ/m <sup>2</sup> ]	5	7.8	12.2	17	19.6	21.5	23.5	18.5	13.5	9.3	5.5	4.7
$T_{ea}$ [°C]	0.4	3.2	8.2	12.5	16.7	21.1	23.3	22.6	18.8	12.6	6.8	2
COSENZA (Lat = 37° 30', Long = 15° 05', CS)												
Months	Jan	Feb	Mar	Apr	May	Jun	Jul	Aug	Sep	Oct	Nov	Dec
G [MJ/m <sup>2</sup> ]	7.7	11.8	17.3	21.8	25.7	29.6	28.9	26	20	12.9	9.4	7.7
$T_{ea}$ [°C]	8.1	8.8	11.3	14.4	18.1	23.1	26	25.8	22.7	17.8	13.4	9.4



Starting from these values, using TRNSYS 17 [59] software, the climatic data relative to the characteristic day of each month were generated. Such climatic data have a period of 24 hours and are represented through the monthly average hourly values of solar radiation on the vertical plane exposed to South, of the sky temperature and of external air temperature. Figure 8 shows the monthly average hourly trends of the characteristic day, for all months of the year and for the two locations considered.

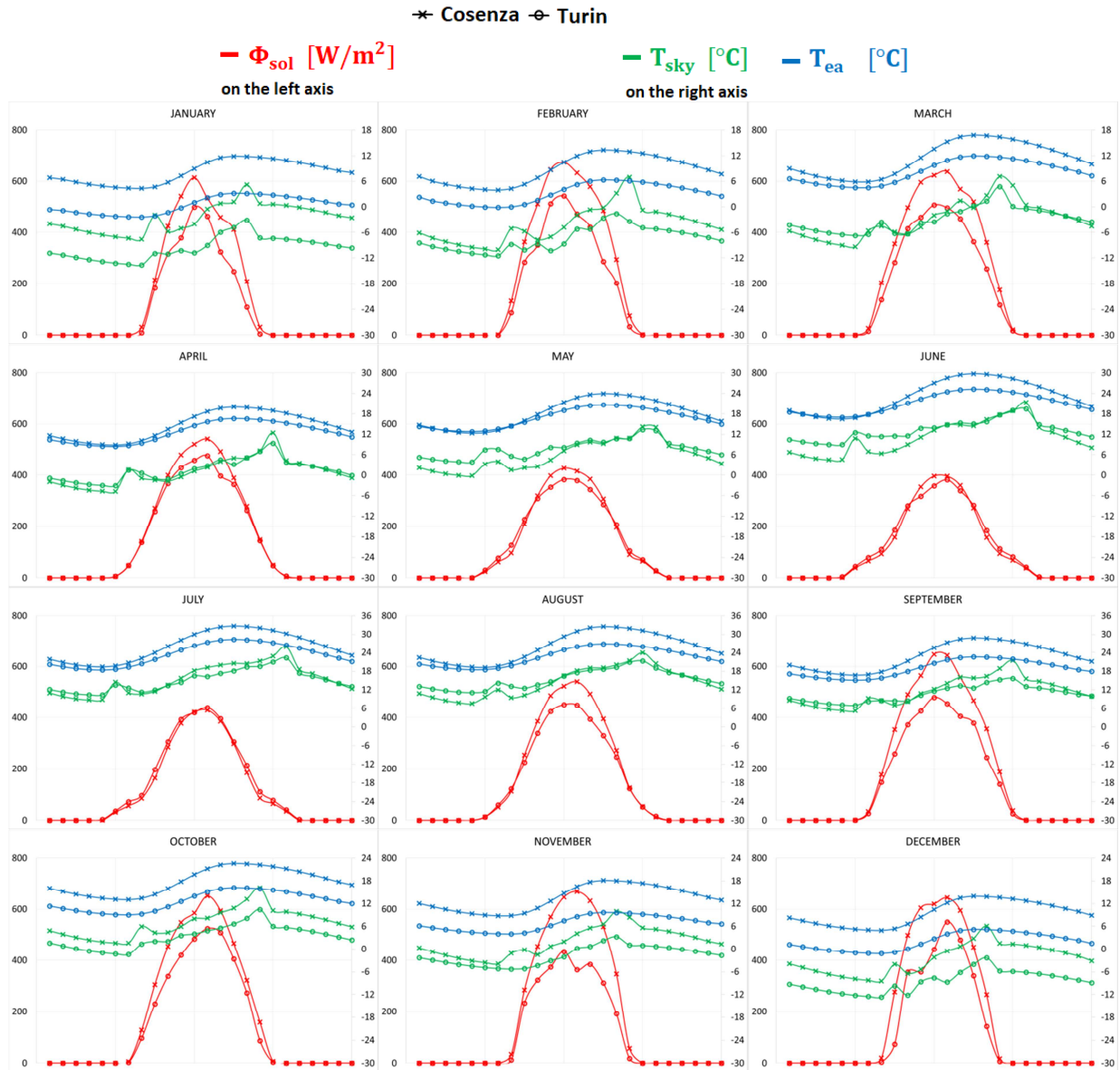


Figure 8 - Characteristic day of the different months in Cosenza and Turin. In each image: incident solar radiation on the vertical plane exposed to South  $\Phi_{sol}$  on the left axis, and sky temperature  $T_{sky}$  and external air temperature  $T_{ea}$  on the right axis.

In the indoor environment, the temperature values in continuous regime were chosen according to the reference standard [60] while the heating period, the cooling period and the intermediate period according to the national regulations [61], see Table 4.

Table 4 - Indoor environment set point temperature in the different months for Turin and Cosenza.

Indoor environment set point temperature [°C]												
Months	Jan	Feb	Mar	Apr	May	Jun	Jul	Aug	Sep	Oct	Nov	Dec
Turin	20	20	20	20	23	26	26	26	23	20	20	20
Cosenza	20	20	20	23	23	26	26	26	26	23	20	20

The numerical simulations considered: on the external surface a solar absorption coefficient equal to 0.60 and a convective and radiative heat transfer coefficient respectively equal to 20 W/m<sup>2</sup> K and 5.35 W/m<sup>2</sup> K; and on the internal surface a heat transfer coefficient equal to 7.7 W/m<sup>2</sup> K. The values of these coefficients were obtained by applying the technical reference standard EN ISO 6946 [62] while for the value of  $h_{r,e}$  reference is made to a previous experimental work by some of the authors [63] developed for a vertical wall with southern exposure and corresponding to the average value of an entire year of measurements.

The layer was discretized with 19 nodes and the equation system was solved by an integration time step  $\Delta t = 5$  s. The choice of the number of nodes was performed by preliminary simulations in order to verify the grid independence. From the results of the simulations performed, varying the number of nodes from 10 to 30 with a step of one, it is possible to deduce that this condition is realized by using nineteen nodes to discretize the PCM layer.

#### 4. Results and discussion

Regarding the different PCMs and for the two locations are shown: in Section 4.1 for each month, the number of bi-phase interfaces which are formed in the layer, the surface on which they originate and the disposition of the phases in the layer; in section 4.2, the monthly and seasonal values of the transferred energy and of the stored energy in latent and sensible form, obtained by applying the relations defined in section 2.3; in section 4.3, the monthly values of dynamic parameters evaluated through the relations defined in section 2.4, the results of the study on the influence of the latent stored efficiency on the dynamic parameters and some correlations obtained amongst dynamic parameters.

4.1. Configuration of the phases in the different typologies of PCM layers.

Figures 9 and 10 show the number of bi-phase interfaces, the surface on which they originate and the disposition of the phases in the layer starting from the outside and going towards the inside, for the considered PCMs and locations in the different months.

		JAN	FEB	MAR	APR	MAY	JUN	JUL	AUG	SEP	OCT	NOV	DEC
<b>S15</b>	N° interfaces	0	1b	3b	3a	2a	0	0	0	1a	2a	2b	1b
	Configuration of the phases in the layer	S	S L	S L S L	S L S L L	S L S L	L	L	L	L S	L S L	L S L	S L S L
<b>LATEST20T</b>	N° interfaces	0	0	0	2a	3b	2a	1b	2a	2a	2a	0	0
	Configuration of the phases in the layer	S	S	S	S L	S L S L	S L L	S L	S L L	S L L	S L L	S L	S
<b>HS22P</b>	N° interfaces	0	0	0	0	1a	2a	2a	2a	2a	0	0	0
	Configuration of the phases in the layer	S	S	S	S	L S	L S L	L S L	L S L	L S L	L S	S	S
<b>SP26E</b>	N° interfaces	0	0	0	0	0	2a	2a	2a	2a	0	0	0
	Configuration of the phases in the layer	S	S	S	S	S	S L	S L	L S	L S	L S	S	S
<b>C32</b>	N° interfaces	0	0	0	0	0	0	0	0	0	0	0	0
	Configuration of the phases in the layer	S	S	S	S	S	S	S	S	S	S	S	S

Figure 9 - Number of bi-phase interfaces present in the layer, surface on which they originate, and arrangement of the phases from the outside to the inside, in the various months of the year and for different PCMs. Turin. a) all the bi-phase interfaces are on the external surface; b) one bi-phase interface is on the internal surface.

		JAN	FEB	MAR	APR	MAY	JUN	JUL	AUG	SEP	OCT	NOV	DEC
<b>S15</b>	N° interfaces	3b	3b	3b	2a	2a	0	0	0	0	2a	2a	3b
	Configuration of the phases in the layer	S L S L	S L S L	S L S L	S L S L	S L S L	L	L	L	L S	L S L	L S L	S L S L
<b>LATEST20T</b>	N° interfaces	0	2a	2a	3b	3b	2a	1a	1a	2a	3b	2a	2a
	Configuration of the phases in the layer	S	S L	S L	S L S L	S L S L	S L	S L	S L	S L	S L L	L S	S L S L
<b>HS22P</b>	N° interfaces	0	0	0	2a	2a	2a	2a	2a	2a	2a	2a	0
	Configuration of the phases in the layer	S	S	S	S L	S L	L S	L S	L S	L S	L S	L S	L S
<b>SP26E</b>	N° interfaces	0	0	0	0	2a	2a	2a	2a	2a	2a	1a	0
	Configuration of the phases in the layer	S	S	S	S	S L	S L	L S	L S	L S	L S	L S	L S
<b>C32</b>	N° interfaces	0	0	0	0	0	0	2a	2a	2a	0	0	0
	Configuration of the phases in the layer	S	S	S	S	S	S	S L	S L	L S	S	S	S

Figure 10 - Number of bi-phase interfaces present in the layer, surface on which they originate, and arrangement of the phases from the outside to the inside in the various months of the year and for different PCMs. Cosenza. a) all the bi-phase interfaces are on the external surface; b) one bi-phase interface is on the internal surface.

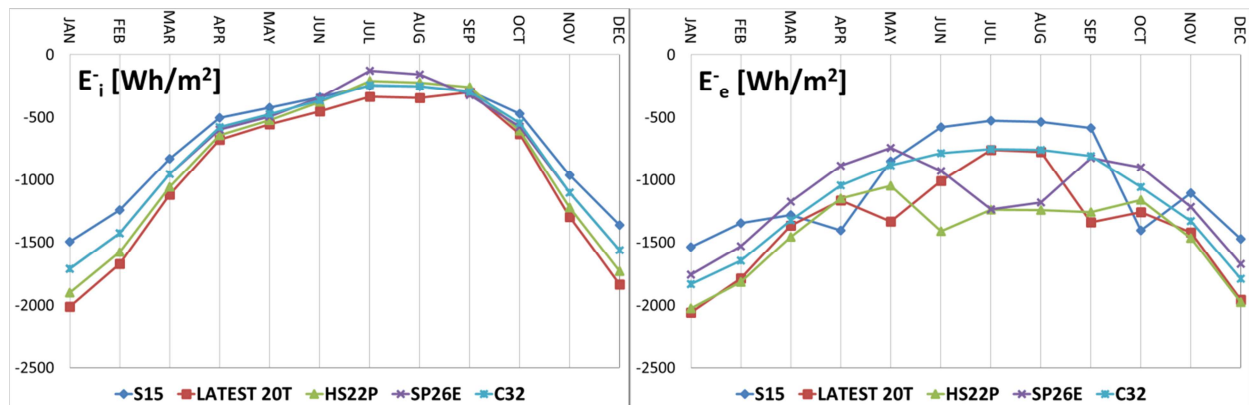
The presence of a bi-phase interface which originates on the external surface is indicated by 1a), and that which originates on the internal surface by 1b). The case of two bi-phase interfaces, both originating on the external surface, is shown by 2a), while the case with one interface on the external surface and another one on the internal surface by 2b); finally, in the case of three bi-phase interfaces, 3a) shows that all the interfaces originate on the external surface, while 3b) shows that two interfaces are formed on the external surface and the other one on the internal surface.

The phase changes occur: for PCM S15 from September to May, except in January, in Turin, and from October to May in Cosenza; for PCM LATEST20T from April to October in Turin, and from February to December in Cosenza; for PCM HS22P from May to September in Turin, and from April to November in Cosenza; for PCM SP26E from June to September in Turin, and from May to November in Cosenza; the PCM C32, due to the high melting temperature, in Turin does not undergo any phase change, while in Cosenza phase changes occur from July to September.

#### 4.2. Evaluation of the transferred and stored energy

The monthly average values of the total energy and fluctuating energy transferred through the two boundary surfaces of the layer, for each month and for each different type of PCM are shown in Figure 11 for Turin and in Figure 12 for Cosenza.

For each month and for each type of PCM, each figure shows: above, the energy leaving the environment through the internal surface  $E_i^-$  and leaving the layer towards the outdoor environment  $E_e^-$ ; in the middle, the energy entering the indoor environment through the internal surface  $E_i^+$  and entering the layer from the external surface  $E_e^+$ ; below, the fluctuating energy through the internal  $\tilde{E}_i$  and external  $\tilde{E}_e$  surface.



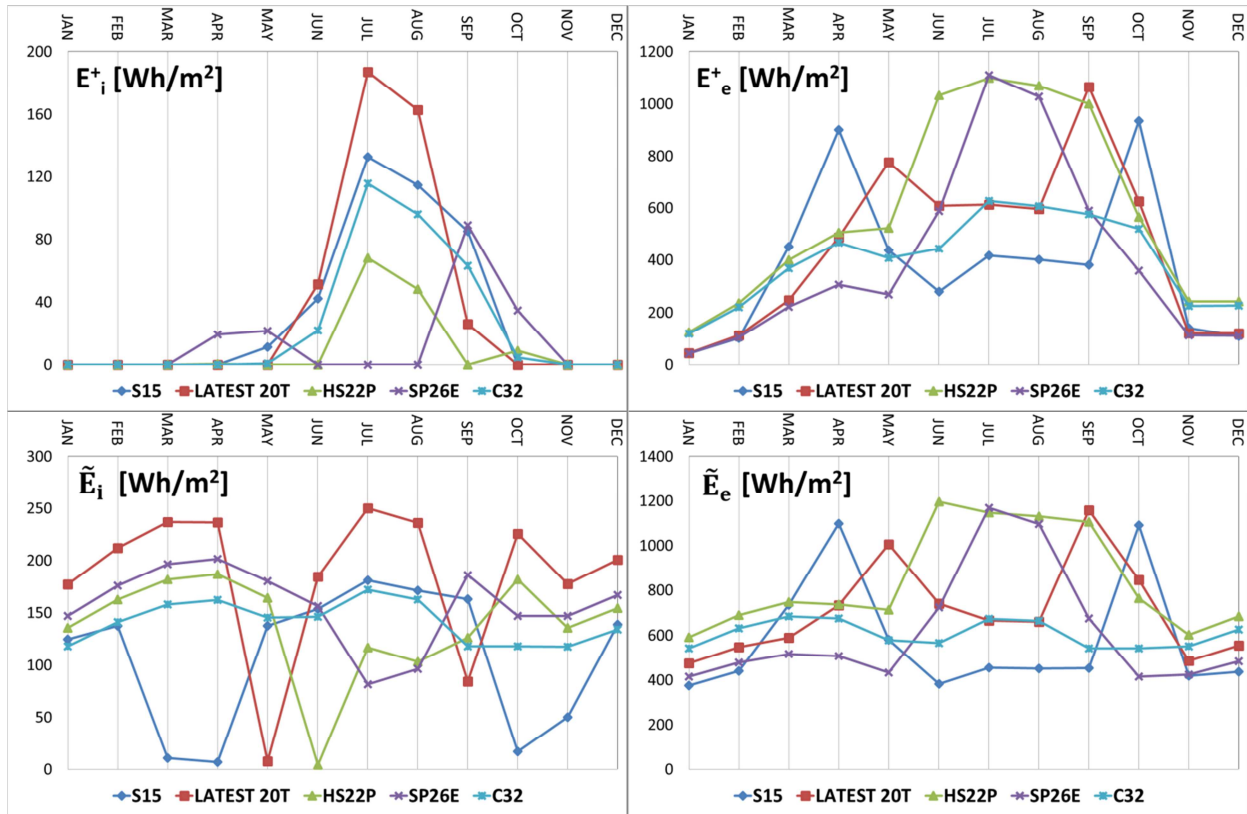
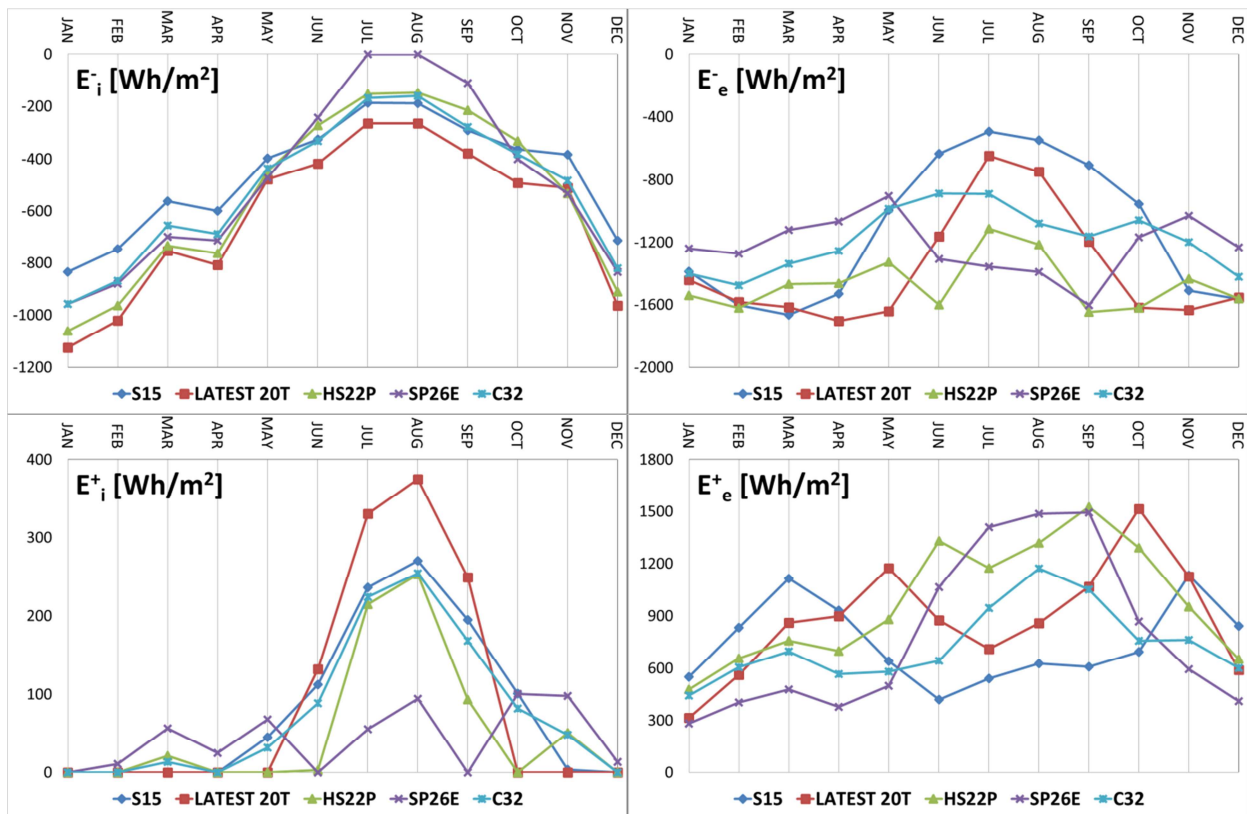


Figure 11 - monthly average daily values of the total energy and of the fluctuating component transferred through the external surface  $E_e^+$ ,  $E_e^-$  and  $\tilde{E}_e$ , and through the internal surface  $E_i^+$ ,  $E_i^-$  and  $\tilde{E}_i$  for the different PCM, Turin.

The monthly trends of such energetic quantities vary according to the PCM and can be synthesized as below for Turin:

- $E_i^-$  shows a regular trend with a minimum value in the summer months and it increases in a monotonous way, proceeding towards the winter months with maximum values in January and December; the PCM LATEST20T provides the highest values in all months, while the lowest values are obtained in July and August with the PCM SP26E and in the other months with the PCMS15;
- $E_e^-$  shows high values during the winter months and lower values in the summer and intermediate months, with a regular trend in absence of phase change, as in the case of PCM C32. The presence of bi-phase interfaces gives rise to a sharp increase of the energy lost through the external surface. In particular, such an increase moves with increasing melting temperature from intermediate months to the summer months. PCM HS22P provides the highest values from November to March and from June to August, S15 in April and in October, and LATEST20T during the other months. The lowest values occur with PCM S15 between November and February and between June and September, and in the other months with SP26E;

- $E_i^+$  shows, usually, the highest values during summer months, with a peak in June, and nil values between November and March. PCM LATEST20T records during June, July and August show the highest values. The behavior of PCM SP26 is quite different, recording nil values during summer months and the highest values during the intermediate months;
- $E_e^+$  shows low values during winter months and higher values during intermediate and summer months. The irregular trend is due to the phase changes, which cause a sharp increase of the energy entering the layer. The monthly behavior of different PCMs is totally analogous to that illustrated regarding the energy exiting from the layer toward the outdoor environment  $E_e^-$ , with higher values and lower values obtained by the same PCMs during the different months;
- $\tilde{E}_i$  and  $\tilde{E}_e$  show a little variable monthly trend in absence of bi-phase interfaces, as highlighted by PCM C32. The phase change determines a modification of the previous trend with significant monthly variations of the heat flux fluctuating components on the internal and external face. Particularly, the stored and then released latent energy causes a sharp reduction of the fluctuating energy through the internal surface, and a marked increase of the fluctuating energy through the external surface.



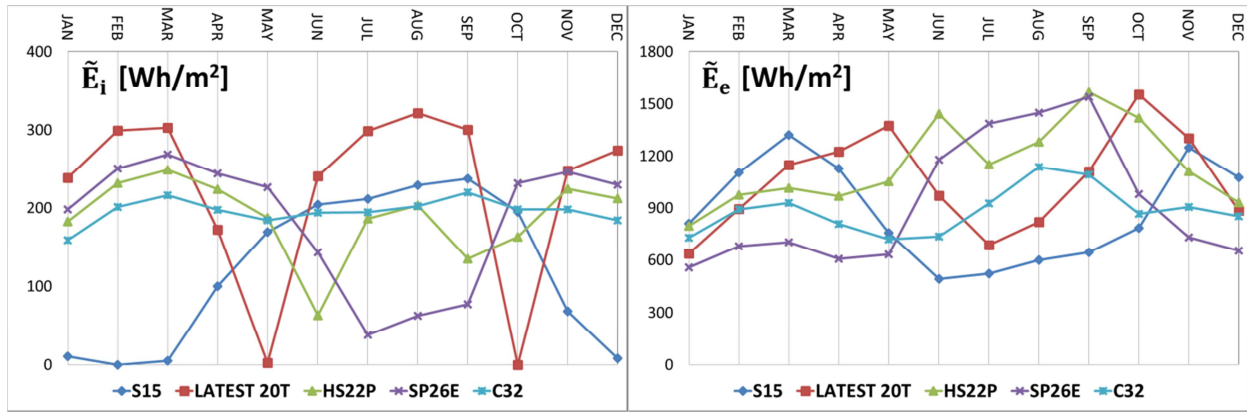


Figure 12 – Monthly average daily values of the total energy and of the fluctuating component transferred through the external surface  $E_e^+$ ,  $E_e^-$  and  $\tilde{E}_e$  and through the internal surface  $E_i^+$ ,  $E_i^-$  and  $\tilde{E}_i$  for the different PCMs, Cosenza.

In Cosenza, unlike Turin:

- $E_i^-$  for the different PCMs shows the same trend with lower values in the different months. Even in this case, the highest values are obtained with PCM LATEST20T. The lowest values are recorded from June to September with PCM SP26E, from November to May with the PCM S15, and in October with PCM HS22P;
- $E_e^-$  shows the same trend with lower values and, during the months in which phase change occurs, the increase switches with the rise in melting temperature from winter to summer months. PCM S15 shows the highest values in March, LATEST20T in April, May and November, SP26E in July and August, and HS22P in all the other months. The lowest values occur with PCM S15 between June and October and with SP26E from November to May.
- $E_i^+$  shows a similar trend with higher values and with a maximum in August. PCM LATEST20T records higher values from June to September, and in all other months nil values. The behavior of PCM SP26E is quite different, showing lower values in the summer months and higher values during intermediate months.
- $E_e^+$  shows higher values and the increases switch, due to the phase changes, according to the rise of the melting temperature from winter to summer months. Even in Cosenza the highest and the lowest values during the different months are obtained with the same PCMs highlighted in the comment about exiting energy.
- $\tilde{E}_i$  and  $\tilde{E}_e$  show analogous behavior as that experienced for Turin.

On the whole, it can be observed that in Cosenza, with its Mediterranean climate, the exiting energy from the air conditioned environment through the internal  $E_i^-$  and external  $E_e^-$  surfaces is lower than that recorded in Turin, while the energies  $E_i^+$  and  $E_e^+$  show higher values in Cosenza. In order to evaluate the energy transferred through the layer, it is necessary to take into account both the energy exiting the environment, which represents a loss in the winter period and a heat gain in the summer period, and the energy entering the environment, which makes a heat gain in the winter period and a thermal load in the summer period.

The results obtained with the different PCMs for Turin and Cosenza are shown in Figure 13, which illustrates at the ordinate the energies in the winter period  $E_{i,win}^+$  and  $E_{i,win}^-$  and during the summer  $E_{i,sum}^+$  and  $E_{i,sum}^-$ , calculated adding the correspondent monthly values, determined starting from the daily average values.

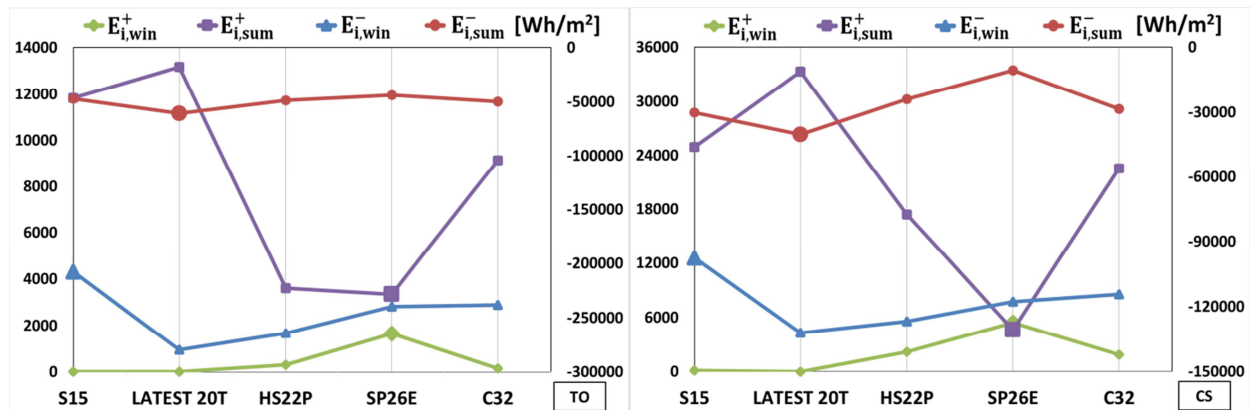
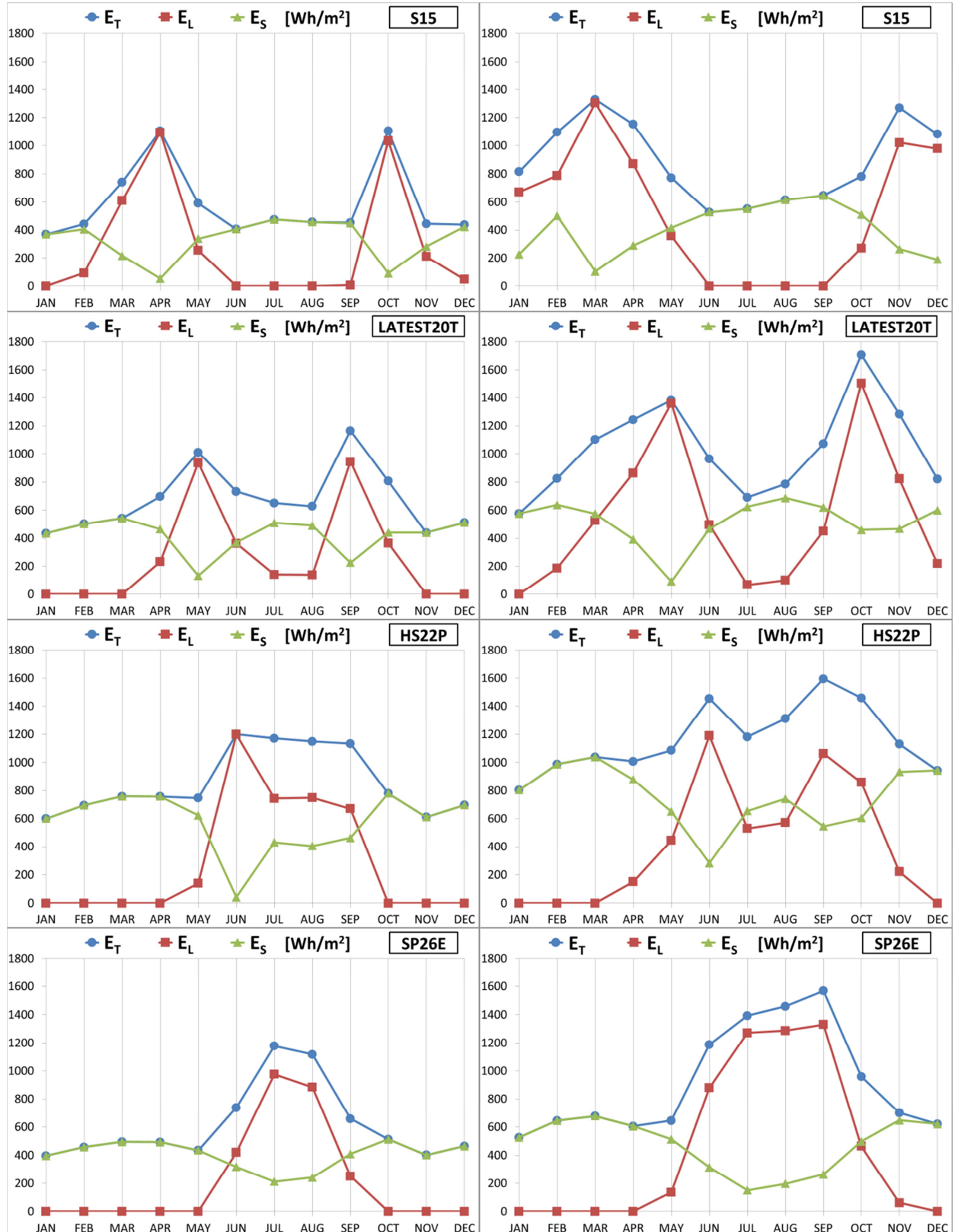


Figure 13 - Seasonal energies entering  $E_{i,win}^+$  and  $E_{i,sum}^+$  the air conditioned environment and energies exiting  $E_{i,win}^-$  and  $E_{i,sum}^-$  from the air conditioned environment, for the different PCMs taken into consideration for Turin and Cosenza.

About Turin: in the winter period, the bigger heat gain is ensured by PCM SP26E and the lowest by PCM LATEST20T and S15, the lowest heat loss by the PCM S15 and the highest by LATEST20T; in the summer period, the most reduced load value is obtained with SP26E and the highest with LATEST20T, the highest heat gain is provided by LATEST20T and the lowest by SP26E. For Cosenza the previous results are confirmed, with higher values of the entering energy  $E_i^+$  and lower values of the exiting energy  $E_i^-$  in both seasons. In the figures, for all considered cases, the largest gains and the lowest loads during the heating and the cooling air conditioning, are identified with a more visible pointer.



The stored energy referring to the monthly average day in each different month is shown in Figure 14, on the left for Turin, and on the right for Cosenza. For each PCM considered, the total energy stored, both the latent and the sensible contribution, is shown.



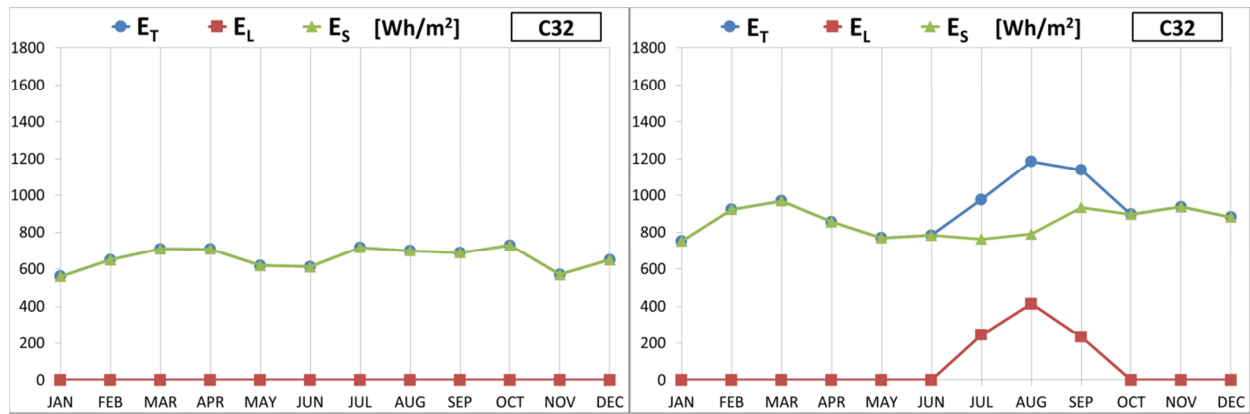


Figure 14 – Monthly average daily total  $E_T$ , latent  $E_L$  and sensible  $E_S$  energy stored in the different months for each type of PCM considered; Turin on the left and Cosenza on the right.

With the increase of the melting temperature, for both locations, the highest values of the stored latent energy switch from winter and intermediate months, as in the PCM S15 case, to summer months, as in the case of PCM SP26E. The behavior of PCM C32 is quite different, which does not supply a latent contribution in Turin during the different months, due to the absence of phase change, while in Cosenza phase changes occur in the summer time. The quantity of latent energy stored during the months in which phase change is recorded depends on the number of bi-phase interfaces, on the size of the portion of the layer involved in the phase change, on the density and on the latent heat of fusion. In Turin, the highest values occur in April and October for PCM S15, in May and September for PCM LATEST 20T, in June for PCM HS22P, and in July and August for PCM SP26E. In Cosenza, the highest values are recorded in March and November for PCM S15, in May and October for PCM LATEST 20T, in June and September for PCM HS22P, between July and September for PCM SP26E, and in August for PCM C32.

The sensible energy storage shows a reduction during the months in which the phase change occurs, while during the other months, it depends on the volumetric heat capacity  $\rho c_p$  of the PCM. In particular, the highest values are shown for PCMs HS22P and C32, and the lowest values for S15.

The total stored energy increases during the months in which the phase change occurs, despite the reduction of the sensible contribution; during the other months, it is determined by only sensible energy. In particular, in Turin the total energy stored is higher with PCM HSP22 from November to March and in June, with PCM S15 in April and October, with PCM LATEST20T in May, with PCMs LATEST20T and HS22P in September and with PCMs HS22P and SP26E in July and in August. In Cosenza, the total energy stored is higher with PCM S15

from November to March, with PCM LATEST20T in April, May and October, with HS22P in June and September and with SP26E in July and August.

The yearly sensible, latent and total stored energy, for the different types of PCM in the two locations, is shown in Figure 15. The highest thermal heat storage for both places is obtained by HS22P. In Turin, the sensible contribution is prevailing on the latent contribution, while in Cosenza this prevalence happens only for PCMs HS22P and C32.

The comparison of the two locations highlights that, independently of the type of PCM, the sensible, latent and total energy stored in the layer are higher in Cosenza compared to Turin.

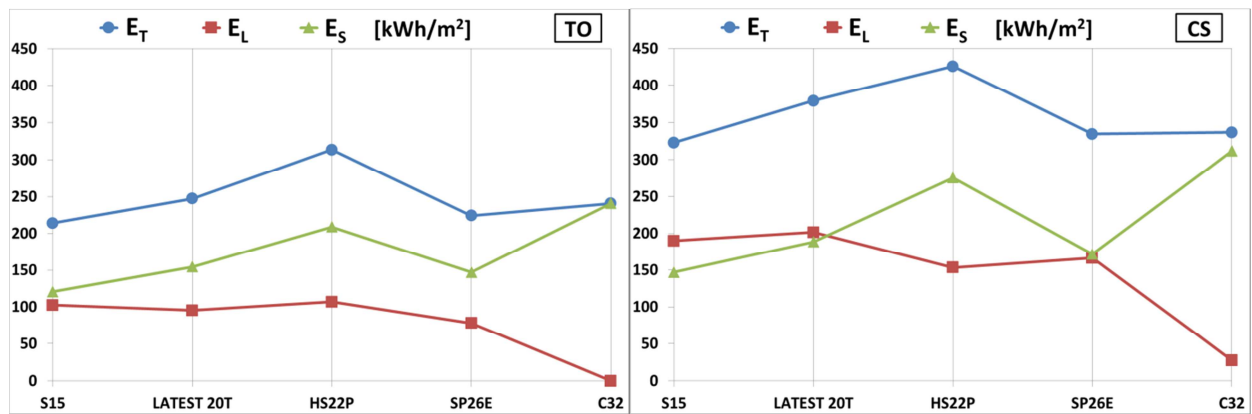


Figure 15 – Yearly sensible  $E_S$ , latent  $E_L$  and total  $E_T$  stored energy for the different PCMs. Values for Turin are on the left; for Cosenza are on the right.

### 4.3. Evaluation of dynamic parameters

#### 4.3.1. Monthly values

Figure 16 shows the values of the fraction of stored latent energy in layer  $\Lambda_L$ , calculated by Eq. 14 and also shows in which months, the latent storage is prevalent on the sensible one.

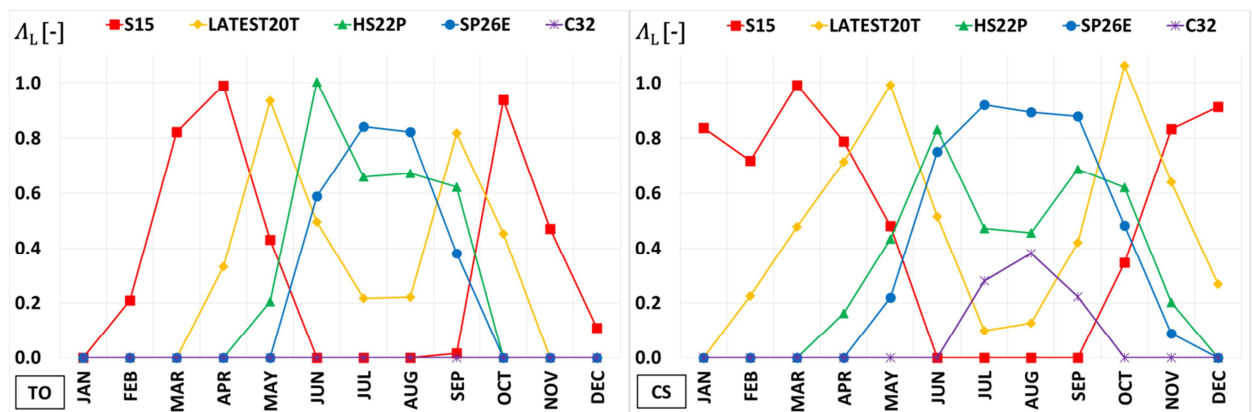


Figure 16 - Stored latent energy fraction in the layer  $A_L$  during the different months for Turin, on the left, and for Cosenza, on the right.

Figure 17 shows values for latent storage efficiency  $\epsilon_L$  calculated by the Eq. 13, and it also shows in which months the part of the layer interested by the phase change is more extended.

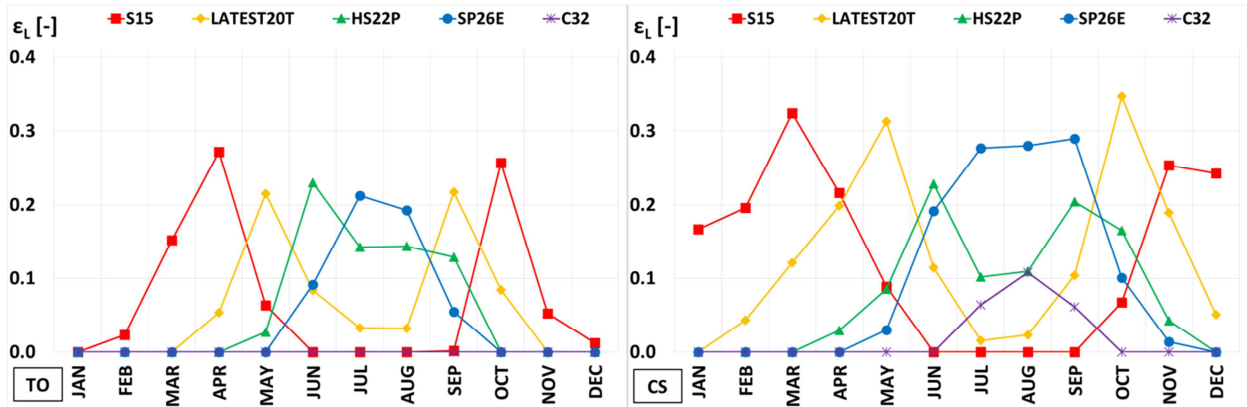


Figure 17 - Latent storage efficiency  $\epsilon_L$  during the different months in Turin, on the left, and in Cosenza, on the right.

In Figures 18-24 values of dynamic parameters are shown in the different months, calculated by Eqs. 15-21.

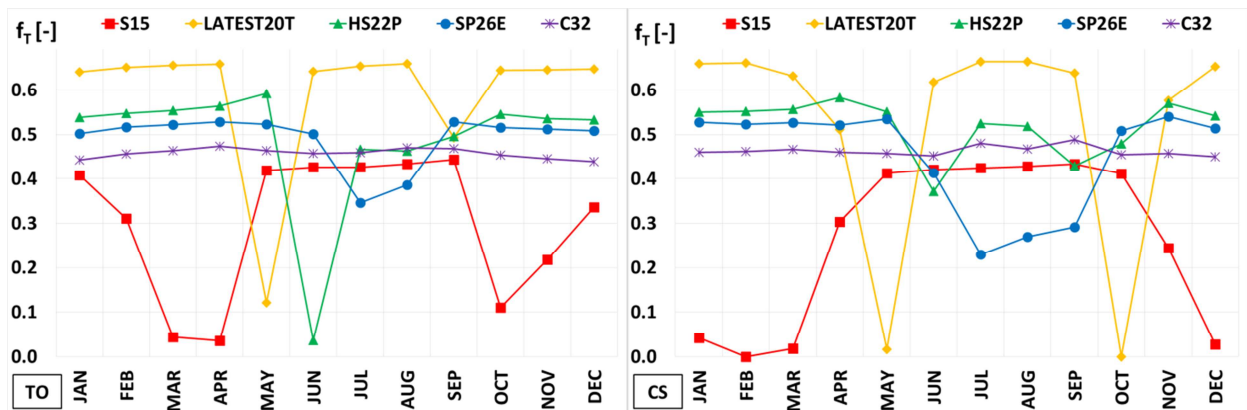


Figure 18 - Decrement factor of the maximum excursion of the temperature  $f_T$  in the different months for Turin, on the left, and for Cosenza, on the right.

Regarding the decrement factor of the maximum excursion of the temperature  $f_T$  (Figure 18):

- for S15, in the absence of phase change, it has values approximately equal to 0.42 in both locations, while in the presence of phase change it significantly decreases to a value of 0.035 in April for Turin, and it is annulled in February for Cosenza;

- for LATEST20T, in absence of phase change, it has values approximately equal to 0.66 in both locations, while in presence of phase change it decreases to a value of 0.12 in May for Turin, and it is almost nil in October and in May for Cosenza;
- for HS22P, in absence of phase change, it has values approximately equal to 0.55 in both locations, while in presence of phase changes it decreases, reaching in June a value of 0.04 for Turin, and of 0.37 for Cosenza;
- for SP26E, in absence of phase change, it has values approximately equal to 0.52 in both locations, while in presence of phase change it decreases reaching in July a value of 0.35 for Turin and of 0.23 for Cosenza;
- for C32, in both locations, over the different months, it is constant and equals 0.46.

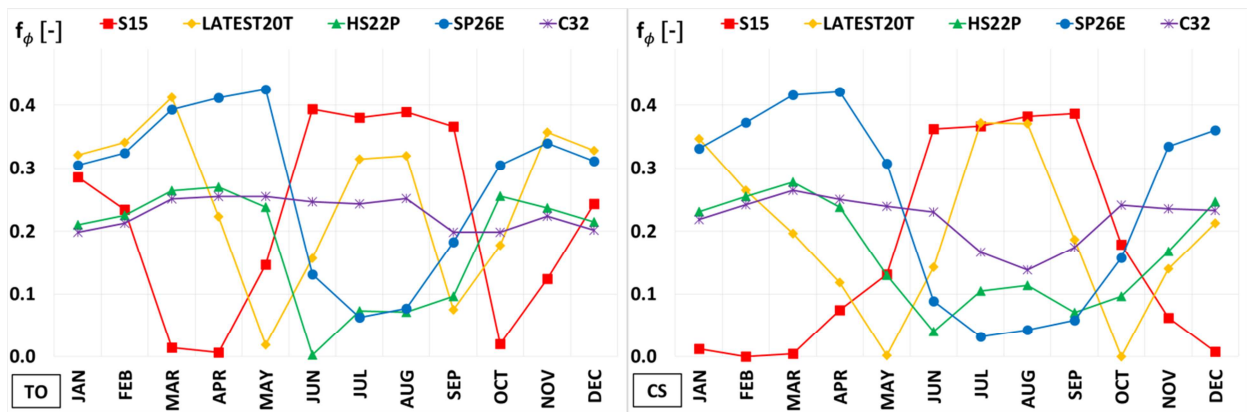


Figure 19 - Decrement factor of the maximum excursion of the heat flux  $f_\phi$  in the different months for Turin, on the left, and for Cosenza, on the right.

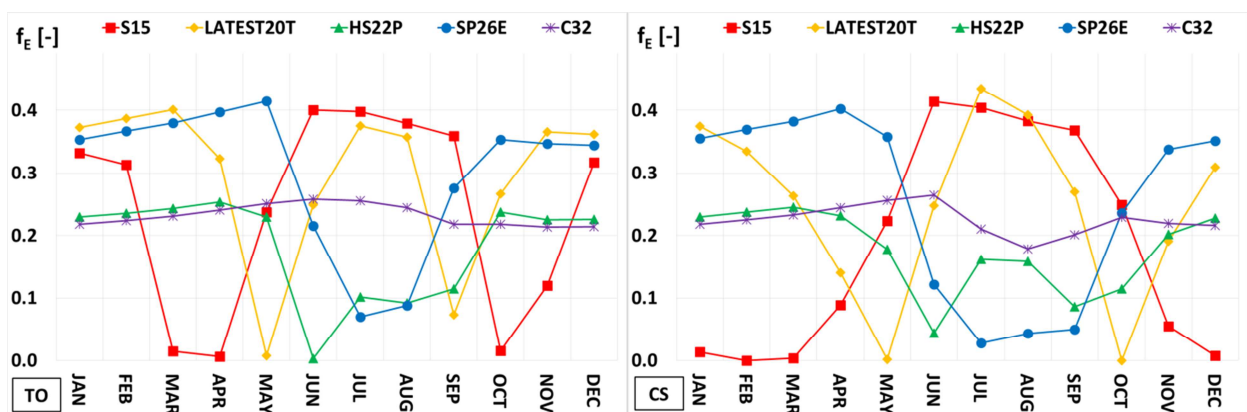


Figure 20 – Energy decrement factor  $f_E$  in the different months for Turin, on the left, and for Cosenza, on the right.

The decrement factor of the maximum excursion of the heat flux  $f_\phi$  (Figure 19) and the energy decrement factor  $f_E$  (Figure 20) show trends and analogous values for the same type of PCM:

- for S15, in the absence of phase change,  $f_{\Phi}$  and  $f_E$  values are approximately equal to 0.38 in both locations; in the presence of phase change, values decrease reaching a value of 0.006 in April for Turin, and are almost nil from December to March for Cosenza;
- for LATEST20T, in the absence of phase change,  $f_{\Phi}$  and  $f_E$  values are approximately equal to 0.35 in both locations; in the presence of phase change, values decrease reaching, respectively, a value of 0.02 and almost nil in May for Turin, and they are annulled in May and in October for Cosenza;
- for HS22P, in the absence of phase change,  $f_{\Phi}$  and  $f_E$  values are approximately equal to 0.25 in both locations; in the presence of phase change, values decrease reaching in June a value almost nil for Turin, and a value of 0.04 for Cosenza;
- for SP26E, in the absence of phase change,  $f_{\Phi}$  and  $f_E$  values vary between 0.30 and 0.40 in both locations; in the presence of phase change values decrease, reaching in July a value of approximately 0.066 for Turin, and of approximately 0.03 for Cosenza;
- for C32, in the absence of phase change,  $f_{\Phi}$  and  $f_E$  values vary between 0.20 and 0.26 in both locations, while for Cosenza in presence of phase change, values decrease and in August become almost the same, respectively 0.14 and 0.18.

In the fraction of the period in which the maximum or minimum peak of the temperature on the internal surface is constant, also the related heat flux peak is constant, due to the fact that the indoor environment temperature is fixed and equal to the set-point value. For this reason, in continuous air-conditioned  $\Pi_{T_i} = \Pi_{\Phi_i}$ .

With reference to all considered cases, only for PCMs S15 and LATEST20T, and for both locations, it can be observed that, in some months the maximum and minimum peaks of the temperature and heat flux, stay constant for a fraction of the period. For these PCMs the values of the parameter  $\Pi_{T_i} = \Pi_{\Phi_i}$  are shown in Table 5.

Table 5 - Constant peak time fraction  $\Pi_{T_i} = \Pi_{\Phi_i}$  during the different months for Turin and Cosenza.

$\Pi_{T_i} = \Pi_{\Phi_i}$	JAN	FEB	MAR	APR	MAY	JUN	JUL	AUG	SEP	OCT	NOV	DEC
S15-TO	0	0.384	0.361	0	0	0	0	0	0	0	0.382	0.235
S15-CS	0.323	1	0	0	0	0	0	0	0	0	0	0.149
LATEST20T-TO	0	0	0	0	0.580	0	0	0	0	0	0	0
LATEST20T-CS	0	0	0	0.351	0.137	0	0	0	0	1	0	0

The constant peak time fraction is different to zero during the months when a bi-phase interface originates on the internal surface, or when a bi-phase interface fluctuates within the layer, close to the internal surface. This can be seen from the comparison between Table 5 and Figures 9 and

10. In those figures, this case is indicated by the letter b, independently of the number of bi-phase interfaces in the layer.

The time lags (Figures 21-24), in absence of phase change, are approximately constant, with the exception of that of the minimum peak of the heat flux, which shows a seasonal variability; in the presence of one or more bi-phase interfaces the time lags are subject to abrupt variations. In particular, in the absence of phase change, for both locations considered and for all the different PCMs, with the change of the months, the  $\Delta t_{T\max}$  and  $\Delta t_{T\min}$  variation field is within 0 and 3 h, while that of  $\Delta t_{\Phi\max}$  is between 2.5 and 6 h. The time lag  $\Delta t_{\Phi\min}$  varies between 5 and 7 h in the summer period and between 13 and 16 h in the winter period.

In the presence of phase change, the extent of variations is dependent on PCM, on the locations and on the month:

- for S15,  $\Delta t_{T\max}$  is equal to about 23 hours in February for both locations;  $\Delta t_{T\min}$  is about 10 hours in April for Turin, and 24 hours in January for Cosenza;  $\Delta t_{\Phi\max}$  is about 13 hours in April for Turin, and 23 hours in February for Cosenza,  $\Delta t_{\Phi\min}$  becomes, in October, equal to 7.7 hours for Turin and 3.7 hours for Cosenza;
- for LATEST 20T,  $\Delta t_{T\max}$  is equal to 5.5 hours in April and October for Turin, and to 22.2 hours in October for Cosenza;  $\Delta t_{T\min}$  is 7.3 hours in September for Turin, and 6.4 hours in June for Cosenza;  $\Delta t_{\Phi\max}$  is 2.5 hours in May for Turin, and 22.5 hours in October for Cosenza,  $\Delta t_{\Phi\min}$  becomes equal to 12 hours in April for Turin and 5.8 hours in October for Cosenza;
- for HS22P,  $\Delta t_{T\max}$  is equal to about 10 hours in June and September for Turin, and in October for Cosenza;  $\Delta t_{T\min}$  is about 15 hours in June for Turin and, approximately 11 hours in July for Cosenza;  $\Delta t_{\Phi\max}$  is about 12 hours in June and September for Turin, and about 10 hours in May and October for Cosenza;  $\Delta t_{\Phi\min}$  is equal in June to about 16 hours for Turin, and about 11 hours for Cosenza.
- for SP26E,  $\Delta t_{T\max}$  is equal to about 14 hours in July for Turin, and in September for Cosenza;  $\Delta t_{T\min}$  stays approximately unvaried for Turin, and it is equal to about 11 hours in July for Cosenza;  $\Delta t_{\Phi\max}$  is about 15 hours in July for Turin, and 17 hours in September for Cosenza;  $\Delta t_{\Phi\min}$  is equal to about 8 hours in June for Turin, and about 12.5 hours during the months May, July and August for Cosenza.
- for C32, in Cosenza  $\Delta t_{T\max}$  becomes approximately 7 hours in July;  $\Delta t_{T\min}$  stays basically unvaried;  $\Delta t_{\Phi\max}$  is about 8 hours in August;  $\Delta t_{\Phi\min}$  is about 12.5 hours from July to September.

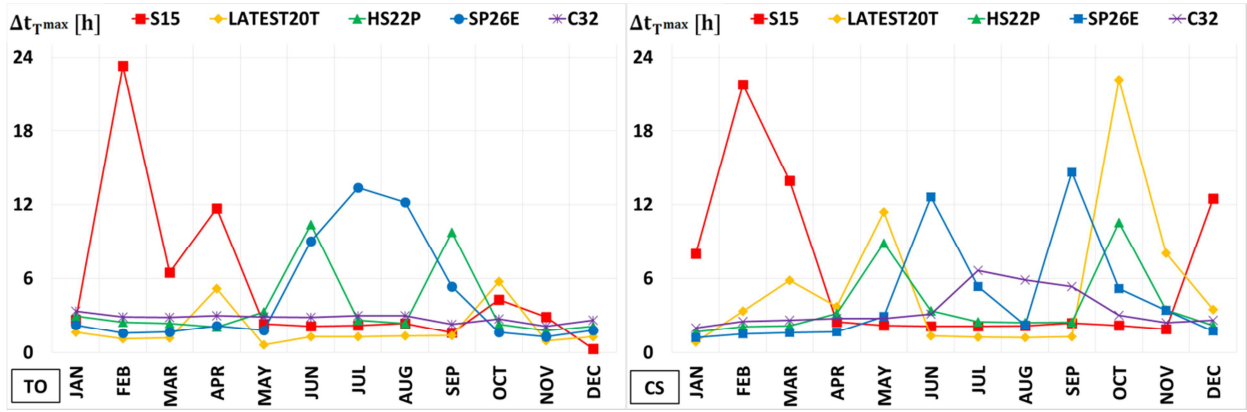


Figure 21 – Time lag of the maximum peak of the temperature  $\Delta t_{Tmax}$  in different months for Turin, on the left, and for Cosenza, on the right.

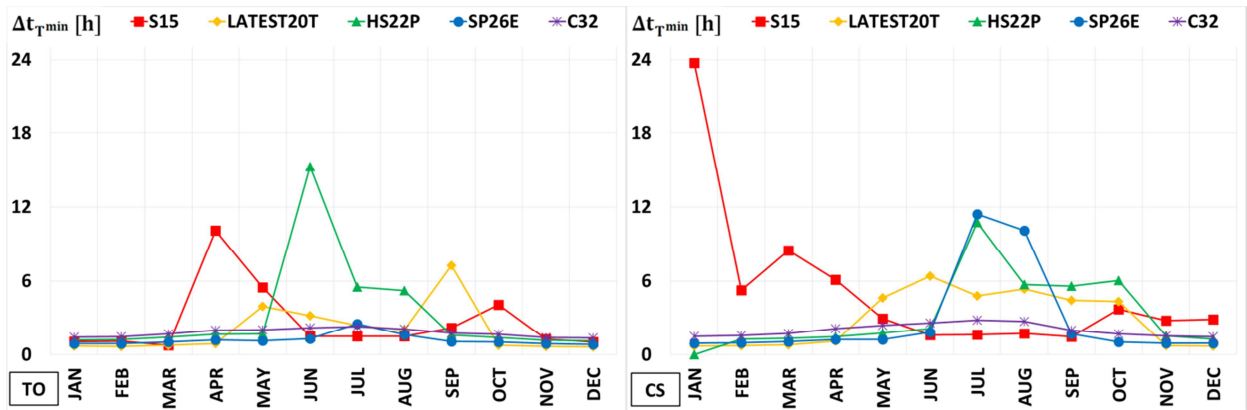


Figure 22 – Time lag of the minimum peak temperature of the  $\Delta t_{Tmin}$  in different months for Turin, on the left, and for Cosenza, on the right.

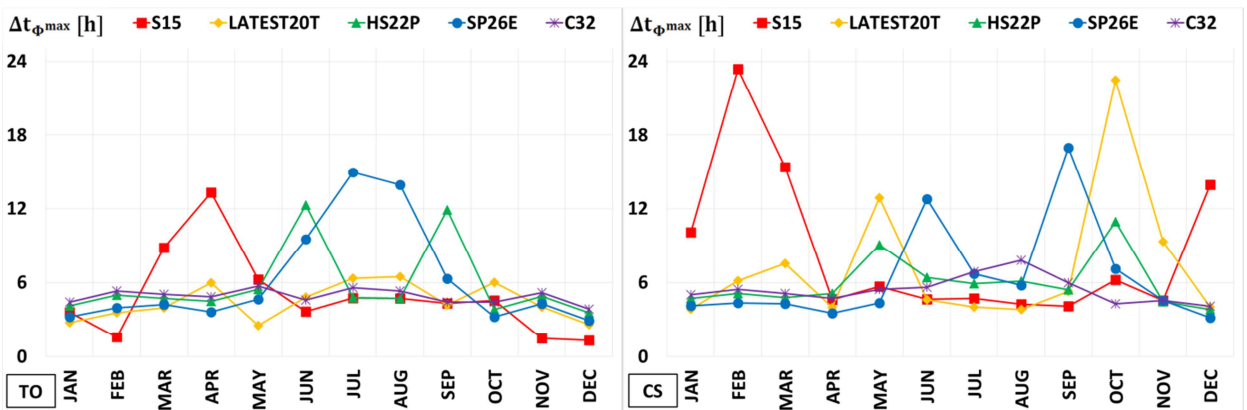


Figure 23 – Time lag of the maximum peak of the heat flux  $\Delta t_{\phi max}$  in different months for Turin, on the left, and for Cosenza, on the right.



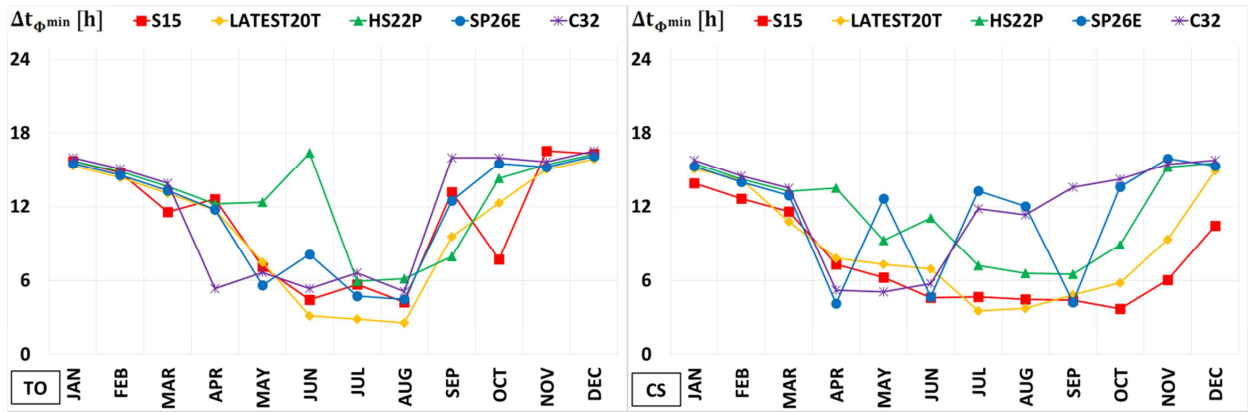


Figure 24 – Time lag of the minimum peak of the heat flux  $\Delta t_{\phi, \min}$  in different months for Turin, on the left, and for Cosenza, on the right.

#### 4.3.2. Influence of the latent storage efficiency on the dynamic characteristics

Data analysis has shown that the dynamic parameters related to the trends of the temperature and heat flux, of the fluctuating energy passing through the layer and of the stored energy in latent and sensible form are correlated to the latent storage efficiency.

Figure 25 shows the values of dynamic parameters related to the monthly average day of the latent energy fraction  $\Lambda_L$ , and the decrement factors  $f_T$ ,  $f_\phi$  and  $f_E$  depending on the latent storage efficiency  $\varepsilon_L$  for the different PCMs. In each image the values related to both locations are reported.

Generally, irrespective of location, of PCM typology and of the air conditioning season, to the increase of latent storage efficiency  $\varepsilon_L$ , the decrement factors of the maximum excursion of the temperature  $f_T$  and of the heat flux  $f_\phi$  as well as the decrement factor of the energy  $f_E$  decrease, while the stored latent energy fraction  $\Lambda_L$  rises significantly. All these trends can be represented by second grade polynomial functions, with concavity facing downwards for parameters  $\Lambda_L$  and  $f_T$  and facing upwards for parameters  $f_\phi$  and  $f_E$ .

Concerning the trend of the decrement factor of the temperature  $f_T$ , it is necessary to specify that, during the months when the constant peak time fraction is different to zero, it is subject to a change of concavity with a reduction of the values. This behavior concerns only PCMs S15 and LATEST20T, as shown in the results from Table 5, which show, in some months, a fraction of the period in which the maximum or minimum peak of the temperature and heat flux, endure in time, due to the presence of a bi-phase interface in proximity of the internal surface. This different behavior is recorded by the correspondent images with two interpolating curves with opposite concavities (conf. *a* and conf. *b*).

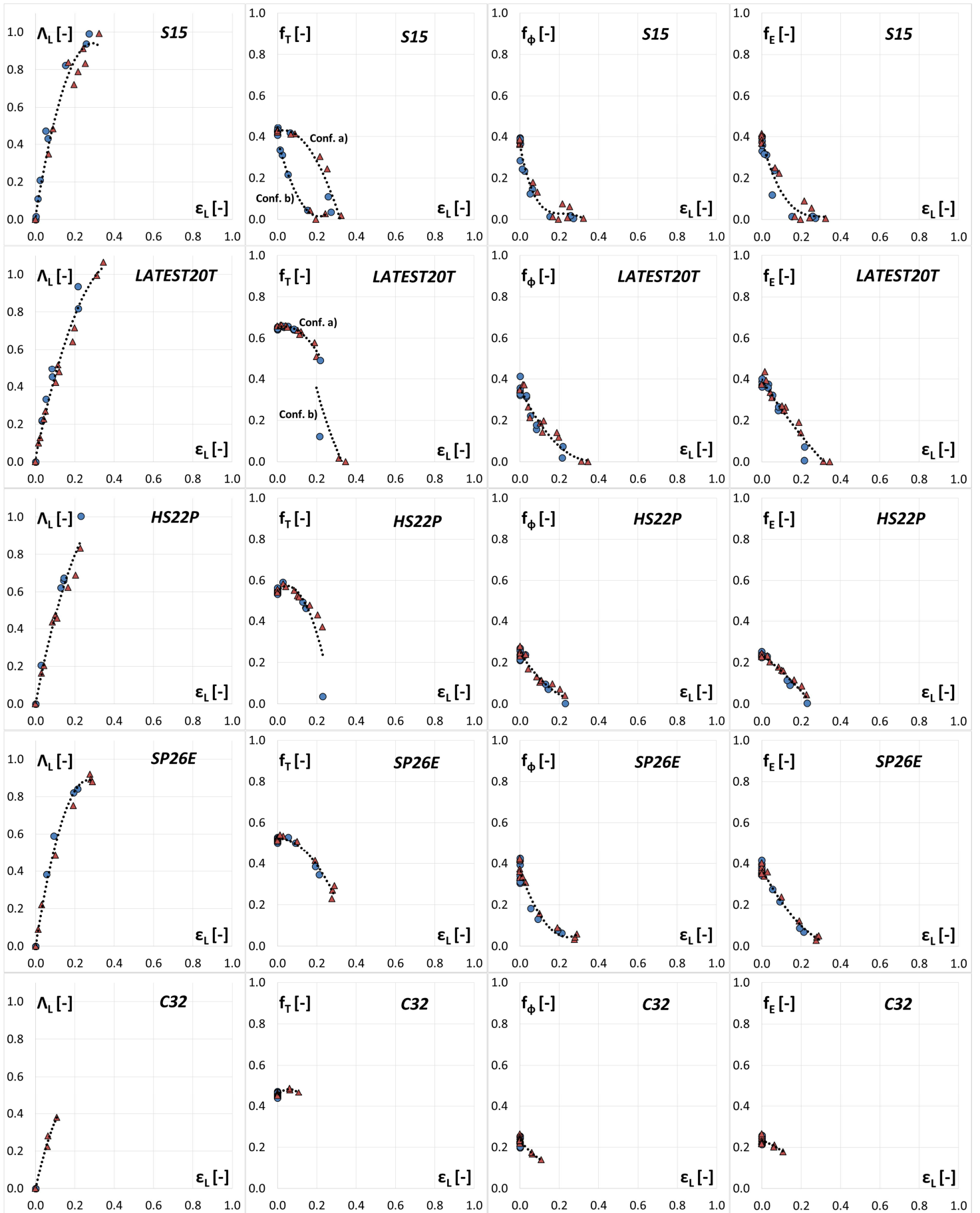


Figure 25 – Latent energy fraction  $\Lambda_L$  and decrement factors of temperature  $f_T$ , heat flux  $f_\phi$  and energy  $f_E$  as a function of the latent storage efficiency  $\varepsilon_L$  for different PCMs.

▲ Turin      ● Cosenza

Regarding the other dynamic parameters, the influence of the constant peak time fraction is very contained and the trends can be considered independent of the configuration of the phases within the layer. Furthermore, graphs show that the functional dependency of the dynamic parameters from  $\varepsilon_L$  is the same for all the typologies of PCMs.

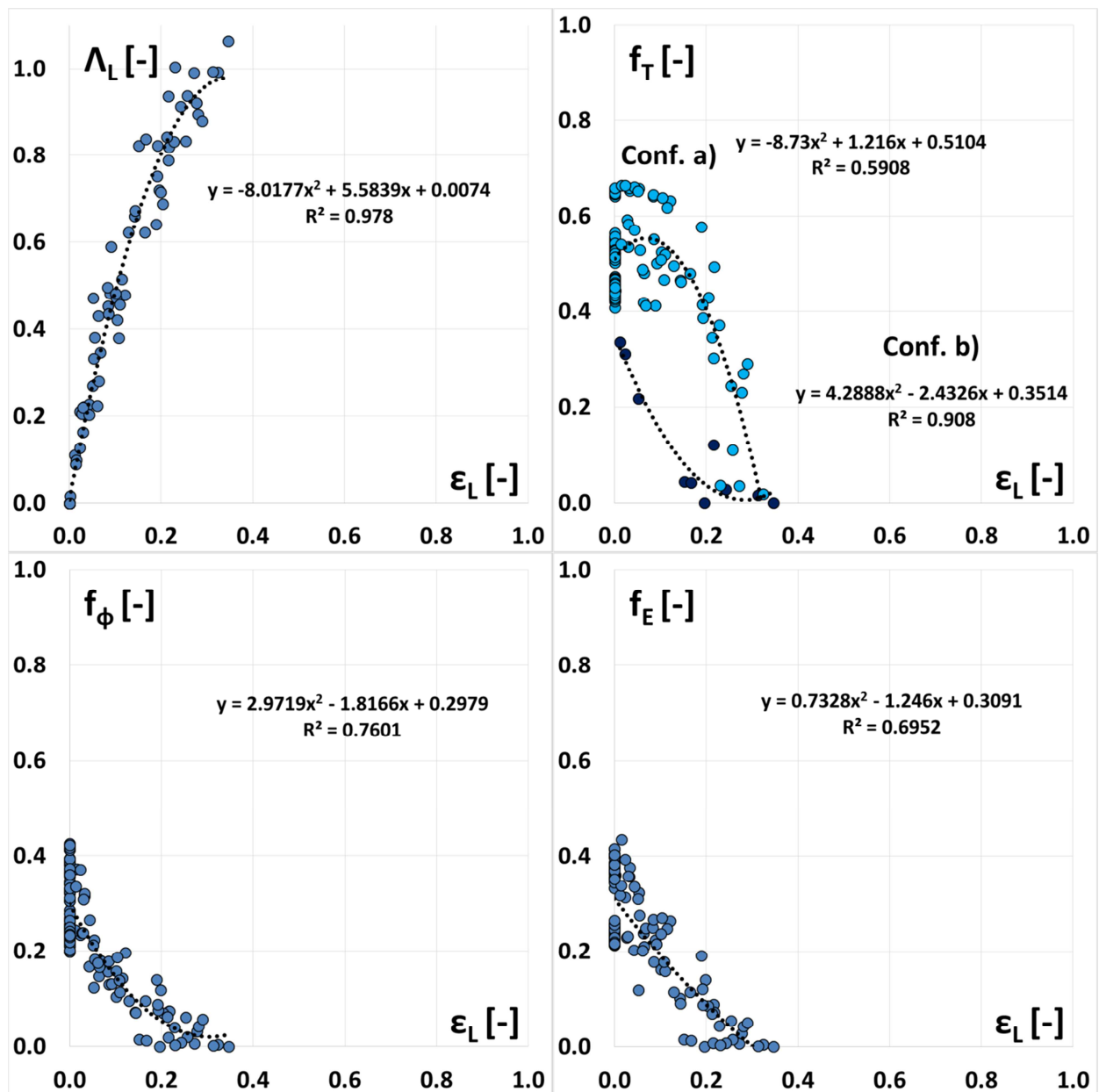


Figure 26 – Latent energy fraction stored  $\Lambda_L$  and decrement factor of temperature  $f_T$ , of heat flux  $f_\phi$  and of the energy  $f_E$  as a function of the latent storage efficiency  $\varepsilon_L$ .

An additional summary has been made by putting the values of previous dynamic parameters in function of  $\varepsilon_L$ , for both locations and for all types of PCM into a graph. This summary is shown in Figure 26.

In general, the image concerning the latent energy fraction  $\Lambda_L$  shows a strict correlation to the latent storage efficiency  $\varepsilon_L$  and it is an indicator that the total stored energy apportionment in latent and sensible energy depends mainly on the latent storage efficiency  $\varepsilon_L$ .

Concerning the decrement factors  $f_T$ ,  $f_\phi$  and  $f_E$ , the images highlight that for reduced  $\varepsilon_L$  values, to which corresponds a greater contribution of the sensible type to the thermal storage, the dispersion of the points around the interpolating curves is greater, due to the different volumetric heat capacity  $\rho c_p$  in the different PCMs. For higher values of  $\varepsilon_L$ , to which corresponds a contribution to the heat storage in latent form prevailing on the sensible one, the points show a lower dispersion.

Furthermore, images show that it is sufficient to obtain a latent storage efficiency  $\varepsilon_L = 0.35$ , to which corresponds a portion of the layer involved in the phase change equal to 35%, in order to attenuate completely the excursion of the temperature and heat flux on the internal surface, to annul the fluctuating energy transferred into the indoor environment and to obtain unitary values of the latent energy fraction.

Similarly to Figure 25, in Figure 27, for each of the different PCMs, the values of the time lag of maximum peak and of the minimum peak of the temperature  $\Delta t_{T_{\max}}$  and  $\Delta t_{T_{\min}}$  and of the heat flux  $\Delta t_{\phi_{\max}}$  and  $\Delta t_{\phi_{\min}}$  as a function of the latent storage efficiency  $\varepsilon_L$  are reported.

On the whole, independently of the location, PCM type, and air-conditioning season, with the rise of latent storage efficiency  $\varepsilon_L$ , time lags  $\Delta t_{T_{\max}}$ ,  $\Delta t_{T_{\min}}$  and  $\Delta t_{\phi_{\max}}$  increase. Such an increase is more contained for the time lag  $\Delta t_{T_{\min}}$ .

Concerning the time lag  $\Delta t_{\phi_{\min}}$ , functional dependency, on the growth of  $\varepsilon_L$ , is different in the two air-conditioning seasons, with a reduction in the winter period and an increase in the summer period. For such a reason, in the image relative to time lag  $\Delta t_{\phi_{\min}}$ , the pointers were differentiated based on the air-conditioning season. All these trends can be represented by a first grade polynomial function.

The time lags of the temperature maximum and minimum peak, analogously to the temperature decrement factor, are distant from the interpolating straight line, for the S15 and LATEST20T PCMs, during the months when the constant peak time fraction is different to zero.

For the other parameters, the influence of the constant peak time fraction is very contained and the trends can be considered independent of the configuration of the phases in the layer.

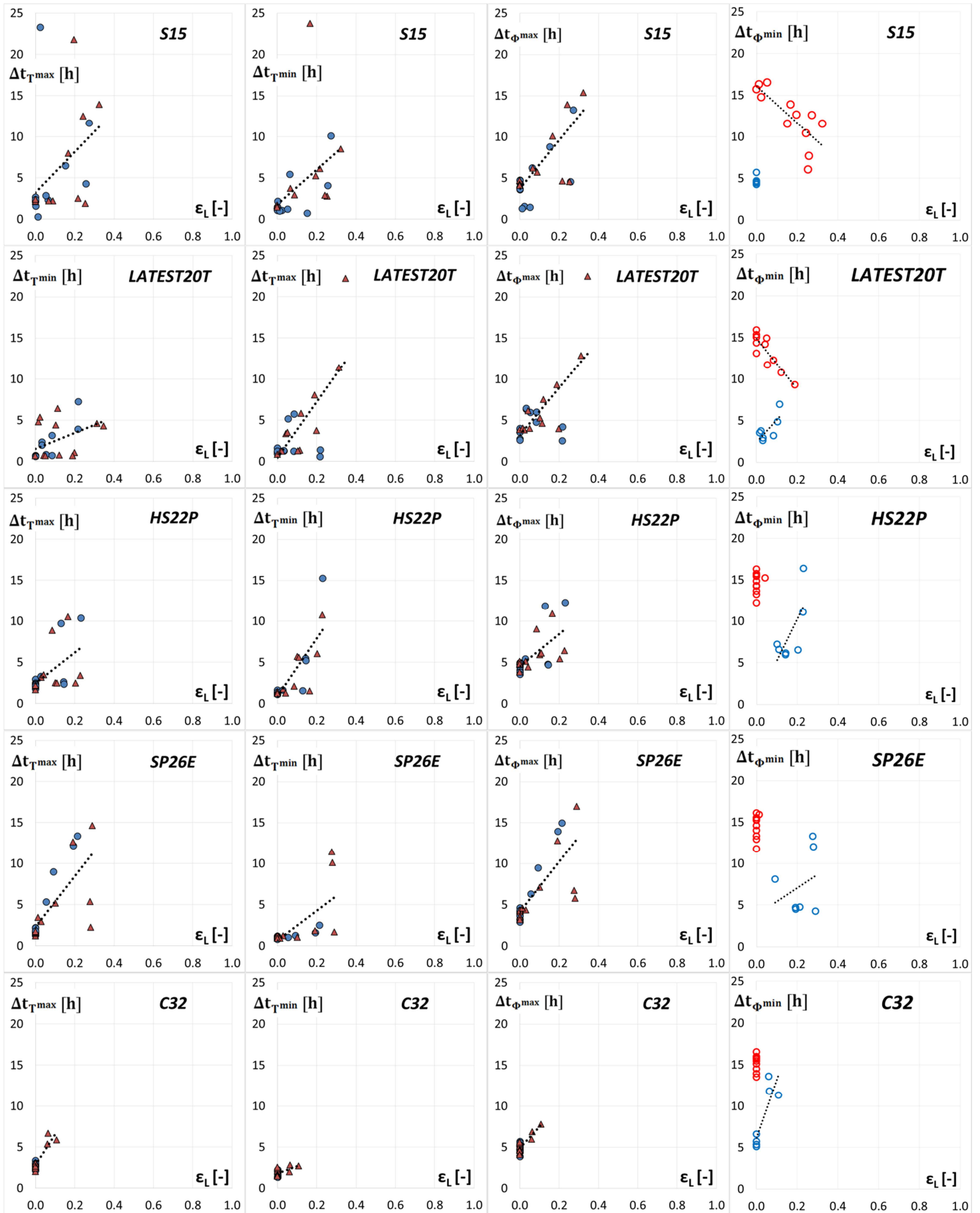


Figure 27 - Time lag of the maximum and minimum peak of the temperature  $\Delta t_{Tmax}$  and  $\Delta t_{Tmin}$  and of the heat flux  $\Delta t_{\phi max}$  and  $\Delta t_{\phi min}$  as a function of latent storage efficiency  $\epsilon_L$  for the different PCMs.

▲ Turin ● Cosenza ○ Winter period ○ Summer period

The summary shown in Figure 28 images, obtained by inserting in a graph, the values of the previous dynamic parameters in function of  $\epsilon_L$ , for both locations and for all types of PCM, highlights that the functional dependency between the dynamic parameters and the latent storage efficiency provides a qualitative trend with a high dispersion.

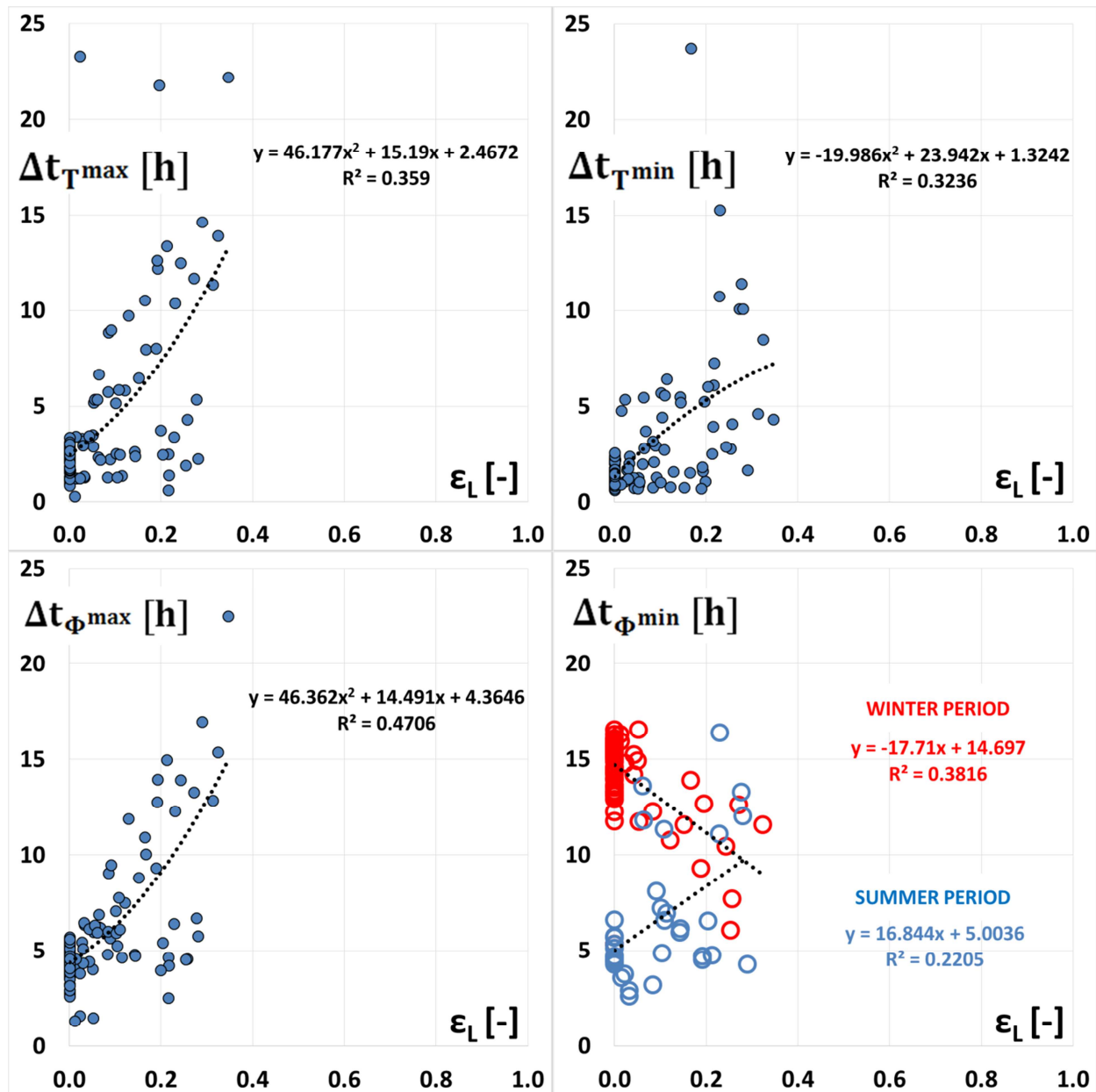


Figure 28 - Time lag of the maximum and minimum peak of the temperature  $\Delta t_{Tmax}$  and  $\Delta t_{Tmin}$  and of the heat flux  $\Delta t_{\phi max}$  and  $\Delta t_{\phi min}$  as a function of the latent storage efficiency  $\epsilon_L$ .

The interpolating curves show that with a storage latent efficiency  $\varepsilon_L = 0.35$ , the time lag of the maximum peak of the temperature and of the heat flux increase by about 10 h, the time lag of the minimum peak of the temperature rises by about 5 h, and the time lag of the minimum peak of the heat flux decreases by about 6 h during the winter period, and increases by about 5 h in the summer period.

#### 4.3.3. Correlations between dynamic parameters

A further study has been developed by correlating dynamic parameters directly among them. The search of such functional links highlighted a strong correlation between the decrement factor of the heat flux maximum excursion  $f_\phi$  and the energy decrement factor  $f_E$ , and between the time lag of the temperature maximum peak  $\Delta t_{Tmax}$  and the time lag of the heat flux maximum peak  $\Delta t_{\phi max}$ . Such dependencies, see Figure 29, result as being independent of the location, of the typology of PCM and of the configuration of the phases in the layer, and of the air-conditioning season.

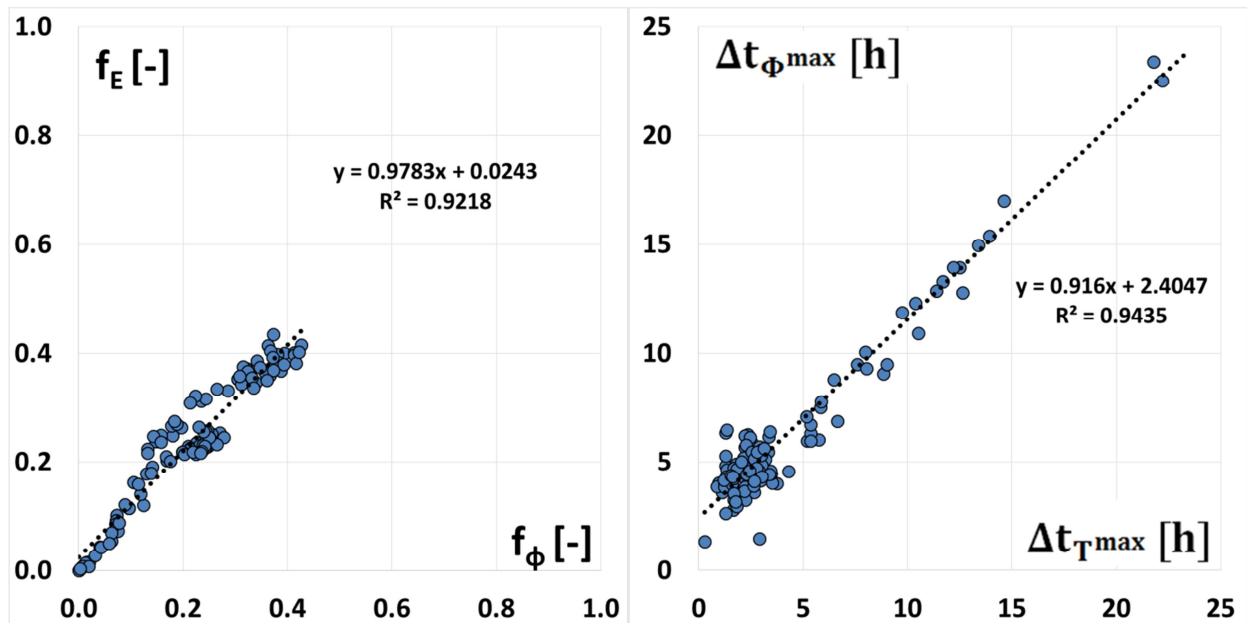


Figure 29 – Energy decrement factor  $f_E$  in function of that of the heat flux  $f_\phi$ , on the left, and heat flux maximum peak time lag  $\Delta t_{\phi max}$  as a function of the temperature maximum peak time lag  $\Delta t_{Tmax}$ .

The decrement factor  $f_E$  increases linearly with a growth of the decrement factor  $f_\phi$  with an angular coefficient close to the unit and, in these conditions, the intercept at the origin represents the difference between the two dynamic parameters, for all the values of  $f_\phi$ , see Eq. (24). Analogously it happens for the time lags  $\Delta t_{\phi max}$  and  $\Delta t_{Tmax}$ , see Eq. (25). In both cases, the

positive value of the intercept at the origin shows that  $f_E$  and  $\Delta t_{\phi \max}$  are, respectively, higher than  $f_{\phi}$  and  $\Delta t_{T \max}$ .

#### 4.3.4 Parameters required for the dynamic characterization

The analysis developed in the previous sections of this chapter shows that, for the complete characterization of a PCM layer subject to a phase change, it is necessary to evaluate only a part of the parameters as defined in Section 2.4. These parameters are: the decrement factor of the temperature  $f_T$  and heat flux  $f_{\phi}$  maximum excursion; the temperature maximum and minimum peak time lag  $\Delta t_{T \max}$  and  $\Delta t_{T \min}$ ; the heat flux minimum peak time lag  $\Delta t_{\phi \min}$ ; the latent storage efficiency  $\varepsilon_L$ ; the constant peak time fraction of the internal surface temperature and heat flux  $\Pi_{T_i}$  and  $\Pi_{\phi_i}$ .

The other parameters can be calculated with a high level of accuracy by Eq. 24 for the fraction of the latent energy stored  $\Lambda_L$ , by Eq. 25 for the energy decrement factor  $f_E$  and by Eq. 26 for the heat flux maximum peak time lag  $\Delta t_{\phi \max}$ .

$$\Lambda_L = -8.0177 \varepsilon_L^2 + 5.5839 \varepsilon_L + 0.0074 \quad (24)$$

$$f_E = 0.9783 f_{\phi} + 0.0243 \quad (25)$$

$$\Delta t_{\phi \max} = 0.916 \Delta t_{T \max} + 2.4047 \quad (26)$$

In the case of continuous air-conditioning, as already highlighted, the two constant peak time fraction parameters, related to the temperature and to the heat flux on the internal surface, correspond  $\Pi_{T_i} = \Pi_{\phi_i}$ .

In the end, in a situation of continuous air-conditioning the number of dynamic parameters required in order to identify in a complete way the dynamic behavior of the layer decreases from eleven to seven. Moreover, with less accuracy, also the decrement factor of the heat flux maximum excursion  $f_{\phi}$  can be correlated to the latent storage efficiency by the relation:

$$f_{\phi} = 2.9719 \varepsilon_L^2 - 1.8166 \varepsilon_L + 0.2979 \quad (27)$$



## 5. Conclusions

In this chapter, an accurate thermal and energetic analysis of PCM layers subject to the typical loadings operating on the external walls of air-conditioned buildings has been developed in the case in which, due to the effect of the periodic boundary conditions one or more bi-phase interfaces are present in the layer. The analysis allowed for the evaluation of the effects produced by the phase change on the heat transfer of the temperature and heat flux fluctuations, and on the thermal storage within the layer. The study highlighted that:

- in the different months of the year the configuration of the phases is variable and the layer can be totally in solid or liquid phase, or it can be the site of the formation of one, two or three bi-phase interfaces;
- the boundary conditions, relating to the melting temperature, determine the abscissa of the phase change formation, the number, the typology and the advancing velocity of the bi-phase interfaces and the stored latent energy in the layer;
- with the effect of the latent storage, on the external and internal surface of the layer, the daily maximum excursions modify, and the maximum and minimum peaks undergo a time lag, and in some cases it can also happen that, in a fraction of the period, they turn out to be constant;
- also the fluctuating energy associated with the surface heat flux fluctuations and the energy exchanged through the external and internal surface change.

The energetic analysis developed on monthly bases in relation to a PCM layer with different thermophysical properties and melting temperatures, subject to different climatic conditions, highlighted that, in Turin during the winter period:

- the lowest energy exiting from the indoor environment is ensured by a PCM with a melting temperature of 15°C (S15);
- the highest contribution of energy entering the indoor environment, mainly due to solar radiation, is recorded for a PCM with a melting temperature of 26°C (SP26).

In the summer period:

- the lowest value of energy entering the indoor environment is obtained by SP26;
- the highest value of energy exiting from the indoor environment is ensured by LATEST20 (with a melting temperature equal to 20°C).

For Cosenza, in both seasons, the previous findings with the highest values of energy entering the indoor environment and lowest values of the exiting energy are confirmed.

In both locations the yearly total stored energy, which characterizes the use of PCM, results at its highest values with the PCM HS22P, with melting temperature intermediate between those of winter and summer set points of the indoor environment. Such PCM is the best compromise between winter and summer energy needs for an air-conditioned environment.

The developed procedure can be used to select the most suitable PCM in summer air-conditioning, or in winter air-conditioning, or even with reference to annual air-conditioning. If the objective is that of reducing energy requirements in a specific air-conditioning season, the criterion to be adopted consists of selecting the PCM that ensures: in summer, the least energy entering the indoor environment; in winter the least energy lost by the indoor environment. If annual energy requirements are considered: if one of the two air-conditioning seasons is more expensive, the choice criterion is the previous one; if the two seasons have comparable energy requirements then the criterion proposed is that of selecting the PCM that assures the maximum total energy stored throughout the year.

For a complete dynamic characterization of the PCM layer, it was necessary to define more parameters in order to identify the change that undergoes the form of the trend of temperature and heat flux, as well as the transferred fluctuating energy and the sensible and latent energy stored. Concerning the temperature fluctuation, the decrement factor of the maximum excursion, the maximum and minimum peak time lag and the constant peak time fraction on the internal surface have to be used in order to quantify the thermal discomfort following the variation of the internal surface temperature, both during the winter and summer season. If the heat flux is considered, the analogue parameters provide the extent of the attenuation and of the time lag of the power peak, entering during the summer and exiting in the winter, for the evaluation of the maximum loads which work on the indoor environment. Furthermore, if the fluctuating energy passing through the layer is considered, the relative decrement factor allows estimation of the fraction of transferred energy into the indoor environment in summer and winter air conditioning, for the determination of the thermal requirements. Finally, the latent storage efficiency and the fraction of stored latent energy allow evaluation of the correct use of the layer as a system of latent heat storage.

The defined parameters have to be utilized for the thermal dimensioning of the layer, which is related to the choice of PCM and to its thickness, and also to identify the thermal behavior of the layer when operating.

Variability of the configuration of the phases in the layer during the course of the year modify the dynamic characteristics of the layer in function to the quantity of the latent energy stored. In particular, it has been found that the dynamic parameters are correlated to the latent storage

efficiency. The latent storage fraction and the decrement factors are strongly correlated, while for the time lags the correlation is less accurate. Independently of the location, of the type of PCM and of the configuration of the phases in the layer, by increasing the latent storage efficiency:

- the maximum excursion decrement factor of the temperature and the heat flux, and the decrement factor of the energy decrease;
- the latent energy fraction stored increases drastically;
- the maximum and minimum peak time lags of temperature and heat flux increase;
- the minimum peak time lag of heat flux decreases in the winter season and increases in the summer season;

Furthermore, it has been found that:

- the latent storage fraction and the decrement factors are strongly correlated to the latent storage efficiency, while for the time lags the correlation is less accurate;
- during the months when the constant peak time fraction is different to zero, the decrement factor of temperature and the maximum and minimum peak time lags of temperature are differently correlated to the latent storage efficiency;
- for the other dynamic parameters, the influence of the constant peak time fraction is very contained and the trends in function of the latent storage efficiency can be considered independent from the configuration of the phases in the layer;
- for the decrement factors, for reduced values of latent storage efficiency, to which corresponds a higher contribution to the heat storage of sensible type, the dispersion of the points around the interpolating curve is higher due to the different volumetric heat capacity of the different PCMs;
- for higher values of the latent storage efficiency, to which corresponds a contribution to the thermal storage of latent type prevailing on the sensible one, the points show a lower dispersion.

Finally, results show that it is sufficient to reach the phase change in a portion of the layer equal to 35% in order to obtain:

- a complete attenuation on the internal surface of the temperature and heat flux maximum excursion;
- an annulment of the fluctuating energy transferred to the indoor environment;
- unitary values of the latent energy fraction;

- a high increase of the time lag of the maximum and minimum peak of temperature, of the maximum peak of the heat flux, of the minimum peak of the heat flux during summer period;
- a high reduction of the minimum peak of the heat flux during the winter period.

The research of further functional dependencies among the dynamic characteristics highlighted a strong correlation between the decrement factor of the maximum excursion of the heat flux and the energy decrement factor, and between the time lag of the maximum peak of the temperature and the time lag of the maximum peak of the heat flux. Such dependencies turn up to be independent from the location, the PCM typology, the configuration of the phases in the layer and the air conditioning season.

Finally, it can be concluded that in order to identify the PCM layer's dynamic behavior in a complete way, seven independent dynamic parameters are necessary, from which it is possible to obtain the remaining parameters.

The results obtained provide valuable indications for improving the thermal performance of the building envelope by using PCM to achieve the net Zero Energy Building targets.

## References

- [1] Hussein Akeiber, Payam Nejat, Muhd Zaimi Abd. Majid, Mazlan A. Wahid, Fatemeh Jomehzadeh, Iman Zeynali Famileh, John Kaiser Calautit, Ben Richard Hughes, Sheikh Ahmad Zaki, A review on phase change material (PCM) for sustainable passive cooling in building envelopes, *Renewable and Sustainable Energy Reviews*, Volume 60, July 2016, Pages 1470-1497.
- [2] Yinping Zhang, Guobing Zhou, Kunping Lin, Qunli Zhang, Hongfa Di, Application of latent heat thermal energy storage in buildings: State-of-the-art and outlook, *Building and Environment*, Volume 42, Issue 6, June 2007, Pages 2197-2209, ISSN 0360-1323, <http://dx.doi.org/10.1016/j.buildenv.2006.07.023>.
- [3] Frédéric Kuznik, Damien David, Kevyn Johannes, Jean-Jacques Roux, A review on phase change materials integrated in building walls, *Renewable and Sustainable Energy Reviews*, Volume 15, Issue 1, January 2011, Pages 379-391, ISSN 1364-0321, <http://dx.doi.org/10.1016/j.rser.2010.08.019>.
- [4] Mario A. Medina, Jennifer B. King, Meng Zhang, On the heat transfer rate reduction of structural insulated panels (SIPs) outfitted with phase change materials (PCMs), *Energy*, Volume 33, Issue 4, April 2008, Pages 667-678, ISSN 0360-5442, <http://dx.doi.org/10.1016/j.energy.2007.11.003>.

- [5] Amar M. Khudhair, Mohammed M. Farid, A review on energy conservation in building applications with thermal storage by latent heat using phase change materials, *Energy Conversion and Management*, Volume 45, Issue 2, January 2004, Pages 263-275, ISSN 0196-8904, [http://dx.doi.org/10.1016/S0196-8904\(03\)00131-6](http://dx.doi.org/10.1016/S0196-8904(03)00131-6).
- [6] L.F. Cabeza, A. Castell, C. Barreneche, A. de Gracia, A.I. Fernández, Materials used as PCM in thermal energy storage in buildings: A review, *Renewable and Sustainable Energy Reviews*, Volume 15, Issue 3, April 2011, Pages 1675-1695, ISSN 1364-0321, <http://dx.doi.org/10.1016/j.rser.2010.11.018>.
- [7] Belén Zalba, José M Marín, Luisa F. Cabeza, Harald Mehling, Review on thermal energy storage with phase change: materials, heat transfer analysis and applications, *Applied Thermal Engineering*, Volume 23, Issue 3, February 2003, Pages 251-283, ISSN 1359-4311, [http://dx.doi.org/10.1016/S1359-4311\(02\)00192-8](http://dx.doi.org/10.1016/S1359-4311(02)00192-8).
- [8] Vineet Veer Tyagi, D. Buddhi, PCM thermal storage in buildings: A state of art, *Renewable and Sustainable Energy Reviews*, Volume 11, Issue 6, August 2007, Pages 1146-1166, ISSN 1364-0321, <http://dx.doi.org/10.1016/j.rser.2005.10.002>.
- [9] Ruben Baetens, Bjørn Petter Jelle, Arild Gustavsen, Phase change materials for building applications: A state-of-the-art review, *Energy and Buildings*, Volume 42, Issue 9, September 2010, Pages 1361-1368, ISSN 0378-7788, <http://dx.doi.org/10.1016/j.enbuild.2010.03.026>.
- [10] Michal Pomianowski, Per Heiselberg, Yinping Zhang, Review of thermal energy storage technologies based on PCM application in buildings, *Energy and Buildings*, Volume 67, December 2013, Pages 56-69, ISSN 0378-7788, <http://dx.doi.org/10.1016/j.enbuild.2013.08.006>.
- [11] N. Soares, J.J. Costa, A.R. Gaspar, P. Santos, Review of passive PCM latent heat thermal energy storage systems towards buildings' energy efficiency, *Energy and Buildings*, Volume 59, April 2013, Pages 82-103, ISSN 0378-7788, <http://dx.doi.org/10.1016/j.enbuild.2012.12.042>.
- [12] Hicham Johra, Per Heiselberg, Influence of internal thermal mass on the indoor thermal dynamics and integration of phase change materials in furniture for building energy storage: A review, *Renewable and Sustainable Energy Reviews*, Volume 69, March 2017, Pages 19-32, ISSN 1364-0321, <http://dx.doi.org/10.1016/j.rser.2016.11.145>.
- [13] Mohammad Saffari, Alvaro de Gracia, Svetlana Ushak, Luisa F. Cabeza, Economic impact of integrating PCM as passive system in buildings using Fanger comfort model, *Energy and Buildings*, Volume 112, 15 January 2016, Pages 159-172, ISSN 0378-7788, <http://dx.doi.org/10.1016/j.enbuild.2015.12.006>.

- [14] Simen Edsjø Kalnæs, Jelle BP. Phase change materials for building applications: a state-of-the-art review and future research opportunities. *Energy Build* 2015;94:150–76. <http://dx.doi.org/10.1016/j.enbuild.2015.02.023>.
- [15] Fabrizio Ascione, Nicola Bianco, Rosa Francesca De Masi, Filippo de' Rossi, Giuseppe Peter Vanoli, Energy refurbishment of existing buildings through the use of phase change materials: Energy savings and indoor comfort in the cooling season, *Applied Energy*, Volume 113, January 2014, Pages 990-1007, ISSN 0306-2619, <http://dx.doi.org/10.1016/j.apenergy.2013.08.045>.
- [16] C.K. Halford, R.F. Boehm, Modeling of phase change material peak load shifting, *Energy and Buildings*, Volume 39, Issue 3, March 2007, Pages 298-305, ISSN 0378-7788, <http://dx.doi.org/10.1016/j.enbuild.2006.07.005>.
- [17] EN ISO 13786, Thermal Performance of Buildings Components e Dynamic Thermal Characteristics e Calculation Methods, 2010.
- [18] G. Evola, L. Marletta, A dynamic parameter to describe the thermal response of buildings to radiant heat gains, *Energy and Buildings*, Volume 65, October 2013, Pages 448-457, ISSN 0378-7788, <http://dx.doi.org/10.1016/j.enbuild.2013.06.026>.
- [19] G. Oliveti, N. Arcuri, D. Mazzeo, M. De Simone, A new parameter for the dynamic analysis of building walls using the harmonic method, *International Journal of Thermal Sciences*, Volume 88, February 2015, Pages 96-109, ISSN 1290-0729, <http://dx.doi.org/10.1016/j.ijthermalsci.2014.09.006>.
- [20] D. Mazzeo, G. Oliveti, N. Arcuri, Influence of internal and external boundary conditions on the decrement factor and time lag heat flux of building walls in steady periodic regime, *Applied Energy*, Volume 164, 15 February 2016, Pages 509-531, ISSN 0306-2619, <http://dx.doi.org/10.1016/j.apenergy.2015.11.076>.
- [21] D. Mazzeo, G. Oliveti, N. Arcuri, Mapping of the seasonal dynamic properties of building walls in actual periodic conditions and effects produced by solar radiation incident on the outer and inner surfaces of the wall, *Applied Thermal Engineering*, Volume 102, 5 June 2016, Pages 1157-1174, ISSN 1359-4311, <http://dx.doi.org/10.1016/j.applthermaleng.2016.04.039>.
- [22] K.J. Kontoleon, D.K. Bikas, The effect of south wall's outdoor absorption coefficient on time lag, decrement factor and temperature variations, *Energy and Buildings*, Volume 39, Issue 9, September 2007, Pages 1011-1018, ISSN 0378-7788, <http://dx.doi.org/10.1016/j.enbuild.2006.11.006>.
- [23] Andrea Gasparella, Giovanni Pernigotto, Marco Baratieri, Paolo Baggio, Thermal dynamic transfer properties of the opaque envelope: Analytical and numerical tools for the assessment of

the response to summer outdoor conditions, *Energy and Buildings*, Volume 43, Issue 9, September 2011, Pages 2509-2517, ISSN 0378-7788, <http://dx.doi.org/10.1016/j.enbuild.2011.06.004>.

[24] Guobing Zhou, Yongping Yang, Hong Xu, Performance of shape-stabilized phase change material wallboard with periodical outside heat flux waves, *Applied Energy*, Volume 88, Issue 6, June 2011, Pages 2113-2121, ISSN 0306-2619, <http://dx.doi.org/10.1016/j.apenergy.2011.01.016>.

[25] Guobing Zhou, Yongping Yang, Xin Wang, Jinming Cheng, Thermal characteristics of shape-stabilized phase change material wallboard with periodical outside temperature waves, *Applied Energy*, Volume 87, Issue 8, August 2010, Pages 2666-2672, ISSN 0306-2619, <http://dx.doi.org/10.1016/j.apenergy.2010.02.001>.

[26] Naser P. Sharifi, Ahsan Aadil Nizam Shaikh, Aaron R. Sakulich, Application of phase change materials in gypsum boards to meet building energy conservation goals, *Energy and Buildings*, Volume 138, 1 March 2017, Pages 455-467, ISSN 0378-7788, <http://dx.doi.org/10.1016/j.enbuild.2016.12.046>.

[27] Haoshu Ling, Chao Chen, Hong Qin, Shen Wei, Jie Lin, Na Li, Mingxing Zhang, Nan Yu, Yin Li, Indicators evaluating thermal inertia performance of envelopes with phase change material, *Energy and Buildings*, Volume 122, 15 June 2016, Pages 175-184, ISSN 0378-7788, <http://dx.doi.org/10.1016/j.enbuild.2016.04.009>.

[28] G. Evola, L. Marletta, F. Sicurella, A methodology for investigating the effectiveness of PCM wallboards for summer thermal comfort in buildings, *Building and Environment*, Volume 59, January 2013, Pages 517-527, ISSN 0360-1323, <http://dx.doi.org/10.1016/j.buildenv.2012.09.021>.

[29] Hong Ye, Linshuang Long, Haitao Zhang, Ruqiang Zou, The performance evaluation of shape-stabilized phase change materials in building applications using energy saving index, *Applied Energy*, Volume 113, January 2014, Pages 1118-1126, ISSN 0306-2619, <http://dx.doi.org/10.1016/j.apenergy.2013.08.067>.

[30] Xiaoqin Sun, Quan Zhang, Mario A. Medina, Kyoung Ok Lee, Shuguang Liao, Parameter design for a phase change material board installed on the inner surface of building exterior envelopes for cooling in China, *Energy Conversion and Management*, Volume 120, 15 July 2016, Pages 100-108, ISSN 0196-8904, <http://dx.doi.org/10.1016/j.enconman.2016.04.096>.

[31] Jiawei Lei, Jinglei Yang, En-Hua Yang, Energy performance of building envelopes integrated with phase change materials for cooling load reduction in tropical Singapore, *Applied*

Energy, Volume 162, 15 January 2016, Pages 207-217, ISSN 0306-2619, <http://dx.doi.org/10.1016/j.apenergy.2015.10.031>.

[32] Stephen D. Zwanzig, Yongsheng Lian, Ellen G. Brehob, Numerical simulation of phase change material composite wallboard in a multi-layered building envelope, Energy Conversion and Management, Volume 69, May 2013, Pages 27-40, ISSN 0196-8904, <http://dx.doi.org/10.1016/j.enconman.2013.02.003>.

[33] Frédéric Kuznik, Joseph Virgone, Experimental assessment of a phase change material for wall building use, Applied Energy, Volume 86, Issue 10, October 2009, Pages 2038-2046, ISSN 0306-2619, <http://dx.doi.org/10.1016/j.apenergy.2009.01.004>.

[34] I. Mandilaras, M. Stamatiadou, D. Katsourinis, G. Zannis, M. Founti, Experimental thermal characterization of a Mediterranean residential building with PCM gypsum board walls, Building and Environment, Volume 61, March 2013, Pages 93-103, ISSN 0360-1323, <http://dx.doi.org/10.1016/j.buildenv.2012.12.007>.

[35] Luisa F. Cabeza, Cecilia Castellón, Miquel Nogués, Marc Medrano, Ron Leppers, Oihana Zubillaga, Use of microencapsulated PCM in concrete walls for energy savings, Energy and Buildings, Volume 39, Issue 2, February 2007, Pages 113-119, ISSN 0378-7788, <http://dx.doi.org/10.1016/j.enbuild.2006.03.030>.

[36] Dong Li, Yumeng Zheng, Changyu Liu, Guozhong Wu, Numerical analysis on thermal performance of roof contained PCM of a single residential building, Energy Conversion and Management, Volume 100, August 2015, Pages 147-156, ISSN 0196-8904, <http://dx.doi.org/10.1016/j.enconman.2015.05.014>.

[37] Francesco Guarino, Andreas Athienitis, Maurizio Cellura, Diane Bastien, PCM thermal storage design in buildings: Experimental studies and applications to solarium in cold climates, Applied Energy, Volume 185, Part 1, 1 January 2017, Pages 95-106, ISSN 0306-2619, <http://dx.doi.org/10.1016/j.apenergy.2016.10.046>.

[38] Alexander M. Thiele, Gaurav Sant, Laurent Pilon, Diurnal thermal analysis of microencapsulated PCM-concrete composite walls, Energy Conversion and Management, Volume 93, 15 March 2015, Pages 215-227, ISSN 0196-8904, <http://dx.doi.org/10.1016/j.enconman.2014.12.078>.

[39] Bogdan M. Diaconu, Mihai Cruceru, Novel concept of composite phase change material wall system for year-round thermal energy savings, Energy and Buildings, Volume 42, Issue 10, October 2010, Pages 1759-1772, ISSN 0378-7788, <http://dx.doi.org/10.1016/j.enbuild.2010.05.012>.



- [40] Xu Wang, Hang Yu, Lu Li, Mei Zhao, Experimental assessment on the use of phase change materials (PCMs)-bricks in the exterior wall of a full-scale room, *Energy Conversion and Management*, Volume 120, 15 July 2016, Pages 81-89, ISSN 0196-8904, <http://dx.doi.org/10.1016/j.enconman.2016.04.065>.
- [41] Chao Chen, Haifeng Guo, Yuning Liu, Hailin Yue, Chendong Wang, A new kind of phase change material (PCM) for energy-storing wallboard, *Energy and Buildings*, Volume 40, Issue 5, 2008, Pages 882-890, ISSN 0378-7788, <http://dx.doi.org/10.1016/j.enbuild.2007.07.002>.
- [42] Waqar A. Qureshi, Nirmal-Kumar C. Nair, Mohammad M. Farid, Impact of energy storage in buildings on electricity demand side management, *Energy Conversion and Management*, Volume 52, Issue 5, May 2011, Pages 2110-2120, ISSN 0196-8904, <http://dx.doi.org/10.1016/j.enconman.2010.12.008>.
- [43] K. Peippo, P. Kauranen, P.D. Lund, A multicomponent PCM wall optimized for passive solar heating, *Energy and Buildings*, Volume 17, Issue 4, 1991, Pages 259-270, ISSN 0378-7788, [http://dx.doi.org/10.1016/0378-7788\(91\)90009-R](http://dx.doi.org/10.1016/0378-7788(91)90009-R).
- [44] A.K. Athienitis, C. Liu, D. Hawes, D. Banu, D. Feldman, Investigation of the thermal performance of a passive solar test-room with wall latent heat storage, *Building and Environment*, Volume 32, Issue 5, September 1997, Pages 405-410, ISSN 0360-1323, [http://dx.doi.org/10.1016/S0360-1323\(97\)00009-7](http://dx.doi.org/10.1016/S0360-1323(97)00009-7).
- [45] Zouhair Ait Hammou, Marcel Lacroix, A new PCM storage system for managing simultaneously solar and electric energy, *Energy and Buildings*, Volume 38, Issue 3, March 2006, Pages 258-265, ISSN 0378-7788, <http://dx.doi.org/10.1016/j.enbuild.2005.06.008>.
- [46] A. Castell, I. Martorell, M. Medrano, G. Pérez, L.F. Cabeza, Experimental study of using PCM in brick constructive solutions for passive cooling, *Energy and Buildings*, Volume 42, Issue 4, April 2010, Pages 534-540, ISSN 0378-7788, <http://dx.doi.org/10.1016/j.enbuild.2009.10.022>.
- [47] Jan Kosny, Elizabeth Kossecka, Andrzej Brzezinski, Akhan Tleoubaev, David Yarbrough, Dynamic thermal performance analysis of fiber insulations containing bio-based phase change materials (PCMs), *Energy and Buildings*, Volume 52, September 2012, Pages 122-131, ISSN 0378-7788, <http://dx.doi.org/10.1016/j.enbuild.2012.05.021>.
- [48] D.A. Neeper, Thermal dynamics of wallboard with latent heat storage, *Solar Energy*, Volume 68, Issue 5, 2000, Pages 393-403, ISSN 0038-092X, [http://dx.doi.org/10.1016/S0038-092X\(00\)00012-8](http://dx.doi.org/10.1016/S0038-092X(00)00012-8).

- [49] Dariusz Heim, Joe A Clarke, Numerical modelling and thermal simulation of PCM–gypsum composites with ESP-r, *Energy and Buildings*, Volume 36, Issue 8, August 2004, Pages 795-805, ISSN 0378-7788, <http://dx.doi.org/10.1016/j.enbuild.2004.01.004>.
- [50] Xu X, Zhang YP, Lin KP, Di HF, Yang R. Modeling and simulation on the thermal performance of shape-stabilized phase change material floor used in passive solar buildings. *Energy Build* 2005;37(10):1084–91.
- [51] Guobing Zhou, Yiping Zhang, Xin Wang, Kunping Lin, Wei Xiao, An assessment of mixed type PCM-gypsum and shape-stabilized PCM plates in a building for passive solar heating, *Solar Energy*, Volume 81, Issue 11, November 2007, Pages 1351-1360, ISSN 0038-092X, <http://dx.doi.org/10.1016/j.solener.2007.01.014>.
- [52] Feng Jiang, Xin Wang, Yiping Zhang, A new method to estimate optimal phase change material characteristics in a passive solar room, *Energy Conversion and Management*, Volume 52, Issue 6, June 2011, Pages 2437-2441, ISSN 0196-8904, <http://dx.doi.org/10.1016/j.enconman.2010.12.051>.
- [53] Axel Arnault, François Mathieu-Potvin, Louis Gosselin, Internal surfaces including phase change materials for passive optimal shift of solar heat gain, *International Journal of Thermal Sciences*, Volume 49, Issue 11, November 2010, Pages 2148-2156, ISSN 1290-0729, <http://dx.doi.org/10.1016/j.ijthermalsci.2010.06.021>.
- [54] Xiaoqin Sun, Quan Zhang, Mario A. Medina, Kyoung Ok Lee, Energy and economic analysis of a building enclosure outfitted with a phase change material board (PCMB), *Energy Conversion and Management*, Volume 83, July 2014, Pages 73-78, ISSN 0196-8904, <http://dx.doi.org/10.1016/j.enconman.2014.03.035>.
- [55] D. Zhou, G.S.F. Shire, Y. Tian, Parametric analysis of influencing factors in Phase Change Material Wallboard (PCMW), *Applied Energy*, Volume 119, 15 April 2014, Pages 33-42, ISSN 0306-2619, <http://dx.doi.org/10.1016/j.apenergy.2013.12.059>.
- [56] Domenico Mazzeo, Giuseppe Oliveti, Natale Arcuri, Multiple Bi-phase Interfaces in a PCM Layer Subject to Periodic Boundary Conditions Characteristic of Building External Walls, *Energy Procedia*, Volume 82, December 2015, Pages 472-479.
- [57] D. Mazzeo, G. Oliveti, M. De Simone, N. Arcuri, Analytical model for solidification and melting in a finite PCM in steady periodic regime, *International Journal of Heat and Mass Transfer*, Volume 88, September 2015, Pages 844-861.
- [58] UNI 10349:1994. Heating and cooling of buildings. Climatic data.
- [59] Solar Energy Laboratory University of Wisconsin-Madison, TRNSYS, Version 17, 2012.

[60] EN ISO 13790:2008. Energy performance of buildings – calculation of energy use for space heating and cooling

[61] UNI TS 11300-1:2008. Energy performance of buildings. Part 1: Evaluation of energy need for space heating and cooling.

[62] EN ISO 6946:1997. Building components and building elements – Thermal resistance and thermal transmittance – Calculation method.

[63] Oliveti G, Arcuri N, De Simone M, Bruno R. Experimental evaluations of the building shell radiant exchange in clear sky conditions. Solar Energy 2012; 86:1785-1795.

### Nomenclature

a	thermal diffusivity [ $\text{m}^2/\text{s}$ ]
c	specific heat capacity [ $\text{J}/\text{kg K}$ ]
E	energy per square meter [ $\text{J}/\text{m}^2$ ]
$E_e$	energy on the external surface [ $\text{J}/\text{m}^2$ ]
$E_i$	energy on the internal surface [ $\text{J}/\text{m}^2$ ]
$f_T$	decrement factor of the temperature maximum excursion [-]
$f_\Phi$	decrement factor of the heat flux maximum excursion [-]
$f_E$	decrement factor of the fluctuating energy transferred [-]
G	monthly average daily solar irradiation on the horizontal plane [ $\text{J}/\text{m}^2$ ]
h	heat transfer coefficient [ $\text{W}/(\text{m}^2 \text{K})$ ]
H	latent heat of fusion [ $\text{J}/\text{kg}$ ]
$j_k$	j-th subvolume including the k-th bi-phase interface [-]
k	thermal conductivity [ $\text{W}/\text{m K}$ ]
L	layer thickness [m]
P	period [s]
t	time [s]
T	Temperature [K]
x	spatial coordinate [m]
$X_M$	position of the bi-phase interface [m]
Greek symbols	
$\alpha$	solar absorption coefficient [-]
$\Delta P$	portion of period P [h]

$\Delta t$	finite difference time step [s]
$\Delta t_{T_{\max}}$	time lag of the temperature maximum peak [h]
$\Delta t_{T_{\min}}$	time lag of the temperature minimum peak [h]
$\Delta t_{\Phi_{\max}}$	time lag of the heat flux maximum peak [h]
$\Delta t_{\Phi_{\min}}$	time lag of the heat flux minimum peak [h]
$\Delta x$	thickness of the subvolume [m]
$\varepsilon_L$	latent energy efficiency [-]
$\Phi$	heat flux [ $\text{W}/\text{m}^2$ ]
$\lambda$	liquid fraction [-]
$\Lambda_L$	latent energy fraction [-]
$\Pi_{T_i}$	constant peak time fraction of the temperature [-]
$\Pi_{\Phi_i}$	constant peak time fraction of the heat flux [-]
$\rho$	density [ $\text{kg}/\text{m}^3$ ]
<b>Subscripts</b>	
c	convective
e	external
eq	equivalent
ea	referring to the external air load
i	i-th subvolume preceeding the subvolume in phase change
ia	internal air
$j_k$	referring to the j-th subvolume including the k-th bi-phase interface
k	k-th bi-phase interface
l	liquid
L	referring to the latent energy stored
$L_{,\max}$	referring to the maximum latent energy stored
M	melting
n	n-th hour
p	at constant pressure
PC	phase change
r	radiative
s	solid
S	referring to the sensible energy stored

s,i	referring to the internal surface
s,e	referring to the external surface
sky	referring to the sky load
sol	referring to the solar load
T	referring to the total energy stored

**Superscripts**

+	entering
-	exiting
max	maximum value
min	minimum value
n	current time instant
n+1	successive time instant
p	peak value
sum	summer period
win	winter period

**Symbols**

~	fluctuating value
---	-------------------

# Chapter 8

## Experimental validation of the exact analytical solution of the steady periodic heat transfer problem in a PCM layer

### Abstract

Phase change materials (PCM) are used in many industrial and residential applications for their advantageous characteristic of high capacity of latent thermal storage by means of an isothermal process. In such a context, it is very useful to have predictive mathematical models for the analysis of the performance and the thermal design of these layers.

In this chapter, an experimental validation of an analytical model that resolves the steady periodic heat transfer problem in a finite layer of PCM is presented. The boundary conditions are such as to give rise to the formation of a sole bi-phase interface, in movement in the layer, which divides the solid phase from the liquid phase. The mathematical model is represented by a system of differential equations that describe conduction in the solid phase and in the liquid phase and the thermal balance equation at the bi-phase interface at the phase change temperature. The problem is

decomposed into two sub-problems, one steady and the other steady periodic sinusoidal; the latter is solved using the phasor method. The solution allows evaluation, upon variation of time, of the position of the bi-phase interface, and starting from this, the temperature and heat flux fields and the energy stored in latent and sensible form. As the principle of superposition of causes and effects is valid, the obtained solution can be also applied in the case of non-sinusoidal periodic boundary conditions.

The experimental investigation was conducted by subjecting the two flat faces of a cylindrical PCM sample, mounted inside an experimental device, to different boundary conditions upon time variation and measuring the temperature at different heights and the surface heat fluxes. The choice of the PCM was made so that the thermophysical and thermochemical behaviour was very close to those hypothesized in the formulation of the analytical model. For the evaluation of the thermophysical properties of the PCM sample used (thermal conductivity and specific heat in the two phases, latent heat and phase change temperature), an experimental procedure created by the authors was used. The experimental procedure consists of subjecting the sample, mounted in the experimental device for verification of the model, to different tests. Each of these tests consists of a thermal transient from an initial steady state to a final steady state. The sample in the first test is entirely in solid phase, in the second test it is entirely in liquid phase and in the third test it undergoes a complete solid-liquid phase change.

Validation of the analytical model was conducted: in a sinusoidal periodic regime, setting temperature boundary conditions on the two faces of the sample, varying the decrement factor, the time lag and the oscillation period; in a non-sinusoidal periodic regime, considering, on the two sample faces, temperature boundary conditions with different shape, represented by means of a Fourier series expansion. In all the cases, the comparison between the measured and calculated trends of the temperature at different sample heights and of the surface heat fluxes resulted as being in excellent agreement, as the thermal fluctuations present steady mean values, and amplitudes and arguments that are very close. Moreover, also having verified the analytical total stored energy, the analytical model constitutes a valid instrument for the evaluation of the latent and sensible contribution and the trend in time of the position of the bi-phase interface in function of time.

Keywords: PCM; Experimental validation; Analytical model; Thermophysical properties; New procedure; DSC

- Experimental verification of an analytical model resolving a Stefan Problem is conducted.
- The exact solution regards a finite PCM layer subjected to a steady periodic regime.

- The experimental device employed is able to measure the temperatures in the sample and the surface heat fluxes.
- A new experimental procedure for the determination of the thermophysical properties is developed.
- The analytical model provides accurate predictive assessments of the thermal fluctuations throughout the layer.
- A high attenuation factor, a nil time lag and a high period give rise to the maximum total energy stored.

*Non dobbiamo dimenticare che quando il radio venne scoperto nessuno sapeva che si sarebbe rivelato utile negli ospedali. Era un lavoro di pura scienza. E questa è la prova che il lavoro scientifico non deve essere considerato dal punto di vista della diretta utilità dello stesso. Deve essere svolto per se stesso, per la bellezza della scienza, e poi c'è sempre la probabilità che una scoperta scientifica possa diventare come il radio un beneficio per l'umanità.*

*(Marie Curie)*



## 1. Introduction

The use of phase change materials (PCM) has been the object of increasing interest that has led to many applications in different contexts. Unlike traditional materials, PCM, due to their solid-liquid phase change, allow the storage of a great quantity of latent energy at a constant temperature. For example, PCM are used in industrial plants for the storage of heating and cooling energy, in the air-conditioning of buildings to reduce energy in transit through the walls both in the summer season and in the winter season. PCM are also used in electronic equipment to ensure correct functioning and in containers used for the transportation of food, drinks and medicines to prevent their deterioration [1].

In many of these applications, the thermal regime can be considered, with a good approximation, as steady periodic. Several authors have addressed the problem of the thermal behavior of a PCM layer in steady periodic regime has been addressed through analytical models, numerically solved, or through experimental investigations. Bransier [2] has analyzed the problem of thermal storage for plates and hollow cylinders in contact with a fluid with a periodically variable temperature. The comparison of the thermal behavior of the two geometries was obtained by means of a numerical model. The same investigation was conducted experimentally by Bardon et al. [3] with reference to a vertical plate and by Kalhori and Ramadhyani [4] in a vertical cylinder with or without fins. Belleci and Conti [5-7] have developed a numerical model to simulate the cyclical behavior of a phase change storage system of solar energy and they supplied a criterion for the optimal design of the storage system. Halford et al. [8] have developed a numerical model in a steady periodic regime of a multilayer wall containing a PCM layer, with an imposed temperature on the external surfaces. They have evaluated the time lag and the attenuation of the peak load varying both layer thickness and the outdoor climatic conditions. Mathieu-Potvin et al. [9] have evaluated the behaviour of an external multilayer wall containing a PCM layer varying its position and the phase change temperature. The analysis was conducted with a finite volume method considering a sinusoidal temperature oscillation and real temperature profiles in order to optimize the annual energy requirement. Neepor [10] has examined three parameters that influence the energy that can be passively absorbed and released during a diurnal cycle by a PCM wallboard subject to an idealized sinusoidal room temperature: the phase change temperature; the temperature range above which melt occurs; and the latent heat capacity per unit area. In a sinusoidal periodic regime, Zhou et al. [11,12] have used a numerical method to study the effects of PCM thermophysical properties, of the inner surface convective heat transfer coefficient and of the thickness of a PCM wallboard on the dynamic characteristics. In the same thermal regime, Sharifi et

al. [13], by means the use of a 2D heat transfer model, have evaluated the dynamic behavior of a based PCM-impregnated gypsum board. In a non-sinusoidal periodic regime, Mazzeo et al. [14] have determined a set of dynamic parameter, for each month of the year, of PCM layers with different melting temperatures and thermophysical properties and subject to climatic conditions of two locations.

If on the one hand a large number of numerical investigations in a steady periodic regime were addressed, only a small amount of this research is supported by analytical or experimental validation. Jariwala et al. [15] have studied the cyclical performance of a latent heat thermal storage system in cylindrical geometry made of paraffin wax and containing a submerged helical coil of copper crossed by a flow. The results of a quasi-stationary one-dimensional model were compared with experimental data. Hasan et al. [16] have numerically and experimentally studied the fusion and solidification of a plate subject to cyclical boundary conditions. This investigation was further extended by Voller et al. also considering convection in the liquid phase [17]. Casano and Piva [18] have formulated an analytical model in a steady periodic regime, in a dimensionless form, of a PCM layer with heat flux boundary conditions. The model was numerically resolved with the finite volume method and validated experimentally. Kuznik et al. [19] have compared a set of experimental data with the results of a numerical model considering cubical test cells subject to a sinusoidal external temperature evolution. Savovic et al. [20] have conducted a numerical study of the heat transfer in a PCM layer with a finite difference model in monodimensional geometry with Dirichlet periodic boundary conditions. The evaluations of the position and velocity of the bi-phase interface and of the temperature fields were compared with those obtained with the Ozisik integral method [21]. Henze et al. [22] have used a simplified numerical model based on a quasi-linear transitory equation to study the phase change in a PCM layer with a thin fin. The model predicts the melt fraction of PCM and the form of the bi-phase interface as a function of time; the results were verified experimentally. Lachheb et al. [23] have evaluated the thermal behavior of a new plaster composite containing a microencapsulated PCM with a numerical and experimental study. Ling et al. [24] have proposed and compared with experimental measurements a method for the evaluation of the thermal inertia performance of a building component with PCM.

From the aforementioned studies, it emerges that, for the analysis of the performance and the thermal design of such layers, it is extremely important to have experimentally validated predictive mathematical models. The use of these models requires the knowledge of the effective thermophysical properties of the layer, measurable with the most widespread experimental methods, namely DSC (Differential Scanning Calorimeter) technique, developed by Watson et al. [25], and the T-History method, proposed by Zhang et al. [26], or with new techniques [27, 28] proposed in

the recent years. Concerning the availability of predictive mathematical models, it is necessary to highlight that the problem of the determination of the temperature field in a layer subject to phase changes, known as Stefan Problem, presents non-linear characteristics, which render the solving of differential equations describing the phenomenon particularly difficult. In particular, the domains of the differential equations are variable in time and depend, on the external surface boundary conditions, as well as on the bi-phase interface conditions. These conditions are expressed by an instantaneous thermal balance equation, which describes conductive heat flux discontinuity, and by the constraint that at the bi-phase interface the temperature is equal to the phase change temperature. The thermal field in the two phases, which present different thermophysical properties, is a function of the position of the bi-phase interface that is variable in time as well as the relative boundary conditions.

The complexity of the problem has led many authors to use numerical procedures that implement simplified models to describe the phase change such as the models known in literature as latent-heat evolution methods [29]. The latter describe the movement of the bi-phase interface through different approaches known as the apparent heat capacity method, the effective heat capacity method, and the enthalpy method. Only a limited number of analytical solutions of the Stefan Problem are available and regard semi-infinite or finite layers with boundary conditions that are not variable in time [21, 29-34]. The analytical solutions present the advantage of directly identifying the physical parameters on which the thermal behavior of the system depends, and the function that connects the unknowns to the physical parameters and to the boundary conditions. Recently, in the laboratory of "Building Energy" of the Applied Physics Area of the Department of Mechanical, Energy and Management Engineering (DIMEG) at the University of Calabria, the exact solution of a Stefan Problem in a finite PCM layer in steady periodic regime was obtained [35]. The model allows for the determination of the bi-phase interface position, of the temperature and heat flux field, and of the energy stored in latent and sensible form.

The objective of this chapter is the experimental validation of such a model that was formulated supposing simplificative hypotheses regarding material behaviour and heat transfer in the layer as valid. Validation was made using a device developed by the GREA Innovació Concurrent research group at the University of Lleida (Lleida, Spain). This device contains two controlled chambers, heated and cooled by copper coils with thermo stated water supplied by water baths, capable of setting different boundary conditions upon variation of time. Furthermore, it is equipped with a system for the measurement and acquisition of temperatures in the sample and of the surface heat fluxes. This equipment was used in a previous work to test the improvement in the thermal response of a gypsum board due to the incorporation of PCM [27]. The considered PCM

presents, for reduced heating/cooling rate values, a reduced phase change temperature range, a melting temperature that is very close to the solidification temperature and a slight difference between the latent heat of fusion and that of solidification. Moreover, the material does not present phenomena of phase segregation nor of subcooling. These properties are very close to those hypothesized in the formulation of the model. The thermophysical properties were determined by means of specific tests in the device conducted on the same PCM sample used for validation of the model. In this regard, a new experimental procedure has been developed, which represents an advancement of the method used in de Gracia et al. [27]. The new procedure allows: (i) the evaluation of the thermophysical properties in the two phases; (ii) the obtainment of both the thermal conductivity and the specific heat with a sole experimental test; (iii) the evaluation of the latent heat and the phase change temperature. The results obtained were compared with those provided by the manufacturer and with those obtained in the laboratory by means of DSC tests. For the validation of the analytical model, different sinusoidal boundary conditions are considered, which give rise to reduced heating/cooling rates, obtained by varying the attenuation and the time lag between the two temperature loadings operating on the two boundary faces and the oscillation period. Moreover, the model was validated considering non-sinusoidal boundary conditions. Validation was made by comparing the measured and analytically calculated trends of the temperatures at different heights in the sample and of the surface heat fluxes, and by comparing the experimental total stored energy and that provided by the model.

In the first part of the chapter, the authors present: (i) a brief description of the analytical model for the determination of the position of the bi-phase interface and of the thermal field in the solid and liquid phases; (ii) a description of the PCM employed and of the experimental device; (iii) the new procedure for the determination of the thermal conductivity and specific heat in the two phases, latent heat and phase change temperature. Successively, the results of the new experimental procedure for the evaluation of the thermophysical properties of the PCM are described and compared with those provided by the manufacturer and with those obtained in the laboratory by means of DSC tests. Finally, the different experimental tests conducted in a steady periodic regime for validation of the analytical model are presented.

## 2. Method and materials

### 2.1. Physical model

#### 2.1.1. Description

The study of thermal exchange in a PCM, known as the Stefan or Moving Boundary Problem, subjected to steady periodic boundary conditions has been developed in Section 4 [35] by simultaneously solving the general equation of conduction in the solid phase and in the liquid phase, coupled by bi-phase interface conditions and by boundary conditions on two faces. At the bi-phase interface, the difference in heat fluxes between the liquid phase and the solid phase is equal to the heat needed for the fusion process per unit time and the temperature is equal to the melting temperature. Interface conditions introduce complexity in the resolution of the temperature field given that the position of the bi-phase interface in various instants is unknown. The Stefan Problem addressed regards a cyclic process, in a steady periodic regime, in which the two phases are active since the boundary conditions regard a temperature oscillation above the melting temperature on one face and a temperature oscillation below the melting temperature on the other face. In such conditions, in the layer, a sole bi-phase interface originates. The model was determined supposing: (i) that the transfer of conductive heat is one-directional in the liquid phase, as well as in the solid phase; (ii) that the bi-phase interface is flat and the phase change is reversible and isothermal: hysteresis phenomena are excluded; (iii) the absence of subcooling phenomena and of phase segregation; (iv) that the thermophysical properties of the PCM are constant with the temperature, but different in the solid and liquid phase; (v) that the difference of density between the solid phase and the liquid phase is negligible. The temperature and heat flux fields and the bi-phase interface position are expressed through a Fourier series expansion. The steady thermal field and the fluctuating thermal field in the two phases are obtained separately. The analytical solution of such a Stefan problem is reported in a synthetic form in Section 2.1.2, while the resolution procedure of the model and some applications of the solution are reported in detail in [35].

#### 2.1.2. Constitutive equations of the analytical model

With reference to figure (1-I), the equations of the model are:

- *General equation of conduction in phase (a) and in phase (b)*

$$\frac{\partial^2 T_a}{\partial x^2} - \frac{1}{\alpha_a} \frac{\partial T_a}{\partial t} = 0 \quad 0 < x < X_M(t) \quad \frac{\partial^2 T_b}{\partial x^2} - \frac{1}{\alpha_b} \frac{\partial T_b}{\partial t} = 0 \quad X_M(t) < x < L \quad (1)$$

with  $X_M(t)$  position of the bi-phase interface,  $T$  temperature at abscissa  $x$  and at time  $t$ ,  $\alpha = \lambda/(\rho c)$  thermal diffusivity,  $\lambda$  thermal conductivity,  $\rho$  density,  $c$  specific heat capacity and  $L$  thickness of the layer. Subscripts (a) and (b) indicate the two phases.

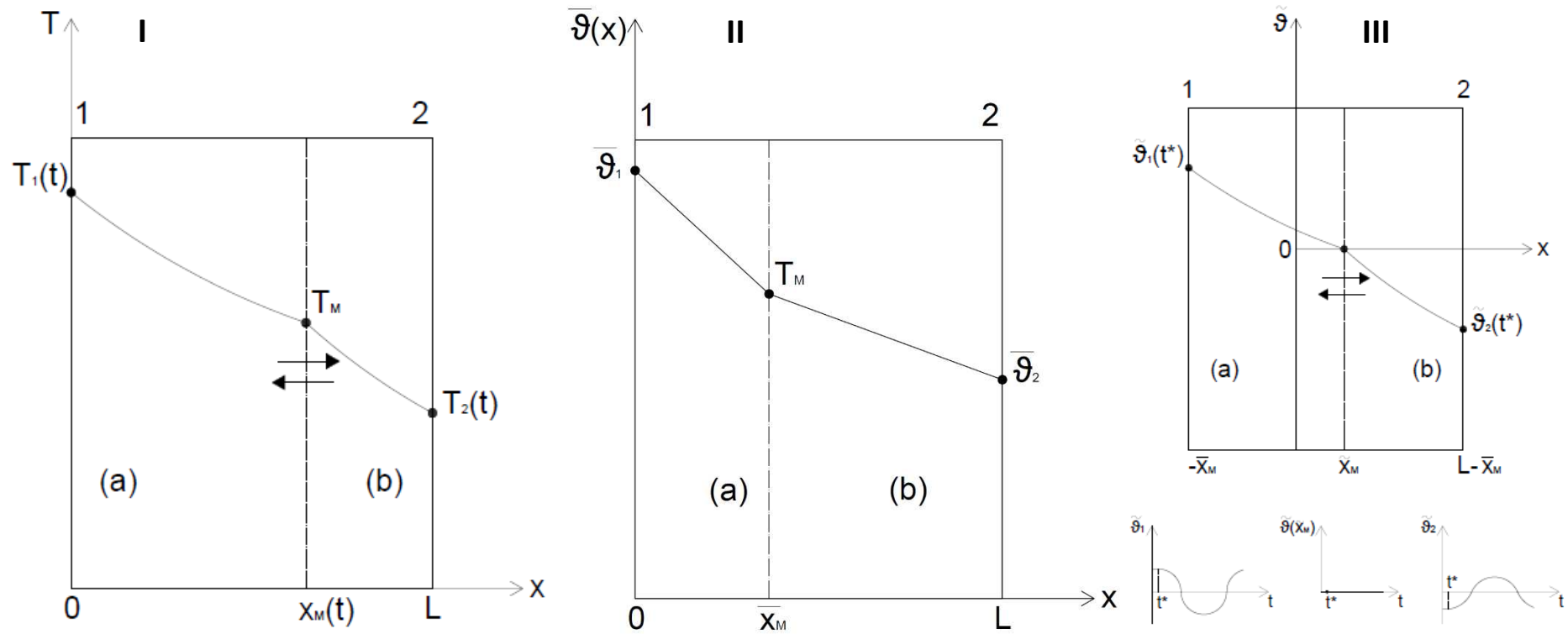


Figure 1 – Reference system of the bi-phase interface position, boundary conditions and temperature trend in the liquid phase a) and in the solid phase b) in the PCM layer; I) Total trend; II) steady component; III) oscillating component.

- *Stefan conditions at the bi-phase interface:*

$$\left[ \lambda_a \frac{\partial T_a}{\partial x} - \lambda_b \frac{\partial T_b}{\partial x} \right]_{x=X_M} = \rho H \frac{dX_M}{dt} \quad (2)$$

$$T_a(X_M, t) = T_b(X_M, t) = T_M \quad (3)$$

In Eq. (2)  $H$  is the latent heat of fusion (J/kg) and  $dX_M/dt$  the advancement velocity of the bi-phase interface at the melting temperature  $T_M$ .

The periodic boundary conditions in terms of temperature on face 1 of abscissa  $x = 0$  of layer (a) and on face 2 of abscissa  $x = L$  of layer (b), using the harmonic method are:

$$T_a(0, t) = T_1(t) = \bar{\vartheta}_1 + \vartheta_1(t) = \bar{\vartheta}_1 + \sum_{k=1}^n \tilde{\vartheta}_{1k}(t) \quad (4)$$

$$T_b(L, t) = T_2(t) = \bar{\vartheta}_2 + \vartheta_2(t) = \bar{\vartheta}_2 + \sum_{k=1}^n \tilde{\vartheta}_{2k}(t) \quad (5)$$

with  $\bar{\vartheta}$  temperature steady component,  $\vartheta(t)$  fluctuation of null mean value,  $k$  order and  $n$  number of harmonics  $\tilde{\vartheta}_k(t)$ .

In such conditions, the thermal field in the layer is steady periodic and is placed in the form:

$$T(x, t) = \bar{\vartheta}(x) + \vartheta(x, t) = \bar{\vartheta}(x) + \sum_{k=1}^n \tilde{\vartheta}_k(x, t) = \bar{\vartheta} + \sum_{k=1}^n |\tilde{\vartheta}_k| \text{sen}(k\omega t + \varphi_k) \quad (6)$$

$$F(x, t) = \bar{\phi} + \phi(x, t) = \bar{\phi} + \sum_{k=1}^n \tilde{\phi}_k(x, t) = \bar{\phi} + \sum_{k=1}^n |\tilde{\phi}_k| \text{sen}(k\omega t + \psi_k) \quad (7)$$

with  $\bar{\vartheta}(x)$  and  $\bar{\phi}$  respectively steady component of the temperature at abscissa  $x$  and steady component of the heat flux,  $\vartheta(x, t)$  and  $\phi(x, t)$  fluctuations of the null mean value at abscissa  $x$  and time  $t$ ,  $\tilde{\vartheta}_k(x, t)$  and  $\tilde{\phi}_k(x, t)$  sinusoidal components with amplitude  $|\tilde{\vartheta}_k|$  and  $|\tilde{\phi}_k|$ , with argument  $\varphi_k$  and  $\psi_k$  and with pulsation  $k\omega$ .

The bi-phase interface also presents a periodic trend:



$$X_M(t) = \bar{\chi}_M + \chi_M(t) = \bar{\chi}_M + \sum_{k=1}^n \tilde{\chi}_{M_k}(t) = \bar{\chi}_M + \sum_{k=1}^n |\tilde{\chi}_{M_k}| \text{sen}(k\omega t + \zeta_k) \quad (8)$$

with  $\bar{\chi}_M$  steady component of the bi-phase interface around which oscillates fluctuation  $\chi_M(t)$ , expressed as the sum of  $n$  harmonics  $\tilde{\chi}_{M_k}(t)$  of amplitude  $|\tilde{\chi}_{M_k}|$  and of argument  $\zeta_k$ .

The steady contribution of the solution is obtained by resolving the equation of conduction in the solid phase and in the liquid phase with the bi-phase interface at the melting temperature  $T_M$  of abscissa  $\bar{\chi}_M$ , not depending on time, and steady boundary conditions  $\bar{\vartheta}_1$  and  $\bar{\vartheta}_2$ .

The resolution of the oscillating thermal field, with reference to a generic harmonic, is obtained with the phasors method. Each generic harmonic  $\tilde{\vartheta}_k$ ,  $\tilde{\Phi}_k$ ,  $\tilde{\chi}_{M_k}$  of pulsation  $k\omega$ , is represented by means of the imaginary part of the relative phasor written in the complex form. For the temperature:

$$\hat{\vartheta}_k = |\hat{\vartheta}_k| [\cos(k\omega t + \varphi_k) + j \text{sen}(k\omega t + \varphi_k)] = |\hat{\vartheta}_k| e^{j\varphi_k} e^{jk\omega t} \quad (9)$$

with  $|\hat{\vartheta}_k| = |\tilde{\vartheta}_k|$  and  $\arg(\hat{\vartheta}_k) = \arg(\tilde{\vartheta}_k)$ .

Table 1 reports the resolute equations of the steady model, with reference to Figure (1-II), and of the oscillating model, with reference to Figure (1-III). In particular, the table contains: the equation of the conduction in the liquid phase and in the solid phase, the Stefan conditions at the bi-phase interface and the boundary conditions on the two external faces that delimit the layer.

In the table, the spatial coordinate in the reference system of the steady model is indicated with  $x$ , with origin on face 1, while in that of the oscillating model, it is indicated with  $x^*$ , with origin in correspondence of the steady component of the position of the bi-phase interface. The two coordinates are bound by the relation  $x^* = x - \bar{\chi}_M$ . The total temperature and heat flux field, with reference to a single harmonic, are obtained respectively with the relations:

$$T(x, t) = \bar{\vartheta}(x) + \tilde{\vartheta}(x - \bar{\chi}_M, t) \quad (10)$$

$$F(x, t) = \bar{\Phi} + \tilde{\Phi}(x - \bar{\chi}_M, t)$$

in which the oscillating component is reported in the reference system of the steady component.

Table 1 - Constitutive equations of the steady model and of the oscillating model.

	Steady model	Oscillating model
Spatial coordinate	$0 \leq x \leq L$	$-\bar{\chi}_M \leq x^* \leq L - \bar{\chi}_M$
Equation of the heat conduction in phase a) and in phase b)	$\frac{d^2 \bar{\vartheta}_a(x)}{dx^2} = 0 \quad 0 \leq x \leq \bar{\chi}_M$ (11)	$\frac{d^2 \hat{\vartheta}_a}{dx^{*2}} - \frac{j\omega}{\alpha_a} \hat{\vartheta}_a = 0 \quad -\bar{\chi}_M \leq x^* \leq 0$ (16)
	$\frac{d^2 \bar{\vartheta}_a(x)}{dx^2} = 0 \quad \bar{\chi}_M \leq x \leq L$ (12)	$\frac{d^2 \hat{\vartheta}_b}{dx^{*2}} - \frac{j\omega}{\alpha_b} \hat{\vartheta}_b = 0 \quad 0 \leq x^* \leq L - \bar{\chi}_M$ (17)
Stefan conditions at the bi-phase interface	$\left[ \lambda_a \frac{d\bar{\vartheta}_a}{dx} - \lambda_b \frac{d\bar{\vartheta}_b}{dx} \right]_{x=\bar{\chi}_M} = 0$ (13)	$\left[ \lambda_a \frac{d\hat{\vartheta}_a}{dx} - \lambda_b \frac{d\hat{\vartheta}_b}{dx} \right]_{x=\hat{\chi}_M} = j\omega\rho H\hat{\chi}_M$ (18)
	$\bar{\vartheta}_a(\bar{\chi}_M) = \bar{\vartheta}_b(\bar{\chi}_M) = T_M$ (14)	$\hat{\vartheta}_a(\hat{\chi}_M) = \hat{\vartheta}_b(\hat{\chi}_M) = 0$ (19)
Boundary conditions	$\bar{\vartheta}_a(0) = \bar{\vartheta}_1 \quad x = 0$ $\bar{\vartheta}_b(L) = \bar{\vartheta}_2 \quad x = L$ (15)	$\hat{\vartheta}_a(-\bar{\chi}_M) = \hat{\vartheta}_1 \quad x^* = -\bar{\chi}_M$ $\hat{\vartheta}_b(L - \bar{\chi}_M) = \hat{\vartheta}_2 \quad x^* = L - \bar{\chi}_M$ (20)

The steady thermal field is that in a slab with two layers, one in solid phase and the other in liquid phase, with temperature  $\bar{\vartheta}_1$  and  $\bar{\vartheta}_2$  assigned on the two faces of the boundary, and with thicknesses defined by the steady component of the bi-phase interface.

For the oscillating thermal field, the use of the phasors method allows transformation of the partial differential equation, which describes heat conduction in the solid phase and in the liquid phase and the discontinuity of the heat flux at the bi-phase interface, in ordinary differential equations. Substituting the boundary conditions in the general solution of the ordinary differential equations that describe heat conduction in the two phases, a system of algebraic equations is obtained. The resolution of such a system provides the phasor associated with the oscillating component of the position of the bi-phase interface, which is successively used to determine the phasors associated with the thermal field.

Table 2 reports the solution of the steady model and of the oscillating model.

Table 2 - Solution of the steady model and of the oscillating model.

	Solution of the steady model	Solution of the oscillating model
Position of the bi-phase interface	$\bar{\chi}_M = \frac{\lambda_a(\bar{\vartheta}_1 - T_M)}{\lambda_a(\bar{\vartheta}_1 - T_M) + \lambda_b(T_M - \bar{\vartheta}_2)} L \quad (21)$	$\frac{\lambda_a \gamma_a}{\sinh[\gamma_a(\bar{\chi}_M + \hat{\chi}_M)]} \hat{\vartheta}_1 + \frac{\lambda_b \gamma_b}{\sinh[\gamma_b(L - \bar{\chi}_M - \hat{\chi}_M)]} \hat{\vartheta}_2 = j\omega\rho H \hat{\chi}_M \quad (25)$
Heat flux field in phase (a) and in phase (b)	$\bar{\Phi}_a = \bar{\Phi}_b = \bar{\Phi} = \frac{\bar{\vartheta}_1 - \bar{\vartheta}_2}{\frac{\bar{\chi}_M}{\lambda_a} + \frac{L - \bar{\chi}_M}{\lambda_b}} \quad (22)$	$\hat{\Phi}_a(x^*) = -\lambda_a \gamma_a \hat{\vartheta}_1 \left\{ \sinh[\gamma_a(x^* + \bar{\chi}_M)] - \frac{\cosh[\gamma_a(x^* + \bar{\chi}_M)]}{\tanh[\gamma_a(\bar{\chi}_M + \hat{\chi}_M)]} \right\} \quad -\bar{\chi}_M \leq x^* \leq - \hat{\chi}_M  \quad (26)$
		$\hat{\Phi}_{ab}(x^*) = \frac{(L - x) \hat{\Phi}_a(x^*) + x \hat{\Phi}_b(x^*)}{L} \quad - \hat{\chi}_M  \leq x^* \leq  \hat{\chi}_M  \quad (27)$
		$\hat{\Phi}_b(x^*) = \lambda_b \gamma_b \hat{\vartheta}_2 \left\{ \sinh[\gamma_b(L - \bar{\chi}_M - x^*)] - \frac{\cosh[\gamma_b(L - \bar{\chi}_M - x^*)]}{\tanh[\gamma_b(L - \bar{\chi}_M - \hat{\chi}_M)]} \right\} \quad  \hat{\chi}_M  \leq x^* \leq L - \bar{\chi}_M \quad (28)$
Temperature field in phase (a) and in phase (b)	$\bar{\vartheta}_a(x) = T_M + \frac{\bar{\chi}_M - x}{\lambda_a} \bar{\Phi} \quad 0 \leq x \leq \bar{\chi}_M \quad (23)$	$\hat{\vartheta}_a(x^*) = \hat{\vartheta}_1 \left\{ \cosh[\gamma_a(x^* + \bar{\chi}_M)] - \frac{\sinh[\gamma_a(x^* + \bar{\chi}_M)]}{\tanh[\gamma_a(\bar{\chi}_M + \hat{\chi}_M)]} \right\} \quad -\bar{\chi}_M \leq x^* \leq - \hat{\chi}_M  \quad (29)$
		$\hat{\vartheta}_{ab}(x^*) = \frac{(L - x^*) \hat{\vartheta}_a(x^*) + x \hat{\vartheta}_b(x^*)}{L} \quad - \hat{\chi}_M  \leq x^* \leq  \hat{\chi}_M  \quad (30)$
	$\bar{\vartheta}_b(x) = T_M - \frac{x - \bar{\chi}_M}{\lambda_b} \bar{\Phi} \quad \bar{\chi}_M \leq x \leq L \quad (24)$	$\hat{\vartheta}_b(x^*) = \hat{\vartheta}_2 \left\{ \cosh[\gamma_b(L - \bar{\chi}_M - x^*)] - \frac{\sinh[\gamma_b(L - \bar{\chi}_M - x^*)]}{\tanh[\gamma_b(L - \bar{\chi}_M - \hat{\chi}_M)]} \right\} \quad  \hat{\chi}_M  \leq x^* \leq L - \bar{\chi}_M \quad (31)$

In the table with  $\gamma_a=(1+j)(\omega/2\alpha_a)^{1/2}$  and  $\gamma_b=(1+j)(\omega/2\alpha_b)^{1/2}$  the propagation constants in the two phases are indicated.

The steady solution defines the position of the bi-phase interface  $\bar{\chi}_M$  (Eq. 21), the temperature field in the two phases  $\bar{\vartheta}_a(x)$  and  $\bar{\vartheta}_b(x)$  (Eqs. 23 and 24), and the transferred heat flux  $\bar{\phi}_a = \bar{\phi}_b = \bar{\phi}$  (Eq. 22).

The oscillating solution is represented: by the equation for the determination of the phasor associated with the oscillating component of the bi-phase interface  $\hat{\chi}_M$  (Eq. 25); by the phasors, function of the phasor  $\hat{\chi}_M$ , associated with the oscillating temperature  $\hat{\vartheta}_a(x^*)$ ,  $\hat{\vartheta}_{ab}(x^*)$  and  $\hat{\vartheta}_b(x^*)$  (Eqs. 29, 30 and 31) and oscillating thermal flux  $\hat{\phi}_a(x^*)$ ,  $\hat{\phi}_{ab}(x^*)$  and  $\hat{\phi}_b(x^*)$  (Eqs. 26, 27 and 28), calculated in the two phases in the portion of the layer subject to phase change. The equation for the determination of  $\hat{\chi}_M$  is an implicit transcendental equation with complex parameters and unknowns, the solution of which cannot be expressed in symbolic explicit form. However, it is possible to determine it by means of dedicated algorithms once the parameter values are known. The oscillating components in the time domain are obtained successively considering only the imaginary part of the preceding phasors expressed in trigonometrical form.

The advancement velocity of the bi-phase interface  $\tilde{u}_M$  is obtained deriving the oscillating component of the bi-phase interface:

$$\tilde{u}_M = \frac{d\tilde{\chi}_M}{dt} = \text{Im}[j\omega\hat{\chi}_M e^{j\omega t}] = \omega|\hat{\chi}_M|\cos(\omega t + \zeta) \quad (32)$$

Substituting Eq. (32) in Eq. (18) the expression of the latent heat stored/released per unit time is obtained:

$$\tilde{\Phi}_H = \rho H \tilde{u}_M \quad (33)$$

## 2.2. Equipment for testing steady and dynamic response of a PCM layer

### 2.2.1. Experimental device

The experimental set-up used for the tests (Figure 2) is constituted by a wooden structure with external dimensions of 32 cm x 28 x 61 cm. All the exterior wooden panels (3 mm) are insulated with 3.5 cm of vacuum panels (thermal resistance = 0.14 m<sup>2</sup>·K/W) and 2 cm of Pyrogel (k = 0.013 W/m K). The internal volume of the structure is divided into two separate air cavities (upper and lower) by a sample holder made of XPS insulation (19 x 19 x 8 cm). A cylindrical hole with dimensions of Ø 75 × 75 mm and two heat-flux meters located on the bottom and top of the sample holder retain the PCM sample in both liquid and solid phases. The

insulating layer allows the lateral surface of the cylinder to be almost adiabatic and obtain a unidirectional heat flux in the axial direction. The two air cavities constitute controlled environments, heated or cooled by means of copper coils connected to two programmable water baths able to simulate different thermal conditions ranging from  $-10\text{ }^{\circ}\text{C}$  to  $140\text{ }^{\circ}\text{C}$ . The temperature of each bath is regulated by hot or cold water flows produced in an individual heater/cooler system. This experimental equipment was developed at GREA Innovació Concurrent, University of Lleida (Spain) and was used by de Gracia et al. [27] in an earlier work to evaluate the improvement in the thermal behaviour by impregnating a PCM in a conventional gypsum board.

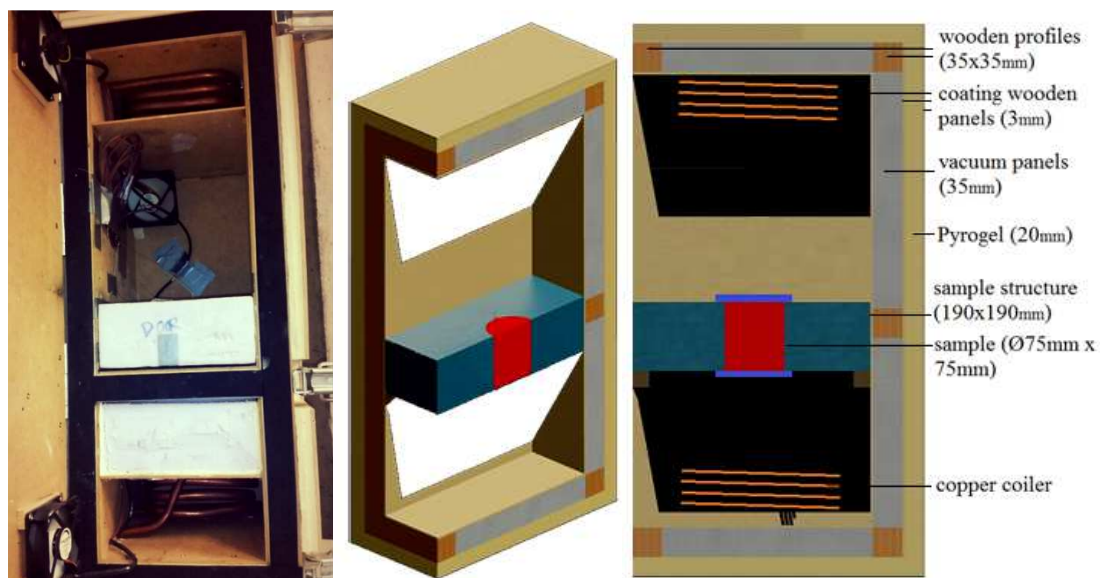


Figure 2 - Sections of the experimental device scheme design.

The measurement of the heat flux on the two faces of the cylindrical sample of PCM is obtained by two heat flux meters (Hukseflux HFP01) with a diameter of 7.5 cm with an accuracy of  $\pm 5\%$ . These two heat flux meters allow testing one-dimensional heat transfer. In these conditions, the steady component (mean value) of the periodic heat flux on the upper surface is equal to that on the bottom surface. The temperature in the sample is measured using  $\text{Ø } 0.5\text{ mm}$  thermocouples type T, with an error of  $\pm 0.75\%$ , in correspondence with the axis, on the upper face (top point) and lower (bot point), and within the layer at 3 different heights (points 2, 3 and 4). The location of the previously introduced sensors is shown in Figure 3. A data logger acquires and registers the measured thermal quantity every 10 seconds.

The surface heat fluxes and the temperatures along the axis of the sample are used for the thermal analysis in a steady regime and in a transient regime for the evaluation of the

thermophysical properties of the PCM, and in a steady periodic regime for validation of the analytical model.

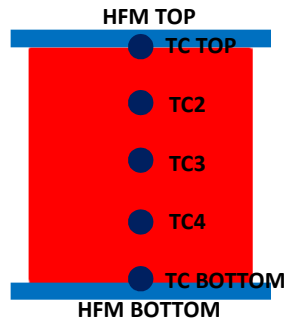


Figure 3- Position of the thermocouples TC and of the heat flux meters HFM in the cylindrical PCM sample.

### 2.2.2. Description of the PCM sample holder Pure Temp 23

The material considered in this study is the commercial PCM PureTemp23, provided by Entropy Solutions [36]. According to the manufacturer, the material presents consistent and repeatable performance over thousands of thermal (melt/solidify) cycles; it is 100% renewable, non-toxic and biodegradable since it is produced from natural agricultural sources (such as palm oil, palm kernel oil, rapeseed oil, coconut oil, and soybean oil). It does not undergo phase segregation and supercooling, the phenomenon in which a substance cools below its freezing point without solidifying.

The thermophysical properties and DSC curve of the Puretemp23 provided by the manufacturer, obtained with a heating rate of  $1^{\circ}\text{C}/\text{min}$ , are reported in Figure 4.

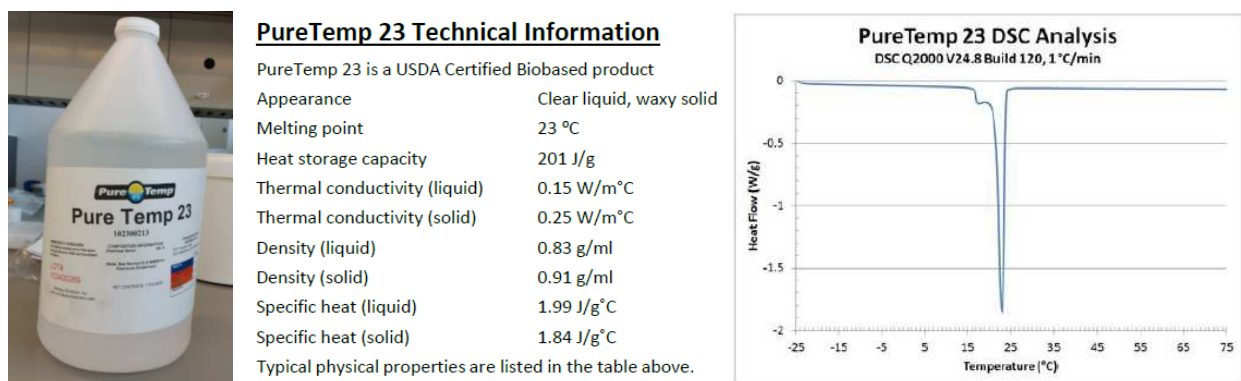


Figure 4 - PCM PureTemp23, thermophysical properties and DSC curve with an heating rate of  $1^{\circ}\text{C}/\text{min}$  [36].

In order to investigate the variability of the melting temperature range and of the latent heat (J/kg) upon variation of the heating/cooling rate, three tests were conducted ( $0.5\text{ K}/\text{min}$ ,  $5\text{ K}/\text{min}$  and  $10\text{ K}/\text{min}$ ), with the DSC method in the GREA Innovació Concurrent center laboratory. The

DSC technique has been widely used to determine the thermophysical properties of different PCM [37, 38] and allows the evaluation of the stored heat trend per time unit and per mass unit upon variation of the temperature. In this study, the DSC has been used for two purposes. The first experiments were designed to investigate the variability of the phase change temperature and of the latent heat (J/kg) upon variation of the heating/cooling rate. In this case three dynamic tests were conducted at 0.5 K/min, 5 K/min, and 10 K/min. The second experiments were designed to determine the specific heat capacity ( $c$ ) at different temperatures in both phases, liquid and solid phase. The methodology to determine the  $c$  follows the one published by Ferrer et al. [39]. A Mettler Toledo DSC 822e was used to perform all the experiments. Two samples of the selected PCM for each experiment were tested under the same conditions to ensure repeatability of the results. The samples were placed in 40 $\mu$ l closed aluminium crucibles under 200 ml/min N<sub>2</sub> flow. Each sample mass was around 12 mg weighed in a Mettler Toledo AG135 analytical balance with a precision of 0.01 mg.

The DSC program for the PCM under study, in the case of a heating/cooling rate equal to 0.5 K/min, is reported in Figure 5a, while the DSC response, for sample 1, in Figure 5b is reported.

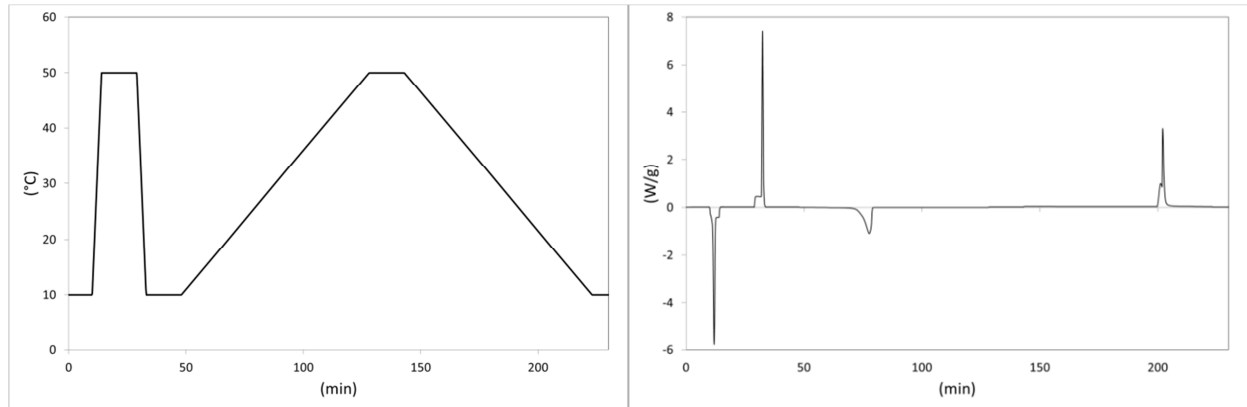


Figure 5 - a) DSC program to obtain the heat latent of fusion and of solidification, and the solidification and melting temperatures. b) DSC response. Sample 1 of PureTemp 23 and heating/cooling rate equal to 0.5 K/min.

A first fast melting and freezing cycle is performed to homogenise the sample and it is not taken into account for determination of the properties (see Figure 5a). The latent heat of fusion and solidification by integration of the area under each peak of the heat stored per unit time and per unit mass is obtained, while the melting temperature by the temperature in correspondence of the peak value is identified.

Table 3 summarizes the experimental results for the two samples in terms of the latent heat of fusion  $H_{\text{fus}}$  and of solidification  $H_{\text{sol}}$ , and of melting  $T_{\text{fus}}$  and of solidification  $T_{\text{sol}}$  temperature, the arithmetic mean values and the standard deviation, for different heating/cooling rates.

Table 3 - Summary of the DSC results for the two samples of PureTemp23 at 0.5 K/min, 5 K/min and 10 K/min.

	0.5 K/min				5 K/min				10 K/min			
Sample	$H_{\text{fus}}$ (kJ/kg)	$H_{\text{sol}}$ (kJ/kg)	$T_{\text{fus}}$ (°C)	$T_{\text{sol}}$ (°C)	$H_{\text{fus}}$ (kJ/kg)	$H_{\text{sol}}$ (kJ/kg)	$T_{\text{fus}}$ (°C)	$T_{\text{sol}}$ (°C)	$H_{\text{fus}}$ (kJ/kg)	$H_{\text{sol}}$ (kJ/kg)	$T_{\text{fus}}$ (°C)	$T_{\text{sol}}$ (°C)
1	215.61	219.1	24.57	21.31	198.65	200.62	24.88	18.17	200.05	200.63	25.91	16.80
2	215.87	214.09	24.46	21.1	200.51	199.65	24.89	18.39	195.41	195.48	26.23	16.77
mean	215.74	216.60	24.52	21.21	199.58	200.14	24.89	18.28	197.73	198.06	26.07	16.79
sd	0.18	3.54	0.08	0.15	1.32	0.69	0.01	0.16	3.28	3.64	0.23	0.02

Latent heat and phase change temperature results of PureTemp 23 obtained by DSC are repeatable, presenting a standard deviation of less than 3.7 kJ/kg for the latent heat and less than 0.16 °C for the phase change temperature in all the different analyses obtained when varying the heating/cooling rate. Moreover, no remarkable differences ( $< 3.4$  °C) between melting and solidification temperatures are observed when applying a heating rate of 0.5 K/min. Nonetheless, this temperature difference becomes significant when increasing the heating/cooling rate, reaching a difference of around 10 K between  $T_{\text{fus}}$  and  $T_{\text{sol}}$  in the case of 10 K/min. This could be due to the sample not achieving thermal equilibrium when applying high heating/cooling rates and also for the crystallization process. This behaviour upon variation of the heating/cooling rate is confirmed in other works available in the scientific literature [40-42]. It is noteworthy that the latent heat provided by the manufacturer, 201 J/g at 1 K/min (see Figure 4), is between the latent heat presented in this chapter (see Table 3) at 0.5 and 5 K/min. On the contrary, this trend is not observed for the melting temperature, with a difference of 1.52 K and 1.89 K between the manufacturer value and the results presented here at 0.5 and 5 K/min, respectively.

In summary, in the case of PureTemp 23, upon diminishment of the heating/cooling rate, the melting temperature decreases, the solidification temperature increases and the phase change temperature range reduces, while the latent heat of fusion is very close to that of solidification in all the different tests, and upon the decrease of the heating/cooling rate undergoes a slight increase. The performed analysis allowed for the establishment that, in the case of PureTemp 23, the experimental tests to be conducted for the validation of the analytical model are necessary to be performed at heating/cooling rates equal or lower than 0.5 K/min. This allows obtaining a



reduced difference between the melting temperature and the solidification temperature and to contain the phase change temperature range.

The program developed to obtain the  $c$ , in both the liquid and solid phase, consists in temperature steps of  $1\text{ }^{\circ}\text{C}$  with constant temperature segments in between to let the sample reach thermal equilibrium (see Images on the top in Figure 6).

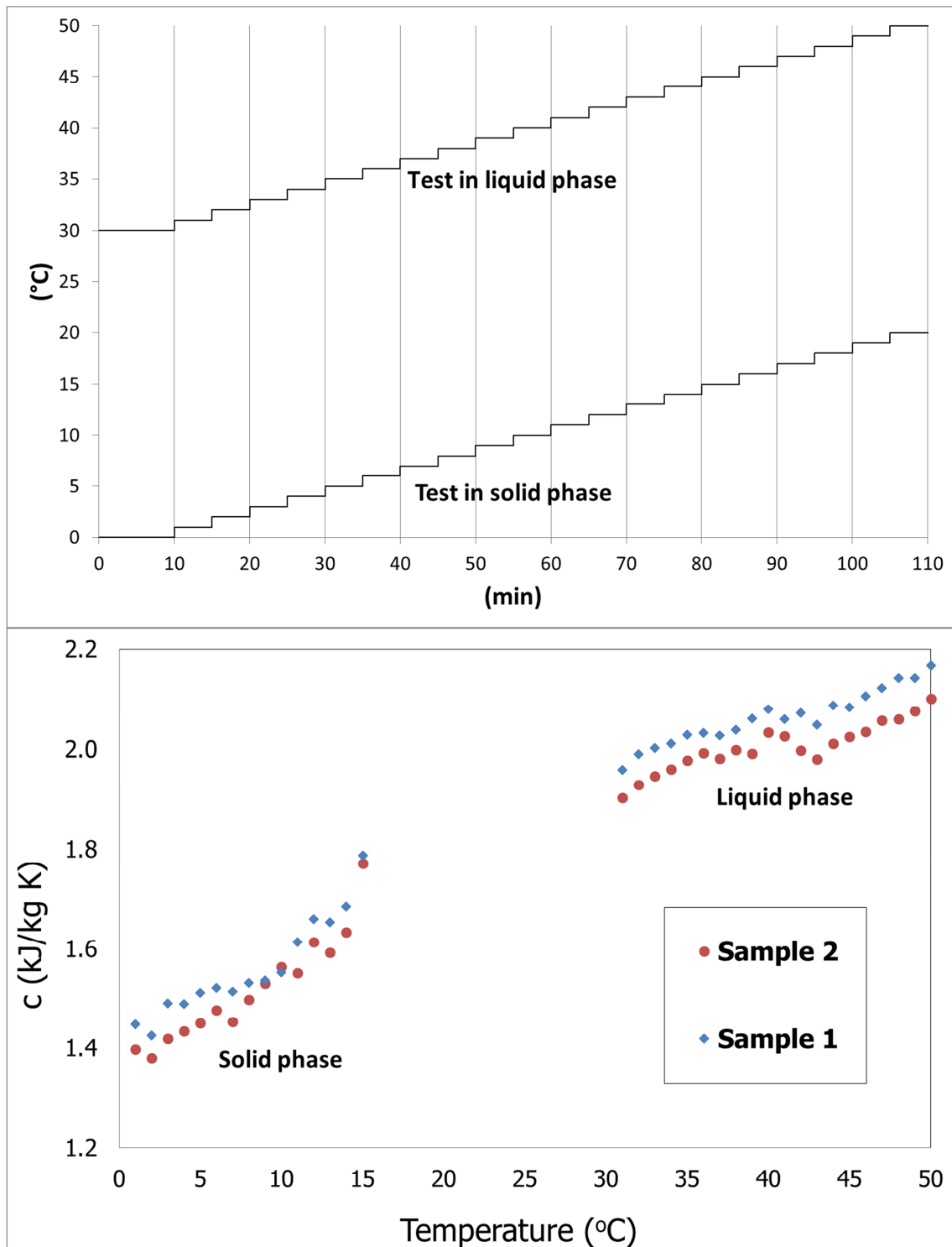


Figure 6 - On the top: DSC Program to obtain  $C_p$  as a function of temperature in solid phase and in liquid phase.

*On the bottom: specific heat capacity as a function of the temperature for the solid phase and liquid phase in the case of Sample 1 and Sample 2.*

The specific heat capacity as a function of temperature for sample 1 and for sample 2 can be observed in Figure 6 on the bottom. The  $c$  of PureTemp 23 is  $1.55 (\pm 0.01)$  kJ/kg·K at  $10\text{ }^{\circ}\text{C}$  and  $2.05 (\pm 0.03)$  kJ/kg·K at  $40\text{ }^{\circ}\text{C}$ . The results obtained with the two samples are in agreement ensuring repeatability of the results. The manufacturer provides the  $c$  at both phases without specifying at which temperature are measured. Nevertheless, if these results are compared, they are also in agreement especially for the liquid phase, which presents a difference of  $0.06$  kJ/kg·K whereas for the solid phase is  $0.29$  kJ/kg·K.

### 2.2.3. Setting of the experiments

#### *Evaluation of the PCM density in liquid and solid phase*

Two samples (A and B) of PCM with volumes equal to 100ml and 250ml and corresponding mass of 83.1g and 207.8g placed in two cylindrical glass containers were used for the determination of the density of the liquid phase. The density of the liquid phase of sample A resulted as being equal to  $0.831$  g/ml while that of sample B is equal to  $0.819$  g/ml. The different values can mainly be attributed to errors in the measurement of the volume. In the subsequent calculations, a value equal to  $0.831$  g/ml was assumed, in accordance with the value provided by the manufacturer.

In order to evaluate PCM density in the solid phase, it is necessary to identify the entity of the variation of volume of the sample and the form that the upper surface assumes due to the effect of the liquid-solid phase change. For each of the preceding samples, two tests were conducted cooling the samples in a cooling cell at a temperature of  $7\text{ }^{\circ}\text{C}$ . In order to avoid a possible introduction of liquid water present inside the cooling cell due to condensation phenomena the glass was covered with an elastic film.

Following the phase change, it was found that the upper surface of the PCM, initially flat in the liquid phase, contracts assuming the shape of a spherical cap with the level of the PCM layer in contact with the lateral surface of the glass unchanged, and a gradually increasing proceeding towards the cylinder axis. We took into consideration that, at the interface with the external air, the solid phase assumed a non-flat shape, schematically shown as a spherical cap, to determine the variation in volume compared to the liquid phase consequent to the phase change. The results obtained through the four tests are reported in Table 4.

Table 4 – Tests conducted with sample A and sample B, volume variation following liquid-solid phase change, solid phase volume, solid phase density.

	TEST	Volume variation $\Delta V$ [ml]	$V_s$ [ml]	$\rho_s$ [g/ml]
CAMPIONE A	1	4.97	95.03	0.874
	2	4.97	95.03	0.874
CAMPIONE B	1	11.33	238.67	0.858
	2	10.37	239.63	0.855
Mean value				0.865

Following the phase change, it was found that the volume variation is contained and is always less than 5%. The density value provided in the solid phase by the manufacturer results as being 5% higher compared to the mean value measured.

#### *Preparation of the sample holder in the experimental device*

In the preparation of the sample, it was necessary to prevent the PCM in the liquid phase from coming out of the sample holder. The liquid leakage in the experimental device was avoided by the use of a double cylinder layer of impermeable film.

Instead, in order to avoid modification of the shape of the upper surface of the cylindrical sample, and the formation of an air cavity between the same surface and the heat flux meter, an enlargement of the diameter for a depth of 1 cm was created in the insulating layer where the sample is located. This allowed the position of the heat flux meter to be made mobile; it can move downwards following the contraction of the volume consequent to the phase change, to maintain direct contact with the PCM also in the solid phase. Furthermore, the enlargement of the diameter prevents the heat flux meter from falling into the liquid phase PCM. A similar enlargement with a reduced depth was also used at the base of the insulation layer around the hole for the placement of the second heat flux meter. The direct contact between the heat flux meter and the PCM is, in this case, ensured by the action of gravity.

#### *Evaluation of the effective PCM length in the test box*

The liquid phase PCM sample used in the experimental device has a mass of  $m = 234.1$  g and a Diameter  $D = 7.1$  cm. Considering the density value measured in the liquid phase, the height of the cylindrical sample results as being equal to 7.11 cm.

#### *Dependence of the temperature of the sample holder from the thermal baths temperatures*

A series of preliminary tests were conducted in the experimental device with the PCM sample installed in order to determine the bath temperature which feeds the coil placed in the

upper cavity of the experimental device  $T_{hf}$ , and that of the bath which supplies the coil placed in the lower cavity of the experimental device  $T_{cf}$ , necessary to obtain a uniform temperature distribution and equal to  $T_{sample}$  in the sample. This calibration is necessary to take into account the heat losses towards the external environment or the heat fluxes from the external environment at temperature  $T_{env}$  through the boundary surfaces of the bath, the surfaces of the conduits that supply the coils, and the surfaces of the walls that delimit the two cavities of the experimental device. In order to obtain a uniform temperature in the sample, the temperatures required of the two baths are different as the thermal losses/heat gains undergone by the two coil supply flows, being different the lengths of tubing, and the heat losses/heat gains through the walls of the two chambers, which have a different volume. The relations obtained, following preliminary tests, for the calculation of the temperature of the two baths  $T_{cf}$  and  $T_{hf}$  in function of the external environment temperature and the temperature of the sample are:

$$T_{cf} = T_{sample} - 6.5 \left( \frac{T_{env} - T_{sample}}{T_{env}} \right) \quad (34)$$

$$T_{hf} = T_{sample} - 10 \left( \frac{T_{env} - T_{sample}}{T_{env}} \right) \quad (35)$$

The successive tests conducted for the determination of thermophysical properties at the initial instant require a uniform temperature within the sample. Such a condition was achieved by determining the temperatures of the two baths with the Eqs. (34) and (35).

#### *Evaluation of the position of the thermocouples*

A test with the sample in the solid phase was conducted by setting two different temperature values on the upper and lower faces, in order to ascertain the exact placement of the thermocouples within the sample along the axis at different heights. After an initial transient, temperatures were detected corresponding to the steady condition at different heights. The measurements of the two steady surface temperatures  $T_{top}$  and  $T_{bot}$  were used to obtain a linear profile of the temperature in the layer, while the other temperature measurements within the sample  $T_2$ ,  $T_3$  and  $T_4$  were used to verify the position of the thermocouples along the axis. The relation used for the calculation of the position of a thermocouple  $x_{TC}$  at temperature  $T(x_{TC})$  is:

$$x_{TC} = \frac{T_{top} - T(x_{TC})}{T_{top} - T_{bot}} L \quad (36)$$

With  $T_{top}$  and  $T_{bot}$  equal respectively to 14.1 °C and 4.3°C and  $T(x_{TC2}) = 11.6$  °C,  $T(x_{TC3}) = 9.1$  °C and  $T(x_{TC4}) = 6.5$  °C, it resulted that  $x_{TC2} = 1.78$  cm,  $x_{TC3} = 3.63$  cm and  $x_{TC4} = 5.51$  cm.

### 2.3. Determination of the solid phase and liquid phase thermophysical properties in the experimental device

Experimental tests were conducted in the experimental device for the determination of the thermal conductivity and of the specific heat capacity in the solid and liquid phases, of the latent heat and of the phase change temperature. Such tests are necessary to compare the thermophysical properties provided by the manufacturer and those obtained in section 2.2.2 on a sample of a very reduced dimension (10-50 mg), with those on the same sample used for validation of the model, which has notably greater dimensions (234 g). As reported in Cheng et al. [28], the thermophysical properties could depend on the sample mass.

#### 2.3.1. Thermal conductivity and specific heat

Two tests were conducted for the determination of the thermal conductivity and of the specific heat. One test was conducted with the sample entirely in a solid phase and the other with the sample entirely in a liquid phase. The test consists of subjecting the sample to a thermal transient from an initial steady thermal state to a successive steady thermal state without allowing the phase change to occur. The temperature and heat flux trends measured on the two faces during the thermal transient regime are used to evaluate the specific heat, while the values corresponding to the final steady regime are used for calculation of thermal conductivity. Figure 7 shows a sketch of the temperature and heat flux trends on the two faces.

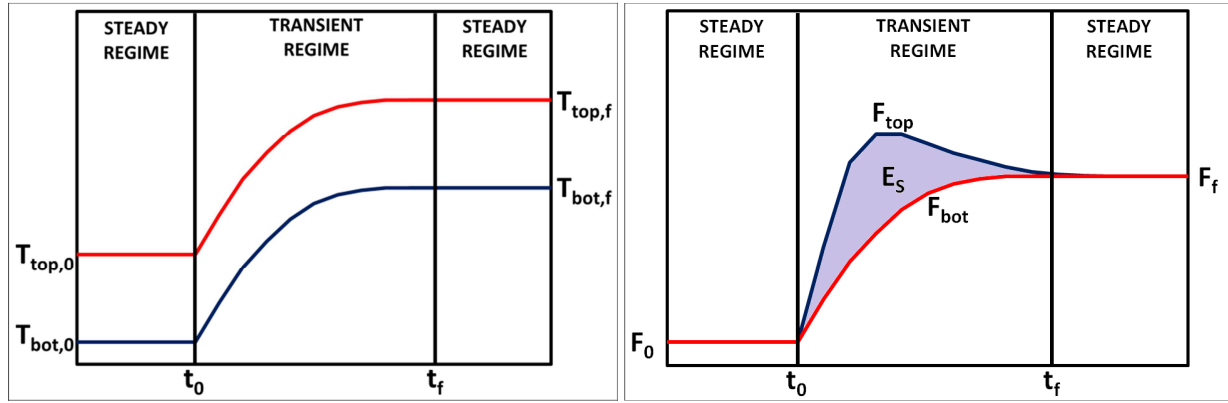


Figure 7 – Schematization of temperature trends  $T_{top}$  and  $T_{bot}$ , on the left, and of surface heat fluxes  $F_{top}$  and  $F_{bot}$  and of the stored sensible energy  $E_S$ , on the right, during the thermal transient between an initial steady state and a final steady state, to be used for the determination of the thermal conductivity and specific heat capacity in the two phases.

The thermal conductivity is obtained using the measurement of the heat flux  $F_f$  and that of the temperatures  $T_{top,f}$  and  $T_{bot,f}$  on the two faces of the sample with the relation:

$$\lambda = \frac{F_f L}{(T_{top,f} - T_{bot,f})} \quad (37)$$

The energy balance relating to the thermal transient between the initial instant  $t_0$ , with a linear temperature profile in the sample  $T_0(x)$ , and the final instant  $t_f$ , with a linear temperature profile in the sample  $T_f(x)$ , is expressed by the relation:

$$E_S = A \int_{t_0}^{t_f} (F_{top}(t) - F_{bot}(t)) dt = Apc \int_0^L [T_f(x) - T_0(x)] dx \quad (38)$$

The resolution of the preceding equation for the specific heat provides the relation:

$$c = \frac{A \int_{t_0}^{t_f} (F_{top}(t) - F_{bot}(t)) dt}{m \left[ \left( \frac{T_{top,0} + T_{bot,0}}{2} \right) - \left( \frac{T_{top,f} + T_{bot,f}}{2} \right) \right]} \quad (39)$$

The created procedure represents an advancement of the method used in de Gracia et al. [27] in that it allows for differentiation of the thermophysical properties in the two phases and also

allows the obtainment of both the thermal conductivity and specific heat with one experimental test.

### 2.3.2. Heat latent of fusion and phase change temperature

The experimental device was also used to determine the latent heat and the melting temperature. The tests conducted consist of a thermal transient with a solid-liquid phase change in the entire sample. The initial state is steady with a uniform temperature and the sample is in a solid phase, and the final state is also steady and the sample entirely in a liquid phase. Since the phase change at the different abscissae starts and ends in different time instants, the energy balance of the sample was obtained as the sum of the energetic balance of the subvolumes associated with the single thermocouples. With reference to Figure 8, if  $t_0$  and  $t_f$  are the initial and final instant of the thermal transient, the total energy stored by generic subvolume  $j$  of thickness  $\Delta x_j$ , expressed by the integral of the difference between the entering and exiting heat flux, is given by the sum: (i) of the sensible energy stored in the time intervals in which the subvolume is in the solid phase, between the instant  $t_0$  and  $t_{1,j}$ , and in liquid phase, between  $t_{2,j}$  and  $t_f$ , (ii) of the stored latent energy due to the phase change in the subvolume, in the interval  $(t_{1,j}, t_{2,j})$ . The sensible energy stored during the solid phase and during the liquid phase is obtained using the respective initial and final temperatures, while the latent energy stored is that corresponding to the phase change of the mass of subvolume  $m_j$ .

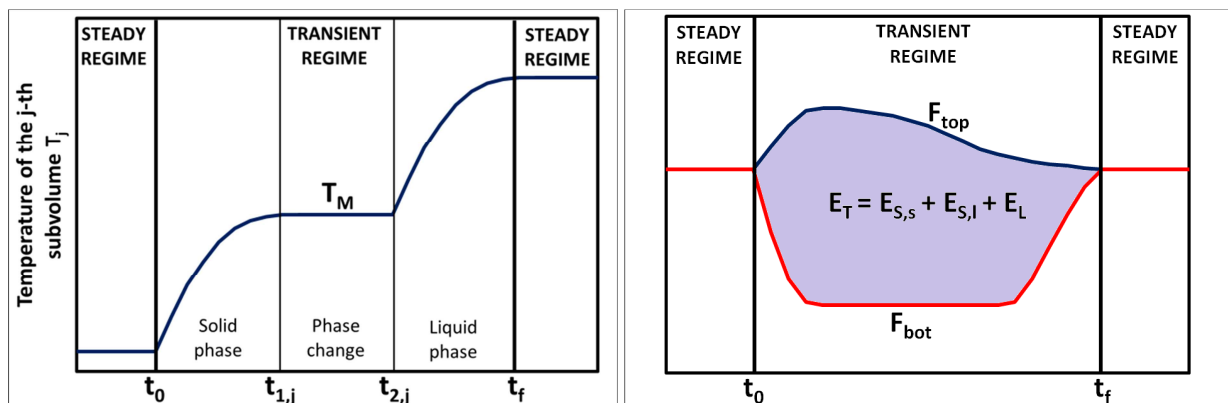


Figure 8 - Schematization of the temperature trend in a  $j$ -th node, on the left, and of the surface heat fluxes  $F_{top}$  and  $F_{bot}$  and of the total stored energy  $E_T$ , on the right, during the thermal transient between an initial steady state and a final steady state, to be used for the determination of the latent heat and of the phase change temperature.

For the entire sample, the total stored energy is obtained by summing the contributions of the  $n$  subvolumes:

$$\begin{aligned}
A \sum_{j=1}^n \int_{t_0}^{t_f} [F(x_j - \Delta x_j/2, t) - F(x_j + \Delta x_j/2, t)] dt \\
= \sum_{j=1}^n \left\{ \rho_s c_{p_s} A \int_{x_j - \Delta x_j/2}^{x_j + \Delta x_j/2} [T_j(t_{1,j}) - T_j(t_0)] dx \right\} + \sum_{j=1}^n \{m_j H\} + \\
+ \sum_{j=1}^n \left\{ \rho_l c_{p_l} A \int_{x_j - \Delta x_j/2}^{x_j + \Delta x_j/2} [T_j(t_f) - T_j(t_{2,j})] dx \right\} \quad (40)
\end{aligned}$$

Developing the summation at the first member, for the total stored energy  $E_T$  the following expression is obtained:

$$A \sum_{j=1}^n \int_{t_0}^{t_f} \left[ F\left(x_j - \frac{\Delta x_j}{2}, t\right) - F\left(x_j + \frac{\Delta x_j}{2}, t\right) \right] dt = A \int_{t_0}^{t_f} [F_{\text{top}}(t) - F_{\text{bot}}(t)] dt = A e_T = E_T \quad (41)$$

In the second member of Eq. (40), the first term represents the sensible energy stored in the solid phase  $E_{S,s}$ , the second term represents the stored latent energy  $E_L$  and the third term represents the sensible energy stored in the liquid phase  $E_{S,l}$ . Finally, resolving Eq. (40) for the latent heat  $H$  the following relation is obtained:

$$H = \frac{A(E_T - E_{S,s} - E_{S,l})}{m} \quad (42)$$

As regards the determination of the phase change temperature, for each subvolume, the temperature value in the interval  $(t_{1,j}, t_{2,j})$ , corresponding to the phase change, was considered.

### 3. Experimental test results for the determination of the thermophysical properties

#### 3.1. Thermal conductivity and specific heat

With reference to the method described in Section 2.3.1, for the determination of the thermal conductivity and of the specific heat in the solid phase, starting from a steady field in the



sample, which was made by setting the temperature in the hot bath at  $T_{hf} = -10^{\circ}\text{C}$  and that of the cold bath at  $T_{cf} = -6.5^{\circ}\text{C}$ ; at the initial instant  $t_0$  the temperature of the hot bath  $T_{hf}$  was modified and set equal to  $18^{\circ}\text{C}$ . For the determination of the thermal conductivity and of the specific heat in the liquid phase, the initial values of the thermal baths are  $T_{hf} = 33.5^{\circ}\text{C}$  and  $T_{cf} = 31.9^{\circ}\text{C}$  and, at initial instant  $t_0$ , the temperature  $T_{hf}$  was modified and set equal to  $90^{\circ}\text{C}$ .

The trends of temperatures at different heights and on the surface heat fluxes recorded during the thermal transient are reported for the solid phase, respectively in Figure 9a and Figure 9b, and for the liquid phase in Figure 9c and Figure 9d. The trends of the sensible energy stored per unit time, calculated as the difference between the surface heat fluxes, are reported in the images showing the trends of the surface heat fluxes.

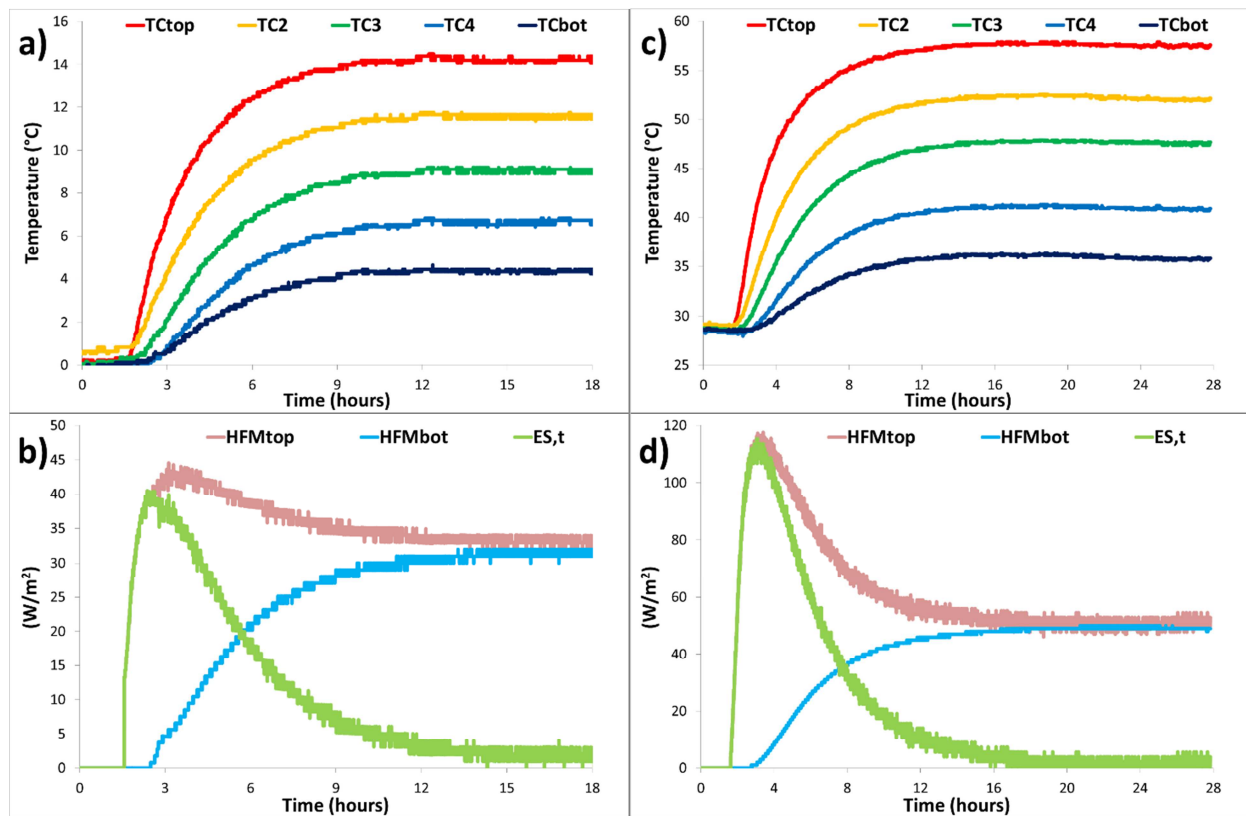


Figure 9 - Trends of the temperatures  $TC$  at different heights, of the surface heat fluxes  $HFM$  and of the sensible energy stored per unit time  $E_{S,t}$ . a) and b) solid phase; c) and d) liquid phase.

Figure 9 highlights that the thermal transient in the test with the sample in a solid phase has a duration of approximately 12 hours, (a) and (b), while in the test with the sample in a liquid phase, it has a duration of approximately 15 hours, (c) and (d). The different duration is due to the different specific heat capacity in the two phases and to the different excursion of temperature imposed at the initial time instant on the top surface.

In both tests the temperature trends and the bottom heat flux trend increase until to become constant once the final steady state was reached. The top heat flux increases at the beginning, it successively reaches a maximum value and at the end decreases and becomes constant in correspondence of the final steady state.

Table 5 presents a summary of the values of the initial and final temperatures and of final heat flux used for the calculation of the thermal conductivity and of the specific heat of the solid phase and the liquid phase, calculated with Eqs. (37, 39).

Table 5 – Measured values obtained of temperatures  $T_{top}$  and  $T_{bot}$  on the two faces of the sample at final instant  $t_f$  and initial instant  $t_0$  of the thermal transient, of steady heat fluxes  $F_f$  at final instant  $t_f$ , of the stored sensible energy  $E_s$ , of the thermal conductivity and of the specific heat, in the two experimental tests with the sample entirely in solid and in liquid phase.

	$T_{top,f}$ (°C)	$T_{bot,f}$ (°C)	$T_{top,0}$ (°C)	$T_{bot,0}$ (°C)	$F_f$ (W/m <sup>2</sup> )	$E_s$ (J/m <sup>2</sup> )	$\lambda$ (W/mK)	$c$ (J/kgK)
Solid phase $s$	14.09	4.33	0.33	0.12	32	3166	0.233	1504.8
Liquid phase $l$	57.60	35.80	28.56	28.58	49	8690	0.160	2047.9

The comparison between the thermal conductivity values provided by the manufacturer and those obtained by the experimental investigation show a deviation of -7.3% for the solid phase and +6.1% for the liquid phase. Regarding the specific heat, the results obtained were compared with those reported in Section 2.2.2, which highlight a dependence of the specific heat on the temperature. The values obtained in the experimental device correspond to an average temperature in the sample in the thermal transient equal to  $T_{sample} = 7.7$  °C for the solid phase test and to  $T_{sample} = 44.5$  °C for the liquid phase test. In correspondence of these temperatures, the curve of  $c(T)$ , shown in Figure 6, for the solid phase provides a value of  $c_s = 1514.2$  J/kg K and for the liquid phase a value of  $c_l = 2049.3$  J/kg K.

### 3.2. Heat latent of fusion and phase change temperature

For the determination of the latent heat and of the phase change temperature, the method considered is that described in Section 2.3.2. Starting from a steady field in the sample in solid phase at a uniform temperature equal to 15°C, made by setting the hot bath temperature at  $T_{hf} = 12.5$ °C and that of the cold bath at  $T_{cf} = 13.4$  °C, at initial instant  $t_0$ , the temperature of the hot bath  $T_{hf}$  was modified and set equal to 33.5 °C while that of the cold bath at  $T_{cf} = 31.9$  °C in

order to obtain a uniform temperature equal to  $29^{\circ}\text{C}$  at the end of the thermal transient in the sample. The temperature values in the two baths necessary to obtain the two uniform temperatures in the sample at the beginning and at the end of the thermal transient, were calculated with Eqs. (35) and (36).

The trends of temperatures at the different heights and of the surface heat fluxes recorded during the thermal transient are reported, respectively, in Figure 10a and Figure 10b. Figure 10b also reports the trend of the energy stored per unit time, sum of the sensible contribution and of the latent contribution.

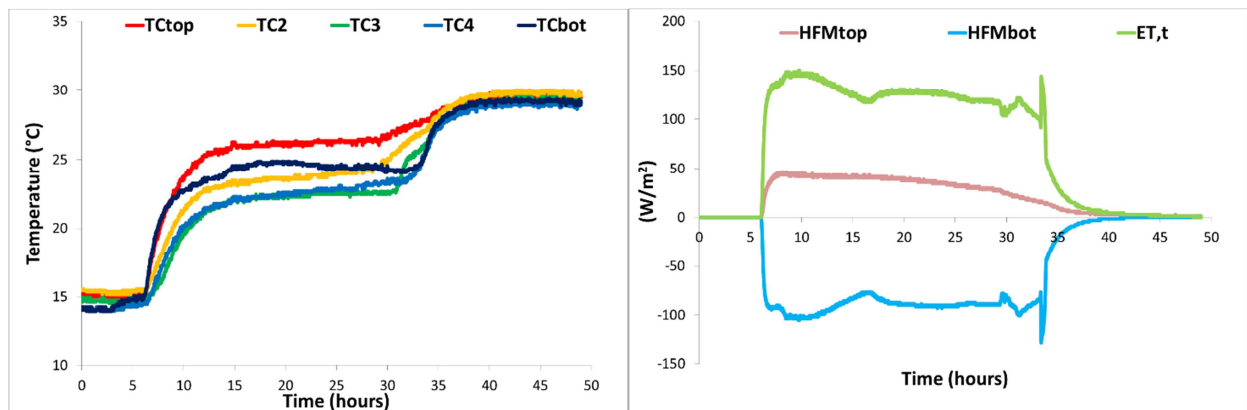


Figure 10 - a) Temperature trends at the different heights. b) trends of the surface heat fluxes and of the sensible energy stored per unit time.

Figure 10 highlights that the thermal transient has duration of approximately 36 hours, proving the high latent storage capacity of the PCM. The solid-liquid phase change in the sample, due to the effect of the considered boundary conditions, initially occurs on the two boundary surfaces and then proceeds towards the inside until it determines the phase change in the entire volume. The recorded temperature trends show that the heating rate during the solid phase reduces proceeding from the two boundary faces *top* and *bot* towards the inside of the sample, in correspondence with thermocouples TC3, TC4 and TC5. Such a reduction determines a decrease of the melting temperature proceeding towards the inside of the sample, as shown by the trends in Figure 10a during the phase change. In particular, the heating rate is equal to  $0.027\text{ K/min}$  on the top face, to  $0.022\text{ K/min}$  on the bot face, and to  $0.017$  in correspondence with TC3, TC4 and TC5. The corresponding melting temperatures approximately are:  $26.2^{\circ}\text{C}$  on the face top;  $24.7^{\circ}\text{C}$  on the face bot;  $22.47^{\circ}\text{C}$  for the three internal thermocouples. The dependence of the melting temperature on the heating rate has already been highlighted with the DSC tests in Section 2.2.2.

In the experimental tests, conducted to verify the analytical model, the periodic trends of the temperatures made in the sample give rise to heating/cooling rates of between 0.001 and 0.01 K/min. For this reason, the phase change temperature used in the analytical model was assumed as equal to 22.47 °C, to which is associated with the lower heating rate, in correspondence with TC3, TC4 and TC5, in the experimental test.

Regarding the evaluation of the latent heat, Table 6 reports the sensible energy stored in the solid phase and in the liquid phase for each subvolume, represented, respectively, by the first and third term of the second member of Eq. (40), and the total energy stored in the entire sample, represented by the first member of Eq. (40).

Table 6 - Sensible energy stored in the solid phase and in the liquid phase by each subvolume and by the entire layer, total sensible energy stored and total energy stored.

Subvolume j	1	2	3	4	5	Tot	$E_{S,tot}$ (J)	$E_T$ (J)
$E_{S,s}$ (J)	99.0	188.2	210.2	209.4	91.0	797.8	1088.5	52867
$E_{S,l}$ (J)	40.5	87.9	74.0	58.6	29.6	290.7		

Applying Eq. (42), taking into account the values in Table 6 and of the mass of the sample equal to  $m = 234.1$  g, a value of  $H = 221.18$  kJ/kg is obtained. Such a result confirms the slight increase undergone by the latent heat upon the decrease of the heating/cooling rate, as highlighted in Section 2.2.2.

### 3.3. Thermophysical properties of PureTemp23 employed for the verification of the analytical model

Table 7 reports the thermophysical properties of the PCM sample used in the experimental device to verify the analytical model, which was presented in Section 4.

Table 7 - Thermophysical properties of the PureTemp23 PCM sample used in the experimental device.

$\rho_s$ (kg/m <sup>3</sup> )	$\rho_l$ (kg/m <sup>3</sup> )	$\rho$ (kg/m <sup>3</sup> )	$\lambda_s$ (W/mK)	$\lambda_l$ (W/mK)	$c_s$ (J/kg K)	$c_l$ (J/kg K)	$T_M$ (°C)	H (kJ/kg)
865.25	831	848.13	0.23	0.16	1504.8	2047.9	22.47	221.18

Regarding the density, since the model provides for an identical value in the two phases, the value  $\rho$  reported in the table is the average between the liquid phase density and the solid phase density.

#### 4. Validation of the analytical model

The experimental equipment was used for validation of the analytical model. The periodic temperature conditions on the two faces of the sample were set by the fluid temperatures in the two thermal baths. The resulting surface temperature were successively interpolated by a Fourier series expansion and used as the boundary conditions in the analytical model. The achievement of the validation of the analytical model with different boundary conditions requires the conduction of: (i) several tests in the sinusoidal periodic regime by varying the attenuation factor and the time lag between the temperature oscillations on the two faces and the period of oscillations; (ii) one test in the non-sinusoidal periodic regime to consider the effect of multiple harmonics. Validation of the model was obtained by means of a comparison between the trends measured of the temperatures at different heights in the sample and of the heat fluxes on the two faces, with those obtained using the analytical solution.

Table 8, in the case of sinusoidal temperature boundary conditions and in the case of non-sinusoidal temperature boundary conditions, reports for each harmonic used in the Fourier expansion: the order  $k$  and the period  $P$ , the mean steady value  $\bar{\vartheta}_1$  and  $\bar{\vartheta}_2$ , the amplitude  $|\tilde{\vartheta}_1|$  and  $|\tilde{\vartheta}_2|$ , and the argument  $\arg(\tilde{\vartheta}_1)$  and  $\arg(\tilde{\vartheta}_2)$  of the surface temperature loadings, the attenuation factor  $f$  and the time lag  $\Delta t$  between the two loadings.

In the different tests, the interpolation of the boundary conditions by the Fourier series expansion was obtained with correlation indexes  $R^2$  very close to the unit. The same value in all the experiments was assigned to the mean value of the temperature of each fluid with the aim to obtain in the various tests the same mean temperature value on the top surface and the same temperature value on the bottom surface. The mean temperature measurements resulted as being equal, respectively, to  $33.8 \pm 0.8$  °C and  $12.5 \pm 0.2$  °C. Thus, the tests differ only in terms of the fluctuating component. Furthermore, the top surface temperature at each instant is greater than the melting temperature, while the bottom surface temperature is always lower than the melting temperature. In such conditions, a sole bi-phase interface is realised in the layer that divides the liquid phase, which is always placed in the upper part of the sample, from the solid phase, placed in the lower part of the sample.

Table 8 - Tests in a sinusoidal and non-sinusoidal regime: order  $k$  and period  $P$  of the harmonics used in the Fourier series expansion, mean steady value  $|\tilde{\vartheta}_1|$  and  $|\tilde{\vartheta}_2|$ , amplitude  $|\tilde{\vartheta}_1|$  and  $|\tilde{\vartheta}_2|$ , and argument  $\arg(\tilde{\vartheta}_1)$  and  $\arg(\tilde{\vartheta}_2)$  of the two boundary conditions, attenuation factor  $f$  and time lag  $\Delta t$  between the two boundary conditions.

TEST IN SINUSOIDAL PERIODIC REGIME										
			Top surface temperature			Bottom surface temperature				
TEST	k	P (hours)	$\bar{\vartheta}_1$ (°C)	$ \tilde{\vartheta}_1 $ (°C)	$\arg(\tilde{\vartheta}_1)$ (rad)	$\bar{\vartheta}_2$ (°C)	$ \tilde{\vartheta}_2 $ (°C)	$\arg(\tilde{\vartheta}_2)$ (rad)	f (-)	$\Delta t$ (rad)
1	1	24	33.000	9.547	0.950	12.260	4.379	7.115	0.459	6.166
2	1	24	33.910	9.985	1.060	12.650	1.034	6.265	0.104	5.205
4	1	12	33.900	8.278	-0.697	12.310	3.389	5.570	0.409	6.267
5	1	24	34.542	10.640	2.647	12.717	3.188	4.155	0.300	1.508
TEST IN NON SINUSOIDAL PERIODIC REGIME										
			Top surface temperature			Bottom surface temperature				
TEST	k	P (hours)	$\bar{\vartheta}_1$ (°C)	$ \tilde{\vartheta}_1 $ (°C)	$\arg(\tilde{\vartheta}_1)$ (rad)	$\bar{\vartheta}_2$ (°C)	$ \tilde{\vartheta}_2 $ (°C)	$\arg(\tilde{\vartheta}_2)$ (rad)	f (-)	$\Delta t$ (rad)
3	1	24	34.092	5.650	-1.366	12.493	1.840	-0.814	0.326	0.552
	2	12		2.766	1.454		0.900	3.005	0.326	1.551
	3	8		3.077	2.184		1.032	4.973	0.335	2.789
	4	6		1.330	0.245		0.372	3.649	0.279	3.404
	5	4.8		0.753	-1.527		0.277	2.273	0.368	3.800

TEST 1 is the reference test and regards boundary conditions that are both sinusoidal with a period equal to 24 hours. The amplitude and the argument of the temperature oscillation on the top face are equal, respectively, to 9.547 °C and 0.950 rad, while on the bottom face, the temperature oscillation is attenuated and undergoes a time lag, respectively, of 0.459 rad and 6.166 rad. In TEST 2 the boundary condition on the bottom face was modified, reducing the attenuation factor to 0.104. This modification gave rise to a slight variation of the time lag. In TEST 5 the boundary condition on the bottom face was modified to obtain a different time lag and equal to 1.508 rad, which led to a slight modification of the attenuation factor. Only the period of the oscillations on the boundary surface of the sample was modified in TEST 4. An additional test to validate the analytical model in non-sinusoidal conditions was conducted. This experimental test regards a non-regular fluctuation with period equal to 24 hours on the top face and on the bottom face described through a Fourier series expansion truncated at the fifth harmonic.

In the different tests, the achievement of a steady periodic regime was held to be satisfied when in two successive cycles, the temperature trends at the different heights present mean deviations of less than 3% and those of the surface fluxes less than 5%. For example, in the case of TEST 1, Figure 11 reports the thermal transient evolution up to the reaching of the steady

periodic regime of the temperatures at the different heights and of the surface heat fluxes. The regime conditions are achieved after four 24-hour cycles.

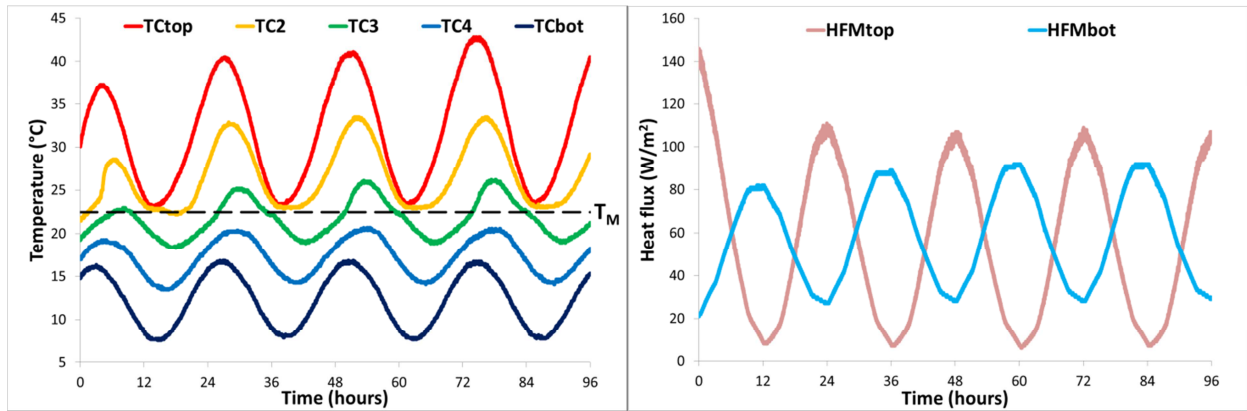


Figure 11 – Thermal transient until attainment of the steady periodic regime of temperatures at different heights and of the surface heat fluxes during TEST 1.

In the case of tests in a sinusoidal periodic regime, Figure 12 reports the comparison between the experimental temperature trends at different heights and of the surface heat fluxes, and the trends obtained analytically with the equations presented in Table 2. The analogue figures relative to the test in a non-sinusoidal periodic regime are reported in Figure 13. In the latter case, the analytical profiles were obtained by applying the equations relative to the steady model and, for the different harmonics, those relative to the oscillating model.

The experimental temperature trends in all the tests confirm that for the boundary conditions considered, represented by trends TC1 and TC5, a sole one bi-phase interface is present in the layer. It remains highlighted in all the tests by the TC3 trends since they intersect the phase change temperature, and in tests 1, 2 and 5 also by the TC2 trends, which for a brief time interval reaches the phase change temperature while during the remaining part of the period it is in liquid phase.

The temperature fluctuations in the solid phase (TC4 and TC5) and in the liquid phase (TC1 and TC2), not involved in the phase change, present regular trends that attenuate and undergo a time lag proceeding from the two boundary surfaces towards the inside of the layer, in proximity to the portion involved in the phase change. In this portion, a smaller amplitude of the temperature fluctuation is recorded as the heat fluxes in transit in the two phases are converted into latent energy.

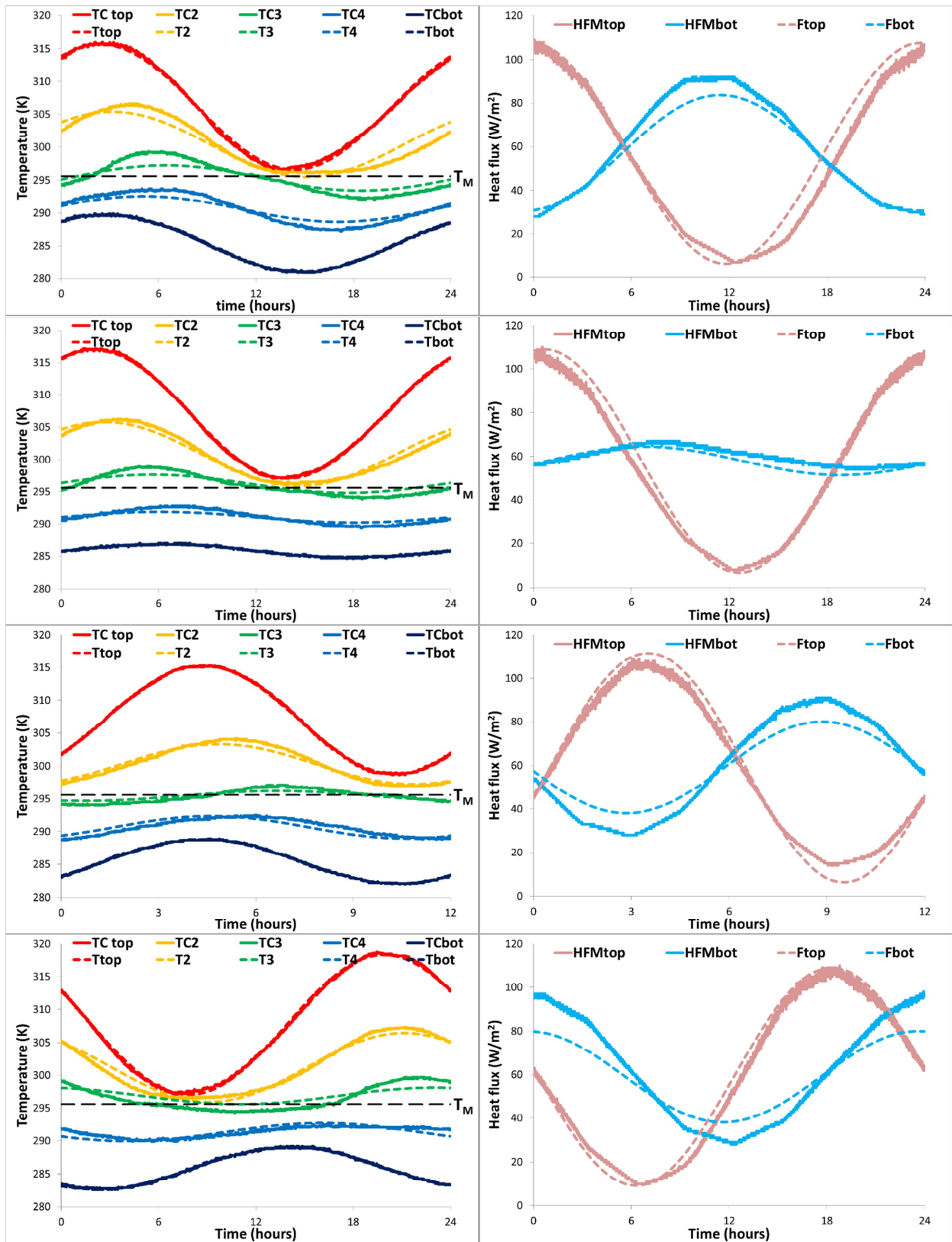


Figure 12 - Comparison between the measured (TC and HFM) and calculated (T and F) temperature trends at different heights, on the left, and of the surface heat fluxes, on the right, in the case of test in a sinusoidal periodic regime.



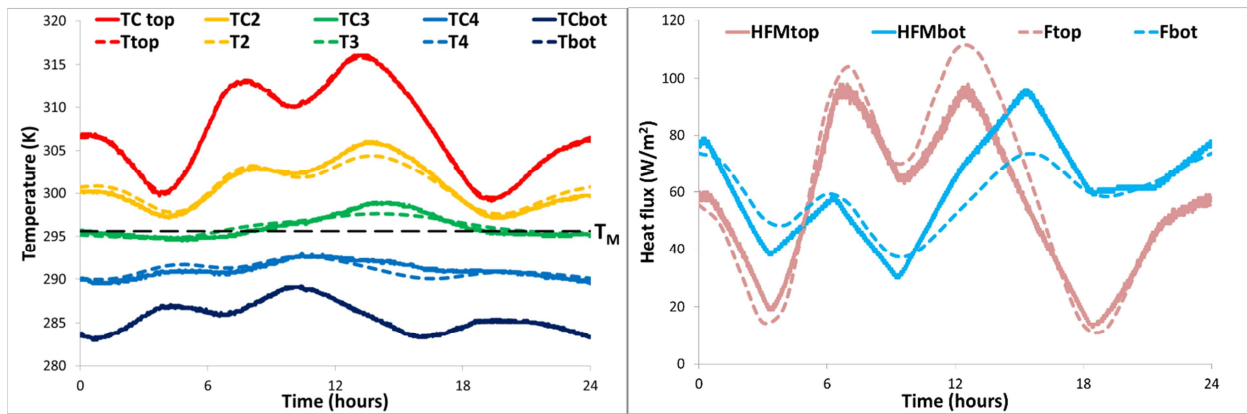


Figure 13 - Comparison between the measured (TC and HFM) and calculated (T and F) temperature trends at different heights, on the left, and of the surface heat fluxes, on the right, in the case of test in a non-sinusoidal periodic regime.

The qualitative comparison between the experimental trends and the trends calculated with the analytical model is, overall, very good in that in all the tests since the periodic fluctuations present similar mean values, amplitudes and appear to be in phase. In particular, the deviations recorded on the temperature trends result as being very reduced in the portions of the layer that are always in liquid phase and in solid phase, while in the portion affected by the phase change, the deviations are more evident. Instead, regarding the measured heat flux, compared to that calculated with the analytical model, on the top surface it presents a slightly lower amplitude, whereas on the bottom it has a slightly greater amplitude.

Such quantitative deviations recorded are to be attributed:

- To the non one-directionality of the heat flux caused by:
  - The imperfect adiabaticity of the lateral boundary surface of the cylindrical sample. In particular, having recorded an external environment temperature close to the melting temperature in all the tests, the liquid phase of the sample transfers heat to the external environment while the solid phase receives heat from the external environment. This finds confirmation in the measured heat flux values, which on the bottom surface present a higher mean steady value and a higher amplitude compared to those calculated with the analytical model, while on the top surface are lower (see Table 9).
  - The convective effects in the portion of the layer in liquid phase which increase the thermal losses towards the external environment. As proposed by other authors [16, 18], addressing similar experimental tests, the convection phenomena can be neglected in a PCM layer with a small thickness.

For each test, Table 9 reports the mean steady value of the heat flux measured on the top and bottom surfaces, the absolute and percentage deviation, the mean steady value of the analytically calculated heat flux and the percentage deviation between the two measured steady heat fluxes and the analytical one.

Table 9 - For the different tests, heat flux steady mean value measured on the top surface  $\overline{HFM}_{top}$  and on the bottom surface  $\overline{HFM}_{bot}$ , absolute  $\Delta_{HFM}$  and percentage  $\Delta\%$  deviation, heat flux steady mean value calculated analytically  $\bar{\phi}$  and percentage deviations  $\Delta_{top}\%$  and  $\Delta_{bot}\%$ , between the two measured heat fluxes and the analytical one.

	TEST 1	TEST 2	TEST 4	TEST 5	TEST 3
$\overline{HFM}_{top}$ (W/m <sup>2</sup> )	53.40	54.99	58.55	57.39	55.54
$\overline{HFM}_{bot}$ (W/m <sup>2</sup> )	60.07	59.95	59.15	61.51	61.31
$\Delta_{HFM}$ (W/m <sup>2</sup> )	-6.67	-4.97	-0.59	-4.11	-5.77
$\Delta\%$	-12.49	-9.04	-1.01	-7.17	-10.38
$\bar{\phi}$ (W/m <sup>2</sup> )	57.12	57.89	58.99	59.09	58.81
$\Delta_{top}\%$	-6.51	-5.02	-0.74	-2.88	-5.57
$\Delta_{bot}\%$	5.17	3.57	0.27	4.08	4.24

The table shows that, since the percentage deviations are of the order of  $\pm 6\%$ , and close to the error of measurement of the heat flux meters, in the experimental device the conditions of adiabaticity can be held to be sufficiently verified and that conduction plays the main role in the heat transfer in the layer. In such conditions, the heat transfer is almost one-dimensional.

- To the hysteresis phenomenon, a function of the heating/cooling rate, which gives rise to a melting temperature that is different to the solidification temperature, and to a melting latent heat that is slightly different to that of solidification; to the dependence of the phase change temperature range and of the latent heat from the heating/cooling rate. Such a phenomenon greatly influences the temperature trends in proximity of the portion of the layer subject to phase change.
- To the variability of the specific heat in the liquid phase and in the solid phase with the temperature, as already shown in figure 6, compared to the analytical model that uses the mean values in the two phases;
- To the slight difference in density in the two phases ( $\pm 2\%$  compared to the mean value), that in the analytical model is assumed as constant and equal to the mean value.
- To the slight variation of the volume following the transition phase, which produces a variation of the length of the sample of 4% in the case in which the entire layer changes phase. In the tests, only a reduced portion of the layer is subject to phase change.

- To experimental trends produced by a steady periodic regime that are respected with an error always lower than 5%, and to the slight difference between the experimental and analytical boundary conditions, represented with a Fourier series expansion truncated at the fifth harmonic.

Despite the abovementioned experimentally detected phenomena, the basic hypotheses and the results of the analytical model result as being sufficiently verified. Therefore, the model can be validly used for the study of the dynamic thermal behaviour of a PCM layer and for the evaluation of stored energy in latent and sensible form. A further validation, in energy terms, of the predictive capacity of the model was obtained by comparing the total stored or released energy of the sample in the different experiments obtained with the analytical model. Table 10 shows the total stored energy determined experimentally and that calculated analytically as well as the percentage deviation.

Table 10 - For the different tests, experimental and analytical value of the total stored energy and percentage deviation.

	TEST 1	TEST 2	TEST 4	TEST 5	TEST 3
$E_{T,exp}$ (kJ)	8.90	5.80	4.22	6.13	4.66
$E_{T,anal}$ (kJ)	8.67	5.81	4.11	5.68	5.51
$\Delta_{E_T}$ %	-2.65	0.17	-2.68	-7.92	15.43

Despite propagation of the error in the calculation of  $E_{T,exp}$  as the integral of the difference between the two surface heat fluxes, measured with an accuracy of  $\pm 5\%$ , and the basic assumptions of the analytical model that have not been perfectly verified, the deviations are less than 8% in a periodic sinusoidal regime and of the order of 15% in a non-sinusoidal periodic regime.

Moreover, Table 10 shows that the maximum total energy stored is recorded in the case of TEST 1, with a higher attenuation factor and boundary conditions that are almost in phase. The reduction of the period gives rise to a reduction of the total stored energy.

The validated analytical model allows for the stored energy in the sensible contribution and in the latent contribution to be divided; it also allows for the determination of the trend upon variation of the time of the bi-phase interface position. Such a results, for the different tests, are reported for the stored energy in Table 11 and for the position of the bi-phase interface in Figure 14.

Table 11 - For the different tests, sensible and latent stored energy.

	TEST 1	TEST 2	TEST 4	TEST 5	TEST 3
$E_{S,anal}$ (kJ)	8.31	5.49	3.91	5.39	5.17
$E_{L,anal}$ (kJ)	0.56	0.38	0.25	0.41	0.36

The reduced value of the stored latent energy, compared to the sensible one, is due to the contained extension of the portion subject to phase change.

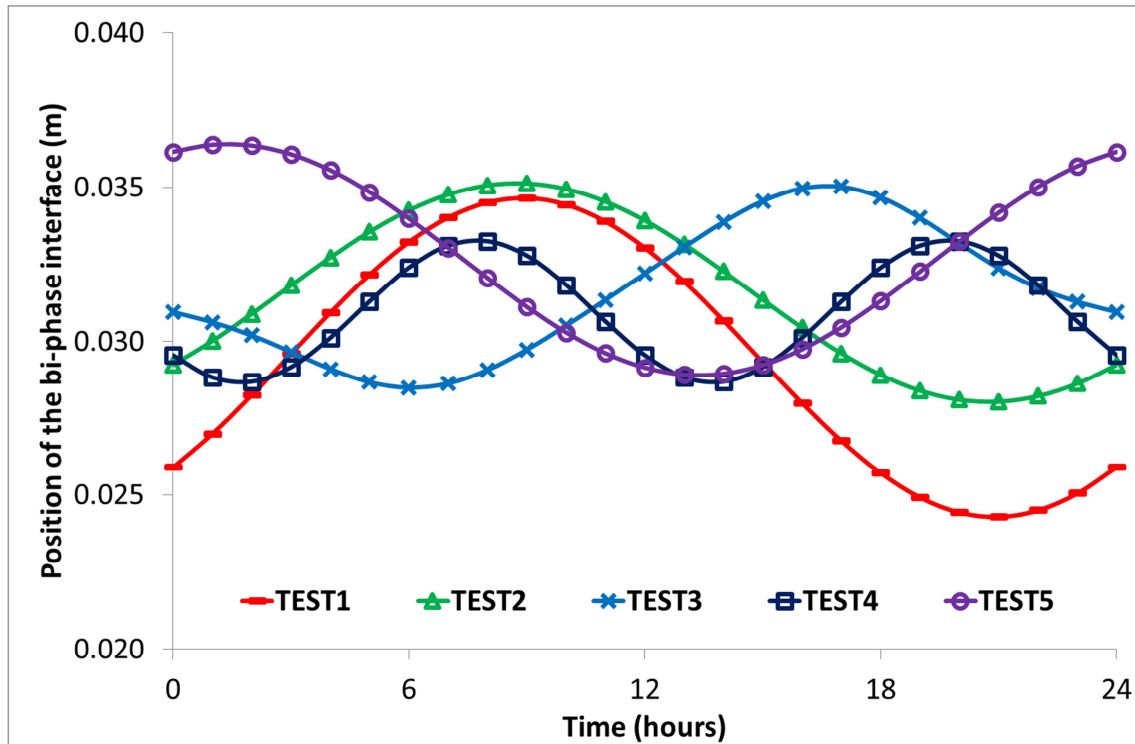


Figure 14 - For the different tests, trend of the position of the bi-phase interface in function of time.

In the different tests, the position of the bi-phase interface fluctuates within the layer between the abscissae  $x = 2.4$  cm and  $x = 3.6$  cm, determining a phase change of, at most, 17% of the thickness of the PCM layer.

### 5. Conclusions

An experimental validation of an analytical model resolving the Stefan Problem in a PCM layer subject to steady periodic boundary conditions that give rise to a sole bi-phase interface was conducted. The considered temperature boundary conditions regard sinusoidal and non-sinusoidal periodic trends. The model was verified by comparing the measured and calculated temperature trends at different heights in the layer, the trends of the surface heat

fluxes, and the total stored energy. Thermophysical properties determined by means of experimental tests, obtained using the same PCM test sample were used. To this end, a new procedure with a limited number of tests in an experimental device, allows for the determining of the thermal conductivity and of the specific heat in the liquid phase and in the solid phase, of the latent heat and the phase change temperature, was used. The values obtained are close to those provided by the manufacturer and those determined by DSC characterization.

The analytical model provides accurate predictive assessments as the temperature fluctuations throughout the layer and the surface heat flux fluctuations result as being very close to the experimental ones. In particular, trends have similar mean values, of the amplitudes and of the arguments. The deviations recorded on the temperature trends are significantly reduced in the portion of the layer that is always in a liquid phase and in a solid phase, while they are more evident in the portion involved in the phase change. As regards the measured heat flux, compared to that calculated with the analytical model, on the top surface it presents slightly higher amplitude, whereas on the bottom it has a slightly lower amplitude. These slight differences are mainly attributable to: the thermal field that is not strictly one-dimensional because of the imperfect adiabaticity of the cylindrical lateral surface of the sample used and the convective heat fluxes which originate in the liquid phase; the variability of thermophysical properties with the temperature. In the area affected by the phase change, the most obvious deviations can mainly be attributed to the presence of a melting temperature range, rather than a single temperature, and to the phenomenon of hysteresis, a function of the heating/cooling rate. Due to this phenomenon, the melting temperature and the latent heat of fusion are, respectively, different from the solidification temperature and the latent heat of solidification. Furthermore, also the phase change temperature range and the latent heat vary upon variation of the heating/cooling rate.

Finally, the predictive capacity of the model in the evaluation of the total stored energy calculating the deviations from that determined experimentally, was verified. The reduced values of these deviations justify the use of the model to determine the energy stored in the sensible and latent form in the layer and the trend of the position of the bi-phase interface in function of time.

The maximum total energy stored is recorded in the case in which the attenuation factor is higher and the arguments are almost close, between the two temperature boundary conditions. The reduction of the period gives rise to a reduction of the total stored energy.

---

**References**

- [1] H. Mehling, L. F. Cabeza, Heat and cold storage with PCM, An up to date introduction into basics and applications, Springer, (2008).
- [2] J. Bransier, Storage periodique par chaleur latente: aspects fondamentaux lies a la cinetique des transferts, International Journal of Heat and Mass Transfer 22 (1979), pp. 875-883.
- [3] J. P. Bardon, E. Vrignaud, D. Delaunay, Etude experimentale de la fusion et de la solidification periodique d'une plaque de paraffine, Revue Générale de Thermique (1979), pp. 212-213.
- [4] B. Kalhori, S. Ramadyani, Studies on heat transfer from a vertical cylinder with or without fins embedded in a solid phase change medium, Journal of Heat Transfer 107(1) (1985), pp. 44-51.
- [5] C. Belleci, M. Conti, Phase change thermal storage: transient behaviour analysis of a solar receiver/storage module using the enthalpy model, International Journal of Heat and Mass Transfer 36 (1993), pp. 146-156.
- [6] C. Belleci, M. Conti, Transient behaviour analysis of latent heat thermal storage module, International Journal of Heat and Mass Transfer 36 (1993), pp. 2157-2163.
- [7] C. Belleci, M. Conti, Latent heat thermal storage for solar dynamic power generation, Solar Energy 51 (1993), pp. 169-173.
- [8] C. K. Halford, R. F. Boehm, Modeling of phase change material peak load shifting, Energy and Buildings 39 (2007), pp. 298-305.
- [9] F. Mathieu-Potvin, L. Gosselin, Thermal shielding of multilayer walls with phase change materials under different transient boundary conditions, International Journal of Thermal Sciences 48 (2009), pp. 1707-1717.
- [10] D. A. Neeper, Thermal dynamics of wallboard with latent heat storage, Solar Energy 68(5) (2000), pp. 393-403.
- [11] G. Zhou, Y. Yang, H. Xu, Performance of shape-stabilized phase change material wallboard with periodical outside heat flux waves, Applied Energy 88(6) (2011), pp. 2113-2121.
- [12] G. Zhou, Y. Yang, X. Wang, J. Cheng, Thermal characteristics of shape-stabilized phase change material wallboard with periodical outside temperature waves, Applied Energy 87(8) (2010), pp. 2666-2672.
- [13] N. P. Sharifi, A. A. N. Shaikh, A. R. Sakulich, Application of phase change materials in gypsum boards to meet building energy conservation goals, Energy and Buildings 138 (2017), pp. 455-467.

- [14] D. Mazzeo, G. Oliveti, N. Arcuri, Definition of a new set of parameters for the dynamic thermal characterization of PCM layers in the presence of one or more liquid-solid interfaces, *Energy and Buildings* 141 (2017), pp. 379-396.
- [15] V. Jariwala, A.S. Mujumdar, M. E. Weber, The periodic steady state for cyclic energy storage in paraffin wax, *The Canadian Journal of Chemical Engineering* 65 (1987), pp. 899-906
- [16] M. Hasan, A. S. Mujumdar, M. E. Weber, Cyclic melting and freezing, *Chemical Engineering Science* 46(7) (1991), pp. 1573-1587.
- [17] V. R. Voller, P. Felix, C. R. Swaminathan, Cyclic phase change with fluid flow, *International Journal of Numerical Methods for Heat & Fluid Flow* 6(4) (1996), pp. 57-64.
- [18] G. Casano, S. Piva, Experimental and numerical investigation of the steady periodic solid-liquid phase-change heat transfer, *International Journal of Heat and Mass Transfer* 45 (2002), pp. 4181-4190.
- [19] F. Kuznik, J. Virgone, Experimental investigation of wallboard containing phase change material: Data for validation of numerical modeling, *Energy and Buildings* 41 (2009), pp. 561-570.
- [20] S. Savovic, J. Caldwell, Numerical solution of Stefan problem with time-dependent boundary conditions by variable space grid method, *Thermal Science* 13 (2009), pp. 165-174.
- [21] M. Ozisik, *Heat conduction*, Wiley, New York, (1980).
- [22] R. Henze, J. Humphrey, Enhanced heat conduction in phase change thermal energy storage devices, *International Journal of Heat and Mass Transfer* 24 (1981), pp. 450-474.
- [23] M. Lachheb, Z. Younsi, H. Naji, M. Karkri, S. B. Nasrallah, Thermal behavior of a hybrid PCM/plaster: A numerical and experimental investigation, *Applied Thermal Engineering* 111 (2017), pp. 49-59.
- [24] H. Ling, C. Chen, H. Qin, S. Wei, J. Lin, N. Li, M. Zhang, N. Yu, Y. Li, Indicators evaluating thermal inertia performance of envelopes with phase change material, *Energy and Buildings* 122 (2016), pp. 175-184.
- [25] E. S. Watson, M. J. O'Neill, Joshua J, B. Nathaniel, A differential scanning calorimeter for quantitative differential thermal analysis, *Analytical Chemistry* 36(7) (1964), pp.1233-1238.
- [26] Y. P. Zhang, Jiang Y, Y. Jiang, A simple method, the T-history method, of determining the heat of fusion, specific heat and thermal conductivity of phase-change materials, *Measurement Science and Technology* 10(3) (1999), pp. 201-205.
- [27] A. de Gracia, C. Barreneche, M. M. Farid, L. F. Cabeza, New equipment for testing steady and transient thermal performance of multilayered building envelopes with PCM, *Energy and Buildings* 43(12) (2011), pp. 3704-3709.

- [28] R. Cheng, M. Pomianowski, X. Wang, P. Heiselberg, Y. Zhang, A new method to determine thermophysical properties of PCM-concrete brick, *Applied Energy* 112 (2013), pp. 988-998.
- [29] H. Hu, S. A. Argyropoulos, Mathematical modelling of solidification and melting: a review, *Modelling and Simulation in Materials Science and Engineering* 4(4) (1996), pp. 371-396.
- [30] L.I. Rubinstein, *The Stefan Problem*, Translations of Mathematical Monographs, vol. 27 American, Mathematical Society, Providence, Rhode Island (1971).
- [31] J. Crank, *Free and Moving Boundary Problems*, Oxford: Clarendon, (1984).
- [32] H. S. Carslaw, J.C. Jaeger, *Conduction of Heat in Solids*, second edition, Oxford Science Publications, (1988).
- [33] V. Alexiades, A. Solomon, *Mathematical Modelling of Melting and Freezing Processes*, Hemisphere Publishing Corporation, Washington (1993).
- [34] S. Liu, Y. Li, Y. Zhang, Mathematical solutions and numerical models employed for the investigations of Pcm' phase transformations, *Renewable and Sustainable Energy Reviews* 33 (2014), pp. 659-674.
- [35] D. Mazzeo, G. Oliveti, M. De Simone, N. Arcuri, Analytical model for solidification and melting in a finite PCM in steady periodic regime, *International Journal of Heat and Mass Transfer* 88 (2015), pp. 844-861.
- [36] <http://www.puretemp.com>. Last access: 25/01/2017
- [37] A. Lazaro, C. Peñalosa, A. Solé, G. Diarce, T. Haussmann, M. Fois, B. Zalba, S. Gshwander, L. F. Cabeza, Intercomparative tests on phase change materials characterisation with differential scanning calorimeter, *Applied Energy* 109 (2013), pp. 415-420.
- [38] C. Barreneche, A. Solé, L. Miró, I. Martorell, A. Inés Fernández, Luisa F. Cabeza, Study on differential scanning calorimetry analysis with two operation modes and organic and inorganic phase change material (PCM), *Thermochimica Acta* 553 (2013), pp. 23-26.
- [39] G. Ferrer, C. Barreneche, A. Solé, I. Martorell, L.F. Cabeza, New proposed methodology for specific heat capacity determination of materials for thermal energy storage (TES) by DSC, *Journal of Energy Storage* 11 (2017), pp. 1-6.
- [40] L. Li, H. Yu, X. Wang, S. Zheng, Thermal analysis of melting and freezing processes of phase change materials (Pcm) based on dynamic DSC test, *Energy and Buildings* 130 (2016), pp. 388-396.
- [41] X. Jin, X. Xu, X. Zhang, Y. Yin, Determination of the PCM melting temperature range using DSC, *Thermochimica Acta*, 595 (2014), pp. 17-21.



[42] E. Günter, S. Hiebler, H. Mehling, Determination of the heat storage capacity of PCM and PCM-Objects as a function of temperature, in: 10th International Conference on Thermal Energy Storage, ECOSTOCK, (2006).

## Nomenclature

(a)	portion of the layer in phase a
(b)	portion of the layer in phase b
c	specific heat capacity [J/(kg K)]
D	sample diameter [m]
E	energy stored [J]
f	attenuation factor [-]
F	heat flux [W/m <sup>2</sup> ]
H	latent heat of fusion [J/kg]
HFM	experimental heat flux [W/m <sup>2</sup> ]
k	harmonic order [-]
L	thickness of the PCM layer [m]
m	sample mass [kg]
n	number of harmonics [-]
P	period of oscillation [s]
t	time [s]
t*	a particular instant in time [s]
t <sub>1</sub>	initial time instant of the phase change [s]
t <sub>2</sub>	final time instant of the phase change [s]
T	temperature [K]
TC	experimental temperature [K]
V	volume [m <sup>3</sup> ]
x	spatial Cartesian coordinates in steady regime [m]
x*	spatial Cartesian coordinates in oscillating regime [m]
X	position of the bi-phase interface [m]

## Greek symbols

$\alpha$	thermal diffusivity [m <sup>2</sup> /s]
$\gamma$	propagation constant [m <sup>-1</sup> ]

---

$\Delta$	deviation
$\Delta t$	time lag [rad]
$\Delta V$	volume variation [m <sup>3</sup> ]
$\Delta x$	thickness of the subvolume [m]
$\zeta$	argument of the oscillating component of the position of bi-phase interface [rad]
$\vartheta$	generic component of the temperature Fourier series expansion [K]
$\vartheta_p, \vartheta_r$	constants of integration [K]
$\lambda$	thermal conductivity [W/(m K)]
$\rho$	density [kg/m <sup>3</sup> ]
$v$	velocity of the bi-phase interface [m/s]
$\varphi$	argument of the temperature oscillation [rad]
$\phi$	generic component of the heat flux Fourier series expansion [W/m <sup>2</sup> ]
$\chi$	generic component of the position of bi-phase interface Fourier series expansion [m]
$\psi$	argument of the heat flux oscillation [rad]
$\omega$	angular frequency [rad/s]

## Subscripts

0	initial time instant of the transient regime
1	face 1
2	face 2
a	phase a
A	sample holder area [m <sup>2</sup> ]
anal	analytical
b	phase b
bot	referring to the sample bottom surface
cf	referring to the thermal bath that provides the cold fluid
env	referring to the external environment of the experimental device
$E_T$	referring to the total energy stored
exp	experimental
f	final time instant of the transient regime
fus	fusion
H	latent heat stored per unit time
hf	referring to the thermal bath that provides the hot fluid

HFM	referring to the experimental heat flux
j	referring to the j-esimo subvolume of the sample
k	k-th harmonic
l	liquid phase
L	latent heat storage
M	melting
s	solid phase
S	sensible heat storage
sample	referring to the sample holder
sol	solidification
T	total heat storage
TC	referring to the experimental temperature
top	referring to the sample top surface
tot	total sensible heat storage

#### Symbols

–	mean value
~	oscillating value in the time domain
^	oscillating value in the complex domain
	amplitude of an oscillating value
arg	argument of an oscillating value

---

# Conclusions

## Sensible heat storage materials

The main proposals, accomplishments and conclusions of this PhD thesis are listed below:

- A proposal for the *extension of the reference standard EN ISO 13786* for the dynamic thermal characteristics of opaque building components in the presence of several temperature and heat flux loadings acting on the external and internal surfaces, both in sinusoidal and non-sinusoidal periodic regime, was developed.
- The *newly defined parameters* were used to compare the thermal performance in different localities of some types of commonly used walls.
- The results obtained, relating to 1152 different boundary conditions, were used for the *construction of maps of dynamic characteristics*, different upon variation of the plant functioning regime and of the shortwave radiant load on the internal surface. The maps show the dependence of the dynamic parameters on the season, on the external surface absorption coefficient, on the orientation and the type of wall, and on the locations.
- The *calculation method was verified* by means of a comparison of the entering and exiting heat fluxes through the wall calculated both analytically and numerically.
- This study offers the possibility of distinguishing the summer and winter behaviour of the wall. Moreover, it can be useful in the *thermal design of the wall* in order to reduce power peaks and energy requirements during summer and winter conditioning.
- In the case of summer or winter air conditioning, the results allow definition of the *most suitable thermal and optical properties* of the wall. If the air conditioning is annual, the choice must lead to an overall reduction in energy and power needed in the two seasons or in the more energetically expensive season.

---

## Latent heat storage materials (PCM)

The main proposals, accomplishments and conclusions of this PhD thesis are listed below:

- An *analytical exact solution of the phase change problem*, known as the Stefan or Moving Boundary Problem, in a phase change material (PCM) layer subject to steady periodic boundary conditions is presented.
- The solution of the model was used to conduct a thermal analysis in different thermodynamic configurations of the PCM layer subject to *sinusoidal periodic temperature boundary conditions* and to determine the thermal behaviour of a PCM layer subject to *multi-harmonic periodic temperature boundary conditions*.
- The analyses conducted have highlighted the conditions necessary to obtain a complete transformation of the oscillating heat fluxes coming from the boundary faces of the layer into stored latent heat. The results obtained also show how the *behaviour of the layer* alters up on *variation of the dimensionless parameters*.
- A *parametric study of the exact analytical solution* of the Stefan problem in steady periodic regime conditions is presented.
- The study of the phasor that describes the oscillating component of the bi-phase interface position, upon the variation of the thermal parameters, has highlighted how the trends of the amplitude and the argument are very similar to a *frequency response* that in the Laplace domain is equal to the *transfer function of a dynamic linear system of the third order with a finite time-delay*.
- An *explicit expression* of the oscillating component of the bi-phase interface position was obtained through a simplification obtained by neglecting sensible heat stored in the two phases.
- The limits of validity of such a solution were determined evaluating the *relative error* that is committed, and the fields of variation of the thermal parameters that ensure a relative error value lower than 3 %.
- This approximate solution also allows the direct obtainment of the thermal field in the two phases as a function of only dimensionless thermal parameters and boundary loadings.
- By means of the development of a *numerical procedure*, a detailed description of the phenomena that occur in a *PCM layer location of several bi-phase interfaces* is presented when it is subject to the typical loadings that operate on the building envelope.

- 
- The numerical model and the resolution algorithm is *validated by means of a comparison with an analytical model*, which resolves the Stefan problem in a finite layer in a steady periodic regime in presence of a sole bi-phase interface.
  - The numerical model and the calculation algorithm can be validly used for the *thermal dimensioning of the PCM layer*. The objective is to obtain a reduction of both the thermal loads and the energy requirements in the two air conditioning seasons, and to improve the thermal comfort within the environment through control of the surface temperature.
  - An accurate *thermal and energetic analysis of PCM layers* subject to the typical loadings operating on the external walls of air-conditioned buildings has been developed in the case in which, due to the effect of the periodic boundary conditions, one or more bi-phase interfaces are present in the layer.
  - The energetic analysis developed on monthly bases in relation to a PCM layer, with different thermophysical properties and melting temperatures, highlighted that the highest values of the yearly total stored energy is obtained with an *intermediate melting temperature between those of winter and summer set points of the indoor environment*, both in a Mediterranean and continental climate. Such a PCM is the best compromise between winter and summer energy needs for an air-conditioned environment.
  - The created procedure allows for a *dynamic thermal characterisation* by means the definition of a *set of new dynamic parameters* able to identify the change that undergone by the form of the trend of temperature and heat flux, as well as the transferred fluctuating energy and the sensible and latent energy stored.
  - The defined parameters have to be utilized for the thermal dimensioning of the PCM layer, which is related to the *thickness* and to the *thermophysical properties*, and to identify the effective thermal behaviour of the layer.
  - It has been found that the *dynamic parameters are correlated to the latent storage efficiency*. The research of further functional dependencies among the dynamic characteristics highlighted a strong correlation between the decrement factor of the maximum excursion of the heat flux and the energy decrement factor, and between the time lag of the maximum peak of the temperature and the time lag of the maximum peak of the heat flux. Such dependencies result as being independent of the location, of the PCM typology, of the configuration of the phases in the layer and of the air conditioning season.

- In order to identify the PCM layer's dynamic behavior in a complete way, *seven independent dynamic parameters are necessary*, from which it is possible to obtain the remaining parameters.
- An *experimental verification of the exact analytical model* resolving the Stefan Problem in a PCM layer subject to steady periodic boundary conditions, that give rise to a sole bi-phase interface, was conducted. The considered temperature boundary conditions regard sinusoidal and non-sinusoidal periodic trends.
- The model was verified by *comparing the measured and calculated temperature trends* at different heights in the layer, the *trends of the surface heat fluxes*, and the *total stored energy*.
- The analytical model provides *accurate predictive assessments* as the thermal fluctuations throughout the layer result as being very close to the experimental ones. In particular, trends have similar mean values, of the amplitudes and of the arguments.
- The reduced values of those deviations justify the use of the model to determine the energy stored in the sensible and latent form in the layer and the trend of the position of the bi-phase interface in function of time.